Dimitris N. Metaxas
Leon Axel (Eds.)

LNCS 6666

Functional Imaging and Modeling of the Heart

6th International Conference, FIMH 2011
New York City, NY, USA, May 2011
Proceedings

Springer

Lecture Notes in Computer Science 6666

Commenced Publication in 1973
Founding and Former Series Editors:
Gerhard Goos, Juris Hartmanis, and Jan van Leeuwen

Dimitris N. Metaxas Leon Axel (Eds.)

Functional Imaging and Modeling of the Heart

6th International Conference, FIMH 2011
New York City, NY, USA, May 25-27, 2011
Proceedings

Springer

Volume Editors

Dimitris N. Metaxas
Rutgers University, Division of Computer and Information Sciences
Piscataway, NJ 08854, USA
E-mail: dnm@cs.rutgers.edu

Leon Axel
New York University, Department of Radiology
560 First Avenue, New York, NY 10016, USA
E-mail: leon.axel@nyumc.org

ISSN 0302-9743 e-ISSN 1611-3349
ISBN 978-3-642-21027-3 e-ISBN 978-3-642-21028-0
DOI 10.1007/978-3-642-21028-0
Springer Heidelberg Dordrecht London New York

Library of Congress Control Number: 2011926695

CR Subject Classification (1998): J.3, I.6, I.3, I.2.1, I.2.10, I.4

LNCS Sublibrary: SL 6 – Image Processing, Computer Vision, Pattern Recognition, and Graphics

Typesetting: Camera-ready by author, data conversion by Scientific Publishing Services, Chennai, India

Printed on acid-free paper

Springer is part of Springer Science+Business Media (www.springer.com)

Preface

It is a great pleasure to present to you this rich collection of papers in the form of the proceedings of the International Conference on Functional Imaging and Modeling of the Heart held in New York City, USA, during May 25–27, 2011. This was the sixth in a series of FIMH conferences, following a very successful meeting in Nice, France in 2009.

FIMH 2011 aimed to integrate the research and development efforts in the fields of cardiovascular modeling, physiology, and image-based analysis, at a range of scales and imaging methods. A major goal is to encourage interaction and collaboration among more technical scientists (e.g., in imaging, signal and image processing, applied mathematics, biomedical engineering and computer science), biologically oriented scientists (e.g., cardiac physiology and biology) and clinicians (e.g., cardiology, radiology and surgery), with a common interest in the heart. The FIMH 2011 program included three invited talks, original research paper presentations, and clinical and industrial panels offering interdisciplinary discussions on related cardiac topics.

The call for papers resulted in 123 submissions. Of these, 105 met the submission guidelines and were subjected to a rigorous review process. Each paper was sent to at least four reviewers. Fifty-four papers whose scores were above a certain threshold were accepted. The top 25 in terms of score were accepted as orals and the remaining 29 as poster papers.

We would like to thank our three invited keynote speakers, Eugene Grossi from New York University Medical Center, Ann Bolger from University of California San Francisco, School of Medicine and Joao Lima from Johns Hopkins University, whose excellent presentations were a highlight of the conference. We would also especially like to thank the team at the Center for Computational Biomedicine Imaging and Modeling (CBIM) and especially Shaoting Zhang, our Publications Chair, for the web support, the published proceedings and being a liaison with the rest of the Organizing Committee. Finally, we would like to thank Naomi Weinberger for all her assistance with the FIMH 2011 organization.

May 2011

Dimitris Metaxas
Leon Axel

Organization

FIMH 2011 was organized by the Department of Computer Science, Rutgers University and New York University Medical Center.

Executive Committee

General Chairs	Dimitris N. Metaxas (Rutgers University) Leon Axel (New York University)
Industrial Chair	Ioannis Pavlidis (University of Houston)
Publications Chair	Shaoting Zhang (Rutgers University)

Program Committee

Alexander Andreopoulos
Elsa Angelini
Nicholas Ayache
Dominique Chapelle
Patrick Clarysse
Dorin Comaniciu
Herve Delingette
James Duncan
Frederick Epstein
Vic Ferrari
Mark Fogel
Alejandro Frangi
Julius Guccione
Jeffrey Holmes
Robert Howe
Mingxing Hu
Junzhou Huang
Xiaolei Huang
Ioannis Kakadiaris
Chandra Kambhamettu
Scott Kulp
Andrew Laine
Boudewijn Lelieveldt
Qingshan Liu
Cristian Lorenz
Rob MacLeod
Isabelle Magnin
Sherif Makram-Ebeid
Nassir Marouche
Andrew Mc Culloch
Viorel Mihalef
Wiro Niessen
Alison Noble
Sebastien Ourselin
Nikos Paragios
Ioannis Pavlidis
Zhen Qian
Osman Ratib
Daniel Rueckert
Frank Sachse
Gunnar Seemann
Maxime Sermesant
Dinggang Shen
Pengcheng Shi
Albert Sinusas
Xubo Song
Barbara Srichai
Larry Staib
Gabor Szekely
James Thomas
Mustafa Uzunbas
Szilard Voros
Raymond Winslow
Graham Wright
Alistair Young
Shaoting Zhang
Jinghao Zhou
Xiahai Zhuang

Table of Contents

Oral Session 1: Cardiac Electrophysiology

Poster Session 1: Cardiac Electrophysiology

Image Analysis

Functional Imaging and Modeling

Oral Session 2: Image Analysis

Oral Session 3: Functional Imaging and Modeling

Poster Session 2

Oral Session 4: Image Analysis

Oral Session 5: Cardiac Mechanics, Cardiac Electrophysiology

Anode Make and Break Excitation Mechanisms and Strength-Interval Curves: Bidomain Simulations in 3D Rotational Anisotropy

Piero Colli-Franzone[1], Luca F. Pavarino[2], and Simone Scacchi[2]

[1] Dipartimento di Matematica, Università di Pavia and IMATI-CNR
Istituto di Matematica Applicata e Tecnologie Informatiche,
Via Ferrata 1, 27100 Pavia, Italy
colli@imati.cnr.it
[2] Dipartimento di Matematica, Università di Milano,
Via Saldini 50, 20133 Milano, Italy
{luca.pavarino,simone.scacchi}@unimi.it

Abstract. The shape of anodal strength-interval curves and make and break excitation mechanisms are investigated in a 2D anisotropic Bidomain model, with different membrane models and action potential durations, and in a 3D rotational anisotropic Bidomain model, with axisymmetric or orthotropic conductivity properties. The results have shown that the LRd model with a long intrinsic APD exhibits a systolic dip threshold lower than the diastolic threshold, in agreement with previous experimental data. The spatial and temporal analysis of the excitation patterns indicates a novel anode make excitation mechanism with delayed propagation within the transition from break to make mechanisms.

1 Introduction

Optical mappings of cardiac transmembrane action potential, starting in the mid nineties, has revealed that the extracellular cardiac stimulation by a unipolar electrode produces a characteristic transmembrane pattern called *virtual electrodes response*, see e.g. [11,26,14,28]. After an anodal stimulus, the transmembrane potential distribution exhibits a *virtual anode* (VA), i.e. a dog-bone shaped hyperpolarized volume around the stimulating electrode, and two *virtual cathodes* (VCs), i.e. depolarized regions adjacent to the concave part of the VA boundary. The central dog-bone VA develops mainly across the fiber direction, while the two adjacent VCs are aligned along the fiber direction. Conversely, after a cathodal stimulus, the polarity is reversed. It is well known that only macroscopic bidomain models of cardiac tissue with unequal anisotropy ratios of the intra- and extracellular media are able to generate the observed *virtual electrode polarization* regions, see [14,28]. During an anodal stimulation, we distinguish between the *anode make* (AM) activation mechanism, if excitation starts at the two VCs before the stimulus end, and the *anode break* (AB) activation mechanism, if excitation starts at the VA after the stimulus end. These excitation

D.N. Metaxas and L. Axel (Eds.): FIMH 2011, LNCS 6666, pp. 1–10, 2011.

mechanisms have been investigated by simulation studies, mostly on 2D sheets or in cylindrical domains, in [22,23,20,27,24,18] and by experimental studies in [11,26]; see also the recent surveys [14,28].

The aim of this work is to investigate the shape of anodal strength-interval curves and make and break excitation mechanisms in a 2D anisotropic Bidomain model, with different membrane models and action potential durations, and in a 3D rotational anisotropic Bidomain model, with axisymmetric or orthotropic conductivity properties.

2 Methods

The anisotropic Bidomain model. The three-dimensional cardiac domain H is in contact with a conducting medium Ω_0, representing either the intracavitary blood or an extracardiac bath. We define $\overline{\Omega} = \overline{H} \cup \overline{\Omega}_0$ and $S = \partial H \cap \partial\Omega_0$ the common not insulated interface. The remaining interface $\partial\Omega$ is assumed insulated. The macroscopic Bidomain model (see e.g. [13,17]) in H is coupled to an elliptic problem for the extracardiac potential u_b. The evolution of the transmembrane potential $v(\mathbf{x},t)$, extracellular potential $u_e(\mathbf{x},t)$, extracardiac potential $u_b(\mathbf{x},t)$, gating variables $w(\mathbf{x},t)$ and ionic concentrations $c(\mathbf{x},t)$ is computed using finite element approximation of the following time splitting method for the Bidomain model, i.e. given (v^n, w^n, c^n) and $i_{app}^{e,n}$ at time t^n:

$$
\begin{cases}
-\operatorname{div}(D\nabla u_e^n) = \operatorname{div}(D_i \nabla v^n) + i_{app}^{e,n} \ \text{ in } H, \quad -\operatorname{div} \sigma_b \nabla u_b^n = i_{app}^{e,n} \ \text{ in } \Omega_0 \\
\mathbf{n}^T D_i \nabla u_e^n = -\mathbf{n}^T D_i \nabla v^n \ \text{ on } \partial H \\
u_e^n = u_b^n, \quad \mathbf{n}^T D_e \nabla u_e^n = \mathbf{n}^T \sigma_b \nabla u_b^n \ \text{ on } S, \quad \mathbf{n}^T \sigma_b \nabla u_b^n = 0 \ \text{ on } \partial\Omega_0 \setminus S \\
w^{n+1} - \tau R(v^n, w^{n+1}) = w^n, \quad c^{n+1} = \tau S(v^n, w^{n+1}, c^n) + c^n, \ \text{ in } H \\
\dfrac{c_m}{\tau} v^{n+1} - \operatorname{div}(D_i \nabla v^{n+1}) = \dfrac{c_m}{\tau} v^n + \operatorname{div}(D_i \nabla u_e^n) + i_{ion}(v^n, w^{n+1}, c^{n+1}) \ \text{ in } H.
\end{cases}
$$

Here $D = D_i + D_e$ with D_i, D_e conductivity tensors, σ_b is the conductivity coefficient of the extracardiac medium, c_m, i_{ion}, i_{app}^e denote the capacitance, the ionic current, the applied current per unit volume, respectively. The reference potential is determined by imposing $\int_H u_e(\mathbf{x},t)dx = 0$ and the compatibility condition $\int_\Omega i_{app}^e = 0$ must be satisfied.

Membrane model. In [21], the bidomain model with unequal anisotropic ratio was first proposed and used to establish a theoretical framework able to explain the *make* and *break* mechanisms of excitability in terms of the underlying virtual electrodes polarization. In addition to the previous *virtual electrodes polarization*, another anode break mechanism has been proposed in [19], related to the so called *funny* current I_f, see e.g. [10,4]. The contribution of I_f to the anode break excitation has been investigated in [19,20,23] by performing bidomain simulations on 2D anisotropic sheets, incorporating I_f into a Luo-Rudy I membrane model [15]. Another active membrane factor contributing to excitation mechanisms is the *electroporation* current [8]. In this work, we use two

membrane models: the LR1 model [15] and the LRd model [12]. Both models are augmented with: the funny current I_f, the electroporation current I_e and the outward current I_a (see [5]), which has been incorporated in several recent studies on the effects of defibrillation shocks, see e.g. [2,18].

Myocardial conductivity tensors and fiber architecture. Recent studies have shown a laminar organization of the fibers structure evidencing two preferential transverse fiber directions, one tangent and the other orthogonal to the laminae, respectively, yielding orthotropic conductivity tensors, see e.g. [3] and the references therein. In this work, we consider both orthotropic conductivity tensors $D_i(\mathbf{x})$ and $D_e(\mathbf{x})$ defined by

$$D_{i,e}(\mathbf{x}) = \sigma_l^{i,e}\ \mathbf{a}_l(\mathbf{x})\mathbf{a}_l^T(\mathbf{x}) + \sigma_t^{i,e}\ \mathbf{a}_t(\mathbf{x})\mathbf{a}_t^T(\mathbf{x}) + \sigma_n^{i,e}\ \mathbf{a}_n(\mathbf{x})\mathbf{a}_n^T(\mathbf{x}) \quad ,\mathbf{x} \in H \qquad (1)$$

and axisymmetric tensors defined analogously but with $\sigma_n^{i,e} = \sigma_t^{i,e}$. $\mathbf{a}_l(\mathbf{x}), \mathbf{a}_t(\mathbf{x}), \mathbf{a}_n(\mathbf{x})$ are unit vectors parallel to the local fiber direction, tangent and normal to the cardiac lamina, respectively. $\sigma_{l,t,n}^{i,e}$ are the effective intra and extracellular conductivity coefficients measured along (l) and across (t,n) the fiber direction. The conductivity values $mScm^{-1}$ of the two different anisotropic calibrations are the following (see also [6,7]):

anisotropy	σ_l^i	σ_t^i	σ_n^i	σ_l^e	σ_t^e	σ_n^e
orthotropic	2.31724	0.24350	0.05690	1.54483	1.04385	0.37221
axisymmetric	2.31724	0.24350	0.24350	1.54483	1.04385	1.04385

Computational domain. The cardiac domain H considered in this study is a cartesian slab of dimensions $0.96 \times 0.96 \times 0.32\ cm^3$, with the lower face (endocardium) in contact with a smaller slab of dimensions $0.96 \times 0.96 \times 0.16\ cm^3$, modeling the extracardiac bath, where $\sigma_b = 6e^{-3}\ \Omega^{-1}cm^{-1}$ similar to the blood conductivity.

Numerical methods. A structured grid of $96 \cdot 96 \cdot 48$ hexahedral isoparametric Q_1 finite elements of size $h = 0.1\ mm$ is used in space, while the time discretization is based on splitting both the ODEs from the PDEs and the elliptic PDEs from the parabolic one. The large linear systems arising at each time step are solved by the conjugate gradient method, preconditioned by a Multilevel Hybrid Schwarz preconditioner (see e.g. [25]) and implemented using the PETSc parallel library [1]. The simulations are run on 24 processors of a Linux Cluster.

Stimulation site. Stimulation pulses are delivered at the center of epicardium in a small region of dimensions $0.06 \times 0.06 \times 0.03\ cm^3$. The compatibility condition is ensured by injecting a stimulation current in a strip of dimensions $0.96 \times 0.96 \times 0.08\ cm^3$ in the extracardiac bath with equal strength and opposite polarity of that used at the subepicardial level. In order to simulate the break excitation mechanisms during systole, we perform an S1-S2 stimulation protocol.

Strength-Interval (S-I) curves. We determine the threshold strength of the premature anodal stimulus S2 able to generate a propagating excitation response

as a function of the time interval elapsed from the previous cathodal excitation stimulus S1 applied to a resting tissue. This yields a S-I curve in the strength-interval plane.

Activation time isochrones. During the simulations, we process the distribution of the transmembrane potential $v(\mathbf{x}, t)$ in order to define the activation time $t_a(\mathbf{x})$ as the first time instant for which $v(\mathbf{x}, t_a(\mathbf{x})) = v_{up}$; we choose $v_{up} = -50\ mV$, a value above threshold able to initiate an action potential.

3 Results

Anodal S-I curve: 2D slab. We study the shape dependence of the S-I curve on the LR1 and LRd models, using a sheet of tissue with parallel fibers. Fig. 1 reports the anodal S-I curves of the LR1 and LRd models with a short intrinsic APD of about $230-210ms$, respectively (panel A), and with a long intrinsic APD of about 380 ms (panel B). All the S-I curves exhibit break, make stimulation mechanisms as well as the presence of the following features: a dip close to the effective refractory period, a subsequent plateau phase and a sudden decrease close to the end of the relative refractory period. The long APD tissue presents a S-I curve with deeper threshold dip than the short APD tissue, (2 mA vs. 2.2 mA for the LR1 model, 1.2 mA vs. 2 mA for the LRd model), and a slightly longer relative refractory period, (25 ms vs. 20 ms for the LR1 model, 35 ms vs. 20 ms for the LRd model).

Anodal S-I curve: 3D slab. Fig. 1-C shows the dependence of the S-I curves on the anisotropy (axisymmetric and orthotropic) for a 3D slab with the LRd model with a short APD of about 210 ms. The curves are similar, except a slightly deeper threshold dip and lower break and make threshold values in the orthotropic case than in the axisymmetric one.

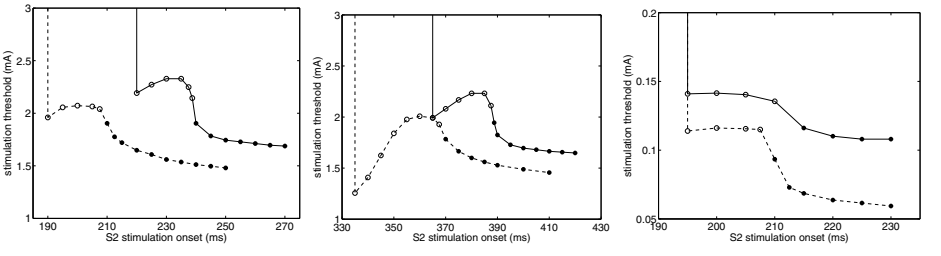

Fig. 1. Anodal strength-interval curves. (A): 2D slab, LR1 and LRd (dashed) models with short APD. (B): 2D slab, LR1 and LRd (dashed) models with long APD. (C): 3D slab, axisymmetric and orthotropic (dashed) anisotropy. Make and break excitation mechanisms are marked with (·) and (o), respectively.

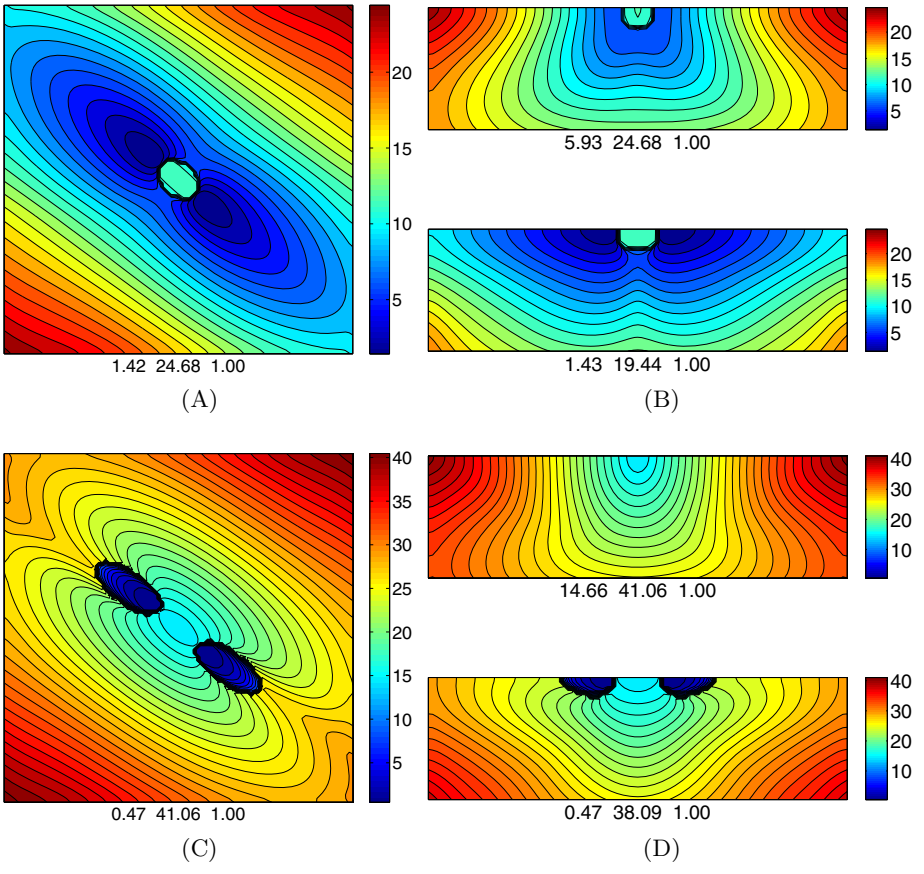

Fig. 2. Orthotropic 3D slab. **Top panels.** Anode make. Diastolic S2 anodal stimulation at 230 ms with amplitude 0.0864 mA and duration 10 ms. **Bottom panels.** Anode break. Systolic S2 anodal stimulation at 205 ms with amplitude 0.1404 mA and duration 10 ms. Isochrones of activation time on the epicardium (A-C) and on the two transmural diagonals (B-D). Below each contour plot are reported the minimum, maximum, and contour step size in ms of the displayed map.

Anode-make excitation mechanism. The epicardial and transmural isochrones in Fig. 2-A,B show that two distinct activation wavefronts arise from the VCs and propagate outward and inward along the diagonal parallel to the fibers direction, but when they reach the VA region, a block of the inward propagation takes place. Excitation starts from the VC regions at about 1.5 ms after S2 onset, hence anode make excitation occurs.

Anode-break excitation mechanism. During the 10 ms of anodal stimulation, on the epicardial face a *dog-bone* shaped region of strongly hyperpolarized tissue (VA) surrounding the stimulated area is generated, with two depolarized regions (VCs) developing along the fiber direction. Although the VCs are

depolarized above threshold, anode make excitation does not occur, because the surrounding regions are in the refractory period and still inexcitable. When the stimulus is turned off, the combined effect of discharge diffusion of currents, flowing from the VCs toward the central anodal region, and of the membrane funny and electroporation currents I_f, I_e depolarizes the tissue inside the VA region, inducing anode break excitation with a delay of about 6 ms. The isochrones of activation time displayed in Fig. 2-C,D show the typical anode break excitation pattern, where the first activated point is the epicardial central site of the anodal region and the excitation wavefronts propagate across fibers with a rim on the inexcitable obstacle located around the VCs.

Stimulation at the transition of break and make mechanisms. We now consider an S2 stimulation at 210 ms, instant of transition between break and make mechanisms (see S-I curve displayed in Fig. 1 C), in order to investigate the dependence of the excitation sequence on the stimulation amplitude.

Axisymmetric 3D slab. For high stimulation amplitude, e.g. 0.2160 mA, anode make excitation occurs, see Fig. 3-A, i.e. excitation emanates from the VCs before the stimulus end. When decreasing the stimulation amplitude to 0.1366 mA, a different type of excitation is observed, i.e. an anode make/break excitation mechanism. In fact, two excitation wavefronts are launched from the VCs edges, thus an anode make mechanism arises, but, since the surrounding tissue is not fully recovered from refractoriness, these two initiated wavefronts can propagate only after 10 ms, i.e. after the stimulus is turned off. Therefore, we are in presence of a break mechanism with respect to the propagating features of the wavefront. Subsequently, at about 18 ms, an additional wavefront arises and propagates from the central VA region, triggered by the I_f and I_e membrane currents, see Fig. 3-B. Hence, this is an additional anode break mechanism. Later on, at 20 ms, three distinct excitation wavefronts spread through the cardiac volume, subsequently colliding and merging. When decreasing further the stimulation amplitude to 0.1355 mA, only anode break excitation mechanism occurs at the center of the VA region, triggered by the I_f and I_e currents, see Fig. 3-C.

Orthotropic 3D slab. For high stimulation amplitude , e.g. 0.1620 mA, anode make excitation mechanism occurs (not shown). sharing the same features of Fig. 3-A. When decreasing the stimulation amplitude to 0.0934 mA, anode make excitation occurs, since before the end of the anodal pulse two wavefronts originates at the edges of the VCs, but they propagate only after the termination of the stimulus. The propagating fronts lie on the edges portion of VCs, crossed by the direction along fiber, and propagate with a counterclockwise twist after 15 ms. Moreover, after the anodal pulse is turned off, the VA region is excited at about 22 ms by the collision of the two excitation wavefronts, see Fig. 3-D. Decreasing further the stimulus amplitude, no excitation response occurs, in particular anode break excitation is not observed.

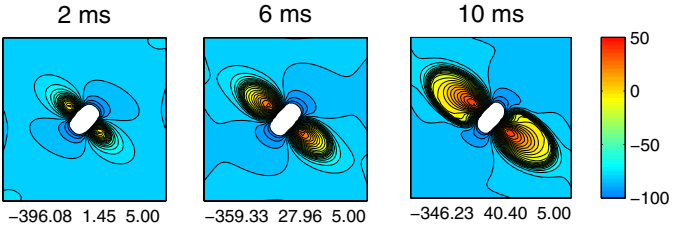

(A) Transmembrane potential on the epicardium 2, 6, 10 ms after the onset of S2 stimulation with amplitude 0.2160 mA. Anode make mechanism of excitation.

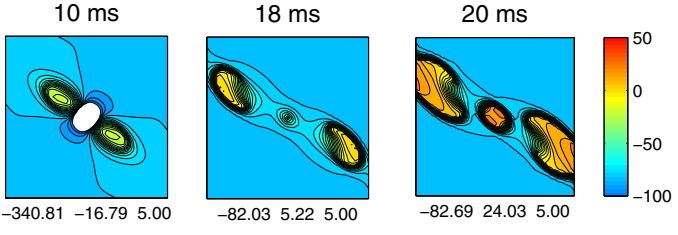

(B) Transmembrane potential on the epicardium 10, 18, 20 ms after the onset of S2 stimulation with amplitude 0.1366 mA. Anode make/break mechanism of excitation.

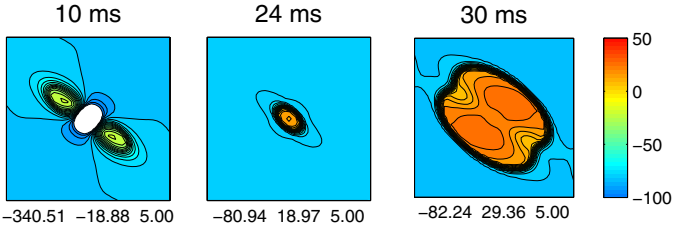

(C) Transmembrane potential on the epicardium 10, 24, 30 ms after the onset of S2 stimulation, amplitude 0.1355 mA. Anode break mechanism of excitation.

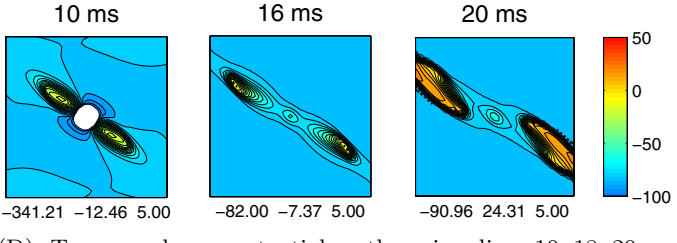

(D) Transmembrane potential on the epicardium 10, 18, 20 ms after the onset of S2 stimulation with amplitude 0.0934 mA. Delayed anode make mechanism of excitation.

Fig. 3. Systolic S2 anodal stimulation at 210 ms, duration 10 ms. (A), (B), (C): axisymmetric slab, (D): orthotropic slab. Below each contour plot are reported the minimum, maximum, and contour step size in mV of the displayed map.

4 Discussion

The behavior of our S-I curves in an anisotropic 2D sheet of parallel fiber shares the same qualitative features observed in previous simulation studies employing various ionic models [22,23]. A qualitative discrepancy is the drop between the anode break and make portion of the S-I curve, which is less abrupt in the LRd model. The features of the S-I curve reproduce some qualitative characteristics of the experimental data, see [9,16]. In particular, the LRd model with a long intrinsic APD, exhibits a threshold dip value lower than the diastolic threshold value, in agreement with the experimental data of [9]. We have found that the S-I curves in a 3D anisotropic slab show lower break and make threshold values in the orthotropic case than in the axisymmetric one. Our result of anode make and break mechanisms in a 3D slab with rotational anisotropy are in agreements with the transmembrane snapshots previously obtained mainly in symmetric cylindrical strand with parallel fibers, see [22,23,14]. Finally, we have investigated the dependence of excitation patterns on the anodal S2 pulse amplitude, applied at a time instant within the break and make transition. We have identified a novel anode make mechanism with delayed propagation, in which two wavefronts emanate from the edges of the two depolarized VCs regions, but they are able to propagate only after 15 ms, i.e. after the end of the anodal pulse as in the anode break mechanism. To our knowledge, the experimental investigation of anodal stimulation mechanisms within the transition from break to make portions of the S-I curve is still lacking in literature.

References

1. Balay, S., et al.: PETSc home page (2001), http://www.mcs.anl.gov/petsc
2. Arevalo, H., Rodriguez, B., Trayanova, N.A.: Arrhythmogenesis in the heart: multiscale modeling of the effects of defibrillation shocks and the role of electrophysiological heterogeneity. Chaos 17(1), 015103 (2007)
3. Caldwell, B.J., et al.: Three distinct directions of intramural activation reveal nonuniform side-to-side electric coupling of ventricular myocytes. Circ. Arrhythmia Electrophysiol. 2, 433–440 (2009)
4. Cerbai, E., Barbieri, M., Mugelli, A.: Characterization of the hyperpolarization-activated current, I_f in ventricular myocytes isolated from hypertensive rats. J. Physiol. 481(3), 585–591 (1994)
5. Cheng, D.K., Tung, L., Sobie, E.A.: Nonuniform responses of transmembrane potential during electric field stimulation of single cardiac cells. Am. J. Physiol. Heart Circ. Physiol. 362, H351–H362 (1999)
6. Colli Franzone, P., Guerri, L., Taccardi, B.: Modeling ventricular excitation: axial and orthotropic anisotropy effects on wavefronts and potentials. Math. Biosci. 188, 191–205 (2004)
7. Colli Franzone, P., Pavarino, L.F., Taccardi, B.: Effects of transmural electrical heterogeneities and electrotonic interactions on the dispersion of cardiac repolarization and action potential duration: a simulation study. Math. Biosci. 204(1), 132–165 (2006)

8. DeBruin, K.A., Krassowska, W.: Electroporation and shock-induced transmembrane potential in a cardiac fiber during defibrillation strength shocks. Ann. Biomed. Eng. 26, 584–596 (1998)
9. Dekker, E.: Direct current make and break thresholds for pacemaker electrodes on the canine ventricle. Circ. Res. 27, 811–823 (1970)
10. DiFrancesco, D., Ferroni, A., Mazzanti, M., Tromba, C.: Properties of the hyperpolarizing-activated current (if) in cells from rabbit sini-atrial node. J. Physiol. 377, 61–88 (1986)
11. Efimov, I.R., Gray, R.A., Roth, B.J.: Virtual electrodes and deexcitation: new insights into fibrillation induction and defibrillation. J. Cardiovasc Electrophysiol. 11, 339–353 (2000)
12. Faber, G.M., Rudy, Y.: Action potential and contractility changes in [Na+](i) overloaded cardiac myocytes: A simulation study. Biophys. J. 78(5), 2392–2404 (2000)
13. Henriquez, C.S., Ying, W.: The Bidomain model of cardiac tissue: from microscale to macroscale. In: Efimov, I.R., et al. (eds.) Cardiac Bioelectric Therapy, ch. 5.1, pp. 401–421. Springer, Heidelberg (2009)
14. Janks, D.L., Roth, B.J.: The bidomain theory of pacing. In: Efimov, I.R., et al. (eds.) Cardiac Bioelectric Therapy, ch. 2.1, pp. 63–83. Springer, Heidelberg (2009)
15. Luo, C., Rudy, Y.: A model of the ventricular cardiac action potential: depolarization, repolarization, and their interaction. Circ. Res. 68(6), 1501–1526 (1991)
16. Mehra, R., Furmann, S.: Comparison of cathodal, anodal and bipolar strength - interval curves with temporary and permanent pacing electrodes. Br. Heart J. 41, 468–476 (1979)
17. Pennacchio, M., Savaré, G., Colli Franzone, P.: Multiscale modeling for the bioelectric activity of the heart. SIAM J. Math. Anal. 37(4), 1333–1370 (2006)
18. Plank, G., et al.: Evaluation intramural virtual electrodes in the myocardial wedge preparation: simulations of experimental conditions. Biophys. J. 94, 1904–1915 (2008)
19. Ranjan, R., et al.: Mechanism of anode break stimulation in the heart. Biophys. J. 74, 1850–1863 (1998)
20. Ranjan, R., Tomaselli, G.F., Marban, E.: A novel mechanism of anode-break stimulation predicted by bidomain modeling. Circ. Res. 84, 153–156 (1999)
21. Roth, B.J., Wikswo Jr., J.P.: Electrical stimulation of cardiac tissue: a bidomain model with active membrane properties. IEEE Trans. Biomed. Eng. 41(3), 232–240 (1994)
22. Roth, B.J.: Strength-Interval curve for cardiac tissue predicted using the bidomain model. J. Cardiovasc. Electrophysiol. 7, 722–737 (1996)
23. Roth, B.J., Chen, J.: Mechanism of anode break excitation in the heart: the relative influence of membrane and electrotonic factors. J. Biol. Systems 7(4), 541–552 (1999)
24. Sambelashvili, A., Nikolski, V.P., Efimov, I.R.: Virtual electrode theory explains pacing threshold increase caused by cardiac tissue damage. Am. J. Physiol Heart Circ. Physiol. 2194, H2183–H2194 (2004)
25. Scacchi, S., et al.: Computing cardiac recovery maps from electrograms and monophasic action potentials under heterogeneous and ischemic conditions. Math. Mod. Meth. Appl. Sci. 20(7), 1089–1127 (2010)

26. Sidorov, V.Y., et al.: Examination of stimulation mechanism and strength-interval curve in cardiac tissue. Am. J. Physiol Heart Circ. Physiol. 2615, H2602–H2615 (2005)
27. Skouibine, K.B., Trayanova, N.A., Moore, P.: Anode/cathode make and break phenomena in a model of defibrillation. IEEE Trans. Biomed. Eng. 46(7), 769–777 (1999)
28. Wikswo Jr., J.P., Roth, B.J.: Virtual electrode theory of pacing. In: Efimov, I.R., et al. (eds.) Cardiac Bioelectric Therapy, ch. 4.3, pp. 283–330. Springer, Heidelberg (2009)

Comparing Simulated Electrocardiograms of Different Stages of Acute Cardiac Ischemia

Mathias Wilhelms, Olaf Dössel, and Gunnar Seemann

Institute of Biomedical Engineering, Karlsruhe Institute of Technology (KIT)
Kaiserstr. 12, 76131 Karlsruhe, Germany
publications@ibt.kit.edu
http://www.ibt.kit.edu

Abstract. Diagnosis of acute cardiac ischemia depends on characteristic shifts of the ST segment. The transmural extent of the ischemic region and the temporal stage of ischemia have an impact on these changes. In this work, computer simulations of realistic ventricles with different transmural extent of the ischemic region were carried out. Furthermore, three stages within the first half hour after the occlusion of the distal left anterior descending coronary artery were regarded. The transmembrane voltage distributions and the corresponding body surface ECGs were calculated. It was observed how the electrophysiological properties worsen in the course of ischemia, so that almost no excitation was initiated in the central ischemic zone 30 minutes after the occlusion. In addition to these temporal effects, also the transmural extent of the ischemic region had an impact on the direction and intensity of the ST segment shift.

Keywords: Cardiac Ischemia, Phase 1b, Electrocardiogram, Mathematical Modeling, ST Segment Shift.

1 Motivation

The occlusion of a coronary artery due to e.g. atherosclerosis leads to a deficient blood supply of the heart muscle. This pathology, which is termed acute cardiac ischemia, leads to lethal heart failure or severe ventricular arrhythmias in many cases. During the first thirty minutes after the occlusion, two different phases of arrhythmias can be identified [1]. The so-called phase 1a peaks between 2 and 10 minutes and phase 1b between 20 and 30 minutes after the onset of ischemia [2].

In phase 1a, mainly three ischemia effects can be observed: hyperkalemia, acidosis and hypoxia. Due to this, the conduction velocity (CV), the action potential (AP) amplitude and duration are reduced and the resting transmembrane voltage is increased [3]. These time-dependent electrophysiological changes are classified with increasing ischemia: 5 to 7 minutes after the occlusion, stage 1 (S1) is reached and stage 2 (S2) after 10 to 12 minutes [4].

Phase 1b is characterized by cellular uncoupling, which means that the gap junctional conductance decreases. In addition, the extracellular potassium concentration ($[K^+]_o$) and the intracellular calcium concentration ($[Ca^{2+}]_i$) increase, which also favors initiation of arrhythmias [1].

D.N. Metaxas and L. Axel (Eds.): FIMH 2011, LNCS 6666, pp. 11–19, 2011.

Depending on the degree of the occlusion and the occlusion site, ischemia effects vary spatially. They appear in the subendocardium at first, which is called *subendocardial ischemia*. Then, they spread transmurally towards the subepicardium, if the occlusion of the artery continues for longer periods (*transmural ischemia*) [5]. However, ischemia effects are stronger in the subepicardial tissue, since, inter alia, the sensitivity of the ATP regulated potassium channels is higher there [6].

The diagnosis of cardiac ischemia is based on changes in the electrocardiogram (ECG), as for example shifts of the ST segment. Depending on the transmural extent of the ischemic region, ST segment elevation or depression can be observed in leads close to the ischemic region. The reason for these deviations is the direction of injury currents, which flow from healthy or less injured towards ischemic tissue [7]. Nevertheless, the exact underlying mechanisms responsible for these ECG alterations and the dynamic changes during the first thirty minutes of ischemia are not completely understood. In order to improve the early diagnosis of acute cardiac ischemia, computer simulations are a helpful tool. For this purpose, the electrocardiograms of different ischemic stages of the heart with varying transmural extent of the ischemic region were investigated *in silico* in this work.

2 Methods and Materials

Aiming at simulation of the impact of acute cardiac ischemia on electrocardiograms, a ventricular cell model was modified to reproduce ischemia effects at different stages. Then, the transmembrane voltage distribution was computed in a realistic model of human ventricles with varying transmural extent of the ischemic region. Finally, the corresponding body surface potential maps (BSPMs) were calculated and the ECGs were extracted.

2.1 Modeling Ischemic Myocytes

The simulation of acute cardiac ischemia was based on the ventricular cell model published in 2006 by ten Tusscher et al. [8]. The model provides an electrophysiological description of endocardial, midmyocardial and epicardial myocytes. Furthermore, the model was modified according to Weiss et al. [3] in order to simulate phase 1a ischemia effects, which are hyperkalemia, acidosis and hypoxia. For both stages S1 and S2, different parameter sets were used. The formulation of the ATP sensitive potassium channel was modified, so that the current was inhibited at healthy ADP concentrations. For this purpose, the half-maximum inhibition constant was adjusted ($K_m = (-151.0919+75.5379 \cdot [ADP]_i^{0.256}) \cdot K_{m,factor}$). As a consequence, the ADP concentrations at stage 1 and phase 1b were adapted (compare Table 1).

For the simulation of phase 1b cardiac ischemia, even more parameters, i.e. the maximal conductances of I_{NaK}, I_{NaCa}, I_{up} and I_{rel} (P_{NaK}, k_{NaCa}, V_{maxup} and V_{rel}), were modified according to Pollard and coworkers [9]. In this way, changes of the intracellular calcium handling, pumps and exchangers were considered.

Table 1. Cell model parameters at different stages of acute ischemia in the central ischemic zone according to [3,9,10,11]. g_{Na} and $g_{Ca,L}$ are the sodium and calcium channel conductivities, $dV_{m,Na}$ is the voltage shift of sodium channels, and $[ATP]_i$ and $[ADP]_i$ are the intracellular concentrations of ATP and ADP

Cell model parameter		control (0 min)	stage 1 (5 min)	stage 2 (10 min)	phase 1b (20–30 min)
$[K^+]_o$	(mmol/l)	5.4	8.7	12.5	15.0
g_{Na},$g_{Ca,L}$	(%)	100	87.5	75	50
$dV_{m,Na}$	(mV)	0	1.7	3.4	3.4
$[ATP]_i$	(mmol/l)	6.8	5.7	4.6	3.8
$[ADP]_i$	(μmol/l)	15	87.5	99	101.5
P_{NaK}	(%)	100	100	100	30
k_{NaCa}	(%)	100	100	100	20
V_{maxup}	(%)	100	100	100	90
V_{rel}	(%)	100	100	100	5

Since the background calcium current I_{bCa} is small compared to other currents and the calcium sensitive nonselective cation current $I_{ns,Ca}$ is not implemented in this model, the metabolic changes of these currents were neglected here. An overview of the modified cell model parameters is given in Table 1.

2.2 Modeling Heterogeneous Excitation Propagation

The anatomical model of the ventricles used in this work was derived from MR images of a healthy volunteer. This dataset was interpolated to an isotropic cubic voxel size of 0.4 mm. The longitudinal intracellular conductivity, which was scaled through the ventricular wall as described in [12], was on average 0.26 S/m resulting in a conduction velocity of approximately 0.65 m/s. The anisotropy factor was set to 2.6. The cardiac fiber orientation was modeled using a rule-based method as in [12].

Different electrophysiological heterogeneities were considered for the simulations shown in this work. For this purpose, the ventricular wall was divided into 20% epicardial, 40% midmyocardial and 40% endocardial tissue [12]. As already included in the cell model of ten Tusscher et al. [8], transmurally differing values for the conductivities of the slow delayed rectifier potassium channel (g_{Ks}), the transient outward potassium channel (g_{to}) and the corresponding channel kinetics were used. Furthermore, an apico-basal gradient of g_{Ks} resulting in a two times larger value at the apex (compare Fig. 1) allowed the simulation of a T-wave comparable to the measurements of the healthy volunteer.

The effects of cardiac ischemia also varied spatially. The half-maximum inhibition constant K_m of the ATP sensitive potassium channel was largest in epicardial and smallest in endocardial tissue. This ensured the transmurally differing sensitivity of this channel to changes of $[ATP]_i$ and $[ADP]_i$ [3]. The ischemic region was described by the so-called zone factor (ZF), which described the regional influence of the occluded coronary artery (see also Fig. 1). Its values ranged from 0 (healthy tissue) to 1 (central ischemic zone, CIZ), intermediate

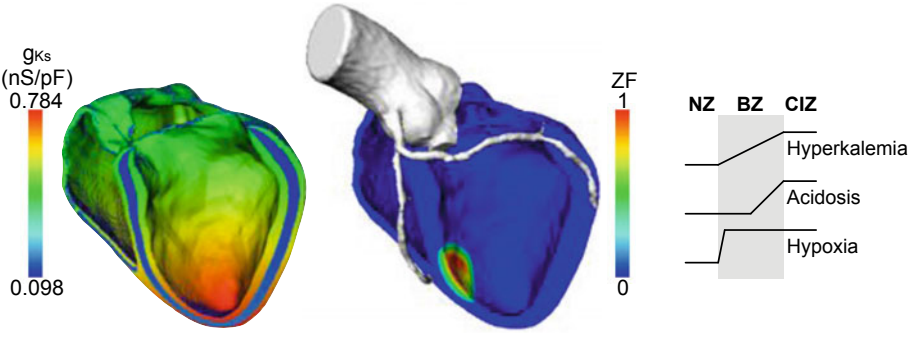

Fig. 1. Ventricular model showing transmural and apico-basal heterogeneity of g_{Ks} (*left*) and zone factor (ZF) with a subendocardial ischemic region and coronary arteries (*middle*). Border zones of different ischemia effects (*right*).

values described the border zone (BZ). The different ischemia effects developed unequally across the BZ, which had a thickness of 5.6 mm in this example. As in [10], the effects of hyperkalemia underwent a linear course from the beginning to the end of the BZ, whereas the impact of acidosis began at 50% of the BZ. However, the effects of hypoxia were fully present after 10% of the BZ (compare Fig. 1). In order to model cellular uncoupling during phase 1b, the intracellular conductivity was linearly decreased from healthy tissue (100%) to the CIZ (12.5%) [11]. The ischemic regions were modeled as ellipsoids with their centers on the endocardial surface. In order to investigate the impact of the transmural extent of the ischemic region on the ECG, a subendocardial, an intermediate and a transmural ischemic region were created. The total size of the ischemic region varied between 2.9% (subendocardial ischemia) and 5.6% (transmural ischemia) of the volume of the left ventricle. The size of the endocardial surface, which was affected by cardiac ischemia, was equal in all three cases. The ischemic region was located at the distal left anterior descending coronary artery (see Fig. 1).

Cardiac ischemia effects at different stages were initialized in a single-cell environment. Afterwards, simulation of cardiac excitation propagation was carried out using the parallel monodomain solver *acCELLerate* [13] with a time step of 20 μs in the 3D ventricular model. For this purpose, an endocardial stimulation profile as in [12] mimicking the His-Purkinje conduction system, which describes the time instant and location of ventricular stimulation, was used.

2.3 Calculation of Body Surface Electrocardiograms

The simulated BSPMs were obtained by solution of the forward problem of electrocardiography. For this purpose, the previously calculated transmembrane voltages in the heart model were interpolated onto a high resolution tetrahedron model of the torso ($\approx$ 1.3 million nodes). This torso contained the following tissue types in addition to the heart: blood, lungs, fat, skeletal muscle, intestine, kidneys, liver and spleen. After the interpolation, the bidomain equations were used to determine the corresponding body surface potentials with inhomogeneous

tissue conductivities as described in [12]. As in the ventricular simulations, the intracellular conductivity of the heart was linearly decreased to 12.5% across the BZ in the ischemic region in case of phase 1b ischemia.

3 Results

3.1 Cell Simulations

The cell model was initialized, so that the effects of the different stages of acute ischemia were fully present. Since the changes due to cardiac ischemia were most prominent in epicardial myocytes, only the results of this cell type are shown here. The APs at different stages of cardiac ischemia are depicted in Fig. 2.

The changes of the action potential parameters were also consequently greatest in epicardial cells (see Table 2). The APD_{90} (measured at 90% repolarization) gradually decreased to 18.2% of the control value after 30 min of cardiac ischemia. The resting transmembrane voltage $V_{m,rest}$ increased and the peak transmembrane voltage $V_{m,max}$ decreased in the course of ischemia.

3.2 Tissue Simulations

Altogether, ten simulations using the 3D ventricular model were carried out: one control case and three setups with different transmural extent of the ischemic

Table 2. Action potential parameters of epicardial myocytes at different stages of acute cardiac ischemia

Action potential parameter		control (0 min)	stage 1 (5 min)	stage 2 (10 min)	phase 1b (20–30 min)
APD_{90}	(ms)	309.1	116.5	72.1	56.3
$V_{m,rest}$	(mV)	-85.6	-73.6	-64.3	-58.1
$V_{m,max}$	(mV)	38.4	34.9	18.8	16.5

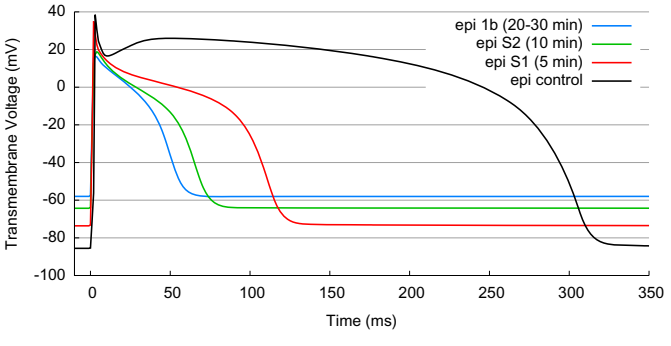

Fig. 2. Action potentials of epicardial myocytes at different stages of acute ischemia

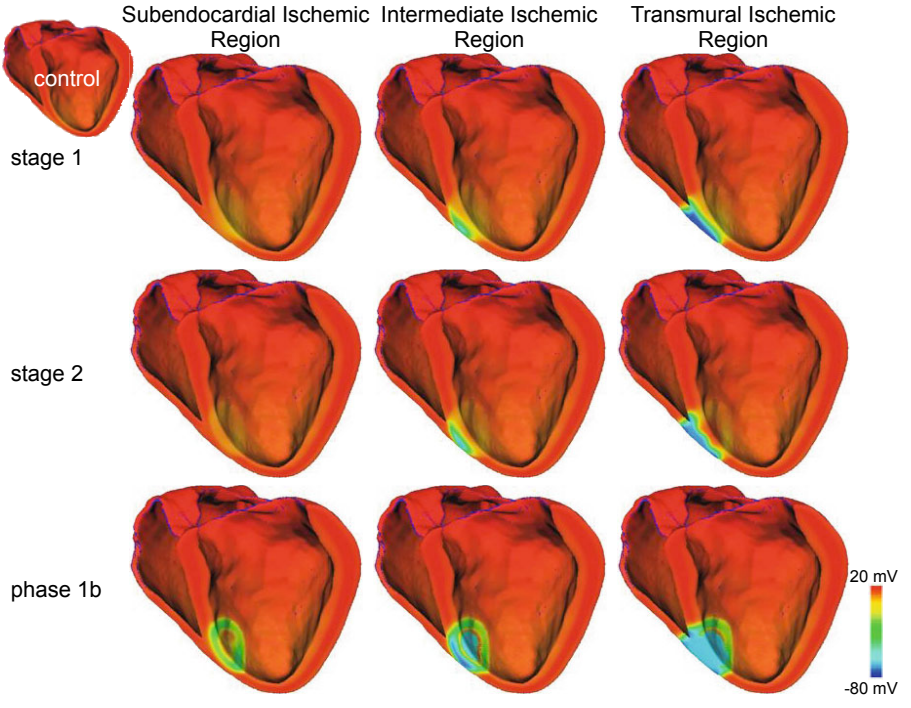

Fig. 3. Transmembrane voltages of different ischemia setups at $t = 200$ ms. The transmural extent of the ischemic region and the stage of ischemia were varied.

region at three ischemia stages each. The resulting transmembrane voltage distributions at $t = 200$ ms after beginning of a normal sinus beat are shown in Fig. 3. The corresponding ECGs, which resulted from these simulations, are plotted in Fig. 4. Since lead V_4 was closest to the ischemic region simulated in this work, the changes due to cardiac ischemia were most prominent in this lead.

In the control case, the ventricles were completely in the plateau phase of the action potential at 200 ms resulting in a nearly zero baseline in lead V_4. During cardiac ischemia, this excitation pattern was changed. In case of subendocardial ischemia, only short APs with low amplitude were initiated in the ischemic region. The ischemia effects intensified with increasing ischemia stage. Since the injury current was flowing from healthy epicardial towards injured endocardial tissue, a pronounced ST segment depression could be observed during phase 1b.

The transmural extent of the ischemic region was slightly increased in the intermediate ischemic region setup. During the first ten minutes, ischemia effects were more pronounced in the midmyocardial and epicardial tissue, which resulted in a slight elevation of the ST segment there. In phase 1b, no excitation was initiated in the endocardial CIZ, whereas the midmyocardial and epicardial BZ were activated. This caused nearly a ST segment depression in the later ischemia stage.

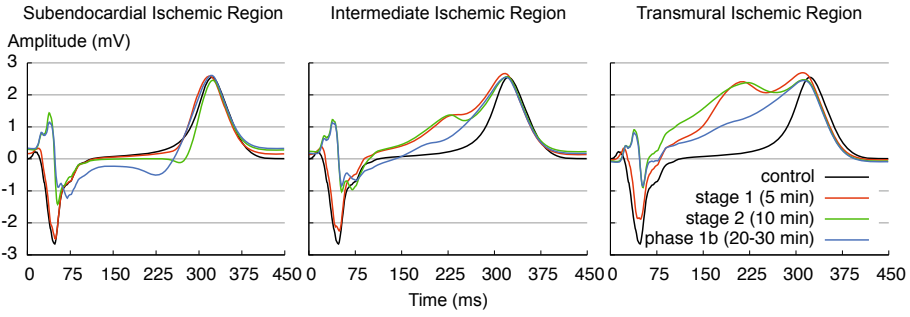

Fig. 4. ECGs (chest lead V_4) of three ischemia cases at different ischemia stages

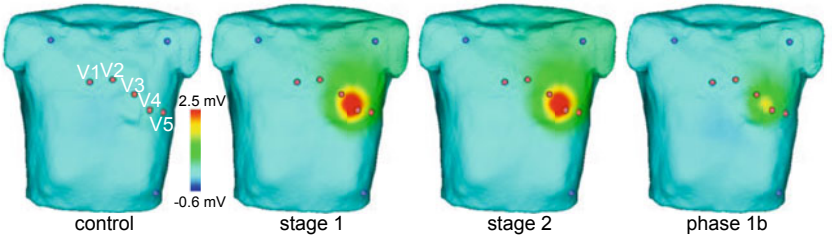

Fig. 5. BSPMs of the transmural ischemia case at $t = 200$ ms at different stages of acute cardiac ischemia

In transmural ischemia, the CIZ of the ischemic region spanned the entire ventricular wall. However, a conduction block was only visible in the epicardium at stage 1 and stage 2. In the endocardium, a delayed activation could be observed. This led to a pronounced elevation of the body surface potential (compare Fig. 5), since the injury current was directed from the less injured endocardium towards the more affected epicardium. During phase 1b, there was also a conduction block in the endocardium. Consequently, the body surface potential was only slightly elevated close to the ischemic region. Next to this area of elevation, the potential was similar to that of the control case.

4 Discussion and Conclusions

In clinical practice, the early diagnosis of cardiac ischemia is based on shifts of the ST segment. In this *in silico* study, we showed that the changes in the ECG depend not only on the transmural extent of the ischemic region, but also on the stage of acute ischemia. Other groups as e.g. [9,10,11] also investigated phase 1b of cardiac ischemia. However, the corresponding body surface ECGs and the differences between several acute ischemia stages were not investigated there.

The effects of cardiac ischemia worsened in the first thirty minutes. On the cellular level, the electrophysiological properties, as e.g. the APD or the AP amplitude, changed gradually. Furthermore, the intracellular conductivity was reduced in the ischemic region during phase 1b. As a consequence, almost no excitation was initiated in the CIZ at this stage. As a result, the ST segment depression was more pronounced in the subendocardial ischemia case and also in the intermediate ischemia case, a ST segment depression can be seen. In the transmural ischemia case, the difference between endocardial and epicardial ischemic tissue decreases during phase 1b compared to the earlier stages. Consequently, ST segment elevation is less pronounced after 20 to 30 minutes. Similar observations have been made in animal experiments [14,15], in which the ST segment elevation decreased at ca. 30 minutes. However, the authors concluded that this could be explained by transitory improvement of the electrophysiological properties of ischemic cells due to a plateau phase of $[K^+]_o$ accumulation. However, lack of experimental data, i.e. human body surface ECGs of the first 30 minutes of cardiac ischemia, do not allow appropriate verification of the findings of these simulations.

The exemplary ischemic region presented in this work shows that the diagnosis of cardiac ischemia based on ST segment shifts can be very difficult. In addition to the transmural extent of the ischemic region, also the temporal stage of ischemia has an impact on the ECG and the direction of the ST segment shift. Some ischemia cases, as e.g. the subendocardial ischemia at stage 1 or stage 2, can hardly be identified in the ECG. As a consequence, early diagnosis of cardiac ischemia should not only rely on 12-lead ECGs. Instead, biomarkers as CK-MB or troponin or multichannel ECG systems should be more emphasized.

In general, the monodomain model is sufficient for the simulation of cardiac excitation propagation and body surface potentials using a high resolution forward model [16]. However, anisotropy ratio may be changed during phase 1b ischemia, which would require use of the bidomain model. As in [9], the model of cardiac ischemia used in this work only indirectly simulates metabolic effects as the inhibition of the Na^+-K^+ pump in order to reduce model complexity. However, detailed metabolic models as in [17] allow more realistic simulations of ischemia effects. Furthermore, a diffusion model of the blood flow in the coronary arteries would create more realistic ischemic regions. Another aspect that should be mentioned is that the spatial resolution of 0.4 mm was a compromise between computing time and accuracy, since the calculation of a single heart beat (450 ms) took approximately 8.5 h on 16 cores. In future simulations, a higher resolution of 0.2 mm will be used. In addition, more simulations with different occlusion sites and varying ischemia size should be carried out in the future.

Acknowledgments

This work has been partially funded within the framework of the nationwide "Initiative for Excellence" from the Karlsruhe Institute of Technology (KIT).

References

1. Carmeliet, E.: Cardiac ionic currents and acute ischemia: from channels to arrhythmias. Physiol. Rev. 79, 917–1017 (1999)
2. Cascio, W., Yang, H., Muller-Borer, B., Johnson, T.: Ischemia-induced arrhythmia: the role of connexins, gap junctions, and attendant changes in impulse propagation. J. Electrocardiol 38, 55–59 (2005)
3. Weiss, D., Ifland, M., Sachse, F.B., Seemann, G., Dössel, O.: Modeling of cardiac ischemia in human myocytes and tissue including spatiotemporal electrophysiological variations. Biomed. Tech. 54, 107–125 (2009)
4. Rodríguez, B., Tice, B., Eason, J., Aguel, F., Ferrero, J., Trayanova, N.: Effect of acute global ischemia on the upper limit of vulnerability: a simulation study. Am. J. Physiol-Heart C 286, 2078–2088 (2004)
5. Colonna, P., Cadeddu, C., Montisci, R., Chen, L., Meloni, L., Iliceto, S.: Transmural heterogeneity of myocardial contraction and ischemia. Diagnosis and clinical implications. Ital Heart J. 1, 174–183 (2000)
6. Furukawa, T., Kimura, S., Furukawa, N., Bassett, A., Myerburg, R.: Role of cardiac ATP-regulated potassium channels in differential responses of endocardial and epicardial cells to ischemia. Circ. Res. 68, 1693–1702 (1991)
7. Foster, D.: Ischemia and Anginal Syndromes. In: Twelve-lead Electrocardiography: Theory and Interpretation. Springer, Heidelberg (2007)
8. ten Tusscher, K., Panfilov, A.: Alternans and spiral breakup in a human ventricular tissue model. Am. J. Physiol-Heart C 291, H1088–H1100 (2006)
9. Pollard, A., Cascio, W., Fast, V., Knisley, S.: Modulation of triggered activity by uncoupling in the ischemic border. A model study with phase 1b-like conditions. Cardiovasc Res. 56, 381–392 (2002)
10. Jie, X., Trayanova, N.: Mechanisms for initiation of reentry in acute regional ischemia phase 1b. Heart Rhythm 7, 379–386 (2010)
11. Ramirez, E., Saiz, J., Trenor, B., Ferrero, J., Molto, G., Hernandez, V.: Influence of 1b ischemic ventricular tissue on the automaticity of purkinje fibers: A simulation study. In: Computers in Cardiology, pp. 617–620 (2007)
12. Keller, D.U.J., Weber, F.M., Seemann, G., Dössel, O.: Ranking the influence of tissue conductivities on forward-calculated ECGs. IEEE Transactions on Biomedical Engineering 57, 1568–1576 (2010)
13. www.ibt.kit.edu/acCELLerate.php Cardiac Electrophysiology and Tension Development Software
14. Kleber, A., Janse, M., van Capelle, F., Durrer, D.: Mechanism and time course of S-T and T-Q segment changes during acute regional myocardial ischemia in the pig heart determined by extracellular and intracellular recordings. Circ. Res. 42, 603–613 (1978)
15. Cinca, J., Warren, M., Carreno, A., Tresanchez, M., Armadans, L., Gomez, P., Soler-Soler, J.: Changes in myocardial electrical impedance induced by coronary artery occlusion in pigs with and without preconditioning: correlation with local ST-segment potential and ventricular arrhythmias. Circ. 96, 3079–3086 (1997)
16. Potse, M., Dubé, B., Richter, J., Vinet, A., Gulrajani, R.: A comparison of monodomain and bidomain reaction-diffusion models for action potential propagation in the human heart. IEEE Trans. Biomed. Eng. 53, 2425–2435 (2006)
17. Terkildsen, J., Crampin, E., Smith, N.: The balance between inactivation and activation of the Na^+-K^+ pump underlies the triphasic accumulation of extracellular K^+ during myocardial ischemia. Am. J. Physiol. 293, H3036–H3045 (2007)

Interpreting Optical Mapping Recordings in the Ischemic Heart: A Combined Experimental and Computational Investigation

Sara Dutta[1], Martin J. Bishop[1], Pras Pathmanathan[1], Peter Lee[2], Peter Kohl[2], T. Alexander Quinn[2], and Blanca Rodriguez[1]

[1] Computing Laboratory, University of Oxford, UK
[2] Harefield Heart Science Centre, Imperial College London, UK

Abstract. The occlusion of a coronary artery results in myocardial ischemia, significantly disturbing the heart's normal electrical behavior, with potentially lethal consequences, such as sustained arrhythmias. Biologists attempt to shed light on underlying mechanisms with optical voltage mapping, a widely used technique for non-contact visualization of surface electrical activity. However, this method suffers from signal distortion due to fluorescent photon scattering within the biological tissue. The distortion effect may be more pronounced during ischemia, when a gradient of electrophysiological properties exists at the surface of the heart due to diffusion with the surrounding environment. In this paper, a combined experimental and computer simulation investigation into how photon scattering, in the presence of ischemia-induced spatial heterogeneities, distorts optical mapping recordings is performed. Dual excitation wavelength optical mapping experiments are conducted in rabbit hearts. In order to interpret experimental results a computer simulation study is performed using a 3D model of ischemic rabbit cardiac tissue combined with a model of photon diffusion to simulate optical mapping recordings. Results show that the presence of a border zone, in combination with fluorescent photon scattering, distorts the optical signal. Furthermore, changes in the illumination wavelength can alter the relative contribution of the border zone to the emitted signal. The techniques developed in this study may help with interpretation of optical mapping data in electrophysiological investigations of myocardial ischemia.

1 Introduction

Sudden cardiac death accounts for over 300, 000 deaths in the US each year [1]. One of the major causes of cardiac arrest is coronary artery occlusion, reducing the supply of blood to the heart, and resulting in a phenomenon known as myocardial ischemia.

The ischemic action potential (AP) displays significant morphological changes: a decrease in upstroke velocity, AP amplitude and duration, and a depolarization of the resting membrane potential. These changes are mainly due to an increase in extracellular potassium concentration ($[K^+]_o$), a decrease in conductance of the main ion channels carrying sodium and calcium (I_{Na} and I_{CaL}) and

D.N. Metaxas and L. Axel (Eds.): FIMH 2011, LNCS 6666, pp. 20–27, 2011.

an increase in conductance of the ATP-sensitive potassium current ($I_{K(ATP)}$) [2]. However, during ischemia, a layer of cells between poorly- and well-perfused tissue, referred to as the border zone (BZ), does not display fully ischemic action potentials (APs) [3,4], and the resulting electrophysiological heterogeneities increase the likelihood of developing disturbed excitation patterns and cardiac arrhythmias [5]. During global ischemia, this occurs at the the epi- and endocardial surface (with a BZ thickness of ≈1mm), due to diffusion of oxygen and ions with the environment surrounding the heart and blood within the ventricles [6].

Optical mapping utilizes voltage-sensitive fluorescent dyes to visualize the electrical activity of the heart. Upon excitation at a specific illumination wavelength, dye molecules transduce differences in membrane potential (V_m) into changes in emitted fluorescence. However, penetration of the illuminating light into the tissue (with depth dependent on illumination wavelength [7]) and scattering of the emitted fluorescent photons, means that the detected signal represents a weighted-average of V_m levels from within a volume of tissue beneath the surface recording site. Such effects have been shown in modeling studies to distort optical recordings [8,9], in particular causing a prolongation of the AP upstroke.

In this study, we combine experiments and computational modeling to investigate how optical mapping recordings are affected by ischemia-induced transmural electrophysiological heterogeneity in the epicardial BZ and photon scattering. We hypothesize that optical signals will be significantly distorted relative to actual epicardial APs due to the collection of signals from a depth of tissue containing the BZ and fully ischemic myocardium. Preliminary dual-wavelength optical mapping experiments were performed on no-flow globally ischemic rabbit hearts. Two excitation wavelengths were used to investigate whether differences between the respective emitted optical signals would appear with time, assuming ischemia-induced transmural heterogeneities became more pronounced. Computational simulations, representing both the BZ and the effects of photon scattering on optical mapping signals, were performed to assist interpretation of experimental data.

2 Methods

2.1 Optical Mapping Experiments

Optical mapping experiments were performed on isolated rabbit hearts (1kg females, n=3), Langendorff-perfused with 37°C Krebs-Henseleit solution bubbled with 95% O_2 / 5% CO_2, and maintained in a heated imaging chamber filled with perfusate. Hearts were stained with voltage-sensitive dye (20μL bolus of 27.3mM di-4-ANBDQPQ), excitation-contraction uncoupled to eliminate motion-induced imaging artifacts (10μM blebbistatin), paced at the apex (2ms, 8V bipolar pulse at 1.25Hz, to ensure maintained capture and avoid alternans during ischemia), and subjected to no-flow global ischemia. Fluorescence was excited using camera frame-synchronized LED illumination, alternating 470 ± 10nm (shallow penetration) and 640 ± 10nm (deep penetration), and acquired with a 690nm long-pass filter (which effectively cuts out excitation light) at 922Hz (64x64 pixel 16-bit

CCD camera resulting in 300μm/pixel resolution). This allowed paired comparison of short and long wavelength excitation.

2.2 Modeling Ischemia-Induced Alterations in Electrophysiology

We constructed a cuboid ventricular segment model (5mm x 5mm x 5mm) of global ischemia, including transmurally-rotating fiber architecture and rabbit ventricular cell membrane dynamics [10], with an added $I_{K(ATP)}$ current [11]. We chose to model the cardiac tissue after 10min of ischemia, as the electrophysiological differences between the healthy and ischemic tissue are assumed to be greatest at that time [6]. The BZ, as shown in Figure 1, was represented by a transmural gradient in ischemia-induced changes [6].

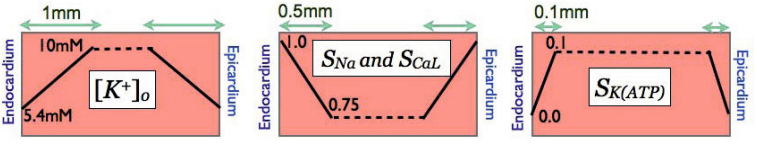

Fig. 1. Diagram of varying ischemic electrophysiological parameters of the cardiac tissue model with a BZ: $[K^+]_o$, S_{Na}, S_{CaL}, and $S_{K(ATP)}$ define a BZ of 1mm, 0.5mm, and 0.1mm, respectively

Bidomain simulations, solved using the finite element method within the Chaste environment [12], were used to simulate propagation of electrical excitation through the tissue following a supra-threshold stimulus applied to the bottom plane of the cube, horizontally aligned to the transmural section. To assess the effects of the BZ, models with/without ischemia-induced spatial heterogeneities were considered.

2.3 Optical Mapping Model

Optical mapping signals were simulated using the model presented by Bishop *et al.* [8]. Briefly, the steady-state photon diffusion equation was solved using the finite element method in the Chaste environment to calculate the distribution of photon density throughout the tissue following both uniform epicardial illumination (Φ_{illum}) and the resulting fluorescent photon emission (Φ_{em}): $D \bigtriangledown^2 \Phi - \mu_a \Phi = -w$, where the optical diffusivity (D) and absorptivity (μ_a) were taken at the illumination/emission wavelength (488/669nm): 0.18/0.36mm, 0.52/0.10mm^{-1} [8]. Zero boundary conditions were used throughout, except during illumination where the source term w was set to an arbitrary value of 1 on the epicardial surface; during emission, w was defined to be a function of Φ_{illum} and V_m, as obtained from the bidomain simulations, at each point in the tissue. The recorded optical signal, V_{opt}, was then calculated as the outward flux of Φ_{em} at each time step across the epicardial surface by applying Fick's Law: $V_{opt} = -D^{em} \bigtriangledown \Phi_{em}.\boldsymbol{n}$, where $\boldsymbol{n}$ is the normal to the epicardial surface.

The degree of distortion due to photon scattering depends highly on the effective optical penetration depth ($\delta = \sqrt{D/\mu_a}$) at both the illumination and emission wavelengths [8]. Therefore, we analyzed the effects of high/default/low values of δ_{eff}^{illum} (2.45/0.59/0.18mm) and δ_{eff}^{em} (3.20/1.90/0.18mm) to represent high and low wavelength penetration depths.

2.4 Data Analysis

The results presented are taken from normalized V_m and V_{opt} values of a node at the center of the epicardium: V_m^* and V_{opt}^*. We calculate the APD as the time difference between the upstroke reaching 0 mV and 90% repolarization and upstroke duration as the time between V_m reaching 10% and 90% depolarization. We define τ_{opt} as the ratio of V_{opt}^* and V_m^*.

3 Results

3.1 Optical Mapping Experiments

Experiments were performed in isolated rabbit hearts to investigate changes in optical mapping signals during no-flow global ischemia. Normalized voltage signals, showing the activation wavefront at different times following apical stimulation can be seen in Figure 2(a). Upstrokes from a 2x2 pixel area on the left ventricular free wall for the two excitation wavelengths at different times of ischemia are shown in Figure 2(b). Differences between the respective emitted optical signals increase with time, showing a prolongation in upstroke duration and a reduced upstroke velocity recorded with 640nm compared to 470nm excitation. We hypothesize that the deeper penetrating wavelength (640nm) displays more ischemic features, as it gathers information from a larger volume that includes more ischemic cells than the shallower penetrating wavelength (470nm). To investigate the source of these differences, we subsequently performed a simulation study.

3.2 Border Zone Effects on Epicardial Transmembrane Potential

Figure 3(a) shows the distribution of V_m^* for the two types of tissue: with and without a BZ. We notice that the repolarization wavefront shapes are significantly different in the two types of tissue. Cells close to the epicardium and endocardium depolarize faster and take longer to repolarize in the tissue with a BZ, than in the homogeneously ischemic tissue.

Figure 3(b) shows that the AP (sampled from the epicardium) of the fully ischemic tissue (without a BZ) displays all of the expected ischemia-induced morphological changes. In the presence of a BZ, the AP displays an upstroke duration 22% shorter and an APD 11% longer than the homogeneously ischemic tissue, characteristics of an AP from less ischemic tissue.

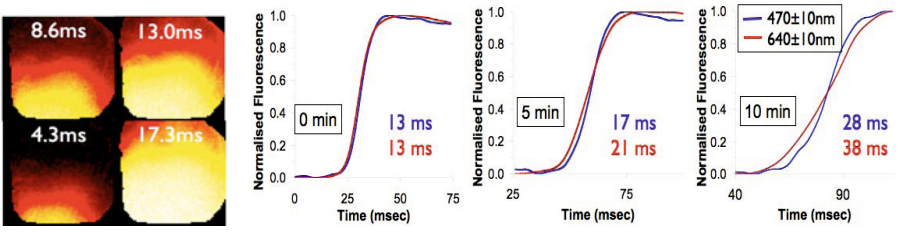

(a) (b)

Fig. 2. (a) Images of normalized fluorescence emitted from the left ventricle of the rabbit heart at different times after apical stimulation. (b) Normalized voltage upstroke after 0, 5 and 10 min of ischemia for 470nm ±10nm and 640 ±10nm excitation with the respective upstroke durations.

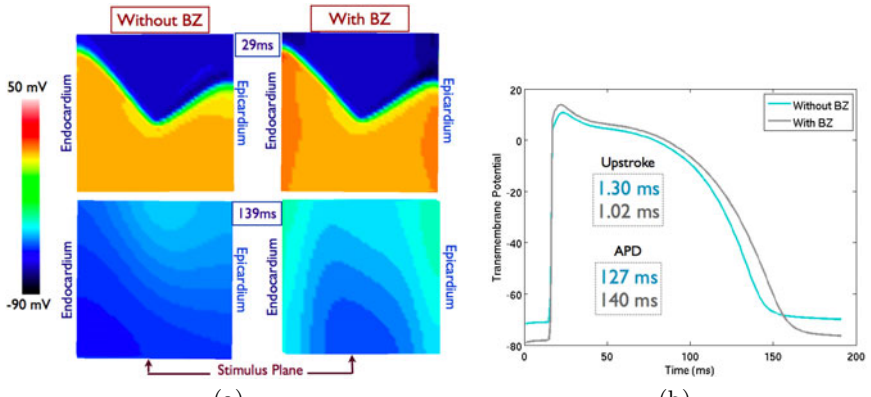

(a) (b)

Fig. 3. Computational model of border zone effects on V_m^*. (a) Snapshots of V_m^* for tissue with and without a BZ during tissue depolarization (29 ms) and repolarization (139 ms) following apical stimulation (b) V_m^* with and without a BZ, including APD and upstroke duration values.

3.3 Optical Signal and Transmembrane Potential Comparison

Figure 4(a) shows the corresponding V_{opt}^* surface optical APs with/without BZ, whilst Figure 4(b) compares differences in upstroke duration and APD relative to the V_m^* traces of Figure 3(b). As has been shown in previous optical mapping studies, the emitted signal represents the transmembrane potential of a weighted average volume of myocardium, due to photon scattering [8,9]. These effects are more noticeable in the upstroke than the APD, as shown in Figure 4(b), even in the homogeneously ischemic tissue. This is caused by the narrow and fast wavefront that occurs during depolarization, such that as it crosses the scattering

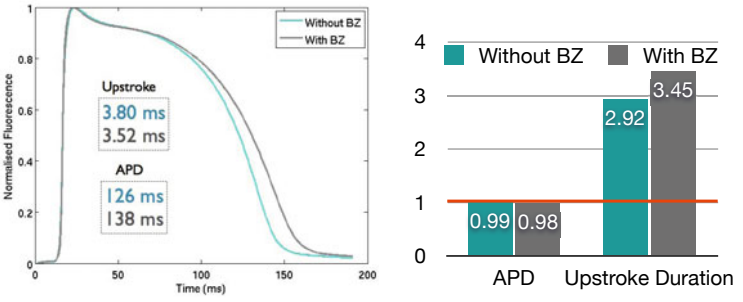

(a) (b)

Fig. 4. (a) Simulated V^*_{opt} with and without BZ. APD and upstroke duration values are shown for the respective APs. (b) Photon scattering effects, represented by τ_{opt}, on APD and upstroke duration for simulations run on a tissue with and without a BZ.

volume, some cells are in their resting state while others are excited. This is not the case during the slower repolarization phase, where most of the cells in the scattering volume will have a similar transmembrane potential. In fact, $\tau_{opt(APD)}$ values are close to 1 while $\tau_{opt(upstroke)}$ values are of 2.92 or greater. Therefore, differences in APD seen in Figure 4(a) are mainly due to the border zone as opposed to photon scattering.

Figure 4(b) shows that τ_{opt} values move away from 1 in the presence of a BZ for both APD and upstroke duration. This arises from the increase in heterogeneities which lead to differences in AP morphology, in conduction velocity and wave front propagation. In the presence of a BZ, V^*_{opt} gathers information from cells exposed to different degrees of ischemia, while V^*_m represents the less ischemic cells at the epicardium. Differences in upstroke duration and APD for simulations with and without a BZ are attenuated in V^*_{opt} (Figure 4(a)) compared to V^*_m (Figure 3(b)) due to the optical signal representing a weighted average volume of tissue.

3.4 Varying Optical Mapping Penetration Depth

The trends mentioned above are accentuated as we change the penetration depth. Figure 5 shows that τ_{opt} values move away from 1 as the penetration depth increases for both APD and upstroke duration in simulations with and without a BZ. Differences between V^*_{opt} and V^*_m increase due to the optical signal averaging over a bigger volume for an increased penetration depth. Furthermore, the differences between τ_{opt} values with and without a BZ become more pronounced for both upstroke duration and APD calculations as the penetration depth increases. As we increase δ_{eff}, the differences between V^*_{opt} with and without a border zone are attenuated due to a larger scattering volume, such that more signal is acquired from the deeper ischemic tissue, decreasing the relative

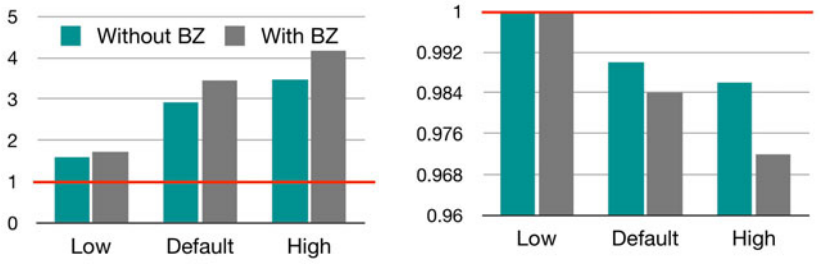

Fig. 5. Varying penetration depth effects, represented by τ_{opt}, for tissue with and without a BZ. (a) Upstroke duration and (b) APD, taken at different penetration depths (Low, Default, and High).

contribution of the BZ. However, a large change remains in V_m^* with/without BZ (Figure 3(b)), thus leading to a larger difference in τ_{opt} as penetration depth increases.

4 Conclusions

The aim of this study was to investigate the combined effects of ischemia-induced transmural heterogeneities and photon scattering on epicardial optical mapping recordings in a globally ischemic heart. We approached this with a combined experimental and simulation study. Preliminary dual wavelength optical mapping experiments in globally ischemic isolated hearts were performed. These showed a clear difference in voltage-sensitive fluorescence emission between the two excitation wavelengths, which we attribute to the presence of an epicardial BZ. We investigated this hypothesis with a model of global ischemia, including transmural variation of electrophysiological parameters, combined with a model of photon density and excitation to simulate the optical signal at the surface of the heart. Simulations of V_m and V_{opt} were conducted on a model of ischemic rabbit tissue with and without a BZ. This demonstrated that the electrophysiological heterogeneities that exist in the presence of an epicardial BZ affect the optical signal, resulting in a decrease in upstroke duration and an increase in APD compared to the optical signal from a homogeneously ischemic slab of tissue. Furthermore, as the penetration depth of the optical signal is increased, the differences between the epicardial V_{opt} and V_m are accentuated.

Overall, this study shows that the electrophysiological heterogeneities that arise at the epicardial surface during ischemia have a significant effect on optical mapping recordings. Furthermore, exciting fluorescent dyes with different wavelengths has an important impact on the resulting optical signal and may be used to investigate transmural heterogeneities. These findings provide new insights into optical mapping data interpretation when investigating the role of heterogeneity during global ischemia.

References

1. Papadakis, M., Sharma, S., Sheppard, M., Panoulas, V., Behr, E.: The magnitude of sudden cardiac death in the young: a death certificate-based review in England and Wales. Europace 11, 1353–1358 (2009)
2. Carmeliet, E.: Cardiac ionic currents and acute ischemia: from channels to arrhythmias. Physiol. Rev. 79, 917–987 (1999)
3. Fiolet, J., Baartscheer, A., Schumacher, C., Terwelle, H., Krieger, W.: Transmural inhomogeneity of energy metabolism during acute global ischemia in the isolated rat heart: dependence on environmental conditions. J. Mol. Cell. Cardiol. 17, 87–92 (1985)
4. Schaapherder, A., Schumacher, A., Coronel, R., Fiolet, J.: Transmural inhomogeneity of extracellular [K+] and pH and myocardial energy metabolism in the isolated rat heart during acute global ischemia; dependence on gaseous environment. Basic Res. Cardiol. 85, 33–44 (1990)
5. Rodriguez, B., Trayanova, N., Noble, D.: Modeling cardiac ischemia. Ann. NY Acad. Sci. 1080, 395–414 (2006)
6. Tice, B., Rodriguez, B., Eason, J., Trayanova, N.: Mechanistic investigation into the arrhythmogenic role of transmural heterogeneities in regional ischemia phase 1A. Europace 9, 47–58 (2007)
7. Walton, R., Benoist, D., Hyatt, C., Gilbert, S., White, E., Bernus, O.: Dual excitation wavelength epifluorescence imaging of transmural electrophysiological properties in intact hearts. Heart Rhythm 7, 1843–1849 (2010)
8. Bishop, M., Rodriguez, B., Eason, J., Whiteley, J., Trayanova, N., Gavaghan, D.: Synthesis of voltage-sensitive optical signals: application to panoramic optical mapping. Biophys. J. 90, 2938–2945 (2006)
9. Hyatt, C., Mironov, S., Wellner, M., Berenfeld, O., Popp, A., Weitz, D., Jalife, J., Pertsov, A.: Synthesis of voltage-sensitive fluorescence signals from three-dimensional myocardial activation patterns. Biophys. J. 85, 2673–2683 (2003)
10. Mahajan, A., Shiferaw, Y., Sato, D., Baher, A., Olcese, R., Xie, L., Yang, M., Chen, P., Restrepo, J., Karma, A., Garfinkel, A., Qu, Z., Weiss, J.: A rabbit ventricular action potential model replicating cardiac dynamics at rapid heart rates. Biophys. J. 94, 392–410 (2008)
11. Michailova, A., Suacerman, J., Belik, M., McCulloch, A.: Modeling regulation of cardiac KATP and L-type Ca2+ currents by ATP, ADP, and Mg2+. Biophys. J. 88, 2234–2249 (2005)
12. Pitt-Francis, J., Pathmanathan, P., Bernabeu, M., Bordas, R., Cooper, J., Fletcher, A., Mirams, G., Murray, P., Osborne, J., Walter, A., Chapman, S., Garny, A., van Leeuwen, I., Maini, P., Rodriguez, B., Waters, S., Whiteley, J., Byrne, H., Gavaghan, D.: Chaste: A test-driven approach to software development for biological modelling. Comput. Phys. Commun. 180, 2452–2471 (2009)

Towards High Resolution Computational Models of the Cardiac Conduction System: A Pipeline for Characterization of Purkinje-Ventricular-Junctions

Daniel Romero[1,⋆], Frank B. Sachse[3], Rafael Sebastian[4], and Alejandro F. Frangi[1,2]

[1] Computational Imaging & Simulation Technologies in Biomedicine, Universitat Pompeu Fabra, and Networking Biomedical Research Center on Bioengineering, Biomaterials and Nanomedicine, Barcelona Spain
daniel.romero@upf.edu
[2] Institució Catalana de Recerca i Estudis Avançats, Barcelona, Spain
[3] Nora Eccles Harrison Cardiovascular Research & Training Institute, University of Utah, and Department of Bioengineering, University of Utah, Salt Lake City, UT, USA
[4] Department of Computer Science, Universitat de Valencia, Spain

Abstract. The cardiac conduction system (CCS) has been in the spot light of the clinical and modeling community in recent years because of its fundament role in physiology and pathophysiology of the heart. Experimental research has focused mainly on investigating the electrical properties of the Purkinje-ventricular-junctions (PVJs). The structure of the PVJs has only been described through schematic drawings but not thoroughly studied. In this work confocal microscopy was used with the aim of three-dimensional characterization of PVJs. Adult rabbit hearts were labeled with fluorescent dyes, imaged with confocal microscopy and Purkinje fibers differentiated from other cardiac tissue by their lack of transverse tubular system on the membrane. A semi-automatic pipeline to segment the network was implemented, using region growing and manual revisions. The resulting three-dimensional reconstructions were used to compute centerlines of the Purkinje fibers. Highly complex structural configurations were found at a subcellular resolution including anastomoses with furcations of up to 5 paths. We suggest that the presented analysis and parametrization of the centerline skeleton of the PVJs will help to improve automated Purkinje network generation algorithms.

Keywords: Purkinje system, cardiac electrophysiology, confocal microscopy, labeling.

1 Introduction

The Purkinje fibers are a specialized myocardial tissue mainly characterized by its ability to conduct electric impulses at higher speed than working myocardium[1].

⋆ Corresponding author.

D.N. Metaxas and L. Axel (Eds.): FIMH 2011, LNCS 6666, pp. 28–35, 2011.

This functionality improves efficiency of the contraction and pumping by ensuring an activation pattern that synchronizes the electrical activation of the ventricular walls. The cardiac conduction system includes several compartments along its extension differing in cell type and localization within the heart. In the ventricles, the portion exiting the atrioventricular node is called the bundle of His, which splits into right and left bundle branches at the basal septum. The fascicular branches then lead to a complex network of Purkinje fibers, which connect to the ventricles, and are the most distal portion of the system. Depending on species, the cardiac conduction system is isolated from the rest of the myocardium by a sheath of connective tissue which prevents the current to flow out from the fibers but at specific contact points. In some species transitional cells between Purkinje and the myocardium can be differentiated, for instance in rabbit, dog or pig, but not in human and bovine [2]. In these species the contact point for transmission of the electric impulse occurs at the terminal points of the Purkinje network (Purkinje-ventricular junctions, PVJs) [3,4,5].

The Purkinje network has hit a spot light in recent years in clinical and academic research, in particular on arrhythmogenesis. On the one hand abnormal activation of the CCS has been reported to cause electrical macro- or micro-reentries. This kind of reentry is produced due to a unidirectional block in the His-Purkinje system and can give rise to ventricular tachycardia [5]. On the other hand, it has been found that targeting Purkinje-like-potentials (PLPs) during radio frequency ablation therapy near the scar border zone in patients with myocardial infarction is an effective way to prevent recurrence of ventricular fibrillation [6]. However there is a lack of detailed description of how ischemia in these sites of PLPs is causing the electrical disturbance. Experimental research has been focussed primarily on electrical coupling of the PVJs. These regions have been studied, for example, on how cadmium and isoproterenol affect the electrical delay of propagation [7]. At a structural level two types of interaction have been found at this interface: a funnel connection and a transitional layer (T cells) between the Purkinjes and working myocytes. Tranum-Jensen et al showed a schematic description of the spatial configuration [2]. But apart from this study based on light microscopy the structural appearance of the PVJ has been only sparsely characterized.

More sophisticated techniques such as confocal microscopy allow 3D imaging at subcellular resolution, which can be used to characterize these junctions in a more precise way. This paper focuses on the construction of 3D models of PVJs from microscopy techniques with the final aim of quantitatively characterize them. This image-based information will provide a solid basis for developing realistic models of the CCS with important applications to clinical treatment of heart disease.

2 Material and Methods

2.1 Tissue Preparation

The complete methodological pipeline is illustrated in Fig. 1. All animal usage was approved by the Institutional Animal Care and Use Committee (IACUC) at

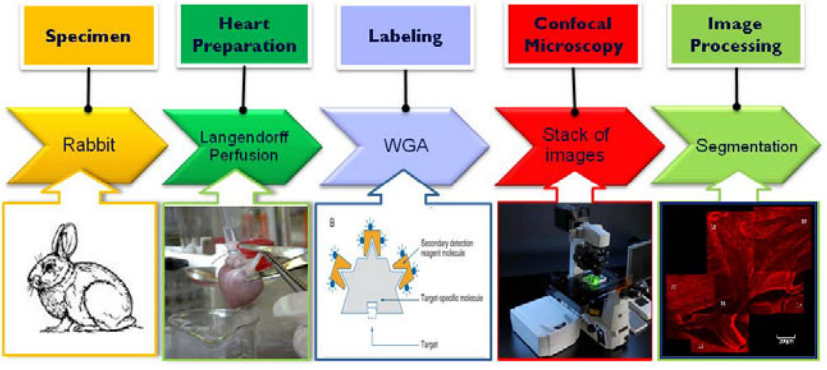

Fig. 1. Methodological pipeline. We isolated, labeled and imaged sections from rabbit subendocardial heart tissue. The image data was processed and analyzed using methods of digital image processing.

the University of Utah. Adult rabbits were anesthetized with pentobarbital and anticoagulated with heparin. Following thoracotomy hearts were quickly excised and placed in a modified oxygenated Tyrode's solution at room temperature. The hearts were perfused and stabilized with a Langendorff preparation. Tyrode's solution including wheat germ agglutinin (WGA) conjugated to Alexa Fluor 555 (Invitrogen, Carlsbad, CA), a fluorescent dye that binds to carbohydrates in the cell membrane and extracellular space, was passed through the hearts. This method allowed for a homogeneous distribution of the dye throughout the heart. The hearts were also fixed through the same line of the Langendorff perfusion with paraformaldehyde. Biopsies were made from left and right ventricle lateral walls (mid and apical), papillary muscles, and septal wall. Afterwards, the biopsies were stored in paraformaldehyde.

2.2 Image Acquisition

Images were obtained within 2 months after heart isolation. 3D image stacks were acquired using a confocal microscope equipped with a 40x oil immersion lens (Zeiss 5 Live, Jena, Germany). Image stacks have a spatial resolution of $0.31 \times 0.31 \times 0.31 \mu m$ and were obtained with a field-of-view (X x Y) of $318 \times 318 \mu m$ extending up to $60 \mu m$ into the myocardium (Z direction). The Z-axis was parallel to the laser beam direction.

2.3 Geometric Reconstruction and Structural Analysis

The image stacks were pre-processed before the segmentation. A deconvolution with the iterative Richardson-Lucy algorithm was applied to all the images using a measured point spread function (PSF) following descriptions from [8]. Images were further processed to remove background signals and corrected for depth-dependent attenuation. These methods were implemented combining a customized C++ and MatLab software (MathWorks, Natick, MA).

3D Slicer software (www.slicer.org) was used for a semi-automatic segmentation of the Purkinje network. Image stacks presented differences due to the varying levels of diffusion of the WGA in the tissue. An approach using region growing together with manual segmentation was found the most appropriate when attempting segmentation on these type of images. Livewire algorithm was used to perform the manual corrections [9]. Problems arose due to the number of discontinuities on the cell membrane, which caused the region growing algorithm to leak through into the extracellular space.

After stacks were fully segmented, centerlines were computed for the reconstructed surfaces of the Purkinje network in order to analyze in a quantitative way their branching pattern in following studies. For this, the implementation of Antiga et al [10] in VMTK was used (www.vmtk.org).

3 Results

The pipeline allowed us labeling, imaging and processing tissue images to characterize PVJs in 3D at high resolutions. First, the field of view and resolution used in the image acquisition with confocal microscopy proved to be adequate for the purpose of differentiating Purkinje fibers from working myocytes by observation of the transverse tubular system (T-system). The WGA labeling marked the clefts between cells (interstitial space) and to some extend fibrous structures of the endocardium. Differentiating Purkinje cells from other cardiac tissue based on the lack of T-system was possible, since Purkinje fibers lack T-system or present a less developed T-system than working myocytes, depending on the species [11]. Our XY-images displayed a characteristic dotted pattern due to the T-tubules in the cell membranes of working myocytes and less pronounced in Purkinje fibers (Fig. 2).

The collagen fibers sheathing the Purkinje fibers provided an effective boundary for its segmentation. Nevertheless, in general the labeling of cell membranes is not homogeneous in the images. Therefore a region growing method failed in

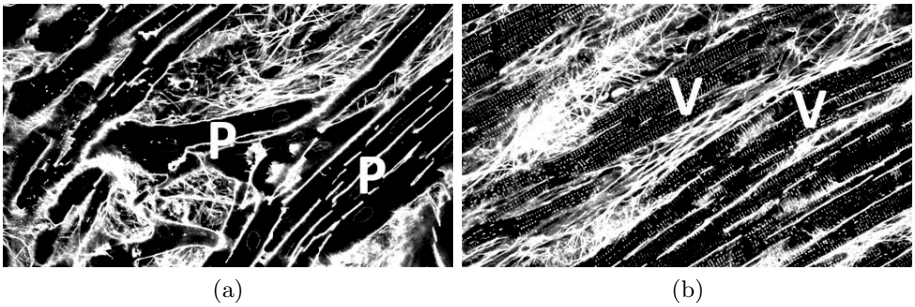

(a) (b)

Fig. 2. Exemplary images from 3D-stack. (a) Purkinje fibers (P). Notice the absence of T-system inside the cells. (b) Ventricular myocytes (V). In these cells the T-system appears as a very regular dotted pattern in the cell.

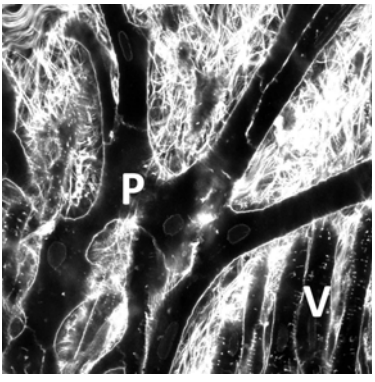

Fig. 3. Multiple-furcation in Purkinje fibers. Star-like arrangement at a branching site of a fiber. Note in the lower right corner working myocytes below the Purkinje fibers. The working myocytes follow preferential direction according to the fiber orientation while Purkinje fibers do not have a particular direction.

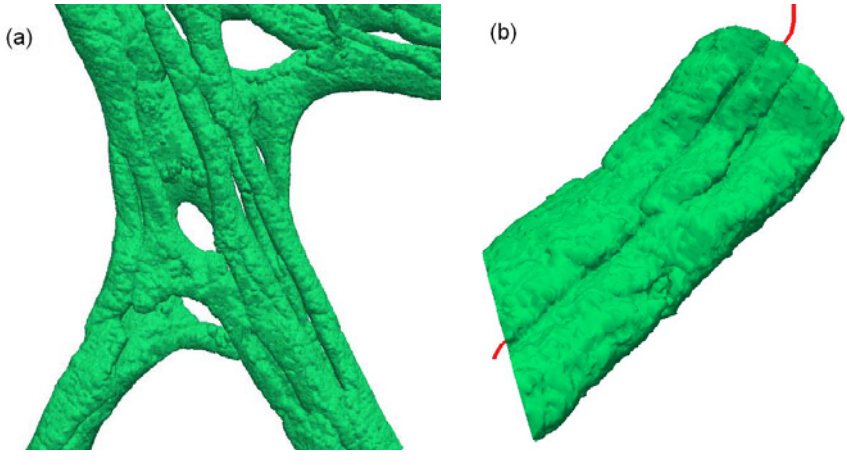

Fig. 4. 3D reconstruction of image stacks. (a) Surface model of a Purkinje network. (b) Zoom into a bundle of cells in a Purkinje fiber. Marked in red is the centerline, averaged for the bundled of fibers.

multiple instances to segment entirely the Purkinje fibers without leaking into extracellular space or ventricular myocytes. To avoid this problem, a manual selection of distributed seeds was necessary to segment the stack. The algorithm worked in 3D, and provided Purkinje structure spanning over the whole stack of images. Manual corrections were needed and the Livewire algorithm was helpful to perform the manual task.

After segmenting a stack the Purkinje network was analyzed in 3D. At fork points, complex furcations were found. Anastomosis yielded alternative paths to ensure the delivery of the electric signal. In some cells up to 5 branches were

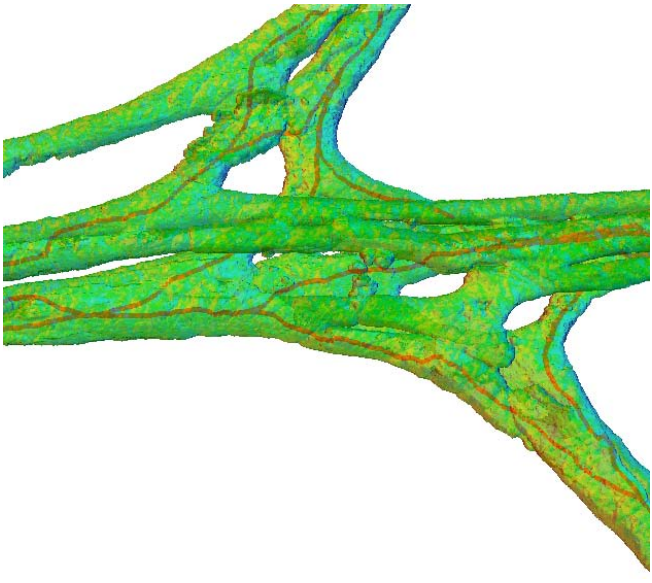

Fig. 5. Surface model with centerlines. The centerlines (lines in red) were computed taking advantage of the tubular shape nature of the Purkinje fibers.

seen spreading from a star like geometry (Fig. 3). To extract quantitative data from the images, binary 3D masks were created. Following, surface meshes were reconstructed for each of the segmentations (Fig. 4a). Purkinje fibers at that resolution form tubular complex structures, which tend to show a clear directionality, and do not run in parallel in many cases. Each fiber was formed by a few group of cells, in the order of three to four. Inconsistencies on membrane continuity also occurred in between Purkinje fibers, and thus the tubular shapes appeared merged at certain segments. These connections might be due to segmentation errors in some cases, although it has been reported that there is lateral electrical connection between bundle fibers. This fact helped to decide a common initial site when choosing seed and target points for the centerline computation; the centerlines bundle a group of cells in the fiber (Fig. 4b).

In Fig. 5 a Purkinje fiber structure shows the centerlines computed for the main directions of a PVJ interface. In this 3D orientation of the structure, ventricular myocytes (endocardial wall) are below the structure. Note the two layers of fibers and the connection between with anastomosis.

4 Discussion and Conclusions

The complexity of interconnection in our study at high spatial resolution is in agreement with previous work [12]. From macroscopic (as early evidenced from Tawara [13]) to microscopic resolution, the Purkinje network forms plexus structures. The reported star-like arrangement of cells in Fig. 3, where a junction

has more than two paths, has not been considered in modeling approaches of the Purkinje tree [14,15]. Here, it was simplified to a parent-branch leading to two child-branches.

The importance of the Purkinje system to realistic modeling has been demonstrated in the past [16]. Further development in imaging technologies will enable us to visualize in vivo the Purkinje network, meanwhile modeling approaches seem to provide a suitable substitution. Nevertheless, these models should be enriched by ex-vivo histological data, in order to be physiologically meaningful. Algorithms for automated construction of Purkinje structures, e.g. [17], will have to be extended in order to represent the level of detail for PVJ interconnection with the surrounding tissue observed in this study.

As future work, the centerlines of the PVJs will be used to quantitatively study the branching pattern, by means of studying the branch length, and furcation angle, and other similar parameters. This parametric characterization of the PVJ structure will be crucial in order to set up spatial growth parameters in an automated algorithm. We hypothesize that from polygonal patterns seen in macroscopic data there is a fractal relationship with the plexus forms observed at microscopic level. This relation could be tested and expanded in the progress of our research.

Acknowledgments

This research has been partially funded by the Industrial and Technological Development Centre (CDTI) under the CENIT Programme (CvRemod Project), the European Community's Seventh Framework Programme (FP7/ICT-2007-224495) under grant agreement n. 224495 (euHeart project), and was also supported by the Richard A. and Nora Eccles Fund for Cardiovascular Research and awards from the Nora Eccles Treadwell Foundation.

References

1. Guyton, A., Hall, J. (eds.): Textbook of Medical Physiology, Saunders, Philadelphia (2006)
2. Tranum-Jensen, J., Wilde, A.A., Vermeulen, J.T., Janse, M.J.: Morphology of electrophysiologically identified junctions between purkinje fibers and ventricular muscle in rabbit and pig hearts. Circ. Res. 69(2), 429–437 (1991)
3. Cates, A.W., Smith, W.M., Ideker, R.E., Pollard, A.E.: Purkinje and ventricular contributions to endocardial activation sequence in perfused rabbit right ventricle. Am. J. Physiol. Heart Circ. Physiol. 281(2), H490–H505 (2001)
4. Dosdall, D.J., Cheng, K.A., Huang, J., Allison, J.S., Allred, J.D., Smith, W.M., Ideker, R.E.: Transmural and endocardial purkinje activation in pigs before local myocardial activation after defibrillation shocks. Heart Rhythm 4(6), 758–765 (2007)
5. Tabereaux, P.B., Walcott, G.P., Rogers, J.M., Kim, J., Dosdall, D.J., Robertson, P.G., Killingsworth, C.R., Smith, W.M., Ideker, R.E.: Activation patterns of purkinje fibers during long-duration ventricular fibrillation in an isolated canine heart model. Circulation 116(10), 1113–1119 (2007)

6. Sinha, A., Schmidt, M., Marschang, H., et al.: Role of left ventricular scar and purkinje-like potentials during mapping and ablation of ventricular fibrillation in dilated cardiomyopathy. Pacing Clin Electrophysiol. 32, 286 (2009)
7. Wiedmann, R., Tan, R., Joyner, R.: Discontinuous conduction at purkinje-ventricular muscle junction. Am. J. Physiol. 271, H1507–H1516 (1996)
8. Savio, E., Goldhaber, J.I., Bridge, J.H.B., Sachse, F.B.: A framework for analyzing confocal images of transversal tubules in cardiomyocytes. In: Sachse, F.B., Seemann, G. (eds.) FIHM 2007. LNCS, vol. 4466, pp. 110–119. Springer, Heidelberg (2007)
9. O'Donnell, L., Westin, C.-F., Grimson, W.E.L., Ruiz-Alzola, J., Shenton, M.E., Kikinis, R.: Phase-based user-steered image segmentation. In: Niessen, W.J., Viergever, M.A. (eds.) MICCAI 2001. LNCS, vol. 2208, pp. 1022–1030. Springer, Heidelberg (2001)
10. Antiga, L., Ene-Iordache, B., Remuzzi, A.: Centerline computation and geometric analysis of branching tubular surfaces with application to blood vessel modeling. Journal of WSCG 1-3(11) (Febuary 2003)
11. Ayettey, A., Navaratnam, V.: The t-tubule system in the specialized and general myocardium of the rat. J. Anat. 127, 125–140 (1978)
12. Canale, E., Campbell, G., Uehara, Y., Fujiwara, T., Smolich, J.: Sheep cardiac purkinje fibers: Configurational changes during the cardiac cycle. Cell Tissue Res. 232, 97–110 (1983)
13. Tawara, S.: Das reizleitungssystem des säugetierherzens. eine anatomisch- histologische studie über das atrioventricularbündel und die purkinjeschen fäden. Jena, Verlag v. Gustav Fischer (1906)
14. Ijiri, T., Ashihara, T., Yamaguchi, T., Takayama, K., Igarashi, T., Shimada, T., Namba, T., Haraguchi, R., Nakazawa, K.: A procedural method for modeling the purkinje fibers of the heart. J. Physiol. Sci. 58(7), 481–486 (2008)
15. Pollard, A., Barr, R.: Computer simulations of activation in an anatomically based model of the human ventricular conduction system. IEEE Trans. Biomed. Eng. 38(10), 982–996 (1991)
16. Romero, D., Sebastian, R., Bijnens, B.H., Zimmerman, V., Boyle, P.M., Vigmond, E.J., Frangi, A.F.: Effects of the purkinje system and cardiac geometry on biventricular pacing: A model study. Ann. Biomed. Eng., 1388–1398 (January 2010)
17. Zimmerman, V., Sebastian, R., Bijnens, B., Frangi, A.: Modeling the purkinje conduction system with a non deterministic rule based iterative method. Computers in Cardiology 36, 461–464 (2009)

Dynamic Classification of Cellular Transmural TransMembrane Potential (TMP) Activity of the Heart

Mohamed Elshrif, Linwei Wang, and Pengcheng Shi

Golisano College of Computing and Information Science,
Rochester Institute of Technology, Rochester, NY 14623, USA
mme4362@rit.edu

Abstract. Understanding the transmembrane potential (TMP) dynamics of the heart provides an essential guidance to the diagnoses and treatment of cardiac arrhythmias. Most existing methods analyze and classify the TMP signal globally depending on extracting silent features such as the activation time. In consequence, these methods can not characterize the dysfunctions of each cardiac cell dynamically. In order to assess the electrophysiology of the heart considering pathological conditions of each cardiac cell over time, one should analyze and classify the TMP behavior that is differentially expressed in a particular set of time. In this paper, we utilize a spectral co-clustering algorithm to disclose the abnormality of the TMP dynamics over a time sequence. This algorithm is based on the observation that the embedding spectrum structures in the TMP dynamics matrices can be found in their eigenvectors through singular value decomposition (SVD). These eigenvectors correspond to the characteristic patterns across cardiac cells or time sequence. To demonstrate the reliability of this approach, our experimental results show great agreement with the ground truth of the simulated data sets that enable efficient use of this scheme for revealing abnormal behavior in TMP dynamics, at the presence of added Gaussian noise to the simulated TMP dynamics. Furthermore, we compare our results against the k-means clustering algorithm outcomes.

1 Introduction

Electrical activity of the heart triggers myocardial contraction and any disturbance of this activity interrupts the rhythmic and coordinated contraction of the heart, and eventually, weaken the strength of the heart to pump the blood. The standard noninvasive observation of this signal is the Electrocardiogram (ECG), and as a result, currently diagnosing cardiac pathology is primary based on classification and pattern recognition of the ECG signal.

However, ECG signal is not able to provide localized information of cardiac electrical activity. Therefore, in the last decades many efforts have been put to localize this electrical activity through estimation of the transmembrane potential (TMP) of personalized electrophysiological models [2,3,4].

D.N. Metaxas and L. Axel (Eds.): FIMH 2011, LNCS 6666, pp. 36–46, 2011.

It is difficult to understand the TMP dynamics, i.e. action potential, thoroughly as it is three-dimensionally distributed over space and evoluted over time (3D+T) problem, and in consequence, people tend to extract certain features from it, especially because early works manifest that certain features are valuable in disclosing dysfunctions of the heart in experimental [9], and simulated [5] studies. Accordingly, many existing methods are based on such approach. In [1], infarct region was identified by extracting two representative features, activation time (AT) and action potential duration (APD), and measuring the diversions of these features from the normal values. K-means clustering algorithm was then used to differentiate between healthy and diseased regions. In [3], he accuracy of the personalized TMP activity was measured by optimizing four features, i.e. AT, APD, conduction velocity restitution and APD restitution, to measure t.

However, various studies [10,11,12,13,14], have shown different morphologies and traits between depolarization segment (DS) and repolarization segment (RS) in discovering cardiac arrhythmias. Therefore, analyzing either period or extracting certain features can not reflect the cardiac electrophysiological states thoroughly and it is important to evaluate both segments dynamically by classifying them based on their time distributions.

Within a cardiac electrophysiology (EP) context, there are numerous data mining techniques that can be applied to identify cardiac arrhythmias and to classify different pathological conditions of heart cells. With knowledge insufficiency of cardiac cells behavior as a function of time classes, it is appropriate to design or use partitioning methods that have capabilities revealing latent classes by benefiting from the correlation between cardiac cells and time sequence. To the best of our knowledge, no work has been done on the topic of classification and quantification of cardiac arrhythmias that consider the dynamics of the TMP, instead existing methods are mostly based on isochrone features such as action potential duration [1], [3], [4]. Therefore, the aim of this paper is to consider the time sequence of the TMP dynamics in disclosing ischemic regions by gaining from a spectral co-clustering algorithm. Dhillon was the pioneer of spectral co-clustering algorithm on a bipartite graph (or bigraph), which is a graph that has two independent sets of vertices and each set of vertices is connected to subset or all vertices in the other set, and it successfully applied to many applications such as linguistics [6], [7], and bioinformatics fields[8]. Within cardiac EP, we can benefit from the duality of cardiac cell and time clustering. Here, cardiac cells clustering induces time clustering, while time sequence clustering induces cardiac cells clustering. We posed the cardiac cells clustering as a bipartite graph-partitioning problem and by performing co-clustering on the TMP dynamics, we could reduce this high dimensional data interaction problem to visualize a selection of abnormal TMP behavior.

2 Methods

We simulate the TMP dynamics using phenomenological monodomain two-variable modified FitzHugh-Nagumo (FHN) model, i.e. Aliev-Panfilov model

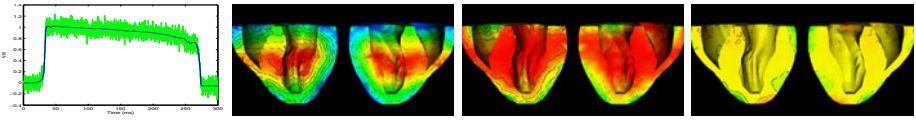

(a) (b) (c) (d)

Fig. 1. Spatiotemporal TMP. (a) Normalized waveform of a single normal left ventricular TMP signal over time (noiseless TMP: blue line and noisy TMP: green line). (b)-(d) Spatial propagation of the TMP signal through the entire myocardium. Left to right: 20.63ms, 47.28ms, 215.42 ms after the onset of the ventricular activation. (b)-(c) Depolarization segment, (d) Repolarization segment.

[19], because it generates realistic TMP shape at macroscopic level. In addition, it offers a flexible control on TMP shapes that make it easy to mimic pathological conditions of the myocardium.

The transmembrane potential signal , as shown in figure 1, represents the normalized electrical activity of a single cardiac cell over time before and after adding Gaussian noise. At the same time, it represents the myocardium electrical activity since it propagates from one cell to adjacent cells throughout the whole cardiac muscle. Since our focus is to cluster the behavior of the TMP dynamics into meaningful physiological conditions, normal/abnormal, we can reformulate this clustering problem utilizing graph partitioning technique.

2.1 Co-clustering within a Cardiac Electrophysiology Context

Co-clustering or bi-clustering is a data mining technique that allows for clustering the samples and features of the data simultaneously. Each data sample is constituted from these features. It is accomplished by relating each class of the data features to a class of the data samples that share certain characteristics and we believe that these characteristics are important in creating such a class. Within cardiology context, representing each cardiac cell as a data sample and each time step as a data feature. The scalar TMP value between each cell and the corresponding time step represent the edge. Therefore, we aim to create clusters that differentiate between normal and abnormal behavior of TMP dynamics by splitting data samples and features into two classes.

Given a data set matrix of TMP dynamics with m nodes (samples) that represent the whole myocardium and n time steps (features), i.e. $A = (a_{ij})_{m \times n}$, we consider the clustering of the time steps t_q into groups as follows:

$$t_1, t_2, t_3, ..., t_{p-1}, t_p, \quad t_q \subseteq \{1, 2, ..., n\}, \quad q = 1, 2, 3, ..., p-1, p. \tag{1}$$

where $\bigcup_{q=1,..,p}^{p} t_q = \{1, 2, ..., n\}$, and $t_q \cap t_r = 0$, such that $q, r = 1, ..., p$, $q \neq r$.

The clustering procedure is done in such a way that time steps are grouped together should share particular characteristics. In a similar manner, each cardiac cell c_q is assigned to one of the cardiac cells groups:

$$c_1, c_2, c_3, ..., c_{p-1}, c_p, \quad c_q \subseteq \{1, 2, ..., m\}, \quad q = 1, 2, 3, ..., p-1, p. \tag{2}$$

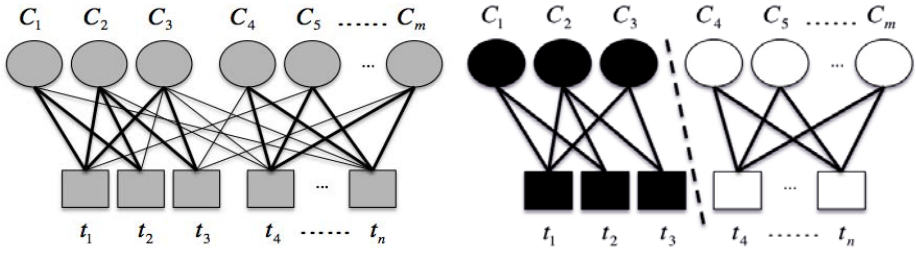

Fig. 2. (a) Constructed bipartite graph: $C_1 ... C_m$ represent cardiac cells and $t_1 ... t_n$ represent time sequence of the TMP dynamics (before clustering). (b) Partitioning of the bipartite graph: The colors (black-white) represent (normal-abnormal) clusters and the dotted line represent the cut of the graph (after clustering).

where $\bigcup_{q=1,..,p}^{p} c_q = \{1, ..., m\}$, and $c_q \cap c_r = 0$, such that $q, r = 1, ..., p, \quad q \neq r$.

With this procedure, cardiac cells that belong to class c_q are responsible for constructing the time steps class t_q. This dual process of classification is called co-clustering.

2.2 Bipartite Spectral Graph Co-clustering Algorithm

In the framework of cardiac electrophysiology discipline, we can represent an undirected weighted bipartite graph, as shown in figure 2, by $G(Vc, Vt, E)$ that consists of two finite sets of vertices Vc that represent cardiac cells (samples) and Vt that represent the time sequence of each cell (features), and a finite set of edges E that signify the association between the two sets of vertices in the graph [6]. One approach to capture the strength of this association is to have dynamic edge-weights equal to normalized TMP dynamics of each cardiac cell at specific time. The cut of this graph captures the separation between different partitions. In [15], it is shown that one can gain from graph spectrum by observing the latent characteristics and structure of a graph, i.e. how to partition a graph. To do so, we can solve matrices that contain eigenvalues and eigenvectors associated with graphs. Furthermore, [6] proposed a new co-clustering approach on bipartite graphs and it is straightforward to fit this approach to our problem, 3D+T, where we can treat each time step as a feature and each cardiac cell as a vector of these features in the feature space. Thus, the entire myocardium can be represented as a cell-time matrix whose rows correspond to cardiac cells and columns represent the time sequence of the TMP dynamics. The underlying assumption is that cardiac cells that have the same behavior at specific time should be clustered together. To achieve the clearest electrophysiological characterization of cardiac cells in TMP dynamics, we subtract the TMP dynamics of each cell from the reference (normal) TMP dynamics. Since we have the preprocessed data set ready, we can now introduce the algorithm:

1. Given a data set matrix $A_{m \times n}$, which represent the TMP dynamics, that measures the association $a_{i,j}$ of the cardiac cell i at particular time step j. Construct the normalized matrix

$$A_n = D_1^{-1/2} A D_2^{-1/2} \tag{3}$$

where $D_1(i,i) = \sum_j A_{ij}$ and $D_2(j,j) = \sum_i A_{ij}$ are diagonal matrices.

2. Compute the associated singular value decomposition (SVD) of the normalized matrix A_n

$$SVD(A_n) = U * \Lambda * V^T \tag{4}$$

where $U_{m\times m}$ and $V^T_{n\times n}$ are unitary matrices, $\Lambda_{m\times n}$ is diagonal matrix.

3. Calculate $l = \lceil \log_2 k \rceil$ singular vectors, $u_2, ..., u_{l+1}$ and $v_2, ..., v_{l+1}$. These l singular vectors usually contain k-modal information of the data set.
4. Construct the l-dimensional data set matrix

$$Z = \begin{bmatrix} D_1^{-1/2} & U_{[2,\ldots,l+1]} \\ D_2^{-1/2} & V_{[2,\ldots,l+1]} \end{bmatrix} \tag{5}$$

5. Run the k-means clustering algorithm on the l-dimensional data set matrix Z to obtain the k-way multi-partitioning.

3 Experimental Results

3.1 Simulated Data Sets

– Modeling Specification: We accomplished our study on the heart model of the University of Auckland with 836 nodes that represent cardiac cells [16]. We tested the algorithm on 100 simulated cases (27 anterior, 25 inferior, 27 lateral, and 21 septal) of myocardial ischemia and infarction that represent the TMP dynamics of each cardiac cell over time. Abnormal TMP dynamics for different pathological conditions are simulated as the gold standard and then corrupted with Gaussian noises with zero mean of 20dB signal-to-noise ratio (SNR) as defined in equation 6. This Gaussian noises are assumed to be spatially variant, but temporarily invariant.

$$SNR = 10log_{10}\frac{power(signal)}{cov(noise)} = 20log_{10}\frac{mean(signal)}{std(noise)} \tag{6}$$

– Infarction procedure: In our experiments, we follow [1], [5] procedure in assigning ischimic and infarct regions of the heart and used the AHA standard 17-segments devision of the left ventricular [17], as shown in figure 6 (a). We define a scar ranging from one to nine combination of segments covering all left ventricular regions. In each case, we decrease the tissue excitability gradually from isthmus to the center of the chosen scar segment(s) that no excitation can be recognized. As an example, we analyze two simulated cases in more detail.

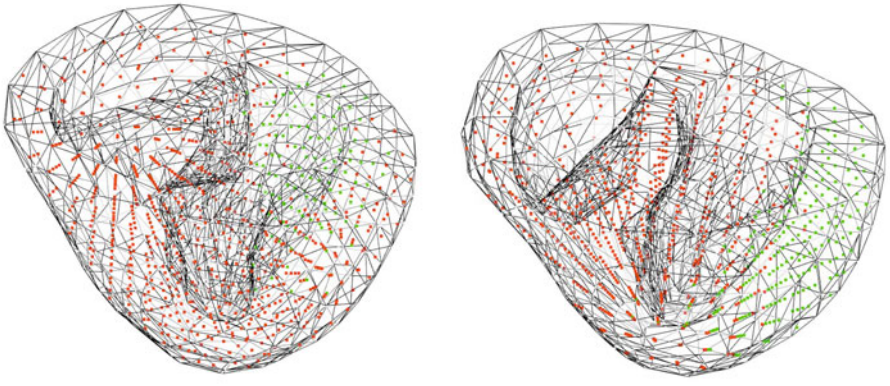

(*a*) (*b*)

Fig. 3. (a) The ground truth of the infarct of case 1 (green area) in a meshfree representation of the ventricles. (b) The ground truth of the infarct case 2 (green area) in a meshfree representation of the ventricles. red: normal tissue excitability.

3.2 Results

1. Case 1: Figure 3 (a) shown the ground truth (GT) of the simulated data for scar location that belongs to segments 4, 10, and 15, which represent basal, mid, and apical inferior region of the left ventricle respectively. Figure 4 depicts the spectral co-clustering results of case 1 where it reveals the embedding spectrum of the TMP behavior of each cell with time and cluster it together. Also, as can be seen from figure 4 the algorithm clusters the normal/abnormal TMP dynamics cells together in certain time steps. As an example, the cardiac cell at row 800 depicts an abnormal behavior (red color) in all time steps. This means that the cell is not excited at all. On the other hand, the cardiac cell at row 650 reveals the abnormality just in the repolarization period. Figure 5 displays the dynamic clustering of the TMP behavior during DS and RS. As can be seen the excitation region difference between this case and the normal case shown in figure 1 is in the inferior region.

   Furthermore, figure 6 (a) shows the clustered abnormal TMP segments with their corresponding abnormality percentages. To present different examples of abnormalities in TMP dynamics, we plot the behavior of abnormal cells in figure 6 (b-d). The percentage identification of the abnormal TMP cells is measured by the ratio: the number of identified abnormal TMP cells behavior to the total number of true abnormal TMP cells behavior. In this case, the percentage of correctly identified abnormal TMP cells behavior before adding the noise is 90.51% where the algorithm can discover 124 nodes out of 137 nodes in the GT. After corrupting the TMP dynamics signal by adding Gaussian noise with 20 dB, the correctly identified abnormal TMP cells behavior is 89.05% where the algorithm can discover 122 nodes out of

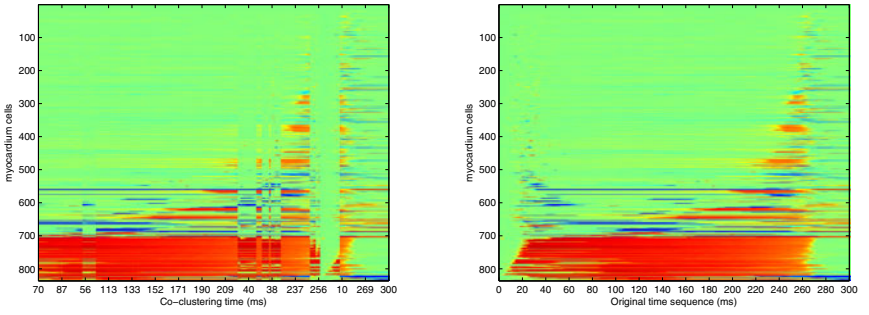

(a) (b)

Fig. 4. Visualization of co-clustering cardiac cells (y-axis) and time sequence (x-axis) of case 1. (a) The results of co-clustering with shuffled time sequence of the TMP dynamics. (b) The results of co-clustering with original time sequence. Colors encode the embedding spectrum of the data. Green: normal TMP dynamics, red: abnormal TMP dynamics.

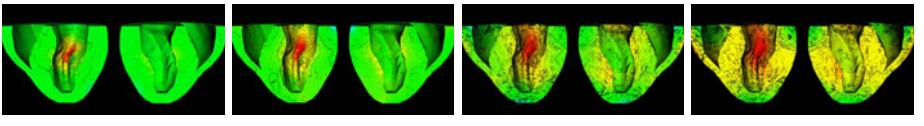

(a) (b) (c) (d)

Fig. 5. (a)-(d) Dynamic co-clustering of the TMP cells in case 1. Left to right: 10.38ms, 20.63ms, 215.42 ms, 235.92ms after the onset of the ventricular activation. The color encodes the TMP value from max (red area) to min (green area) while the black contours represent isochrones of the TMP.

137 nodes in the GT. In addition, we characterize the regions where the abnormality of the TMP cells behavior appears, and found that 84.67% are in the infarct scar segments, 12.09% are in the isthmus region, and 3.23% are in distant regions.

2. Case 2: Figure 3 (b) shown the ground truth (GT) of the simulated data for scar location that belongs to segments 5, 6, 11, 12, and 16, which represent left circumflex region. Due to the space constraints we display the dynamic clustering of the TMP during DS and RS periods, figure 7. The distinction in excitation regions compared with the normal case depicted in figure 1 is in the lateral region. In this case, the percentage of correctly identified abnormal TMP cells behavior before adding the noise is 91.95% and 95.48% after adding the Gaussian noise. Also, we quantify the regions where the abnormality of the TMP cells behavior manifests, and it is found that 95.08% are in the true infarct scar segments, 4.37% are in the boundary scar region, and 0.55% are in remote regions.

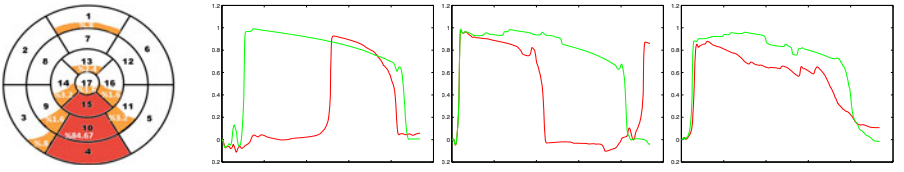

(a) (b) (c) (d)

Fig. 6. (a) Final clustering results of the TMP abnormality regions with corresponding percentage of each abnormal segment in case 1. Red area: infarct scar segments and orange area: isthmus and distant scar segments. (b) Exemplify the delay activation cell that belongs to infarct scar segments. (c) Exemplify the early repolarization cell that belongs to isthmus scar segments. (d) Exemplify the decreasing potential magnitude cell that belongs to distant scar segments. Green line: normal TMP and red line: abnormal TMP.

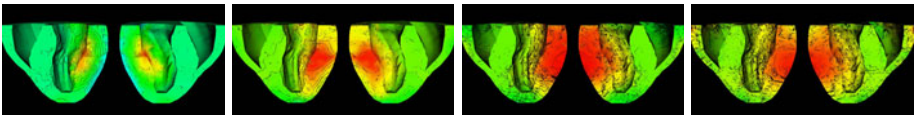

(a) (b) (c) (d)

Fig. 7. (a)-(d) Dynamic co-clustering of the TMP cells in case 2. Left to right: 10.38ms, 20.63ms, 215.42 ms, 246.18ms after the onset of the ventricular activation. The color encodes the TMP value from max (red area) to min (green area) while the black contours represent isochrones of the TMP.

Table 1. The (mean ± SD) percentages of cells that have abnormality TMP dynamics on each region

Size of the infarct region	Infarct scar region	Isthmus scar region	Distant scar regions
0 - 10 %	30.25% ± 14.35%	29.25% ± 7.22%	40.58% ± 8.26%
10 - 20 %	52.8% ± 14.88%	23% ± 7.17%	24.4% ± 10.8%
≥ 20 %	74.83% ± 9.66%	13.5% ± 5.57%	11.67% ± 8.57%

Table 2. The (mean ± SD) percentages of cells that have abnormality TMP dynamics on each location

Location of the infarct	Infarct scar region	Isthmus scar region	Distant scar regions
anterior	69.8% ± 20.32%	14.4% ± 8.82%	15.8% ± 12.67%
inferior	62% ± 16.29%	18.6% ± 7.36%	19.4% ± 11.88%
lateral	75% ± 10.81%	14.8% ± 6.09%	10.2% ± 7.82%
septal	57% ± 10.74%	32% ± 5.19%	10.8% ± 6.45%

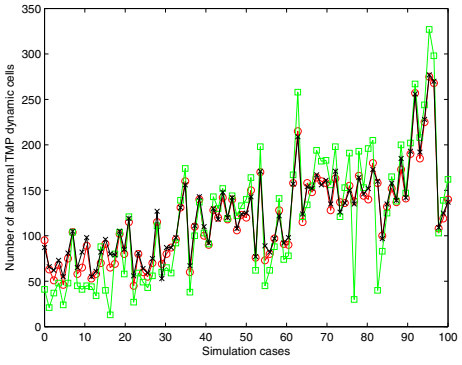

Fig. 8. Comparison results: red line: ground truth (GT), black line: co-clustering results after adding Gaussian noise, green line: K-means results

3.3 Quantitative Analysis

We test the algorithm on 100 simulated cases and observe that the number of cells with abnormal TMP dynamics changes with the size and location of the infarct region. This observation coincides with [18], which indicates that there is a delay of electrical activation in the isthmus region and additional activation delay occurred in remote regions. Tables 1 and 2 summarize the percentages of cells with abnormality TMP dynamics of three different regions based on the size and location of the infarction. In the infarct scar region, we notice that while the infarct scar size becomes larger, the TMP dynamics abnormality increases. Contrarily, in the border and remote regions, when the infarct scar size gets larger the TMP dynamics abnormality decreases. Also, we observe that the lateral and anterior segments have larger abnormality TMP dynamics cells in the infarct scar region. The septal segments have the largest abnormality TMP dynamics cells in the boarder region, while the inferior segments have the largest abnormality TMP dynamics cells in remote regions.

4 Discussion and Conclusion

In this study, we presented a novel approach in analyzing TMP dynamics through spectral co-clustering of cardiac cells and time sequence (3D+T) performed on a TMP data matrix. The clustered TMP dynamics, i.e. normal/abnormal, exhibits high correlation with certain time steps. The adapted algorithm is robust because it out performs the simple K-means clustering algorithm even when adding Gaussian noise, as depicted in figure 8. Furthermore, our experimental results exhibit the advantage of this scheme in discovering latent classes of the TMP dynamics with different locations and sizes of the transmural infarct scars. This opens up new themes that can be investigated for understanding the TMP dynamics and tissue excitability simultaneously, and considering spatial classification of the TMP dynamics.

References

1. Wang, L., Wong, K., Zhang, H., Liu, H., Shi, P.: Noninvasive Computational Imaging of Cardiac Electrophysiology for 3D Infarct Quantitation. IEEE Transactions on Biomed. Eng. 13 (December 2010)
2. Wang, L., Zhang, H., Wong, K., Liu, H., Shi, P.: Physiological Model Constrained Noninvasive Reconstruction of Volumetric Myocardial Transmembrane Potentials. IEEE Transactions on Biomedical Engineering 57(2) (February 2010)
3. Relan, J., Pop, M., Delingette, H., Wright, G.A., Ayache, N., Sermesant, M.: Estimation of Reaction, Diffusion and Restitution Parameters for a 3D Myocardial Model Using Optical Mapping and MRI. In: Camara, O., Pop, M., Rhode, K., Sermesant, M., Smith, N., Young, A. (eds.) STACOM 2010. LNCS, vol. 6364, pp. 270–280. Springer, Heidelberg (2010)
4. Relan, J., Sermesant, M., Pop, M., Delingette, H., Sorine, M., Wright, G.A., Ayache, N.: Volumetric Prediction of Cardiac Electrophysiology using a Heart Model Personalized to Surface Data. In: MICCAI Workshop, pp. 19–27 (2009)
5. Miller III, W.T., Geselowitz, D.B.: Simulation Studies of the Electrocardiogram; II. Ischemia and Infarction. J. ACM. Circ. Res. 43(2), 315–323 (1978)
6. Dhillon, I.S.: Co-clustering documents and words using bipartite spectral graph partitioning. In: Proceedings of the the Seventh ACM SIGKDD (2001)
7. Weiling, M., Nerboone, J.: Bipartite spectral graph partitioning to co-cluster varieties and sound correspondence in dialectology. In: Choudhuri, M. (ed.) Proc. Workshop on Graph-based Methods for Natural Lang. Processing, pp. 26–34 (2009)
8. Kluger, Y., Basri, R., Chang, J.T., Gerstein, M.: Spectral biclustering of microarray data: co-clustering genes and conditions. Genome Research 13, 703–716 (2003)
9. Kardesch, M., Hogancamp, C.E., Bing, R.J.: The effect of complete ischemia on the intracellular electrical activity of the whole mammalian heart. Circ. Res. 6, 715–720 (1958)
10. Samson, W.E., Scher, A.M.: Mechanism of S-T segment alteration during acute myocardial injury. Circ. Res. 8, 780–787 (1960)
11. Spach, M.S., Barr, R.C., Lanning, C.F., Tucek, P.C.: Origin of body surface QRS and T-wave potentials from epicardial potential distributions in the intact chimpanzee. Circulation 55, 268–278 (1977)
12. Ramanathan, C., Jia, P., Ghanem, R., Ryu, K., Rudy, Y.: Activation and repolarization of the normal human heart under complete physiological conditions. PNAS 103(16), 6309–6314 (2006)
13. Janse, M.J., Wit, A.L.: Electrophysiological mechanisms of ventricular arrhythmias resulting from myocardium ischemia and infarction. Physiol. Rev. 69, 1049–1169 (1989)
14. Taccardi, B.: Distribution of heart potentials on the thoracic surface of normal human subjects. Circ. Res. 12, 341 (1963)
15. Chung, F.: Spectral Graph Theory. American Mathematical Society Press, Providence (1997)
16. Nash, M.: Mechanics and material properties of the heart using an anatomically accurate mathematical model. Ph.D. dissertation, Univ. of Auckland (May 1998)
17. Cerqueira, M.D., Weissman, N.J., Dilsizian, V., Jacobs, A.K., Kaul, S., Laskey, W.K., Pennell, D.J., Rumberger, J.A., Ryan, T., Verani, M.S.: Standardized myocardial segmentation and nomenclature for tomographic imaging of the heart. Circulation 105, 539–542 (2002)

18. Shuros, A.C., Salo, R.W., Florea, V.G., Pastore, J., Kuskowski, M.A., Chandrashekhar, Y., Anand, I.S.: Ventricular Preexcitation Modulates Strain and Attenuates Cardiac Remodeling in a Swine Model of Myocardial Infarction. Circ. Res. 116, 1162–1169 (2007)
19. Aliev, R.R., Panfilov, A.V.: A simple two-variable model of cardiac excitation. Chaos, Solitions and Fractals 7(3), 293–301 (1996)

Cardiac Deformation from Electro-Anatomical Mapping Data: Application to Scar Characterization

A.R. Porras[1], G. Piella[1], Oscar Cámara[1], E. Silva[2], D. Andreu[2], A. Berruezo[2], and A.F. Frangi[1,3]

[1] CISTIB - Universitat Pompeu i Fabra, CIBER-BBN, Barcelona, Spain
[2] Hospital Clinic, IDIBAPS, Universitat de Barcelona, Barcelona, Spain
[3] Institucio Catalana de Recerca i Estudis Avanats (ICREA), Barcelona, Spain

Abstract. We propose in this paper a new way of calculating an endocardial end-systolic deformation parameter from electro-anatomical data acquired intra-operatively during electrophysiology interventions. The estimated parameter is then used to study deformation in regions with different viability properties: scar, border zone and normal myocardial tissue. These regions are defined based on electrophysiological data acquired with a contact mapping system, specifically with the bipolar voltage maps and a set of routinely used thresholds. The obtained results when applying our methodology on a set of 8 cases show statistically significant differences between the average deformation values of the scar, border zone and normal myocardial tissue areas, thus demonstrating the feasibility of detecting changes in deformation between normal and non-healthy tissue from electro-anatomical maps. Nevertheless, although low deformation regions more often correspond to non-healthy tissue, deformation is not an accurate indicator of viability abnormalities.

1 Introduction

Scar presence and its characteristics play a fundamental role in several cardiac pathologies. Most of ventricular tachycardias (VTs) present in patients with ischemia are produced by a re-entrance mechanism associated to the presence of scars [1], which are composed by areas of dense fibrosis that cause a conduction block, as well as other areas of fibrosis where it is possible to find myocardial cells with low-speed conduction [2]. Catheter ablation is an option for recurrent VT treatment. To improve its applicability and effectiveness, a detailed knowledge of the ventricular scar and border zone is required. In addition, it has been proven that scar location, morphology and physiology play an essential role on Cardiac Resynchronization Therapy (CRT) planning [3].

Several methods have been used to identify the region affected by the scar. Delay-Enhancement Magnetic Resonance Imaging (DE-MRI) allows quantifying the area with fibrosis and its level of transmurality, making it possible to detect and assess the myocardial viability. However, these images are obtained prior to the intervention, being its use for guidance during the ablation procedure hampered.

D.N. Metaxas and L. Axel (Eds.): FIMH 2011, LNCS 6666, pp. 47–54, 2011.

Therefore, electro-anatomical mapping is the most used way to locate the area to be treated. It basically consists in introducing one catheter into the ventricle and, with a tracking system, recording the position and electrical activity of different points on the endocardium wall. Since reduced endocardial voltage indicates electrically abnormal tissue, scar, border zone and normal tissue can be delimited according to their electrical activity. This approach has the advantage that it is an intra-procedure method and the same catheter can be used to perform the ablation. However, some studies have concluded that it is hard to establish absolute values that can be used to differentiate between scar, border zone and normal tissue for all patients [4]. Moreover, spatial resolution in this kind of procedures is usually very low.

To complement electrical information, mechanical properties can also be analyzed. This is actually possible with current electro-anatomical mapping systems since trajectories for each acquired point are recorded, allowing motion of the heart wall to be estimated and hence providing information on cardiac mechanics [5]. During the last few years, the idea of extracting motion/deformation from electro-anatomical mapping systems has started to be exploited, as it is the case of NOGA system (Biologics Delivery Systems Group, Cordis Corporation, Irwindale CA, USA), which provides a linear local shortening index [6] as an indicator of local contraction of the myocardium.

The main goal of this paper is to propose a new way to calculate deformation from CARTO XP (Biosense Webster, Haifa, Israel) electro-anatomical data [7] and to analyze how tissue viability defined by electrical data behaves in terms of deformation. We focus on deformation analysis rather than motion, since passive non-deforming regions can show motion due to tethering to adjacent regions and overall heart motion [8]. The deformation parameter is computed with a strain-like equation after point filtering, but projecting all points onto an estimation of the plane tangent to the endocardial surface.

2 Cardiac Deformation Estimation

CARTO XP is an electrophysiological contact mapping system mostly used for anatomical guidance of ablation procedures. The obtained electro-anatomical maps consist of electrical signals (recorded at 1kHz) and position data of the catheter (recorded at 100Hz) over 2.5s.

2.1 Data Pre-processing

Before the deformation analysis, some of the tracked points were removed to filter out possible acquisition errors, i.e. the catheter sliding over the endocardial wall or the contact of the catheter on the wall being unstable. For this study, points were removed according to the following two criteria:

1. Points whose positions in two consecutive cardiac cycles are too far away. We filtered those points whose distances between two consecutive end diastoles were greater than 10mm, in a similar way as proposed in [9]. End-diastole is

taken as reference because CARTO XP synchronizes all points according to the R-peak of the electro-cardiogram (end-diastole), so it is a good reference.
2. Isolated points that did not have any point closer than 25mm, since it makes local deformation estimation not reliable enough. This threshold has been chosen regarding to the mean distance between the points.

Furthermore, since motion and electrical data are sampled with different rates, motion data have been linearly interpolated.

2.2 Deformation Estimation

The following step in our proposed methodology is the deformation analysis, once position data have been resampled. For each analyzed point, the Endocardial End-Systolic Deformation (EESD) can be estimated from its Euclidean distance to the closest points in space by using the following expression:

$$EESD = \frac{L_{ED} - L_{ES}}{L_{ED}} \tag{1}$$

where L_{ED} is the distance between points at end-diastole, and L_{ES} represents the same distance at end-systole.

According to Eq. 1, areas with high deformation should ideally have a higher value (close to 1) for EESD than areas with low deformation (which should be close to 0), as long as the distance between points in end-systole is smaller than in end-diastole (which should be the normal situation).

This approach cannot, however, be directly applied over electro-anatomical data because each point is acquired in different time instants. Even though the mapping system synchronizes all points to the R-peak of the electro-cardiogram, there is a lack of synchronization away from this instant that is intrinsic to the acquisition procedure. This is illustrated in Fig. 1, where we can see two simplified examples of endocardial wall displacement between diastolic and systolic phases. In the ideal case, when there are no synchronization errors between neighboring points away from the trigger point, L_{ES} is shorter than L_{ED}. On the other hand, when two adjacent points are not in the same time instant of the cardiac cycle, L_{ES} can be equal or larger than L_{ED}.

In Fig. 1, we can appreciate that most of the error is introduced in the radial direction. Thus, part of the synchronization problem could be eliminated if we filter motion in this direction. This can be done by projecting the length vectors in a plane tangent to the endocardial wall surface.

However, we do not have enough data to accurately calculate such a tangent plane. Thus, we have estimated this plane by finding the spatial center of all points at end-diastole, so that a vector from one point to this center is a very coarse approximation to the radial direction. Since this direction is normal to the tangent plane, we just have to project point distances onto this plane and calculate the deformation parameter in Eq. 1 by using these projections rather than real distances, as illustrated in Fig. 2.

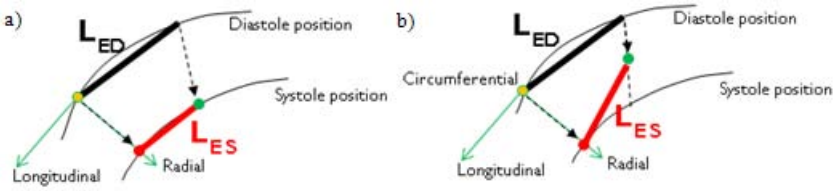

Fig. 1. a) Ideal situation for points acquired with electro-anatomical mapping systems, where L_{ES} is shorter than L_{ED}. b) Situation where for a certain acquisition time, two points are not in the same time instant of the cardiac cycle, so L_{ES} can be equal or larger than L_{ED}.

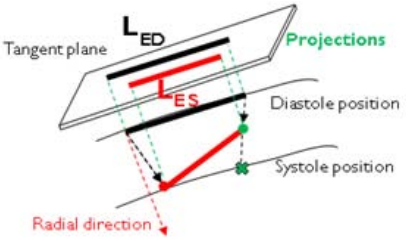

Fig. 2. Projection of end diastolic and end systolic distances onto the tangent plane. When projecting, L_{ES} is smaller or equal than L_{ED} in most cases.

2.3 Statistical Analysis

Data are expressed as mean ± standard deviation. Comparisons between all data were done using a Student's t-test and results were considered statistically significant at a p value lower than 0.05.

Moreover, a ROC analysis has been carried out to find out whether EESD can discriminate between normal and un-healthy tissue.

2.4 Clinical Data

For the deformation analysis, we have used electro-anatomical maps from 4 VT patients and 4 CRT patients (age 72.25 ± 4.71 years). The maps were acquired with CARTO XP and had an average of 380 ± 219 points (range 83 - 548 points) for VT patients and 76 ± 35 points (range 49 - 124) for CRT patients.

3 Results

Before the deformation analysis, 27.9 ± 11.6% points were filtered. Afterwards, EESD maps have been compared between scar, border zone and normal myocardial tissue. Tissue type has been defined according to their electrical activity, which is the currently used gold standard [10]. Hence, points whose maximum

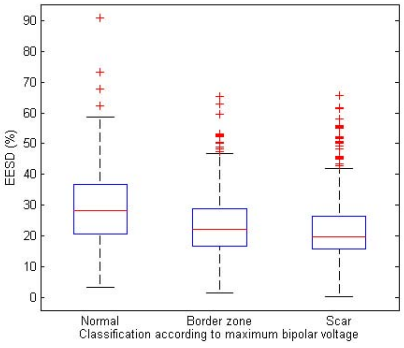

Fig. 3. Box plots showing the EESD distribution for all points. For each box, the central mark represents the median, the boxes represent the first and third quartiles and the crosses represent outliers.

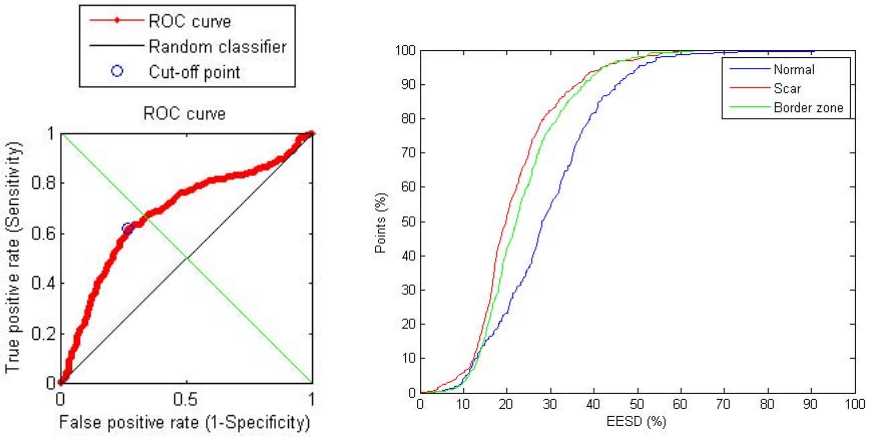

Fig. 4. On the left, a ROC curve when classifying normal from un-healthy tissue is represented. On the right, the cumulated percentage of points as function of deformation value for scar, border zone and normal tissue is shown.

bipolar voltage is lower than 0.5mV are considered as scar, while points with maximum bipolar voltage between 0.5mV and 1.5mV are defined as border zone.

Normal tissue showed a larger mean deformation than the border zone ($29 \pm 13\%$ vs. $24 \pm 10\%, p \leq 0.05$) and scar regions ($29 \pm 13\%$ vs. $22 \pm 10\%, p \leq 0.05$), while scar regions showed lower mean deformation than border zone ($22 \pm 10\%$ vs. $24 \pm 10\%, p \leq 0.05$). Fig. 3 shows the box plots of the EESD distribution for the points from all patients.

The ROC analysis for the EESD is shown in Fig. 4, where the obtained cut-off value that best discriminates un-healthy from normal tissue is 25.8%. The cumulated percentage of points for each deformation value is also represented.

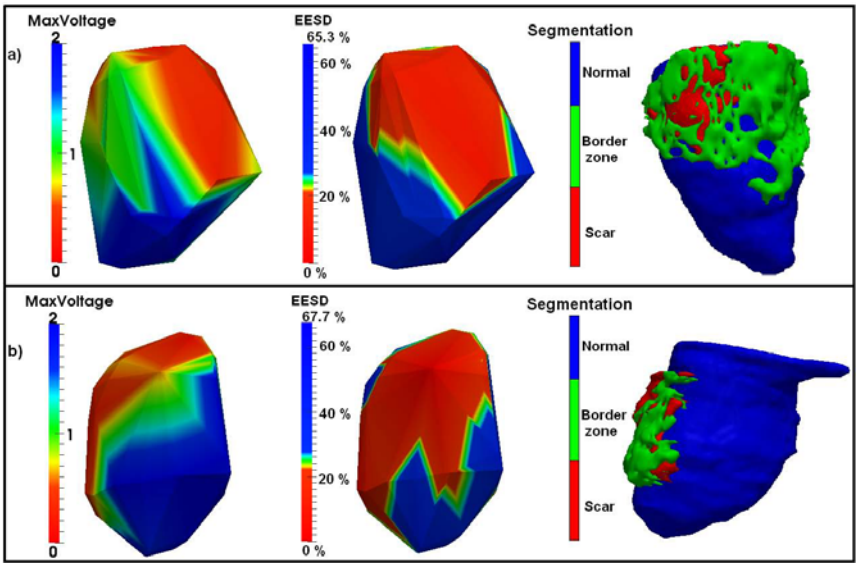

Fig. 5. Reconstruction of the left ventricle for two patients (a and b) from CARTO XP data. For each patient, maximum bipolar voltages (scale in mV) are shown on the left, EESD values are shown on the middle and manual segmentation from DE-MRI on the right. For the voltage maps, regions in red correspond to scar and regions in blue are related to normal tissue. For EESD maps, colors range from red (low EESD value) to blue (high EESD value).

Finally, in Fig. 5, a view of two patient's left ventricle reconstruction (with Delaunay triangulation) from CARTO XP data is shown, where both electrical and EESD data are represented. For visual comparison, a manual segmentation of scar, border zone and normal tissue from DE-MRI performed by experts has also been included.

4 Discussion

The obtained results suggest that points in normal myocardial tissue have a higher deformation than points in the scar. Moreover, points on the border zone seem to have a higher deformation than scar, but lower than normal tissue.

However, although the differences in EESD between the three kind of tissue are statistically significant, one can appreciate in Fig. 3 that there is a considerable overlap in their ranges. This is in agreement with previous studies using the NOGA system [11].

The ROC analysis shown in Fig. 4 suggests that, for the optimal EESD cut-off value, specificity and sensitivity are low. Moreover, 25% of normal points have a lower value for EESD than the cut-off value, and 29% of points in scar have a higher value. Hence, we can conclude that discrimination based only in the EESD would not be reliable with the data analyzed in this paper.

Under the hypothesis that regions with scar have a reduced deformation when compared to normal tissue, there is a considerable mismatching (as shown in Fig. 5) with respect to tissue classification based on electrical activity. This fact was partially expected, because deformation and electrical activity show two different and complementary characteristics of endocardial tissue. It is important to point out that the classification based on electrical activity has been done using absolute thresholds for bipolar voltages.

EESD computation is very dependent on the quality and proximity of the acquired points and thus, we are very conditioned by the acquisition method. The underlying problem is that, beside the measurement error of the tracking system, every point is acquired independently, so there is a general lack of synchronization that introduces an error. Furthermore, when acquiring a point, the catheter usually slides over the endocardial surface, as can easily be appreciated when visualizing its trajectory. Since deformation is very sensitive to small changes in motion between every two points, it is very affected by all these errors. It would be possible to filter out some of the artifacts present in the recorded motion signal if their nature was known. For example, the error introduced by respiration motion could be removed by filtering the frequencies associated to it, or the lack of synchronization between points could be overcome by applying signal re-synchronization methods. Nevertheless, the most important artifact is produced by the catheter sliding over the endocardial and it would be very difficult to automatically detect and remove it.

5 Conclusions

In this paper, we have proposed a new way for estimating deformation from electro-anatomical data acquired with a widely used contact mapping system. We found that, even though there is a statistically significant difference between the mean of EESD for scar, border zone and normal tissue, low deformation is not always an indicator of low electrical activity. Dually, high deformation does not always correspond to normal electrical activity.

These results are limited by the sparse spatial information and the various sources of error derived from the acquisition procedure. Hence, it would be necessary to use data from other intra-operative modalities to improve on the reliability of the deformation computation.

Future work includes a co-registration of CARTO data to DE-MRI segmentation to quantify its correspondence with the EESD proposed.

Aknowledgements

This research has been partially funded by the Industrial and Technological Development Center (CDTI) under the CENIT-cvREMOD program. The work by O. Camara is supported by the Spanish Ministry of Science and Innovation through the Ramon y Cajal Program.

References

[1] Svenson, W.G.: Ventricular scars and ventricular tachycardia. Transactions of the American Clinical and Climatological Association 120, 403–412 (2009)
[2] de Bakker, J., van Capelle, F., Janse, M., Tasseron, S., Vermeulen, J., de Jonge, N., Lahpor, J.: Slow conduction in the infarcted human heart. 'zigzag' course of activation. Circulation 88(3), 915–926 (1993)
[3] Duckett, S.G., Ginks, M., Shetty, A.K., Knowles, B.R., Totman, J.J., Chiribiri, A., Ma, Y.L., Razavi, R., Schaeffter, T., Carr-White, G., Rhode, K., Rinaldi, C.A.: Realtime fusion of cardiac magnetic resonance imaging and computed tomography venography with x-ray fluoroscopy to aid cardiac resynchronisation therapy implantation in patients with persistent left superior vena cava. Europace (2010)
[4] Botker, H.E., Lassen, J.F., Hermansen, F., Wiggers, H., Sogaard, P., Kim, W.Y., Bottcher, M., Thuesen, L., Pedersen, A.K.: Electromechanical mapping for detection of myocardial viability in patients with ischemic cardiomyopathy. Circulation 103, 1631–1637 (2001)
[5] Camara, O., Oeltze, S., De Craene, M., Sebastian, R., Silva, E., Tamborero, D., Mont, L., Sitges, M., Bijnens, B.H., Frangi, A.F.: Cardiac motion estimation from intracardiac electrical mapping data: Identifying a septal flash in heart failure. In: Ayache, N., Delingette, H., Sermesant, M. (eds.) FIMH 2009. LNCS, vol. 5528, pp. 21–29. Springer, Heidelberg (2009)
[6] Psaltis, P., Worthley, S.: Endoventricular electromechanical mapping the diagnostic and therapeutic utility of the noga xp cardiac navigation system. Journal of Cardiovascular Translational Research 2, 48–62 (2009)
[7] Ben-Haim, S., Osadchy, D., Schuster, I., Gepstein, L., Hayam, G., Josephson, M.: Nonfluoroscopic, in vivo navigation and mapping technology. Nature Medicine 2(12), 1393–1395 (1996)
[8] Gorcsan, John, I.: Echocardiographic Strain Imaging for Myocardial Viability: An Improvement Over Visual Assessment? Circulation 112(25), 3820–3822 (2005)
[9] Klemm, H., Ventura, R., Franzen, O., Baldus, S., Mortensen, K., Risius, T., Willems, S.: Simultaneous mapping of activation and motion timing in the healthy and chronically ischemic heart. Heart Rhythm 3(7), 781–788 (2006)
[10] Dickfeld, T., Lei, P., Dilsizian, V., Jeudy, J., Dong, J., Voudouris, A., Peters, R., Saba, M., Shekhar, R., Shorofsky, S.: Integration of three-dimensional scar maps for ventricular tachycardia ablation with positron emission tomography-computed tomography. JACC: Cardiovascular Imaging 1(1), 73–82 (2008)
[11] Samady, H., Liu, Y., Choi, C., Ragosta, M., Pfau, S., Cleman, M., Powers, E., Kramer, C., Wackers, F., Beller, G., Watson, D.: Electromechanical mapping for detecting myocardial viability and ischemia in patients with severe ischemic cardiomyopathy. The American Journal of Cardiology 91(7), 807–811 (2003)

Comparing Image-Based Respiratory Motion Correction Methods for Anatomical Roadmap Guided Cardiac Electrophysiology Procedures

YingLiang Ma[1], Andy P. King[1], Nicolas Gogin[2], Geert Gijsbers[3], C. Aldo Rinaldi[4], Jaswinder Gill[4], Reza Razavi[1], and Kawal S. Rhode[1]

[1] Division of Imaging Sciences, King's College London, SE1 7EH, UK
[2] Medisys Research Lab, Philips Healthcare, France
[3] Philips Healthcare, Netherlands
[4] Department of Cardiology, Guy's & St. Thomas' Hospitals NHS Foundation Trust, London, SE1 7EH, UK
y.ma@kcl.ac.uk

Abstract. X-ray fluoroscopically guided cardiac electrophysiological procedures are routinely carried out for diagnosis and treatment of cardiac arrhythmias. X-ray images have poor soft tissue contrast and, for this reason, overlay of static 3D roadmaps derived from pre-procedural volumetric data can be used to add anatomical information. However, the registration between the 3D roadmap and the 2D X-ray data can be compromised by patient respiratory motion. Three methods were evaluated to correct for respiratory motion using features in the X-ray image data. The first method is based on tracking either the diaphragm or the heart border using the image intensity in a region of interest. The second method detects the tracheal bifurcation using the generalized Hough transform and a 3D model derived from pre-operative image data. The third method is based on tracking the coronary sinus (CS) catheter. All three methods were applied to X-ray images from 18 patients undergoing radiofrequency ablation for the treatment of atrial fibrillation. The 2D target registration errors (TRE) at the pulmonary veins were calculated to validate the methods. A TRE of 1.6 mm ± 0.8 mm was achieved for the diaphragm tracking; 1.7 mm ± 0.9 mm for heart border tracking; 1.9 mm ± 1.0 mm for trachea tracking and 1.8 mm ± 0.9 mm for CS catheter tracking. We also present a comparison between our techniques with other published image-based motion correction strategies.

1 Introduction

Cardiac electrophysiological (EP) procedures are traditionally carried out under X-ray fluoroscopic guidance to diagnose and treat cardiac arrhythmias. However, X-ray images have poor soft tissue contrast and it is difficult to interpret the anatomical context directly from these images. To overcome the lack of soft tissue contrast, a three-dimensional (3D) roadmap can be generated from 3D high-resolution computed tomography (CT)/ magnetic resonance images (MRI), registered and overlaid in real-time with X-ray fluoroscopy images [1]. Currently, the 3D roadmap remains static and does not move with the patient's respiratory motion. In some cases, respiratory motion can cause a two-dimensional (2D) registration error of over 14 mm [2], which

D.N. Metaxas and L. Axel (Eds.): FIMH 2011, LNCS 6666, pp. 55–62, 2011.

is a significant compromise in the accuracy of guidance. A number of groups have addressed the issue of respiratory motion correction in the literature. Motion-compensated navigation for coronary interventions based on magnetic tracking was suggested in [3], but it required additional special hadware. Several image-based approaches have been developed that use only information from the X-ray fluoroscopic images themselves. Shechter et al. [4] constructed a model of cardiac and respiratory motion of the coronary arteries from biplane contrast-enhanced X-ray image sequences. The model was applied by tracking the motion of the diaphragm in subsequent (non-enhanced) X-ray images. However, forming the model from X-ray images under contrast injection means that it will be constructed from a limited amount of data. Furthermore, the diaphragm is not always in the X-ray field of view, particularly for obese patients. Brost et al. [5] developed an image-based respiratory motion correction method for EP procedures by tracking the 3D position of a lasso catheter from biplane X-ray images. Unlike tracking the diaphragm, this method directly tracks an instrument very close to the target region of the EP procedure. However, it also has some limitations. Firstly, the lasso catheter is particular for only a subset of EP procedures and it does not always remain stationary inside the heart. Secondly, the majority of X-ray systems are monoplane systems. Finally, the maximum frame rate of the lasso catheter tracking was only 3 frames per second and the tracking method required manual initialization.

The aim of our study was to develop and clinically evaluate respiratory motion compensation techniques for anatomical roadmapping for guiding cardiac EP interventions, particularly catheter radiofrequency ablation (RFA) for atrial fibrillation (AF), which is now one of the most common reasons for cardiac catheterization. The techniques needed to have accuracy within the clinical requirement of less than 5mm (determined by the typical size of the targeted structures, i.e. the PVs). They needed to be clinically robust and also have minimal interference with the routine clinical workflow. For the latter reason, we opted for approaches that used features present in the X-ray fluoroscopy image data, i.e. 2D image-based motion correction methods. Three approaches were implemented and clinically evaluated. The first method was based on tracking the diaphragm or the heart border, both of which are commonly observed in cardiac fluoroscopic images, even at very low radiation doses. This method tracks the image intensity within a manually defined rectangular region of interest (ROI) that lies across the diaphragm or heart border. The second approach that was used was to automatically track the tracheal bifurcation using the generalized Hough transform (GHT) for detection. The third method was to track the coronary sinus (CS) catheter from X-ray images using a catheter detection technique. We validate these three methods by computing the 2D target registration errors (TRE) at the pulmonary veins. In addition, we compare our methods with other published methods in the terms of speed, accuracy and robustness.

2 Method

2.1 Diaphragm or Heart Border Tracking

For the diaphragm or heart border tracking technique, a rectangular ROI was manually selected in which the motion of the diaphragm or heart border was visible

and no other radiographically dense features were present (see figure 1). One X-ray image was chosen as a reference. The diaphragm or heart border motion of subsequent X-ray images was determined by computing the 1D translation (along the long axis of the rectangle) that minimised the mean sum of squared differences between the intensities in the current image and the reference image within the ROI. A simple translational model similar to the one commonly employed in MRI image acquisition [6] was used to apply the 1D displacement of the diaphragm or heart border to the 3D heart roadmap. The 1D motion scaling factor for diaphragm was set to 0.6 (same as used in MRI) and the 1D motion scaling factor for heart border was set to 1 as heart was tracked directly. Finally, the 3D heart roadmap was translated along the head-to-foot vector of the patient by the 1D displacement.

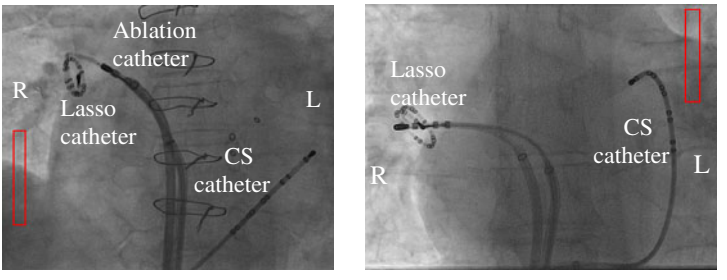

(a) diaphragm tracking (b) heart border tracking

Fig. 1. Tracking diaphragm (panel a) and tracking heartborder (panel b) in EP X-ray images. Red rectangle is the region of interest.

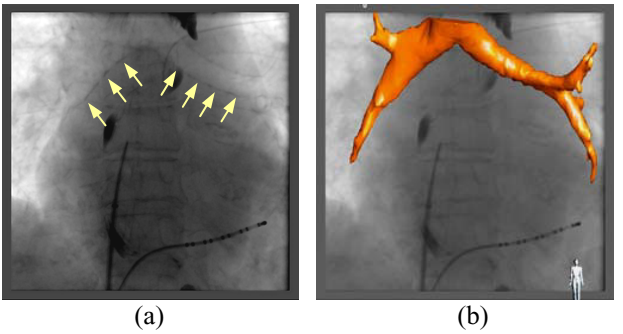

(a) (b)

Fig. 2. (a) An X-ray image showing the tracheal bifurcation. (b) A 3D model of the tracheal bifurcation derived from CT data is overlaid on to the X-ray fluoroscopic image.

2.2 Tracheal Bifurcation Detection

The tracheal bifurcation is located immediately above the LA and moves in a similar way to the LA during respiratory motion. It is clearly visible in cardiac X-ray fluoroscopic images (figure 2a). The Generalized Hough Transform (GHT) was used to detect the bifurcation in the X-ray images. A 3D model of the trachea (figure 2b) was derived from the pre-operative image data and then registered and projected onto the X-ray images to produce a 2D contour model. The contour model was used as a

template to match similar shapes in the X-ray images using the GHT. For tracking the tracheal bifurcation in X-ray fluoroscopic images, a Gaussian smoothing filter was first applied to the X-ray image followed by a Canny edge detector using the Sobel operator to find all edges. The edge map was then binarized using Otsu's algorithm [7] and the edges were iteratively thinned until they were one-pixel wide. Finally the contour model is used to search the optimal matched position in the binarized edge map using the GHT.

2.3 CS Catheter Detection

We developed a real time CS catheter tracking technique in [8]. This method first uses a fast multi-scale blob detection method to detect all possible electrode-like objects in the X-ray image. Based on prior knowledge of the CS catheter geometry, a cost function was designed to identify the CS catheter from all catheter-like objects. The reason for choosing the CS catheter instead of other catheters is that it is ubiquitously present during EP procedures. The CS catheter has several electrodes which are highly visible in normal dose and low dose X-ray images. Furthermore, the CS catheter remains in place throughout the procedure, its position is not routinely altered and it is normally not close to other catheters. Figure 3 gives an example of CS catheter detection.

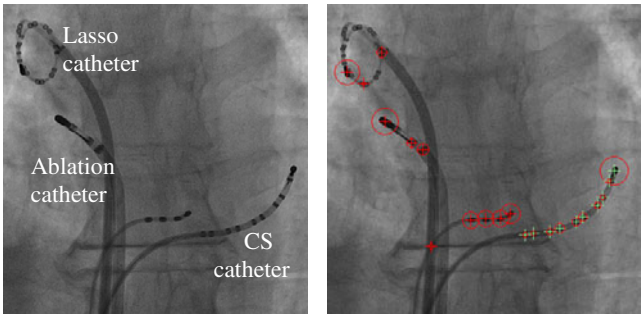

Fig. 3. An example result from the CS catheter detection method. Green crosses are the positions of CS catheter electrodes. Red crosses are the positions of other catheter electrodes. The size of the red circles represents the strength of the blobs.

3 Results

The tracking errors of the methods are first given. CS catheter tracking error was presented in [8] and we achieved 2D detection error of 0.39 mm ± 0.22 mm for all electrodes of the CS catheter. Then the validation of the motion correction methods is presented using the lasso catheter.

3.1 Diaphragm and Heart Border Tracking Errors

A clinical expert manually picked a center point along the border of the diaphragm or heart within the rectangular ROI. The error of tracking is defined as the 1D absolute

difference between the manually tracked point and the automatically tracked point along the long axis of the region of the interest. 1145 clinical X-ray fluoroscopic images were used to test the accuracy of tracking. There were a total of 25 different clinical fluoroscopy sequences which came from 18 clinical EP cases. 29% of the clinical X-ray images that were tested were low dose and contained high frequency noise. All X-ray images were 512×512 pixels in resolution. To estimate the ratio from pixel to mm R_{xray} in X-ray images, the X-ray DICOM file header information is used. Although the DICOM header gives the ratio R_{dicom} from pixel to mm, it is only correct when the magnification factor M of X-ray system is 1.0. The magnification factor M is computed using $M = D_{\det} / D_{pat}$, where $D_{\det}$ is the distance from X-ray source to the detector and D_{pat} is the distance from X-ray source to the patient. Finally, $R_{xray} = R_{dicom} / M$. The errors of diaphragm and heart border tracking in normal dose X-ray images were 1.2 ± 0.9 pixels (0.3 ± 0.2 mm). The errors in low dose X-ray images were 1.9 ± 1.3 pixels (0.5 ± 0.3 mm).

3.2 Tracheal Bifurcation Detection Errors

The tracheal bifurcation detection method was evaluated on the same dataset. However, only the X-ray sequences with the tracheal bifurcation within the field of view were selected. The total number of X-ray images used was 954 from 20 sequences which came from 18 clinical EP cases. 32% of the X-ray images were low dose and contained high frequency noise. The 3D models of the tracheal bifurcation were derived from pre-operative image data. There were 6 clinical cases using CT data, 4 cases using rotation X-ray angiography (RXA) and 8 cases using MRI. The tracheal bifurcation was automatically segmented from 3D high-resolution whole heart image data using a region growing algorithm followed by manual correction. To evaluate the detection errors, the bifurcation point was manually annotated on each X-ray frame by a clinical expert. This provided the ground-truth. The 3D trachea model was manually registered with a 2D X-ray image. In the subsequent frames, 2D translations were applied to the 2D trachea contour model. The detection errors were defined as the 2D distance between the manually defined bifurcation point and the bifurcation point in the trachea contour model. The model was positioned in 2D by the highest score from the GHT. Table 1 gives the errors of the trachea detection. All calculations were carried out on 512×512 resolution X-ray images.

Table 1. The 2D errors of the tracheal bifurcation detection. (Two figures are given for each modality: the 50% and 95% percentile errors. These represent the maximum detection errors of the lowest 50% and 95% of the tests respectively.).

	CT		MR		RXA	
	50%	95%	50%	95%	50%	95%
Normal dose image	1.9 pixels 0.5 mm	2.7 pixels 0.7 mm	7.7 pixels 2.1 mm	48.7 pixels 12.8 mm	2.0 pixels 0.5 mm	3.1 pixels 0.8 mm
Low dose image	5.8 pixels 1.5 mm	40.4 pixels 10.5 mm	44.5 pixels 11.7 mm	55.5 pixels 14.6 mm	N/A	N/A

3.3 Validation Using the Lasso Catheter

The intended application of the image-based tracking techniques was to update the position of a 3D roadmap. Therefore, the target registration error (TRE) was computed for the main validation of the approaches. Previous papers [2, 4] have reported motion error figures as a percentage of the total motion recovered. The percentage of motion recovered is calculated as

$$M_{rec} = 100\% * (TRE_{before} - TRE_{after}) / TRE_{before}$$

where TRE_{before} and TRE_{after} are the TREs before and after respiratory motion correction. A lasso catheter is often used in EP procedures. The lasso catheter is normally placed inside the PVs to be used as a mapping/measurement catheter. For the image sequences in which the lasso catheter was used for validation of accuracy, it remained stable in one of the PVs for all the X-ray frames evaluated (assessed by a clinical expert). For validation using the lasso catheter, 1D or 2D translational motion is applied to the 2D position of the lasso catheter tip electrode which acts as a surrogate for the position of the PVs since it is rigidly placed within these structures during the procedure. For the diaphragm and heart border tracking based motion correction strategies, the 1D translation along the long axis of the ROI was used. For the trachea tracking based approach, 2D translational motion was directly used. For the CS catheter based approach, filtered 2D translational motion was used. The TRE was computed as the distance error between this predicted position of the lasso catheter tip electrode and the actual position of the lasso catheter tip electrode in the X-ray data. The positions of the lasso catheter tip were manually annotated by a clinical expert. The TRE was calculated at the PVs on 418 fluoro images (8 patients). All X-ray images are normal dose which is suitable for the trachea-based motion compensation approach. The pre-operative image was either CT or RXA data. Table 2 gives the comparison of TREs among all motion correction strategies.

Table 2. TRE before and after motion correction using lasso catheter validation

TRE (mm)	Diaphragm	Heart border	Trachea	CS catheter
Before	4.7 ± 1.7	4.7 ± 1.7	4.7 ± 1.7	4.7 ± 1.7
After	1.6 ± 0.8	1.7 ± 0.9	1.9 ± 1.0	1.8 ± 0.9
Motion Recovered	45%~75%	41%~74%	39%~71%	37%~72%

4 Conclusion and Discussions

Three image-based motion correction approaches have been developed and evaluated. Image-based approaches do not require any fiducial markers, additional contrast agent or special hardware and do not interfere with the clinical work-flow. Each approach has its advantages and disadvantages. Diaphragm tracking is fast and free of cardiac cycle motion. Heart border tracking is also fast but can be influenced by cardiac cycle

motion. However, considering the case of an obese patient, the diaphragm is not often in the field of view so heart border tracking can be used instead. Furthermore, diaphragm tracking requires a motion correction factor (0.6) which may not be valid for all patients. Both methods require manually defined ROIs which are free of other features such as guide wires or catheters. The ROI may have to be changed often due to C-arm rotation, changing contrast and features moving into the region of interest. However, from the experience of 18 clinical EP cases, tracking the heart border is easier than tracking the diaphragm as the heart border shadow often has better contrast than the shadow of the diaphragm and it is always in the field of view. In 2 cases, when the left heart border was tracked and the patient heart was aligned to the iso-center of the X-ray system, the ROI did not have to be changed even if the C-arm was rotated through the normal clinical range. Both methods are computationally efficient and simple to implement. Furthermore, as both methods track soft tissue, they can be used at anytime during EP procedures.

Tracking the trachea gives only respiratory motion and the trachea is very close to the primary target of left atrium of the procedures. However, it becomes less robust and accurate when it is used for low dose X-ray images. This is because low dose X-ray images have fewer strong edges for the tracheal bifurcation and this causes the GHT method to detect the wrong object. The trachea detection method requires a 3D model to generate the 2D GHT contour model. In this study, it was found that the pre-operative 3D MRI image data was least suitable for generating the 3D tracheal model. This was caused by the low contrast of the tracheal bifurcation in the MR images and the region growing method yielded a noisy and truncated model of the trachea. Truncated bronchi generate less edge information for the GHT contour model and the GHT becomes less robust. As a conclusion, the trachea detection based motion correction approach should be used in normal dose X-ray fluoroscopic images with a pre-operative 3D image data set acquired using CT or RXA. The 2D translational motion of the tracheal bifurcation can be directly applied to the 3D roadmap to correct respiratory motion.

As a fully automatic method, real-time CS catheter detection in X-ray fluoroscopy images was developed and it is accurate and robust even in low dose fluoroscopy images as CS catheter electrodes remain highly visible. A sub-millimeter accuracy of CS catheter detection method was achieved. Updating the 3D roadmap by the filtered 2D motion of the CS catheter can significantly improve the accuracy of fluoroscopy overlays for cardiac EP procedures. The CS catheter detection method has several advantages. First, it is real-time so that as well as being used to detect respiratory motion it could potentially also be applied to the detection of the much faster cardiac cycle motion. Secondly, it does not require any user interaction and can detect the CS catheter position without defining a ROI in the X-ray image. Similar to the diaphragm and heart border tracking based approaches, the CS catheter detection based motion correction does not restrict which kind of pre-operative 3D image data can be used. However, the presence of cardiac cycle motion in the CS catheter is a potential disadvantage for respiratory motion correction. Table 3 summarizes the comparison among the methods as well as the lasso catheter tracking based motion correction method [5], King et al.'s patient-specific motion correction method [2] and Shechter's prospective motion correction method [4].

Table 3. Comparison among respiratory motion correction methods. (unit of tracking speed is frames per second).

	Tracking error (mm)	Success rate	With cardiac motion	Tracking Speed	Motion Recovered (average)	X-ray Image Dose
Diaphragm	0.4 ± 0.3	100%	No	>30	65%	Low/Normal
Heart border	0.4 ± 0.3	100%	Yes	>30	63%	Low/Normal
Tracheal bifurcation	0.8 ± 0.2	96.7% *	No	3	61%	Normal
CS catheter	0.4 ± 0.2	99.3%	Yes	21	60%	Low/Normal
Lasso catheter	0.6 ± 0.3	N/A	Yes	3	N/A	N/A
King *et al.* Method	N/A	100%	No	>30	66%	Low/Normal
Shechter's Method	N/A	N/A	Yes	N/A	63%	Normal

A successful detection is defined as the detection error is within 5 mm, which is the radius of the pulmonary veins.
*Please note that the success rate of trachea detection excludes tests carried out on the low dose X-ray images and the clinical cases using MR pre-operative image data.

References

1. Rhode, K.S., Hill, D.L.G., Edwards, P.J., Hipwell, J., Rueckert, D., Sanchez-Ortiz, G., Hegde, S., Rahunathan, V., Razavi, R.: Registration and Tracking to Integrate X-ray and MR Images in an XMR facility. IEEE Transactions on Medical Imaging 24(11), 810–815 (2003)
2. King, A.P., Boubertakh, R., Rhode, K.S., Ma, Y.L., Chinchapatnam, P., Gao, G., Tangcharoen, T., Ginks, M., Cooklin, M., Gill, J.S., Hawkes, D.J., Razavi, R.S., Schaeffter, T.: A Subject-specific Technique For Respiratory Motion Correction in Image-guided Cardiac Catheterisation Procedures. Med. Image. Anal. 13(3), 419–431 (2009)
3. Timinger, H., Krueger, S., Dietmayer, K., Borgert, J.: Motion Compensated Coronary Interventional Navigation by Means of Diaphram Tracking and Elastic Motion Models. Phys. Med. Biol. 50(3), 491–503 (2005)
4. Shechter, G., Shechter, B., Resar, J.R., Beyar, R.: Prospective Motion Correction of X-ray Images for Coronary Interventions. IEEE Transactions on Medical Imaging 24(4), 441–450 (2005)
5. Brost, A., Liao, R., Hornegger, J., Strobel, N.: 3-D Respiratory Motion Compensation during EP Procedures by Image-based 3-D Lasso Catheter Model Generation and Tracking. In: Yang, G.-Z., Hawkes, D., Rueckert, D., Noble, A., Taylor, C. (eds.) MICCAI 2009. LNCS, vol. 5761, pp. 394–401. Springer, Heidelberg (2009)
6. Wang, Y., Riederer, S.J., Ehman, R.L.: Respiratory Motion of the Heart: Kinematics and the Implications for the Spatial Resolution in Coronary Imaging. Magnetic Resonance in Medicine 33(5), 713–719 (1995)
7. Otsu, N.: A Threshold Selection Method from Gray-level Histograms. IEEE Transactions on Systems, Man and Cybernetics 9(1), 62–66 (1979)
8. Ma, Y., King, A.P., Gogin, N., Rinaldi, C.A., Gill, J., Razavi, R., Rhode, K.S.: Real-Time Respiratory Motion Correction for Cardiac Electrophysiology Procedures Using Image-Based Coronary Sinus Catheter Tracking. In: Jiang, T., Navab, N., Pluim, J.P.W., Viergever, M.A. (eds.) MICCAI 2010. LNCS, vol. 6361, pp. 391–399. Springer, Heidelberg (2010)

Automatic Segmentation of Left Atrial Scar from Delayed-Enhancement Magnetic Resonance Imaging

Rashed Karim[1], Aruna Arujuna[1,2], Alex Brazier[1], Jaswinder Gill[1,2], C. Aldo Rinaldi[1,2], Mark O'Neill[1,2], Reza Razavi[1,2], Tobias Schaeffter[1], Daniel Rueckert[3], and Kawal S. Rhode[1]

[1] Division of Imaging Sciences and Biomedical Engineering, King's College London, UK
[2] Department of Cardiology, Guy's and St. Thomas' Hospitals NHS Trust, London, UK
[3] Department of Computing, Imperial College London, London, UK
{rashed.karim,aruna.arujuna,alex.brazier,
tobias.schaeffter,kawal.rhode}@kcl.ac.uk,
{jaswinder.gill,aldo.rinaldi,mark.oneill}@gstt.nhs.uk,
d.rueckert@imperial.ac.uk

Abstract. Delayed-enhancement magnetic resonance imaging is an effective technique for imaging left atrial (LA) scars both pre- and post- radio-frequency ablation for the treatment of atrial fibrillation. Existing techniques for LA scar segmentation require expert manual interaction making them tedious and prone to high observer variability. In this paper, we propose a novel automatic segmentation algorithm for segmenting LA scar based on a probabilistic tissue intensity model. This is implemented as a Markov random field-based energy formulation and solved using graph-cuts. It was evaluated against an existing semi-automatic approach and expert manual segmentations using 9 patient data sets. Surface representations were used to compare the methods. The segmented LA scar was expressed as a percentage of the total LA surface. Statistical analysis showed that the novel algorithm was not significantly different to the manual method and that it compared more favorably with this than the semi-automatic approach.

Keywords: delayed enhancement MRI, atrial fibrillation, scar segmentation, graph-cuts, Markov random fields.

1 Introduction

Atrial fibrillation (AF) is the most common cardiac arrhythmia and affects approximately 2.2 million people in the USA. A common treatment for AF is minimally-invasive catheter-based radio-frequency ablation (RFA) that aims to electrically isolate the pulmonary veins (PVs) from the left atrial body. The procedure is successful in 50-80% of patients. Assessment of the LA substrate in terms of scarring is important both pre- and post-RFA. The successful imaging of LA scars has been demonstrated using Gadolinium delayed enhancement (DE) magnetic resonance imaging (MRI) [1, 2] (see Fig. 1a). However, clinical interpretation of these data is difficult from tomographic images. Several strategies have been proposed for visualization including maximum intensity projection (MIP) onto a thick slice [1],

D.N. Metaxas and L. Axel (Eds.): FIMH 2011, LNCS 6666, pp. 63–70, 2011.

MIP onto a LA surface model [3] (see Fig. 1b), and 3D volume rendering [2]. Such visualization techniques provide more intuitive visualization and may have a role for guiding redo procedures [4], which are very common (20-50%). Quantification of the DE-MRI has been proposed using thresholding techniques for either endocardial surface-based segmentation [3] or volumetric segmentation [2]. Such quantification has been shown to predict likely response to RFA in clinical studies [5]. It will also be critical for applying cardiac biophysical models of AF for patient selection and RFA planning [6].

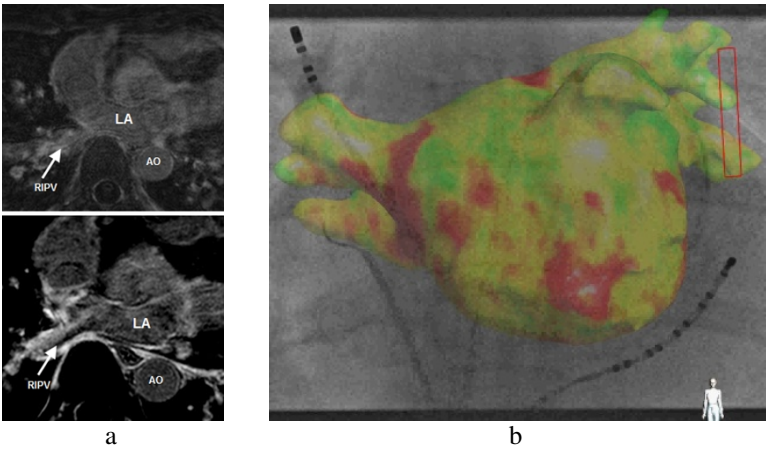

Fig. 1. (a) Example of left atrial Gadolinium delayed enhancement MR images; (top) pre-ablation; (bottom) post-ablation showing enhancement around the pulmonary veins. (b) Left atrial surface model with color-code scar information (red is scar) generated using maximum intensity projection of DE-MRI intensity to left atrial surface along surface normals [3]. The model is superimposed onto live X-ray fluoroscopy data to guide a redo ablation procedure.

Existing techniques [2, 3] for LA scar segmentation require expert user interaction making them tedious and prone to high inter- and intra-observer variability. In this paper, we propose a novel automatic LA scar segmentation algorithm based on a probabilistic tissue intensity model of DE-MRI data. This is implemented as a Markov random field (MRF)-based energy formulation and solved using graph-cuts. We evaluated our automatic method using 9 patient data and compare to expert manual and semi-automatic approaches [3].

2 Methods

2.1 Patient Protocol

9 patients with paroxysmal AF were recruited into the study under a local ethics committee approved protocol. The patients underwent RFA using wide area circumferential ablation to achieve isolation of the PVs. At 6 months post-ablation, the patients underwent MRI (1.5T Achieva, Philips Healthcare, The Netherlands).

The MR examination included (a) a 3D magnetic resonance angiography (MRA) scan with whole-heart coverage, reconstructed to 1mm isotropic resolution, following injection of a 0.4ml/kg double dose of a Gd-DTPA contrast agent; (b) a 3D respiratory-navigated and cardiac-gated, balanced steady state free precession (bSSFP) acquisition with whole-heart coverage, reconstructed to 1.3mm isotropic resolution; and (c) 20 minutes after contrast injection, the delayed enhancement scan, which was a 3D respiratory-navigated and cardiac-gated, inversion recovery turbo field echo with whole LA coverage, reconstructed to 1.3x1.3x2mm^3 resolution.

2.2 Left Atrium Segmentation and Image Registration

The best quality anatomical scan was selected from either the bSSFP or MRA scans and the endocardial boundary of the LA was segmented using an automatic approach based on a statistical shape model [7]. The automatic segmentation was verified by a clinical expert and manual corrections were made whenever required to achieve a high-fidelity result. The anatomical images were registered to the DE images using initialization by the DICOM header data, followed by affine registration [8]. Thereby the endocardial LA boundary was defined in the DE images.

2.3 Segmentation of Atrial Lesions

Segmentation Framework. The segmentation approach is based on a MRF-based energy formulation solved using graph-cuts [9]. Segmentation of scars from DE-MRI images can be described as assigning a label $f_p \in \{0,1\}$ to every voxel p in the image. Voxels representing scar tissue are assigned to the foreground class label $f_p = 1$ and non-scar tissues are assigned to the background class label $f_p = 0$. Given the observed intensities in the image and prior knowledge about scars, the segmentation problem can be solved using a probabilistic framework where the maximum *a posteriori* (MAP) estimate is computed using Bayes' theorem:

$$\text{argmax}_{\mathbf{f}}\, p(\mathbf{f}|\mathbf{I}) = \frac{p(\mathbf{I}|\mathbf{f})p(\mathbf{f})}{p(\mathbf{I})} \tag{1}$$

where $\mathbf{f}$ is the total label configuration and $\mathbf{I}$ are all observed intensities in the image. The image likelihood $p(\mathbf{I}|\mathbf{f})$ describes how likely is the observed image given a label configuration $\mathbf{f}$. The prior $p(\mathbf{f})$ encodes any prior knowledge of the tissue class labels (i.e. non-scar and scar tissue classes). Eq. 1 is commonly transformed into an MRF-based energy function over the neighborhood system N and labeling f:

$$E(f) = \lambda \sum_{p \in P} E_{\text{data}}(f_p) - \sum_{\{p,q\} \in N} E_{\text{prior}}(f_p, f_q). \tag{2}$$

The introduction of a weighting term λ weights the influence of the energy terms. The intensity energy E_{data} measures the disagreement between the *a prior* probabilistic model and the observed data, and E_{prior} is a smoothness term within a tissue class that penalizes any discontinuities between voxel pairs $\{p, q\}$. The scar segmentation problem is solved by minimization of the energy function described in Eq. 2. In the context of images, certain MRF-based energy functions are efficiently solved using

graph-cuts [9]. In this approach the image is represented as a graph $G = \langle V, E \rangle$ where each voxel in the image corresponds to a node. However, the node set V contains two special *terminal* nodes called the *source* and the *sink.* These represent the foreground (i.e. scar) and background (i.e. non-scar tissue) classes respectively. Every node in the graph has an edge to these terminal nodes, as well as neighbour-to-neighbour edge links that exist between neighboring nodes. The MRF-based energy function in Eq. 2 is coded into the edge weights. The optimal *cut* or partitioning of the graph into two disjoint sets with each set containing a terminal node solves the segmentation problem. The cost of the graph-cut is equal to the total energy of the corresponding segmentation.

Non-scar Tissue Priors. The intensity model for non-scar tissue provides the source edge weights in the graph. This is based on prior knowledge about different tissue classes that could possibly interface with scar. As scar tissue normally borders with a multitude of tissues, it is not possible to model non-scar tissues using a single, uni-modal Gaussian distribution. A multi-modal distribution is used that can be represented as a mixture of Gaussian distributions:

$$\sum_{i=1}^{n} a_i \, \mathbf{G}_i(\mu_i, \sigma_i) \tag{3}$$

where $\mathbf{G}_i$ is a Gaussian distribution for tissue i with mean μ_i and variance σ_i for some mixture proportion $a_i \in [0,1]$ and $\sum_{i=1}^{n} a_i = 1$. The non-scar tissue model is derived from the image to be segmented (i.e. unseen image). Given our segmentation of the LA endocardium from the anatomical images, regions of blood pool, atrial wall and pericardium can be approximated. This is accomplished by obtaining regions within fixed distances from the LA endocardium. For example, regions of blood pool and pericardium are obtained 5mm inside and outside the endocardial border, respectively. The atrial wall region is obtained 0-5 mm from the endocardium. See Fig. 2 for examples of the healthy tissue mixture model taken from two patients. However, as scarred tissue is also part of the atrial wall, the Gaussian in the mixture model most likely resulting from scar tissue is identified and eliminated. This is possible using an ROI corresponding to scar tissue that is selected by the operator. Assuming that the mean and variance of scar are μ_S and σ_S^2 respectively, then the Gaussian corresponding to index t has the maximum amount of overlap with the scar Gaussian within unit standard deviation and is subsequently eliminated:

$$t = \text{argmax}_i \big| |\mu_i \pm \sigma_i| - |\mu_S \pm \sigma_S| \big|. \tag{4}$$

Following the elimination of Gaussian $\mathbf{G}_t$, the weights of the remaining Gaussians of the mixture model are normalized to sum to one. It is also useful to take as user-input an ROI on normal myocardium selected by the operator. To incorporate this new normal myocardium Gaussian with mean and variance μ_M and σ_M into the existing tissue mixture model, the weights are adjusted based on ρ which weights the degree of confidence on the manual operator's normal myocardium selection with a higher ratio assigned for expert operators:

$$p\big(\mathbf{I} \big| f_p = 0\big) = (1-\rho) \sum_{i=1}^{n-\{t\}} a_i \, \mathbf{G}_i(\mu_i, \sigma_i) + \rho \mathbf{G}(\mu_M, \sigma_M). \tag{5}$$

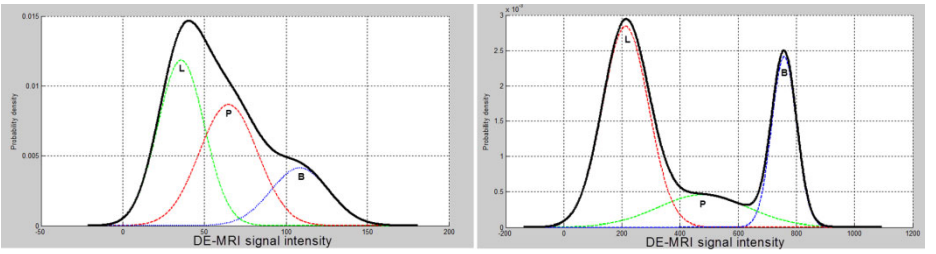

Fig. 2. The healthy tissue model computed in two patients. A Gaussian mixture density curve (in bold) is computed from individual Gaussians of the three tissue classes (L – lungs, P – pericardium, B – blood pool).

The parameters (a_i, μ_i, σ_i) of the Gaussian mixture model are obtained using the Expectation-Maximization (EM)-algorithm [10].

Scar Tissue Priors. The intensity model for scar is built from training data. This model corresponds to the intensity energy E_{data} in the MRF model (Eq. 2), and thus the sink edge weights in the flow-graph G. Scar tissue appears predominantly as areas of bright regions in DE-MRI. To derive an intensity distribution model for scar tissues, a Gaussian density function can be used:

$$p(\mathbf{I}|f_p = 1) = \frac{1}{\sqrt{2\pi\sigma^2}} \exp\left[-\frac{1}{2}\left(\frac{r-\mu}{\sigma}\right)^2\right] \tag{6}$$

where r is the ratio of DE-MRI signal of scar tissue to interfacing tissues with mean μ and variance σ. These are tissue classes which could possibly interact with scar tissues in the image. The parameters μ and σ are derived from training images which are expert hand-segmentations of scars in DE-MRI. The ratio r for each voxel in the unseen image is determined as the ratio of its intensity to mean blood pool and pericardium intensity.

Tissue Class Boundaries for Smoothness. To ensure continuity and smoothness within voxels of a tissue class through the E_{prior} term of the MRF energy function, neighboring voxels sharing similar intensities incur an exponentially high cost if they are classified into different tissue classes. The Lorentzian error norm [11] is employed, which is a robust metric for measuring intensity differences within a neighborhood:

$$\zeta(p,q) = \left(1 + \frac{1}{2}\left(\frac{|I_p - I_q|}{\sigma}\right)^2\right). \tag{7}$$

The scale σ can be estimated from the DE-MRI image and depends on the variance of the *actual* scar and non-scar tissue class intensity distributions. With decreasing scale, the algorithm becomes less forgiving to small difference in intensities. Given that it is technically challenging to acquire high quality DE-MRI scans that show a clear distinction between scar and non-scar tissue, a larger value for the scale σ is almost always preferred. For convenience, neighbour-to-neighbour edge links are

bounded above and below by $[0,1]$ and thus the edge-link weight assigned between neighbouring nodes is simply given by $1/(1+\zeta(p,q))$.

2.4 Evaluation of Novel Approach

The proposed automatic algorithm was evaluated with the 9 patient data using the leave-one-out principle, with 8/9 data used for training and 1/9 used as the unseen data. For comparison, the LA scars were manually segmented by two expert observers using the ITKSnap tool (www.itksnap.org). Furthermore, each data set was processed using the previously published semi-automatic approach of Knowles et al. [3]. This approach projects the maximum signal intensity from the DE data onto the LA endocardial surface along the surface normals. The segmentation is then achieved by applying a user-interactive threshold on the projected data. In order to make a comparison between the automatic, semi-automatic and manual segmentations, all segmentation results were projected onto the LA endocardial surfaces. All processing was carried out a 2.8 GHz PC.

3 Results

The pre-processing (LA segmentation and registration) was the same for each approach, i.e. automatic, semi-automatic and manual, and took typically 5 minutes. The novel automatic algorithm completed the segmentation process for each DE image in typically 30 seconds whereas the semi-automatic approach took typically 5 minutes. Manual segmentation of the scars took typically 45 minutes. See Fig. 3 for example results.

For each segmentation method, the amount of detected scar expressed as a percentage of the total LA surface was calculated (Fig. 4). Segmentations using the automatic algorithm approximated more closely to the manual segmentations than

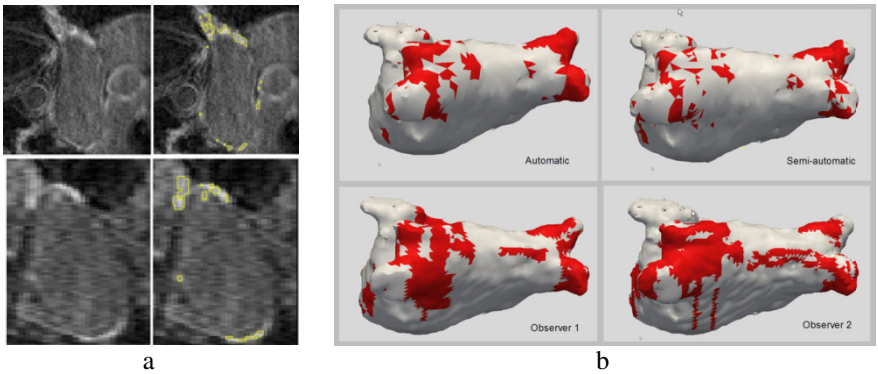

Fig. 3. Results from segmentation methods. (a) Automatic segmentations for patient 1 showing 2 example slices from the DE-MRI data; (left) original image data; (right) with segmentation annotations. (b) Surface representations for segmentations results for patient 2 showing automatic, semi-automatic and manual segmentations.

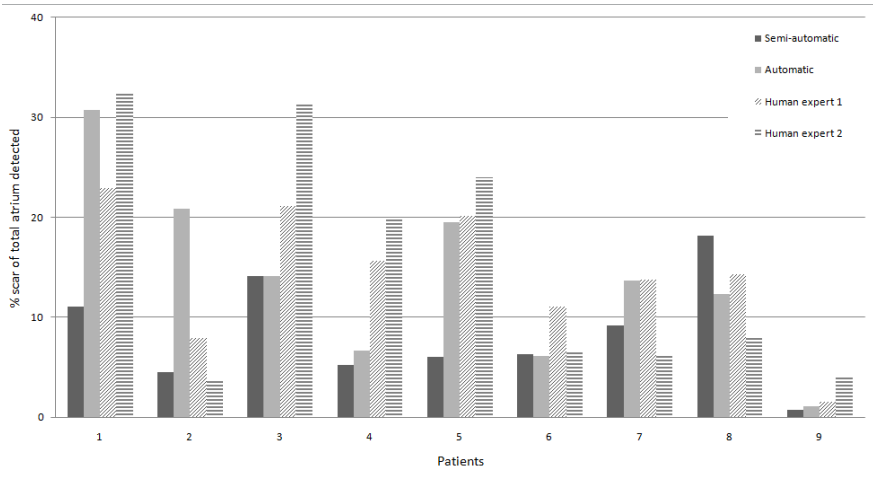

Fig. 4. Comparison of percentage scar in each patient for the different methods. Detected scar was expressed as a percentage of total LA surface.

Table 1. *p*-values from paired t-tests between each method with significant differences underlined. The significance level was set at 0.05.

p-values	Semi-auto	Auto	Observer 1	Observer 2
Semi-auto		0.09	0.10	0.01
Automatic			0.72	0.87
Observer 1				0.70

those using semi-automatic method, as confirmed this using a statistical paired *t*-test (Table 1). At a significance level of 0.05, there was no significant difference between the percentage scar detected in automatic and manual methods. In contrast, a significant difference was found between semi-automatic and one of the expert observers.

4 Discussion and Conclusion

In this paper, we have presented a novel automatic technique for segmenting scars in the LA using DE-MRI. The technique was applied to 9 patient data sets and the results compared to expert manual segmentations and segmentations from an existing semi-automatic approach. The automatic method was not significantly different from the manual method and compared more favorably to this than the semi-automatic approach. Furthermore, using the automatic method produces a considerable time-saving over using manual segmentation (30 seconds vs. 45 minutes) and some saving over the using semi-automatic method (30 seconds vs. 5 minutes). Most importantly, the automatic method results in a volumetric segmentation as opposed to a surface

segmentation, as for the semi-automatic method. This will be important for assessing transmurality of post-RFA scars. It is envisaged that user-independent lesion segmentation with low computational cost, as proposed in this paper, will allow for standardization of DE-MRI as a marker of cardiac injury. Future work will focus on improved training of the probabilistic intensity model and validation using a larger patient cohort with more expert segmentations per data set.

References

[1] Peters, D.C., Wylie, J.V., Hauser, T.H., Kissinger, K.V., Botnar, R.M., Essebag, V., Josephson, M.E., Manning, W.J.: Detection of pulmonary vein and left atrial scar after catheter ablation with three-dimensional navigator-gated delayed enhancement MR imaging: initial experience. Radiology 243(3), 690–695 (2007)

[2] McGann, C.J., Kholmovski, E.G., Oakes, R.S., Blauer, J.J., Daccarett, M., Segerson, N., Airey, K.J., Akoum, N., Fish, E., Badger, T.J., DiBella, E.V., Parker, D., MacLeod, R.S., Marrouche, N.F.: New magnetic resonance imaging-based method for defining the extent of left atrial wall injury after the ablation of atrial fibrillation. J. Am. Coll. Cardiol. 52(15), 1263–1271 (2008)

[3] Knowles, B.R., Caulfield, D., Cooklin, M., Rinaldi, C.A., Gill, J., Bostock, J., Razavi, R., Schaeffter, T., Rhode, K.S.: 3-D visualization of acute RF ablation lesions using MRI for the simultaneous determination of the patterns of necrosis and edema. IEEE Trans. Biomed. Eng. 57(6), 1467–1475 (2010)

[4] Reddy, V.Y., Schmidt, E.J., Holmvang, G., Fung, M.: Arrhythmia recurrence after atrial fibrillation ablation: Can magnetic resonance imaging identify gaps in atrial ablation lines? Journal of Cardiovascular Electrophysiology 19(4), 434–437 (2008)

[5] Oakes, R.S., Badger, T.J., Kholmovski, E.G., Akoum, N., Burgon, N.S., Fish, E.N., Blauer, J.J., Rao, S.N., DiBella, E.V., Segerson, N.M., Daccarett, M., Windfelder, J., McGann, C.J., Parker, D., MacLeod, R.S., Marrouche, N.F.: Detection and quantification of left atrial structural remodeling with delayed-enhancement magnetic resonance imaging in patients with atrial fibrillation. Circulation 119(13), 1758–1767 (2009)

[6] Reumann, M., Bohnert, J., Seemann, G., Osswald, B., Dössel, O.: Preventive ablation strategies in a biophysical model of atrial fibrillation based on realistic anatomical data. IEEE Trans. Biomed. Eng. 55(2 Pt 1), 399–406 (2008)

[7] Peters, J., Ecabert, O., Meyer, C., Schramm, H., Kneser, R., Groth, A., Weese, J.: Automatic whole heart segmentation in static magnetic resonance image volumes. Med. Image Comput. Comput. Assist. Interv. 10(Pt 2), 402–410 (2007)

[8] Schnabel, J.A., Rueckert, D., Quist, M., Blackall, J.M., Castellano-Smith, A.D., Hartkens, T., Penney, G.P., Hall, W.A., Liu, H., Truwit, C.L., Gerritsen, F.A., Hill, D.L.G., Hawkes, D.J.: A generic framework for non-rigid registration based on non-uniform multi-level free-form deformations. Med. Image Comput. Comput. Assist. Interv. 4, 573–581 (2001)

[9] Boykov, Y., Veksler, O., Zabih, R.: Fast approximate energy minimization via graph cuts. IEEE Transactions on Pattern Analysis and Machine Intelligence 23(11), 1222–1239 (2002)

[10] Dempster, A.P., Laird, N.M., Rubin, D.B.: Maximum likelihood from incomplete data via the EM algorithm. Journal of the Royal Statistical Society, Series B (Methodological) 39(1), 1–38 (1977)

[11] Rousseeuw, P.J., Leroy, A.M.: Robust regression and outlier detection. Wiley Series in Probability and Statistics. John Wiley & Sons Inc., Chichester (1987)

Estimation of Activation Times in Cardiac Tissue Using Graph Based Methods

Mikael Wallman[1,2], Nic Smith[3], and Blanca Rodriguez[1]

[1] Oxford University Computing Laboratory, Oxford, United Kingdom
[2] Fraunhofer-Chalmers Centre, Chalmers Science Park, Gothenburg, Sweden
[3] Division of Imaging Sciences, King's College London, United Kingdom

Abstract. The bidomain and monodomain equations are well established as the standard set of equations for the simulation of cardiac electrophysiological behaviour. However, the computational cost of detailed bidomain/monodomain simulations limits their applicability to scenarios in which results are needed in real time (e.g. clinical scenarios). In this study, we present a graph based method which relies on point to point path finding to estimate activation times in cardiac tissue with minimal computational costs. Activation times are compared to bidomain simulation results for heterogeneous tissue slabs and an anatomically-based rabbit ventricular model. Differences in activation times between our proposed graph based method and bidomain results are less than 10% of the total activation time and computational performance is orders of magnitude faster with the graph based method. These results suggest that the graph based method could provide a viable alternative to the bidomain formalism for the fast estimation of activation times when the need for fast performance justifies limited loss of accuracy.

1 Introduction

During the last two decades, the bidomain equations, and the closely related monodomain equation, have emerged as a gold standard for simulating cardiac electrophysiology [1]. Although able to provide a sophisticated representation of cellular mechanisms and intercellular interactions, solving the resulting PDEs is very computationally expensive. Additionally, in many situations, e.g. when determining the activation times in a steady state setting, the level of complexity provided by the bidomain formalism is higher than necessary, making bidomain simulations inefficient solutions to the problem at hand.

For such situations, several alternative ways of describing cardiac propagation exist, ranging from early models relying on Huygens principle [2], via cellular automata models [3], to models explicitly derived from the bidomain equations, such as the eikonal equations [4]. Common between all of these simplified models is that finding the order of activation requires a sequence of computations for all the spatial nodes. Thus, in each step of the algorithm, all data needed to find the wavefront are computed. While this is desirable in many situations, for some applications, even focussing the computational efforts on locating the wavefront is inefficient.

D.N. Metaxas and L. Axel (Eds.): FIMH 2011, LNCS 6666, pp. 71–79, 2011.

Instead of computing the wavefront, we might determine the path the current takes from a point of initial activation to any point in the tissue, representing the fastest route between the two points. The analytic calculation of these paths in a continuous setting remains an open problem for most situations. However, some progress has been made towards closed form solutions [5], and several algorithms exist for solving the corresponding problem on graphs. Cardiac tissue can thus be described as a connected graph, allowing activation times to be approximated in a very efficient manner.

This paper presents a novel approach to estimating activation times in cardiac tissue using a graph-based method. Results are compared to finite element solutions to the bidomain equations in an attempt to characterise method accuracy. The comparison is performed in three different models: (1) a succession of 7 cardiac tissue slabs of decreasing resolution to evaluate methods convergence; (2) a cardiac tissue slab incorporating fiber rotation and a central region of slow conduction; (3) an anatomically-based rabbit ventricular model.

2 Methods

2.1 The Bidomain Model

The bidomain equations describe the cardiac tissue as two continuous and completely interpenetrating domains. At each point in space, two electrical potentials exist, one intra-cellular (ϕ_i), and one extra-cellular (ϕ_e). This also implies a transmembrane potential, v, at each point in space, defined as

$$v = \phi_i - \phi_e \ . \tag{1}$$

With the transmembrane potential defined is this way, the bidomain equations can be written as

$$\begin{aligned} &\beta(C_m \frac{\partial V_m}{\partial t} + I_{ion}(\eta, V_m)) - \nabla \cdot (\sigma_i \nabla (V_m + \phi_e)) = I_{S_i}, \\ &\nabla \cdot ((\sigma_i + \sigma_e)\nabla \phi_e + \sigma_i \nabla V_m) = I_{S_e}, \end{aligned} \tag{2}$$

where β is the cell surface to volume ratio, C_m is the membrane capacitance per unit area, σ_i is the intracellular conductivity tensor, σ_e is the extracellular conductivity tensor, I_{S_i} is an external stimulus applied to the intracellular space and I_{S_e} is an external stimulus applied to the extracellular space. I_{ion} is the ionic current, a function dependent on the cell model coupled to the bidomain model. η is a vector containing the state variables for the cell model.

2.2 The Graph Based Model

By considering the cardiac tissue as a connected graph, very fast approximations of activation sequence can be obtained. In this context, a graph consists of spatial nodes, connected by edges. Every edge in the graph is assigned a cost, based on

the time it takes the activation wavefront to traverse the corresponding path between two points in the tissue. Activation is initiated at one or several nodes, corresponding to the point or points where the tissue is initially stimulated. From there, the activation travels from node to node along the edges of the graph. At each node, an estimate of its activation time can be obtained by finding the accumulated cost of all edges traversed in order to reach it along a specific path. Typically, a very large number of paths can be taken between two nodes in the graph, so in order to obtain the best estimate of the activation time, the path with the lowest cost needs to be found.

Path Finding with the A* Algorithm. In this work, the A* algorithm has been used to find the lowest cost path though the network [6]. The A* works by keeping a priority queue of nodes to search. Each node n in the priority queue is assigned a score, based on the expected cost $f(n)$ of reaching the goal along a path passing through n, and the queue is ordered according to these scores. The score $f(n)$ is a sum of two other scores $g(n)$ and $h(n)$. $g(n)$ represents the accumulated cost of all the edges traversed in order to reach n, while $h(n)$ is a heuristic estimate of the cost that will be accumulated along the path from n to the goal.

Starting from a node s in the graph, a basic version of the A* algorithm can be described as follows:

1. Add s to the priority queue and calculate $f(s)$.
2. Select the node n on the queue whose value of f is smallest.
3. If n is the goal node, terminate the algorithm.
4. Otherwise, find all connected nodes n_i connected to n, calculate $f(n_i)$ for each and add them to the queue.
5. Goto step 2.

In the context of this work, two different heuristics have been employed. For the succession of slabs of decreasing resolution, a weighted Euclidean distance was used. For the more complex models, the heuristic estimate was based on another path finding procedure, performed on a down-sampled mesh, which itself used the heuristic $h(n) = 0$ for all nodes. The final estimates resulting from this procedure can thus be viewed as a refinement of initial coarser ones.

Graph Construction. As stated in the introduction, 9 different meshes were used in this work: 8 discretized slabs and 1 anatomically-based ventricular mesh. The nodes of the discretized slabs were regularly spaced in the shape of a Cartesian grid, while the nodes of the ventricular mesh had a less ordered distribution, conforming to the more complex geometry. For the regular meshes, the graphs presented here were constructed by successively processing cubic subgraphs of $2\times2\times2$ nodes, ensuring that all nodes in the subgraphs were 7-connected, so that an edge existed between any pair of nodes in the subgraph. For the anatomically-based ventricular geometry, the finite element mesh was used as the graph.

For each edge in the resulting graphs, costs of traversal was calculated according to

$$c_{i,i+1} = \sqrt{v_{i,i+1}^T M_{i,i+1} v_{i,i+1}}, \tag{3}$$

where $v_{i,i+1}$ is the vector from node n_i to node $n_i + 1$ and $M_{i,i+1}$ is a tensor describing conduction costs for that edge. For the 3D case, M can be written as

$$M = [m_l \lambda_l^2, m_t \lambda_t^2, m_n \lambda_n^2] \ . \tag{4}$$

Here, the set of vectors $\{m_l, m_t, m_n\}$ form an orthonormal system, describing the local fiber direction, while the scalars λ_l, λ_t, λ_n are the costs of traversal in the longitudinal, transversal and normal directions defined by this system.

In the results presented below, the conduction costs for the graphs were estimated using the full set of activation times resulting from the bidomain simulations. Starting from the bidomain simulation output, the activation time for each node was defined as the time when V_m changed sign from negative to positive. The three principal directions of conduction in the graph, corresponding to the m_l, m_t and m_n elements of M (i.e. the fibre direction), were the same as those used in the bidomain simulations. Conduction costs for these directions, corresponding to λ_l, λ_t and λ_n, were estimated using the Nelder-Mead simplex algorithm. As an objective function, the RMS error between the activation times estimated using the graph based method and those calculated from the bidomain simulations was used.

Recently, van Dam et al. [7] used a graph based method to estimate activation times on a ventricular surface. Although superficially similar, the method differs from ours in several important ways. While the previous method only considers nodes on the cardiac surface, our method also takes into account nodes that are situated within the cardiac walls. Additionally, while the previous method uses a fully connected graph, our method uses a sparser graph with a comparatively small number of connections for each node, allowing it to be applied to larger graphs. Furthermore, our method treats fibre directions in a more explicit way, using information about the the principal conduction directions in each node when determining the conduction costs for the graph. Finally, our method relies on a heuristic path finding algorithm, leading to very low computational costs for estimating the activation time in individual nodes.

3 Results

Activation times obtained using the graph-based method were compared to corresponding bidomain simulations in each of the three different settings: The succession of seven slabs of decreasing resolution, the slab incorporating fiber rotation and conduction heterogeneity, and the full ventricular mesh. The slab succession provides means to compare how the two methods perform for different mesh resolutions, while the two more complex settings elucidate how well the graph based method is able to mimic a given bidomain activation pattern.

All bidomain simulations presented were done using the Chaste software package [8]. The relative errors were calculated as $E_i = (\hat{AT}_i - AT_i)/AT_{\text{tot}}$, where E is relative error, i is the node index, $\hat{AT}$ is the approximate activation time, AT is the correct activation time, and AT_{tot} is the time it takes for all the nodes in the considered mesh to become activated. For the tissue slab with varying mesh resolution, the activation times from the finest mesh was considered correct, while for the remaining simulations, the activation times calculated from the bidomain simulations were considered correct, giving the errors a subtly different interpretation.

3.1 Method Comparison for Different Mesh Resolutions

The first set of bidomain simulations were performed on a cuboid geometry, measuring $1.80 \times 0.73 \times 0.29$ cm. The cuboid was discretized at seven different levels, producing seven tetrahedral meshes with homogeneous element size. The average node distance for each of the 7 meshes was 684 μm, 622 μm, 442 μm, 306 μm, 179 μm, 132 μm and 75 μm respectively.

For the bidomain simulations, activation of cardiac tissue was initiated by point stimulation at one of the corners of the mesh. After stimulation, activation time at each mesh node was calculated. These activation times were also estimated using the graph based approach, resulting in another set of activation times. For the bidomain simulation at a mesh resolution of 75 μm mesh, AT_{tot} was 34 ms.

For comparison between the different discretizations and methods, a grid of 250 points was chosen, with the points evenly distributed throughout the volume. The activation time values in these points, obtained from the bidomain simulations and the graph based approximations, were found using the built in linear interpolation functionality in MATLAB. Results are shown in Fig. 1.

From the histograms and graph in Fig. 1 it can be seen that the bidomain simulations have a lower relative error than the graph based method up to a discretization of 300 μm, while for coarser discretizations the graph based method has a lower relative error. The results also show that while the average relative error of the bidomain equations greatly increases for discretizations above 400 μm, the corresponding error for the graph based method remains almost constant.

3.2 Method Comparison in a Slab of Heterogeneous, Anisotropic Tissue

Next, propagation in a tissue slab of 4×4×1 cm (for the x,y and z directions respectively), with a spatial discretization of 300 μm was simulated. The conductivity was anisotropic, with fiber directions according to the Streeter model [9]. For the current geometry this implies that fibres were oriented in planes of homogeneous fibre orientation, perpendicular to the z-axis, with the fibre direction gradually rotating 120° between the planes $z = 0$ and $z = 1$. Additionally, a region of low conductivity was incorporated at the centre of the tissue, centred at the point $(x, y, z) = (2, 2, 0)$ and defined by two ellipsoids. The conductivity

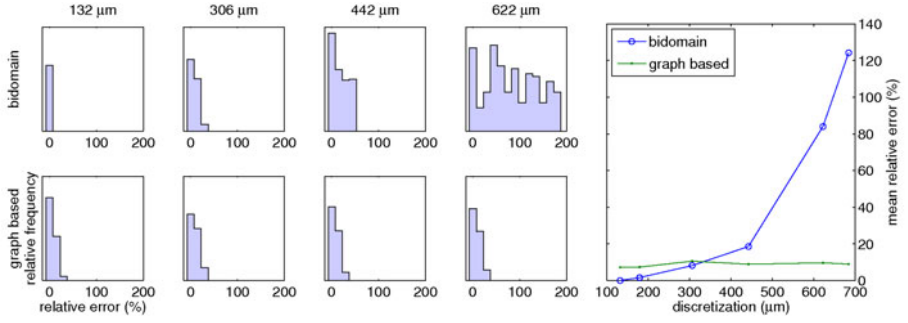

Fig. 1. Left panel shows histograms of relative errors in activation time for bidomain (upper row) and the graph based method (lower row). The columns correspond to different mesh discretizations, with the node spacing increasing from left to right. Right panel shows the mean relative error in activation time of bidomain (blue line, points marked with circles) and graph based approximations (green line, points marked with dots).

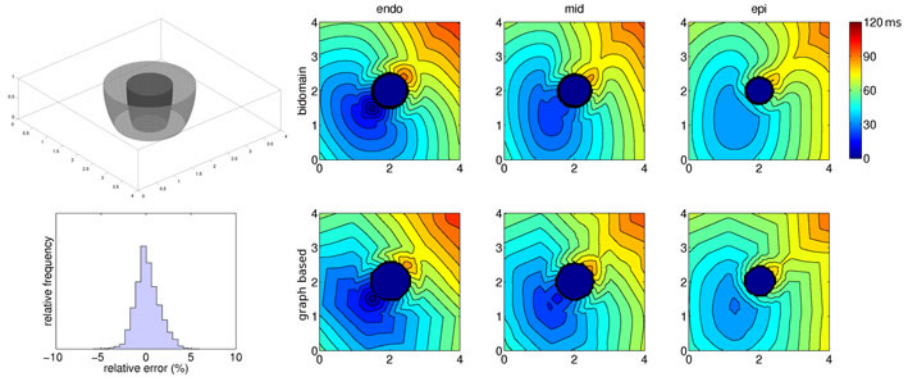

Fig. 2. The upper left panel illustrates the tissue slab with its central low conductivity region. The lower left panel shows a histogram of the relative errors of the graph based activation time approximations. The six right panels show activation isochrones of the six slab simulations. The upper row corresponds to bidomain results, while the lower row shows graph based approximations. The columns from left to right correspond to endocardium, mid-myocardium and epicardium.

inside the larger ellipsoid was 10 times lower than outside. Additionally, in the region overlapping the smaller ellipsoid, the tissue was modelled using passive diffusion only. Conductivity in the slow region was isotropic. A bidomain simulation of the activation was performed, with the initially stimulated area situated just outside the low conductivity region. Again, activation times were computed for each node, and corresponding activation times were also estimated using the graph based method. The total activation time for the bidomain simulation was

120 ms. The geometric model, along with a histogram of relative errors and activation isochrones for 3 cross sections of the slab, are shown in Fig. 2.

From the histogram in Fig. 2 it can be seen that the errors of the graph based activation time approximations keep within 5% of the total activation time. Considering the activation isochrones on the right side of Fig. 2, it can be observed that although polygonal in shape, the activation isochrones from the graph based method (lower row) show strong similarities in shape to the isochrones from bidomain (upper row).

3.3 Method Comparison in a Rabbit Ventricular Mesh

Finally, a realistic mesh of the rabbit heart ventricles, derived from MRI [10], was simulated. The mesh resolution was 420 μm, giving a total of 82619 nodes. The model was activated at several endocardial points in the lower half of the ventricles, emulating purkinje activation. Subsequently, the activation times for each node as obtained from the bidomain simulations were compared to the corresponding approximations obtained using the graph based method. The total activation time for the model was 71 ms. Results are shown in Fig. 3.

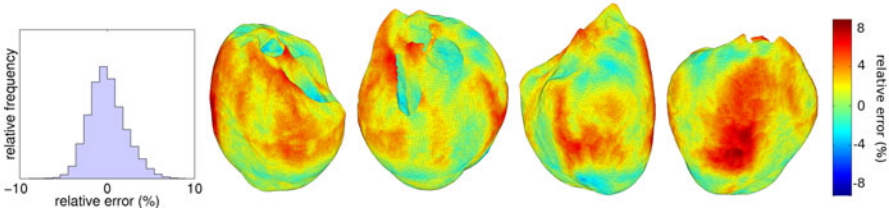

Fig. 3. Left panel shows a histogram of relative errors in activation time for graph based approximations. Right panel shows four rotated views of the distribution of relative errors in activation time on the epicardium of the rabbit ventricular mesh. The geometry is rotated 90 degrees between consecutive frames.

The histogram in Fig. 3 shows a fairly narrow distribution of errors, keeping well within 10% of the total activation time. The spatial distribution of errors show a largely irregular pattern, with no strong correlation between the distance from the area of initial stimulation and the magnitude of the errors. The rightmost view show a central accumulation of relatively high positive errors, which might be due to the greater wall thickness of this area, accentuating effects of wavefront curvature in the bidomain propagation.

4 Conclusions

We have presented a fast, graph based method for cardiac activation time estimation under steady state conditions. The comparison between the graph based method and the succession of increasingly coarse slabs show that while the average relative error for the bidomain greatly increases at discretizations above

300 μm, the corresponding error for the graph based method stays almost constant for the entire range of resolutions investigated. Additionally, results from both the slab with anisotropic, heterogeneous conduction and from the ventricular mesh show that the graph based algorithm is able to approximate activation times to well within 10% of the total activation time. This suggest that the method provides a viable alternative for situations where need for fast performance justifies limited loss of accuracy.

In the simulations presented here, the wall time for approximating activation times of isolated nodes in the most complex meshes were of the order of 10 ms on a standard desktop computer, making them 10^4 - 10^5 times faster than the bidomain simulations for that particular task. The authors are aware of the existence of alternative fast methods for activation time approximations, such as the fast marching method [11]. However, the primary aim of this work has been to investigate the accuracy of the proposed method. For this purpose the bidomain equations, representing the state of the art in cardiac electrophysiological modelling, provide a good basis of comparison. A full comparison of all alternative methods in terms of computational performance is beyond the scope of this manuscript. It should however be noted that the computational complexity of Dijkstra-like methods, such as the fast marching method (FMM), is $O(NlogN)$ for N nodes, while for the A* algorithm, this complexity provides a very rare worst case scenario. Additionally, each node expansion is likely to be much more computationally expensive for FMM than for the A* algorithm. While these considerations do not quantify the difference in performance, they strongly suggest that the proposed method is less computationally expensive than the bulk of competing fast methods.

Acknowledgements

This work was supported by the European Commission as part of the euHeart project FP7-ICT-2007-224495 and the preDiCT grant (DG-INFSO-224381). BR holds a UK Medical Research Council Career Development Award.

References

1. Keener, J., Sneyd, J.: Mathematical Physiology, 2nd edn. Springer, New York (1998)
2. Plonsey, R., Barr, R.C.: Mathematical modeling of electrical activity of the heart. Journal of electrocardiology 20(3), 219–226 (1987)
3. Ye, P., Entcheva, E., Grosu, R., Smolka, S.A.: Efficient modeling of excitable cells using hybrid automata. In: Proc. of CMSB, pp. 216–227 (2005)
4. Tomlinson, K.A., Hunter, P.J., Pullan, A.J.: A finite element method for an eikonal equation model of myocardial excitation wavefront propagation. SIAM J. Appl. Math. 63(1), 324–350 (2002)
5. Pashaei, A., Sebastian, R., Zimmerman, V., Bijnens, B.H., Frangi, A.F.: A meshless approach for fast estimation of electrical activation time in the ventricular wall. In: Computers in Cardiology 2009, pp. 209–212 (2010)

6. Hart, P., Nilsson, N.J., Raphael, B.: A formal basis for the heuristic determination of minimum cost paths. IEEE Transactions on Systems Science and Cybernetics 4(2), 100–107 (1968)
7. van Dam, P.M., Oostendorp, T.F., Oosterom, A.: Application of the fastest route algorithm in the interactive simulation of the effect of local ischemia on the ECG. Medical & Biological Engineering & Computing 47(1), 11–20 (2008)
8. Pitt-Francis, J., Pathmanathan, P., Bernabeu, M.O., Bordas, R., Cooper, J., Fletcher, A.G., Mirams, G.R., Murray, P., Osborne, J.M., Walter, A., et al.: Chaste: a test-driven approach to software development for biological modelling. Computer Physics Communications 180(12), 2452–2471 (2009)
9. Streeter, D.D., Spotnitz, H.M., Patel, D.P., Ross, J., Sonnenblick, E.H.: Fiber orientation in the canine left ventricle during diastole and systole. Circulation Research 24(3), 339–347 (1969)
10. Corrias, A., Jie, X., Romero, L., Bishop, M.J., Bernabeu, M., Pueyo, E., Rodriguez, B.: Arrhythmic risk biomarkers for the assessment of drug cardiotoxicity: from experiments to computer simulations. Philosophical Transactions of the Royal Society A: Mathematical, Physical and Engineering Sciences 368(192), 3001–3025 (1921)
11. Sethian, J.A., Vladimirsky, A.: Fast methods for the eikonal and related Hamilton Jacobi equations on unstructured meshes. Proceedings of the National Academy of Sciences of the United States of America 97(11), 5699–5703 (2000)

Automatic Segmentation of Cardiac CTs - Personalized Atrial Models Augmented with Electrophysiological Structures

Peter Neher[1,2], Hans Barschdorf[2], Sebastian Dries[2], Frank M. Weber[1], Martin W. Krueger[1], Olaf Dössel[1], and Cristian Lorenz[2]

[1] Institute of Biomedical Engineering, Karlsruhe Institute of Technology (KIT), Germany
[2] Philips Research Hamburg, Germany

Abstract. Electrophysiological simulations of the atria could improve diagnosis and treatment of cardiac arrhythmia, like atrial fibrillation or flutter. For this purpose, a precise segmentation of both atria is needed. However, the atrial epicardium and the electrophysiological structures needed for electrophysiological simulations are barely or not at all detectable in CT-images. Therefore, a model based segmentation of only the atrial endocardium was developed as a landmark generator to facilitate the registration of a finite wall thickness model of the right and left atrial myocardium. It further incorporates atlas information about tissue structures relevant for simulation purposes like Bachmann's bundle, terminal crest, sinus node and the pectinate muscles. The correct model based segmentation of the atrial endocardium was achieved with a mean vertex to surface error of 0.53 mm for the left and 0.18 mm for the right atrium respectively. The atlas based myocardium segmentation yields physiologically correct results well suited for electrophysiological simulations.

Keywords: automatic segmentation, computed tomography, cardiac atrium, atrial fibrillation, electrophysiological structures.

1 Introduction

Although not lethal by itself, atrial fibrillation is the most widespread cardiac arrhythmia and a possible cause of apoplectic seizures and serious cardiac diseases like cardiac insufficiency and heart failure. According to the "Copenhagen Stroke Study", 18% of all stroke patients are also atrial fibrillation patients [1]. Electrophysiological (EP) simulations of the atria could improve diagnosis and treatment of cardiac arrhythmia, like atrial fibrillation or flutter [2,3]. For this purpose, precise segmentation and patient specific model generation of both atria are needed. Due to the recent advances in computed tomography, which allow sub millimetre resolution 3D images of the human heart, the preconditions for the automatic segmentation of the atrial endocardium are given [4,5]. However due to the lack of contrast it is still not possible to automatically detect the atrial epicardium as well

D.N. Metaxas and L. Axel (Eds.): FIMH 2011, LNCS 6666, pp. 80–87, 2011.

as the tissue structures contained in the atrial myocardium needed for the electrophysiological simulations mentioned above. To overcome this lack of information, we propose an atlas based segmentation procedure of the atrial myocardium with its respective wall thickness information in the different atrial regions. The resulting segmentation further incorporates atlas information about tissue structures relevant for simulation purposes like Bachmann's bundle, terminal crest, sinus node and the pectinate muscles [6]. This atlas based segmentation is guided by a model based segmentation of the atrial endocardium yielding the landmarks used for the atlas registration. The atlas information is incorporated in a tetrahedral mesh structure of the atrial complex.

2 Materials and Methods

The segmentation process of the atrial myocardium was separated into three major steps. A data and atlas generation step, the endocardial surface segmentation and the atlas registration. Section 2.1 and 2.2 cover the first step, the endocardial segmentation is introduced in section 2.3 and in section 2.4 the registration of the atlas with the patient image via thin plate spline transform (TPS) is explained. Figure 1 shows an overview of the whole process.

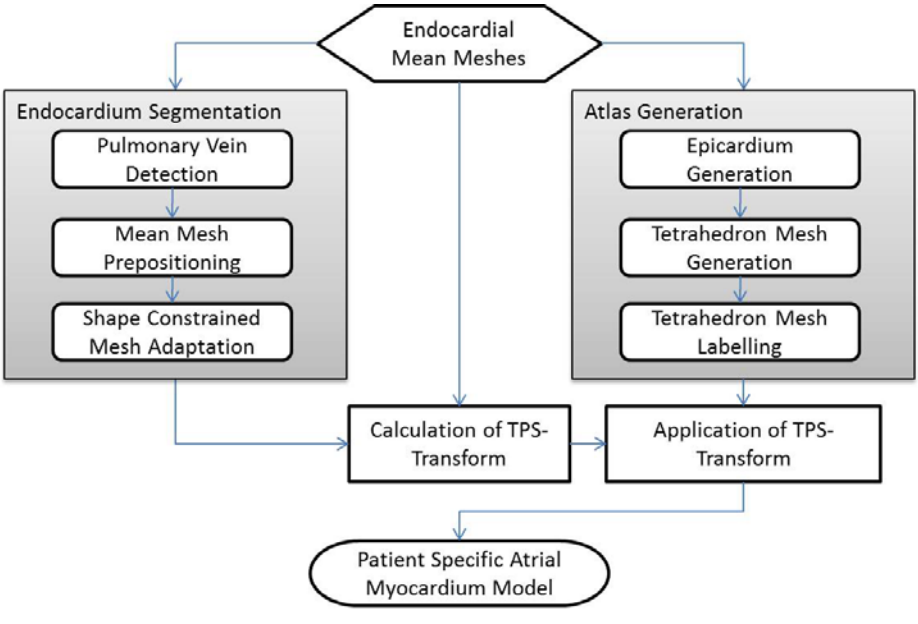

Fig. 1. Generation of patient specific atrial myocardium models

2.1 Wall Thickness from MR-Data

For the left atrium the wall thickness values for five different areas were used as proposed by Hall *et al.* [7]. However, for the right atrium there are only few and coarse wall thickness values obtainable through literature research. In order to overcome this lack of information, the right atrium wall thickness values were manually extracted from 7 magnetic resonance images obtained from 7 different volunteers via a targeted black blood, fat suppressed, ECG triggered spin echo sequence [8]. All images had a resolution of about 1.0 mm along the x- and y-axis and 5.0 mm along the z-axis. The atrium was divided into five different regions each of which was again subdivided into one to three subregions with different wall thickness values. The final wall thickness values were determined by 940 manual measurements in eleven different regions of the atrium. Additionally 32 reference measurements of the left atrial wall were conducted in order to detect a possible systematic error resulting from the chosen imaging modality.

2.2 Atlas Mesh Generation

An atlas, describing the wall thickness in the different atrial regions and the EP-structures needed for EP-simulations, was incorporated into a tetrahedral mesh structure. Therefore, mean surface meshes of the atrial endocardium were generated from the manually segmented atria in 30 and 44 different patient images for the left and right atrium respectively and labeled according to the different tissue types, EP-structures and the orifices present in the atrial wall. The labels representing the specific tissue structures are inserted manually based on the results of the approaches presented by Krueger *et al.* [6], Ho *et al.* [9] and Saremi *et al.* [10]. A list of all inserted electrophysiological structures can be seen in Table 1.

These mean meshes are then dilated, according to the wall thickness determined for the respective anatomical region in section 2.1, to represent the epicardial surface of each atrium. To combine the two still separate left and right atrial meshes they are connected by removing their overlapping parts and afterwards closing the thus produced gap. Secondly, the orifices to the ventricles, the caval

Table 1. Electrophysiological structures inserted into the atrial tissue. Abbreviations: PM – pectinate muscles, TC – terminal crest, BB – Bachmann's bundle.

Right atrium	Left atrium	Septum
Sinus node	BB (left branch)	Septum
TC	BB end point	BB
BB (right branch)	BB starting point	
PM onsets		
PM 1-7		
TC inflexion point		
TC end point		
BB end point		

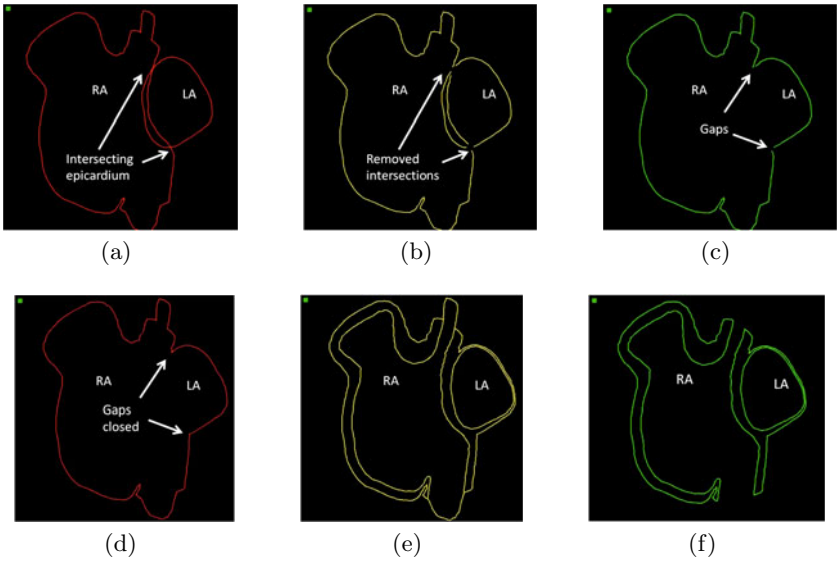

Fig. 2. Construction of a double walled atrial mesh consisting of the epi- and endocardium of both atria including the orifices to the ventricles and veins. (a) Depicts the overlapping epicardium meshes. (b) Shows the two meshes after the intersecting triangles have been removed. (c) Both atrial meshes after the overlap has been removed. Next the resulting gap between the meshes is closed (d), the epi- and endocardium meshes are merged (e) and afterwards the orifices are inserted (f).

vein and the pulmonary veins are inserted at the previously labeled locations. The process is illustrated in Figure 2.

Next the surface mesh which consists of the merged endo- and epicardium of both atria, was used to generate the tetrahedron mesh. The open source tool *TetGen* [11] was used to generate a Delaunay tetrahedralization of the input mesh, suitable for finite element and finite volume methods. Due to the fact that *TetGen* does not preserve the mesh labeling, the electrophysiological labeling was automatically transferred from the triangles of the surface mesh to the respective closest elements of the tetrahedron mesh. The final results of the atlas mesh generation process can be seen in Figure 3.

2.3 Model Based Segmentation of the Atrial Endocardium

The actual adaptation of the atrial endocardium in cardiac CT images was conducted with a model based approach similar to the one introduced by Weese *et al.* [12]. This segmentation method was enhanced by a label specific parameter selection to account for the specific situations at the different anatomical regions of the atrium which each requires different parametrization of the segmentation process. The mesh used for the segmentation has nine differently labeled regions, each of which has its own set of adaptation parameters. The most important parameters are the allowed range of the image gradient feature, the maximum

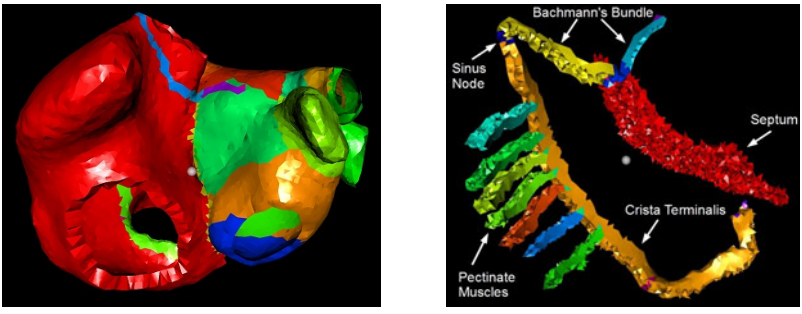

(a) (b)

Fig. 3. Figure (a) shows the final atlas mesh augmented with all EP-structures listed in Table 1. In (b) the mesh consisting only of the EP-structures but without the surrounding myocardium is illustrated.

feature search distance, the weighting of the external energy as well as a feature distance penalty. These parameters are automaticaly changed after each iteration during the segmentation process in order to cope with the different situations at the different stages of the process. The first step in the segmentation process is the prepositioning of the endocardial mean meshes introduced in section 2.2 in the patient image. This initialization was achieved by the detection of the atria via generalized hough transform. The thus yielded affine transform was applied to the atrial mean meshes. To allow for explicit adaptation to the different configurations of the pulmonary venous drainage a method for the detection of the correct number of right pulmonary veins was applied. According to the detected number of pulmonary veins a fitting mean mesh can be chosen which prevents mis-segmentation of the left atrium in this region. The different pulmonary vein configurations considered here are based on a study performed by Marom *et al.* on the anatomical variation of the pulmonary veins using contrast-enhanced CT data [13]. The correct pattern of the right pulmonary veins is detected by using a 3D image based region grower which is constrained to grow into the direction of a cone originating at a seed point located in the right part of the left atrium and stretching into the direction of the right pulmonary veins.

2.4 Registration of the Atlas Mesh with Patient Images

To register the volumetric atlas mesh generated in section 2.2 to patient images a transformation based on thin plate splines is used [14]. The vertices of the endocardial surface as detected in section 2.3 are used as landmarks for the registration. The transformation is computed between the vertices of the respective mean endocardium mesh and the according target vertices of the adapted mesh. The transformation, describing the deformation between the the mean surface model and the adapted surface model, can now be applied to adapt the mean

tetrahedron mesh to the patient image. The registration of this mesh results in a complete segmentation of the atrial myocardium including the electrophysiological structures introduced in table 1.

3 Results

The average wall thickness of 3.3 mm determined in section 2.1 combined with the wall thickness values of the left atrium described in [7], yielded an average value for both atria of about 2.5 mm. The reference measurements of the left atrial wall resulted in an average wall thickness of 2.1 mm.

To evaluate the segmentation result of our approach the model based segmentation of the endocardial surface was evaluated automatically as well as, in case of the right atrium, manually by a physician. The evaluation of the model based endocardium segmentation yielded a mean vertex to surface error of 0.53 mm for the left and 0.18 mm for the right atrium and was conducted for 30 reference meshes of the left atrium and 44 reference meshes of the right atrium in a leave-one out-manner. In the human evaluation approach, all the automatically segmented right atria were scored on a scale from 1 to 5 where 1 is the worst and 5 is the best result. Additionally each result was commented with respect to the accuracy of the segmentation. The evaluation yielded an over all positive result with no segmentation scored worse than 3. The average score for all segmentations was 4.2. The CT-images used for the evaluation where acquired with an average resolution of about 0.5 mm in all three spatial directions.

Due to the lack of ground truth data, the atlas based registration of the atrial myocardium was not evaluated via automatically computed error measurements. A visual evaluation of the correct positioning of the EP-structures yielded an over all very positive result which is a direct result of the very accurate model based segmentation discussed before and the used registration method. The voxelized results of the patient specific tetrahedron mesh for one exemplary dataset are visualized in Figure 4. To ensure the fitness of the generated atrial myocardium model for electrophysiological simulations, the correct labeling of the electrophysiological structures in the generated mean tetrahedron meshes had to be evaluated. The most important task in the tissue labeling process was the insertion of the undisrupted terminal crest and Bachmann's bundle to facilitate the correct simulation of the electrical behavior of these conduction lines as well as the complete segregation of the left and right atrial myocardium by the septum layer. To check the first characteristic a conduction test was performed to check whether every part of the conduction system could be reached by a region grower starting from the sinus node. To test whether the septum layer between both atria is leak proof the region grower was modified to grow over all triangles but the triangle labeled as septum or the part of the Bachmann's bundle passing through the septum. If the layer is leak proof, the grower will not spread into the left atrium. The generation process proposed in this work meets all these requirements.

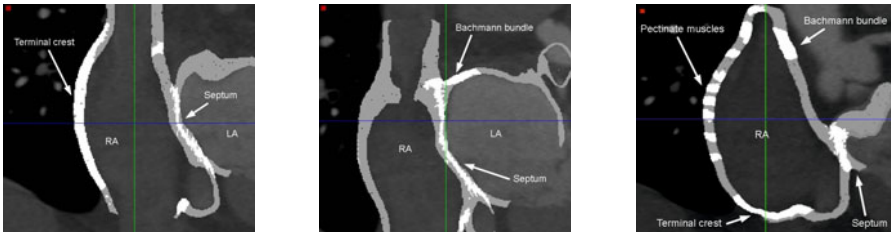

(a) (b) (c)

Fig. 4. Exemplary voxelized patient specific tetrahedron mesh. (a) Depicts the terminal crest and the septum, (b) shows Bachmann's bundle and the septum and (c) illustrates the pectinate muscles and the lower part of the terminal crest.

4 Discussion and Conclusion

An automatic method for the complete segmentation of both atria and its electrophysiological structures is proposed. The method consists of a model based segmentation approach of the atrial endocardium and an atlas based segmentation of the atrial myocardium using the results of the endocardium segmentation as scaffolding for the registration. The models yielded by this segmentation approach incorporate statistical information about the wall thickness of the different atrial regions, as well as different electrophysiologically relevant tissue structures like Bachmann's bundle, terminal crest, sinus node and the pectinate muscles.

One important advantage of the method proposed in this work is its high flexibility regarding the information incorporated in the model. The model can easily be extended with additional label regions. This way, further structures that could be electrophysiologically relevant, such as the fossa ovalis or the cavotricuspid isthmus, can be added. Furthermore, supplemental information can be defined for each volume element, containing e.g. muscle fibre orientation.

A very good segmentation accuracy of the atrial endocardium has been achieved. Regarding the manually extracted wall thickness values of the right atrium, the resulting wall thickness of both atria is not completely consistent with the results stated in [15]. The difference might result from an overestimated wall thickness in the MR-images due to signals received from unsuppressed blood near the atrial walls. The comparison of the left atrial reference measurements to literature values support this assumption of a systematical error and made a correction of the overestimated wall thickness possible. The registration of the atlas mesh and the incorporated EP-structures also yields very good results. Nevertheless, the actual validity of the adapted meshes will not be proven until extended electrophysiological simulations are conducted on the basis of these meshes. Future work will focus on the application of the method to other organs and modalities like MRI as well as the further validation of the proposed method by extensive conduction of electrophysiological simulations on the basis of the models generated with our approach. Such simulations could be of great

value to improve the diagnosis and treatment of cardiac arrhythmia, like atrial fibrillation or flutter.

References

1. Jørgensen, H.S., et al.: The copenhagen stroke study (1996), http://stroke.ahajournals.org/ (accessed May 14, 2010)
2. Weber, F.M., Schilling, C., Straub, D., Gurm, S., Seemann, G., Lorenz, C., Dössel, O.: Extracting Clinically Relevant Circular Mapping and Coronary Sinus Catheter Potentials from Atrial Simulations. In: Ayache, N., Delingette, H., Sermesant, M. (eds.) FIMH 2009. LNCS, vol. 5528, pp. 30–38. Springer, Heidelberg (2009)
3. Jacquemet, V., et al.: Modeling atrial arrhythmias: Impact on clinical diagnosis and therapies. IEEE Reviews in Biomedical Engineering 1 (2008)
4. Lorenz, C., et al.: A comprehensive shape model of the heart. Medical Image Analysis 10, 657–670 (2006)
5. Ecabert, O.: Automatic model-based segmentation of the heart in ct images. IEEE Transactions on Medical Imaging 27, 1189–1201 (2008)
6. Krueger, M.W., et al.: Semi-automatic segmentation of sinus node, bachmann's bundle and terminal crest for patient specific atrial models. IFMBE Proceedings 25, 673–676 (2009)
7. Hall, B., et al.: Variation in left atrial transmural wall thickness at sites commonly targeted for ablation of atrial fbrillation. Journal of Interventional Cardiac Electrophysiology 17, 127–132 (2006)
8. Stehning, C., et al.: Black-blood restricted field of view sequence for pre-ablation imaging of the atria. Proc. Intl. Soc. Mag. Reson. Med. 18, 1409 (2010)
9. Ho, S.Y., et al.: Atrial structure and fibres: morphologic bases of atrial conduction. Cardiovascular Research 54, 325–336 (2002)
10. Saremi, F., et al.: Cardiac conduction system: anatomic landmarks relevant to interventional electrophysiologic techniques demonstrated with 64-detector ct. Radiographics 27, 1539–1565 (2007)
11. Si, H.: TetGen A Quality Tetrahedral Mesh Generator and Three-Dimensional Delaunay Triangulator. Weierstrass Institute for Applied Analysis and Stochastics. Version 1.4 edn. (2006)
12. Weese, J., Kaus, M.R., Lorenz, C., Lobregt, S., Truyen, R., Pekar, V.: Shape constrained deformable models for 3D medical image segmentation. In: Insana, M.F., Leahy, R.M. (eds.) IPMI 2001. LNCS, vol. 2082, pp. 380–387. Springer, Heidelberg (2001)
13. Marom, E.M., et al.: Variations in pulmonary venous drainage to the left atrium: implications for radiofrequency ablation. Radiology 230, 824–829 (2004)
14. Bookstein, F.L.: Principal warps: Thin-plate splines and the decomposition of deformations. IEEE Transaction on Pattern Analysis and Machine Intelligence 2, 567–585 (1989)
15. Coffey, J., et al.: Specific absorbed fractions for photon sources uniformly distributed in the heart chambers and heart wall of a heterogeneous phantom. Journal of Nuclear Medicine 22, 65–71 (1981)

Construction of Left Ventricle 3D Shape Atlas from Cardiac MRI

Shaoting Zhang[1], Mustafa Uzunbas[1], Zhennan Yan[1], Mingchen Gao[1], Junzhou Huang[1], Dimitris N. Metaxas[1], and Leon Axel[2]

[1] Rutgers, the State University of New Jersey, Computer Science Department
[2] New York University, Radiology Department

Abstract. In this paper, we present an effective algorithm to construct a 3D shape atlas for the left ventricle of heart from cardiac Magnetic Resonance Image data. We derive a framework that creates a 3D object mesh from a 2D stack of contours, based on geometry processing algorithms and a semi-constrained deformation method. The geometry processing methods include decimation, detail preserved smoothing and isotropic remeshing, and they ensure high-quality meshes. The deformation method generates subject-specific 3D models, but with global point correspondences. Once we extract 3D meshes from the sample data, generalized Procrustes analysis and Principal Component Analysis are then applied to align them together and model the shape variations. We demonstrate the algorithm via a set of experiments on a population of cardiac MRI scans. We also present modes of variation from the computed atlas for the control population, to show the shape and motion variability.

1 Introduction

In the last decade, Magnetic Resonance Imaging (MRI) has been proven to be a non-invasive tool that can be used to measure the myocardial mass and functional deformation of the heart [8]. Quantification of ventricular mass and function are important for early diagnosis of cardiac disorders and quantitative analysis of cardiac diseases. Recent developments in Cine MRI further help diagnose the presence of heart disease by analyzing the heart function throughout the cardiac cycle. MRI is becoming considered as a gold-standard for cardiac function [2,6]. In this context, the construction of an anatomical shape atlas of the structures in the heart has been of particular interest and its importance has been emphasized in a number of recent studies [10,11,13].

In clinical applications, particularly the delineation of left ventricle endocardium and epicardium, automatic and quantitative approaches are highly desired to facilitate the analysis of comprehensive MR data sets. Regarding the needs for automated and quantitative methods in clinical applications, an atlas can provide a reference shape for a family of shapes or can be used to model the consistent deformation of a structure of interest. This could be useful in numerous applications including, but not limited to, statistical analysis of different populations, the segmentation of structures of interest, motion characterization, functional analysis, and the detection of various diseases [5,11,13]. The 3D size and shape characteristics of the left ventricle, and its deformation over a cardiac cycle, are relatively consistent and can be fairly well characterized by specific

D.N. Metaxas and L. Axel (Eds.): FIMH 2011, LNCS 6666, pp. 88–94, 2011.

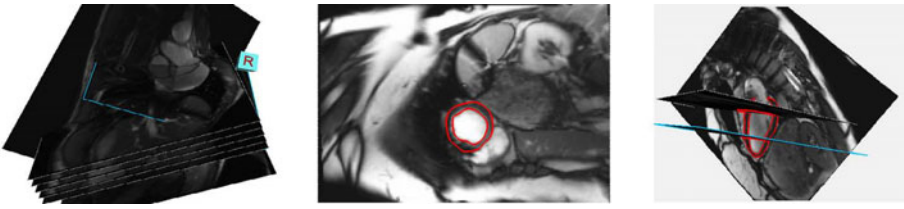

Fig. 1. From left to right: visualization of 2D slices from MR scans; annotation in the short axis; annotation in the long axis

models. 2D delineations of the left ventricle is already available from manual segmentation. Accurate 3D manual annotation, however, is difficult and time-consuming.

In this paper, we propose a method for creating a 3D shape atlas of the left ventricle from 2D manual delineations. It employs currently available 2D databases and could lead to further novel segmentation methods if further developed. The input to our algorithm is a cloud of points marked on a set of sparse, 2D cardiac slices, as shown in Fig. 1. Note here, that the slice thickness is typically several times larger than the pixel size in cardiac MR images, so that the resolution is poorer in the direction orthogonal to the slice. Thus, creating a 3D model from such sparse data is challenging. Our proposed framework is based on several steps. First, a 3D binary image is generated by interpolating 2D labeling. Then a surface is obtained from the 3D binary file, using Marching Cubes algorithm. Second, geometry processing methods are applied to obtain a high quality mesh. These methods include decimation, detail-preserved smoothing, and isotropic remeshing. In the third step, the one-to-one correspondence for each vertex is obtained among the sample set of the model by registering a reference shape model to all the other samples. The transformation is done based on a nonrigid local deformation method. The mapping of a unique template to all instances provides a consistency among not only the motion model of one cardiac image series, but also shape and textures model of many cardiac series from different patients, if needed. In the final step, shape statistics are computed straightforwardly, using generalized Procrustes analysis and PCA. The mean shape and major variations are then obtained. Note here, that the manual delineations do not have to be constrained with any anatomical point correspondence. Our method automatically resolves that issue, both among multiple instances of the same phase of a cardiac cycle or sequential phases of one cycle. The ability to fit the atlas to all temporal phases of a dynamic study can benefit the automatic functional analysis.

2 Methods

2.1 Algorithm Framework

Fig. 2 shows the algorithm framework. The typical input data is MRI scans, acquired in different locations, along with their 2D contour labeling. The MRI data can be relatively sparse. Note that the input data can also be previously constructed 3D binary images or meshes. In such cases the algorithm will just start from the second or the

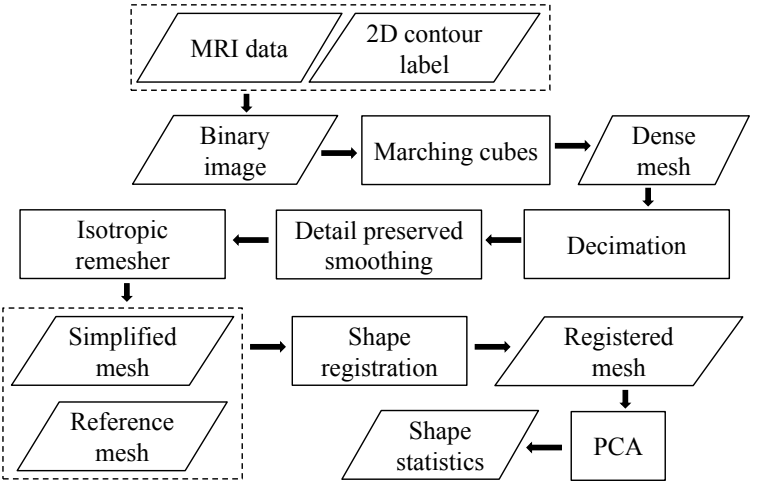

Fig. 2. The algorithm flowchart. The diamond shape represents data, and the rectangular shape denotes algorithms.

third step. Given MRI and 2D contour data, a 3D binary image is generated by interpolating values among slices. Then, the Marching Cubes method [4] is employed to derive the corresponding isosurfaces. The mesh of this surface may be very dense and contain hundreds of thousands vertices. Furthermore, the shape of this may contain artifacts caused by the sharp transitions at contours. It is necessary to downsample and smooth it, without removing the shape detail information. After these geometry processing steps, a simplified and high-quality shape is generated. Then, a reference shape is deformed to fit it, using a shape registration method. Since all resulting shapes are registered with the same reference shape, they share the same topology and all vertices have one-to-one correspondences. Finally, generalized Procrustes analysis [1,3] and Principal Component Analysis (PCA) are used to compute the mean shape and major variations.

2.2 Geometry Processing

In our system, the input data is converted to a isosurface after the preprocessing. Because of the properties of Marching Cubes, such surface may contain too many vertices and also may have local artifacts. Thus it is desirable to obtain a simplified and high-quality mesh, with shape details preserved. We use mesh decimation to downsample the input shape, and also use isotropic remeshing to guarantee that each vertex has six neighbors. The remaining difficulty is to smooth the shape without losing the important details. We use Laplacian Surface Optimization [7] to achieve this. This method has previously been employed to reconstruct the left ventricle from tagged MRI [12].

Let the mesh $\mathbf{M}$ of the shape be described by a pair $(\mathbf{V}, \mathbf{E})$, where $\mathbf{V} = \{v_1, ..., v_n\}$ describes the geometric positions of the vertices in $\mathbf{R}^3$ and $\mathbf{E}$ describes the connectivity. The neighborhood ring of a vertex i is the set of adjacent vertices $\mathbf{N}_i = \{j|(i,j) \in \mathbf{E}\}$ and the degree d_i of this vertex is the number of elements in $\mathbf{N}_i$. Instead

of using absolute coordinates $\mathbf{V}$, the mesh geometry is described as a set of differentials $\Delta = \{\delta_i\}$. Specifically, coordinate i will be represented by the difference between v_i and the weighted average of its neighbors: $\delta_i = v_i - \sum_{j \in \mathbf{N}_i} w_{ij} v_j$, where w_{ij} is computed from cotangent weights [7]. Assume V is the matrix representation of $\mathbf{V}$. Using a small subset $\mathbf{A} \subset \mathbf{V}$ of m anchor points, a mesh can be reconstructed from connectivity information alone. The x, y and z positions of the reconstructed object ($V'_p = [v'_{1p}, ..., v'_{np}]^T, p \in \{x, y, z\}$) can be solved for separately by minimizing the quadratic energy:

$$\|L_u V'_p - \Delta\|^2 + \sum_{a \in \mathbf{A}} \|v'_{ap} - v_{ap}\|^2, \tag{1}$$

where L_u is the Laplacian matrix from uniform weights, and the v_{ap} are anchor points. $\|L_u V'_p - \Delta\|^2$ tries to smooth the mesh when keeping it similar to the original shape, and $\sum_{a \in \mathbf{A}} \|v'_{ap} - v_{ap}\|^2$ keeps the anchor points unchanged. The cotangent weights approximate the normal direction, and the uniform weights point to the centroid. By minimizing the difference of these two (i.e., $L_u V'$ and Δ), the vertex is actually moved along the tangential direction. Thus the shape is smoothed without significantly losing the detail. With m anchors, (1) can be rewritten as a $(n+m) \times n$ overdetermined linear system $AV'_p = b$:

$$\begin{bmatrix} L_u \\ I_{ap} \end{bmatrix} V'_p = \begin{bmatrix} \Delta \\ V_{ap} \end{bmatrix} \tag{2}$$

This is solved in the least squares sense using the method of normal equations $V'_p = (A^T A)^{-1} A^T b$. The conjugate gradient method is used in our system to efficiently solve it. The first n rows of $AV'_p = b$ are the Laplacian constraints, corresponding to $\|L_u V'_p - \Delta\|^2$, while the last m rows are the positional constraints, corresponding to $\sum_{a \in A} \|v'_{ap} - v_{ap}\|^2$. I_{ap} is the index matrix of V_{ap}, which maps each V'_{ap} to V_{ap}. The reconstructed shape is generally smooth, with the possible exception of small areas around anchor vertices.

2.3 Shape Registration and Shape Statistics

These simplified and high-quality meshes do not share the same topology. They may have different numbers of vertices, and there is no one-to-one correspondence for each vertex. Our solution is to use shape registration to deform a reference shape to fit to all the others. Since all deformed shapes are registered to the reference one, they effectively have one-to-one correspondences for each vertex. It is also important that the deformed reference shape should be almost identical to the target shape. We use an Adaptive-Focus Deformable Model (AFDM) [9] to do the shape registration task. This algorithm was originally designed for automatic segmentation and has the property of maintaining the topology. We have simplified it for shape registration without using image information. After applying AFDM for each shape, all shapes share the same topology.

Once the one-to-one correspondence is obtained for each vertex among all shapes, the shape statistics can be computed straightforwardly using generalized Procrustes

analysis and PCA, like the Active Shape Model [1] does. Given any two shapes, they can be fitted to each other using a similarity transformation. Procrustes analysis is used to find the translational, rotational and scaling components. Since there is no mean shape in the beginning, generalized Procrustes analysis arbitrarily chooses a shape to use as the reference and transforms all the rest to fit it. After that, a mean shape is computed by averaging all transformed shapes. Then, this mean shape is used as a reference shape in the next round. We repeat this procedure until the mean shape converges to a stable state. Note that normalization is necessary, as otherwise the mean shape will degenerate to a single point.

After the alignment, each resulting shape is filled into a matrix as a column vector. PCA is applied to get the Point Distribution Model (PDM). The important "modes" (i.e., eigenvectors corresponding to the largest eigenvalues) are selected to cover more than 80% of the variance. Combining the mean shape and the modes, the PDM is able to summarize and describe the sample shapes concisely and accurately. Such shape statistics are used as the atlas or shape prior information.

3 Experiments

We validated our method on 36 3D MRI scans. They are from sequences of images over the full cardiac cycle. Thus, the shape variances are large. Manual segmentation was applied in each 2D slice. Then a 3D binary data was obtained by interpolating values among slices. The Marching Cubes method was used to generate a 3D mesh.

These meshes may contain artifacts and too many vertices. Thus geometry processing methods were necessary to downsample and smooth these meshes without removing the shape details. Some decimated meshes are shown in Fig. 3. Fig. 4 visualizes the errors after all geometry processing. The distance between the original surface and the processed surface is computed and visualized. Most errors of vertices are within one voxel. Compared to the initial mesh in Fig. 3, the processed shapes are more smooth and most artifacts are removed, while the shape detail is still preserved. Then, shape

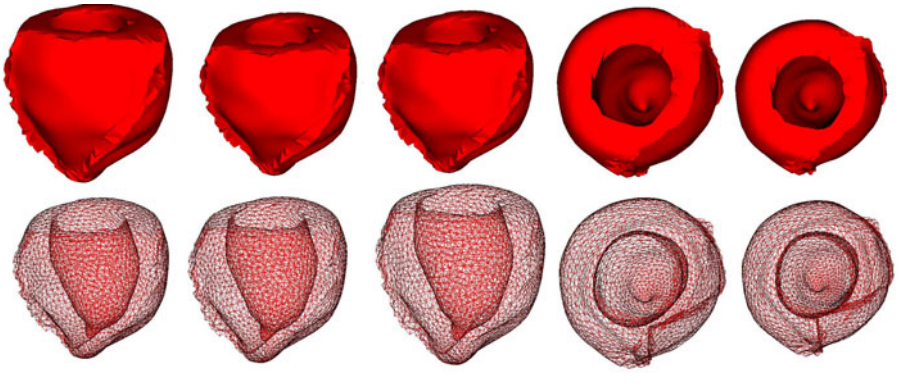

Fig. 3. Samples of decimated 3D meshes. The artifacts along the long axis can still be observed. Note that these shapes don't have one-to-one correspondence for vertices.

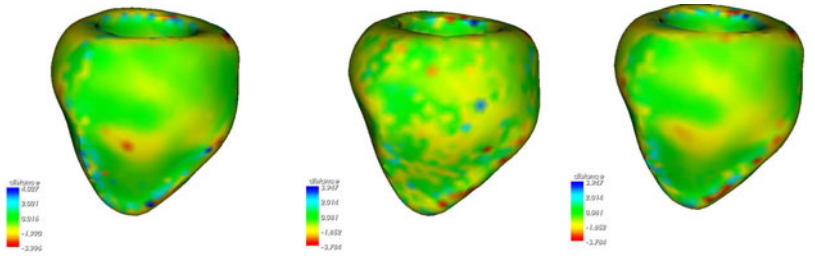

Fig. 4. Visual validation of geometry processing methods. The errors of each vertex is plotted using different color. Green means that the error is within one voxel. Blue and yellow denote errors within two voxels.

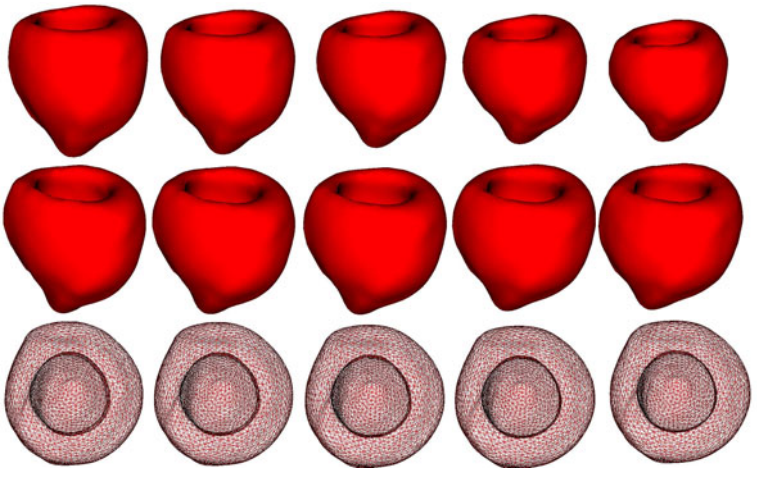

Fig. 5. Three modes with largest variations, from -3σ to 3σ. The first row: the first mode represents the contraction. The second row: the second mode is the movement along the short axis. The third mode is the twisting.

registration was employed to fit a reference mesh to all the others. This method uses non-rigid local deformation. Thus, the fitted shape is nearly identical to the target shape. Furthermore, the resulting meshes have the same topology and one-to-one correspondence since they all start from the same reference mesh.

After obtaining one-to-one correspondence, it is straightforward to compute the mean shape and its variations, by using generalized Procrustes analysis and PCA. Fig. 5 shows the major modes having largest variances. The first three modes cover more than 80% of the variance. Although the shapes of original data are diverse, the modes are very simple. By changing the variations from -3σ to 3σ, where σ is the standard deviation, the first mode just represents the contraction of the heart. The second mode is the movement along the short axis. The third mode is the twisting.

We implemented this method using Python 2.5 and C++ on a Quad CPU 2.4GHZ PC. It took about 20 seconds to do geometry processing and shape registration for each

data, and 5 seconds to construct the atlas and shape statistics from 36 meshes. The processing time may increase when there are more vertices in each shape. In our test, each mesh contained around 2,800 vertices and 5,600 triangles.

4 Conclusions

In this paper we presented a framework to construct a 3D shape atlas of the left ventricle from MRI scans. The framework includes geometry processing, shape registration, and Principal Component Analysis. It was tested on 36 annotated 3D data. The benefits of our atlas method are twofold. First, the 3D mesh is generated from existing 2D labeling and MR scans. Thus, 3D training data can be obtained from 2D annotations. Such high-quality meshes can also improve the training performance since points evenly distribute on the surface. Second, the one-to-one correspondences thus established can be used to generate PDM, which is very important for many segmentation methods such as ASM. In the future, we plan to use this atlas to facilitate the segmentation and tracking algorithms, using it as the shape prior information. We will also use this framework to obtain an atlas for other anatomies, such as liver.

References

1. Cootes, T.F., Taylor, C.J., Cooper, D.H., Graham, J.: Active shape model - their training and application. CVIU 61, 38–59 (1995)
2. Frangl, A.F., Rueckert, D., Duncan, J.S.: Three-dimensional cardiovascular image analysis. TMI 21(9), 1005–1010 (2002)
3. Goodall, C.: Procrustes methods in the statistical analysis of shape. J. Roy. Statistical Society 53, 285–339 (1991)
4. Lorensen, W.E., Cline, H.E.: Marching cubes: A high resolution 3D surface construction algorithm. In: SIGGRAPH, pp. 163–169 (1987)
5. Lötjönen, J., Kivistö, S., Koikkalainen, J., Smutek, D.: Statistical shape model of atria, ventricles and epicardium from short-and long-axis MR images. In: Medical Image (January 2004)
6. Metaxas, D., Axel, L., Qian, Z., Huang, X.: A segmentation and tracking system for 4D cardiac tagged MR images. In: EMBC, pp. 1541–1544 (2008)
7. Nealen, A., Igarashi, T., Sorkine, O., Alexa, M.: Laplacian mesh optimization. In: GRAPHITE, pp. 381–389 (2006)
8. Pettigrew, R., Oshinski, J.: MRI techniques for cardiovascular imaging. Journal of Magnetic Resoance Imaging 10, 590–601 (1999)
9. Shen, D., Davatzikos, C.: An adaptive-focus deformable model using statistical and geometric information. TPAMI 22(8), 906–913 (2000)
10. Wang, X., Schaerer, J., Huh, S., Qian, Z., Metaxas, D., Chen, T., Axel, L.: Reconstruction of detailed left ventricle motion from tMRI using deformable models. In: Sachse, F.B., Seemann, G. (eds.) FIHM 2007. LNCS, vol. 4466, pp. 60–69. Springer, Heidelberg (2007)
11. Zhang, H., Wahle, A., Johnson, R., Scholz, T., Sonka, M.: 4D cardiac MR image analysis: Left and right ventricular morphology and function. TMI 29(2), 350–364 (2010)
12. Zhang, S., Wang, X., Metaxas, D., Chen, T., Axel, L.: LV surface reconstruction from sparse tMRI using laplacian surface deformation and optimization. In: ISBI, pp. 698–701 (2009)
13. Zhu, Y., Papademetris, X., Sinusas, A., Duncan, J.: Segmentation of the left ventricle from cardiac MR images using a subject-specific dynamical model. TMI 29(3), 669–687 (2010)

Simulation of Diffusion Anisotropy in DTI for Virtual Cardiac Fiber Structure

Lihui Wang[1,2], Yue-Min Zhu[2], Hongying Li[2],
Wanyu Liu[1,2], and Isabelle E. Magnin[2]

[1] Harbin Institute of Technology, 150001, Harbin, China
[2] CREATIS, CNRS UMR5220, Inserm U1044, INSA Lyon, University of Lyon1,
University of Lyon. 69100 Villeurbanne, France
{lihui.wang,yuemin.zhu,hongying.li,
isabelle.magnin}@creatis.insa-lyon.fr
wanyu.liu@hit.edu.cn

Abstract. Diffusion anisotropy is the most fundamental and important parameter in the description of cardiac fibers using diffusion tensor magnetic resonance imaging (DTI), by reflecting the microstructure variation of the fiber. It is, however still not clear how the diffusion anisotropy is influenced by different contiguous structures (collagen, cardiac myocyte, etc.). In this paper, a virtual cardiac fiber structure is modeled, and diffusion weighted imaging (DWI) and DTI are simulated by the Monte Carlo method at various scales. The influences of the water content ratio in the cytoplasm and the extracellular space and the membrane permeability upon diffusion anisotropy are investigated. The simulation results show that the diffusion anisotropy increases with the increase of the ratio of water content between the intracellular cytoplasm and the extracellular medium. We show also that the anisotropy decreases with the increase of myocyte membrane permeability.

Keywords: DTI, cardiac myocyte, diffusion anisotropy, myocardial fiber, Monte Carlo simulation.

1 Introduction

The myocardial fiber structure plays an important role in determining the mechanical and electrical properties of the ventricles of the human heart. It is very useful for analyzing the normal and pathologic states of the heart. Up to now, most research on myocardial fiber structure focuses on fiber orientation, which can be provided by diffusion magnetic resonance imaging (DMRI). DMRI measures the displacement of water molecules subject to Brownian motion within the tissues. Since the mobility of the molecules is conditioned by the microstructure of the tissue, especially the direction, we can infer the structural orientation information of the later from the anisotropy of the molecular displacements.

A number of approaches for analyzing the DMRI have been proposed, and the most popular ones are diffusion tensor magnetic resonance imaging (DTI) [1, 2], high angular resolution diffusion imaging (HARDI) [3], q-space imaging (QSI) [4] and

D.N. Metaxas and L. Axel (Eds.): FIMH 2011, LNCS 6666, pp. 95–104, 2011.

q-ball imaging (QBI) [5]. These methods provide more and more precise knowledge about the orientation distribution of fibers. However, for typical DMRI, an image voxel is of the order of about 10 mm^3. For cardiac applications, it means that such voxel contains thousands of cardiac myocytes and other extracellular tissues. In this condition, it would be difficult to know exactly whether the diffusion anisotropy measured by the above imaging modalities arises from the intra myocyte compartment or the extracellular compartment or their combination [6,7]. Meanwhile, the diffusion of water molecules in each compartment (e.g., collagen, intercalated disk, membrane, and cytoplasm) is affected by the local viscosity, component, geometry and membrane permeability, etc. As a result, using DMRI techniques, it is impossible to analyze the influence of these factors on diffusion anisotropy, because of the so small size of myocytes, whose length ranges from 50~100μm, and diameter from 10~25μm [8].

In order to overcome the technical limitations of these imaging techniques, several modelling and simulation methods have been developed. In [9], the Brownian motion of molecules by the Monte Carlo (MC) was simulated in a restricted space to obtain the diffusion signal. The authors of [10] introduced the concept of spin phase memory loss during the MC simulation and applied it to describe the diffusion-induced signal attenuation. In [11] the diffusion anisotropy was simulated with the digital fiber phantom. The authors of [12] compared the experimental diffusion signal and the simulated signal for a cylinder fiber. In the present work, we propose to model virtual cardiac fiber structures (VCFS) and simulate the diffusion behavior of water molecules in this VCFS. We use the quantum spin theory to compute virtual diffusion magnetic resonance (MR) images and analyze the contribution of various structure parameters (such as water content in extracellular space and intracellular cytoplasm) and the membrane permeability to the diffusion anisotropy. The rest of this paper is organized as follows. The simulation method is presented in Section 2, the obtained results and discussion in Section 3, and the conclusion in Section 4.

2 Method

2.1 VCFS Model

In order to mimic the realistic structure of a myocyte as well as that of a myocardial fiber, and find an easy way to describe some of known variations in the tissue structure, such as the shape and the location of the myocyte, and their small shape variation during the beat of the heart, we model the VCFS as a three-dimensional matrix of realistically shaped myocytes organized into fibers. They are connected with intercalated disks and plunged in within an extracellular medium. In order to reduce computation consuming resources, the spatial resolution of the model was selected as 5 μm. The model consists of the mixture of two regions, the intracellular cytoplasm and the extracellular space. Each myocyte in the model has a size of about 15×25×90 μm^3 and all the myocytes share the same direction along the long axis but they are arranged differently in space, which means from a macroscopic viewpoint, that the anisotropy is uniform, but from a microscopic view, it is not.

2.2 Diffusion MRI Simulation Theory

The diffusion process can be seen as a sequence of small random walks of water molecules. If the walk of molecules obeys the stochastic properties of a Brownian particle, the random 3D walking displacement $\Delta\vec{r}_i$ of a molecule i during time interval δt between two random walks is then given by [12]:

$$\Delta\vec{r}_i = \sqrt{6D_0\delta t} \quad . \tag{1}$$

where D_0 is the diffusion coefficient of water molecules.

According to the basic theory of DMRI [13], the phase shift induced by this displacement is

$$\Delta\phi_i = 2\pi\vec{q}\cdot\Delta\vec{r}_i \quad . \tag{2}$$

where $\vec{q}$ is related to the diffusion gradient $\vec{G}(t)$, $q = \frac{\gamma}{2\pi}\int\vec{G}(t)dt$ and γ is the gyromagnetic ratio.

Thus, the diffusion signal can be numerically approximated by

$$E(\Delta\phi) = \frac{1}{n}\sum_{i=1}^{n}\cos(\Delta\phi_i)\ ; \qquad \Delta\phi_i \in P(\Delta\phi) \quad . \tag{3}$$

where n designates the number of molecules involved and i the index of the molecules. The phase $\Delta\phi_i$ should conform to the distribution $P(\Delta\phi)$. By combining equations (2) and (3), the diffusion signal can be further written as

$$E(\phi) = \frac{1}{n}\sum_{i=1}^{n}\cos(2\pi\vec{q}\cdot\Delta\vec{r}_i)\ ; \qquad \Delta\vec{r}_i \in P(\Delta\vec{r}) \quad . \tag{4}$$

If the diffusion gradient is a constant, according to equation (2), the distribution of $P(\Delta\vec{r})$ will be the same as that of $P(\Delta\phi)$. In our research, this distribution is simulated by a Monte Carlo method. Designating the diffusion time as Δ, then the number of random walk steps m for one molecule is

$$m = \frac{\Delta}{\delta t} \quad . \tag{5}$$

If the displacement for the i^{th} molecule induced by the j^{th} walk step is $\Delta\vec{r}_{ij}$, the corresponding phase shift is

$$\phi_{ij} = 2\pi\vec{q}\cdot\Delta\vec{r}_{ij} \quad . \tag{6}$$

At the end of the diffusion, the total phase shift for the i^{th} molecule is

$$\phi_i = \sum_{j=1}^{m}\phi_{ij} = \sum_{j=1}^{m}2\pi\vec{q}\cdot\Delta\vec{r}_{ij} \quad . \tag{7}$$

According to equation (4), we then obtain the diffusion signal

$$E(\phi) = \frac{1}{n}\sum_{i=1}^{n}\cos(\phi_i) = \frac{1}{n}\sum_{i=1}^{n}\cos(\sum_{j=1}^{m} 2\pi \bar{q}\cdot\Delta\bar{r}_{ij}) \quad . \tag{8}$$

Due to the complex structure of the cardiac fibers, the diffusion of water molecules in the VCFS model is not free. Therefore, the interaction between the molecules and the membrane of the myocyte should be considered in the simulation. In this work, such interaction is modeled by elastic collision and reflection, which means that, after the collision with the membrane, the molecule does not lose energy and will be reflected by the membrane in an arbitrary direction.

Based on the above hypothesis, we add diffusion gradients along different directions to get the diffusion weighted images of the VCFS model. In order to analyze the influence of different parameters upon the diffusion anisotropy, we calculated the diffusion tensor [14, 15] and fractional anisotropy (FA). In the present work, the number of gradient directions was selected as 30, which were obtained from the Siemens MRI machine. Let λ_1 , λ_2 and λ_3 represent respectively the three eigenvalues of the diffusion tensor. The FA is then given by [14, 15]

$$\mathrm{FA} = \sqrt{\frac{1}{2}}\frac{\sqrt{(\lambda_1-\lambda_2)^2+(\lambda_1-\lambda_3)^2+(\lambda_2-\lambda_3)^2}}{\sqrt{(\lambda_1^2+\lambda_2^2+\lambda_3^2)}} \quad . \tag{9}$$

3 Results and Discussion

In order to choose an appropriate distribution $P(\Delta\bar{r})$ of random walking step lengths, we compare two situations with respectively Gaussian and uniform distributions, which are often used in simulations [10-12]. Then, the diffusion weighted images (DWI) of the myocytes are simulated and the influence of the water content ratio in different compartments upon diffusion anisotropy is analyzed by means of the diffusion tensor. Finally, the influence of membrane permeability upon diffusion anisotropy is also investigated.

3.1 Monte Carlo Simulation of the Restricted Diffusion

We assume that water molecules diffuse in two infinite parallel plates spaced by a distance of $2a$ (Eq.10). If the diffusion gradient is applied along the direction normal to the plates, the thus resulting diffusion corresponds to the restricted diffusion. However, if the gradient is added in the direction parallel to the plates, it then concerns free diffusion of the water molecules in this direction. For the restricted diffusion and the free diffusion, the corresponding analytical diffusion equations are given respectively by

$$E_{\mathrm{retrict}} = \sin^2(\pi qa)/(\pi qa)^2 \quad . \tag{10}$$

$$E_{\mathrm{free}} = \exp(-bD_0) \quad . \tag{11}$$

which correspond to two modeling situations.

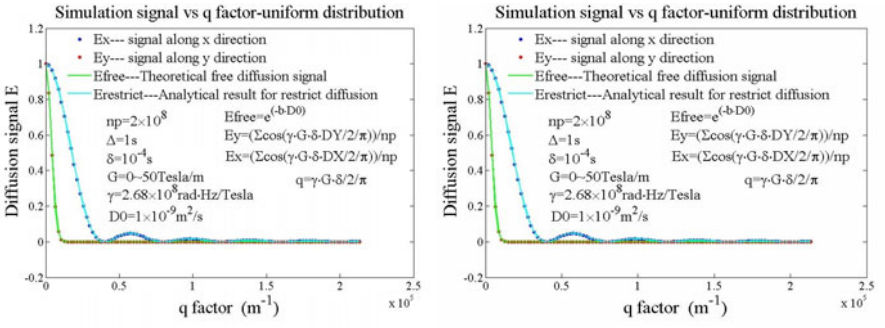

Fig. 1. Monte Carlo simulation of DMRI signal of diffusion between two plates

In all the simulations, the number of molecules was set to 2×10^8 in order to obtain the results with high accuracy. At the beginning, the molecules are uniformly distributed in space. Then, they walk randomly with either uniform or Gaussian distribution of walk step lengths, but with the same distribution of directions (between 0 and 2π). After a given time, according to equation (8), the diffusion signals in the directions both normal and parallel to the plate are calculated. All simulations were performed on a PC machine cluster; the computation time was about 16 hours. The simulation results with the corresponding parameters are illustrated in Fig. 1. It can be seen that the simulation with the uniform distribution conforms better to the theoretical results. For this reason, in the following, all the diffusion processes will be simulated using the uniform distributed walking step length.

3.2 Simulation of VCFS

In order to approximate the actual structure of myocytes, we represent it by a random hexagons combination. In the transverse plane, the myocyte location is randomly distributed on the surface. Based on the Voronoi theory, a myocyte is formed by combining the nearest neighbor hexagons. Fig.2 provides a histological image for the transverse section of myocytes and its corresponding simulation model. It can be seen that our model is fairly realistic, and that it can generate myocytes with certain regular organization but varying shapes.

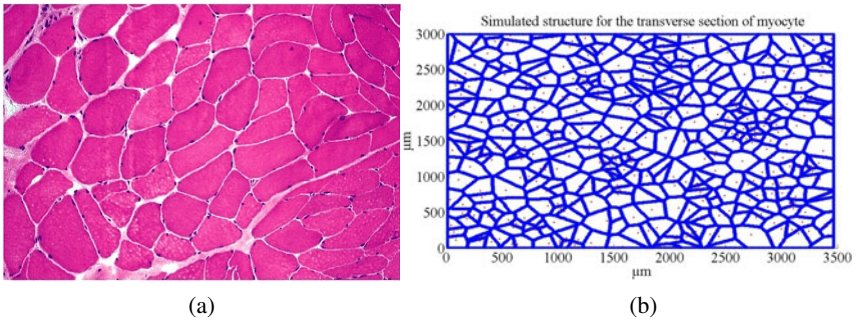

(a) (b)

Fig. 2. (a) histological image for the transverse section of myocyte (Reference [16]) (b) The VCFS transverse model

From this transverse slice, a three-dimensional myocyte is constructed by changing the length of the myocytes. By choosing the hexagon as the basic modeling element, we can control various parameters of diffusion simulation such as the boundary condition for the random walk, the simulation spatial resolution, the computation complexity, etc. In the present study, the hexagon edge length was chosen as 5μm.

3.3 DTI Simulation and Anisotropy Analysis

As mentioned in Section 2.2, diffusion tensor imaging data can be simulated by applying diffusion gradients along different directions. The DTI data are simulated at three different scales. The first DTI scale concerns that of one hexagon, which corresponds to one voxel having a dimension of 5x5x5 μm^3. The second scale is at the level of one myocyte whose spatial resolution is about 25μm, and the final scale is dealt with the simulation of several myoyctes. In the present study, we chose only four myocytes with a resolution of about 100μm, for the sake of the heavy computation load.

3.3.1 Influence of Water Content on Diffusion Anisotropy

From the research of Denis Le Bihan [17], it is considered that water molecules diffuse quickly in the intra and extra spaces, but diffuse slowly near and across the membrane. The dimension of the membrane of cardiac myocytes being about 7.5 nm [18], it is so small in comparison with that of cytoplasm and extracellular space that it will be ignored in the present simulation. The diffusion coefficient in the cytoplasm and the collagen is selected as the same, which is $D_0 = 1000\mu m^2/s$, because both of them belong to the quick diffusion region. Moreover, the dimension of water molecules is about 3.2Å, and in the cytoplasm the water content is 78%, of which 92% is immobilized [19]. Thus, for our voxel (8x8x8 μm^3), there are about 3×10^{11} water molecules. In practice, it is almost impossible to simulate with such a number of water molecules. A trade-off between computing time and simulation accuracy should then be done. We selected 1000 molecules for one voxel. For the diffusion gradient, the amplitude was chosen as 2 Tesla/μm (note however that, in real imaging, it is about 1.5 Tesla/m), the diffusion time as 50 ms, and the number of random walks during this period as 300. Since there are some contradictory conclusions in the literature about the water content in the myocyte and extracellular space, it is necessary to simulate the effects of the ratio of water contents on diffusion anisotropy. Fig. 3(a) shows a 3D simulated structure of myocytes, (b) a single transverse slice and (c) the corresponding diffusion image of the later in one gradient direction d (red color) which is illustrated in Fig.3(d). For this illustrated situation, water was distributed only in the extracellular space in order to distinguish it from the structure information.

To investigate the influence of water content in different compartments, the ratio of water content in cytoplasm and extracellular space was chosen respectively as 1/6, 1/5, 1/4, 1/3, 1/2, 1(Point1, Fig. 4(a)), 2, 3 (Point2, Fig. 4(a)), 4, 5 and 6. The simulation results are given in Fig. 4, where Fig. 4(a) shows the variation of diffusion anisotropy with the water content ratio changes in extracellular and intracellular spaces. We compare the diffusion images along the same direction for different water content ratio. It can be seen that for each pixel the diffusion signal intensity changes a

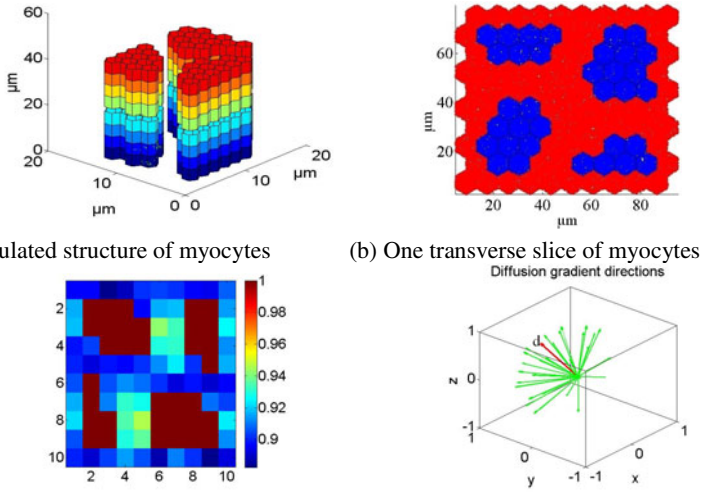

(a) 3D simulated structure of myocytes (b) One transverse slice of myocytes

(c) Simulated DWI for slice (b) indirection d (red) (d) Directions of diffusion gradient

Fig. 3. 3D Myocyte structure and diffusion image

little, which means, from a microscopic view, that the change in water content ratio does not influence greatly the anisotropy. This can also be verified by the diffusion tensor for each voxel shown in Fig. 4(b) and 4(c). However, for a larger scale of single myocyte or several myocytes, the diffusion FA increases if the water content in the myocyte is bigger than that in the extracellular medium, as illustrated by global diffusion tensor comparison in Fig. 4(b) and 4(c). This phenomenon is caused by the combination effects of diffusion in the intra- and extra- cellular compartments in the large scale measurement. All these imply that for modeling MRI diffusion signal with DTI in large scales, the water content influence should be taken into account.

3.3.2 Influence of Permeability on Diffusion Anisotropy

According to [20], there are some aqueous pores in the myocyte membrane, which allow water molecules to exchange between different compartments (intra- and extra-cellular). Following [21], the membrane permeability of a myocyte ranges from 0 to 100 μm/s. During their random walk process, water molecules will pass through the membrane with a certain probability p, determined by the permeability p_t, the diffusion coefficient D_0 and the random walk step length s. Their relationships is ruled by

$$p = p_t \times s / D_0 \quad . \tag{12}$$

The simulation results are shown in Fig. 5.

The results show that the diffusion anisotropy decreases with the increase of the membrane permeability. In the present work, walk step length is 1μm that corresponds to a diffusion time of 1/6 ms for one step. In this condition, when the membrane permeability is smaller than 50μm/s, its influence can be ignored.

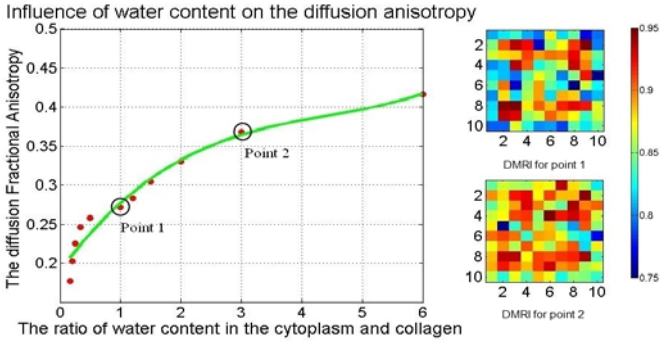

(a) Influence of water content on the FA and DWI of the myocyte slice (Fig.4(b)) in the same gradient direction d for two different water content ratios 1 (Point 1) and 3 (Point 2)

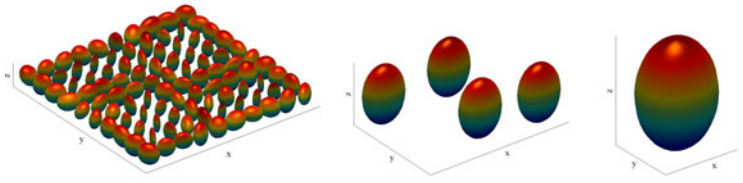

(b) 3D Diffusion Tensor of one hexagon, one myocyte and four myocytes for Point 1

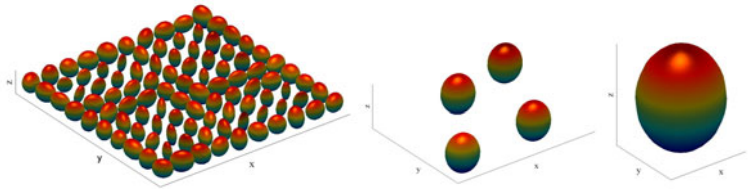

(c) 3D Diffusion Tensor of one hexagon, one myocyte and four myocytes for Point 2

Fig. 4. Influence of water content on the diffusion FA

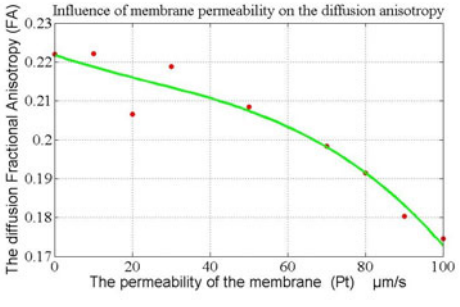

Fig. 5. Influence of membrane permeability on the FA

In practice, diffusion time in DMRI ranges from several ms to several seconds. As a result, for such long diffusion process, the contribution of permeability to FA should be considered accordingly.

4 Conclusion

A fairly realistic virtual cardiac fiber structures (VCFS) model has been constructed, and its diffusion weighted image and diffusion tensor image were simulated by Monte Carlo method. From the thus simulated images, the influences of the water content and membrane permeability upon diffusion anisotropy have been investigated. The results show that the diffusion anisotropy increases with the increase of ratio of water content between intra- and extra- cellular media, and that it decreases with the increase of membrane permeability. Consequently, for different spatial resolutions in practical imaging, the contribution to FA of water content in different compartments and permeability should be taken into account accordingly. For the future work, we will improve the VCFS model to make it more realistic and compare the thus obtained results with practical imaging techniques such as polarized optical imaging.

Acknowledgements

This work was supported by the National Natural Science Foundation of China (60777004), International S&T Cooperation Project of China (2007DFB30320), and French ANR 2009 (under ANR-09-BLAN-0372-01).

References

1. Le Bihan, D.: Looking into the functional architecture of the brain with diffusion MRI. International Congress Series. Elsevier, Amsterdam (2006)
2. Kingsley, P.B.: Introduction to diffusion tensor imaging mathematics: Part I. Tensors, rotations, and eigenvectors. Concepts in Magnetic Resonance Part A 28, 101–122 (2006)
3. Descoteaux, M., Angelino, E., Fitzgibbons, S., Deriche, R.: Apparent diffusion coefficients from high angular resolution diffusion imaging: Estimation and applications. Magnet. Reson. Med. 56, 395–410 (2006)
4. Özarslan, E., Koay, C.G., Basser, P.J.: Remarks on q-space MR propagator in partially restricted, axially-symmetric, and isotropic environments. Magnetic Resonance Imaging 27, 834–844 (2009)
5. Tuch, D.S.: Q-ball imaging. Magnet. Reson. Med. 52, 1358–1372 (2004)
6. Le Bihan, D., Poupon, C., Amadon, A., Lethimonnier, F.: Artifacts and pitfalls in diffusion MRI. Journal of Magnetic Resonance Imaging 24, 478–488 (2006)
7. Assaf, Y., Freidlin, R.Z., Rohde, G.K., Basser, P.J.: New modeling and experimental framework to characterize hindered and restricted water diffusion in brain white matter. Magnetic Resonance in Medicine 52, 965–978 (2004)
8. Severs, N.J.: The cardiac muscle cell. Bioessays 22, 188–199 (2000)
9. Duh, A., Mohori, A., Stepinik, J.: Computer simulation of the spin-echo spatial distribution in the case of restricted self-diffusion. Journal of Magnetic Resonance 148, 257–266 (2001)
10. Cai, C., Chen, Z., Cai, S., Zhong, J.: Propagator formalism and computer simulation of restricted diffusion behaviors of inter-molecular multiple-quantum coherences. Physica B: Condensed Matter 366, 127–137 (2005)

11. Fieremans, E., De Deene, Y., Delputte, S., Özdemir, M.S., D'Asseler, Y., Vlassenbroeck, J., et al.: Simulation and experimental verification of the diffusion in an anisotropic fiber phantom. Journal of Magnetic Resonance 190, 189–199 (2008)
12. Avram, L., Özarslan, E., Assaf, Y., Bar-Shir, A., Cohen, Y., Basser, P.J.: Three-dimensional water diffusion in impermeable cylindrical tubes: theory versus experiments. NMR in Biomedicine 2, 888–898 (2008)
13. Heidi, J.B., Timothy, E.J.B.: Diffusion MRI, 1st edn., p. 8. Elsevier, Amsterdam (2009)
14. Kingsley, P.B.: Introduction to diffusion tensor imaging mathematics: Part II. Anisotropy, diffusion-weighting factors, and gradient encoding schemes. Concepts in Magnetic Resonance Part A 28, 123–154 (2006)
15. Kingsley, P.B.: Introduction to diffusion tensor imaging mathematics: Part III. Tensor calculation, noise, simulations, and optimization. Concepts in Magnetic Resonance Part A 28, 155–179 (2006)
16. Skeletal, M., Reid, R.H.J., Lucia, L.B.: Histology for Pathologists, 3rd edn., p. 201. Williams & Wilkins, Baltimore (2009)
17. Bihan, D.L.: The 'wet mind': water and functional neuroimaging. Physics in medicine and biology 52, R57–R90 (2007)
18. Iaizzo, P.A.: Handbook of Cardiac Anatomy, Physiology, and Devices, 2nd edn. (2009)
19. Friedrich, M.G.: Myocardial edema—a new clinical entity? Nature Reviews Cardiology (2010)
20. Egan, J.R., Butler, T.L., Au, C.G., Tan, Y.M., North, K.N., Winlaw, D.S.: Myocardial water handling and the role of aquaporins. Biochimica et Biophysica Acta (BBA)-Biomembranes 1758, 1043–1152 (2006)
21. Ogura, T., Imanishi, S., Shibamoto, T.: Osmometric and water-transporting properties of guinea pig cardiac myocytes. The Japanese Journal of Physiology 52, 333–342 (2002)

On the Estimation of Transmural Myocardial Shear by Means of MRI Tagging

Alessandro C. Rossi, Theo Arts, and Tammo Delhaas

Department of Biomedical Engineering,
Maastricht University,
Universiteitssingel 50,
6229 ER Maastricht, The Netherlands
alessandro.rossi@maastrichtuniversity.nl

Abstract. The reliability of non-invasive myocardial shear measurements based on MRI tagging is evaluated in relation to the influence of possible edge effects close to myocardial borders. Automatic cardiac motion tracking is performed with SinMod, a method based on sinusoidal wave modeling. Shear results are evaluated for simulated images with a known imposed motion field, as well as for real short-axis acquisitions from 10 healthy volunteers. To evaluate accuracy and precision *in vivo*, automatic results are compared with manual tracings. Results show that estimation of circumferential-radial shear is feasible *in vivo*, where edge effects close to myocardial borders play a minor role as compared with those found in synthetic images. In healthy subjects, circumferential-radial shear and rotation of the myocardium appear negatively correlated.

Keywords: MRI tagging, left ventricle, myocardial mechanics, transmural gradient, shear, SinMod, Harp.

1 Introduction

Transmural deformation gradients in the left ventricle (LV), estimated non-invasively by means of MRI tagging (MRIT), have been reported in literature for healthy subjects [1] as well as for aortic stenosis patients [2]. Being closely related to the myocardial fiber arrangement in the LV, such gradients can be used, along with torsion and circumferential shortening, to analyze and validate computational models of cardiac mechanics [3].

The amount of tags along the radial direction in MRIT images of the heart is limited, due to the fact that tag spacing usually ranges between 1/2 and 1/3 of the myocardial thickness. Edge effects inducing errors in displacement estimation close to epicardial and endocardial borders could therefore hamper the assessment of transmural displacement gradients. In this regard, the aim of this study is to evaluate the accuracy and precision in measuring LV rotation angle and circumferential-radial shear (E_{cr}) using MRIT. The automatic tracking method used, SinMod [4], is based on local sine wave modeling. Measurements have been evaluated using synthetic images with a known imposed motion field, as well as comparing automatic and manual tracings of endocardial and epicardial markers in real MRIT acquisitions from 10 healthy subjects.

D.N. Metaxas and L. Axel (Eds.): FIMH 2011, LNCS 6666, pp. 105–112, 2011.

2 Materials and Methods

2.1 MRIT Acquisitions and Bandpass Filtering

Horizontal and vertical MRIT image sequences of the LV, acquired from 10 healthy adults using spatial modulation of magnetization [5], were analyzed. Short-axis MR images were acquired with a 1.5 T Gyroscan NT Intera (Philips, The Netherlands). Tag spacing was set to 6 mm in both directions. Grid images were generated by subtracting horizontally tagged images from the vertically tagged ones, and were stored for processing. For each subject, 3 short axis slices were considered: basal, equatorial and apical. The distance of basal and apical slices from the equatorial one ranged between 8 and 12 mm, depending on heart size. The first frame in each sequence was acquired 21 ms after the R-top of the ECG. The frame rate varied between 42 and 56 Hz, depending on the heart rate of the subject. Motion tracking was carried out on the first 12 frames in each sequence, starting at end diastole and covering most of the ejection period.

MRIT images were bandpass filtered in the frequency domain. The center frequency corresponded to the spatial frequency of the tags. The bandwidth to center frequency ratio was set to 1.0. The transmission factor of the bandpass filter was a squared cosine window, circularly symmetric in the domain of the complex logarithm of frequency [4].

2.2 LV Motion Tracking with SinMod

SinMod, an automatic MRIT tracking method, was implemented as described in [4]. MRIT images were modeled as moving sinusoidal wavefronts. The displacement components along horizontal ($u_x(x,y)$) and vertical ($u_y(x,y)$) directions were obtained, yielding a complete displacement map evolving in time. The center frequency ω_c of the bandpass filter was tuned to either direction x or y. Thereafter, two additional filters were defined in the passband, respectively skewed towards low and high frequencies. At each pixel of the deformed image, estimates of ω_p and u along either direction were calculated from low frequency power (P_{Lf}), high frequency power (P_{Hf}) and cross-power maps (P_{CC}) of the complex images resulting from the skewed filters:

$$\omega_p(x, y) = \omega_c \sqrt{\frac{P_{Hf}(x, y)}{P_{Lf}(x, y)}} \tag{1}$$

$$u(x, y) = \frac{\arg(P_{CC}(x, y))}{\omega_p(x, y)} \tag{2}$$

The implementation of SinMod took advantage of a shift in the frequency domain, allowing faster calculations in the spatial domain thanks to lower amounts of processed pixels. Furthermore, noise was suppressed by using a local criterion for fit quality of the sinusoidal model [4].

2.3 Lagrangian Shear Strain in Synthetic and Acquired Images

The Lagrangian circumferential-radial shear (E_{crL}) was automatically estimated both for real and for synthetic MRIT images. The latter were generated by imposing a known motion field to a myocardium-like tagged circular region, with either uniform or tagged external background (fig. 1).

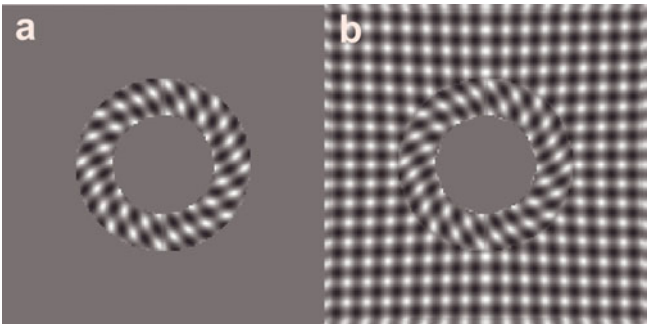

Fig. 1. Synthetic MRIT images. The circular myocardium is subject to a motion field combining rigid rotation, circumferential shortening, radial thickening and circumferential-radial shear. a) and b) show the last frame of the sequence in the cases of uniform and tagged background, respectively.

Lagrangian E_{crL} can be estimated using the u_x and u_y displacement maps obtained pixel-by-pixel with SinMod. The Cartesian components of the Lagrangian strain tensor **E**, namely E_{xx}, E_{yy} and E_{xy}, were computed by properly combining the spatial derivatives of the displacements [6]. E_{crL} was then expressed as:

$$E_{crL} = \sin(\theta) \cdot \cos(\theta) \cdot \left(E_{yy} - E_{xx}\right) + \left(\cos^2(\theta) - \sin^2(\theta)\right) \cdot E_{xy} \ , \qquad (3)$$

where θ represents the angular coordinate with respect to the LV center position at the reference frame. To compensate for potential edge-effects near myocardial borders, a Hanning weighing in the radial direction was used. This weighing enhanced the midwall values of E_{crL} when averaging over the myocardial region of interest (ROI), which for acquired images was retrieved with manual endocardial and epicardial delineation.

2.4 Rotation and Shear Estimated with 16 Markers

To validate *in vivo* automatic estimation of myocardial rotational shear, 16 markers (8 endocardial and 8 epicardial) were manually tracked throughout all the analyzed MRIT frames. Markers were placed on tag centers, trying as much as possible to distribute them equally along the circumferential direction. The images were tracked after bandpass filtering in order to reject noise. An example is shown in fig.2.

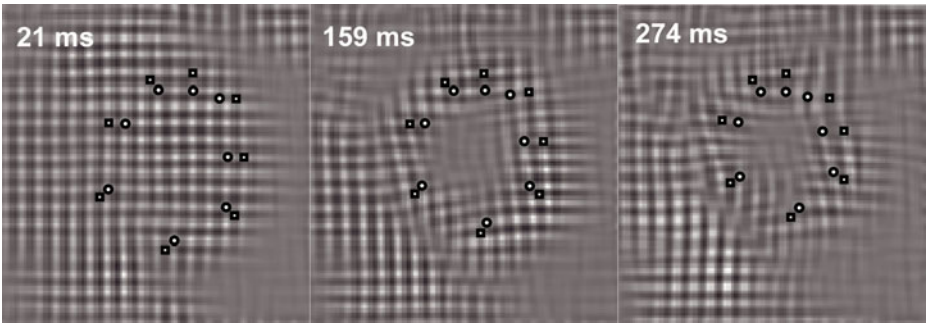

Fig. 2. End-diastolic, mid-systolic and end-systolic frames (from left to right) of an MRIT acquisition (apical slice). Manually tracked epicardial and endocardial markers are represented by white squares and white circles, respectively. Timing of each frame with respect to the ECG R-top is also shown. Images are bandpass filtered as reported in section 2.1.

Manual and automatic tracings of the 16 markers were compared. The rotation angle α of each marker with respect to the left ventricular center point was calculated, both for manually and automatically tracked positions. Rotation is positive counterclockwise, looking from the apex. The LV center point was retrieved at frame 1 by means of a best-fit circle over the myocardial ROI. To avoid the interference of rigid body translation with the calculation of rotation, the center point position was adjusted at each time frame using the average LV displacement.

Once the rotation angle was known for each marker, the mean rotation of all 16 markers and the average transmural rotation difference $\Delta\alpha_T = (\alpha_{epi} - \alpha_{endo})$ were calculated. Based on the latter, the time course of the circumferential-radial shear E_{cr} can be estimated for each analyzed MRIT slice:

$$E_{cr}(t) = \frac{R_{epi}(t) + R_{endo}(t)}{2} \cdot \frac{\Delta\alpha_T(t)}{R_{epi}(t) - R_{endo}(t)} \ , \tag{4}$$

where R_{epi} and R_{endo} are the average epicardial and endocardial radiuses, respectively.

3 Results

In order to compare SinMod results with a standard tracking method for MRIT images, Harp [7] was also implemented after the bandpass filtering described in section 2.1. Harp estimates myocardial displacements based on the differences in harmonic phase between consecutive images.

In synthetic images, E_{crL} errors depend strongly on the background texture and on the amount of rigid rotation applied. Both for SinMod and Harp, high errors in the estimation of E_{crL} are present for the tagged background case (fig. 1b), reaching on average 180% of the true E_{crL} value when a rigid rotation of 20 degrees is superimposed to shear. With uniform background (fig. 1a), E_{crL} errors are about 10 times lower.

Fig. 3 shows *in vivo* manual and SinMod results for E_{cr} estimated by means of marker tracking (eq. 4), as well as SinMod-based estimates of E_{crL} (eq. 3) for the whole myocardium. Since E_{crL} is an element on the secondary diagonal of a symmetric tensor [6], it is expected from theory that the ratio E_{cr}/E_{crL} is on average about 2.

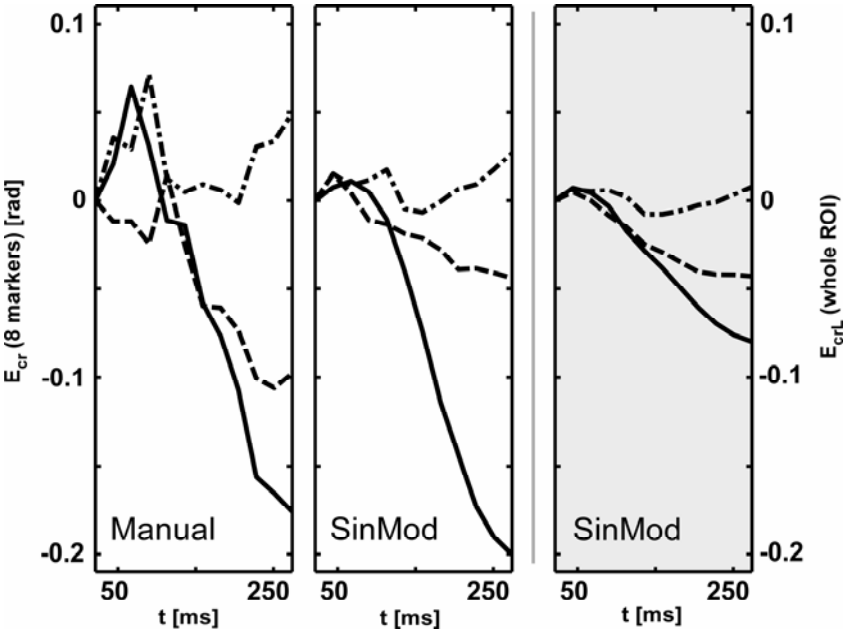

Fig. 3. Circumferential-radial shear results in a healthy subject. White panels: manual and SinMod estimations of E_{cr} combining 8 epicardial and 8 endocardial markers; grey panel: Lagrangian E_{crL} tracks averaged throughout the whole LV ROI. The ratio E_{cr}/E_{crL} is on average about 2. A systematic difference in circumferential-radial shear is present at end systole between apical (solid), equatorial (dashed) and basal (dash-dotted) tracks.

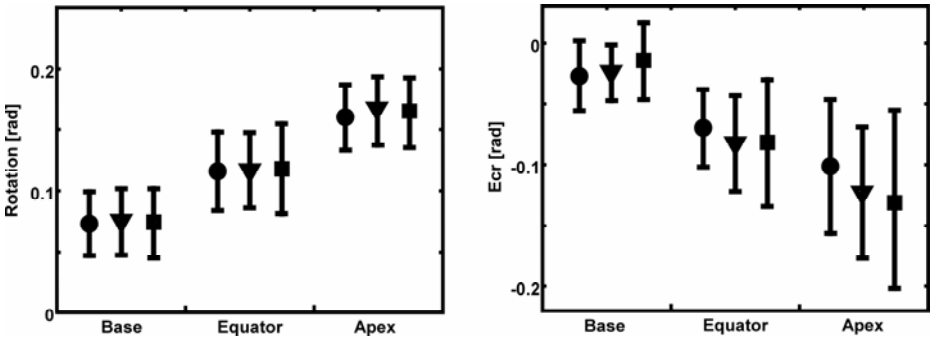

Fig. 4. Rotation (left panel) and E_{cr} (right panel) averaged among 10 healthy subjects in late systole (frames 7 to 12 of the analyzed MRIT sequences). Estimations are performed with manual tracings (circles), SinMod (triangles) and Harp (squares). Vertical bars indicate ± 1 standard deviation. Rotation and E_{cr} appear negatively correlated.

Basal, equatorial and apical rotation and E_{cr} in late systole are shown in fig. 4, averaged over all of the 10 healthy subjects analyzed. Mean rotation is assessed accurately by both SinMod and Harp. It is also clear how, contrarily to what found in synthetic images, the estimation of circumferential-radial shear is feasible *in vivo*. E_{cr} values assessed with either SinMod or Harp follow the ones measured manually, and the bias is low (fig. 4).

Bland-Altman plots [8] relating the performance of SinMod with respect to manual tracking for rotation and E_{cr} are presented in Fig. 5.

Table 1 presents, for both rotation angle and E_{cr}, the standard deviation of the differences between manual and automatic estimates in all images, expressed as percentage of the mean value across all subjects for the specific slice.

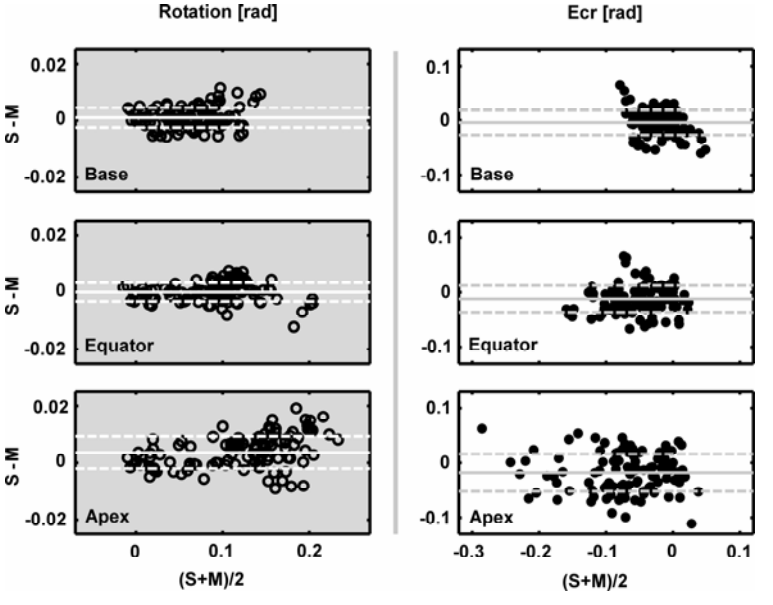

Fig. 5. Bland-Altman plots for SinMod (S) with respect to manual tracking (M). Grey panels (left) represent rotation, and white panels (right) E_{cr}, for base, equator and apex respectively (top to bottom). Solid horizontal lines represent the average difference (bias) between SinMod and manual tracking, whereas dashed lines delimit the ± 1 standard deviation range.

Table 1. Standard deviation (SD_d) of the *in vivo* estimation error, for both rotation and E_{cr}, expressed as percentage of the respective mean measured values in base, equator and apex. Estimations with SinMod are less affected by noise, especially for base and equator.

	Rotation SD_d [%]		**E_{cr} SD_d [%]**	
	SinMod	**Harp**	**SinMod**	**Harp**
Base	5.9	8.3	115.1	168.4
Equator	4.0	6.4	49.5	67.4
Apex	5.1	4.9	52.5	59.9

4 Discussion and Conclusion

When testing automatic tracking on synthetic images, the results for E_{cr} are not indicative of E_{cr} inaccuracies *in vivo* for SinMod and Harp, but are due to the unrealistically abrupt gradients found at the myocardial borders in synthetic images. Compared to fig. 1b, for instance, images acquired *in vivo* do not present the same high grey level discontinuities across the epicardial border. Hence, edge effects *in vivo*, even though being present due to the limited bandwidth of the bandpass filtering (section 2.1) and of the tagging imaging protocol, are not affecting the estimates as much as in simulations. This is also supported by the fact that, for the calculation of Lagrangian E_{crL} in real MRIT acquisitions, hardly any effect is noticed when switching on or off the Hanning weighing across the myocardial thickness.

Both Harp and SinMod accurately estimate rotation (fig. 4). SinMod performs better than Harp for the estimation of E_{cr}. The right panel of fig. 4 indicates that inter-subject bias and variability of E_{cr} estimation are lower for SinMod than for Harp. Also, Table 1 shows that SinMod presents lower errors with respect to Harp.

The standard deviation of the E_{cr} estimation error shown in Table 1 is relatively high because the myocardial thickness is relatively small with respect to tag spacing. Thus, small errors in displacement estimation on either epicardium or endocardium have a large impact on the measurement of transmural angle differentials and E_{cr}. However, fig.4 shows that the standard deviations of manual and automatic estimates across the analyzed population are similar. The slice with the lower relative precision for E_{cr} is the base (Table 1). Interestingly, as shown in fig. 4, the base is also the slice with the lower absolute variations in E_{cr}. Bland-Altman plots (fig. 5) show that SinMod is not biased when compared to manual tracings. These plots also show that errors are not dependent on the mean value of either rotation or E_{cr}.

In conclusion, this study suggests that automatic estimation of myocardial rotation and transmural shear *in vivo* can be performed accurately and precisely, by tracking non-invasive MRI tagging images. SinMod proves to be a reliable algorithm for such task. Edge effects in real images play a minor role as compared with those found in synthetic images. It is observed that at end ejection the LV apex presents a circumferential-radial shear higher in amplitude with respect to the base. This pattern has already been reported in previous studies [3], and is consistent with a base-to-apex gradient in the maximum transmural component of myofiber orientation. The negative linear correlation between the apex-to-base courses of rotation and circumferential-radial shear (fig. 4) is a feature of LV motion, and not an artifact, because both manual and automatic assessments show it. Further developments could include investigating the relation of myocardial shear strain with other quantities such as torsion and circumferential shortening, both for healthy and pathological subjects. Also, further investigations could be aimed at the comparison between SinMod and DENSE [9] for the calculation of E_{cr}. Non-invasive estimates of transmural circumferential-radial shear have the potential to unveil mechanistically relevant patterns of myocardial motion.

References

1. Russel, I.K., Gotte, M.J., Kuijer, J.P., Marcus, J.T.: Regional assessment of left ventricular torsion by CMR tagging. J. Cardiovasc. Magn. Reson. 10, 26 (2008)
2. Van Der Toorn, A., Barenbrug, P., Snoep, G., Van Der Veen, F.H., Delhaas, T., Prinzen, F.W., Maessen, J., Arts, T.: Transmural gradients of cardiac myofiber shortening in aortic valve stenosis patients using MRI tagging. Am. J. Physiol. Heart Circ. Physiol. 283, H1609–H1615 (2002)
3. Bovendeerd, P.H., Kroon, W., Delhaas, T.: Determinants of left ventricular shear strain. Am. J. Physiol. Heart Circ. Physiol. 297, H1058–H1068 (2009)
4. Arts, T., Prinzen, F., Delhaas, T., Milles, J., Rossi, A.C., Clarysse, P.: Mapping Displacement and Deformation of the Heart With Local Sine-Wave Modeling. IEEE Trans. Med. Imaging 29, 1114–1123 (2010)
5. Axel, L., Dougherty, L.: MR imaging of motion with spatial modulation of magnetization. Radiology 171, 841–845 (1989)
6. Malvern, L.E.: Introduction to the mechanics of a continuous medium. Prentice-Hall, Englewood Cliffs (1969)
7. Osman, N.F., McVeigh, E.R., Prince, J.L.: Imaging heart motion using harmonic phase MRI. IEEE Trans. Med. Imaging 19, 186–202 (2000)
8. Bland, J.M., Altman, D.G.: Statistical methods for assessing agreement between two methods of clinical measurement. Lancet 327, 307–310 (1986)
9. Zhong, X., Spottiswoode, B.S., Meyer, C.H., Kramer, C.M., Epstein, F.H.: Imaging three-dimensional myocardial mechanics using navigator-gated volumetric spiral cine DENSE MRI. Magn. Reson. Med. 64, 1089–1097 (2010)

Multi-frame Radial Basis Functions to Combine Shape and Speckle Tracking for Cardiac Deformation Analysis in Echocardiography

Colin B. Compas[1], Ben A. Lin[2], Smita Sampath[1,3], Congxian Jia[5], Qifeng Wei[6], Albert J. Sinusas[2,3], and James S. Duncan[1,3,4]

Departments of
[1] Biomedical Engineering, [2] Internal Medicine, [3] Diagnostic Radiology,
[4] Electrical Engineering,
Yale University, New Haven, CT USA
[5] Department of Biomedical Engineering, University of Michigan, Ann Arbor, MI
[6] Philips Medical Systems, Andover, MA

Abstract. Quantitative analysis of left ventricular motion can provide valuable information about cardiac function. Echocardiography is a non-invasive, readily available method that can generate real time images of heart motion. Two methods that have been used to track motion in echocardiography are shape tracking and speckle tracking. Shape tracking provides reliable tracking information on the boundaries of the myocardium, while speckle tracking is reliable across the myocardium. The complementary nature of these methods means that combining them can lead to a better overall understanding of ventricular deformation. The methods presented here use radial basis functions to combine displacements generated from the two methods using information from multiple sequential frames. Ultrasound data was acquired for six canines at baseline and also, for three of these, after myocardial infarction induced by surgical coronary occlusion. Mean segmental radial strain values showed significant decreases in the infarct regions. Comparison to tagged MRI strain values for two of the animals showed good correlation.

1 Introduction

Left ventricular (LV) deformation analysis has long been an active area of research in the medical imaging community. Quantitative analysis of LV deformation can provide information about the location and extent of myocardial injury, as well as information about treatment efficacy. In order to obtain this type of quantitative information, accurate tracking of myocardial deformation is required. Many different methods have been proposed to quantify myocardial deformation over the cardiac cycle. Shape tracking methods have been used to track feature points between image frames [1,2]. The feature points used in these methods are generally located on the endocardial and epicardial boundaries of the myocardium. These feature points are matched between adjacent frames to find a sparse set of displacements. The sparse displacements are then interpolated

D.N. Metaxas and L. Axel (Eds.): FIMH 2011, LNCS 6666, pp. 113–120, 2011.

into a dense displacement field over the entire myocardium for deformation analysis. Image noise is especially difficult to overcome in echocardiography, which makes it difficult to calculate feature points.

Echocardiography has excellent temporal resolution and portability while being relatively inexpensive. The high frame rate at which images can be acquired allows for real time imaging of cardiac deformation. In ultrasound, speckle tracking methods have been proposed to track cardiac deformation [3]. Speckle is a unique pattern generated in an ultrasound image by the underlying tissue micro-structure. This pattern remains temporally consistent for small deformations and can be used as a feature for motion tracking. Tracking is performed by calculating the maximum correlation between speckles in neighboring frames. Performing speckle tracking on the raw radio frequency (RF) signal has proven to be effective for tracking small deformations, which can be achieved by imaging at a high frame rate [4]. Speckle tracking provides good tracking results across the myocardium where the temporal coherence of the signal remains more consistent. Speckle tracking methods perform poorly on the endo- and epicardial boundaries due to inhomogeneities in the signal at the tissue boundaries.

The displacements calculated through shape and speckle tracking methods provide complementary information. Shape tracking gives more reliable information on the boundaries of the myocardium, while speckle tracking gives more reliable displacement values across the myocardium. For this reason combining these two methods can lead to improved quantification of myocardial deformation over the cardiac cycle. Since speckle tracking provides displacement values across the myocardium, models are no longer required to calculate dense displacement fields (as when using shape information alone). Speckle tracking has difficulty tracking motion lateral to the ultrasound beam due to the lower sampling rate and lack of phase information in the RF signal. Shape tracking information can be used to improve lateral tracking because it is not affected by beam orientation. The methods presented here use radial basis functions (RBFs) in a multilevel framework to combine displacement information from shape and speckle tracking. RBFs have been used extensively in scattered data approximation [5,6], as well as in medical imaging for modeling the deformation field in image registration [7] and motion tracking [8,9]. A major advantage of using RBF methods for interpolation is that data is not required to be in a regular grid. This makes them very suitable for sparse displacements that are scattered over the complex geometry of the left ventricle. Using RBFs avoids the complicated meshing step that is required in some other modeling strategies [2,10].

2 Methods

2.1 Shape Tracking Methods

A brief description of the generalized robust point matching (G-RPM) used for shape tracking is provided here. For a more detailed description of the algorithm see [10]. G-RPM is used to track a set of feature points, with associated feature values, across a set of image frames. The G-RPM algorithm uses soft-assign and

deterministic annealing techniques to jointly estimate a nonrigid transformation and correspondences between point sets. For a data point-set X, with template point-set Y, and their associated feature values an objective energy function is minimized to find the displacements from X to Y. A correspondence matrix is calculated to determine the quality of the point matches. The feature points for shape tracking are found directly from image intensity information using area based operators. Partial derivatives are taken on the image intensity values in order to find Gaussian curvature values at each point. These curvature values are then thresholded and non-maximum suppression is performed to find feature points that will remain consistent through the cardiac cycle.

2.2 Speckle Tracking Methods

Methods for RF speckle tracking have been presented in [3] and are briefly discussed here. Each pixel in the initial analytic image has both a magnitude and a phase. A two-dimensional correlation kernel is defined with a spatial extent equal to approximately one speckle. A speckle is defined as the full-width at half maximum in both dimensions of the two-dimensional auto correlation function of the initial complex image [11]. Following deformation the kernel in one image is cross-correlated with the next complex image. Initial correlations are found using only the magnitudes and then refined using the phase information. The peak correlation is found and the two-dimensional values are given for the displacement. The magnitude of the correlation can be used as a confidence measure for the quality of the displacement values. Speckle tracking feature points are found by using displacement values that correspond to a correlation value above a set threshold.

2.3 Combined Method with RBFs

Combining the shape and speckle tracking data can be posed as a data interpolation problem for a given set of distinct nodes $X = \{x_i\}_{i=1}^{N+M} \subset \mathbb{R}^2$ with function values $\{f_i\}_{i=1}^{N+M} \subset \mathbb{R}^2$. We need to find an interpolant $s : \mathbb{R}^2 \rightarrow \mathbb{R}$ such that $s(x_i) = f_i$, $i = 1, \ldots, N$. Where $\{x_1, \ldots, x_N\}$and $\{f_1, \ldots, f_N\}$ are from shape tracking, and $\{x_{N+1}, \ldots, x_M\}$ and $\{f_{N+1}, \ldots, f_M\}$ are from speckle tracking. These methods are performed here on two-dimensional data, but the nature of radial basis functions will allow for transition to three-dimensions in the future.

For data at nodes $\mathbf{x_1}$,...,$\mathbf{x_N}$ in d dimensions, the general form of an RBF approximation is

$$F(\mathbf{x}) = \sum_{i=1}^{N} \lambda_i \phi \left(||\mathbf{x} - \mathbf{x}_i|| \right) \tag{1}$$

where $||\cdot||$ denotes the Euclidean distance between two points and $\phi(r)$ is defined for $r \geq 0$. Scalar function values of $f_i = f(x_i)$ can be found from calculated displacements and the coefficients λ_i can be found by solving a system of linear equations

$$\mathbf{A}\lambda = \mathbf{f} \tag{2}$$

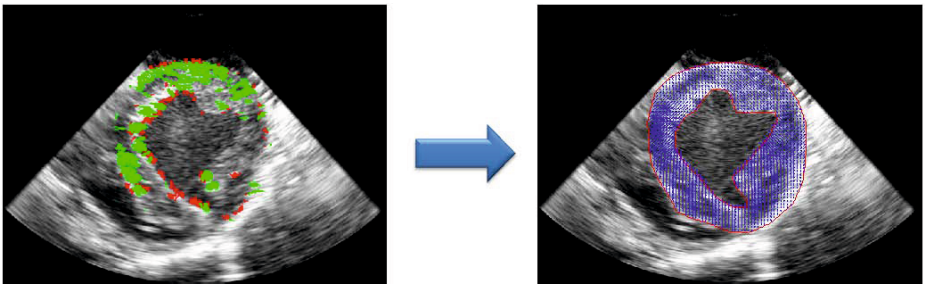

Fig. 1. Sparse input vectors (left) with shape tracking shown in red and speckle tracking showing in green. Output of dense displacement field (right).

where the interpolation matrix A is defined as $a_{ij} = \phi\left(||\mathbf{x}_i - \mathbf{x}_j||\right)$. The interpolation matrix, A, is guaranteed to be non-singular for many choices of ϕ [12]. In this work we use a compactly supported RBF (CS-RBF) for $\phi(r)$. CS-RBFs use only local information to calculate a displacement value at a given point. When solving Equation 2, CS-RBFs also provide a computational advantage over globally supported functions. Wu's compactly supported positive definite RBFs were used:

$$\phi_s\left(x\right) = \phi\left(\frac{||x||}{s}\right),\ x \in \mathbb{R}^d \tag{3}$$

$$\phi\left(r\right) = \left(1-r\right)_+^4 \left(3r^3 + 12r^2 + 16r + 4\right) \text{ for r} \geq 0 \tag{4}$$

where $\left(1-r\right)_+ = \max\left(1-r, 0\right)$, and s is the region of support for the basis function. This function was selected because it exhibits C^2 continuity and the function ϕ is guaranteed to be positive definite for dimensions up to three [5].

To combine the two sources of information CS-RBFs are implemented in a hierarchical fashion with varying levels of support. Large scale functions capture the larger motion trends while the smaller scale functions fill in finer details of the displacement field. The final deformation field, $F(x)$, can then be computed as $F(x) = F_1(x) + \cdots + F_L(x)$ with L being the total number of levels used. In this work $L = 4$. A level is defined as a given center spacing and region of influence. Centers are initially spaced equally over the myocardium at diastole. At each subsequent level the number of centers increases and the spacing between centers decreases. The region of influence for each level is set to twice the spacing distance between centers. This value was found experimentally to be the smallest value that would yield smooth results.

For each level of the algorithm a decision is made to determine if a specific region needs to be modeled using smaller scale functions. Regions with fine detail would need smaller scale functions in order to avoid smoothing out important information. Some regions that appear to have a high level of detail may be image noise and we use larger scale functions to smooth the noise. In order to determine if a region contains important details or noise we look at the displacement variance and correlation values within the region. A noisy region is

characterized by high variance with low correlation and modeled by a small number of functions with a large region of support. A region with fine details would have high variance with high correlation and is modeled in subsequent levels of the algorithm with an increasing number centers with decreasing regions of support. The values for variance and correlation that determine if a region needs further sampling have been determined experimentally.

For a given basis function center there will be a set of feature points from speckle tracking and a set of points from shape tracking that lie within the region of influence. The periodic nature of cardiac motion also allows this region of influence to be extended temporally. For image frame i, information from the previous two frames $i-2$ and $i-1$ and information from the following two frames $i+1$ and $i+2$ is used. The weighting used on the displacements from neighboring frames is inversely proportional to time. These feature values are used to generate the f_c values to solve Equation 2. For a given center c at frame i the value f_c is found as a weighted sum of speckle and shape tracking values.

$$f_i = \alpha f_{\text{speckle}} + (1-\alpha) f_{\text{shape}} \tag{5}$$

$$f_{\text{speckle}} = w(t) f_{\text{speckle},i} + \sum_{t=1}^{2} w(t) \left(f_{\text{speckle},i-t} + f_{\text{speckle},i+t} \right) \tag{6}$$

$$f_{\text{speckle}} = \frac{1}{N} \sum_{i=1}^{N} \phi \left(||x_c - x_{\text{speckle},i}|| \right) d_{\text{speckle},i} \tag{7}$$

$$f_{\text{shape}} = w(t) f_{\text{shape},i} + \sum_{t=1}^{2} w(t) \left(f_{\text{shape},i-t} + f_{\text{shape},i+t} \right) \tag{8}$$

$$f_{\text{shape}} = \frac{1}{M} \sum_{i=1}^{M} \phi \left(||x_c - x_{\text{shape},i}|| \right) d_{\text{shape},i} \tag{9}$$

where f_{speckle} and f_{shape} are the weighted means of the values contained within the region of influence in the current frame and in the two neighboring frames weighted by $w(t)$. For a given center location, x_c, x_{speckle} and x_{shape} are the locations for the N and M number of points with displacement values d_{speckle} and d_{shape} from speckle and shape tracking respectively. The parameter α weights the contribution of each of the two data sources.

3 Results

2D cardiac short-axis US images were acquired at 122-149 fps using a modified Philips iE33 system with an X7-2 phased array transducer at 4.4 MHz. The probe was suspended in a water bath over the heart for six anesthetized, open-chested canines. All subjects were imaged at baseline and three subjects were also imaged after surgical occlusion of the left anterior descending coronary artery. All studies were performed with approval of the Institutional Animal Care and Use Committee. RF and B-mode ultrasound data were exported for speckle and shape

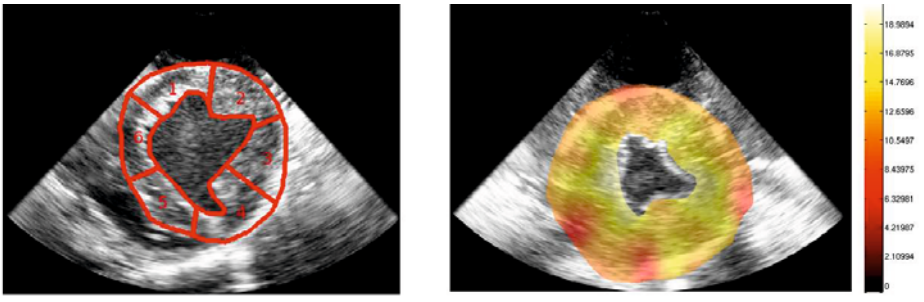

Fig. 2. (Left) Six Region Partition: (1) Anterior, (2) Anterolateral, (3) Inferolateral, (4) Inferior, (5) Inferoseptal, (6) Anteroseptal and (Right) Sample radial strain map over the myocardium for a baseline frame near peak systole

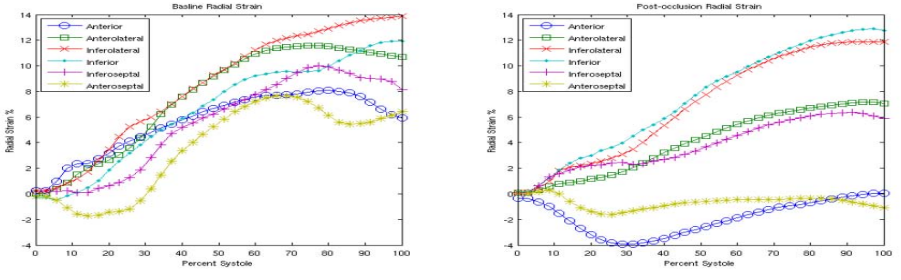

Fig. 3. Radial strain values for six cardiac segments in a single canine pre- and post-occlusion

tracking, respectively. Tagged magnetic resonance (MR) imaging was performed for two baseline animals on a 1.5T Sonata MR scanner using a 1:1 SPAMM pulse sequence [13] and a harmonic phase (HARP) MR software analysis package to compute radial strains [14].

For US data, manual contours of the endocardium and epicardium are traced were traced at end-diastole. The displacement fields were calculated between subsequent frames using the methods outlined in Section 2. The initial contours were warped to each subsequent frame using the calculated displacement field. In this way, the regions of interest were defined with minimal manual input. Radial strains were then calculated from the accumulated frame to frame displacements. For analysis radial strain values were calculated over the entire myocardium and mean radial strain values were also obtained for each of the six regions shown in Figure 2. The radial strain map is shown for a single frame of a baseline acquisition in Figure 2. The radial strain is greatest near the endocardium with lower values closer to the epicardium, as expected.

Figure 3 shows the differences in radial strain values between the baseline and post-occlusion conditions for a single animal. Physiologically, the anterior and anteroseptal regions of the myocardium are most affected by the left anterior

Table 1. Mean correlation of radial strain values across six cardiac segments for two baseline US data sets and corresponding MR data sets

	Ant.	Anterolat.	Inferolat.	Inf.	Inferosep.	Anterosep.
R	0.916	0.880	0.825	0.976	0.984	0.924

descending coronary artery occlusion. This is shown by the large scale changes in radial strain values in those regions. The inferoseptal and anterolateral regions border the area affected by the occlusion and also show a slight decrease in strain, while the inferolateral and inferior regions do not change significantly. Analysis of pooled data from all animals showed similar behavior. Mean radial strain values in the anterior and anteroseptal regions were found to have statistically significant differences pre- and post-occlusion by ANOVA analysis ($p<0.01$ and $p=0.01$, respectively).

Data in Table 1 shows that there is good correlation between the strains generated from the combined method on US data and the strains generated from MR. For the baseline data we see reasonable correlation between the two methods. The differences in how these strains are calculated could lead to the discrepancies in the strain values on the borders of the infarct. The combined US methods generate a strain map over the entire myocardium, while the MR methods calculate strains along three hand traced contours placed on the endocardium, mid-wall, and epicardium.

4 Conclusion

A new method for combining shape tracking and speckle tracking displacement values in echocardiography has been presented. This method uses RBFs in a multi-level fashion to calculate a deformation field for a single image frame using multiple frames for analysis. These methods take advantage of the complementary nature of the two tracking methods to find dense displacement and strain fields over the entire myocardium without the need for a complex meshing step or model based interpolation. We have shown that our combined method is able to distinguish between normal and infarcted regions of the myocardium. We also see consistency with corresponding MR tagged data. Future directions will extend these methods to 3D to ensure that out of plane motion of the myocardium is captured.

Acknowledgments

This project involves collaborative efforts by a large group including: Dr. Jennifer Hu, Donald P. Dione and Christi Hawley of Yale University, Dr. Karl Thiele of Philips Medical Systems, Drs. Lingyun Huang and Matthew O'Donnell of University of Washington, and Dr. Tanveer Syeda-Mahmood of IBM Almaden Research Center. This work was supported by NIH Grant 5R01HL082640-04.

References

1. Paragios, N.: A level set approach for shape-driven segmentation and tracking of the left ventricle. IEEE Transactions on Medical Imaging 22(6), 773–776 (2003)
2. Yan, P., Lin, N., Sinusas, A.J., Duncan, J.S.: A boundary element-based approach to analysis of LV deformation. In: Duncan, J.S., Gerig, G. (eds.) MICCAI 2005. LNCS, vol. 3749, pp. 778–785. Springer, Heidelberg (2005)
3. Lubinski, M., Emelianov, S., O'Donnell, M.: Speckle tracking methods for ultrasonic elasticity imaging using short-time correlation. IEEE Trans. Sonics 46(1), 82–96 (1999)
4. Yu, W., Yan, P., Sinusas, A.J., Thiele, K., Duncan, J.S.: Towards pointwise motion tracking in echocardiographic image sequences–comparing the reliability of different features for speckle tracking. Medical Image Analysis 10(4), 495–508 (2006)
5. Schaback, R.: Creating surfaces from scattered data using radial basis functions. Mathematical Methods for Curves and Surfaces, 477–496 (1995)
6. Morse, B., Yoo, T., Rheingans, P., Chen, D., Subramanian, K.: Interpolating implicit surfaces from scattered surface data using compactly supported radial basis functions. In: Proceedings International Conference on Shape Modeling and Applications, pp. 89–98 (2001)
7. Rohde, G.K., Aldroubi, A., Dawant, B.M.: The adaptive bases algorithm for intensity-based nonrigid image registration. IEEE Transactions on Medical Imaging 22(11), 1470–1479 (2003)
8. Duan, Q., Herz, S., Ingrassia, C., Costa, K., Holmes, J., Laine, A., Angelini, E., Gerard, O., Homma, S.: Dynamic cardiac information from optical flow using four dimensional ultrasound. IEEE Engineering in Medicine and Biology Society 4, 4465–4468 (2005)
9. Bistoquet, A., Oshinski, J., Skrinjar, O.: Myocardial deformation recovery from cine MRI using a nearly incompressible biventricular model. Medical Image Analysis 12(1), 69–85 (2008)
10. Lin, N., Papademetris, X., Sinusas, A.J., Duncan, J.S.: Analysis of left ventricular motion using a general robust point matching algorithm. In: Ellis, R.E., Peters, T.M. (eds.) MICCAI 2003. LNCS, vol. 2878, pp. 556–563. Springer, Heidelberg (2003)
11. Kaluzynski, K., Chen, X., Emelianov, S.Y., Skovoroda, R., O'Donnell, M.: Strain rate imaging using two-dimensional speckle tracking. IEEE Trans. Sonics 48(4), 1111–1123 (2001)
12. Buhmann, M.: Radial Basis Functions: Theory and Implemetations. Cambridge University Press, Cambridge (2003)
13. Young, A., Hitoshi, I., Chang, C.N., Axel, L.: Two-dimensional left ventricular deformation during systole using magnetic resonance imaging with spatial modulation of magnetization. Circulation 89(2), 740–752 (1994)
14. Osman, N.F., Prince, J.L.: Visualizing myocardial function using HARP MRI. Physics in Medicine and Biology 45(6), 1665–1682 (2000)

Monitoring Treatment Outcome: A Visualization Prototype for Left Ventricular Transformation

Stefan Wesarg

Interactive Graphics Systems Group (GRIS), TU Darmstadt, Germany

Abstract. The analysis of cardiac dynamics – especially of the left ventricle – is a means for evaluating the healthiness of the heart. In case that a malfunction has been detected and afterwards has been treated, the question arises whether the treatment was successful or not. On a longer time scale, it is of clinical interest to compare the results of follow-up studies with those of former examinations.

In this paper, we address both issues by presenting a visualization prototype for the comparison of left ventricular dynamics obtained from cine-MRI data. Our approach is based on the computation of differences for standard cardiac parameters between two time series which have been acquired prior to and after treatment. For their visualization, we use a series of bull's-eye displays allowing for an in-depth examination of the treatment outcome. Here, we focus on the special clinical application *ventricular reduction surgery* where we perform a retrospective evaluation for cine-MRI data acquired prior to and right after surgery as well as several months later. We compare our results with diagnosis information obtained from clinical experts.

1 Introduction

In cardiac imaging, the heart is captured at multiple points in time allowing for an examination of its dynamics. There, cardiologists are mainly interested in detecting any abnormalities related to the contraction and relaxation of the left ventricle (LV). For this purpose, cine-MRI (magnetic resonance imaging) is the imaging modality of choice that provides a series of 3D volumes which cover the whole cardiac cycle. In these data sets, the blood pool of the LV has different gray values compared to the myocardium, which permits to easily segment these two regions. Based thereon, the volume of the LV can be computed, and the two boundaries of the myocardium – endocardium and epicardium – can be defined.

Standard LV analysis uses the volume of the blood pool in order to extract end-systole (ES) as well as end-diastole (ED). Afterwards, cardiac parameters are computed [1]. In 2002, the American Heart Association (AHA) has published a set of recommendations concerning LV analysis [2]. The most important issues are the segmentation of the LV into 16/17 regions and the usage of a *bull's-eye* (BE) display for a standardized visualization.

Hennemuth et al. [3] employed a BE display for the visualization of perfusion information and delayed-enhancement image data. The approach presented by

D.N. Metaxas and L. Axel (Eds.): FIMH 2011, LNCS 6666, pp. 121–128, 2011.

de Sa Rebelo et al. [4] uses BE displays in order to show the three components of velocity vectors for the endocardial wall motion. Mantilla et al. [5] visualized computed radial and longitudinal contraction as well as torsion values for the LV in a BE display. A method for computing the degree of asynchronous wall motion and wall thickening has been introduced by Wesarg & Lacalli [6]. There, a BE display is used for the visualization of the corresponding values. A visualization combining 3D rendering and a BE display has been proposed by Termeer et al. [7]. Coronary territories derived from simulated perfusion data are color coded in both visualizations, and in addition, the coronary arteries are projected onto the BE plot. In order to distinguish between a normal and a hypokinetic heart, Kermani et al. [8] compute the *path length* and visualize these values in a BE display.

Most of the aforementioned works employ one single, static BE display for the parameter visualization. Solely, the approach by de Sa Rebelo et al. [4] uses simultaneously two BE displays – one showing the parameters at ED and a second one for ES. A visualization method for cardiac dynamics which employs a set of polar plots and that is closely related to our work has been introduced by Breeuwer [9]. The so-called *uptake movie* consists of successive images which represent the uptake of a contrast agent in the myocardium for the purpose of perfusion examination. In conjunction with the *perfusogram* – a rectangular layout of temporal and spatial perfusion parameters – a convenient navigation through the uptake movie is provided.

The computation of cardiac parameters can be performed for a single study only, i.e. analyzing cine-MRI data acquired at one specific day. However, the examination of changes of LV dynamics over a longer period is also of clinical interest. This may be a monitoring of medication related effects or a follow-up

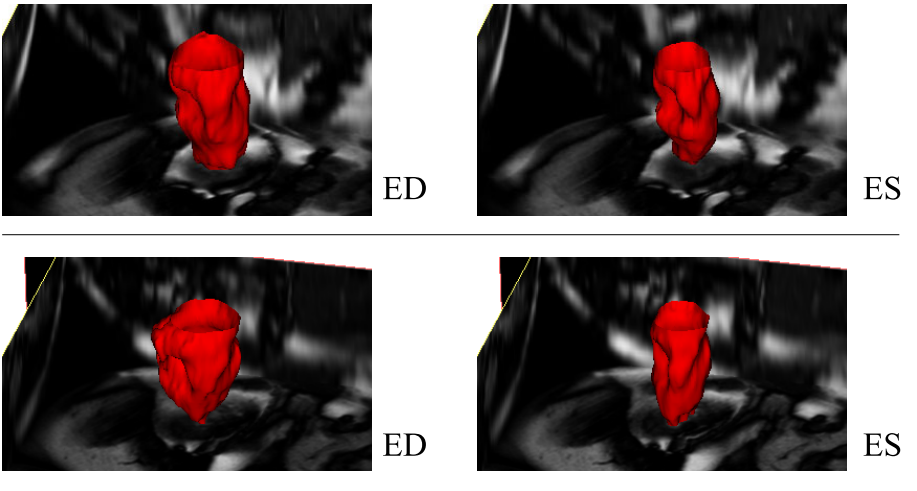

Fig. 1. Ventricular reduction surgery where the apical region is modified. The upper row shows the pre-operative situation, the lower row the status a few days after surgery.

study for investigating surgery outcome. In this work, we focus on the latter where the change of cardiac parameters caused by *ventricular reduction surgery* (VRS) [10,11] is examined. Our data sets originate from patients where the apical region has been reduced in order to give the LV a *better* overall shape (Fig. 1). For the visualization of surgery outcome, the standard static $2D$ representation of the BE display is extended to a $2D+t$ representation. Dynamic BE data is computed for two cine-MRI data sets: a first one acquired prior to surgery and a second one a few days and a few months, respectively, after the intervention. Computing the differences of cardiac parameters between these two data sets allows for a quantification and a detailed examination of left ventricular transformation.

2 Computation of Left Ventricular Transformation

Cardiac image data. Clinical cine-MRI data used for the analysis of left ventricular dynamics is typically represented as short axis (SA) slices. Employing an algorithm specifically designed for the segmentation of the left ventricle, the endocardium as well as the myocardium of the LV can be extracted for all N time steps. We use our own semi-automatic segmentation approach [12] for the extraction of the left ventricular blood pool as well as endocardial borders. However, the method described here is independent from the used segmentation algorithm. In addition to the LV extraction, we obtain a division of the LV into 16 segments (apex is neglected) for each single volume of the time series. For each of the segments, the regional volume is computed and the endocardial (and epicardial) boundaries are sampled on a regular grid of size $I \times J$ (Fig. 2, *left*). Thus, the BE data consists of a number of equally distributed values which represent a specific parameter.

Based on the delineated cine data, the geometrical measure *endocardial distance* Λ^n $n \in \{1, \ldots, N\}$ – being the distance of the sampled wall positions from

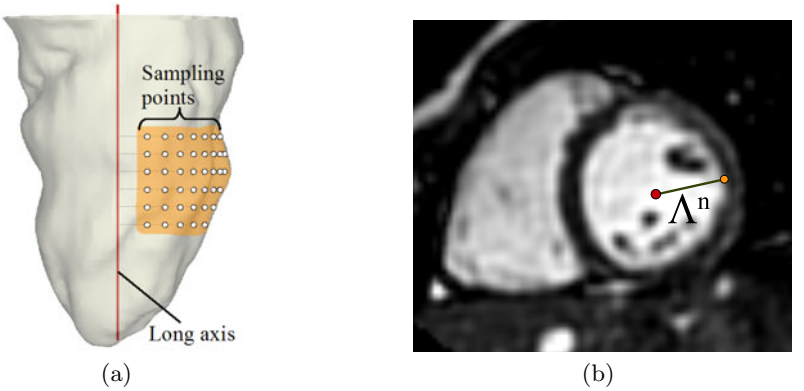

Fig. 2. Sampling of the endocardial border for one mid-cavity segment. The $I \times J$ sampling points are equally distributed over the segment of the endocardium (a) and the corresponding distances Λ^n from the long axis can be computed (b).

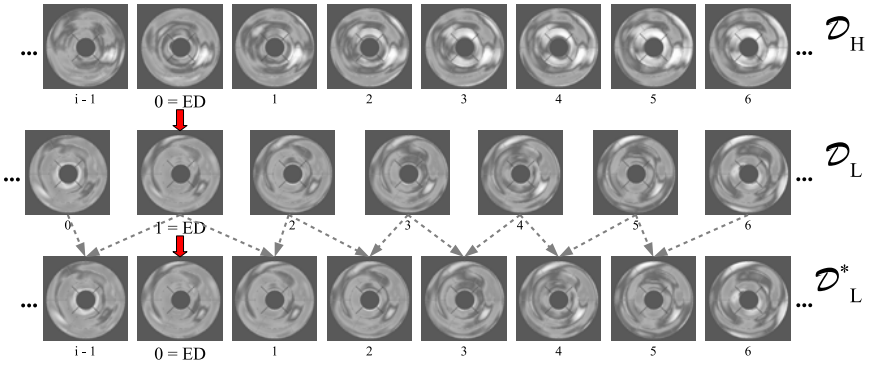

Fig. 3. Two sets $\mathcal{D}_H$ and $\mathcal{D}_L$ of dynamic BE data with different temporal resolution i and j are aligned in order to match ED. The lower resolution data set $\mathcal{D}_L$ (*middle*) is upsampled to $\mathcal{D}^*_L$ using a linear interpolation of the values (*bottom*).

the LV long axis – (Fig. 2, *right*) can easily be computed. Similarly, the *regional volume* Ω^n of the blood pool covered by each of the 16 segments can be derived. If these values are available for each of the N time steps, a series of BE data can be obtained. Thus, in contrast to the conventional approach, where one single BE display – typically related to ED and ES – is computed, we generate a series of BE data comprising all time steps. (Here, we consider only the blood pool and its boundary – the endocardium. But, similar computations can also be performed for the myocardial wall thickness.)

Temporal alignment. We aim on the comparison of two cine-MRI data sets. Assuming that for each of them the segmentation, the sampling of the boundaries as well as the computation of the BE data has been done for all time steps, the BE data has to be aligned spatially as well as temporally in order to compute differences for the cardiac parameters. This alignment could be done on the cine-MRI data directly. For this, several methods have been proposed: spatio-temporal free-form registration [13], level-set motion [14], multichannel diffeomorphic demons [15].

In contrast to these works, we follow a straightforward matching approach based on the BE data and not on the cine-MRI data itself. Spatial correspondence between the BE data is given, since the initial image data has been aligned corresponding to the AHA recommendations and the boundaries are sampled with the same number of points. Due to the fact that in the majority of cases, the temporal resolution is different, a temporal interpolation for the BE data has to be performed. Here, we ignore the rotational motion and deformation since the temporal resolution of our data sets differs only slightly: up to 2 time steps per cardiac cycle.

For performing the temporal alignment, the BE data $\mathcal{D}_H$ with the higher temporal resolution is selected and the BE data $\mathcal{D}_L$ for the other data set is interpolated (Fig. 3). This is done by first aligning the ED phases of both data

sets and afterwards computing the missing information. For each time step where data exists in $\mathcal{D}_H$, new values for $\mathcal{D}_L$ are interpolated linearly. Thus, a temporally upsampled data set $\mathcal{D}_L^*$ is obtained.

Computation of difference values. After the temporal alignment, the difference values for the parameters *endocardial distance* Λ^n as well as *regional volume* Ω^n between two image acquisition dates can be computed. For instance, the differences between pre-operative and post-operative situation are given as: $\mathcal{L} = \mathcal{D}^{\Lambda}_{post} - \mathcal{D}^{\Lambda}_{pre}$ and $\mathcal{O} = \mathcal{D}^{\Omega}_{post} - \mathcal{D}^{\Omega}_{pre}$, respectively. This results in new dynamic BE data sets $\mathcal{L}$ and $\mathcal{O}$ describing each parameter change caused by the treatment.

Visualization. The computational output of the above steps is a set of difference values which are related to specific positions in a BE display. Considering the fact that these values are available for all time steps, *dynamic BE displays* for the changes of endocardial distances as well as regional volumes can be created. For their visualization, several approaches can be used: interactively scrolling through the stack of BE displays, using a multiple window layout, dynamic visualization as animation loop. The computed parameter values are displayed by mapping them to color. For this, we use a perceptually based color map[1] (Fig. 4). The value ranges for this mapping are $(-10 \ldots 10\,mm)$ for the endocardial distance differences and $(-5 \ldots 5\,ml)$ for the regional volume differences. These settings are based on normal value ranges given in the literature [16,17].

3 Clinical Example

Our clinical partner provided us cine-MRI data obtained from over 30 patients who underwent VRS. That data comprised the pre-operative situation, the post-operative status a few days later as well as image data from a follow-up study performed several months after surgery. Due to space constraints, we show results for only one representative patient who underwent VRS.

The diagnosis reported a slightly improved overall LV function right after surgery (global EF increased from 36 % to 38 %) but a re-deterioration – occuring quite often for those patients [11] – seen in the follow-up study with a newly increased size of the LV and dramatically reduced EF (now only 28 %). Using our method, these findings are confirmed and can be investigated in more detail. For this, the differences between the values of the endocardial distances and of regional volumes related to the pre-operative situation (18 time steps) and those values for the post-operative (18 time steps) and follow-up data (16 time steps), respectively, are displayed.

Right after surgery (Fig. 4, *top*), the apical wall does virtually not move at all. The endocardial distances for these regions are larger around ES but smaller around ED compared to the pre-operative ones. In addition, the distances in the basal regions are increased around ED, thus compensating for the reduced apical

[1] Taken from `http://colorbrewer2.org`

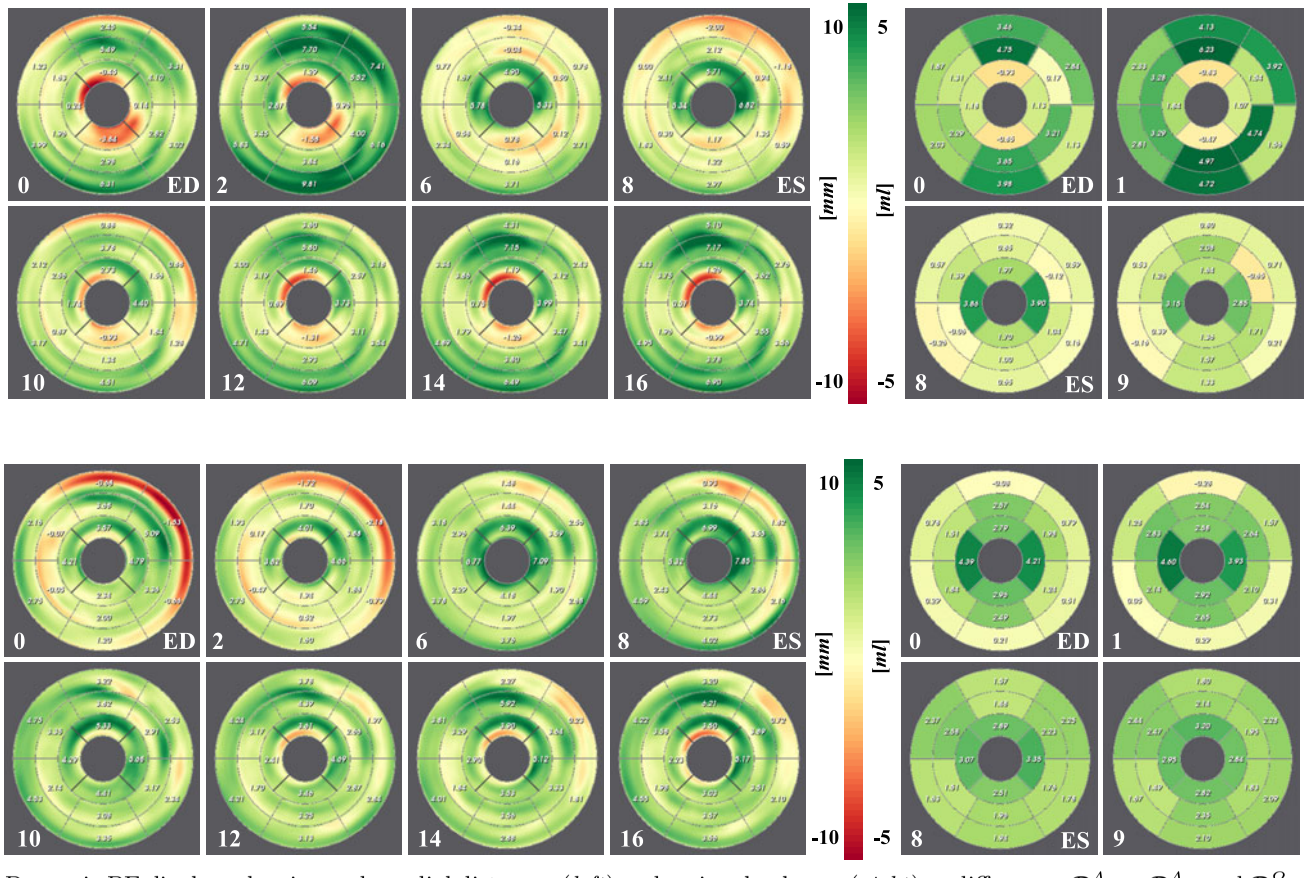

Fig. 4. Dynamic BE displays showing endocardial distances (*left*) and regional volumes (*right*) as differences $\mathcal{D}^{\Lambda}_{post} - \mathcal{D}^{\Lambda}_{pre}$ and $\mathcal{D}^{\Omega}_{post} - \mathcal{D}^{\Omega}_{pre}$, respectively (*top*) as well as differences $\mathcal{D}^{\Lambda}_{f.-up} - \mathcal{D}^{\Lambda}_{pre}$ and $\mathcal{D}^{\Omega}_{f.-up} - \mathcal{D}^{\Omega}_{pre}$, respectively (*bottom*). See text for further explanations.

regions. Consequently, the regional volume displays show significantly increased values for the apical region around ES and an increase for the mid-cavity and basal segments around ED.

Nine months later (Fig. 4, *bottom*), the wall distances for the apical regions are even larger than before surgery. Between basal anterior and lateral regions the endocardial distances are decreased. The end-systolic volume values for basal and mid-cavity regions are increased showing a lowered contractibility of the LV. In addition, the apical LV volume values are globally increased.

4 Discussion

In this work, we have presented an approach for an improved visualization of cardiac parameters related to left ventricular transformation. For this, we have adopted the idea of Breeuwer [9] to display a set of successive polar plots and extended it to a comparison of two dynamic cardiac image data sets. In case that two or more 4D data sets for the same patient are available, our method allows for an in-depth examination of the temporal evolution of cardiac parameters. Differences between the cardiac parameters can be computed and dynamic BE data can be generated. Choosing the clinical application VRS, we have shown how to benefit from our approach for gaining more insight into the changes of cardiac anatomy and function. Furthermore, it can directly be applied to other clinical purposes where the monitoring of treatment outcome after cardiac surgery or drug administration is of interest.

As an extension of the recommended usage of a BE display as preferred means for visualizing the analysis results for the LV [2], the dynamic BE display can easily be understood by cardiologists. There is no need for adapting to a new visualization method, nor is the visualization overloaded with too much information. Solely the temporal dimension is added to the display, making the information accessible which is available in any case. The visualization method presented in this work is currently in a prototypic stage. Initial tests with clinical images from our database related to VRS patients – containing data for over 30 patients – show evidence for providing more detailed information. However, an extensive clinical evaluation is needed for an ultimate verification of the assumed benefit.

Acknowledgment. We want to thank the Department of Thoracic and Cardiovascular Surgery of the J.W. Goethe University Frankfurt, Germany for providing us the image data and sharing the diagnosis information.

References

1. Frangi, A.F., Niessen, W.J., Viergever, M.A.: Three-Dimensional Modeling for Functional Analysis of Cardiac Images: A Review. IEEE Trans. Med. Imaging 20, 2–25 (2001)
2. Cerqueira, M.D., Weissman, N.J., Dilsizian, V., et al.: Standardized Myocardial Segmentation and Nomenclature for Tomographic Imaging of the Heart. Circulation 105, 539–542 (2002)

3. Hennemuth, A., Behrens, S., Kühnel, C., et al.: Novel methods for parameter-based analysis of myocardial tissue in MR images. In: Manduca, A., Hu, X.P. (eds.) Medical Imaging 2007. Proc. of SPIE, vol. 6511 (2007)
4. de Sa Rebelo, M., Meneghetti, J.C., Gutierrez, M.A.: Functional bull's eye based on three dimensional velocity information to quantify left ventricle motion in gated-SPECT. In: 30th Annual International Conference of the IEEE, Engineering in Medicine and Biology Society, EMBS 2008, pp. 209–213 (2008)
5. Mantilla, J., Bravo, A., Medina, R.: A 3-D Multi-modality Image Framework for Left Ventricle Motion Analysis. In: International of Machine Vision and Image Processing Conference, IMVIP 2008, pp. 130–135 (2008)
6. Wesarg, S., Lacalli, C.: Computation and Visualization of Asynchronous Behavior of the Heart. In: Botha, C., et al. (eds.) EG Workshop on Visual Computing for Biomedicine, pp. 29–36. Eurographics Association (2008)
7. Termeer, M., Bescos, J., Breeuwer, M., et al.: Visualization of Myocardial Perfusion Derived from Coronary Anatomy. IEEE Trans. on Visualization and Computer Graphics 14, 1595–1602 (2008)
8. Kermani, S., Moradi, M., Abrishami-Moghaddam, H., et al.: Quantitative analysis of left ventricular performance from sequences of cardiac magnetic resonance imaging using active mesh model. Computerized Medical Imaging and Graphics 33, 222–234 (2009)
9. Breeuwer, M.: Comprehensive visualization of first-pass myocardial perfusion: The uptake movie and the perfusogram. In: Proc. of the International Society for Magnetic Resonance in Medicine, 10th Scientific Meeting (2002)
10. Szabó, G., Soós, P., Seres, L., Beller, C., Juhász-Nagy, A.: Computer-assisted ventricular reduction surgery. International Congress Series 1281, 779–782 (2005); CARS 2005: Computer Assisted Radiology and Surgery
11. Ascione, R., Wilde, P., Angelini, G.D.: Left ventricular volume reduction. MMCTS 2005(0628), 760 (2005)
12. Wesarg, S., Nowak, S.: An Automated 4D Approach for Left Ventricular Assessment in Clinical Cine MR Images. In: Hochberger, C., Liskowsky, R. (eds.) Informatik 2006. Band 1. GI-Lecture Notes in Informatics, vol. P-93, pp. 483–490 (2006)
13. Perperidis, D., Mohiaddin, R.H., Rueckert, D.: Spatio-temporal free-form registration of cardiac MR image sequences. Medical Image Analysis 9(5), 441–456 (2005)
14. Firle, E.A., Nowak, S., Wesarg, S.: Dynamic registration of Cardiac MR Images. In: Proc. of the International Society for Magnetic Resonance in Medicine, 15th Scientific Meeting (2007)
15. Peyrat, J.-M., Delingette, H., Sermesant, M., Pennec, X., Xu, C., Ayache, N.: Registration of 4D Time-Series of Cardiac Images with Multichannel Diffeomorphic Demons. In: Metaxas, D., Axel, L., Fichtinger, G., Székely, G. (eds.) MICCAI 2008, Part II. LNCS, vol. 5242, pp. 972–979. Springer, Heidelberg (2008)
16. Krahwinkel, W., Haltern, G., Gülker, H.: Echocardiographic quantification of regional left ventricular wall motion with color kinesis. The American Journal of Cardiology 85, 245–250 (2000)
17. Köster, R.: A Small Primer on the Clinical Use of MSCT for Heart Exams. TOSHIBA Visions(5), 6–11 (2004)

An Ultrasound-Driven Kinematic Model of the Heart That Enforces Local Incompressibility

Dan Lin, Jeffrey W. Holmes, and John A. Hossack

Department of Biomedical Engineering,
University of Virginia, Charlottesville, Virginia, USA
{dl7ac,holmes,jh7fj}@virginia.edu

Abstract. Local incompressibility can be used to improve fitting and analysis of ultrasound-based displacement data using a heart model. An analytic mathematical model incorporating inflation, torsion, and axial extension was generalized for the left ventricle. Short-axis and long-axis images of mouse left ventricles were acquired using high frequency B-mode ultrasound and myocardial displacements were determined using speckle tracking. Deformation gradient components in the circumferential and longitudinal directions were fitted using linear regressions. The slopes of these lines were then used to predict motion in the radial directions. The optimized kinematic model accurately predicted the motion of mouse left ventricle during filling with normalized root mean square error of 4.4±1.2%.

1 Introduction

While diagnoses and therapies for cardiovascular diseases (CVD) have improved in recent years, CVD remain a major global health concern. In the United States, heart disease is the leading cause of death, accounting for 33.6% of all deaths in 2007 [1]. In an effort to curtail CVD mortality, patient-specific left ventricular (LV) modeling has been introduced to facilitate improved and individualized diagnoses [2,3,4]. Unfortunately, patient-specific modeling is currently a labor-intensive process, involving multiple medical imaging modalities (typically magnetic resonance imaging (MRI) and computed tomography (CT)), and detailed geometric modeling using finite element analysis (FEA) that requires extensive manual tracings. Thus, current approaches to patient-specific modeling are very expensive. We therefore sought a modeling approach to fitting and interpreting ultrasound data that could provide some of the advantages of patient-specific FEA, such as incorporating known aspects of myocardial mechanics, without requiring detailed knowledge of fiber structure, material properties, etc., for each heart.

Models using simple geometric shapes appropriate to the LV have been influential in studying cardiac mechanics. Cylindrical models have been used to predict distribution of stress and strain around the myocardium [5]. They have also been used to estimate material properties of the myocardium [6]. While these models have been instrumental in understanding regional ventricular function,

D.N. Metaxas and L. Axel (Eds.): FIMH 2011, LNCS 6666, pp. 129–136, 2011.

they are only accurate at the mid-ventricular section of the LV and are inadequate in modeling regions near the apex. Other models using prolate spheroidal and actual heart geometries have had better success in describing motion near the apex as well as other modes of motion observed in LV that cannot be modeled with a cylinder [7].

While there is a plethora of established cylindrical heart models [6,8], existing models are similar in that the radial motion is often assumed to be uniform and axisymmetric around the myocardium. In this paper, we derive a kinematic model describing myocardial deformation using a classic cylindrical model and myocardial incompressibility. We then generalize the model by using actual heart geometry to allow radial motion to vary as a function of R, Θ and Z. This formulation allows more freedom in describing cardiac motion but retains the incompressibility of myocardium as a constraint on the fitted displacement field.

In addition to studying cardiac mechanics, geometric models can also operate as a filter by imposing geometric constraints on allowed myocardial motion. This can be used to discard and correct improbable motion estimates derived from motion tracking techniques. For example, the incompressibility constraint has been used to improve both automated segmentation [9,10] and motion estimation [11,12,13]. This is particularly useful in small animal imaging using ultrasound, where motion estimates using speckle tracking techniques are often noisy. In mouse heart imaging, high heart rate and associated low number of image frames per cardiac cycle can result in significant decorrelation between frames. Additionally, signal dropout, attenuation and anatomical related artifacts (e.g. sternum, rib or lung related multipath reverberation) can also degrade image quality. Under these scenarios, motion estimates are frequently inaccurate and unreliable. While there are disadvantages in using ultrasound images, there exist many post image processing techniques to partially compensate for poor image quality, including clutter and artifact reduction using finite impulse response (FIR) filters [14] and principal component analysis via blind source separation method [15]. Compared to MRI and CT, medical ultrasound imaging is inexpensive, radiation free, and has high temporal image resolution. For these reasons, patient-specific modeling may therefore be feasible in a clinical setting.

2 Methods

2.1 Model Formulation

A general form of cylindrical model describing inflation, torsion and extension of a deformable thick-walled cylinder was adopted from Adkins [16]. A cylinder can inflate and deflate radially, corresponding to LV expansion from end-systole (ES) to end-diastole (ED) and LV contraction from ED to ES, respectively. Simple torsion occurs on the plane perpendicular to the axis of the cylinder, and axial extension and compression along the axis of the cylinder. In the initial cylinder

model, undeformed and deformed states were defined at ES and ED, respectively. Left ventricular filling from ES to ED is simulated using equation (1):

$$r = r(R), \theta = \theta(\Theta) + \tau Z, z = z(Z). \tag{1}$$

(R,Θ,Z) and (r,θ,z) are the radial, circumferential and longitudinal components in undeformed and deformed cylindrical coordinates, respectively. During filling, the LV expands radially as a function of R; twists circumferentially as a function of Θ and proportionally to Z by constant τ; and extends longitudinally as a function of Z. We generalized this model to account for spatial nonuniformity expected in an actual heart due to mismatch between the assumed (cylindrical) and actual geometry, regional ischemia, dyssynchrony, etc. Specifically, we allowed radial inflation to vary with circumferential and longitudinal coordinates:

$$r = r(R, \Theta, Z), \theta = \theta(\Theta, Z), z = z(Z). \tag{2}$$

LV deformation from ES to ED can be described using a deformation gradient tensor. In cylindrical polar coordinates and using equation (2), the deformation gradient matrix, F, is [17]:

$$F = \begin{pmatrix} \frac{\partial r}{\partial R} & \frac{1}{R}\frac{\partial r}{\partial \Theta} & \frac{\partial r}{\partial Z} \\ r\frac{\partial \theta}{\partial R} & \frac{r}{R}\frac{\partial \theta}{\partial \Theta} & r\frac{\partial \theta}{\partial Z} \\ \frac{\partial z}{\partial R} & \frac{1}{R}\frac{\partial z}{\partial \Theta} & \frac{\partial z}{\partial Z} \end{pmatrix} = \begin{pmatrix} \frac{\partial r}{\partial R} & \frac{1}{R}\frac{\partial r}{\partial \Theta} & \frac{\partial r}{\partial Z} \\ 0 & \frac{r}{R}\frac{\partial \theta}{\partial \Theta} & r\frac{\partial \theta}{\partial Z} \\ 0 & 0 & \frac{\partial z}{\partial Z} \end{pmatrix}. \tag{3}$$

To find a closed form solution to equation (2), the myocardium is assumed to be incompressible. This is a reasonable assumption since the myocardium is composed of 80% water [18,19], and water is almost perfectly incompressible. While studies have shown that myocardial volume is not isovolumetric due to blood perfusion in the heart, the change in volume is no more than 4% [20]. Using incompressibility, the determinant of the deformation gradient matrix is equal to unity:

$$\det(F) = \left(\frac{\partial r}{\partial R}\right)\left(\frac{r}{R}\frac{\partial \theta}{\partial \Theta}\right)\left(\frac{\partial z}{\partial Z}\right) = 1. \tag{4}$$

Integrating equation (4) and applying boundary condition at the endocardium gives:

$$r(R, \Theta, Z) = \sqrt{\frac{R^2 - R_0^2}{f(\Theta, Z)} + r_0^2}, f(\Theta, Z) = \left(\frac{\partial \theta}{\partial \Theta}\right)\left(\frac{\partial z}{\partial Z}\right). \tag{5}$$

R_0 is the endocardial radius at ES and r_0 is the endocardial radius at ED. The solutions to $\theta = \theta(\Theta, Z)$ and $z = z(Z)$ can be determined by fitting circumferential and longitudinal displacement data, and are used to predict the radial deformation that is consistent with local geometry (R_0 and r_0), circumferential and axial deformation, and myocardial incompressibility.

2.2 Mouse Heart Imaging and Motion Estimates

Short-axis (SA) and long-axis (LA) cine B-mode images of 6 healthy male C57BL/6 mice (10- to 12- weeks old, 24 to 26 g) were acquired using a VisualSonics Vevo2100 scanner (Toronto, Ontario, Canada) with a MS400 transducer operating at 30 MHz. Imaging frame rate was approximately 350 fps, and the average heart rate of mice under anesthesia was 462±14 bpm. Serial SA images were acquired at 0.5 mm interval, with 10 to 12 slices throughout the LV for each mouse. One LA cine loop through the major axis of the LV was acquired for each mouse.

Displacement fields across the myocardium were determined by speckle tracking with approximately 0.2 mm × 0.2 mm pixel block size using a minimum sum absolute difference (MSAD) algorithm and parabolic fit derived sub-pixel resolution [21]. Displacement components were transformed into cylindrical polar coordinates and fitted to the model.

2.3 Optimization of Model Parameters

For normal mouse hearts, a linear relationship was observed between θ and Θ, and between z and Z. From this observation, the final system of equations is expressed as follows:

$$r(R,\Theta,Z)=\sqrt{\frac{R^2-R_0^2}{ac}+r_0^2},\theta(\Theta,Z)=a\Theta+\tau Z+b,z(Z)=cZ+d. \quad (6)$$

In diseased mouse hearts, higher order polynomials or piece-wise functions might better explain the motions in circumferential and longitudinal directions. For healthy mouse hearts, the constants a, b, c, and d can be determined using linear regression on the observed displacement data in the circumferential and longitudinal directions; however, these constants, specifically a and c, do not optimize the model as a whole, since errors in the radial direction are not taken into consideration. To optimize these constants, the normalized root mean square error (NRMSE) between observed, (r_i,θ_i,z_i), and predicted, $(\hat{r_i},\hat{\theta_i},\hat{z_i})$, position after deformation in each direction is calculated:

$$NRMSE=\frac{1}{3\sqrt{n}}\sum_{x\in(r,\theta,z)}\frac{\sqrt{\sum_{i=1}^{n}(x_i-\hat{x_i})^2}}{x_{max}-x_{min}}. \quad (7)$$

The combination of parameter values that yields the minimum NRMSE is determined to be the optimal values:

$$(a,b,c,d,\tau)=\arg\min(NRMSE(a,b,c,d,\tau)). \quad (8)$$

3 Results

Motions in the circumferential and longitudinal directions were modeled using linear functions. Longitudinal motion is obtained using lateral displacement data derived from tracking LA cine loops. The 0 mm-position is defined at the apex at ES. As shown in figure 1A, tissues that are slightly above the apex did not have any longitudinal displacement, while tissues at the basal level move upward and tissues at the apical level move slightly downward. This effectively results in LV extension. Circumferential motion is illustrated in figure 1B. The 0-rad reference is defined at the section between the papillary muscles, and increases in counterclockwise direction. A difference in phase shift is observed at different levels of the LV. Using the midventricular layer as a reference, the basal and apical layers are observed to rotate in opposite directions. This results in LV torsion.

The coefficients determined using linear regression are optimized in their respective components. Therefore, they are not necessarily optimal for the system. Since b, d, and τ are not used in $r(R, \Theta, Z)$, these parameters can be easily optimized individually after a and c are optimized for the system. A range of values in the neighborhood of the regression coefficients a and c are simulated using the model, and the NRMSE of each combination are shown in figure 2. These coefficients were determined individually for each mouse. A statistical summary of the mean and standard deviation of the values for these coefficients are reported in table 1.

The NRMSE of the system using the optimized value is 4.4±1.2%, represented by the minimum value of the surface in figure 2. Figure 3 shows predicted radial motion at different levels of the LV. The fact that the model captures radial motion at different SA levels with a single choice of parameters for $\partial\theta/\partial\Theta$ and $\partial z/\partial Z$ suggests that most of the variation in radial motion in the normal mouse heart arises from spatial variation in geometry (R_0 and r_0 in equation (6)). As shown in figure 3C, the apical section contributes most of the error; this error near the apex is largely due to tracking error, as shown in the sparsely observed data in figure 3C.

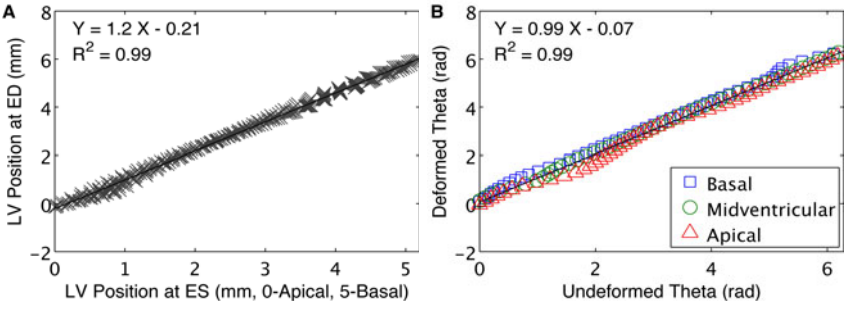

Fig. 1. Linear regression of LV wall motion in longitudinal (A) and circumferential (B) directions. LV extension and torsion are observed, where motions at the basal and apical layers are moving in opposite directions in both components.

Table 1. Optimized values for model Parameters

Parameter	Value
a	1.03±0.12
b	-0.09±0.04 rad
c	1.12±0.08
d	-0.18±0.03 mm
τ	-0.01±0.004 rad/mm

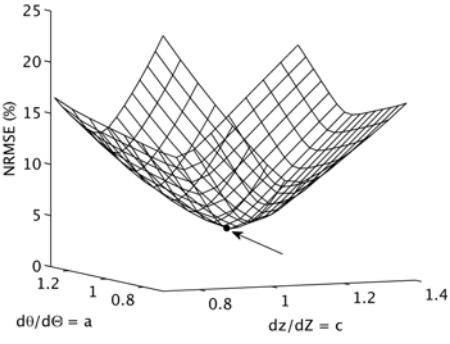

Fig. 2. Model simulation using different combinations of a and c. The NRMSE is calculated for each simulation and the combination with the minimum NRMSE (*arrow*) represents the optimal parameter values.

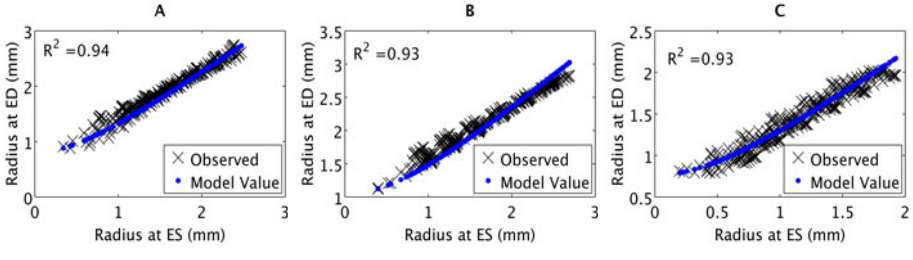

Fig. 3. Observed and predicted radial motion at the base (A), midventricular (B) and apical (C) levels of the LV

4 Conclusion

A unique kinematic model of mouse LV has been shown to accurately predict the motions of the myocardium by enforcing myocardial incompressibility. Compared to a standard cylindrical model, our generalized model can be extended to allow sufficient spatial variation in radial motion to model diseased hearts. In situations with substantial regional variation in deformation, a linear fit will not capture motion in the circumferential component; instead, higher order polynomials or piecewise functions can be used. In these cases, the value for parameter is no

longer a constant, and therefore asymmetric motion can be modeled. Asymmetric motion in the LV can be used to describe the dyssynchrony that is associated with diseased hearts.

Compared to existing geometric models of the LV, the model presented here is simple, and also accurate with 4.4% NRMSE. The presented model is shown to work well with ultrasound datasets. This model offers a lower cost approach to patient-specific modeling by using relatively noisy ultrasound image data as opposed to more expensive imaging modalities.

Acknowledgements. This work was supported by NIH NIBI grant EB001826.

References

1. Roger, V.L., Go, A.S., Lloyd-Jones, D.M., Adams, R.J., Berry, J.D., Brown, T.M., Carnethon, M.R., Dai, S., de Simone, G., Ford, E.S., Fox, C.S., Fullerton, H.J., Gillespie, C., Greenlund, K.J., Hailpern, S.M., Heit, J.A., Ho, P.M., Howard, V.J., Kissela, B.M., Kittner, S.J., Lackland, D.T., Lichtman, J.H., Lisabeth, L.D., Makuc, D.M., Marcus, G.M., Marelli, A., Matchar, D.B., McDermott, M.M., Meigs, J.B., Moy, C.S., Mozaffarian, D., Mussolino, M.E., Nichol, G., Paynter, N.P., Rosamond, W.D., Sorlie, P.D., Stafford, R.S., Turan, T.N., Turner, M.B., Wong, N.D., Wylie-Rosett, J.: Heart Disease and Stroke Statistics 2011 Update: A Report From the American Heart Association. Circulation 123, e18–e209 (2011)
2. Taylor, C.A., Figueroa, C.A.: Patient-specific Modeling of Cardiovascular Mechanics. Annu. Rev. BioMed. Eng. 11, 109–134 (2009)
3. Mihalef, V., Ionasec, R., Wang, Y., Zheng, Y., Georgescu, B., Comaniciu, D.: Patient-specific Modeling of Left Heart Anatomy, Dynamics and Hemodynamics from High Resolution 4D CT. In: IEEE ISBI, pp. 504–507 (2010)
4. Niederer, S., Rhode, K., Razavi, R., Smith, N.: The Importance of Model Parameters and Boundary Conditions in Whole Organ Models of Cardiac Contraction. In: Ayache, N., Delingette, H., Sermesant, M. (eds.) FIMH 2009. LNCS, vol. 5528, pp. 348–356. Springer, Heidelberg (2009)
5. Humphrey, J.D., Yin, F.C.: Constitutive Relations and Finite Deformations of Passive Cardiac Tissue II: Stress Analysis in the Left Ventricle. Cir. Res. 65, 805–817 (1989)
6. Guccione, J.M., McCulloch, A.D., Waldman, L.K.: Passive Material Properties of Intact Ventricular Myocardium Determined From a Cylindrical Model. J. Biomech. Eng. 113, 42–55 (1991)
7. Arts, T., Hunter, W.C., Douglas, A.D., Muijtjens, A.M., Reneman, R.S.: Description of the Deformation of the Left Ventricle by a Kinematic Model. J. Biomechanics 25, 1119–1127 (1992)
8. Costa, K.D., Hunter, P.J., Rogers, J.M., Guccione, J.M., Waldman, L.K., McCulloch, A.D.: A Three-Dimesional Finte Element Method for Large Elastic Deformations of Ventricular Myocardium: I–Cylindrical and Spherical Polar Coordinates. J. Biomech. Eng. 118, 452–463 (1996)
9. Garson, C.D., Li, B., Acton, S.T., Hossack, J.A.: Guiding Automated Left Ventricular Chamber Segmentation in Cardiac Imaging Using the Concept of Conserved Myocardial Volume. Comp. Med. Imag. Graph 32, 321–330 (2008)

10. Zhu, Y., Papademetris, X., Sinusas, A.J., Duncan, J.S.: A Coupled Deformable Model for Tracking Myocardial Borders from Real-time Echocardiography Using an Incompressibility Constraint. Med. Image Analysis 14, 429–448 (2010)
11. Bistoquet, A., Oshinski, J., Skrinjar, O.: Myocardial Deformation Recovery from Cine MRI Using a Nearly Incompressible Biventricular Model. Med. Image Analysis 12, 69–85 (2008)
12. Mansi, T., Pennec, X., Sermesant, M.: iLogDemons: A Demons-Based Registration Algorithm for Tracking Incompressible Elastic Biological Tissues. Int. J. Comput. Vis. 92, 92–111 (2010)
13. Wang, Y., Georgescu, B., Comaniciu, D., Houle, S.: Learning-Based 3D Myocardial Motion Flow Estimation Using High Frame Rate Volumetric Ultrasound Data. In: IEEE ISBI, pp. 1097–1100 (2010)
14. Lediju, M.A., Pihl, M.J., Hsu, S.J., Dahl, J.J., Gallippi, C.M., Trahey, G.E.: A Motion-Based Approach to Abdominal Clutter Reduction. IEEE Trans. Ultrason. Ferro. Freq. Cont. 56, 2437–2449 (2009)
15. Gallippi, C.M., Trahey, G.E.: Adaptive Clutter Filtering Via Blind Source Separation for Two-Dimensional Ultrasonic Blood Velocity Measurement. Ultrason. Imag. 24, 193–214 (2002)
16. Adkins, J.E.: Some General Results in the Theory of Large Elastic Deformation. Proc. R. Soc. 231, 75–90 (1955)
17. Spencer, A.J.M.: Continuum Mechanics. Longman Press, London (1980)
18. Aliev, M.K., Santos, P.D., Hoerter, J.A., Soboll, S., Tikhonov, A.N., Saks, V.A.: Water Content and Its Intracellular Distribution in Intact and Saline Perfused Rat Hearts Revisited. Cardio. Res. 53, 48–58 (2002)
19. Vinnakota, K.C., Bassingthwaighte, J.B.: Myocardial Density and Composition: A Basis for Calculating Intracellular Metabolite Concentrations. Am. J. Physiol. Heart Circ. Phyiol. 286, H1742–H1749 (2004)
20. Judd, R.M., Levy, B.I.: Effects of Barium-induced Cardiac Contraction on Large- and Small-Vessel Intramyocardial Blood Volume. Circulation 68, 217–225 (1991)
21. Li, Y., Garson, C.D., Xu, Y., Beyers, R.J., Epstein, F.H., French, B.A., Hossack, J.A.: Quantification and MRI Validation of Regional Contractile Dysfunction in Mice Post Myocardial Infarction Using High Resolution Ultrasound. Ultrasound in Med. & Biol. 33, 894–904 (2007)

Driving Dynamic Cardiac Model Adaptation with MR-Tagging Displacement Information

Christopher Casta[1], Patrick Clarysse[1], Jérôme Pousin[2], Joël Schaerer[1], Pierre Croisille[1], and Yue-Min Zhu[1]

[1] Université de Lyon, CREATIS, CNRS UMR5220, INSERM U1044, INSA-Lyon;
[2] Université de Lyon, ICJ, CNRS UMR5208, INSA-Lyon;
Université Lyon 1, 69621 Villeurbanne, France

Abstract. The dynamic deformable elastic template (DET) model has been previously introduced for the retrieval of personalized anatomical and functional models of the heart from dynamic cardiac image sequences. Dynamic DET model is a finite element deformable model, for which the minimum of the energy must satisfy a simplified equation of Dynamics. In this paper, we extend its scope to the retrieval of cardiac deformation within tagged magnetic imaging, using precomputed displacement fields as prior data to drive the model. Evaluation conducted on simulated sequences shows the performance of the model to track heart motion as a function of the quantity and quality of prior displacement information.

1 Introduction

Retrieving personalized anatomical and functional models from clinical cardiac images remains a challenging task. Magnetic resonance imaging (MRI) is a versatile imaging modality, able to provide the required data to reconstruct patient specific models. MR-tagging has been extensively used to extract in a non invasive way local myocardial deformation *in vivo*. This modality generates grids within the myocardium as temporary markers, allowing to retrieve deformation throughout the whole cycle.

Several papers have tackled motion and strain estimation from MR-tagging. Axel et al. calculated the 2D Lagrangian strain by tracking and interpolating deformation tags, using a spline method to obtain dense displacement maps [1]. Osman et al. calculated the myocardial velocity field using the phase map in the HARP method [2]. Arts et al. proposed the SinMod method to extract motion from MR-tagging image sequences, by modeling image intensity in the environment of each pixel as a moving sine wavefront [3].

A few papers have targeted the spatio-temporal modeling of the heart function from dynamic MR image sequences. Sermesant et al. proposed a bio-inspired electromechanical model of the heart designed both for the simulation of its electrical and mechanical activity [4]. Billet et al. extended this approach to cardiac motion recovery from the adjustment of the previous electromechanical heart model to cine MR images [5].

D.N. Metaxas and L. Axel (Eds.): FIMH 2011, LNCS 6666, pp. 137–144, 2011.

In a previous paper [6], we introduced the dynamic deformable elastic template model for the automatic segmentation and tracking of the heart in dynamic cine MRI sequences. This spatio-temporal approach imposes temporal smoothness and periodicity constraints to improve the regularity and continuity of the extracted contours throughout the cardiac cycle. In [7], we proposed to improve the robustness and accuracy of the results by introducing prescribed displacements to some contour model nodes. In this study, we propose to provide such point prescription by using a motion field extracted from MR-tagging. Using more or less of this information allows us to assess the behaviour of the model depending on the quantity and quality of the available motion information.

First, the principle of the dynamic DET model is briefly recalled. Then, the methodology to impose prescribed displacements from MR-tagging into dynamic DET is introduced. Then, the evaluation protocol is presented, with results on both simulated and real human MR-tagging sequences. In the last section, we discuss the behaviour of the model when dealing with a lack of prior data.

2 Dynamic DET Model

2.1 Model Main Equations

The dynamic DET model is a deformable volumetric model submitted to external constraints imposed by the image [6]. The equilibrium of the model is obtained through the minimization of an energy E which is the sum of an elastic deformation energy $E_{elastic}$ and energy E_{data} due to the action of external image forces f.

The *a priori* left ventricular (LV) model is an annulus in 2D. The material is considered to be isotropic, homogenous and completely defined by its Young modulus and its Poisson coefficient. The energy terms can be approximated by discretizing the displacement u and the force f, using the finite element method (FEM). The displacement is approximated by linear functions on these elements, while the forces are sampled at nodal points. Under this approximation, the minimum of the energy must satisfy the following simplified Dynamics equation (where acceleration is neglected):

$$\mathbf{D}\dot{\mathbf{U}} + \mathbf{K}\mathbf{U} = \mathbf{F}(\mathbf{U}, t) \tag{1}$$

where $\mathbf{K}$ is the stiffness matrix corresponding to the response of the elastic material, and $\mathbf{U}$ and $\mathbf{F}$ are respectively the displacement and force vectors on mesh nodes. We consider the matrix $\mathbf{D}$ to be a multiple of identity, with scalar coefficient α.

Note that solutions to equation (1) do not necessarily satisfy the periodicity and smoothness constraints. Hence, we look for solutions in a finite-dimensional subspace $\mathcal{F}$ generated by a set of Fourier harmonics (see [6] for details).

2.2 Algorithm Implementation

Solution to equation (1) is achieved through a pseudo-instationary process. Roughly speaking, it consists in introducing a parameter τ, and considering

a pseudo-instationary problem with respect to τ derived from the original problem. Let's define the operator $\mathbf{A} = \alpha\frac{d}{d\tau} + \mathbf{K}$ and consider,

$$\begin{cases} \frac{d\mathbf{U}}{d\tau} & = \mathbf{F}(\mathbf{U}) - \mathbf{A}\mathbf{U} \\ \mathbf{U}(0) & = 0. \end{cases} \tag{2}$$

If $\mathbf{U}$ converges when $\tau \to +\infty$, then it tends towards a limit which is a solution of the nonlinear time dependent problem. Discretizing the previous equation with finite differences to solve the temporal equation leads to (see [6] for details):

$$(\frac{1}{\Delta\tau} + \frac{\alpha}{\Delta n} + \mathbf{K})\mathbf{U}_n^\tau = \mathbf{F}(\mathbf{U}_n^{\tau-1}) + \frac{1}{\Delta\tau}\mathbf{U}_n^{\tau-1} + \frac{\alpha}{\Delta n}\mathbf{U}_{n-1}^\tau \tag{3}$$

which is a linear system and thus straightforward to solve.

3 A Priori Information Applied to the Model

In the context of the dynamic segmentation of the LV contours within conventional cine MRI sequences, the model was driven only by image based forces, which are obtained from extracted contours with gradient operators.

In [7], we investigated two different approaches to prescribe displacements on certain mesh nodes. We briefly recall the principle of the Payne's method and the way it is used to take into account displacement information from tag data.

3.1 Payne's Method for Prescribed Displacement

In the static case, the complete system of equations can be written:

$$\begin{cases} K_{11}u_1 + K_{12}u_2 + ... + K_{1n}u_n = F_1 \\ K_{21}u_1 + K_{22}u_2 + ... + K_{2n}u_n = F_2 \\ \qquad\qquad etc. \end{cases}$$

To impose the displacement of a node, for example $u_i = \tilde{u}_i$, a large value $\beta\mathbf{I}$ is attributed to the coefficient K_{ii}. The second member of the equation is replaced by $\beta\tilde{u}_i$. If β is much larger than the other coefficients of the stiffness matrix, this modification is equivalent to replacing the initial equation by $\beta u_i = \beta\tilde{u}_i$. Thus, the displacement of the node is set to the required value. This process can be extended to the dynamical scheme, and the displacement of any node at any given time point of the sequence can be imposed (see [7] for details).

3.2 MR-Tagging Data

Prescribed displacements were previously used to locally drive the model in order to obtain better LV segmentations in cine MRI sequences, especially when dealing with large contraction throughout the cardiac cycle, or highly pathological cases [7].

We propose to control the model convergence to patient data by introducing displacement information obtained from tagged MRI data, which is considered

as a reference for myocardial motion studies. Therefore, displacement fields estimated from MR-tagging are used as prescribed displacement within the Payne's scheme. Several methods have been proposed to extract motion fields from MR-tagging sequences. In the context of this study, the SinMod [3] method will be used.

We operate as follows: prescribed displacements **U** are attributed to selected nodes, depending on *a priori* data, and the stiffness matrix **K** is modified accordingly. Non prescribed nodes are displaced using a combination of forces extracted from both prescribed points and computed image based forces. In the case of cine MRI sequences, only points at end diastole (ED) and end systole (ES) phases are usually prescribed. In the case of MR-tagging sequences, prescribed displacements were attributed to every phases.

An objective is to extend the approach to 3D. However, to stay as close as possible to clinical protocols, motion information will be very sparse and only available in a limited number of short axis and long axis planes. Therefore, we are interested to evaluate the behaviour of the model when motion information is partially given. The following experimental study is designed to this aim.

4 Method Evaluation Protocol

To evaluate the impact of the proportion of tag-based motion information onto the model convergence, reference MR-tagging sequences were simulated using a parametric model. Dynamic DET model is applied to the sequence with displacement prescription randomly selected from the known reference motion. Experiment is repeated with less and less proportion of imposed displacements. Impact of actual motion measurements vs ideal motion data and the locality of missing data are studied as well.

4.1 Simulated MR-Tagging Sequences

The performance of the method was quantitatively estimated using simulated 2D-MR-tagging sequences of the heart. The sequences are generated as follows: a 2D-MR-tagging short-axis slice of the heart is taken as the first image of the simulated sequence. Then, the motion model is focused onto the myocardial area (defined with two concentric circles) and a dense displacement field is computed at successive time points in the cardiac cycle, using a simple cardiac motion model [8]. Finally, the reference real image is warped according to these fields. This results in a series of MR-tagging images that ressemble a real MR-tagging sequence, for which the whole motion is known. In this paper, the real displacement fields are later refered to as "Reference". Two sequences of 21 images covering the cardiac cycle (systole and diastole) have been generated. Ref-d30 sequence has a 30% contraction value, while Ref-d30r20 sequence has a 30% contraction value mixed with a 20 degrees rotation parameter. Figure 1 shows two sample images generated using this procedure.

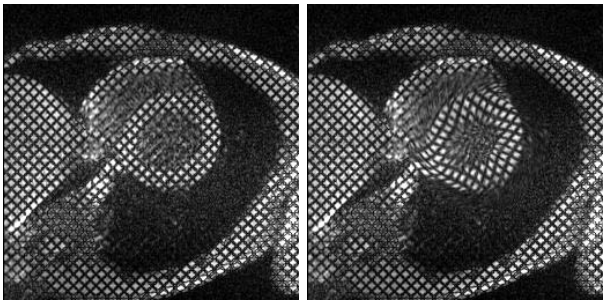

Fig. 1. Two sample images of the computer simulated 2D-MR-tagging Ref-d30r20 sequence, respectively at ED and ES

4.2 Study of Motion Prescription onto the Model

To study the impact of prior motion data, a predefined amount of model's nodes is prescribed by true motion (from analytical model). The motion resulting from the application of DET model is compared with the true one over the myocardium domain. A whole range of percentage of prescribed nodes is sweeped.

The DET model was applied to the Ref-d30 and Ref-d30r20 sequences, using the ring mesh, defined with 5 layers and 40 sectors, as the initial shape of the model. The Young modulus was set to 5 and the Poisson coefficient to 0.2 (this is to cope with the adaptation of the initial template to the data and the myocardial area variation during the cardiac cycle, in 2D). The center of the annulus, its radius and thickness were set manually. The stopping criterion was set to 10^{-5} and the parameter β (from Payne's method) to 50 (which represents a good compromise between image based-forces and prescribed-based forces).

The model was run onto the simulated sequences several times, using less and less prior data (from 100% to 10% of prescribed nodes), and the mean absolute displacement error averaged over the whole sequence was computed as:

$$\bar{err} = \frac{1}{N} \sum_{N} \sum_{i \in \Omega} \sqrt{(dx_i^{DET} - dx_i^R)^2 + (dy_i^{DET} - dy_i^R)^2}$$

where N is the number of phases, Ω is the model domain (myocardium), d_i^{DET} (resp. d_i^R) is the displacement of node i with respect to the initial position, with the DET model (resp. Reference) method.

Figure 2 shows the mean absolute displacement error for Ref-d30 and Ref-d30r20 sequences, depending on how much prescribed information is removed. The blue curve corresponds to the mean error using the reference field (Reference) as prior data. For Ref-d30, the mean error goes from 0.52mm to 1.01mm, with StD<0.007mm. For Ref-d30r20, the mean error goes from 0.53mm to 4.52mm, with StD<0.04mm.

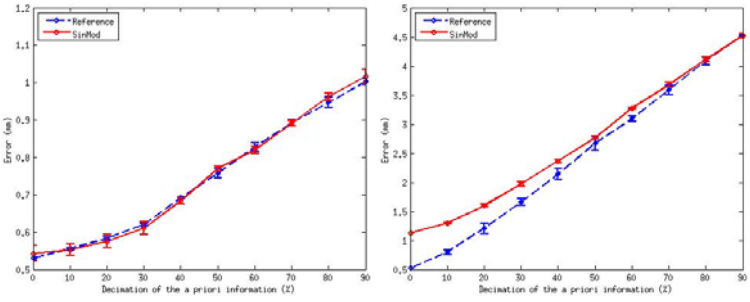

Fig. 2. Mean absolute displacement error (mm) for Ref-d30 (left) and Ref-d30r20 (right) sequence, depending on the decimation of *a priori* information, for both Reference and SinMod prescription

4.3 The Case of Noisy Motion Data

To take into account the imperfection within the motion measurements, an approach consists in adding noise to the reference displacement values. Here, we prefered to use the measurements provided by the SinMod motion estimator which is representative of what can be obtained from MR-tagging analysis. The same sensitivity analysis as the one in the previous section is performed from estimated motion measurements. In figure 2, the red curve corresponds to the error using the field extracted with the SinMod estimator as *a priori* data. For Ref-d30, the mean error goes from 0.51mm to 1.01mm, with StD<0.008mm. For Ref-d30r20, the mean error goes from 1.13mm to 4.49mm, with StD<0.02mm.

4.4 Global vs. Local Absence of Data

Previous experiments were based on a "homogeneous" distribution of motion data. To study the impact of a local absence of data, motion information was cancelled in a selected sector of the myocardium and the quality of the retrieved motion by DET model was localy assessed. Results on Ref-d30r20 sequence are shown in figure 3, where motion information was cancelled in the posteroseptal sector, in a 30 degrees sector. All the model nodes outside this sector were prescribed normally. The mean error averaged over the whole sequence is 0.64mm. The error is maximum at ES, near the endocardium, where contraction and rotational motion are the highest. However, the model accounts well for the lack of information, especially near the epicardium.

4.5 In Vivo Data

The method is experimented on real MR-tagging sequences without any additional modification. Typical results are shown in figure 4. We observed the very good propention of the method to accurately follow motion deformations.

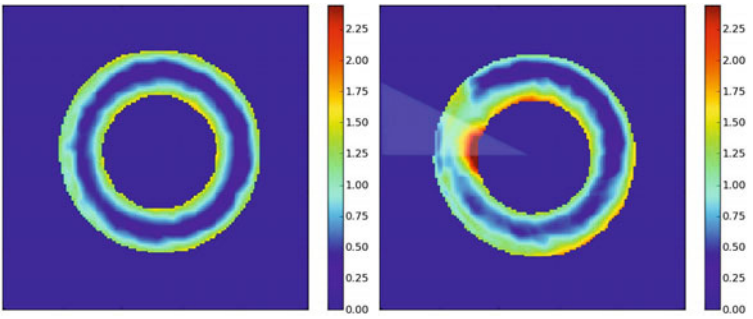

Fig. 3. Mean absolute displacement error (mm) for the Ref-d30r20 sequence at ES, with full data prescription (left), with data cancelling in the posteroseptal sector (right). The transparent layer is the region where data is cancelled.

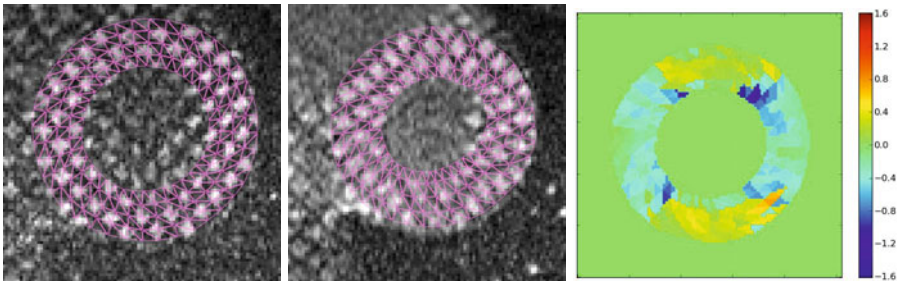

Fig. 4. DET model superimposed onto the images of a real MR-tagging sequence at a median slice of the heart, at ED (left) and ES (middle) phase. Strain map (following the vertical axis in this case) is provided by DET model (right).

5 Discussion

We used motion information from MR-tagging to drive the deformation of dynamic DET model. The performance of the method is evaluated based on simulated MR-tagging sequences, for which the motion at each myocardial point is known. In particular, we investigated the ability of the model to cope with partial miss of data.

On Ref-d30 sequence, results for both Reference and SinMod method are similar, with a small error compared to sequence Ref-d30r20. This is due to the fact that the sequence has only radial motion, hence image based forces can drive the model correctly when data prescription is missing. On Ref-d30r20 sequence, while the mean error over the whole sequence when dealing with complete prescription is about 1mm, the error difference between motion prescribed with both Reference and SinMod method becomes smaller as displacement information is removed. The mean error becomes the same between both methods when decimation is over 50%, since the model and image based forces (which only capture

radial motion) have a higher impact. It rises linearly as we remove information, which shows a good ability of the model to follow the motion of the heart even when the information is not very dense. In each case, the error is larger at end-systole because the total motion (computed relatively to end-diastole) is greater at maximum of contraction.

6 Conclusion

We have presented an improved dynamic DET, for the segmentation and tracking of the heart in MRI sequences, using displacement information from MR-tagging to drive the deformation. Experiments on simulated sequences show a good overall ability of the model to track the motion of the heart even when some amount of information is missing.

The next step will be extending DET model to track heart borders and motion in 3D, from both cine and tagged MR image sequences. Such an extension does not require any further theoretical developments, since the equations remain valid for the 3D case. However, 3D MR image processing poses a number of purely technical problems, such as inter-slice alignement, 3D interpolation and data visualization.

References

1. Axel, L., Chen, T., Manglik, T.: Dense myocardium deformation estimation for 2D tagged MRI. In: Frangi, A.F., Radeva, P., Santos, A., Hernandez, M. (eds.) FIMH 2005. LNCS, vol. 3504, pp. 446–456. Springer, Heidelberg (2005)
2. Osman, N.F., McVeigh, E.R., Prince, J.L.: Imaging heart motion using harmonic phase MRI. IEEE Trans. Med. Imaging 19(3), 186–202 (2000)
3. Arts, T., Prinzen, F.W., Delhaas, T., Milles, J.R., Rossi, A.C., Clarysse, P.: Mapping Displacement and Deformation of the Heart With Local Sine-Wave Modeling. IEEE Trans. Med. Imaging 29(5), 1114–1123 (2010)
4. Sermesant, M., Delingette, H., Ayache, N.: An Electromechanical Model of the Heart for Image Analysis and Simulation. IEEE Trans. Med. Imaging 25(5), 612–625 (2006)
5. Billet, F., Sermesant, M., Delingette, H., Ayache, N.: Cardiac Motion Recovery and Boundary Conditions Estimation by Coupling an Electromechanical Model and Cine-MRI Data. In: Ayache, N., Delingette, H., Sermesant, M. (eds.) FIMH 2009. LNCS, vol. 5528, pp. 376–385. Springer, Heidelberg (2009)
6. Schaerer, J., Casta, C., Clarysse, P., Rouchdy, Y., Pousin, J.: A Dynamic Elastic Model for Segmentation and Tracking of the Heart in MR Image Sequences. Medical Image Analysis 14(6), 738–749 (2010)
7. Casta, C., Clarysse, P., Pousin, J., Schaerer, J., Croisille, P., Zhu, Y.-M.: Incorporating Low-Level Constraints for the Retrieval of Personalised Heart Models from Dynamic MRI. In: Camara, O., Pop, M., Rhode, K., Sermesant, M., Smith, N., Young, A. (eds.) STACOM 2010. LNCS, vol. 6364, pp. 174–183. Springer, Heidelberg (2010)
8. Clarysse, P., Basset, C., Khouas, L., Croisille, P., Friboulet, D., Odet, C., Magnin, I.E.: 2D spatial and temporal displacement field fitting from cardiac MR tagging. Medical Image Analysis 3, 253–268 (2000)

Towards Patient Specific Catheter Selection: Computation of Aortic Geometry Based on Fused MRI Data

Eugen Flehmann[1], Sami ur Rahman[1], Stefan Wesarg[1], and Wolfram Voelker[2]

[1] Interactive Graphics Systems Group, Fraunhoferstr. 5, 64283 Darmstadt, Germany
{eflehmann,srahman,stefan.wesarg}@gris.tu-darmstadt.de
[2] Universitaetsklinikum Wuerzburg, Oberduerrbacher Str.6 / Haus A1, 97080, Wuerzburg, Germany
Voelker_W@medizin.uni-wuerzburg.de

Abstract. In coronary angiography, a catheter's tip has to be directed through the aorta towards the ostium – the region where the coronary arteries arise. Due to the anatomical variation in different humans, there is no common catheter which can be used for all patients. Thus, in a *trial and error* procedure cardiologists find a catheter that fits to the patient's anatomy. To replace this time consuming approach by providing a computer aided planning tool to be used prior to the intervention is the focus of our work. First of all, it is necessary for such a system to derive geometrical parameters for the patient's aorta as well as for the different available catheters. Based thereon, the best fitting catheter can be selected. In this paper, we discuss the first step: the computation of geometrical parameters from the patient's image data. Due to the setting defined by our clinical partner, two MRI data sets are acquired and should be used for the computation. This requires a specific image processing pipeline which we present here and which has to our knowledge not been proposed so far. Furthermore, we show first results obtained for real clinical data sets and discuss the subsequent steps for the development of the catheter selection tool.

1 Introduction

Coronary angiography is used for the diagnosis of any narrowing or occlusion of the coronary arteries. During this procedure, a catheter is pushed through the aorta towards the ostium – the region where the coronary arteries arise. Due to the anatomical variation in different humans, there is not a common catheter to be used for all patients. In fact, the cardiologist selects based on his or her experience a catheter that may fit to the patient's anatomy. However, on average, several catheters have to be tried out until the one that fits is found – especially in cases of anomalous anatomy. For instance, Sarkar et al. [1] tried out 79 catheters on 24 patients in order to find the correct one, which corresponds to an average of three catheters per patient.

D.N. Metaxas and L. Axel (Eds.): FIMH 2011, LNCS 6666, pp. 145–152, 2011.

Obviously, performing the procedure in this way is time consuming. And in addition, there is a slight chance of cancer from excessive exposure to radiation. Furthermore, it is also possible that a catheter which does not match the aortic anatomy punctures the wall tissue causing internal bleeding. For the cardiologist, it would be a huge benefit to be able to select the optimal catheter in advance – before starting the angiography. In the medical literature, aorta and coronary arteries shapes are discussed [2,3] and suggestions for suitable catheter selections are given [4,5]. Nevertheless, there is a lack of work dealing with patient specific catheter selection based on previously acquired image data.

This is where we start with our work. The idea is to use image data routinely acquired prior to a coronary angiography and to develop a planning tool that helps the cardiologist to select the catheter that is most appropriate. The imaging protocol used by our clinical partner dictates that the planning has to be performed on specifically acquired MRI data. On one hand, a low resolution 3D data set covering the complete ascending as well as large parts of the descending aorta is acquired. And on the other hand, a high resolution data set containing only that part of the aorta where the ostia are located is provided. Combining the information contained in these two MRI data sets serves as the basis for the computation of several geometrical parameters. The segmentation of the relevant anatomical structures as well as the computation of geometrical parameters being the first step for the intended planning tool is the focus of this work.

To the best of our knowledge, there has not been published any other work so far, dealing with patient specific catheter selection based on image data. However, there exist previous work focusing on the segmentation of aorta and coronary arteries from 3D image data sets. For example a stochastic relaxation based method for the aorta segmentation is given by Rueckert et al. [6]. A model-based segmentation is proposed by Kovacs [7,8] taking six minutes for segmentation. Wörz and Rohr [9,10] propose a 3-D cylindrical parametric intensity model which needs user interaction for the two points describing the initial 3-D position and orientation. The two level thresholding algorithm of Sauer et al. [11] needs user interaction for the two thresholding levels. The work of Lorenz et al. [12] for coronary arteries segmentation needs to select the seed point for each coronary artery. Hennemuth [13] propose a method where the user has to select a seed point above the branching points of the coronary arteries. An automatic coronary artery segmentation in X-ray images is described by Fallavollita [14]. Wang [15] propose a fully automated level set base method for CT data which needs parameter tunning wheras Shoujan [16] proposes a segmentation algorithm in X-ray projections. Most of these methods are used for CT data with sub millimeter resolution.

2 Material and Methods

For the planning of a coronary angiography, the imaging protocol used by our clinical partner defines the acquisition of two 3D MRI data sets: one containing nearly the complete aorta at low resolution ($0.83 \times 0.83 \times 1.5\,mm^3$) and a second one covering only the region of the aorta close to the ostia of the coronary

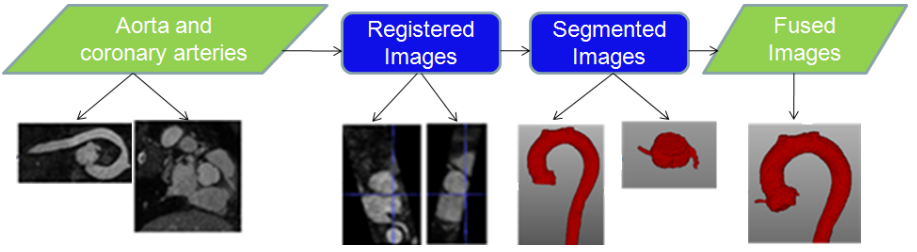

Fig. 1. Segmentation pipeline

arteries but being acquired at high resolution ($0.68 \times 0.68 \times 0.5\ mm^3$). The clinical requirement is to generate from these two data sets a single patient specific model of the aorta and the adjacent coronary arteries arising from the ascending part while masking the other arteries (e.g. subclavian and carotid). From this model, a set of geometrical parameters should be derived. This requires at first a segmentation of the relevant anatomical structures, then a fusion of the regions delineated in both data sets, and finally the generation of a skeleton of the vascular structures. We want to emphasize that the standardized image acquisition protocol as well as our developed methods allow a fully automatic segmentation as well as computation of the geometrical parameters.

2.1 Whole Aorta Segmentation

The segmentation of the aorta in the low resolution image data is performed in a slice-wise manner. We combine a Hough transform [17] with a *Fast Marching Method* (FMM) [18]. In a pre-processing step, the image data is smoothed with an anisotropic diffusion filter and a gradient magnitude filter as well as a sigmoid filter are applied.

An initial start point for the FMM is found automatically by searching for circles with the strongest Hough peaks in the gradient magnitude filtered image slices. This approach has some similarities to the work of Kovács et al. [7]. But in contrast to their method, we start from the middle slice of the stack of image data and search in 10 % of the neighboring slices for three circles with the strongest Hough peaks. Two of them represent the ascending and descending aorta, respectively. The third one is another more or less circular structure with varying location over the different slices. Searching for three circles garanties that the two parts of the aorta are found in each slice. In a next step, the circles in neighboring slices are combined to cylindrical shapes. There, two cylinders which are the largest ones emerge. The one with the largest diameter represents the ascending aorta close to the aortic root, the other one the descending aorta. The center of the latter one defines the start point for the FMM based segmentation.

Beginning at this position, the sigmoid filtered image slices are segmented stepping down the descending aorta. An FMM is applied to each slice and the center-of-gravity (COG) of the segmented region is propagated to the next slice as starting point for the FMM. Similarly, the algorithm steps upwards along the

descending aorta until the size of the segmented region abruptly decreases. This avoids that the subclavian and carotid arteries are included into the segmentation. A few slices below, the size of the segmented region has been abruptly increased. This is the position where ascending and descending aorta join. For the left half of the segmented region in this slice, the COG is computed and serves as start point for the segmentation of the ascending aorta. This part is segmented the same way as the descending aorta by stepping down towards the aortic valves. The segmentation is stopped in case that the size of the segmented region abruptly increases which occurs just below the aortic valves.

2.2 Coronary Artery Ostia Segmentation

The high resolution data set is preprocessed the same way as the low resolution one and in addition, two *vesselness filtered* [19] image data sets are created. The vesselness filters have to be used with proper smoothing of the Hessian matrix for getting the structure we are looking for. We set $\sigma = 1$ for highlighting the coronary arteries (Fig. 2 (a)) and $\sigma = 4$ for the aorta (Fig. 2 (b)). These two data sets represent additional input for the following segmentation. In order to initialize it, we first perform a rigid registration of both data sets employing a *Mean Squares Metric* and upsampling the low resolution data set to the voxel sizes of the high resolution one. We restrict the low resolution data set to fifteen slices lying above the aortic valves, whose position is known from the whole aorta segmentation described above. This increases the speed and robustness of the registration. Once the alignment is done, the COG of the aorta region already segmented in the low resolution data set and having an overlap with the high resolution data set is taken as start point. We explicitly segment the high resolution data set instead of simply transferring the segmented region from the low resolution data set since we need an accurately delineated aorta in the region of the coronary artery ostia.

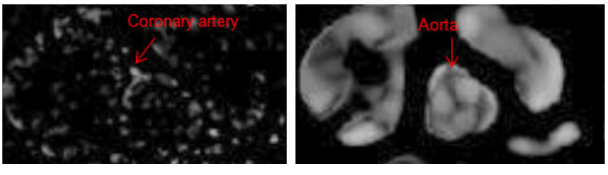

Fig. 2. Vesselness filter applied to the high resolution data set ($\sigma = 1$ (a), $\sigma = 4$ (b))

The aorta and the coronary arteries are extracted in two steps, each of them employing one of the vesselness filter output image data sets. First, the one with $\sigma = 4$ is multiplied voxel-wise with the sigmoid filter's output. Then, an FMM based slice-wise segmentation downwards and upwards the aorta, respectively, as described above is performed. Afterwards, the vesselness filtered image data with $\sigma = 1$ is added voxel-wise to the output of the FMM and the FMM is run again – but in this case in 3D. This extracts in addition to the aorta the coronary arteries being the only small structures which are directly connected to the aorta. The final step is a fusion of the segmentation results. Since the registration of low resolution and high resolution data sets has already been

done, we can simply add both segmentation results after an upsampling of the whole aorta segmentation output to the voxel sizes of the high resolution data set. When adding the results, priority is given to the segmentation derived from the high resolution image data set in the region of the ostia. Thus, we obtain a patient specific aorta model.

2.3 Geometrical Parameter Estimation

Providing a planning tool for the selection of the best fitting catheter requires to compute the geometrical parameters of the segmented structures. Clinically relevant are the following.

Centerline extraction: We use a *binary thinning* algorithm for 3D image data [20] to get the centerline of the image.

Aorta and coronary arteries diameter: We create a plane which is normal to each of the centerline's points. Along that plane, the averaged distances of the points lying on the surface of the segmented region are determined, providing values for the aorta as well as the coronary artery diameters.

Coronary artery ostium: For finding the ostium of the right coronary artery we start from the right endpoint of the skeleton (Fig. 3, point B), compute the diameter at this point, move to the next point on the skeleton and compute the diameter. We proceed to next points and by calculating the ratio between current value and the previous one we determine the skeleton point where this ratio exceeds 2.0 indicating that this point is already inside the aorta. The skeleton between the previous point and the corresponding endpoint of the skeleton is marked as coronary artery ostium. Similarly we find the ostium of the left coronary artery.

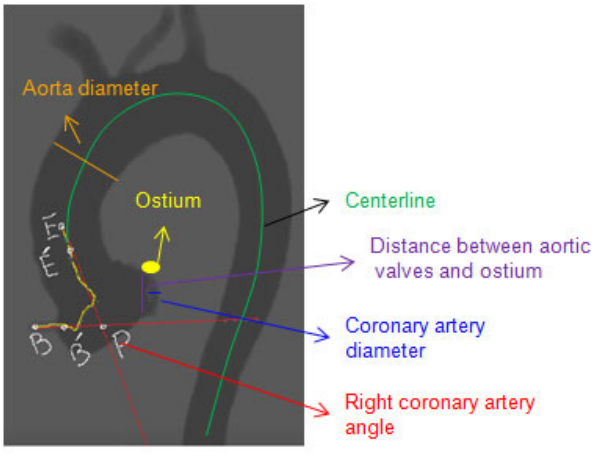

Fig. 3. The set of computed geometrical parameters illustrated for the right coronary artery curve angle

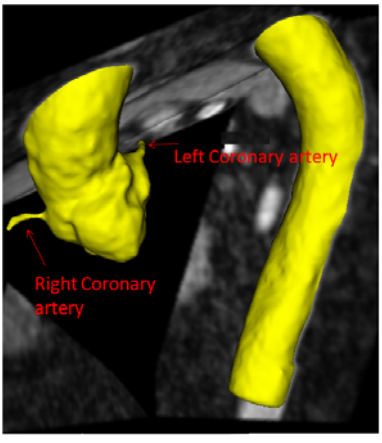

Fig. 4. Segmented aorta and coronary arteries

Coronary artery angle: For the computation of the angles of both coronaries arteries with respect to the aorta, the coronary arteries' skeleton parts as well as the skeleton part belonging to the ascending aorta are projected onto a 2D plane. Straight lines are interpolated for these projected segments and the corresponding angles between them are computed. We refer to [21] for more details.

Aortic valves position: The aortic valve position which has already been estimated during the segmentation of the whole aorta is refined. For this, the intensities in the low resolution data set within the segmented area in the slices which are close to the estimated valve position are considered. The valves appear as darker structures compared to the aorta lumen. Thus, by stepping upwards from the slice containing the initially estimated aortic valve position we search for the first slice where the mean intensity within the segmented region increases by a factor of 1.5 and consider the slice just below as the position of the aortic valves.

3 Results

For testing our developed automatic method for the segmentation and geometrical parameter derivation, a limited number of data sets from eight patients was available. Thus, we present here only initial results. For all patients, low resolution image data covering the whole aorta was available. The segmentation quality was judged visually by an experienced cardiologist. In all cases the aorta was successfully segmented. For three of the patients, additional high resolution image data was available. There, our proposed method was effective too: the segmentation as well as the fusion of the two data sets run successfully – judged again by an experienced cardiologist. Figure 4 shows segmented aorta with adjacent coronary arteries. Also, the calculation of the geometrical

parameters worked well for these three patients. The average time for the aorta segmentation and for the coronary arteries segmentation was 22 *sec* and 55 *sec*, respectively, running on a system with an *Intel* 2.67 GHz processor. There, the preprocessing of the image data sets – smoothing, gradient as well as sigmoid filtering and the computation of the vesselness in case of the coronary arteries – consumed a significant amount of time. This initial processing step took about 15 *sec* for the low resolution aorta data sets and approximately 20 *sec* for the coronary artery data sets.

4 Discussion and Conclusion

We have presented a novel segmentation and geometrical parameter estimation method for the aorta and the coronary arteries. The specialty of our method is the fact that we base our computation on two MRI data sets with different resolution and varying coverage of the aorta. From the segmentation results independently generated for the two data sets, we build a fused model of the aorta and the adjacent coronary arteries. In contrast to other methods, our approach is fully automatic. However, a limitation of our approach is that it cannot model abnormal aorta shape.

In order to meet the requirements for the derivation of geometrical parameters defined by our clinical partner, our segmentation method explicitly excludes subclavian as well carotid arteries. Based thereon, a set of patient specific geometrical parameters is derived. This serves as a basis for the recommendation of the best fitting catheter to be used during angiography. The subsequent step is the development of a procedure for computing how well a specific catheter matches the patient's anatomy [21]. Furthermore, we will do additional tests with more data sets and work on speed improvements. With the work presented here, we have done the first step towards a patient specific catheter selection.

References

1. Sarkar, K., Sharma, S., Kini, A.: Catheter Selection for Coronary Angiography and Intervention in Anomalous Right Coronary Arteries. Journal of Interventional Cardiology 22, 234–239 (2009)
2. Kimbiris, D., Iskandrian, A., Segal, B., Bemis, C.: Anomalous Aortic Origin of Coronary Arteries. Circulation 58(4), 606–615 (1978)
3. Brinkman, A., Baker, P., Newman, W., Vigorito, R., Friedman, M.: Variability of human coronary artery geometry: An angiographic study of the left anterior descending arteries of 30 autopsy hearts. Annals of Biomedical Engineering 22, 34–44 (1994), 10.1007/BF02368220
4. Myler, R., Boucher, R., Cumberland, D., Stertzer, S.: Guiding catheter selection for right coronary artery angioplasty. Catheterization and Cardiovascular Diagnosis 19 (1990)
5. Schneider, P.: Endovascular Skills: Guidewire and Catheter Skills for Endovascular Surgery, 2nd edn. Marcel Dekkar Inc., New York (2003)

6. Rueckert, D., Burger, P., Forbat, S., Mohiaddin, R., Yang, G.: Automatic tracking of the aorta in cardiovascular MR images using deformable models. IEEE Transactions on Medical Imaging 16(5), 581–590 (1997)
7. Kovács, T., Cattin, P., Alkadhi, H., Wildermuth, S., Székely, G.: Automatic Segmentation of the Vessel Lumen from 3D CTA Images of Aortic Dissection. In: Brauer, W., Handels, H., Ehrhardt, J., Horsch, A., Meinzer, H.P., Tolxdorff, T. (eds.) Bildverarbeitung für die Medizin 2006. Informatik aktuell, pp. 161–165. Springer, Heidelberg (2006)
8. Kovács, T., Cattin, P.C., Alkadhi, H., Wildermuth, S., Székely, G.: Automatic segmentation of the aortic dissection membrane from 3D CTA images. In: Yang, G.-Z., Jiang, T.-Z., Shen, D., Gu, L., Yang, J. (eds.) MIAR 2006. LNCS, vol. 4091, pp. 317–324. Springer, Heidelberg (2006)
9. Wörz, S., Rohr, K.: Segmentation and Quantification of Human Vessels Using a 3-D Cylindrical Intensity Model. IEEE Transactions on Image Processing 16(8), 1994–2004 (2007)
10. Wörz, S., von Tengg-Kobligk, H., Henninger, V., Rengier, F., Schumacher, H., Böckler, D., Kauczor, H.U., Rohr, K.: 3-D Quantification of the Aortic Arch Morphology in 3-D CTA Data for Endovascular Aortic Repair. IEEE Transactions on Biomedical Engineering 57(10), 2359–2368 (2010)
11. Saur, S., Kühnel, C., Boskamp, T., Székely, G.: Automatic Ascending Aorta Detection in CTA Datasets (2008)
12. Lorenz, C., Renisch, S., Schlathoelter, T., Buelow, T.: Simultaneous segmentation and tree reconstruction of the coronary arteries in MSCT images. SPIE, vol. 5031, pp. 167–177 (2003)
13. Hennemuth, A., Boskamp, T., Fritz, D., Kühnel, C., Bock, S., Rinck, D., Scheuering, M., Peitgen, H.O.: One-click coronary tree segmentation in CT angiographic images. International Congress Series 1281, 317–321 (2005); CARS 2005: Computer Assisted Radiology and Surgery
14. Fallavollita, P., Cheriet, F.: Towards an Automatic Coronary Artery Segmentation Algorithm. In: 28th Annual International Conference of the IEEE Engineering in Medicine and Biology Society, EMBS 2006 (30, 2006)
15. Wang, Y., Liatsis, P.: A Fully Automated Framework for Segmentation and Stenosis Quantification of Coronary Arteries in 3D CTA Imaging. In: 2009 Second International Conference on Developments in eSystems Engineering (DESE), pp. 136–140 (2009)
16. Shoujun, Z., Jian, Y., Yongtian, W., Wufan, C.: Automatic segmentation of coronary angiograms based on fuzzy inferring and probabilistic tracking. BioMedical Engineering OnLine 9(1), 40 (2010)
17. Ballard, D.: Generalizing the Hough transform to detect arbitrary shapes. Pattern Recognition 13(2), 111–122 (1981)
18. Sethian, J.: Fast Marching Methods. SIAM Rev. 41, 199–235 (1999)
19. Frangi, A., Niessen, W., Hoogeveen, R., van Walsum, T., Viergever, M.: Quantitation of Vessel Morphology from 3D MRA. In: Taylor, C., Colchester, A. (eds.) MICCAI 1999. LNCS, vol. 1679, pp. 358–367. Springer, Heidelberg (1999)
20. Homann, H.: Implementation of a 3D thinning algorithm. Oxford University, Wolfson Medical Vision Lab. (2007)
21. Rahman, S.U., Wesarg, S., Völker, W.: Patient Specific Optimal Catheter Selection for Right Coronary Artery, SPIE Medical Imaging (to appear, 2011)

4D Cardiac Reconstruction Using High Resolution CT Images

Mingchen Gao[1], Junzhou Huang[1], Shaoting Zhang[1],
Zhen Qian[2], Szilard Voros[2], Dimitris Metaxas[1], and Leon Axel[3]

[1] CBIM Center, Rutgers University, Piscataway, NJ, 08550, USA
[2] 2 Piedmont Heart Institute, Atlanta, GA, 30309, USA
[3] New York University, 660 First Avenue, New York, NY, 10016, USA

Abstract. Recent developments on the 320 multi-detector CT technologies have made the volumetric acquisition of 4D high resolution cardiac images in a single heart beat possible. In this paper, we present a framework that uses these data to reconstruct the 4D motion of the endocardial surface of the left ventricle (LV) for a full cardiac cycle. This reconstruction framework captures the motion of the full 3D surfaces of the complex anatomical features, such as the papillary muscles and the ventricular trabeculae, for the first time, which allows us to quantitatively investigate their possible functional significance in health and disease.

1 Introduction

Most countries face high and increasing rates of cardiovascular diseases. Therefore, it is critical to detect and diagnose such diseases in early stages. Computed tomography (CT) and Magnetic resonance imaging (MRI), as non-invasive methods to generate three dimensional images of an organ, have been widely used over the decades. If the detailed cardiac shape features are accurately reconstructed from these images, we can potentially obtain additional clinically valuable information besides the widely used wall thickness and global function features. Many cardiac reconstruction methods have been developed to build 3D models of the heart from cardiac MR images, such as, but not limited to registration-based propagation framework [12] and deformable model [8] [9]. However, due to the sparsity of the data in usual MRI data sets, important anatomic structures, such as the papillary muscles, the ventricular trabeculae and the valves, are often difficult to capture in this modality.

There has also been work on the 3D cardiac reconstruction from CT images [10,7,2]. However, despite the higher level of structural detail potentially available in CT data, most of the prior work has not sought to capture the finer detail structures of the myocardium, such as papillary muscles and trabeculae. The conventional approach to reconstructing cardiac structures from 3D images (e.g., for generating generic or patient-specific models of the heart) is a model-based one that uses a smooth parametric model to guide the segmentation of the cardiac structures from the 3D images. Such parametric models capture the

D.N. Metaxas and L. Axel (Eds.): FIMH 2011, LNCS 6666, pp. 153–160, 2011.

overall shape of the heart wall, but are too coarse to capture or incorporate many of the finer scale anatomical features. For example, Zheng et al. proposed an automatic method to segment the four-chamber heart [10]. Their method employs Active Shape Model to exploit a large database of annotated CT volumes. It efficiently segments all the four chambers of heart. However, the inner wall of the chambers is simply modeled as a smooth surface.

Recent advances in CT technology have made the acquisition of higher resolution cardiac images possible, which can capture previously unseen cardiac structure details. However, these anatomical details are currently only visualized using methods such as volume rendering, which do not lend themselves to the quantitative analysis of the 3D anatomical structures. Segmentation and reconstruction of the endocardial surface of the ventricles with incorporation of finer details can potentially greatly assist doctors in diagnosis and functional assessment. Chen et al. proposed a hybrid framework for 3D cardiac reconstruction [1]. That method has provided high resolution segmentation results of the complex cardiac structure. Their results captured the papillary muscles and detail structure of the myocardium. However, CT data sets from different time frames were segmented independently. Prior model knowledge from neighboring time frames is not used in their framework. Topological consistency between consecutive time frames is not guaranteed, either.

For the case of 4D cardiac images, two problems have to be considered simultaneously: 1) a heart wall segmentation problem in each image and 2) a tracking problem of the left ventricle motion given the data set. In [3], Mcinerney et al. proposed a method for 4D cardiac reconstruction, in which the output of the previous time frame is used as the initial guess for the current time frame in order to do a sequential segmentation. They used a finite element surface model which may not be able to handle topology changes. Montagnat et al. proposed an extended deformable framework by introducing time-dependent constraints. Thus, in addition to computing an internal force to enforce the regularity of the deformable model, prior motion knowledge is introduced in the deformation process through either temporal smoothing or trajectory constraints [4]. However, these 4D reconstruction methods do not capture detailed features.

In this paper, we present a framework for 4D left ventricle (LV) segmentation with inclusion of small scale anatomical features. Semi-automatic segmentation is used to get the initial segmentation from high resolution CT data for an initial (3D) frame of data. This semi-automatic segmentation is time consuming and tedious, so it is not efficient to use it for segmentation of all the frames. The initial high resolution mesh model is generated as an isosurface of the segmentation. Geometric processing is then applied to the initial model to get a smooth and regular mesh with an appropriate number of vertices. Based on the initial model from one time frame, our method deforms it towards the boundaries on the other frames. During the formation, the topology of the model is kept unchanged. We can also get the one-to-one correspondence between frames, as an additional benefit during the segmentation process. With the one-to-one correspondence, we can easily do interpolation among different time frames to get a

smoother heart cycle animation. We have applied our framework on a whole cardiac cycle. The results have been validated based on the ground truth segmented by multiple clinical experts. These novel and powerful methods can extract the full 3D surfaces of these complex anatomical structures, which allows us for the first time to quantitatively investigate their possible functional significance.

2 Methodology

We propose a framework to reconstruct the cardiac model. This framework includes: initial model construction, deformable model based segmentation, and interpolation between time frames. The initial model is generated using 3D snake-based segmentation on one time frame of the CT image. The initial model needs geometry processing, such as decimating, detail-preserving smoothing and isotropic remeshing to get high-quality meshes. Based on the initial model, segmentation of the rest of the CT images is automatically performed using the deformable model. The segmentation of a sequence of CT images is interpolated in time to get a higher effective temporal resolution.

2.1 Model Initialization

The model initialization framework is illustrated in Fig. 1. We use a 3D snake-based semi-automatic segmentation method to get the initial model [11]. This segmentation process is very time consuming and could not be used to segment all frames. Usually it takes several hours to finish a semi-automatic segmentation on one time frame. However, once this model has been generated, it is used to segment the rest of other frames automatically.

Segmentation results are represented as binary images. Isosurface detection is then applied to generate the mesh. However, the resulting mesh is usually bulky, noisy and irregular. To get a better initialization model, some geometric processing should be done on that mesh, such as decimating, detail-preserving smoothing and isotropic remeshing. First, the initial model is too large to readily modify, edge collapses are performed during decimation. After decimation, we get a mesh with much fewer vertices, but that still retains most of the shape details. The meshes have been decimated to about $20,000$ vertices. Detail-preserving smoothing is then performed after decimation. The smoothing is restricted to

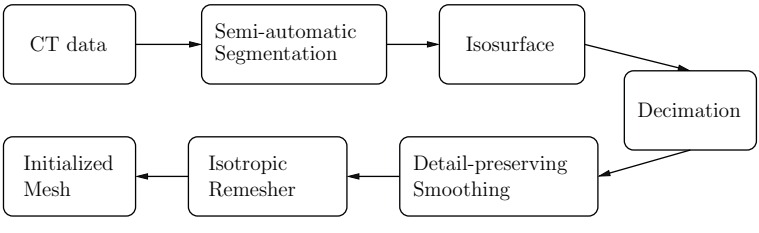

Fig. 1. Initial model construction

the tangential direction. Instead of moving each vertex towards the centroid of its neighbors, which would smooth out the shape details and sharp features, detail-preserving smoothing ensures higher quality meshes without losing details. Isotropic remeshing is important for the mesh quality. In irregular meshes, the vertices with high valences exert strong internal forces to drag other vertices, which can cause unrealistic results in deformable models [6]. An incremental isotropic remeshing technique is used to remesh the given triangular mesh so that all edges have approximately the same target edge length and the triangles are as regular as possible. This process would generally be iterated several times to get the final results.

After all these geometric processing steps, we finally get a high-quality triangular mesh with an appropriate number of vertices. This mesh is used as an initialization for other frames.

2.2 Deformable Model Based Segmentation

We want to deform our model normal to the boundaries during tracking. To do so, we define an energy function, including a term, *external energy*, derived from the image so that it is smaller at the boundaries. By minimizing the energy function, it drags the model towards the boundaries. We also want to keep the shape of the model unchanged during deformation. For that, we use another energy term, *model energy*, which reflects the differences between the original model and the deformed model.

Given a gray level image $I(x, y)$, viewed as a function of continuous position variables (x, y). The model M_{t-1} derived from the previous frame is used to fit the current frame M_t. The energy function we want to minimize is defined as follows:

$$E(M_t, I_t, M_{t-1}) = E_{ext}(M_t, I_t) + E_{model}(M_t, M_{t-1}). \tag{1}$$

The external energy E_{ext} is designed to move the deformable model towards object boundaries.

$$E_{ext}(M_t, I_t) = -\left|\nabla I\right|^2, \tag{2}$$

where ∇ is the gradient operator.

Model energy is defined as the differences of attribute vectors. An attribute vector is attached to each vertex of the model [5], which reflects the geometric structure of the model from a local to global level. In 3D, for a particular vertex V_i, each attribute is defined as the volume of a tetrahedron on that vertex. The other three vertices form the tetrahedron are randomly chosen from the lth level neighborhood of V_i. Smaller tetrahedrons reflect the local structure near a vertex while larger tetrahedrons reflect a more global information around a vertex. The attribute vector, if sufficient enough, uniquely characterizes different parts of a surface of a boundary. The normalized attribute vectors are affine-invariant [5].

The volume of a tetrahedron is defined as $f_l(V_i)$. The attribute vector on a vertex is defined as:

$$F(V_i) = [f_1(V_i), f_2(V_i), ..., f_{R(V_i)}(V_i)], \tag{3}$$

where $R(V_i)$ is the neighborhood layers we want to use around V_i.

As we elaborated earlier in this section, the model energy term reflects the differences of attribute vectors between the original model and the deformed model.

$$E_{model}(M_t, M_{t-1}) = \sum_{i=1}^{N} \sum_{l=1}^{R(V_i)} \delta_l (f_{t,l}(V_i) - f_{t-1,l}(V_i))^2, \tag{4}$$

where $f_{t,l}(V_i)$ and $f_{t-1,l}(V_i)$ are components of attribute vectors of the model and deformed model at vertex V_i, respectively. δ_l here denotes the importance of the lth neighborhood layers. $R(V_i)$ is the number of neighborhood layers around vertex V_i.

A greedy algorithm is used here to minimize the energy function. The proposed algorithm is iterative. During each iteration, the first step is to minimize the external energy, moving vertices towards the minimum gradient of a image; the second step is to minimize the model energy; a neighborhood of a vertex has been examined and the point in the neighborhood with the minimum model energy would be chosen as the new location of the vertex. The iterations continue until the energy converges. While this greedy algorithm might fall into a local minimum, the experiments show satisfactory results.

During the deformation, we suggest moving a surface segment as a whole, rather than a single vertex. This would avoid this risk of getting trapped in a local minimum, and also speed up the convergence. Let V_i be the vertex to be deformed during a particular iteration. The first to $R(V_i)$th neighborhood layers are about to move together as a surface segment. Suppose V_i is to move to $V_i + \Delta$ as a tentative position. Then the new position of each vertex $nbr_{l,m}(V_i)$, the mth vertex on lth neighborhood layer, is set to move to

$$nbr_{l,m}(V_i) + \Delta \cdot \exp(-\frac{l^2}{2\delta^2}), \tag{5}$$

where δ is a parameter determining the locality of the transformation. We make the deformation unchanged on the boundary of the surface segment, such that the continuity has been maintained.

The parameter $R(V_i)$ that determines the locality if the deformation is chosen to be large in the initial iteration, and is then gradually reduced to 1. Therefore, initially there are more vertices involved in the deformation. More global features are used in deformation. In later states, more local deformations are performed.

2.3 Interpolation

Segmentation for all frames are deformed from one single model, such that not only the topology is consistent, but also we have one-to-one correspondence of different time frames. All the meshes are interpolated in time to get a smooth animation of the cardiac cycle. We use periodic cubic spline interpolation. The last frame is set as the previous frame of the first frame in the interpolation process to get a circular animation of the heart cycle. Periodic cubic spline

interpolation makes heart meshes continuous on the second derivatives. The interpolation results are used in simulation of blood flow in the left ventricles.

3 Results and Validation

We applied our reconstruction framework to 10 cardiac CT volumes, which captures a whole cycle of cardiac contraction. The CT data were acquired on a 320-MDCT scanner using a conventional ECG-gated contrast-enhanced CT angiography protocol. The imaging protocol parameters include: prospectively triggered, single-beat, volumetric acquisition; detector width 0.5 mm, voltage 120 KV, current $200 - 550$ mA. Reconstructions were done at 10 equally distributed time frames in a cardiac cycle. The resolution of each time frame is 512 by 512 by 320.

Our reconstruction method successfully captured the papillary muscles and the trabeculae of the left ventricle. Figure 2 illustrates the anatomic structure of the papillary muscles and the trabeculae of the left ventricle. The three-dimensional structures, their relationship and their movement during the cardiac cycle are much more readily appreciated from the model than from the original volumetric image data.

We compare our results to the ground truth from the annotations of clinical experts. Figure 3 shows the differences of the results from the manual segmentations. The color indicates the distance from each vertex of our results to the manual segmentation.

Figure 3(d) shows the quantitative evaluation of the results. The mean distance from every vertex to the semi-automatic segmentation is about one voxel. During the diastolic frames, which are frames 4 to frame 9, there are smaller

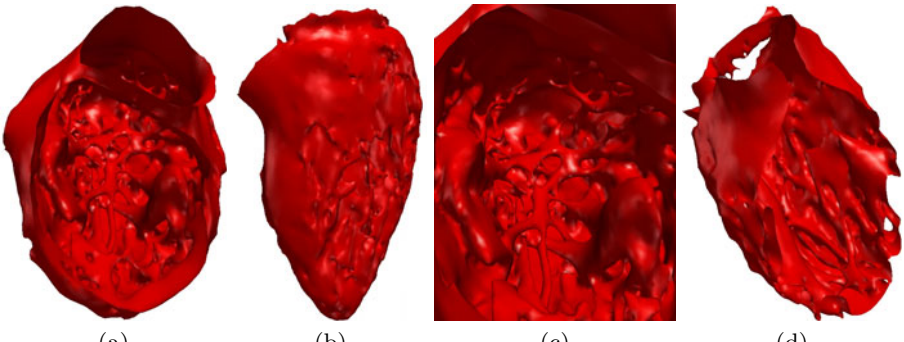

Fig. 2. Reconstruction results of left ventricle at one time frame. Papillary muscles and the trabeculae are clearly captured. (a) shows a view of the left ventricle from the top, through valves (b) shows a view of the trabeculae of left ventricle from the front (c) shows a zoom-in view of the papillary muscles and the trabeculae. (d) shows that papillary muscles and trabeculae being clipped by a user-defined plane.

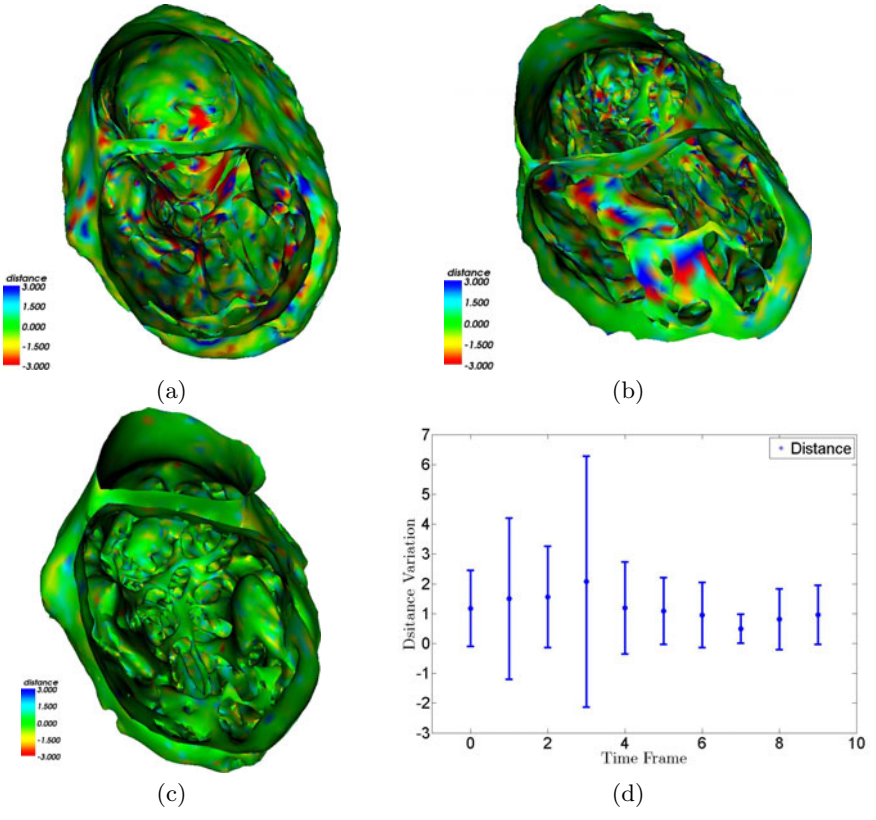

Fig. 3. Differences of the left ventricle to the ground truth. Green colors mean that the distances are within one voxel. Red colors mean under-segmentation while blue colors mean over-segmentation. (a)(b)(c) Different frames of the differences of the left ventricle to the ground truth. (d) Distances distribution of every frame.

distances and less distance variations. On the other hand, during cardiac systole, because of large deformations between neighboring frames, the results have larger errors.

The interpolation results have made possible a smooth animation of the full cardiac movement cycle.

4 Conclusion

In this paper, we have presented a framework using high resolution CT data to reconstruct 4D motion of the left ventricle for a full cardiac cycle. The framework has been applied to a sequence of cardiac CT volumes. High resolution details, such as papillary muscles and ventricular trabeculae, were successfully captured

in this framework. In the future, we plan to use this framework to capture more fine structures of the heart, e.g., the valves and wall surfaces of all the four chambers.

References

1. Chen, T., Metaxas, D., Axel, L.: 3D cardiac anatomy reconstruction using high resolution CT data. In: Barillot, C., Haynor, D.R., Hellier, P. (eds.) MICCAI 2004. LNCS, vol. 3216, pp. 411–418. Springer, Heidelberg (2004)
2. Lorenz, C., von Berg, J.: A comprehensive shape model of the heart. Medical Image Analysis 10(4), 657–670 (2006)
3. Mcinerney, T., Terzopoulos, D.: A dynamic finite element surface model for segmentation and tracking in multidimensional medical images with application to cardiac 4D image analysis. Computerized Medical Imaging and Graphics 19, 69–83 (1995)
4. Montagnat, J., Delingette, H.: 4D deformable models with temporal constraints: application to 4D cardiac image segmentation. Medical Image Analysis 9(1), 87–100 (2005)
5. Shen, D., Davatzikos, C.: Adaptive-focus statistical shape model for segmentation of 3D MR structures. In: Delp, S.L., DiGoia, A.M., Jaramaz, B. (eds.) MICCAI 2000. LNCS, vol. 1935, pp. 206–215. Springer, Heidelberg (2000)
6. Shen, T., Li, H., Qian, Z., Huang, X.: Active volume models for 3d medical image segmentation. In: CVPR, pp. 707–714 (2009)
7. von Berg, J., Lorenz, C.: Multi-surface cardiac modelling, segmentation, and tracking. In: Frangi, A.F., Radeva, P., Santos, A., Hernandez, M. (eds.) FIMH 2005. LNCS, vol. 3504, pp. 1–11. Springer, Heidelberg (2005)
8. Wang, X., Chen, T., Zhang, S., Metaxas, D., Axel, L.: LV motion and strain computation from tMRI based on meshless deformable models. In: Metaxas, D., Axel, L., Fichtinger, G., Székely, G. (eds.) MICCAI 2008, Part I. LNCS, vol. 5241, pp. 636–644. Springer, Heidelberg (2008)
9. Zhang, S., Wang, X., Metaxas, D.N., Chen, T., Axel, L.: LV surface reconstruction from sparse TMRI using laplacian surface deformation and optimization. In: ISBI, pp. 698–701 (2009)
10. Zheng, Y., Barbu, A., Georgescu, B., Scheuering, M., Comaniciu, D.: Four-chamber heart modeling and automatic segmentation for 3D cardiac CT volumes using marginal space learning and steerable features. TMI 27(11), 1668–1681 (2008)
11. Zhu, S., Lee, T., Yuille, A.: Region competition: unifying snakes, region growing, energy/Bayes/MDL for multi-band image segmentation. In: ICCV, pp. 416–423 (June 1995)
12. Zhuang, X., Rhode, K., Razavi, R., Hawkes, D., Ourselin, S.: A registration-based propagation framework for automatic whole heart segmentation of cardiac MRI. TMI 29(9), 1612–1625 (2010)

3D Fusion Echocardiography Improves Transoeosphageal LV Assessment

Kashif Rajpoot[1], Daniel Augustine[2], Christos Basagiannis[2], J. Alison Noble[1], Harald Becher[3], and Paul Leeson[2]

[1] Institute of Biomedical Engineering, University of Oxford, Oxford, UK
[2] John Radcliffe Hospital, Oxford, UK
[3] University of Alberta Hospital, Edmonton, Canada

Introduction

Accurate left ventricular (LV) assessment by transoesophageal echocardiography (TOE) can be clinically important particularly in intensive care or intraoperative settings. Assessment from TOE views is limited by foreshortened imaging planes and mitral valve pathology. Transgastric short-axis (SAX) views allow better alignment but may be limited by patient tolerability or patient-related factors (e.g. post gastric surgery). Fusion of multiple 3D volume datasets is now technically possible and improves LV visualisation from transthoracic windows. We hypothesized that fusion of full 3D TOE volumes would improve LV image quality and allow SAX image reconstruction from the oesophagus with improved image quality vs. transgastric SAX views.

Methods

3D 2 chamber or 4 chamber volumes were obtained in 30 sequential patients undergoing TOE study. The optimal 2 or 4 chamber view on 2D imaging was visually assessed and a 3D dataset acquired in that position. 2-5 further 3D volumes were acquired following small probe manoeuvres (1cm withdrawal or advancement; minor lateral/medial rotation; and angle adjustment (<5). Transgastric SAX views were attempted in the same patients when clinically appropriate and feasible (n = 14, 12 successful). 3D images were fused together using an in-house developed programme. The optimal and fused 2 or 4 chamber views with their corresponding mid SAX image were analysed (using Philips QLAB 7.1 iSlice) to compare quality (using the standard segmental approach) and field of view (FOV). Each segment was assigned a rating 0-3 depending on the amount of visualised endocardial border defined as: 0 (<50%), 1 (50-75%), 2 (75-99%), and 3 (100%).

Contrast-to-noise ratio (CNR) was used as a quantitative measurement of the image quality defined as the ratio of the signal intensity differences between image regions (myocardium and blood pool) to the image noise (variance of image regions). Two readers analysed all images.

Results

Each reader analysed 720 segments. Image quality of both 4 or 2 chamber and SAX views improved with fusion (mean 1.8 vs. 2.2 ($p<0.05$)). There were fewer 0 ratings

D.N. Metaxas and L. Axel (Eds.): FIMH 2011, LNCS 6666, pp. 161–162, 2011.

post fusion (68 vs. 28) and greater 2/3 ratings (135 vs.187). The FOV improved in all images post fusion. The image quality of the optimal (unfused) mid SAX TOE view was similar to the transgastric view (mean 2.0 vs. 2.0 ($p = 0.8$) and improved with 3D fusion (mean 2.5, $p < 0.05$)). CNR improved post fusion by 64% ($p < 0.05$). Interobserver agreement showed a mean difference in image quality assessment of 0.2 image points (CI 0-0.3) and good correlation ($r = 0.78$, $p < 0.05$).

Conclusions

3D fusion TOE significantly improves LV segmental image quality and allows acquisition of SAX views from the oesophagus in all patients. Fused datasets were noted to have increased FOV in the near field. This approach may reduce requirement for transgastric images; improve patient procedure tolerability/safety as well as shorten procedure time.

Automatic Segmentation of Different Pathologies from Cardiac Cine MRI Using Registration and Multiple Component EM Estimation

Wenzhe Shi[1], Xiahai Zhuang[2], Haiyan Wang[1], Simon Duckett[3], Declan Oregan[4], Philip Edwards[1], Sebastien Ourselin[2], and Daniel Rueckert[1]

[1] Biomedical Image Analysis Group
Imperial College London
[2] Centre for Medical Image Computing
University College London
[3] The Rayne Institute
Kings College London
[4] Robert Steiner MRI Unit
Hammersmith Hospital

Abstract. In this paper, we develop a framework for the automatic detection and segmentation of the ventricle and myocardium from multi-slice, short-axis cine MR images. The segmentation framework has the ability to deal with large shape variability of the heart, poorly defined boundaries and abnormal intensity distribution of the myocardium (e.g. due to infarcts). We integrate a series of state-of-the-art techniques into a fully automatic workflow, including a detection algorithm for the LV, atlas-based segmentation, and intensity-based refinement using a Gaussian mixture model that is optimized using the Expectation Maximization (EM) algorithm and the graph cut algorithm. We evaluate this framework on three different patient groups, one with infarction, one with left ventricular hypertrophy (both are common result of cardiovascular diseases) and another group of subjects with normal heart anatomy. Results indicate that the proposed method is capable of producing segmentation results that show good robustness and high accuracy (Dice 0.908 ± 0.025 for the endocardial and 0.946 ± 0.016 for the epicardial segmentations) across all patient groups with and without pathology.

1 Introduction

Accurate estimation of indices of cardiac function, such as ejection fraction and wall thickness or thickening, is important in routine clinical applications as well as in cardiovascular research aimed at better understanding the function of the heart. In order to compute these measurements of cardiac function, one of the essential steps is to identify the ventricles and the myocardium and to delineate their boundaries. Manual segmentation tends to lead to significant inter- and intra-observer variations and is extremely time-consuming, it is hence highly desirable to develop an automated method to obtain a reproducible and unbiased result.

D.N. Metaxas and L. Axel (Eds.): FIMH 2011, LNCS 6666, pp. 163–170, 2011.

Model-based segmentation [1,2,3,4] achieves automatic delineation by deforming the surface of a pre-constructed model towards the detected boundaries, while at the same time constraining the model within a reasonable shape based on *a-priori* knowledge of the model. The detection of candidate boundaries in these methods is usually confined to a local region around the model surface. Therefore, constructing an appropriate prior model, whose shape variability can adequately capture the shape of the heart in unseen images, is crucial for segmentation techniques in this category. An alternative technique for segmentation is to propagate a pre-constructed atlas to the unseen images using image registration [5,6,7]. By using a locally affine registration method (LARM), this technique is able to deal with large shape variations of the heart. However, the segmentation accuracy reported using LARM is limited, in particular for the segmentation of the epicardium [7]. This problem becomes particularly evident when the intensities in the myocardium exhibit locally varying contrast, e.g. due to infarction.

Voxel-based segmentation identifies differences between the intensity distribution of different tissues[8,9,10,11]. The method is able to achieve sub-voxel accuracy but requires a good initialization. However, the lack of geometric information makes it difficult to achieve such a good initialization due to the large shape variation of the heart within a given population of subjects. Furthermore, most of the automatic segmentation methods, including model-based and atlas-based methods, assume homogenous tissue intensities. This leads to problems when segmenting subjects with myocardial infarction, as the infarcted myocardium often has a heterogeneous intensity distribution in contrast to normal myocardium which is characterized by a more homogeneous intensity distribution. These problems are further compounded by the fact that these heterogeneous intensity distributions are difficult model using prior knowledge since the position and intensity of infarcted myocardium varies across different subjects.

In this paper we propose an integrated framework (Figure 1) to deal with the challenges described above. This framework includes a Haar feature-based cascade classifier for heart detection, image registration for propagating prior information built from a group of healthy subjects, and a multiple component EM (MCEM) estimation and graph cut-based method for segmentation refinement. Using Gaussian mixture modelling in the EM estimation has been proposed by [12] to cope with partial volume voxels which exist at the interface between different tissue classes. We extend this approach with spatial weighting to emphasize on that the components are clustered and choose number of Gaussian models explicitly from number of potential components (for example myocardium consist of normal and infarcted myocardium and background consist of blood tissue and air).

In the following sections, the proposed method is described in Section 2, validation results are presented in Section 3, and finally the conclusion and discussion can be found in Section 4.

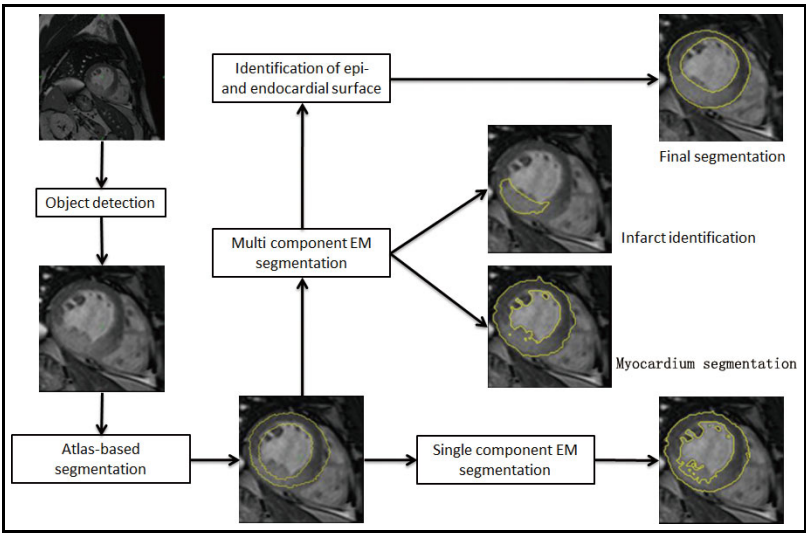

Fig. 1. Workflow of the automatic segmentation framework and MCEM against EM

2 Methods

2.1 Initial Atlas-Based Segmentation of the Heart

Once a region of interest containing the cardiac anatomy has been located via variant of the object detection approach proposed by Viola and Jones [13], we use image registration to propagate an atlas to the unseen images. Zhuang *et al.* [6,7] proposed a locally affine registration method (LARM) to address the large local shape variability of cardiac anatomy, commonly seen across large populations with pathologies. LARM is integrated into the registration process as an intermediate registration step between a global affine registration and a fully non-rigid registration. Compared to traditional registration schemes, LARM is capable of providing a good initial alignment between the images of patients with pathologies and the atlas constructed from normal subjects.

2.2 Multi-component EM Estimation

To enable voxel-based classification, we propagate a probabilistic atlas to the unseen images using the result of the previous registration process as a spatial constraint. We then use the EM algorithm [5] to classify each voxel into 3 labels $\Lambda = \{L_k, L_b, L_m\}$ for background, blood pool, and myocardium respectively. The probabilistic atlas has been constructed from 25 healthy subjects and is used as *a-priori* information for the EM algorithm. However, the probabilistic atlas has been constructed from healthy subjects. In normal anatomical MR images, the intensity of myocardium is relatively homogeneous and the EM-based segmentation is able to segment normal myocardium in healthy subjects

with high accuracy (mean distance and standard deviation reported in [5] is $2.05 \pm 2.19mm$). For the subjects with myocardial infarction, the intensity of the infarcted region can be significantly different from the healthy myocardium. This leads to inaccurate delineation of the myocardium in the infarcted region when using the traditional EM-based algorithm as the example in Figure 1 shows.

We propose to use a multiple component EM (MCEM) algorithm to cope with this abnormal intensity distribution. The MCEM algorithm models the myocardial tissue using multiple Gaussian distributions and thus can better adapt to the heterogeneous intensity distribution. Let K be the number of labels and n be the number of voxels in the image. Let $G(y_i, \mu, \sigma)$ represent a Gaussian distribution where y_i is the intensity, and μ and σ are the mean and standard deviation respectively. Furthermore let $p_L^m(i)$ be the probabilistic estimate of the segmentation of v_i for label L at the m-th iteration; $p_L^{atlas}(i)$ is the prior probability propagated from the probabilistic atlas after the registration step. The MCEM algorithm is then initialized as follows:

$$p_L^0(i) = p_L^{atlas}(i) \tag{1}$$

$$\mu_L^0 = \frac{\sum_{i=1}^n y_i p_L^0(i)}{\sum_{i=1}^n p_L^0(i)} , \qquad (\sigma_L^0)^2 = \frac{\sum_{i=1}^n (y_i - \mu_L^0)^2 p_L^0(i)}{\sum_{i=1}^n p_L^0(i)} \tag{2}$$

Given that label L is modelled using $|l|$ components, the initial probability segmentation of each component, $p_{L_j}^0(i)$, is given by:

$$p_{L_j}^0(i) = \frac{G(y_i, \mu_{L_j}^0, \sigma_{L_j}^0) p_L^{atlas}(i)}{\sum_{k=1}^K \sum_{o=1}^{|l|} G(y_i, \mu_{k_o}^0, \sigma_{k_o}^0) p_k^{atlas}(i)} \tag{3}$$

where $\mu_{L_j}^0 = \mu_L^0 - \sigma + \frac{2\sigma_L^0 (j-1)}{|l|-1}$, $(\sigma_{L_j}^0)^2 = (\sigma_L^0)^2/|l|$, and $\delta_{L_j}^0 = \frac{\sum_i^n p_{L_j}^0(i)}{\sum_{i,o=1}^{n,|l|} p_{L_o}^0(i)}$ is the proportion of component j.

The algorithm then interleaves the following E- and M-steps:. To estimate the probabilistic segmentation, a spatial coefficient C_{Lj} which measures how close v_i is to the gravity center of label L's component j is also computed. where v_i the location of the i-th voxel This is important to avoid misclassifying similar intensities which are remote from the location of the infarction.
E-step:

$$C_{Lj} = \frac{\sum_{i=1}^n G(y_i, \mu_{L_j}^m, \sigma_{L_j}^m) p_L^{atlas}(i) v_i}{\sum_{i=1}^n G(y_i, \mu_{L_j}^m, \sigma_{L_j}^m) p_L^{atlas}(i)} \tag{4}$$

$$\omega_{L_j}^{m+1}(i) = \frac{1}{||v_i - C_{Lj}|| + 1} \tag{5}$$

$$p_{L_j}^{m+1}(i) = \frac{G(y_i, \mu_{L_j}^m, \sigma_{L_j}^m) p_L^{atlas}(i) \delta_{L_j}^m \omega_{L_j}^m(i)}{\sum_{k=1}^K \sum_{o=1}^{|l|} G(y_i, \mu_{k_o}^m, \sigma_{k_o}^m) p_k^{atlas}(i) \delta_{k_o}^m \omega_{k_o}^m(i)} \tag{6}$$

$$p_L^{m+1}(i) = \sum_{o=1}^{|l|} p_{L_o}^{m+1}(i) \tag{7}$$

M-step:

$$\mu_{L_j}^{m+1} = \frac{\sum_i^n y_i p_{L_j}^{m+1}(i)}{\sum_i^n p_{L_j}^{m+1}(i)}\ , \qquad (\sigma_{L_j}^{m+1})^2 = \frac{\sum_i^n (y_i - \mu_{L_j}^{m+1})^2 p_{L_j}^{m+1}(i)}{\sum_i^n p_{L_j}(i)^{m+1}} \tag{8}$$

$$\delta_{L_j}^{m+1} = \frac{\sum_i^n p_{L_j}^{m+1}(i)}{\sum_{i=1}^n \sum_{o=1}^{|l|} p_{Lo}^{m+1}(i)} \tag{9}$$

The EM optimization iterates until the sum of the log likelihood of the Gaussian estimation at every voxel converges and changes by less than a given small value. As a result, areas of myocardial infarction can be segmented using the Gaussian mixture model.

2.3 Segmentation of the Epi- and Endocardial Surfaces

Using the traditional EM-based segmentation, it is difficult to separate the papillary muscle from the myocardium because of the lack of tissue contrast and relatively high probability of myocardium in the area of the papillary muscle. Therefore, we propose to use an energy functions based on Markov Random Fields (MRF) in combination with graph cuts [14,10,15] to improve the smoothness of the segmentation. The data term $D_p(f_p)$ is estimated using the previous MCEM results.

To identify the endocardial contours and to remove the papillary muscle completely we computed the convex hull of the blood pool segmentation. This is done in 2D since the cardiac longitudinal contour is not always convex. Then,

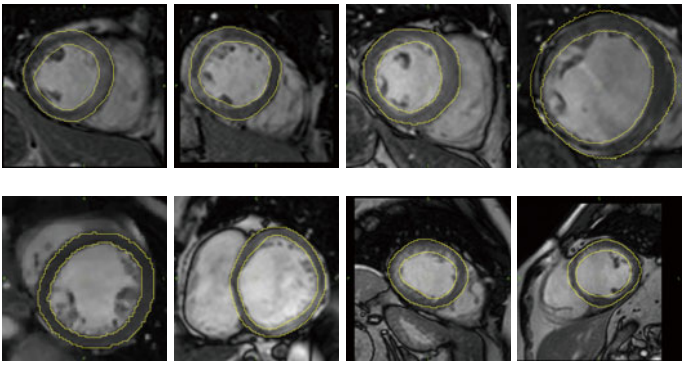

Fig. 2. Random selected segmentation results of different patients

a Fourier representation of the epi- and endocardial contour is computed and the first 6 harmonic phases are retained to obtain a final, smoothed segmentation [16,17,11]. A 3D surface model of the myocardium can be constructed using shape based interpolation [18] and marching cubes [19]. Some example of the segmentation results are shown in Figure 2.

3 Results

We acquired 90 subjects, using multi slice cine steady state free precession MR sequence acquired voxel size $1.44 \times 1.44 \times 8mm$. Images were divided into three different groups according to pathologies, including patients with myocardial infarction (49 cases), patients with ventricular hypertrophy (30 cases), and healthy subjects (11 cases). Manual segmentations were performed by a cardiologist to extract myocardium and left ventricle, and then compared to segmentation results obtained via three different techniques: (a) the technique by Lorenzo et al. [5] which uses affine and non-rigid registration of a probabilistic atlas followed by EM-MRF segmentation, (b) the technique by Zhuang et al. [6] which employs registration for atlas propagation, and (c) the technique proposed in this paper. For comparisons between the methods we used the Dice metric, $D = (2||S_a \cap S_b||)/(||S_a|| + ||S_b||)$ where S_a and S_b are the manual label segmentation and automatic label segmentation, and the surface-to-surface distance [7,20,1]. The results are summarized in Table 1 and 2.

Table 1. Validation results: The Dice overlap measure for the endocardial segmentation (L_b) and epicardial segmentation ($L_b + L_m$) results between automatic and manual segmentation"s label results

Group	Segmentation	Lorenzo et al. [5]	Zhuang et al. [7]	MCEM
normal	endocardial	0.921 ± 0.013	0.919 ± 0.016	0.927 ± 0.013
	epicardial	0.935 ± 0.016	0.936 ± 0.013	0.946 ± 0.018
infarction	endocardial	0.841 ± 0.045	0.853 ± 0.036	0.899 ± 0.029
	epicardial	0.932 ± 0.015	0.933 ± 0.012	0.950 ± 0.011
hypertrophy	endocardial	0.748 ± 0.228	0.917 ± 0.031	0.917 ± 0.028
	epicardial	0.761 ± 0.210	0.929 ± 0.028	0.940 ± 0.023

Table 2. Validation results: The average surface-to-surface distances for the endocardial surfaces and epicardial surfaces between manual and automatic segmentation"s surface results

Group	Surface	Lorenzo et al. [5]	Zhuang et al. [7]	MCEM
normal	endocardial	2.274 ± 0.115	2.119 ± 0.101	1.990 ± 0.150
	epicardial	2.154 ± 0.167	2.122 ± 0.191	1.830 ± 0.185
infarction	endocardial	2.931 ± 0.545	2.637 ± 0.590	1.926 ± 0.342
	epicardial	2.192 ± 0.325	2.326 ± 0.598	1.775 ± 0.195
hypertrophy	endocardial	6.738 ± 8.198	2.446 ± 0.459	2.349 ± 0.418
	epicardial	7.581 ± 8.073	2.862 ± 0.528	2.162 ± 0.337

The results indicate that our proposed segmentation scheme performed consistently better than the other two methods. In our experiments, the global affine registration failed for 8 out of 30 patients with ventricular hypertrophy, leading to failures using the segmentation technique proposed by Lorenzo et al. [5]. On the other side the registration-based approach by Zhuang et al. [6] uses the LARM registration technique, thus the segmentation results were significantly better on subjects with ventricular hypertrophy due to its ability to address the large local shape variability. Furthermore, the proposed method outperformed both other techniques due to its ability to model infarcted myocardium using multiple tissue class components. Finally, the MCEM segmentation achieved high accuracy for the fully automated segmentation across all three groups, which compares favourably to other recent techniques [7,20,1].

4 Discussion and Conclusion

In this paper we have developed a framework for automatic segmentation of MR images the cardiac anatomy with different pathologies. We evaluated our proposed method using a test data set with a wide diversity including healthy controls, patients with myocardial infarction and patients with cardiac myopathy. The proposed segmentation algorithm was compared to two other, state-of-the-art, segmentation schemes. The results showed a consistent improvement, particularly in the segmentation of subjects with myocardial infarction for which registration-based segmentation tends to perform poorly. Also, the voxel-based techniques[5] alone did not demonstrated a robust performance without a good initialization from LARM propagation in the group with ventricular hypertrophy. The proposed integration of registration- and voxel-based segmentation has shown the ability to achieve both the robustness and accuracy. Finally, the segmentation performance achieved by the proposed method is very competitive and outperforms some other recent approaches [7,20,1], although a direct comparison is often difficult due to the different image data sets used.

This work was funded in part by EPSRC grant EP/H019847/1.

References

1. Huang, S., Liu, J., Lee, L., Venkatesh, S., Teo, L., Au, C., Nowinski, W.: An image-based comprehensive approach for automatic segmentation of left ventricle from cardiac short axis cine mr images. Journal of Digital Imaging, 1–11 (2010) 10.1007/s10278-010-9315-4
2. Pluempitiwiriyawej, C., Moura, J., Wu, Y., Ho, C.: STACS: New active contour scheme for cardiac MR image segmentation. IEEE Transactions on Medical Imaging 24(5), 593–603 (2005)
3. Kaus, M., Berg, J., Weese, J., Niessen, W., Pekar, V.: Automated segmentation of the left ventricle in cardiac MRI. Medical Image Analysis 8(3), 245–254 (2004)
4. Rouchdy, Y., Pousin, J., Schaerer, J., Clarysse, P.: A nonlinear elastic deformable template for soft structure segmentation. Inverse Problems 23, 1017–1035 (2007)

5. Lorenzo-Valdés, M., Sanchez-Ortiz, G., Elkington, A., Mohiaddin, R., Rueckert, D.: Segmentation of 4D cardiac MR images using a probabilistic atlas and the EM algorithm. Medical Image Analysis 8(3), 255–265 (2004)
6. Zhuang, X., Rhode, K.S., Arridge, S.R., Razavi, R.S., Hill, D., Hawkes, D.J., Ourselin, S.: An atlas-based segmentation propagation framework using locally affine registration – application to automatic whole heart segmentation. In: Metaxas, D., Axel, L., Fichtinger, G., Székely, G. (eds.) MICCAI 2008, Part II. LNCS, vol. 5242, pp. 425–433. Springer, Heidelberg (2008)
7. Zhuang, X., Rhode, K., Razavi, R., Hawkes, D.J., Ourselin, S.: A Registration-Based Propagation Framework for Automatic Whole Heart Segmentation of Cardiac MRI. IEEE Transactions on Medical Imaging, 1612–1625 (2010)
8. Zhang, Y., Brady, M., Smith, S.: Segmentation of brain MR images through a hidden Markov random field model and the expectation-maximization algorithm. IEEE Transactions on Medical Imaging 20(1), 45–57 (2001)
9. Kedenburg, G., Cocosco, C.: Automatic cardiac MRI myocardium segmentation using graphcut. In: Proceedings of SPIE, vol. 6144, 61440A (2006)
10. Boykov, Y., Kolmogorov, V.: Computing Geodesics and Minimal Surfaces via Graph Cuts. In: Proceedings of the Ninth IEEE International Conference on Computer Vision, p. 26. IEEE Computer Society, Los Alamitos (2003)
11. Jolly, M.: Automatic segmentation of the left ventricle in cardiac MR and CT images. International Journal of Computer Vision 70(2), 151–163 (2006)
12. Ashburner, J., Friston, K.J.: Unified segmentation. NeuroImage 26(3), 839–851 (2005)
13. Viola, P., Jones, M.: Robust real-time object detection. International Journal of Computer Vision 57(2), 137–154 (2002)
14. Greig, D., Porteous, B., Seheult, A.: Exact maximum a posteriori estimation for binary images. Journal of the Royal Statistical Society. Series B (Methodological) 51(2), 271–279 (1989)
15. Khan, S.M., Shah, M.: A multiview approach to tracking people in crowded scenes using a planar homography constraint. In: Leonardis, A., Bischof, H., Pinz, A. (eds.) ECCV 2006. LNCS, vol. 3954, pp. 133–146. Springer, Heidelberg (2006)
16. Lu, Y., Radau, P., Connelly, K., Dick, A., Wright, G.A.: Segmentation of Left Ventricle in Cardiac Cine MRI: An Automatic Image-Driven Method. In: Ayache, N., Delingette, H., Sermesant, M. (eds.) FIMH 2009. LNCS, vol. 5528, pp. 339–347. Springer, Heidelberg (2009)
17. Huang, S., Liu, J.: Segmentation of the Left Ventricle from Cine MR Images Using a Comprehensive Approach. In: Proceedings of the 5th International Conference on Functional Imaging and Modeling of the Heart, pp. 339–347. Springer, Heidelberg (2009)
18. Grevera, G., Udupa, J.: Shape-based interpolation of multidimensional grey-level images. IEEE Transactions on Medical Imaging 15(6), 881–892 (2002)
19. Lorensen, W., Cline, H.: Marching cubes: A high resolution 3D surface construction algorithm. In: Proceedings of the 14th Annual Conference on Computer Graphics and Interactive Techniques, pp. 163–169. ACM, New York (1987)
20. Schaerer, J., Casta, C., Pousin, J., Clarysse, P.: A dynamic elastic model for segmentation and tracking of the heart in mr image sequences. Medical Image Analysis 14(6), 738–749 (2010)

Statistical Analysis of the Human Cardiac Fiber Architecture from DT-MRI

Herve Lombaert[1,2], Jean-Marc Peyrat[3], Pierre Croisille[4], Stanislas Rapacchi[4], Laurent Fanton[5], Patrick Clarysse[4], Herve Delingette[2], and Nicholas Ayache[2]

[1] École Polytechnique de Montréal, Canada
[2] Asclepios, INRIA Sophia-Antipolis, France
[3] Siemens Molecular Imaging, Oxford, UK
[4] CREATIS, Université de Lyon, France
[5] Institut Universitaire de Médecine Légale, Université de Lyon, France

Abstract. A statistical atlas of the cardiac fiber architecture is built for the first time with a human dataset of 10 healthy *ex vivo* hearts acquired using DT-MRI. The atlas is constructed using an efficient semi-automated method where limited interactions are only required to segment the myocardium. All hearts are registered automatically by an efficient and robust non linear registration method. The statistical atlas gives a better understanding of the human cardiac fiber architecture. The study on the global variability of the human cardiac fiber architecture reveals that the fiber orientation is more stable than the laminar sheet orientation. The variability is also consistent across the left ventricular AHA segments. Moreover this atlas could be used for cardiac electromechanical modeling as well as a basis for more precise extrapolation models, essential for *in vivo* cardiac DT-MRI acquisition.

1 Introduction

The beating heart undergoes complex deformations, and the study of the cardiac fiber architecture gives an opportunity to better understand these dynamics. Early studies relied on fiber dissections and histological slices [12]. Nowadays, with advances in imaging technologies, the cardiac fibers can be imaged via diffusion tensor magnetic resonance imaging (DT-MRI) [3,10]. Various acquisition schemes have been proposed for *in vivo* diffusion weighted imaging (DWI) [5,7]. However, due to the fast cardiac motion, its application is currently limited to single DT-MRI slices (2D). The full 3D *in vivo* imaging of the cardiac architecture should still rely on an extrapolation model [17] in the near future. Localized and direct *in vivo* measurements with a dedicated catheter is also possible [11], but is limited to sparse locations on the endocardial surface. The availability of a full 3D atlas of the cardiac architecture opens the door to not only the construction of more accurate extrapolation models for *in vivo* acquisitions, but also to a better understanding of various cardiac mechanical functions, cardiac electrophysiology patterns, and remodeling processes. So far only *ex vivo* canine

D.N. Metaxas and L. Axel (Eds.): FIMH 2011, LNCS 6666, pp. 171–179, 2011.

DT-MRI studies [9,13] have been considered, and in humans, only cases using a single *ex vivo* heart has been studied [15] and visualized in 3D [16]. Histological and DT-MRI studies all lead to similar findings. The fibers, locally organised as laminar sheets, appear to be consistently structured as two counter wound spirals where the fibers smoothly change orientation from the endocardium to the epicardium. Their orientation seems to be more stable than the laminar sheet orientation [9,13].

The availability of human hearts is extremely difficult (they are rather transplanted than used for research), and thanks to a unique post-mortem human dataset [6,14], we have built a statistical atlas from *ex vivo* DT-MRI and extended previous studies [9,13] to humans. The next section explains the semi-automatic method used to construct such atlas. The last section provides global statistics on the fiber architecture as well as more local properties within several myocardial segments.

2 Materials and Method

A method requiring the least possible interactions has been developed. The user provides two paint strokes in a B_0 image, one in each ventricle, and the method finds automatically the myocardium, registers it to the other myocardia, and constructs the statistical atlas of the fiber architecture. The construction of the atlas requires thus minimal user interaction, is reproducible, and can be quickly extended with additional hearts. From this atlas, the fiber variability is analyzed using state-of-the-art statistical tools on diffusion tensors within an efficient Log-Euclidean framework.

2.1 Data Acquisition

The human dataset [6,14] consists of 10 *ex vivo* human hearts acquired during forensic autopsies (6 of them are presented in Fig. 1(a)). MR imaging was performed within 24 hours after death, prior to the examination of the heart and lungs by the pathologist. All cases were from extra cardiac sudden deaths, and hearts were classified as healthy after controlling their weight, wall thickness, and subsequent pathology examination. The excised hearts were placed in a plastic container and filled with hydrophilic gel to maintain a diastolic shape. All images have been acquired on a 1.5T MR scanner (Avanto Siemens) with a bipolar echo planar imaging using 4 repetitions of 12 gradient images. The volumes are of size 128x128x52 with an isotropic resolution of 2mm. Each tensor image is globally normalized by aligning the histograms of the traces of the tensor matrices to compensate for any acquisition variability. This normalization does not affect the orientations of the eigenvectors.

2.2 Segmentation

The myocardium segmentation is a crucial part in our atlas construction, and the Graph Cut algorithm [4] has been chosen for its efficiency and ease of use.

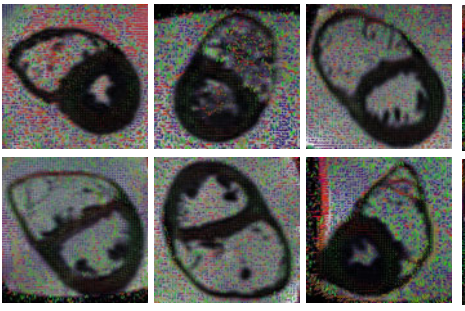

(a) Original tensor fields overlaid by the B_0 images

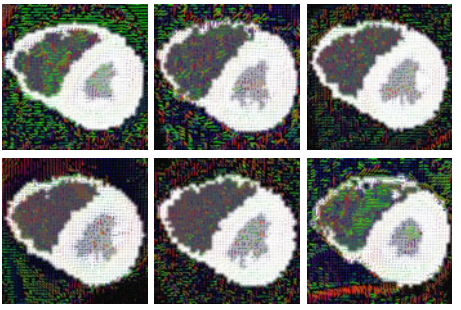

(b) Segmented B_0 images and registered tensor fields

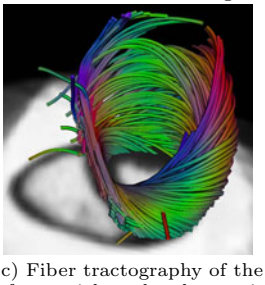

(c) Fiber tractography of the left ventricle and a short axis slice

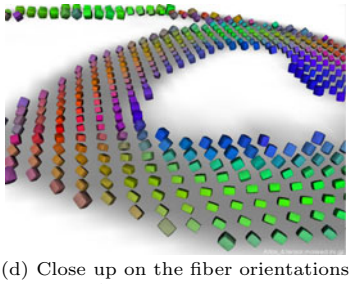

(d) Close up on the fiber orientations of a short axis slice

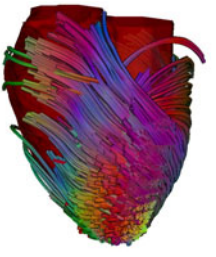

(e) Fiber tractography around the left ventricular blood pool

Fig. 1. A *statistical atlas* of the human cardiac fiber architecture is constructed from *(a)* 10 *ex vivo* human hearts (only 6 of them are shown). *(b)* They are segmented and registered to an average heart shape. The transmural variation of the fiber orientations in the left ventricle is visible in the fiber tractography (computed with MedINRIA) of the average tensor field. *(c)* It is overlaid with a short axis slice (with a close up view on *(d)*). *(e)* A long axis view of the left ventricle with the blood pool in red. The fiber coloring is dependent on the fiber orientation.

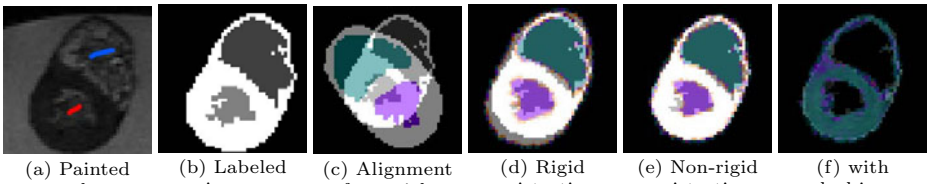

(a) Painted strokes (b) Labeled image (c) Alignment of ventricles (d) Rigid registration (e) Non-rigid registration (f) with masked images

Fig. 2. *Segmentation*: (a) The user marks the left and right blood pools on B_0 images (red and blue strokes), (b) a segmented image is created via Graph Cuts. *Registration*: The method (c) aligns the ventricles of the segmented images, (d) performs a rigid registration, and finds the non-rigid registration between (e) the segmented and (f) the masked B_0 images.

From a B_0 image, an underlying 3D graph is constructed and a global optimal solution partitions the graph into an *object* and a *background*. Fast interactions are possible to correct any missed segmentation. In our application, the user

marks on a 3D slice a few pixels, the *seeds* ([4]), in the left and right blood pools (red and blue strokes in Fig. 2 (a)). From these marks, three 3D binary segmentations are performed: *i)* the heart is isolated from its background using the marked pixels as *object seeds* [4] and the pixels lying on a surrounding box (large enough to be outside the heart) as *background seeds*, *ii)* the myocardium is delineated using the pixels on the inner boundary of the heart mask as *object seeds* and the marked pixels as *background seeds*, and *iii)* the blood pool is partitioned into the left and right sides using each paint stroke as *seeds*. From these binary masks, a 3D segmentation image is created with four labels: background, left and right ventricles, and myocardium (Fig. 2(b)).

2.3 Registration and Atlas Construction

To construct the atlas of DT-MRIs, the population of hearts must be registered to a common reference heart shape. The registration is solely based on B_0 images and their segmented images. Information on the fiber architecture are purposely omitted in order to avoid any bias in the study of the fiber variability. After aligning the centers of mass of each ventricle (Fig. 2(c)), a block matching algorithm performs a rigid registration on the segmented images (Fig. 2(d)). Once correctly aligned, a non-rigid registration of the segmented images is performed (Fig. 2(e)). The resulting transformation initializes the registration of the masked B_0 images (Fig. 2(f)). The symmetric log-domain diffeomorphic demons [18] provides an efficient non-rigid registration method. Moreover, averaging and inverting diffeomorphic deformation fields are straightforward in the log-domain. The construction of the atlas follows Guimond's *et al.* method [8], where the average of inverse transforms brings iteratively the reference heart toward an average shape. In practice, the reference image becomes stable after two or three iterations. Finally, the tensor fields associated with each B_0 image are warped to the converged average heart shape. Among two possible reorientation strategies [1], the Finite Strain strategy is preferred to the Preservation of the Principal Direction for its preservation of geometric features [13].

2.4 Statistical Analysis

A voxel-wise statistical analysis is performed on our atlas (i.e., a population of diffusion tensors warped to a reference heart). The Log-Euclidean metric [2] provides a fast and valid framework for the study of the variability of the diffusion tensors. Our study uses classical statistical tools (such as the mean or the covariance) in the Log-Euclidean framework rather than in the Euclidean space. A tensor is described with a condensed form, $\text{vec}(D) = (D_{11}, \sqrt{2}D_{12}, D_{22}, \sqrt{2}D_{31}, \sqrt{2}D_{32}, D_{33})^t$, where redundant terms in the tensor matrix $(D_{ij})_{i,j=1,2,3}$ are removed. With N tensor fields, $\{D^{(i)}\}_{i=1,\ldots,N}$, the mean is computed, $\bar{D} = \exp\left(\frac{1}{N}\sum_{i=1}^{N}\log(D^{(i)})\right)$, along the covariance matrix, $\Sigma = \frac{1}{N-1}\sum_{i=1}^{N}\text{vec}(\Delta D^{(i)})\cdot\text{vec}(\Delta D^{(i)})^t$ where $\Delta D^{(i)} = \log(D^{(i)}) - \log(\bar{D})$. The trace of the covariance matrix (i.e., the sum of its eigenvalues) gives an assessment on the global

variability of the tensor field. To express it as a percentage ratio from the mean tensor $\bar{D}$, we use its square root:

$$\sqrt{\mathrm{Tr}(\Sigma)} = \sqrt{\frac{1}{N-1}\sum_{i=1}^{N} \|\mathrm{vec}(\Delta D^{(i)})\|}. \quad (1)$$

To gain further information on the variability of the tensor field, The covariance matrix is projected onto orthonormal bases [13]. These bases are formed with a combinations of the different eigenvectors $\mathbf{v_1}, \mathbf{v_2}, \mathbf{v_3}$ of the mean tensor matrix $\bar{D}$. The bases of particular interest are $W_{2,3} = 1/\sqrt{2}\,(\mathbf{v_3} \cdot \mathbf{v_2}^t + \mathbf{v_2} \cdot \mathbf{v_3}^t)$, $W_{1,3} = 1/\sqrt{2}\,(\mathbf{v_3} \cdot \mathbf{v_1}^t + \mathbf{v_1} \cdot \mathbf{v_3}^t)$, and $W_{1,2} = 1/\sqrt{2}\,(\mathbf{v_2} \cdot \mathbf{v_1}^t + \mathbf{v_1} \cdot \mathbf{v_2}^t)$. The standard deviation of orientation differences, $\{\theta_{i,j}\}_{i,j=1,2,3}$, between the coupled $(\mathbf{v_i}, \mathbf{v_j})$ axes around $\mathbf{v_k}$ (i.e., the variability of how the orthogonal axes $(\mathbf{v_i}, \mathbf{v_j})$ rotates around $\mathbf{v_k}$) are revealed by projecting the covariance matrix Σ onto $W_{2,3}$, $W_{1,3}$, and $W_{1,2}$ ($\lambda_{1,2,3}$ are the tensor eigenvalues):

$$\theta_{i,j} = \arctan\left(\frac{1}{2(\lambda_i - \lambda_j)^2}[\mathrm{vec}(W_{i,j})^t \cdot \Sigma \cdot \mathrm{vec}(W_{i,j})]\right)^{\frac{1}{2}} \quad (2)$$

3 Results

The variability of the global fiber architecture is first presented, followed by a more local study on the 17 AHA (American Heart Association) cardiac zones in the left ventricle.

3.1 Fiber Variability

The tractography of the cardiac fibers in Figure 1 shows the average fiber structure. The transmural variation of the fiber orientation is clearly seen in all views. The fibers form a double spiral with different orientations on each side of the myocardium mid-wall. The histogram of the trace (Fig. 3 using Eq. 1) shows a peak of variability at 13.2%. It is however important to note that this variability

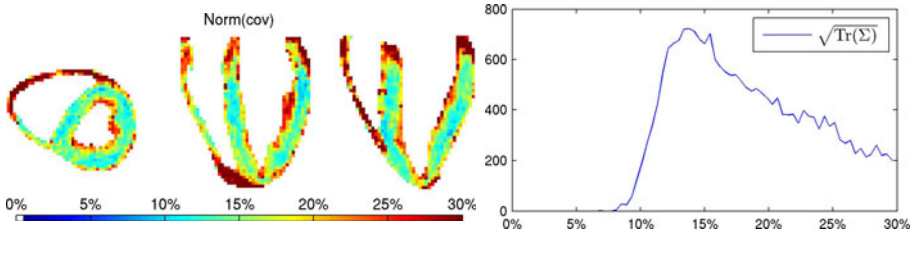

Fig. 3. Global variability ($\sqrt{\mathrm{Tr}(\Sigma)}$, Eq. 1) (expressed in percentage) of the human cardiac fiber structure. The histogram shows a mode of 13.2%.

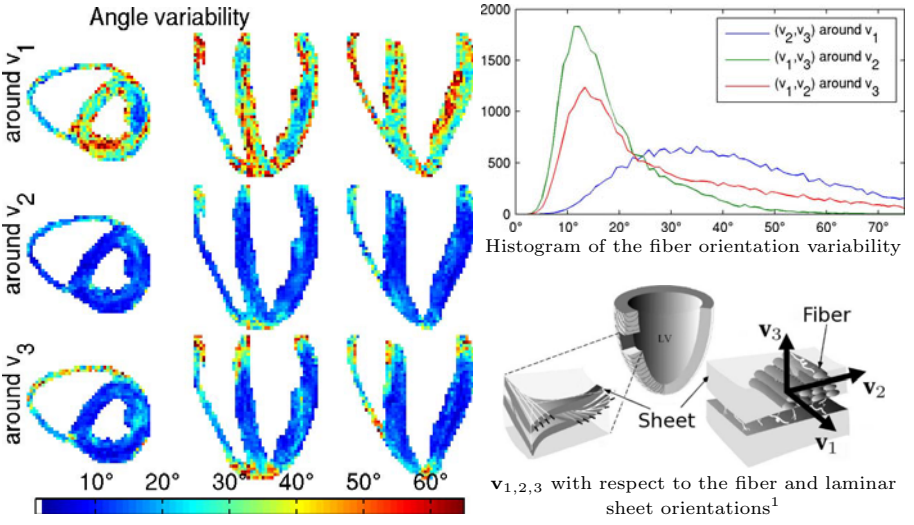

Fig. 4. Standard deviation of the fiber orientation (expressed in degree). *Top row of the image and in the blue histogram*: Variability of the laminar sheet orientation, $\theta_{2,3}$ around $\mathbf{v}_1$, with a mode at 31.1°. *Middle row and in the green histogram*: Variability of the fiber orientation, $\theta_{1,3}$ around $\mathbf{v}_2$, with a mode at 11.5°. *Bottom row and in the red histogram*: Variability of the fiber orientation, $\theta_{1,2}$ around $\mathbf{v}_3$, with a mode at 13.0°.

also includes registration errors. The registration can be difficult and challenging (large deformations, low resolutions) and could certainly be the cause of a higher variability in the right ventricle, the papillary muscles, and around the apex. The variability of the eigenvectors (Fig. 4) reveals a disparity among the different directions. Indeed, the rotations of the planes containing the first eigenvector (i.e., the fiber orientation) around perpendicular axes $\mathbf{v_2}$ and $\mathbf{v_3}$ ($\theta_{1,3}$ and $\theta_{1,2}$ using Eq. 2) show a rather stable cardiac fiber orientation with a standard deviation of $\theta_{1,3} = 11.5°$and $\theta_{1,2} = 13.0°$. However, the orientation of the coupled axes $(\mathbf{v_2}, \mathbf{v_3})$ (i.e., the laminar sheets) around the fiber orientation $\mathbf{v_1}$ shows a much greater variability in the laminar sheet structure with $\theta_{2,3} = 31.1°$. This concurs with a previous canine study [13] where the fiber orientation (with $\theta_{1,3} = 7.9°$and $\theta_{1,2} = 7.7°$) is more stable than the laminar sheet orientation (with $\theta_{2,3} = 22.7°$).

3.2 Variability across Myocardial Segments

We register and map the statistical atlas onto a prolate ellipsoid, and analyze the transmural variation of the fiber orientation in the 17 AHA segments of the left ventricle. The figure 5 shows the helix angle (between the fiber orientation and a short axial line) and the transverse angle (between the fiber orientation and a long axial line) against the transmural width. The helix angle varies globally

[1] Illustration adapted from LeGrice *et al.*, *Am. J. of Phys. - Heart and Circ. Phys.*, 269(2), 1995.

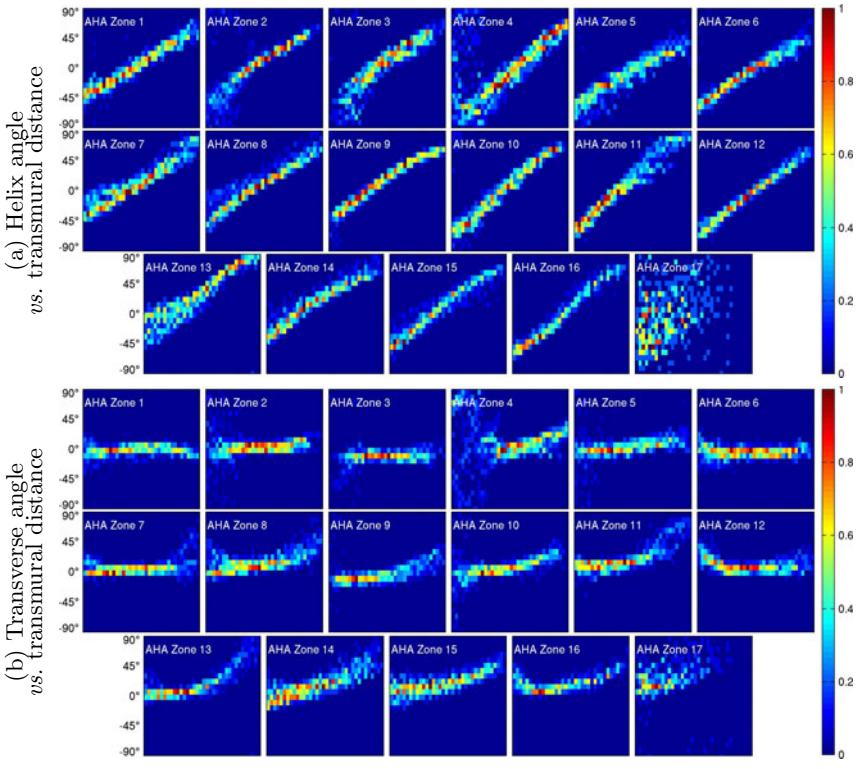

Fig. 5. Joint histograms showing the distribution of the *(a)* helix angle and the *(b)* transverse angle of the human cardiac fibers across the myocardial wall in the 17 AHA segments of the left ventricle. The x axis of each joint histogram represents the transmural distance from epicardium *(left)* to endocardium *(right)*. The y axis is the helix or transverse angle.

from -51°on the epicardium to +66°on the endocardium (the range is 117°- a canine study [13] showed a range of 110°). It appears to be consistent across all myocardial segments. There is however a drastic difference at the apex. While this might be due to missed registrations in the apex area, this could also mean that the fiber structure at the apex varies among the human population. The helix angle is strongly correlated to the transmural distance with a correlation factor of $\rho = 0.831$. The transverse angle is less correlated with $\rho = 0.286$ (i.e., it depends less on the transmural width). It is stable at 0°and appears to be always close to zero on all myocardial segments.

4 Conclusion

This paper brings the first statistical description of the human cardiac fiber architecture from 10 *ex vivo* DT-MRI images. The statistical atlas has been

built thanks to a unique access to 10 *ex vivo* human hearts. The fiber variability has been studied across the whole myocardium. The results show that the orientations of the cardiac fibers are more stable than the cardiac laminar sheet orientations. Knowing that the fibers are globally stable, it was interesting to study the fiber orientation in a more local manner in the left ventricular AHA zones. The observed orientation is consistent across nearly all myocardial segments. Only the apex shows a higher variability. This might show that the fiber structure at the apex might not have a consistent structure. The results of this study also extend a previous canine study [13]. Moreover, a semi-automatic method has been described to build a morphological atlas with easy user interactions. It can be reused for other future studies using more samples or other species. The fiber architecture plays a key role in mechanical and electrical cardiac functions. This first statistical atlas of the human cardiac fiber architecture allows thus a better understanding of the human heart. With recent advances in *in vivo* DT-MRI, it is possible to foresee the use of this statistical model of the heart to extrapolate sparse *in vivo* acquisitions and thereupon paving the way for personalized *in vivo* DT-MRI.

Acknowledgement

The authors wish to thank the financial support of the National Science and Environment Research Council (NSERC), the Michael Smith Scholarship (CGS-MSFSS), and the EGIDE/INRIA Scholarship.

References

1. Alexander, D.C., Pierpaoli, C., Basser, P.J., Gee, J.C.: Spatial transformations of diffusion tensor magnetic resonance images. IEEE Trans. on Medical Imaging 20(11) (2001)
2. Arsigny, V., Fillard, P., Pennec, X., Ayache, N.: Log-Euclidean metrics for fast and simple calculus on diffusion tensors. Mag. Res. in Med. 56(2) (2006)
3. Basser, P.J., Mattiello, J., LeBihan, D.: MR diffusion tensor spectroscopy and imaging. Biophysics Journal 66(1) (1994)
4. Boykov, Y., Jolly, M.-P.: Interactive organ segmentation using graph cuts. In: Delp, S.L., DiGoia, A.M., Jaramaz, B. (eds.) MICCAI 2000. LNCS, vol. 1935, pp. 276–286. Springer, Heidelberg (2000)
5. Dou, J., Tseng, W.-Y.I., Reese, T.G., Wedeen, V.J.: Combined diffusion and strain MRI reveals structure and function of human myocardial laminar sheets in vivo. Mag. Res. in Med. 50(1) (2003)
6. Frindel, C., Robini, M., Croisille, P., Zhu, Y.-M.M.: Comparison of regularization methods for human cardiac diffusion tensor MRI. Med. Im. An. 13(3) (2009)
7. Gamper, U., Boesiger, P., Kozerke, S.: Diffusion imaging of the in vivo heart using spin echoes–considerations on bulk motion sensitivity. Mag. Res. in Med. 57(2) (2007)
8. Guimond, A., Meunier, J., Thirion, J.P.: Average Brain Models: A Convergence Study. Comp. Vis. and Im. Und. (2000)

9. Helm, P.A., Tseng, H.-J.J., Younes, L., McVeigh, E.R., Winslow, R.L.: Ex vivo 3D diffusion tensor imaging and quantification of cardiac laminar structure. Mag. Res. in Med. 54(4) (2005)
10. Hsu, E.W., Henriquez, C.S.: Myocardial fiber orientation mapping using reduced encoding diffusion tensor imaging. J. of Card. Mag. Res. 3(4) (2001)
11. Lasher, R.A., Hitchcock, R.W., Sachse, F.B.: Towards modeling of cardiac microstructure with catheter-based confocal microscopy: a novel approach for dye delivery and tissue characterization. IEEE Trans. on Medical Imaging 28(8) (2009)
12. Nielsen, P.M., Le Grice, I.J., Smaill, B.H., Hunter, P.J.: Mathematical model of geometry and fibrous structure of the heart. Am. J. of Phys. - Heart and Circ. Phys. 260(4) (1991)
13. Peyrat, J.-M., Sermesant, M., Pennec, X., Delingette, H., Xu, C., McVeigh, E.R., Ayache, N.: A Computational Framework for the Statistical Analysis of Cardiac Diffusion Tensors: Application to a Small Database of Canine Hearts. IEEE Trans. on Medical Imaging 26(11) (2007)
14. Rapacchi, S., Croisille, P., Pai, V., Grenier, D., Viallon, M., Kellman, P., Mewton, N., Wen, H.: Reducing motion sensitivity in free breathing DWI of the heart with localized Principal Component Analysis. In: ISMRM (2010)
15. Rohmer, D., Sitek, A., Gullberg, G.T.: Reconstruction and visualization of fiber and laminar structure in the normal human heart from ex vivo diffusion tensor magnetic resonance imaging (DTMRI) data. Investigative Radiology 42(11) (2007)
16. Seemann, G., Keller, D.U.J., Weiss, D.L., Dossel, O.: Modeling human ventricular geometry and fiber orientation based on diffusion tensor MRI. In: Comp. in Card. (2006)
17. Toussaint, N., Sermesant, M., Stoeck, C.T., Kozerke, S., Batchelor, P.G.: In vivo human 3D cardiac fibre architecture: Reconstruction using curvilinear interpolation of diffusion tensor images. In: Jiang, T., Navab, N., Pluim, J.P.W., Viergever, M.A. (eds.) MICCAI 2010. LNCS, vol. 6361, pp. 418–425. Springer, Heidelberg (2010)
18. Vercauteren, T., Pennec, X., Perchant, A., Ayache, N.: Symmetric log-domain diffeomorphic registration: A demons-based approach. In: Metaxas, D., Axel, L., Fichtinger, G., Székely, G. (eds.) MICCAI 2008, Part I. LNCS, vol. 5241, pp. 754–761. Springer, Heidelberg (2008)

Morphological Classification: Application to Cardiac MRI of Tetralogy of Fallot

Dong Hye Ye[1], Harold Litt[2], Christos Davatzikos[1], and Kilian M. Pohl[1]

[1] SBIA, University of Pennsylvania, Philadelphia, USA
[2] Cardiovascular Imaging Section, University of Pennsylvania, Philadelphia, USA

Abstract. This paper presents an image-based classification method, and applies it to classification of cardiac MRI scans of individuals with Tetralogy of Fallot (TOF). Clinicians frequently diagnose cardiac disease by measuring the ventricular volumes from cardiac MRI scans. Interrater variability is a common issue with these measurements. We address this issue by proposing a fully automatic approach for detecting structural changes in the heart. We first extract morphological features of each subject by registering cardiac MRI scans to a template. We then reduce the size of the features via a nonlinear manifold learning technique. These low dimensional features are then fed into nonlinear support vector machine classifier identifying if the subject of the scan is effected by the disease. We apply our approach to MRI scans of 12 normal controls and 22 TOF patients. Experimental result demonstrates that the method can correctly determine whether subject is normal control or TOF with 91% accuracy.

Keywords: Tetralogy of Fallot, Morphological classification, Manifold learning, Computational anatomy.

1 Introduction

Cardiac MRI has become essential for pre- and post-operative management of tetralogy of Fallot patients [1]. This non-invasive technique can yield detailed 3D anatomical images of the beating heart with constant image quality through time. Clinicians use cardiac MRI to perform volumetric measurements of anatomical structures, such as left/right ventricular end-diastolic/end-systolic volumes, mass, stroke volumes, and ejections fractions. However, these measurements are often not sensitive enough to detect certain cardiac disease as they do not fully utilize the rich information provided by cardiac MRI. In addition, clinicians often find it difficult to produce reliable prediction of disease progression due to the high inter- and intra-rater variability associated with these measurements. We address this issue in this paper by suggesting an alternative approach for accurately detecting heart disease.

Our approach is based on a popular concept in the vision community, where high-dimensional features are extracted from the images and then fed into a classifier. The classifier automatically labels the image, which in our case corresponds to differentiating cardiac MRIs of patients effected by a certain disease

D.N. Metaxas and L. Axel (Eds.): FIMH 2011, LNCS 6666, pp. 180–187, 2011.

from healthy individuals. One issue with this type of analysis with respect to cardiac MRI is the relative low sample size in comparison to the high dimensionality of the image features. The number of training subjects impacted by a disease is often limited to hundreds while the number of voxels in a medical scan is typically more than a million. The community has addressed this issue by mapping the high-dimensional features into a lower dimensional space.

Principal component analysis (PCA) performs a linear mapping of the high dimensional features to a lower dimensional space such that the variance of the features in the lower dimensional representations is maximized [2]. However, PCA is not appropriate for nonlinear features, because it is employed in a linear way. Alternatively, manifold learning techniques can map nonlinear high-dimensional data to low-dimensional space [3], [4]. Manifold learning techniques assume that the data of interest lies on an embedded non-linear manifold within the high-dimensional space while preserving neighborhood relations between nearest neighbors. Therefore, they can perform nonlinear dimensionality reduction by applying embedding to high-dimensional features.

In the remainder of this paper, we describe our disease classification approach, which first extracts morphological features from short-axis cine MRI of a subject by finding the spatial transformation that places the scan into a common space. We then compute the Jacobian determinants of the transformations which we relate to tissue density maps. The Jacobian determinants are then embedded into a lower-dimensional space via manifold learning. We then use the resulting embedding coordinates as the lower-dimensional features for disease detection. The method is applied to MRI scans of 12 normal controls and 22 tetralogy of Fallot patients and evaluated by classification rates using leave-one-out method.

2 Method

Fig. 1 summarizes our morphological classification framework. We first extract morphological features for each subject from the given ventricular segmentations of patients' medical scan image. We then use the morphological features to learn a low-dimensional embedding via a manifold learning technique targeted towards dimensionality reduction. Each scan is now represented by coordinates in the low-dimensional embedding. We then apply these coordinates to a non-linear support vector machine classifier to produce the class label. In followings, we will explain each component in detail.

2.1 Feature Extraction

We use the RAVENS maps as a morphological descriptor characterizing the images [5]. RAVENS maps are the results of deformable registration of cardiac images to a common template while generating maps that are proportional to each individual's regional tissue amount. They capture tissue density, which tetralogy of Fallot patients often affect.

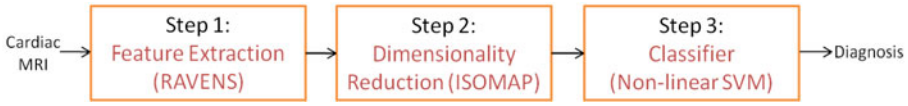

Fig. 1. Overview of proposed framework

Suppose S_k denotes the segmented image for tissue k in the individual image $S : \Omega_S \to \mathbf{R}$ and $T : \Omega_T \to \mathbf{R}$ is the template to be registered. Then a RAVENS map, $\mathcal{D}_k : \Omega_T \to \Omega_T$, for tissue k is defined as:

$$\mathcal{D}_k(x) := J(h(x))S_k(h(x))$$

with h being the deformation map from Ω_S to Ω_T and $J(h(x))$ is the Jacobian determinant of h at voxel x.

We create the RAVENS map, by registering the images to the common atlas via fast diffeomorphic demons algorithm [6]. When registering the images, the choice of a template plays an important role in the accuracy of the morphological features. Therefore, it is necessary to select the optimal template for better morphological representations. In order to select the optimal template, we adopt GRAM framework [7] which finds the geodesic mean of the data. GRAM computes the geodesic distance between two images by viewing the dataset as undirected graph with the nodes of the graph representing the images of the data set. $g(I_i, I_j)$, the geodesic distance between two images I_i and I_j, is approximated by the shortest path between the two corresponding nodes in the graph. The geodesic mean template T is then defined by the image in the data set with minimum distance to all other images:

$$T = \arg\min_i \sum_j g(I_i, I_j).$$

After registering all images to T, we reduce the noise in the RAVENS maps via Gaussian kernel smoothing. We further reduce the number of features by only using the RAVENS map $\mathcal{D}_{RV}$ of the right ventricle for classification. We do so because right ventricle is the most significant tissue type related to Tetralogy of Fallot.

2.2 Dimensionality Reduction

Even after confining the RAVENS maps to the right ventricle, its dimensionality is still very high compared to the limited sample size. As mentioned, this generally negatively influences the accuracy of the classifier. We address the issue by performing dimensionality reduction via the ISOMAP algorithm [4].

In order to apply the ISOMAP algorithm, we represent the data as a graph whose vertex corresponds to the image samples. First, we define the edge length $d(i, j)$ between two subjects i and j as a $L2$ distance of RAVENS maps:

$$d(i, j) := \sum_{x \in \Omega_T} (\mathcal{D}^i_{RV}(x) - \mathcal{D}^j_{RV}(x))^2,$$

We then construct a connected k-NN graph based on the edge lengths $d(i, j)$. We then use the k-NN graph to infer the geodesics between all pairs of subjects. This results are stored in a matrix with the size corresponding to the number of samples. We then generate the low-dimensional embedding of the data by computing the eigenvalues and -vectors of the matrix. The eigenvectors of the 9 highest eigenvalues then define the coordinate system of the low-dimensional embedding of the data set. Finally, each data set is described by its (embedding) coordinates in that coordinate system. By doing so, we reduced the number of features describing each data set from 172800 to 9.

2.3 Non-linear SVM

The embedding coordinates of each image are fed into classifier, which labels each data set based on those features. We choose the support vector machine (SVM) classifier [8] for this task. SVM is a popular approach pattern classification. It separates the data into two clusters hopefully representing the healthy and diseased population. This separation is described through a hyperplane. The hyperplane is generated by training the algorithm on a pre-classified training set. From this training set, the algorithm selects a relatively small number of samples that are close to the opposite group. These samples are called support vectors and are used for defining the dividing hyperplane. By doing so, the classifier inherently focuses on the subtleties of the morphological differences between normal controls and tetralogy of Fallot patients and not on data sets that are easy to detect.

While the SVM classifier is very effective in finding this hyperplane, selecting the type of hyperplane is very important. If the hyperplane is too stiff then the algorithm might not perfectly separate the two groups. On the other hand, if the hyperplane is too flexible then the algorithm will overfit the data. The type of hyperplane is characterized by the kernel that maps the data to a higher-dimensional where linear separation is possible. Based on our experience, we choose the Gaussian radial basis function as kernel [9].

$$K(u, v) := exp(-\gamma||u - v||^2),$$

where u and v are data points and γ is a model parameter.

In summary, we conduct supervised classification with embedding coordinates on the cardiac MRI scans of 34 subjects. In our application, we consider tetralogy of Fallot as a positive data, and normal controls as a negative data. We choose the support vector machine with radial basis function kernel as a classifier due to its effectiveness and efficiency. The classifier is trained on the 33 subjects and trained classifier was applied to the 1 left-out data. We select the model parameter γ in the radial basis function by grid search using cross validation.

3 Experiment

We evaluate our method by applying it on short-axis cardiac MRIs of 12 normal volunteers and 22 Tetralogy of Fallot patients. Tetralogy of Fallot patients

were post-repaired and age-matched to normal controls. Steady-state free precession cardiac MRIs were obtained at end-diastole. The acquired short-axis slice covered the whole heart. To prevent other organs from influencing analysis, the images were cropped using manually defined rectangular regions that enclosed the complete left ventricle and right ventricle on the short axis, respectively. The left ventricular endocardium, left ventricular epicardium, and right ventricular epicardium were semi-automatically segmented in the data set on short-axis slices [10]. We then applied the data set to our pipeline. We measuring the accuracy of our approach via leave-one-out cross validation comparing the classification of the test subject with the diagnosis of an expert. For comparison, we also computed the accuracy of the non-linear SVM classifier using the left and right ventricular volume as input features.

3.1 Features

Fig. 2 shows the distribution of the features used as input to the SVM classifier. Fig. 2a plots the left and right ventricular volume features and Fig. 2b shows the two-dimensional embedding of RAVENS map. It is worth to mentioning that for classification of the RAVENS map we actually used 9 dimensional features. However, it is practically impossible to visualize 9 dimensional features. Therefore, we confine our low-dimensional embedding to the first two largest eigenvalues for visualization purpose. A subset of images is also shown with embedding in Fig. 2b. The embedding conveniently summarizes the change in right ventricle size as the most dominant parameter. These type of observation support the impression that neighborhoods in the embedding coordinates represent images that are similar in terms of the size of right ventricle. Furthermore, we note that ventricular volume features have more overlap between normal controls and tetralogy of fallots in the feature space than embedding coordinates. Therefore, embedding coordinates can have more discriminative power than ventricular volume features. In addition, distribution of embedding coordinates is not linearly separable. This indicates that non-linear kernel mapping is necessary for these features.

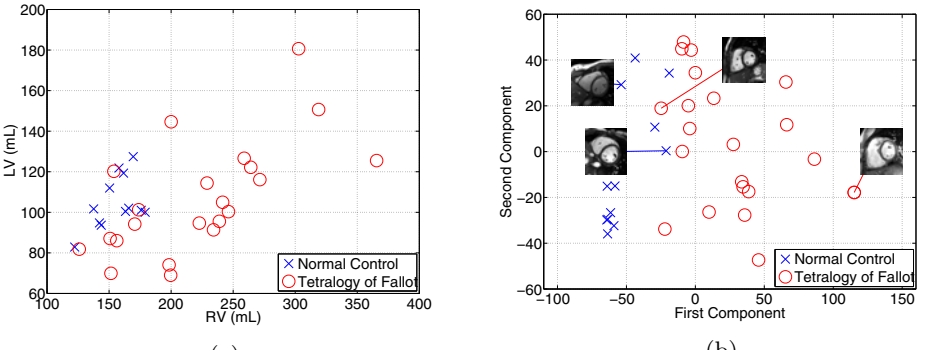

(a) (b)

Fig. 2. Feature distribution (a) Ventricle volume (b) 2D ISOMAP of RAVENS maps

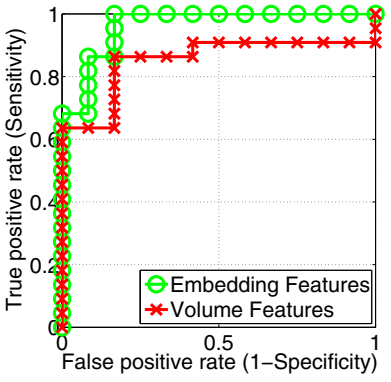

Fig. 3. Receiver Operating Characteristics(ROC) curves for embedding features and ventricular volumetric features

Table 1. Recall rates between Normal Control versus Tetralogy of Fallot

	Sensitivity(%)	Specificity(%)	AUC(%)
Ventricular volumes	86.36	75	85.2
Embedding coordinates	**95.45**	**83.33**	**96.4**

3.2 Classification Accuracy

The classification performance was measured by precision recall rate. In the binary classification of positive tetralogy of fallot and negative normal hearts, the results are represented by numbers of true positive(TP), false positive(FP), true negative(TN), and false negative(FN). The sensitivity and specificity were computed by

$$sensitivity = \frac{TP}{TP + FN}, specificity = \frac{TN}{TN + FP}$$

In addition, area under the curves (AUC) are computed by ROC analysis in Fig. 3. Table 1 shows precision recall rates and AUC for ventricular volume features and embedding coordinates. Compared to ventricular volume features, embedding coordinates achieves higher sensitivity (10.09% increase), specificity (11.07% increase) and AUC (11.2% increase). This result indicates that the features generated by ISOMAP applied to the RAVENS maps better characterize the disease compared to ventricular volume features often used in the clinical setting.

3.3 Group Comparisons via Voxel-Based Analysis

Although nonlinear classification methods are generally effective in resolving spatially complex group differences, they do not easily lend themselves to intuitive interpretation of the result. For clinical evaluation, we need to identify

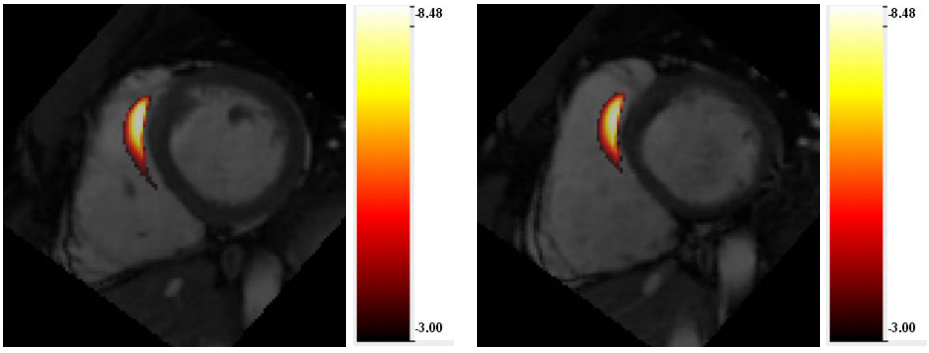

Fig. 4. Maps of the t statistics showing differences between normal controls and tetralogy of fallot patients. T-maps are presented in different mid slices of the cropped template image. Regions in which tetralogy of fallot patients are significantly different from normal controls are highlighted in red, reflecting right ventricular outflow tract (RVOT) obstruction. T-maps were thresholded at the $p = 0.001$ level. Color bar represents logarithm of p value.

abnormalities such as progressive hypertrophy and chamber dilation. However, the high dimensional features are generally not displayable in a single image. We thus choose an alternative approach called voxel-based group comparisons to visualize the differences between healthy and diseased subjects [11]. Fig. 4 shows the t-statistics thresholded at $p = 0.001$ level in different mid slices. This figure shows significant right ventricular shape changes in tetralogy of fallot compared to healthy hearts. Right ventricular outflow tract, which are generally implicated in tetralogy of fallot, are highlighted (red color). This implies that our classification method can precisely localize the region of pathology in tetralogy of fallot patients compared to normal subjects.

4 Conclusion

We presented a disease classification frame work to diagnose tetralogy of Fallot patients. Mass-preserving morphological descriptors were used to extract morphological features from cardiac MRI. We then reduced the dimensionality of features via ISOMAP. The reduced features were fed into the non-liner support vector machine classifier to produce labellings of healthy and diseased patient group. On a small data set, classification based on our features outperformed conventional clinical analysis based on the volume of the ventricle. We believe this improved performance was due to better morphological descriptors and non-linear classifier.

Acknowledgment. The research was supported by an ARRA supplement to NIH NCRR (P41 RR13218).

References

1. Helbing, W.A., Roos, A.: Clinical application of cardiac magnetic resonance imaging after repair of tetralogy of Fallot. Pediatric Cardiology 21(1), 70–79 (2000)
2. Sirovich, L., Kirby, M.: Low-dimensional procedure for the characterization of human faces. Journal of the Optical Society of America A(4), 519–524 (1987)
3. Roweis, S., Saul, L.: Nonlinear Dimensionality Reduction b Locally Linear Embedding. Science 290, 2323–2326 (2000)
4. Tenenbaum, J.B., Silva, V., Langford, J.C.: A Global Geometric Framework for Nonlinear Dimensionality Reduction. Science 290(5500), 2319–2323 (2000)
5. Davatzikos, C., Genc, A., Xu, D., Resnick, S.M.: Voxel-based morphometry using the ravens maps: methods and validation using simulated longitudinal atrophy. Neuroimage 14(6), 1361–1369 (2001)
6. Vercauteren, T., Pennec, X., Perchant, A., Ayache, N.: Diffeomorphic demons: efficient non-parametric image registration. Neuroimage 45(supp.1), S61–S72 (2009)
7. Hamm, J., Ye, D.H., Verma, R., Davatzikos, C.: Gram: A framework for geodesic registration on anatomical manifolds. Med. Image Anal. 14(5), 633–642 (2010)
8. Burges, C.J.C.: A tutorial on support vector machines for pattern recognition. Data Mining and Knowledge Discovery 2, 121–167 (1998)
9. Keerthi, S., Lin, C.: Asymptotic behaviors of support vector machines with Gaussian kernel. Neural Computation 15(7), 1667–1689 (2003)
10. Heiberg, E., Wigstrom, L., Carlsson, M., Bolger, A.: Time Resolved Treedimensional Automated Segmentation of the Left Ventricle. Proceedings of IEEE Computers in Cardiology 32, 599–602 (2005)
11. Ashburner, J., Friston, K.J.: Voxel-based morphometry–the methods. Neuroimage 11(6 Pt 1), 805–821 (2000)

Cardiac MRI Intervention and Diagnosis via Deformable Collaborative Tracking

Yan Zhou, Nikolaos V. Tsekos, and Ioannis T. Pavlidis

Department of Computer Science, University of Houston, Houston, TX 77024, USA

Abstract. The high contrast and lack of ionizing radiation, renders Magnetic Resonance Imaging (MRI) a suitable modality for continuous intra-operative imaging. Tracking the motion of key locations in cardiac MRI is of paramount importance in control and guidance in emerging robot-assisted interventions. Tracking can also be used to assess myocardial wall motion for diagnostic purposes. This article presents an expanded collaborative tracking algorithm to facilitate both interventions and diagnosis in MRI. Specifically, the network of trackers not only follows anatomical landmarks on the beating heart but also computes its evolving deformable surface on a specific plane. Experimental investigations with both CINE and real-time MRI demonstrate that the collaborative tracker network achieves robust real-time performance over long periods, outperforming the MIL tracker. Pilot experimental results also demonstrate that the evolution of the network's deformation mesh can be used for blood volume estimation and computation of the ejection fraction - both of great diagnostic value.

1 Introduction

Image-guided robot-assisted interventions promise to improve patient management and reduce the cost of delivered health care. Real-time tracking of cardiac anatomical landmarks is paramount in such intra-operative interventions to maneuver the robotic manipulator around critical tissue. A major drawback of legacy procedures is that the anatomical information is not updated intra-operatively. Hence, any tissue shifts induced by the advancement of the interventional tools cannot be compensated for. Tissue dislocations are difficult to predict as they depend on tissue elastic properties and the speed of advancement [1] [2] [3] [4] [5] [6]. Moreover, conventional MRI guided procedures that entail the insertion of the tool while the patient is outside the scanner followed by validating scanning, become lengthy and cause additional discomfort to the patient. They may also result to more surgical trauma and increased chances for complications due to multiple insertion attempts.

To keep track of a specific anatomical landmark over time, one approach is to segment the underlying structures in each slice. Such approach may entail defining an appropriate optimization scheme to iteratively minimize a cost function, and the computational cost can be significant. For example, in [7], while the proposed boundary segmentation method achieved very high accuracy, the computational time was 10 seconds per slice. In contrast, Yuen et al. [8] achieved

D.N. Metaxas and L. Axel (Eds.): FIMH 2011, LNCS 6666, pp. 188–194, 2011.

real-time performance in Ultrasound images with an extended Kalman filter tracker. Zhou et al. [9] proposed to use multiple particle filter trackers to track a single region. For each tracker, a decision is made to classify it as "survivor" or "failed". Tracker interaction is modeled via a Bayesian network. The approach is able to achieve accurate overall state estimation in real-time, as an evidence for the motion estimation of a specific landmark point.

In this article we extend Zhou's method to handle tissue surface deformation and not just motion of single landmark points. Different trackers in the network may have different motion patterns due to non-linear tissue deformation. This motivates to take advantage of each tracker's specific location, and form a deformation mesh. The deformed region captures the heart's surface undergoing non-linear deformations. The surface area from the deformation mesh shows periodical rhythm during heart's contraction and extraction - a feature that may be used in diagnosis. We also compare our approach to the state-of-art Multiple Instance Learning (MIL) tracker [10]. MIL tracker uses an online-boosting approach to train the appearance model at each time step. And the training examples are presented in "bags" rather than individual instances. The experimental results show that although MIL tracker captures abrupt motion and appearance changes at first, it gradually drifts and finally loses the target as time passes by. Our tracking approach outperforms the MIL tracker both in speed and robustness in long tracking sequences.

In section 2 we describe in detail the methodological approach. In section 3 we present analysis of the experimental performance of the method.

2 Methodology

2.1 Collaborative Tracking

We have adopted as a baseline methodology the collaborative tracking algorithm proposed by Zhou et al. [9]. The algorithm tracks the region of interest via a grid of particle filter trackers. After each tracker's motion state is estimated as an independent particle filter tracker, the tracker network is formed. For each individual tracker T_i in the 3×3 grid, a decision is made whether to include it or not into the survivor group. The adjacent trackers $\{T_j, ..., T_m\}$ provide evidence to make this decision via a Bayesian network.

$$p(W_{i,t}, \hat{\Theta}_{i,t} | G_{i,t-1}, Z_{i,t}) \propto p(G_{i,t-1}) \prod_k N(\hat{\theta}_{i,t} | \hat{\theta}_{k,t}, \sigma^2) \prod_k p(\hat{\theta}_{k,t} | z_{k,t}). \quad (1)$$

The surviving probability of $T_{i,t}$ is computed in Equation (1); please note that $\hat{\Theta}_{i,t} = \{\hat{\theta}_{i,t}, \hat{\theta}_{j,t}, ..., \hat{\theta}_{m,t}\}$ and $Z_{i,t} = \{z_{i,t}, z_{j,t}, ..., z_{m,t}\}$ are the estimated states and observations of T_i and its adjacent trackers at time t. $W_{i,t}$ represents the event that tracker T_i is in the survivor group at time t. $G_{i,t-1}$ is the Bayesian network at time $t-1$, whose probability $p(G_{i,t-1})$ is known at time t. $N(\hat{\theta}_{i,t} | \hat{\theta}_{k,t}, \sigma^2)$ is the probability density of $\hat{\theta}_{i,t}$ on the Normal distribution centered at $\hat{\theta}_{k,t}$ with variance σ^2.

$p(W_{i,t}, \hat{\Theta}_{i,t}|G_{i,t-1}, Z_{i,t})$ serves as evidence in deciding whether to include or not tracker T_i in the survivor group. If the evidence exceeds a certain threshold (0.05 in our implementation), then it is included in the survivor group, otherwise it is excluded.

The overall motion state is determined by the trackers in the survivor group and computed as follows:

$$\hat{\theta}_{overall} = \frac{1}{\sum_{i=1}^{|W|} \beta_i} \sum_{i=1}^{|W|} \hat{\theta}_i \beta_i, \tag{2}$$

where $|W|$ is the cardinality of the survivor group and β_i is the impact factor of each linked tracker. The latter is determined from:

$$\beta_i = \frac{p(W_{i,t}, \hat{\Theta}_{i,t}|G_{i,t-1}, Z_{i,t})}{D_{i,t}}, \tag{3}$$

where the enumerator is the conditional probability computed in Equation (1) and $D_{i,t}$ is the Euclidean distance from the point of interest (landmark) to the center of the tracker.

2.2 Deformed Region Computation

The multi-tracker network concept presented in [9] is quite powerful but is grossly underutilized. It is used to track single landmark points in cardiac MRI. Here we expand the algorithm to perform deformation mesh computation and track tissue surfaces, not just points.

Specifically, we compute the deformation mesh out of all the surviving trackers in the network. The deformation mesh M_t is composed of a set of nodes $c = (c_1, c_2, ..., c_n)$, which are distributed over the selected target region during the initialization step. Each node is linked to several trackers (Figure 1) and its location is decided by the linked survivor trackers as described in Equation (4):

$$c_i = \frac{1}{\sum_{k=1}^{u_i} \beta_k} \sum_{k=1}^{u_i} p_k \beta_k, \tag{4}$$

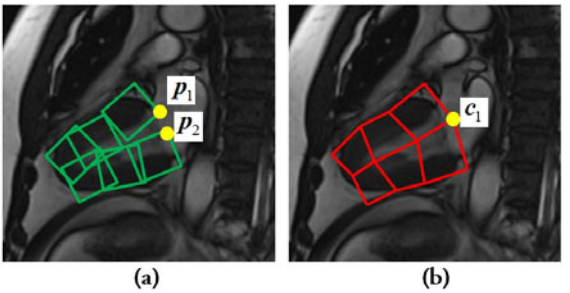

Fig. 1. Deformation mesh computation: (a) Survivor group is selected and colored in green. (b) Computed deformation mesh.

where $\{p_k\}_{k=1}^{u_i}$ indicates all the corner coordinates of the linked survivor trackers at a certain location and β_k is the impact factor of each linked tracker; u_i is the total number of surviving trackers. We use the conditional probability computed in Equation (1) as the impact factor here.

The deformation mesh follows the heart surface while undergoing non-linear tissue deformations. The surface region contracts and expands periodically with the beating heart. This motivates us to examine the surface area of the deformation mesh, which is computed in Equation (5): $polyArea(M_t)$ is the polygon area covered by the deformation mesh, and u_i is the total number of surviving trackers. Experiments in Section 3.2 demonstrate the potential applications of the mesh's evolution.

$$surf = \frac{polyArea(M_t)}{u_i} \tag{5}$$

3 Experimentation

In this study we compare the performance of the collaborative tracker [9] with that of MIL [10] in tracking landmarks in long cardiac MRI sequences. This is in contrast to the short sequences reported in [9], where no comparison was attempted. This part of the experimentation solidifies the baseline algorithm' potential in interventional MRI. Furthermore, we present initial experimental results regarding the computation of cardiac function out of the evolution of the deformation mesh - an algorithmic extension introduced in the present article. This is a development with great diagnostic potential.

3.1 Collaborative versus MIL Tracking in Interventional MRI

The MIL [10] tracking code was downloaded from the authors' webpage. Figure 2 shows a sample visualization from the comparative study. The MRI sequence used in testing consists of 60 repeating cycles, and each cycle includes 25 frames of short-axis view images. The entire sequence has a total of 1500 frames, and lasts 1 minute. Each column shows one snapshot from the tracking sequence by different approaches. The first row shows snapshots of the deformation mesh's evolution as computed by the collaborative tracker. The second row shows the corresponding anatomical landmark locations as computed by the collaborative tracker. The third row shows the corresponding anatomical landmark locations as computed by the MIL tracker. One can observe that the MIL tracker performs well at first, but gradually it drifts to other locations. This could be a fatal problem in interventional MRI, where the operation is expected to last several minutes. A likely reason for the drift is that MIL constantly updates its appearance template through an online-boosting approach. Although this boosting method uses a bag of appearance patches, it is fuzzy about how the exact appearance of the target during evolution; consequently, small errors start accumulating with time. On the contrary, the collaborative tracker, thanks to its redundancy, achieves stable results, which is paramount in robotic interventions.

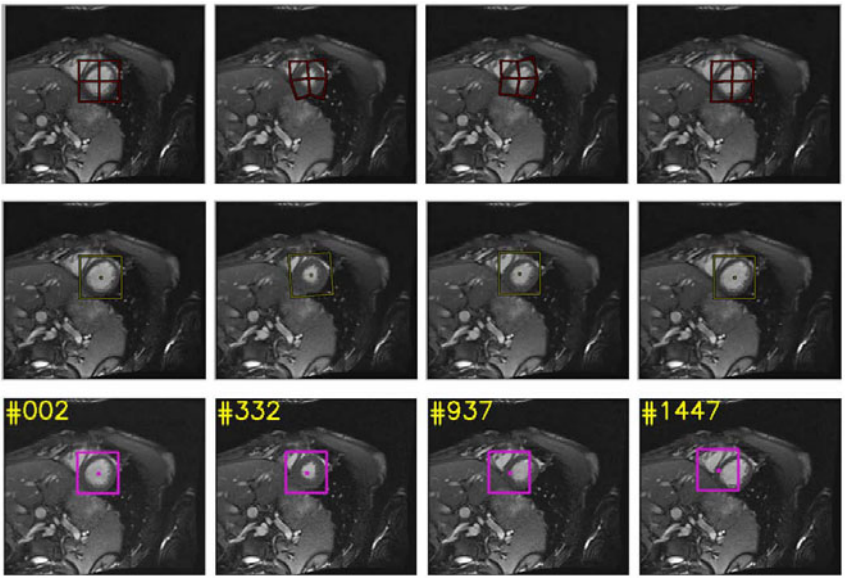

Fig. 2. Comparison results with MIL tracker

Despite this redundancy, the collaborative tracker remains highly efficient and achieves 28 fps on a standard PC versus the 9 fps of the MIL tracker. This has to do with the simple nature of the individual particle filter trackers in the network. Hence, the collaborative tracker renders itself to real-time implementation.

3.2 Surface Area Computation

We computed the evolved area of the deformation mesh and formed respective signals. We applied this analysis on two data sets: the CINE (Figure 3) and the single axis ultrafast dynamic cardiac MRI (Figure 4).

Results from a representative CINE set are shown in Figure 3; the signal clearly tracks the cardiac cycle. One can discern the rapid squeeze of the heart during systole (the lower peak), then the recovery of the relaxing myocardium, and finally reaching the end-diastolic phase (the highest peak). Such dynamic pattern was observed in all slices and subjects we studied.

Results from a sequence with 1350 images at a speed of 50 ms/slice are shown in Figure 4. In this case the same single slice was collected for a far longer period as compared to the CINE sequence in Figure 3. Although, Figure 4 illustrates the same periodicity, because it does not have the time resolution of CINE it does not provide us with the same high resolution assessment of the heart phase changes. In addition, the maxima (end-diastole) and the minima (end-systole) are not as regular as it would be been expected, due to highly varying contrast encountered in such rapid continuous acquisitions.

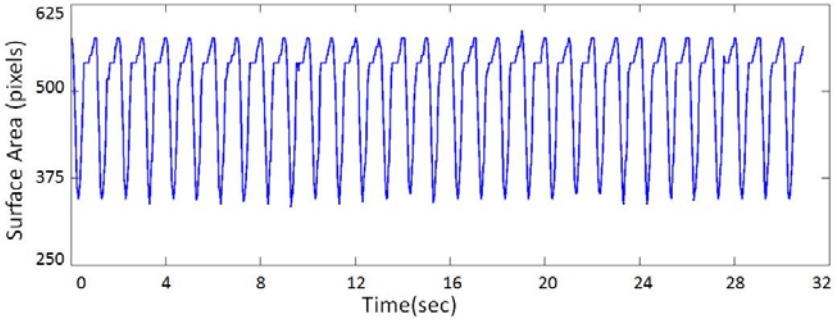

Fig. 3. Deformation mesh evolution signal for a CINE sequence

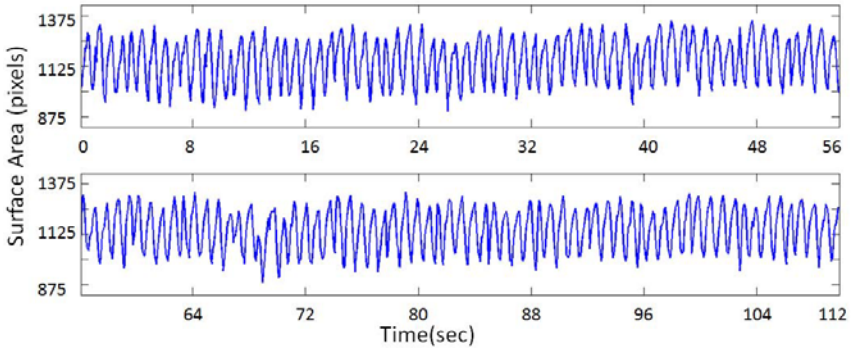

Fig. 4. Deformation mesh evolution signal for a true dynamic sequence. To fit the page, the long signal was split into two parts.

4 Conclusion

The superiority of the collaborative tracking algorithm [9] in long MRI sequences is demonstrated against a state of the art algorithm (MIL - [10]). The collaborative tracker excels in stable behavior and speed - both of paramount importance in interventional MRI. Furthermore, an algorithmic expansion introduced in the present article enables the computation of the deformed heart's surface through the cardiac cycle. The formed signal holds great potential not only as an interventional aid but also as a diagnostic tool. Specifically, this approach can be used for on-the-fly analysis of CINE (while the patient is still in the scanner), that is, for rapid extraction of hemodynamic or heart wall motion parameters. For example, it may provide valuable information about blood volume/velocity estimation and ejection fraction. Still, additional experimental studies are required to fully investigate the relationship of the deformation mesh signals to the hemodynamics of the LV.

Acknowledgements

This material is based upon work supported by the National Science Foundation (NSF) under grants No. #IIS-0812526 and #CNS-0932272. Any opinions, findings, and conclusions or recommendations expressed in this material are those of the authors and do not necessarily reflect the views of the funding agency.

References

1. Saikus, C.E., Lederman, R.J.: Interventional cardiovascular magnetic resonance imaging: A new opportunity for image-guided interventions. JACC Cardiovascular Imaging 2, 1321–1331 (2009)
2. Jolesz, F.A.: Future perspectives for intraoperative MRI. Neurosurgery Clinics of North America 16(1), 201–213 (2005)
3. Tsekos, N.V., Khanicheh, A., Christoforou, E., Mavroidis, C.: Magnetic resonance-compatible robotic and mechatronics systems for image-guided interventions and rehabilitation: A review study. Annual Review of Biomedical Engineering 9, 351–387 (2007)
4. McVeigh, E.R., Guttman, M.A., Lederman, R.J., Li, M., Kocaturk, O., Hunt, T., Kozlov, S., Horvath, K.A.: Real-time interactive MRI-guided cardiac surgery: Aortic valve replacement using a direct apical approach. Magnetic Resonance Medicine 56(5), 958–964 (2006)
5. Dowsey, A.W., Keegan, J., Lerotic, M., Thom, S., Firmin, D., Yang, G.: Motion-compensated MR valve imaging with COMB tag tracking and super-resolution enhancement. Medical Image Analysis 11(5), 478–491 (2007)
6. Spottiswoode, B.S., Zhong, X., Lorenz, C.H., Mayosi, B.M., Meintjes, E.M., Epstein, F.H.: 3D myocardial tissue tracking with slice followed cine DENSE MRI. Journal of Magnetic Resonance Imaging 27(5), 1019–1027 (2008)
7. Fradkin, M., Ciofolo, C., Mory, B., Hautvast, G., Breeuwer, M.: Comprehensive Segmentation of Cine Cardiac MR Images. In: Metaxas, D., Axel, L., Fichtinger, G., Székely, G. (eds.) MICCAI 2008, Part I. LNCS, vol. 5241, pp. 178–185. Springer, Heidelberg (2008)
8. Yuen, S.G., Kesner, S.B., Vasilyev, N.V., del Nido, P.J., Howe, R.D.: 3D Ultrasound-Guided Motion Compensation System for Beating Heart Mitral Valve Repair. In: Metaxas, D., Axel, L., Fichtinger, G., Székely, G. (eds.) MICCAI 2008, Part I. LNCS, vol. 5241, pp. 711–719. Springer, Heidelberg (2008)
9. Zhou, Y., Yeniaras, E., Tsiamyrtzis, P., Tsekos, N., Pavlidis, I.: Collaborative Tracking for MRI-Guided Robotic Intervention on the Beating Heart. In: Jiang, T., Navab, N., Pluim, J.P.W., Viergever, M.A. (eds.) MICCAI 2010. LNCS, vol. 6363, pp. 351–358. Springer, Heidelberg (2010)
10. Babenko, B., Yang, M.H., Belongie, S.: Visual tracking with online multiple instance learning. In: Proceedings of the IEEE Computer Society Conference on Computer Vision and Pattern Recognition, San Diego, California, pp. 983–990 (2009)

A 3D MRI-Based Cardiac Computer Model to Study Arrhythmia and Its In-vivo Experimental Validation

Mihaela Pop[1], Maxime Sermesant[2,3], Jean-Marc Peyrat[4], Eugene Crystal[1], Sudip Ghate[1], Tommaso Mansi[5], Ilan Lashevsky[1], Beiping Qiang[1], Elliot R. McVeigh[6], Nicholas Ayache[2], and Graham A. Wright[1]

[1] Sunnybrook Research Institute, Univ. of Toronto, Canada
[2] INRIA (Sophia-Antipolis), France
[3] Div. Imaging Science, KCL, London, UK
[4] Siemens Molecular Imaging, Oxford, UK
[5] Siemens Corporate Research, Princeton, NJ, USA
[6] Johns Hopkins University, Baltimore, USA
mihaela.pop@utoronto.ca, gawright@sri.utoronto.ca

Abstract. The aim of this work was to develop a simple and fast 3D MRI-based computer model of arrhythmia inducibility in porcine hearts with chronic infarct scar, and to further validate it using electrophysiology (EP) measures obtained in-vivo. The heart model was built from MRI scans (with voxel size smaller than $1mm^3$) and had fiber directions extracted from diffusion tensor DT-MRI. We used a macroscopic model that calculates the propagation of action potential (AP) after application of a train of stimuli, with location and timing replicating precisely the stimulation protocol used in the in-vivo EP study. Simulation results were performed for two infarct hearts: one with non-inducible and the other with inducible ventricular tachycardia (VT), successfully predicting the study outcome like in the in-vivo cases; for the inducible heart, the average predicted VT cycle length was 273ms, compared to a recorded VT of approximately 250ms. We also generated synthetic fibers for each heart and found the associated helix angle whose transmural variation (in healthy zones) from endo- to epicardium gave the smallest difference (i.e., approx. 41°) when compared to the helix angle corresponding to fibers from DW-MRI. Mean differences between activation times computed using DT-MRI fibers and using synthetic fibers for the two hearts were 6 ms and 11 ms, respectively.

Keywords: electrophysiology, computer modelling, cardiac MR imaging.

1 Introduction

Abnormal heart rhythms are often associated with infarct scars and are a major cause (>85%) of sudden cardiac death [1]. One dangerous manifestation is ventricular tachycardia (VT), where a "reentry circuit" facilitates an abnormal re-excitation of the tissue. In such cases, the electrical wave (i.e., the action potential, AP) loops fast around the scar and through a channel which contains viable bundles of muscle

D.N. Metaxas and L. Axel (Eds.): FIMH 2011, LNCS 6666, pp. 195–205, 2011.

interdigitated within nonconductive collagen [2]. Should the VT circuit fails to be interrupted (e.g., via RF ablation lesions placed onto this channel), the abnormal propagation degenerates into lethal fibrillation, VF. The arrhythmogenic substrate is often located at the border zone (BZ) of the scar and is identified during a clinical electrophysiology (EP) study. The EP study uses surface measurements via invasive catheters and aggressive stimulation protocols to induce VT. More-over, many patients are hemo-dynamically unstable and the inducibility of VT can not be performed in the EP laboratory; thus, the substrate is difficult to identify and to ablate [1]. To complement the EP study in identifying the potential VT patients, 3D non-invasive imaging modalities (e.g., MRI) and computer modelling could be exploited. Several groups have shown that MRI can provide good characterization of the VT substrate by using contrast methods (i.e., delayed-enhanced DE-MRI) [3]. However, the in-vivo voxel size currently used in DE-MRI clinical studies suffers from partial volume effects that might affect the accuracy of the substrate identification, thus higher resolution is desirable.

Computer modelling is a valuable tool used in cardiac EP to understand the normal electrical activity and abnormal propagation of action potential (AP) waves [4]. Considerable efforts have been made by the cardiac computational community to develop multi-scale models (from molecular to tissue level), integrating micro-structures and biophysical details into complex models [5, 6]. Several groups recently worked on developing MRI-based models suitable EP studies. One group [7] has focused on developing virtual models for mouse, rabbit, dog and human hearts from diffusion weighted DW-MRI scans, and further used them in combination with detailed, ionic equations to study VT inducibility, but their study lacked any EP experimental validation. Other researchers focused on using fast eikonal models, which can be attractive for patient-specific applications using clinical cardiac MRI models [8] but are not adequate for modelling reentry (since this model lacks the repolarization phase of AP wave); in addition, they used fibers from atlases which have unclear impact on the accuracy of computed activation times. On the other side, simple macroscopic formalisms based on two-variable equations [9] could be used to model re-entrant waves [10, 11]. We chose to explore this mathematical model, as well as to develop pre-clinical animal models to validate computations that would replicate exactly the in-vivo EP experiments.

The specific aim of this paper was to use a 3D MRI-based model together with a simple macroscopic formalism, to study VT inducibility in infarct hearts. For this, we used our recently developed experimental model in swine with chronic infarct hearts [12]. Here, we perform: i) the construction of the 3D MRI-based model (integrating anatomy, scar extent and fiber directions from DW-MRI); ii) the simulation of VT inducibility (replicating exactly the EP experiment); and iii) comparison of model predictions with those observed during the in-vivo EP study. Figure 1 illustrates the workflow of the current study.

Finally, to study the influence of anisotropy on VT inducibility, we generated synthetic datasets by allowing the helix angle to vary within a wide range (between epi- and endocardium). We then performed simulations with the synthetic dataset for which we found the smallest difference between the helix angle corresponding to synthetic fibers and to the fibers from DT-MRI.

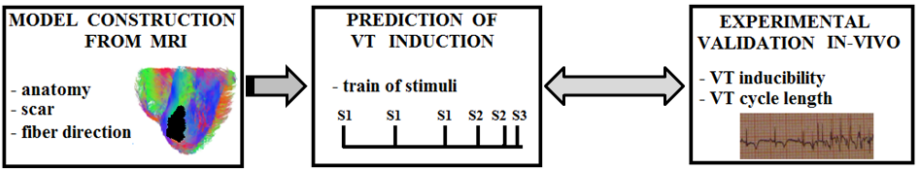

Fig. 1. Diagram of the comparison between the computer model output and in-vivo EP experiments

2 Methodology

2.1 Electrophysiology Study

Myocardial infarction was generated in a swine model by a 90'-min coronary artery occlusion, followed by reperfusion (to create potentially heterogeneous infarct areas), in accordance to the animal protocol approved by our research centre [12]. In this current paper, we focused on two cases in which VT induction was performed: one animal had the left anterior descending (LAD) artery occluded (as shown in Fig. 2a, where the white arrow indicates the occluding balloon), while the other one had the left circumflex (LCX) artery occluded. The in-vivo EP studies were performed at 4-5 weeks post-occlusion and involved the inducibility of VT by following a precise stimulation protocol. This protocol employed the application of a train of stimuli S1 that paced the heart fast (to override the sinus rhythm SNR), followed by several S2-S3 extra stimuli, delivered from the tip of a catheter inserted into the apex of the right ventricle RV (Fig. 2b). The ECG waves were recorded on a paper (allowing us to calculate the resulting VT cycle length when VT was induced).

2.2 Construction of the 3D MRI-Based Computer Model of the Heart

At the completion of the in-vivo EP study, the hearts were explanted, preserved in formalin for few days, and then MR-imaged for anatomy, scar characterization and myocardial fiber directions, using the diffusion weighted DW-MR pulse sequence described in [13]. The MR parameters were given in our previous EP studies [12, 14], together with the methodology regarding the construction of the 3D model from

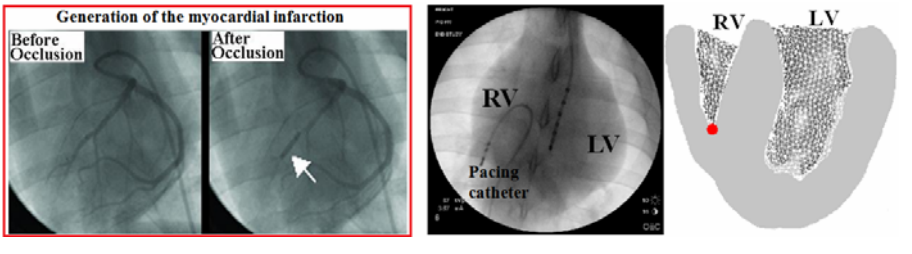

(a) (b) (c)

Fig. 2. Generation of LAD-infarct (a); EP catheters viewed under fluoroscopy (b); and the stimulation point (red dot) in the model, with location corresponding to the catheter tip (c)

apparent diffusion coefficient (ADC) maps, which were next used to segment the heart into three zones: healthy tissue, BZ and infarct scar. Surface meshes were then created for each heart from the 3D anatomy MR scan, and volumetric tetrahedral meshes were generated with TetGen package. Lastly, for each heart, several datasets of synthetic fibers were computer-generated, allowing large transmural variations of fiber direction, such that the helix (inclination) angle from endocardium to epicardium varied on a large range (each from 30º to 90º, with a 5º increment). The calculations of fiber directions and helix angle were performed with Matlab.

2.3 Mathematical Model

We used the macroscopic model developed by Aliev and Panfilov, which is simple, fast, and is based on reaction-diffusion type of equations [8]. In the system of equations given in (1-2) we solve for the action potential (V) and the recovery variable contribution (r) using the Finite Element Method, with an explicit Euler time integration scheme. The term $-kV(V-a)(V-1)$ controls the fast processes (initiation and upstroke of action potential) via the threshold parameter a, while r, determines the dynamics of the repolarization phase.

$$\frac{\partial V}{\partial t} = \nabla \cdot (D\nabla V) - kV(V-a)(V-1) - rV \tag{1}$$

$$\frac{\partial r}{\partial t} = -(\varepsilon + \frac{\mu_1 r}{\mu_2 + V})(ku(u-a-1)+r)\,. \tag{2}$$

This simple model accounts for the heart anisotropy via the diffusion tensor D (which also depends on tissue 'bulk' conductivity d). For instance, the value in the anisotropy ratio is set to 0.14 for a wave propagating almost 2.7 times as fast along the fiber as in the transverse direction. The input values for model parameters were taken from our recent optical fluorescence imaging study performed in infarct hearts [14], and these values were assigned per zone (i.e., infarct, BZ and healthy) and are given in Table 1. Specifically, the values for a (tuning the duration of AP), k (tuning the up-stroke of AP) and the normalized conductivity d were set as in Table 1 (note that a and k values in the scar zone are similarly set like those for BZ, but are in fact irrelevant because the scar is unexcitable, thus d is to 0 (i.e., the AP wave does not propagate through the scar).

Table 1. Electrophysiological parameters in the mathematical model (assigned per zone)

Zone	Parameters		
	a (adimensional)	*k (adimensional)*	*d*
Healthy myocardium	0.112	8	3
Border zone (BZ)	0.2	2	1
Scar (dense)	0.2	2	0

The heart stimulation in the computer model was achieved as follows: i) the sinus rhythm was simulated by applying a square pulse of maximum amplitude (i.e., $V = 1$ since the model output has normalized values for AP) and of 5 ms duration, on both endocardial surface of RV and LV (to mimic Purkinje activation); and, ii) the pacing was simulated by applying a combination of stimuli S1-S2(-S3). These were square pulses 5 ms in duration, of maximum amplitude (i.e., $V = 1$) replicating precisely the stimuli duration and timing like in the EP study, as well as the location of the pacing catheter (at the apex of the RV-endocardium, indicated by the red dot in Fig 2c).

3 Results

3.1 Assessment of VT Inducibility in the EP Study

During the EP experiments, the LCX-infarct heart had non-inducible VT after thirteen pacing stimuli S1 = 550 ms, followed by two S2 extra stimuli at 400 ms and one S3 at 300 ms (thus, S2-S3 coupling interval was 100ms). S3 failed to induce VT, and, consequently, the sinus rhythm was recorded after that (Fig 3a). For the LAD-infarct heart the VT was induced after pacing with eight stimuli S1 = 800 ms, followed by three S2 extra stimuli at 300 ms which induced VT; several VT cycles were recorded, of approximately 250 ms length (Fig 3b).

3.2 Assessment of VT Inducibility in the 3D MR Image-Based Model

Figure 4 shows the results obtained in the LVX-infarct heart, illustrating the construction and parametrization of the 3D MRI-based computer model, together with an example of theoretical propagation of AP wave computed for this heart with non-inducible VT. Specifically, the left panel shows an example of ADC map (2D axial view through the heart) with elevated values of ADC in the scar area, together with the fibers from DT-MRI (with notable severe fibers' disarray in the scar zone). The 3D conductivity map corresponding to the MRI-based model is also illustrated (note that d is set to zero in the scar zone shown in black, and has reduced values in the BZ, as per the input values given in Table 1). The input model parameters also resulted in different EP characteristics for AP wave per zones, for instance: i) the AP duration at 90% recovery is 320 ms for healthy tissue and 275 ms for BZ (as measured in [14]); and ii)

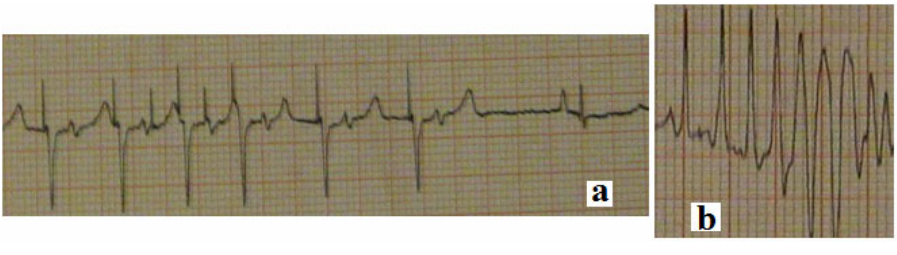

Fig. 3. Non-inducible VT in the LCX-infarct heart, ECG waves recorded at 25 mm/s (a); and inducible VT in the LAD-infarct heart (ECG waves recorded at 10 mm/s), with resulting mean VT cycle length of 250ms (b)

the AP wave has reduced amplitude in BZ (only 0.9) and a slower up-stroke speed compared to the AP wave in the healthy zone. The right panel of Fig. 4 presents simulated activation maps; illustrated are isochronal maps of depolarization times for sinus rhythm (SNR) and following paced cycle (S1), as well as computed all AP waves.

All 3D heart images in Fig. 4 are in presented in a lateral-posterior view.

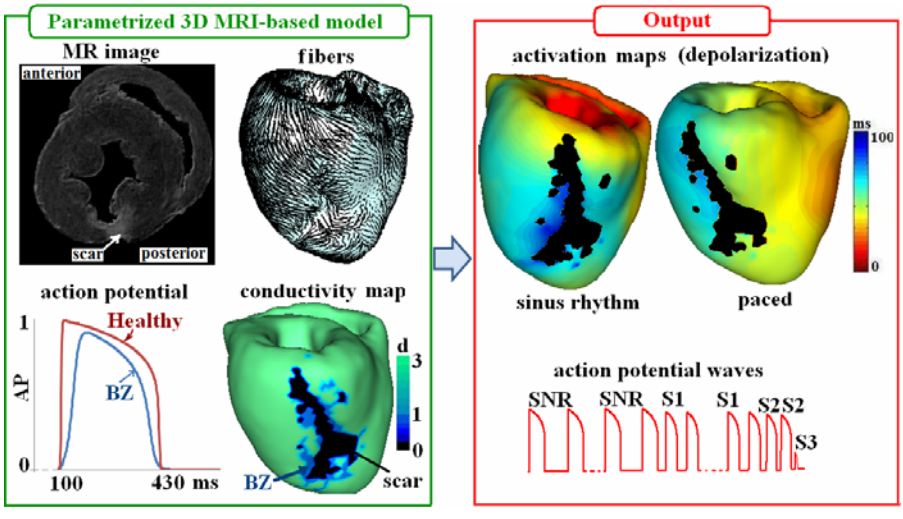

Fig. 4. *Left panel*: The 3D MRI-based parametrized model for the LCX-infarct heart (from segmented ADC maps, and fibers from DT-MRI), together with input 3D conductivity map (with scar in black, healthy in green, BZ in light-blue) and corresponding AP waves (with smaller AP amplitude and shorter duration in the BZ than in the healthy zone). *Right panel*: simulated isochronal maps (depolarization times, with color scale corresponding to early activation times in red and late activation times in blue) during SNR & pacing, and computed AP waves before and after the application of S1-S2-S3 train (resulting in non-inducible VT).

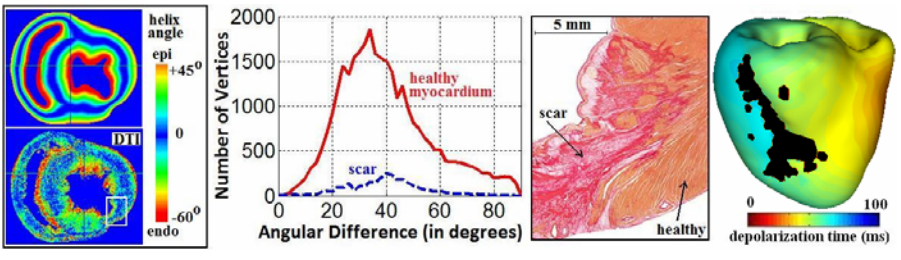

(a) (b) (c) (d)

Fig. 5. Effect of fiber architecture in the LCX-infarct heart: (a) computed helix angle (in a short-axis view) corresponding to synthetic fibers (up) and fibers from DTI (bottom); (b) histogram of angular difference plotted over the vertices in the heart mesh; (c) histological sample taken from the scar area; and (d) and isochronal map of depolarization times during S1 pacing, computed using the synthetic fibers (color scale as in Fig. 4)

Figure 5 shows an example from the results obtained by computer generated synthetic fibers, for which the helix angle varied from +45° on the epicardium to -60° on the endocardium the for LCX-heart. This dataset gave the smallest angular difference (mean ± SD) between the helix angle of synthetic and DTI fibers (i.e., 41.7 ± 20.7° in the healthy heart, and 40.7 ± 18.6° in the scar zone, respectively), see figure caption for more details.

Histological image of Picrosirius Red stain (corresponding to the white square selected in Fig 5a), demonstrated collagen deposition in the transmural scar (in red) and alteration in myofibers' architecture (Fig 5c). Figure 5d shows the activation times obtained using this synthetic dataset, which gave us a mean difference value of 6 ms (over all vertices), compared with the activation times obtained for the case in Fig.4.

Figure 6 presents the 3D MRI-based model obtained for the LAD-infarct heart. The same values for *a, k,* and *d* parameters were assigned per zones as for the LCX-heart. The volume of the scar and border zone was significantly larger than for the LCX-infarct hear; the scar geometry and heterogeneity are notable in the conductivity map. These could explain the inducibility of VT in this LAD-heart.

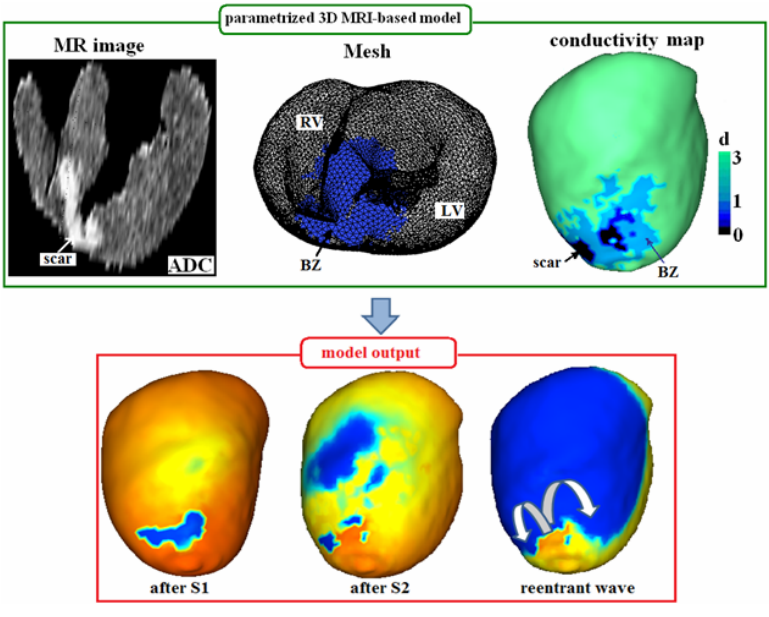

Fig. 6. *Upper panel*: The 3D MRI-based parametrized model for the LAD-infarct heart from segmented ADC maps, together with a top view through the mesh (note the BZ in blue, is visible through the mesh) and the input 3D conductivity map (with *d*-values assigned per zone: with scar in black, healthy in green, BZ in blue). *Lower panel*: simulated isochrones maps (depolarization times) after the S1-S1-S1 train and an extra stimulus S2, resulting in inducible VT and reentrant wave propagating around the scars, in the directions indicated by the white arrows (color scale corresponding to early activation times in red and late activation times in blue).

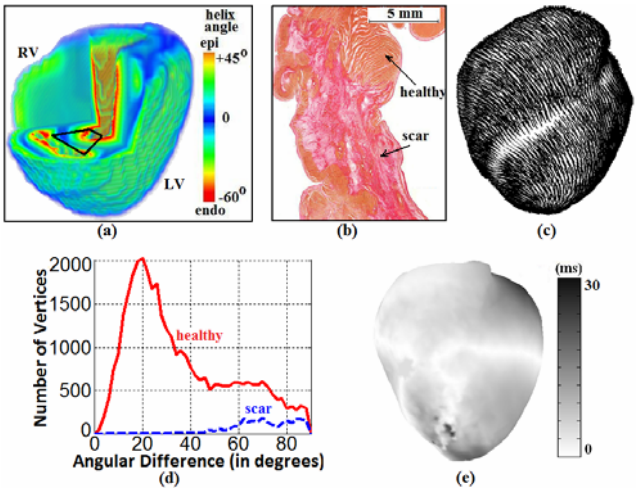

Fig. 7. Effect of fiber architecture in the LAD- heart: (a) computed helix angle (seen through the 3D volume) for synthetic fibers; (b) histological sample take from the septum area indicated by the black rectangle in (a); (c) synthetic fibers displayed on the 3D mesh; (d) histogram of angular difference plotted over the mesh; and (e) absolute difference between activation times computed with DTI-fibers and synthetic fibers (after S1 pacing)

Table 2. Quantitative error analysis associated with differences between activation times computed with DTI fibers and synthetic fibers, respectively

Heart	*r*	RMS-error	mean ± S.D (ms)
LCX-infarct heart	0.97	11.4	6.2 ±4.7
LAD-infarct heart	0.91	22.5	11.1 ±8.1

Figure 7 shows results obtained for the synthetic fibers generated for LAD-infarct heart. Fig 7a shows the 3D image of the helix angle for the dataset that gave the smallest angular difference (mean ± SD) between this helix angle for synthetic set (with fibers direction shown in Fig 7c) and DTI fibers, that is, 39.8 ± 23.7° in the healthy heart and 64.1 ± 18.5° in the scar zone, respectively (Fig 7d).

Histological image of picrosirius red stain is presented in Fig 7b (for the sample corresponding to the black rectangle selected in the ventricular septum, as seen in Fig 7a). The histopathology demonstrated severe dense collagen deposition and fibers' disarray in the scar area, with islands of viable myocytes at the BZ. Figure 7e shows the absolute difference between computed activation times using DTI fibers and synthetic fibers, and errors indicated in Table 2. Note also that an absolute difference of 12 ms was obtained between the activation times computed during VT using DTI-fibers (with a cycle length of approx 273 ms) and the synthetic fibers (CL of approx 285ms).

Table 2 summarizes the errors associated with the differences between the activation times computed using DTI-fibers and using synthetic fibers (for the dataset that had the helix angle varying from 45° on the epi- to -60° on the endo-cardium). For this comparison, we calculated the Pearson's correlation coefficient (*r*), RMS

error and mean ± S.D. (over the vertices in each heart mesh). Notable is the higher *r* value and a smaller RMS-error and mean difference, for the LCX-infarct heart; we attributed this result to the very small volume of BZ in this heart.

The mesh for the LCX-infarct heart had 212,678 elements, whereas for the LAD-infarct heart the mesh had 245,591 elements. A time step of $5x10^{-5}$s yielded a computational time of 50 min for 1s of simulated heart cycle on a regular PC.

4 Discussion and Future Work

To study the key characteristics of VT potentially observable with non-invasive imaging modalities and to predict VT inducibility, one needs to construct patient-specific models and identify the substrate associated with chronic infarct scars. However, prior to integration into clinical applications, such models have to be properly validated using experiments selected to reflect the electrophysiological phenomena at spatio-temporal scales similar to those considered in simulations.

In summary, in this work we developed and tested a simple and fast 3D MRI-based computer model of arrhythmia inducibility in porcine hearts with chronic infarct scar, and validated it using in-vivo EP measures. Simulation results were performed for two infarct hearts: one with non-inducible and another with inducible VT, successfully predicting the outcome as in the in-vivo EP studies. For the inducible heart the average predicted VT cycle length was slightly longer 273 ms compared to recorded cycle 250 ms, possibly due to model input parameters or simplified global parameterization. A finer tuning could be performed by partitioning the heart in smaller zones as in the optical study presented in [14].

Currently, in our experimental model, we have chosen to use juvenile swine (weighing approximately 40-45kg at the sacrifice time), because they do not have yet M-cells (which account for heterogeneities in AP duration in mature endo-, mid- and epicardial cells). Therefore, our experimental model has simplified restitution properties, with APD constant within the cardiac wall. We thus parameterized the model with constant values for *k, a* and *d* throughout the heart mesh. However, one study limitation is that the values of these parameters were derived from an ex-vivo optical study [14]. Further experimentation is needed to measure restitution properties in-vivo and to customize these model parameters from in-vivo pacing scenarios.

The simulation results obtained with synthetic fibers were encouraging, with rather small differences between activation times. Synthetic fibers are also feasible to use for predicting the VT inducibility. The smallest variation of helix angle between DTI-fibers and synthetic fibers corresponded to a transmural variation of this angle from -60° on endocardium to +45° on epicardium. These values are within ranges reported by other studies performed in sheep, swine and canine hearts [13, 15, 16, 17].

This study used only two hearts, thus further experimentation is needed to fully validate the model. Moreover, to better understand the physical conditions associated with VT inducibility in various reentry circuits, future work will focus on study the influence of scar location, geometry, size and transmurality. Furthermore, we will also focus on building accurate EP models for individual hearts by incorporating in-vivo MR data. For the in-vivo characterization of infarct heterogeneities we can use contrast-agent methods instead of DW-MRI (since the latter is not currently suitable to routine clinical investigations due to image noise and motion, as well as long scans

associated with many directions of gradient diffusion [17]). In a recent MR study performed ex-vivo in porcine hearts with chronic infarct (with voxel size $0.63x0.63x0.6mm^3$), we reported very good agreement between delineation of infarct heterogeneities in MR images obtained using contrast agent method and DW method [18]. This gives us confidence to build, in the future, similar contrast MR-based heart models, and, based on the results of this paper, to use synthetic fibers when DTI data is not available.

References

1. Stevenson, W.G.: Ventricular scars and VT tachycardia. Trans. Am. Clin. Assoc. 120, 403–412 (2009)
2. Ursell, P.C., Gardner, P.I., Albala, A., Fenoglio, J., Wit, A.: Structural and EP changes in the epicardial border zone of canine myocardial infarcts during healing. Circ. Research. 56, 436–451 (1985)
3. Bello, D., Fieno, D.S., Kim, R.J., et al.: Infarct morphology identifies patients with substrate for sustained ventricular tachycardia. J. Am. College of Cardiology 45(7), 1104–1108 (2005)
4. Clayton, R.H., Panfilov, A.V.: A guide to modelling cardiac electrical activity in anatomically detailed ventricles. Progress in Biophysics & Molecular Biology (review) 96(1-3), 19–43 (2008)
5. Hunter, P.J., Crampin, E.J., Nielsen, P.M.: Bioinformatics, multi-scale modeling and the IUPS Physiome project. Brief Bioinform. 9(4), 333–343 (2008)
6. Hunter, P.J., Nielsen, P.M.: A strategy for computational integrative physiology. Physiology 20, 316–325 (2005)
7. Vadakkumpadan, F., Rantner, L., Tice, B., Boyle, P., Prassl, A., Vigmond, E., Plank, G., Trayanova, N.A.: Image-based models of cardiac structure with applications in arrhythmia and defibrillation studies. J. Electrocardiology 42(2), 15 (2009)
8. Chinchapatnam, P., et al.: Model-Based imaging of cardiac apparent conductivity and local conduction velocity for planning of therapy. IEEE Trans. Med. Imaging 27(11), 1631–1642
9. Aliev, R., Panfilov, A.V.: A simple two variables model of cardiac excitation. Chaos, Soliton and Fractals 7(3), 293–301 (1996a)
10. Aliev, R., Panfilov, A.V.: Modeling of heart excitation patterns caused by a local inhomogeneity. Journal of Theoretical Biology 181, 33–40 (1996b)
11. Nash, M.P., Panfilov, A.V.: Electromechanical model of the excitable tissue to study reentrant cardiac arrhythmias. Progress in Biophysics and Molecular Biology 85, 501–510 (2004)
12. Pop, M., Sermesant, M.M., Mansi, T., Crystal, E., Fefer, P., McVeigh, E.R., Dick, A.J., Ayache, N., Wright, G.A.: Characterization of postinfarct scars in porcine models: a combined experimental and theoretical study. In: Ebner, M., O'Neill, M., Ekárt, A., Vanneschi, L., Esparcia-Alcázar, A.I. (eds.) EuroGP 2007. LNCS, vol. 4445, pp. 1–10. Springer, Heidelberg (2007)
13. Helm, P., Tseng, H.J., Younes, L., McVeigh, E.R., Winslow, R.L.: Ex-vivo 3D diffusion tensor imaging and quantification of cardiac laminar structure. Magn. Res. Med. 54, 850–859 (2005)
14. Pop, M., Sermesant, M., Liu, G., Relan, J., Mansi, T., Soong, A., Truong, M., Fefer, P., McVeigh, E.R., Delingette, H., Dick, A., Ayache, N., Wright, G.A.: Construction of 3D MR image-based computer models of pathologic hearts, augmented with histology and optical imaging to characterize the action potential propagation (under revision at Medical Image Analysis (2010)

15. Peyrat, J.-M., Sermesant, M., Delingette, H., Pennec, X., Xu, C., McVeigh, E.R., Ayache, N.: A computational framework for the statistical analysis of cardiac diffusion tensors. IEEE Tran. Medical Imaging 26(11), 1500–1514 (2005)
16. Harrington, K., Rodriguez, F., Cheng, A., Langer, F., Ashikaga, H., Daughters, G., Criscione, J., Ingels, N., Miller, D.: Direct measurement of transmural laminar architecture in the antero-lateral wall of the ovine left ventricles. Am. J. Physiol. Heart Circ. Physiol. 288(3), H1324 (2005)
17. Wu, M.T., Tseng, W.Y., Su, M.Y., Chiou, K.R., Reese, T.G., Yang, C.F.: Diffusion tensor MRI mapping of the fiber architecture remodeling in human myocardium after infarction. Circulation 114, 1036–1045 (2006)
18. Pop, M., Ramanan, V., Yang, Y., Ghugre, N., Qiang, B., McVeigh, E.R., Dick, A., Wright, G.A.: Comparison of scar morphology by 3D multi contrast LE-MRI, 3D DW-MRI and histology in a pig model of chronic infarct. In: Proc. of the 18th ISMRM Conference, Stockholm, Sweden (2010)

An Automated Segmentation and Classification Framework for CT-Based Myocardial Perfusion Imaging for Detecting Myocardial Perfusion Defect

Zhen Qian, Parag Joshi, Sarah Rinehart, and Szilard Voros

Piedmont Heart Institute, Piedmont Healthcare, Atlanta, GA, USA

Abstract. Thanks to the recent development of the high-resolution and high-speed multi-sliced CT, CT-based perfusion imaging has become possible. In this paper, we have developed a 320-MDCT-based perfusion imaging framework to detect myocardial ischemia. We designed a rest/stress perfusion imaging protocol, developed an automated LV segmentation algorithm, and adapted a LDA-based classifier to predict myocardial ischemia using the intensity profiles in rest perfusion images. Experiments were done on 6 stress/rest CT perfusion data sets from patients with obstructive coronary artery disease (CAD) and 6 rest CT perfusion data sets from normal subjects. Experimental results have shown that rest perfusion images have the potential of accurately predicting ischemia caused by obstructive CAD.

1 Introduction

Myocardial perfusion imaging is a widely-used cardiovascular diagnostic tool that detects myocardial ischemia and evaluates cardiac function by assessing the blood flow to the heart muscle. Convention myocardial perfusion imaging is based on a nuclear medicine procedure (SPECT), or a first-pass contrast-enhanced MRI. In order to study the reversibility of the myocardial ischemia, myocardial perfusion imaging is usually done at rest and stress, which is induced by physical exercise or drug stimulation.

Cardiac CT is a fast, non-invasive, sub-millimeter resolution imaging modality used to image the heart and the coronary arteries. Thanks to the recent development of the high-resolution and high-speed multi-sliced CT, CT-based perfusion imaging has become possible. Studies [1] [2] have reported that CT-based perfusion imaging on 64- and 256-MDCT single and dual source scanners are predictive of myocardial perfusion defects by visually comparing the myocardial intensity at stress and rest [1] or calculating the transmural perfusion ratio [2]. Compared to nuclear imaging modalities, CT-based perfusion imaging has the potential of achieving higher image resolution and lower radiation dose. Compared to myocardial perfusion MRI, CT technique is more applicable to patients who have metal implants or are too sick to hold their breath for a

D.N. Metaxas and L. Axel (Eds.): FIMH 2011, LNCS 6666, pp. 206–214, 2011.

few heart beats as required by MRI. The additive value of perfusion imaging to imaging the coronary arteries makes cardiac CT a potential "one-stop-shop" procedure for cardiac imaging.

In a recent study [3], a quantitative CT perfusion method on a 320-MDCT was developed. This study demonstrated that CT perfusion at stress and rest is able to quantitatively detect myocardial ischemia by validating against angiography and the measurement of fluid pressure drop caused by the vessel stenosis (fractional flow reserve). Compared to 64- and 256-MDCT, 320-MDCT is unique in cardiovascular imaging: it covers up to $16cm$ length of the scan area in a single gantry rotation. Therefore 320-MDCT is able to scan the whole heart in a single heart beat, and potentially achieve an improved temporal uniformity, or contrast homogeneity, throughout the whole heart. Additionally, 320-MDCT has the potential of lowering the overall contrast media and the overall radiation dose, because it shortens the acquisition time and avoids the helical acquisition.

In this paper, we designed a 320-MDCT-based rest and stress myocardial perfusion imaging protocol and developed an image post-processing framework for the prediction of myocardial ischemia. Fig. 1 shows the flowchart of the framework. The CT perfusion imaging protocol consists of acquiring two sets of contrast-enhanced CT scans of the heart, one at rest and the other under stress, which are acquired 10 minutes apart. We adapted a 3D deformable model-based segmentation algorithm [4] and extended it to a dual-layer structure to segment the endocardial and epicardial surfaces of the left ventricle. The segmented left ventricle is further automatically divided into 17 segments according to the AHA's standard 17-segment model [5]. The intensity profile in each of the 17 segments, as well as in the ventricular blood pool and the whole left ventricle myocardium are derived to train a linear discriminant analysis (LDA)-based classification algorithm to predict ventricular ischemia.

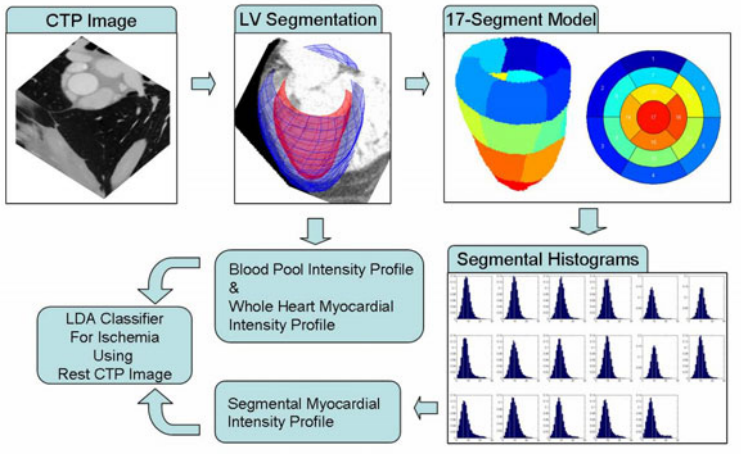

Fig. 1. The flowchart of the CT-based myocardial perfusion imaging framework in predicting myocardial ischemia

In order to validate our proposed approach, in the experiment, we collected 6 CT perfusion data sets from ischemic patients with obstructive coronary artery disease, as defined by invasive angiography and fractional flow reserve. In addition, we also collected 6 normal CT angiography data sets whose imaging protocols are essentially the same as the CT perfusion imaging at rest. In order to avoid unnecessary radiation, we did not acquire stress CT perfusion image on those normal subjects. The myocardial ischemia classifier is trained by using the rest CT perfusion images of those ischemic patients and the normal CT angiography images. Training and testing are done on a strict leave-one-out basis. Experimental results have shown that based on CT rest images, the diagnostic accuracy of ischemia of our method is 91.7% on a strict leave-one-out basis. This suggests CT-based perfusion imaging has the potential to accurately diagnose myocardial ischemia even at rest.

2 Methodology

2.1 CT Perfusion Imaging Protocol

The imaging protocol of the CT-based myocardial perfusion imaging are shown in Fig. 2. The patient first undergoes a rest contrast-enhanced cardiac CT scan with the administration of β-blocker, a medicine that lowers the patient's heart rate. After 10 minutes, the patient undergoes a stress contrast-enhanced cardiac CT scan with the administration of regadenoson, a vasodilator. The detailed imaging parameters for both rest and stress imaging include: 320-MDCT with prospectively triggered, single-beat, volumetric acquisition; detector width was 0.5 mm, voltage was 120 kV, current range was $200 - 550$ mA; reconstruction was done at $65 - 75\%$ R-R. Essentially, the rest CT perfusion protocol is the same as the conventional CT angiography protocol used in clinical practice.

2.2 LV Segmentation in 3D

Much work has been done on myocardial segmentation of the left ventricle in multiple imaging modalities [6].In [7], endocardial surface of the left ventricle was segmented using a Gibbs prior model, a marching-cubes surfacing method, and a local deformable model at the voxel level so that a very detailed surface segmentation can be achieved, including small structures such as the papillary muscles. However, in our application, there is a need to segment the left ventricle,

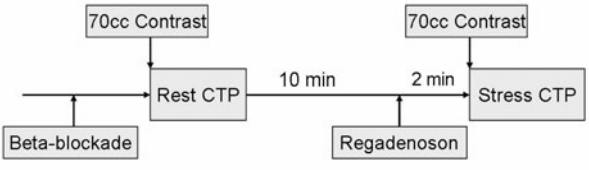

Fig. 2. The imaging protocol of the CT-based myocardial perfusion imaging

including not only the endocardial surface, but also the epicardial surface and the outer boundaries of the left ventricular septum, which is actually part of the endocardial surface of the right ventricle. In addition, there is a need to exclude the papillary muscles and trabeculae structures from the endocardial surface, because the perfusion quantification should be done only in the myocardium. Some of the previous work solved these problems by applying a model to guide the segmentation. In [8], a statistical shape model (ASM) was trained to segment the 4 chambers of the heart. In [9], left ventricle (LV) segmentation was done on a slice-by-slice fashion using morphological operations.

In our study, we did not have a large enough data set to train a model as in [8], and we still needed a strong shape prior to guide the segmentation so that we could exclude the small structures such as the papillary muscle and obtained a smooth boundary surface. Therefore, we adapted a parametric deformable model that consists of two layers of surface meshes, where the distance between the surfaces is constrained by an empirically chosen ventricular thickness. In addition, CT image has a unique characteristic: different tissue has its relatively fixed intensity range in Hounsfield unit (HU). For example, in contrast-enhanced CT image, the myocardium usually has an intensity range of $0 - 250$ HU, while the epicardial fluid and lipid tissue has an intensity below 0 HU. In our approach, the model external force is derived using such characteristic.

Model Initialization. We chose an incomplete ellipsoid shape with rectangular tessellation to model both the endocardial and epicardial surfaces, as illustrated in Fig. 3(a,b). In the surface coordinate system $\mathbf{u} = (u, v)$, $u \in [-\frac{\pi}{2}, \frac{\pi}{4}]$, $v \in [-\pi, \pi)$. In the Cartesian coordinate, the node position $X_o = [x, y, z]'$ can be retrieved by:

$$X_o = \begin{pmatrix} a_x \cos u \cos v \\ a_y \cos u \sin v \\ a_y \sin v \end{pmatrix} \tag{1}$$

where a_x, a_y, and a_z are the scaling parameters in the x, y, and z coordinates.

In contrast-enhanced CT image, the blood pool in the left ventricle is relatively easy to segment because of the increased intensity. We adapt a levelset-based segmentation algorithm [10] to derive the left ventricle blood pool surface first, and use it to guide the model initialization. We denote the nodes of the LV blood surface surface as B_i. As shown in Fig. 3(c), the LV blood pool surface is first manually trimmed to exclude the mitral and aortic valves. Then, the center, long axis orientation and size of B are derived to translate, rotate and scale the surface model in 1. In order to exclude the detailed structure in Fig. 3(c), we impose internal forces of the first and second derivatives of X, and deform the endocardial surface (in red) by iteratively updating $X \leftarrow X + \Delta X$, where,

$$\Delta X = \gamma \cdot F + \alpha\left(\frac{\partial X}{\partial u} + \frac{\partial X}{\partial v}\right) + \beta\left(\frac{\partial^2 X}{\partial u^2} + \frac{\partial^2 X}{\partial v^2}\right) \tag{2}$$

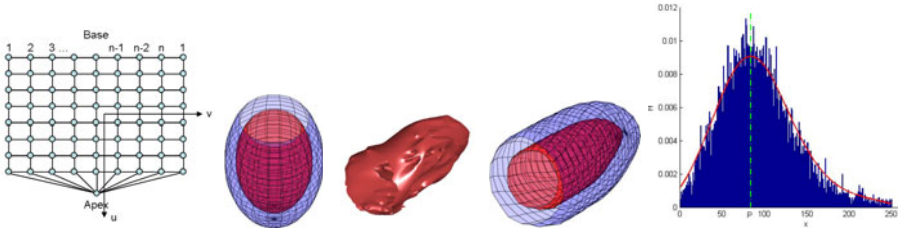

Fig. 3. a) The mesh tessellation. b) The initial parametric model. c) The endo-surface from levelset segmentation. d) the initialized dual-layer surface. e) The intensity histogram is first filtered using a Gaussian filter. Then, the peak location P is found.

where γ, α, β are empirically set weighting parameters that balance the external and internal forces, and F is the external force exerted on the nodes, which is defined by:

$$F = \max_i (N^T \bullet (B_i - X) \cdot N) \tag{3}$$

where N is the outward surface norm of X, and we denote dot product as $\bullet$.

After the endocardial surface is initialized using the blood pool surface, the epicardial surface is initialized by simply expanding the endocardial surface for a certain distance D_o:

$$X_{epi} = X + D_o \cdot N \tag{4}$$

In Fig. 3(d), an example of the initialized endo- and epi-cardial surfaces are illustrated using the LV blood pool surface in Fig. 3(c).

Model Fitting. In the model fitting stage, the deformation update is similar to Equation 2, except for the definition of the external force, which are derived from image intensity profile. The input 3D CT image is first smoothed by a 3D Gaussian filter. Voxel with intensity value off the range of $[0, 250]$ HU are considered off the myocardium, and is replaced with an intensity value of 1000 HU. At each node on the endocardial surface X, we sample a set of the smoothed image intensity value i_m along the outward norm N that is centered at X. The external image force F_{endo} for the endocardial model fitting is defined by:

$$F_{endo} = sign(\operatorname*{argmax}_m \frac{\mathrm{d} \exp \frac{(i_m - \mu)^2}{\sigma^2}}{\mathrm{d}m}) \cdot |\max_m \frac{\mathrm{d} \exp \frac{(i_m - \mu)^2}{\sigma^2}}{\mathrm{d}m})| \tag{5}$$

where μ and σ are empirically selected mean and standard deviation values of the myocardial intensity. Similarly, the external image force F_{epi} for epicardial is defined by:

$$F_{epi} = sign(\operatorname*{argmin}_m \frac{\mathrm{d} \exp \frac{(i_m - \mu)^2}{\sigma^2}}{\mathrm{d}m}) \cdot |\min_m \frac{\mathrm{d} \exp \frac{(i_m - \mu)^2}{\sigma^2}}{\mathrm{d}m})| \tag{6}$$

where the intensity profile is centered at X_{epi}. However, the epicardial surface is more difficult to segment because of the less reliable image information at the

epicardial surface. For instance, it is common that the right ventricle is not filled with contrast, and there is no distinguishable boundary between the septal and the right ventricle blood pool. Therefore, we imposed a stronger internal force that smoothes the inter-surface distance. We define $X_{epi} = X + D$, where X is the endocardial surface, D is the inter-surface distance. We derive X_{epi} by updating $D \leftarrow D + \Delta D$, where

$$\Delta D = \gamma \cdot F_{epi} + \alpha(\frac{\partial D}{\partial u} + \frac{\partial D}{\partial v}) + \beta(\frac{\partial^2 D}{\partial u^2} + \frac{\partial^2 D}{\partial v^2}) \tag{7}$$

2.3 Segmental Intensity Profile

As shown in Fig. 1, the segmented LV is divided into 17 segments using the AHA 17-segment model. In each segment, we first exclude voxels with intensity value off the HU range of $[0, 250]$. Then, the intensity histogram is filtered by a Gaussian filter, and we find the location P of the intensity histogram $H(x)$'s peak, as illustrated in Fig. 3(e). The variation width W of the histogram can be derived by:

$$W = \sqrt{\frac{\sum_x (x - P)^2 \cdot H(x)}{\sum_x H(x)}} \tag{8}$$

2.4 Ischemia Classification Using Linear Discriminant Analysis

In order to investigate the effectiveness of our proposed approach, we adapted a linear discriminant analysis (LDA) [11] algorithm to classify ischemic and normal patients using rest CT perfusion images, because in normal patients, the stress images are not available. A typical two-class LDA classifier can be trained to separate the feature vectors in one class from the other by finding a proper linear projection function. LDA aims to maximizes the between-class scatter and minimizes the within-class scatter. Since in our study, the training sample size is small, we limited the length of the feature vector to avoid over-fitting. We only include the peak location P and variation width W of the blood pool and the whole myocardium, and the variation width W of the segmental myocardial in the feature vector. We did not include the whole intensity histogram profile nor the segmental P values. Therefore, LDA projects the $2+2+17 = 21$ dimensional feature vector to a subspace of $C-1$ dimensions, where C is the number of the classified classes. In this application, $C = 2$. Therefore, the 21 dimensional vector was projected to a 1D scalar. Classification is done by comparing in the 1D subspace, using a k-nearest neighbor scheme. We empirically tested $k = 1$ and 3.

3 Experiments and Results

We collected 6 stress/rest CT perfusion image sets from ischemic patients with obstructive coronary artery disease, and 6 rest CT perfusion image sets from normal subjects. Myocardial perfusion defect is defined by X-ray angiography (XRA) and fractional flow reserve (FFR): XRA $\leq 70\%$ or FFR ≤ 0.75.

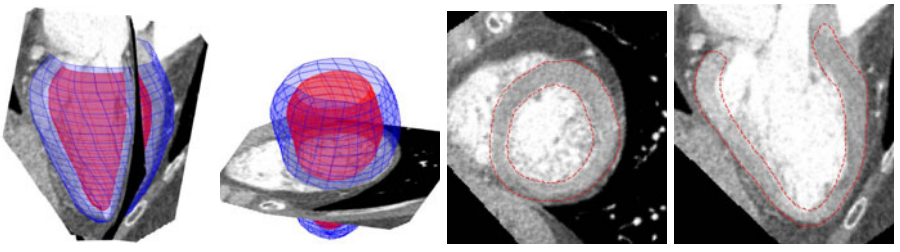

Fig. 4. An example of LV segmentation results in 3D and 2D

3.1 Myocardial Segmentation

We applied our LV myocardial segmentation algorithm on the 6 stress/rest patient data and the 6 rest normal data (18 data sets in total), and obtained very accurate and reliable segmentation results. In Fig. 4, an example of the segmentation results is shown, illustrating that the segmented endocardial surface successfully excludes the papillary muscles from the LV, and the epicardial surface accurately delineates the LV from the epicardial fluid and fat.

Since we do not have manual segmentation results as the ground truth, for quantitative validation, we calculate the percentage of the number of voxels that are off the range of $[0, 250]$ HU in the total voxel number within the segmented LV. Although not exact, this value partially estimates the amount of voxels that are inappropriately included into the LV. From the segmentation results of the 18 data sets, we find the mean and standard deviation of this value are $10.6\% \pm 5.8\%$. Since the LV is a wall structure whose thickness varies in the range of $[0.5, 1.2]$cm in most cases, we can estimate the average combined segmentation error from the endocardial and epicardial surface to be below 1.5mm. In addition, since we excluded all the off-range voxels in the intensity profile analysis and focused on the histogram analysis in the HU range of $[0, 250]$, our experiment shows that such segmentation errors have very limited effects on the subsequent perfusion analysis.

3.2 Visual and Quantitative Assessment of CT Perfusion Image

In the first row of Fig. 5, the stress/rest CT perfusion images from a patient with obstructive left anterior descending artery lesion were shown. The ischemic area, indicated by the red arrow, is easy to visualize in the stress image, but not so apparent in the rest image. In the second row, quantitative analysis shows that the intensity histogram peak location P and variation width W exhibit very similar patterns in the stress and rest perfusion images, but with relatively lower amplitude in the rest images. This suggests that the pattern of intensity profile of the rest CT perfusion image might be potentially predictive of ischemia.

Therefore, we train the LDA classifier using the rest CT perfusion image from 6 ischemic patients and 6 normal subjects. The feature vector of the LDA consists of the P and W of the blood pool in LV and the myocardium in the whole LV, and W of the segmental LV regions. Experiments are done on a strict

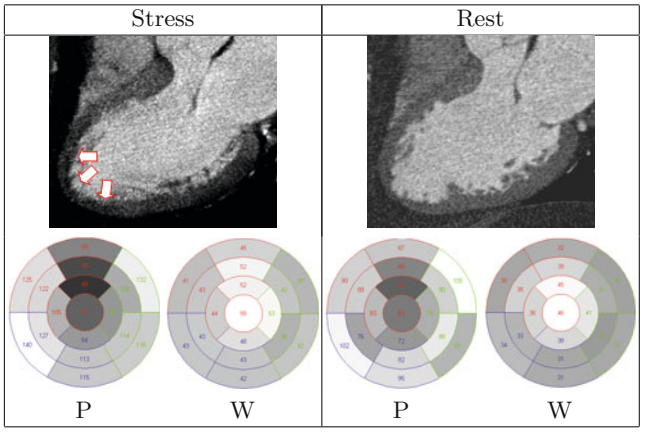

Fig. 5. Visual and quantitative comparison of the stress and rest CT perfusion images

leave-one-out basis, and the LDA classifier accurately classified 11 out 12 data sets, using either $k = 1$ or 3 nearest neighbors.

4 Discussion and Conclusion

In this paper, we have developed a CT-based perfusion imaging framework to detect myocardial ischemia. We designed the rest/stress perfusion imaging protocol for the 320-MDCT, developed an automated LV segmentation algorithm, and adapted a LDA-based classifier to predict myocardial ischemia using the rest perfusion image. Experiments have shown that rest perfusion images have the potential of accurately predicting severe ischemia caused by obstructive CAD. It is probably due to existing myocardial perfusion defects even at rest in those obstructive CAD patients.

There is only one mis-classification in our experiment; however, when substituting that patient's stress image into the LDA testing, the LDA re-classifies it correctly. This suggests that stress imaging amplifies the defects of myocardial perfusion, and in mild to moderately ischemic patients, CT-based stress imaging might be more accurate than rest imaging.

In selecting the feature vector of LDA, we also tested inclusion of the segmental P values, but the accuracy worsens. This may be partially due to the small training sample size. In addition, this suggests the timing of the contrast arriving in the myocardium and then being washed away is difficult to predict and control, which leads to the variation in the overall myocardium intensity levels in CT perfusion images. However, the intensity variation within each local myocardial segment reveals how evenly the blood flow is distributed in the local region, which may be more predictive of obstructive diseases and perfusion defects in the myocardium.

References

1. Blankstein, R., Shturman, L., Rogers, I., et al.: Adenosine-induced stress myocardial perfusion imaging using dual-source cardiac computed tomography. J. Am. Coll. Cardiol. 54, 1072–1084 (2009)
2. George, R., Arbab-Zadeh, A., Miller, J., et al.: Adenosine stress 64- and 256-row detector computed tomography angiography and perfusion imaging: a pilot study evaluating the transmural extent of perfusion abnormalities to predict atherosclerosis causing myocardial ischemia. Circ. Cardiovasc Imaging 2(3), 174–182 (2009)
3. Qian, Z., Vasquez, G., et al.: Validation of quantitative vasodilator stress-rest 320-detector row volumetric ct perfusion imaging against invasive x-ray coronary angiography and fractional flow reserve measurements. In: Annual Scientific Meeting of Society of Cardiovascular Computed Tomography (2010)
4. Metaxas, D.: Physics-Based Deformable Models. Kluwer Academic Publishers, Dordrecht (1996)
5. Cerqueira, M.D., Weissman, N.J., Dilsizian, V., Jacobs, A.K., Kaul, S., Laskey, W.K., et al.: Standardized myocardial segmentation and nomenclature for tomographic imaging of the heart. Circulation 105, 539–542 (2002)
6. Frangi, A., Niessen, W., Viergever, M.: Three-dimensional modeling for functional analysis of cardiac images: A review. IEEE Trans. Med. Imaging 20(1), 2–5 (2001)
7. Chen, T., Metaxas, D., Axel, L.: 3D cardiac anatomy reconstruction using high resolution CT data. In: Barillot, C., Haynor, D.R., Hellier, P. (eds.) MICCAI 2004. LNCS, vol. 3216, pp. 411–418. Springer, Heidelberg (2004)
8. Zheng, Y., Georgescu, B., Barbu, A., Scheuering, M., Comaniciu, D.: Four-chamber heart modeling and automatic segmentation for 3D cardiac CT volumes. In: SPIE, Medical Imaging, vol. 6914 (2008)
9. Silva, S., Sousa Santos, B., Madeira, J., Silva, A.: Left ventricle segmentation from heart MDCT. In: Araujo, H., Mendonça, A.M., Pinho, A.J., Torres, M.I. (eds.) IbPRIA 2009. LNCS, vol. 5524, pp. 306–313. Springer, Heidelberg (2009)
10. Li, C., Huang, R., Ding, Z., Gatenby, C., Metaxas, D., Gore, J.: A variational level set approach to segmentation and bias correction of images with intensity inhomogeneity. In: Metaxas, D., Axel, L., Fichtinger, G., Székely, G. (eds.) MICCAI 2008, Part II. LNCS, vol. 5242, pp. 1083–1091. Springer, Heidelberg (2008)
11. Martinez, A.M., Kak, A.C.: PCA versus LDA. IEEE Trans. on Pattern Analysis and Machine Intelligence 23(2), 228–233 (2001)

Modeling Mitral Valve Leaflets from Three-Dimensional Ultrasound

Robert J. Schneider[1], William C. Burke[1], Gerald R. Marx[3], Pedro J. del Nido[2], and Robert D. Howe[1]

[1] Harvard School of Engineering and Applied Sciences, Cambridge, MA, USA
[2] Department of Cardiac Surgery, Children's Hospital, Boston, MA, USA
[3] Department of Cardiology, Children's Hospital, Boston, MA, USA

Abstract. The geometry of the mitral leaflets, most commonly viewed using three-dimensional ultrasound, is an important input for mechanical models predicting valve closure. Current methods for leaflet modeling from ultrasound either require extensive user interaction, rely on inaccurate assumptions, or produce generic results. The presented method for modeling the mitral leaflets from three-dimensional ultrasound of an open mitral valve is automatic and able to capture patient specific geometry. The method requires as an input the location of the mitral annulus, which we generate semi-automatically using our previously designed method. No additional user interaction is required. The leaflet modeling algorithm operates by first constructing an extended surface at the location of the leaflets which extends beyond the leaflet edges into the blood pool, and then trims the surface to the observed length of the leaflets. Preliminary results suggest the leaflet modeling method, combined with our previous method for annulus segmentation, generates accurate patient-specific mitral valve models.

1 Introduction

The mitral valve is a complex three-dimensional anatomic structure which controls the blood flow between the left atrium and left ventricle in the heart. While it can be imaged using magnetic resonance or computed tomography imaging, the shape and motion of the mitral valve is most accurately captured using three-dimensional ultrasound (3DUS). Ultrasound, in addition to being inexpensive, portable, and non-ionizing, is fast enough to capture the fast moving structures of the valve. The geometry of the mitral valve is used in several applications, including mechanical modeling to predict valve closure [1,2]. While these models typically included only generalized leaflet geometry, more recent efforts have been made to predict valve closure using patient specific geometry [2]. For this reason, several efforts have been made to model the leaflets from 3DUS.

The methods for modeling the leaflets from 3DUS can be categorized as either volumetric, mesh, or parametric. An example of a volumetric method for 3DUS was shown in [3], which used an intensity-based level set method to locate the leaflets. Unfortunately the method included not only the leaflets but anything

D.N. Metaxas and L. Axel (Eds.): FIMH 2011, LNCS 6666, pp. 215–222, 2011.

connected to the leaflets with similar intensity, such as the left ventricle wall, thus failing to isolate the leaflets. A method for modeling the valve as a mesh was presented in [4], which used a thin tissue detector and level sets to locate the leaflets and surrounding tissue. The method subsequently required manual intervention and the assumption of a planar annulus to construct an isolated leaflet mesh geometry. The method presented in [5] segmented and tracked the locations of several features of the mitral and aortic valve structures in 3DUS using machine learning techniques. It then fit a parametric model to the segmented locations. However, in fitting the model to only a few points, the model lacked patient-specific detail.

To compensate for the highlighted insufficiencies of previous methods, we have developed an automatic method for modeling the leaflets. The method is designed for open mitral valves because we want to differentiate between anterior and posterior leaflets, and making this distinction for coapted leaflets in 3DUS is extremely difficult even for a human observer. After finding the location of the annulus using our previously developed semi-automatic algorithm [6] and an automated optical flow tracking method based on the work by Lucas & Kanade [7], the leaflet modeling method automatically finds the location and extent of the mitral leaflets and generates a mesh to represent the geometry with no additional user interaction. We chose to represent the leaflets as a mesh because this representation can be easily used to generate either a volumetric or parametric representation if needed, is a suitable input for mechanical modeling, and is representative of the the thin leaflet tissue.

The method uses the location of the annulus as a means to enforce knowledge about the location and orientation of the leaflets. The method then uses a series of steps to estimate and refine a search space coordinate system and the shape and location of the leaflets. A mesh at the location of the leaflets is then constructed as a natural consequence of the geometry of the search space. The details of the algorithm are described in Section 2. A study quantifying the performance of the method as compared to manual leaflet tracings is then shown in Section 3.

2 Methods and Materials

2.1 Algorithm Summary and Components

The mitral leaflet modeling algorithm is comprised of five main components organized in a two-pass strategy that drives the algorithm to accurately locate the leaflets (Figure 1). The components can be described as defining the search space, redefining the search space axis based on the availability of new information, estimating an extended leaflet surface using a graph cut method, refining the extended leaflet surface using an active surface method, and finally trimming the extended leaflet surface using dimensional reduction and a level set method.

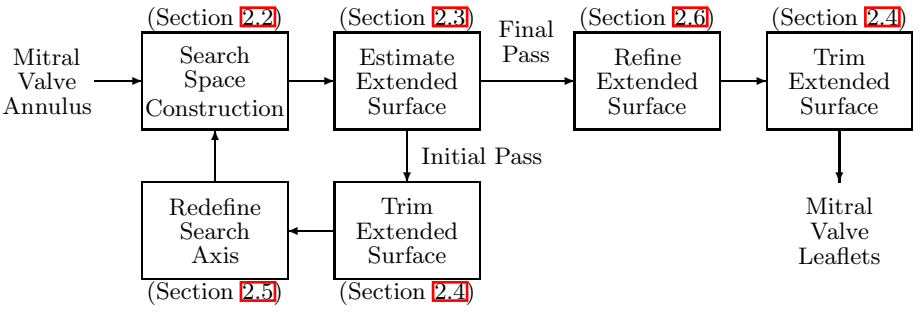

Fig. 1. Flow chart summary of the leaflet modeling algorithm. A description of each component appears in the corresponding section.

2.2 Constructing the Search Space

The location of the mitral leaflets in the heart is such that they attach to and rotate about the mitral annulus. Therefore, we search for the location of the mitral leaflets by constructing a search space that is comprised of an arc system that is centered about the annulus (Figure 2). The arcs are constructed in planes that are rotated about a defined axis. Initially, little is known about the leaflets aside from their orientation, and so the axis is generically defined as the direction of least variance as determined from a principal component analysis of the mitral annulus. For the final pass, the axis location is refined, as described in Section 2.5, to account for the estimated leaflet orientation and position. The search planes are evenly spaced at an angular offset of $\Delta\Theta_p$. The arcs are evenly spaced at a radial offset of ΔR, and points are sampled along the arcs at an angular offset of $\Delta\Theta_s$. The search space is designed around the assumption that the leaflets will intersect the search arcs, at most, at a single location along each arc. This point along each arc is found first using a graph-cut method to estimate the leaflet location, and in the final pass, the location is refined to account for surface curvature and the image.

2.3 Estimating an Extended Leaflet Surface

The location of the leaflets is estimated by fitting a surface to their believed location. The surface is found as the min-cut of a graph [8], where the source connects to all points at the minimum Θ_s and the sink to all points at the maximum. The undirected edges of the graph, Γ, connect neighboring points at $\Theta_p \pm \Delta\Theta_p$, $R \pm \Delta R$, and $\Theta_s \pm \Delta\Theta_s$, making Γ 6-connected. The edges of the graph have a capacity that is a function of a drive image, which is computed at each point. The drive image on the first pass is a product of the original 3DUS intensity ($\mathbf{I}$) and a thin tissue detector ($\mathbf{TTD}$) [6], $\mathbf{I}_{drv} = (\mathbf{I})\,(\mathbf{TTD})$. For the final pass, because we have an estimate for the leaflet location, a weighting function, $\mathbf{W}$, is incorporated into the drive image, $\mathbf{I}_{drv} = (\mathbf{I})\,(\mathbf{TTD})\,(\mathbf{W})$, to encourage the min-cut to be found at the estimated leaflet location. The edge capacity between points i and j is then defined as

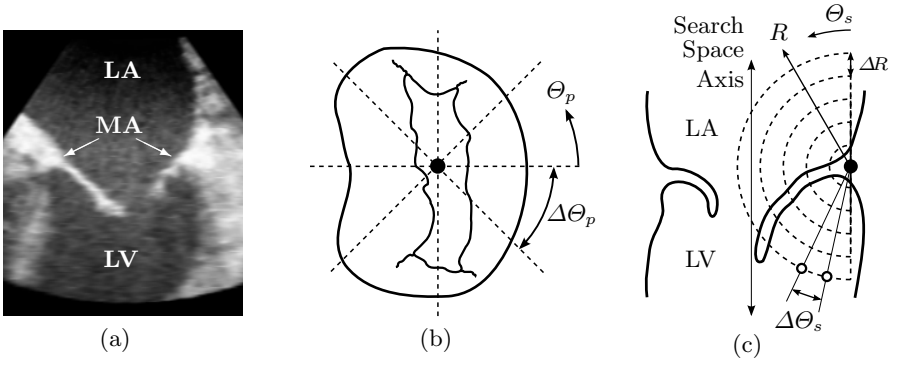

Fig. 2. Example of the location (relative to the mitral valve) and spacing of the search space axis, planes, arcs, and sample points. (a) Open mitral valve in a clinical 3DUS slice. (b) Atrial view of an open mitral valve showing search planes oriented about the search axis. (c) Cut-plane view of an open mitral valve showing the search arc and sample point configurations. (LA - left atrium; LV - left ventricle; MA - mitral annulus).

$$E_{ij} = \frac{1}{1 + \omega \left(\mathbf{I}_{drv,i} + \mathbf{I}_{drv,j}\right)^2}, \tag{1}$$

where ω is a scalar weight. The min-cut of the graph is found using Kolmogorov's implementation [9]. The point representing the leaflet surface location along each arc is herein referred to as a leaflet node.

2.4 Trimming an Extended Leaflet Surface

The extended leaflet surface should reside at the location of the leaflets and extend past the edges of the leaflets into the blood pool of the left ventricle. It is therefore necessary to trim the surface at the leaflet edge so that the remaining leaflet geometry accurately portrays the location and geometry of the mitral leaflets. The trimming operation is done by isolating the nodes that reside at the leaflets from those that reside in the blood pool. This is done by first reducing the ultrasound intensity information at the surface nodes to a two-dimensional image, where the axes of the image are the search plane angle and the arc radial offset (Figure 3). The leaflet nodes are then separated from the blood pool nodes using the RCAC level set method [3], where the level set function is initialized using a k-means algorithm. The annulus nodes are always made to be included in the leaflet group during the level set evolution, and the continuity between the first and last search plane is maintained. Nodes that are not found to be a member of the leaflet group are considered to be part of the blood pool and removed from the surface.

2.5 Redefining the Search Space Axis

The search space axis is initially defined with only the knowledge about the general orientation of the leaflets. The problem with this generic assignment is

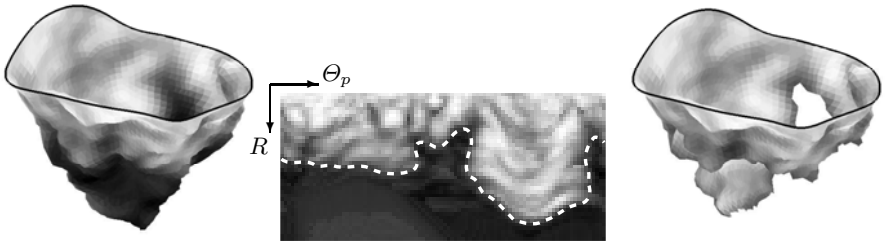

Fig. 3. (a) Example of an extended and refined leaflet surface. The gray level of the triangles reflect the 3DUS intensity. (b) The intensity image formed from the ultrasound intensity at the surface nodes. Also shown is the computed trimming contour (dashed white line) found using a level set formulation. (c) The surface from (a) that is trimmed according to the contour shown in (b). The black contours in (a) and (c) indicate the location of the mitral annulus.

that information about the leaflet position is unknown, and so the axis could potentially pass through the leaflet tissue, thereby creating an inconsistency in the estimated leaflet location. However, as information about the estimated leaflet location becomes available, the axis can be better defined to account for the position of the leaflets. This is done by making the axis the vector that passes through the mitral annulus center point and the center of the estimated leaflet opening. In doing so, the axis will not pass through any leaflet tissue, and will provide for a more appropriate search space in which to find the leaflets.

2.6 Refining an Extended Leaflet Surface

The min-cut algorithm is well suited for estimating the location of the extended leaflet surface, but oftentimes fails to capture finer leaflet detail. Therefore, a surface refinement method treats the surface as an active surface and drives the it toward the location of the leaflets in the image and also regulates surface curvature. In the refinement process, the nodes are restricted to move along their respective arcs in the search space. An image energy, $\mathbf{E}_{img}$, which is the inverse of the ultrasound intensity, drives surface nodes to the leaflet location along the arc. An internal energy, $\mathbf{E}_{crv}$, regulates surface curvature by driving surface nodes to locations that will result in uniform edge length. The minimized surface energy equation is then $\mathbf{E}_{surf} = \omega_{img}\mathbf{E}_{img} + \omega_{crv}\mathbf{E}_{crv}$, where ω_{img} and ω_{crv} are scalar weights.

2.7 Mesh Generation

The nodes of the trimmed leaflet surface are formed into a triangular mesh by first connecting nodes to those neighbors that exist at $\Theta_p \pm \Delta\Theta_p$ and $R \pm \Delta R$. Diagonal edges are then defined between nodes at (Θ_p, R) and $(\Theta_p + \Delta\Theta_p, R + \Delta R)$. The normals of the triangles are defined such that the positive normal direction points toward the top (atrial) side of the mitral leaflets.

3 Performance and Validation

We assessed the performance of the mitral leaflet modeling algorithm on a group of four anonymized clinical pediatric cases. The mitral valves in these cases were imaged using transesophageal echocardiography (iE33 Echocardiography System with X7-2t transesophageal probe, Philips Healthcare, Andover, MA, USA). A frame showing an open valve was manually selected from each of the four cases. The annulus, which acted as the input to the algorithm, was found using our semi-automatic annulus segmentation method [6] and a tracking algorithm based on the Lucas & Kanade method [7]. Using the location of the tracked annulus in the manually selected frame with an open valve, the leaflets were then found using the presented method.

The leaflets in the chosen frames were manually traced in cut planes taken every 10° about the search space axis and compared to the meshes generated by the algorithm (Figure 4). The intersection of the leaflet mesh with the cut planes generated contour segments in the plane. A histogram of the distances of points along these contours from the manually traced leaflet contours were then computed (Figure 5). As indicated in the histogram plot, on average 95%

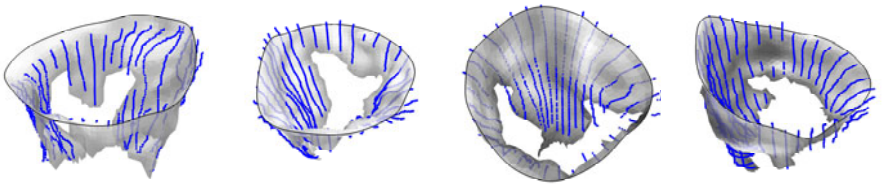

(a) Valve 1 (b) Valve 2 (c) Valve 3 (d) Valve 4

Fig. 4. Comparison of the algorithm-generated leaflet model (shaded surfaces) to manual tracings (contours) made in cut planes about the search space axis

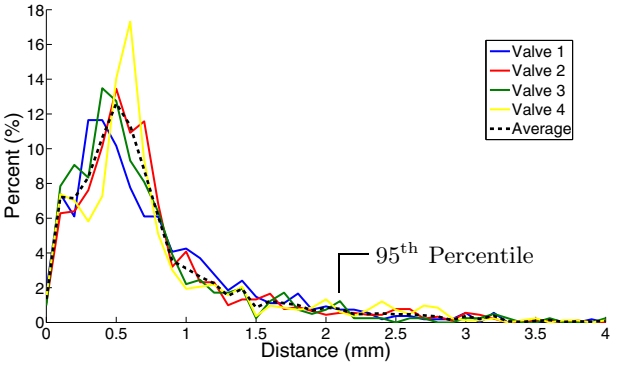

Fig. 5. Histogram of the distances of the algorithm mesh from the manually traced points in each cut plane for each valve in Figure 4 and for the group average. The 95th percentile is shown for the group average.

of the leaflet mesh points resided within 2.10mm of the manually traced leaflets, with the average distance being roughly 0.76 ± 0.65mm. These errors were on the order of the ultrasound volume resolutions (0.5-1.0mm/voxel) and leaflet thicknesses observed in the volumes (2-3mm).

4 Discussion

This paper presents a method that automatically generates a model of the leaflets for an open mitral valve in a 3DUS volume given the location of the mitral annulus. The presented method differs from previous leaflet modeling methods in that it does not require extensive user interaction and generates a detailed, patient-specific leaflet mesh. The method uses a two-pass strategy that defines and refines a search space coordinate system and the leaflet surface to generate a mesh at the location of the leaflets. We showed the accuracy of this method by comparing the mesh to manual tracings of the leaflets made in cut planes taken about a designated axis, where it was found that 95% of the points along the mesh were less than 2.10mm away from the manual tracings.

The leaflet modeling is robust and accurate partly due to the fact that it exploits prior knowledge about where to find the leaflets based on the location of the mitral annulus. Accurately locating the annulus is therefore important as its location directly affects the leaflet model. To find the annulus, we first use our annulus segmentation algorithm to find the annulus in a frame with a closed valve [6]. We then track that annulus to all other frames using a modified version of the Lucas & Kanade optical flow method [7]. We compared the location of the tracked annulus to manual delineations made by three experts across 30 frames and found an average RMS error of 1.67 ± 0.63mm between the tracked annulus and the expert mean. The accuracy of both the annulus and leaflet modeling methods makes for one of the most accurate and robust mitral valve modeling methods capable of capturing detailed patient-specific valve geometry.

A limitation of the presented leaflet modeling method is that the 3DUS images of the mitral valve need to show the leaflets as a thin structure in an open valve state. This suggests that short-axis views of the valve will not suffice, as the chordal structure that becomes visible in this approach gives the leaflets a thick appearance. Also, the valve cannot be completely open (peak diastole) as the leaflets are pushed up against the left ventricle wall and are typically indistinguishable from the wall as seen in 3DUS. The recommended images are then those that use either an enface or apex view of the mitral valve and capture the valve during the process of opening or closing. In these views, the anterior and posterior leaflets should be differentiable.

Future work includes using the defined leaflet mesh as a geometric prior to be tracked to other frames in a 3DUS sequence to provide for a four-dimensional image-driven model of the leaflets. The benefit in this approach is that anterior and posterior mitral leaflets will be differentiated throughout a sequence, and because leaflet geometry can be preserved and collisions resolved, a coaptation line and surface should be found.

Acknowledgments

This work is supported by the U.S. National Institutes of Health under grant NIH R01 HL073647-06.

References

1. Kunzelman, K., Einstein, D., Cochran, R.: Fluid–structure interaction models of the mitral valve: function in normal and pathological states. Philosophical Transactions of the Royal Society B: Biological Sciences 362, 1393 (2007)
2. Hammer, P., Perrin, D., Pedro, J., Howe, R.: Image-based mass-spring model of mitral valve closure for surgical planning. In: Proc. SPIE - Medical Imaging, vol. 6918, 69180Q1–8 (2008)
3. Shang, Y., Yang, X., Zhu, L., Deklerck, R., Nyssen, E.: Region competition based active contour for medical object extraction. Computerized Medical Imaging and Graphics 32, 109–117 (2008)
4. Burlina, P., Sprouse, C., DeMenthon, D., Jorstad, A., Juang, R., Contijoch, F., Abraham, T., Yuh, D., McVeigh, E.: Patient-Specific Modeling and Analysis of the Mitral Valve Using 3D-TEE. In: Navab, N., Jannin, P. (eds.) IPCAI 2010. LNCS, vol. 6135, pp. 135–146. Springer, Heidelberg (2010)
5. Ionasec, R., Voigt, I., Georgescu, B., Wang, Y., Houle, H., Vega-Higuera, F., Navab, N., Comaniciu, D.: Patient-Specific Modeling and Quantification of the Aortic and Mitral Valves From 4-D Cardiac CT and TEE. IEEE Transactions on Medical Imaging 29, 1636–1651 (2010)
6. Schneider, R., Perrin, D., Vasilyev, N., Marx, G., del Nido, P., Howe, R.: Mitral Annulus Segmentation from 3D Ultrasound Using Graph Cuts. IEEE Transactions on Medical Imaging 29, 1676–1687 (2010)
7. Lucas, B., Kanade, T.: An iterative image registration technique with an application to stereo vision. In: Proc. 7th International Joint Conference on Artificial Intelligence, Vancouver, B.C., Canada, pp. 674–679 (1981)
8. Boykov, Y., Kolmogorov, V.: An experimental comparison of min-cut/max-flow algorithms for energy minimization in vision. IEEE Transactions on Pattern Analysis and Machine Intelligence 26, 1124–1137 (2004)
9. Kolmogorov, V.: Software (2004), `http://www.cs.ucl.ac.uk/staff/V.Kolmogorov/-software.html` (accessed: October 1, 2008)

Modeling Atrial Fiber Orientation in Patient-Specific Geometries: A Semi-automatic Rule-Based Approach

Martin W. Krueger[1], Viktor Schmidt[1], Catalina Tobón[2], Frank M. Weber[1], Cristian Lorenz[3], David U.J. Keller[1], Hans Barschdorf[3], Michael Burdumy[1], Peter Neher[1,3], Gernot Plank[4], Kawal Rhode[5], Gunnar Seemann[1], Damien Sanchez-Quintana[6], Javier Saiz[2], Reza Razavi[5], and Olaf Dössel[1]

[1] Institute of Biomedical Engineering, Karlsruhe Institute of Technology (KIT), Germany
martin.krueger@kit.edu
http://www.ibt.kit.edu
[2] Grupo Bioelectrónica- I3BH, Universidad Politécnica de Valencia, Spain
[3] Philips Research Hamburg, Germany
[4] Institute of Biophysics, Medical University of Graz, Austria
[5] Division of Imaging Sciences and Biomedical Engineering, King's College London, United Kingdom
[6] Department of Anatomy, Universidad de Extramadura, Badajoz, Spain

Abstract. Atrial myofiber orientation is complex and has multiple discrete layers and bundles. A novel robust semi-automatic method to incorporate atrial anisotropy and heterogeneities into patient-specific models is introduced. The user needs to provide 22 distinct seed-points from which a network of auxiliary lines is constructed. These are used to define fiber orientation and myocardial bundles. The method was applied to 14 patient-specific volumetric models derived from CT, MRI and photographic data. Initial electrophysiological simulations show a significant influence of anisotropy and heterogeneity on the excitation pattern and P-wave duration (20.7 % shortening). Fiber modeling results show good overall correspondence with anatomical data. Minor modeling errors are observed if more than four pulmonary veins exist in the model. The method is an important step towards creating realistic patient-specific atrial models for clinical applications.

Keywords: patient-specific modeling, atrial modeling, fiber orientation, atrial heterogeneity, atrial anisotropy.

1 Introduction

Atrial anisotropy has strong influence on excitation propagation, activation pattern and P-wave duration (PWd). Simulated P-waves from isotropic models show longer PWds compared to measurements. The use of atrial models in clinical practice therefore requires realistic patient-specific conduction properties.

D.N. Metaxas and L. Axel (Eds.): FIMH 2011, LNCS 6666, pp. 223–232, 2011.

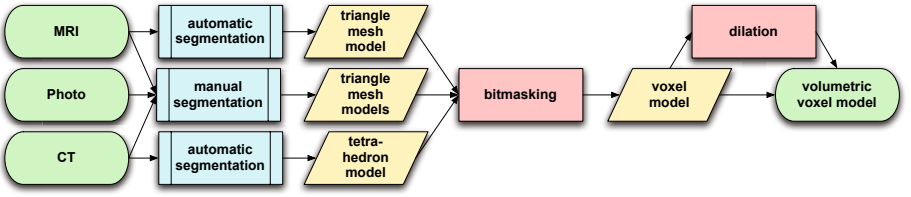

Fig. 1. Workflow to generate volumetric voxel models from various data entities

Atrial myocardial fibers also play an important role in the development and perpetuation of atrial arrhythmias [1].

Incorporating myocardial fiber orientation in atrial models has been going on for nearly a decade now [2,3]. So far, only singular anatomies were manually enhanced with fiber orientation [1,2,3,4,5,6]. Due to most models being 3D surface models [2,3,4,5] they cannot reproduce complex, multi-layer atrial anisotropy. Available volumetric models show only transmurally constant myofiber orientation [1,6], neglecting intersecting fiber bundles. In contrast, ventricular myofiber information is commonly placed automatically in patient-specific models using rule-based or statistical [7] approaches. Recently semi-automatic approaches to add sparse anisotropy in atrial models were reported [8,9,10].

We present a robust semi-automatic method to incorporate complete multi-layer myocardial fiber orientation in patient-specific 3D volumetric models of the human atria. Myocardial tissue is classified to incorporate known atrial heterogeneities [11]. Knowledge about atrial myofiber orientation was gained from literature [12,13,14] as well as from photographic data of human atrial preparations.

2 Methods

2.1 Patient-Specific Atrial Models

Patient-specific isotropic atrial models were created from six volunteers and six patients. The model generation workflow is shown schematically in Figure 1. From the image data, surface models were generated. MRI datasets (n=8) were segmented using automatic (n=5) [15] and manual (n=3) approaches. CT datasets (n=4) were segmented using an automatic method [16]. Photographic data (n=2, Visible Human Man, Visible Human Female) were segmented manually. Volumetric voxel models were created from the surface models. Data segmented with a method described in [15] lack epicardial surface meshes. The endocardium was therefore dilated to produce a model with a homogeneous wall thickness of 2.5-3 mm [17], which corresponds to 7-10 voxels transmurally at a resolution of 0.33 mm.

2.2 Tissue Classification and Fiber Generation

Tissue classification and fiber generation can be separated into multiple sequential steps (Fig. 2). The method uses a volumetric atrial voxel model as input and

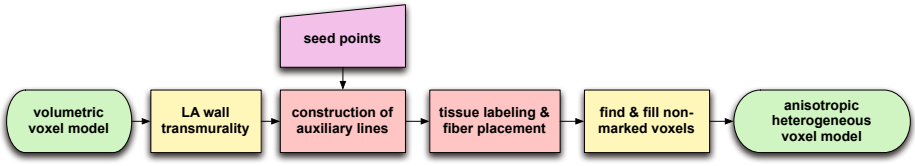

Fig. 2. Workflow of the presented method. Green: input / output; yellow: pre- and post-processing steps; red: algorithm steps; pink: user input.

enhances this with anisotropy and heterogeneity information. In a preparation step, the left atrial wall is split into two equidistant layers through the computation of a virtual static electric field. The steady state "potential distribution" between blood pool and epicardium is thereby calculated by solving Poisson's equation and the left atrial wall is separated at mid potential.

The algorithm requires the user to provide coordinates of 22 seed points in the right and left atrium (Fig. 3 blue points). From the seed points, auxiliary lines and further landmarks (intersection of auxiliary lines) were calculated (Fig. 3 dashed lines) using an adapted 3D fast marching level set method [18] to determine the shortest paths between different coordinates (Fig. 4a). For some myocardial structures (e. g. Crista Terminalis, points R3-R4 in Fig. 3) the shortest path method did not provide the best possible results. In these cases, a corridor along specific planes derived from three seed or auxiliary points was created as boundary condition of the fast marching algorithm. For all seed points used to generate circular muscle bundles (e. g. R1-3, R7-9, L1-3 in Fig. 3) we noted that the points needed to be about equally spaced around the rim, as the shortest paths between the points were used to generate the circular structure of the muscle.

Some of the constructed paths (Fig. 3, solid lines) were used as borders for atrial regions (Fig. 4, bottom row) or as center line for myocardial bundles (Fig. 4, top row). The voxels belonging to these paths were labeled for the corresponding tissue type and the fiber orientation was set along the paths (Fig. 4a,b). Constructed fibers were spatially linear low pass filtered afterwards (Fig. 4c). Thereby, the orientations of the five preceding and five succeeding fiber vectors were averaged. This effectively smoothened abrupt changes in fiber direction and discretization artifacts.

The voxels enclosed by the paths were marked using a 3D implementation of the region growing method [19] to classify their tissue properties (Fig. 4d). If a path marked a muscle bundle (e. g. Crista Terminalis, interatrial bundles, ring muscles), the center line was dilated to produce transverse extension. Fiber orientations within the region were calculated from the average of distance-weighted border voxel orientations (Fig. 4e). In a post-processing step (Fig. 2, yellow) all non-classified voxels were appended to the closest region. Fiber orientation in these voxels was calculated from the average of the surrounding border orientations. Output of this procedure was a volumetric anisotropic heterogeneous bi-atrial voxel model with bundles and regions having smoothly varying fiber

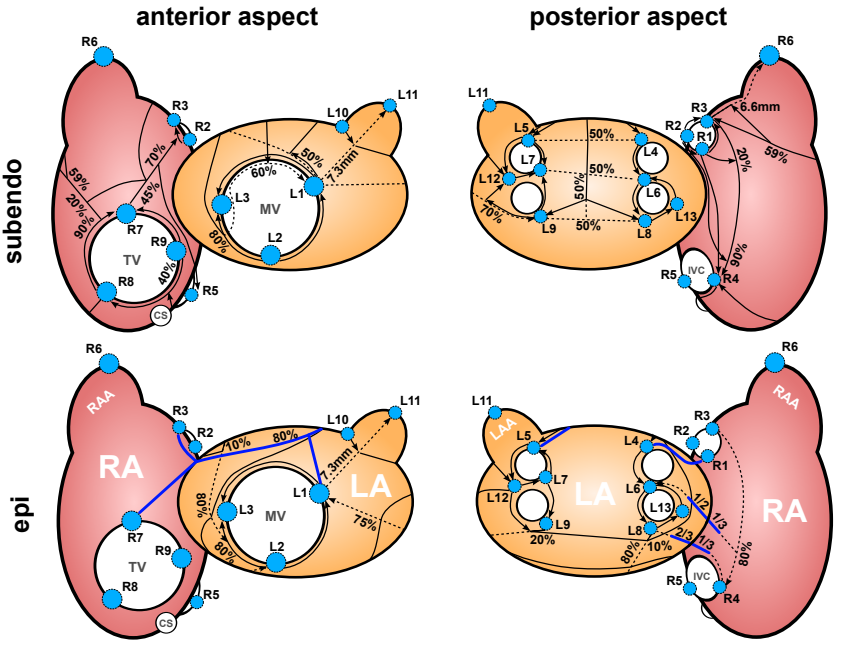

Fig. 3. Seed points (light blue), auxiliary lines (dashed) and region borders (solid lines). Interatrial connections are shown in blue. Arrows indicate the directions of fast marching shortest paths. RA(A): right atrium (appendage); LA(A): left atrium (appendage); TV: tricuspid valve; MV: mitral valve; CS: coronary sinus; IVC: inferior caval vein.

orientation within them, but can cross each other in different transmural layers in a discontinuous manner.

2.3 Electrophysiological Simulations

Two simulations were performed with one model (volunteer, MRI, automatic segmentation, Δx=0.33 mm) to investigate the impact of the anisotropy on atrial excitation. The Courtemanche-Ramirez-Nattel (CRN) model of human atrial electrophysiology [20] was used to simulate atrial action potentials. Maximum ion conductances for three potassium currents were adjusted such that the CRN model was able to reproduce action potentials from various atrial tissues [6]. Cell coupling was considered by the monodomain equation. Finite elements and the explicit Euler method with a time increment of 20 μs were used to discretize the equations in a C++ simulation framework [21]. Transversal conductivity was set to 0.075 S/m for regular atrial myocardium, appendages, valve rings and the right atrial isthmus, to 0.181 S/m for Bachmann's Bundle, 0.075 S/m for Crista Terminalis, 0.03 S/m for pectinate muscles and 0.275 S/m for the sinus node. Ratios for transverse to longitudinal conductivity were to set to 3.75 for regular atrial myocardium and appendages, 3.63 for valve rings, 1.0 for isthmus

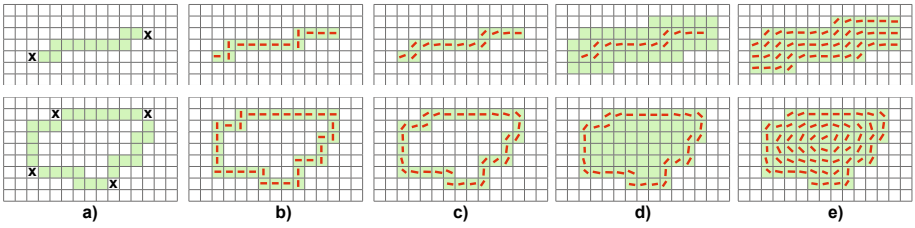

Fig. 4. Region classification and fiber placement in bundles (upper row) and regions (lower row) exemplary shown in a 2D grid. Methods are implemented in 3D and work analogue to the shown examples. a) Shortest path between seed and/or auxiliary points mark region borders. b) Fiber orientation is set along borders. c) Fiber orientation smoothened by averaging of pre- and succeeding orientations. d) Inner region marked using region growing. e) Fiber orientation calculated from the average of distance-weighted border orientations.

and the sinus node, 3.88 for Bachmann's Bundle, 6.56 for Crista Terminalis and 23.25 for pectinate muscles to produce conduction velocities comparable to [22]. Atrial activation was initiated at the location of the sinus node with a basic cycle length of 800 ms. Prior to the coupled cell simulation, 50 cycles of isolated cell simulations were run to reach steady state conditions.

3 Results

3.1 Fiber Orientation and Tissue Classification

We applied the presented method to 14 patient-specific atrial models derived from CT, MR and photographic data. Global fiber orientation in the atrial models showed circulating muscle bundles around the valve openings (Fig. 5d), around the orifice of the superior caval vein and around the pulmonary vein orifices. Atrial appendages had circular fibers, showing some discretization error at their tip. Right atrial appendage fibers arose from the septum spurium and the tricuspid valve musculature (Fig. 5a). Septo-atrial and septo-pulmonary bundles were overlaying each other in the LA roof (Fig. 5c). Bachmann's Bundle, Crista Terminalis and pectinate muscles had well aligned fibers along their longitudinal extent. Fifteen pectinate muscles arose perpendicular from Crista Terminalis in the right atrium and end at the tricuspid ring in the same manner (Fig. 5a,c). Crista Terminalis was crossed by fibers of the intercaval bundles in the subepicardium, which were merging with the pectinate muscles fibers afterwards (Fig. 5a). The area between the intercaval bundle and the orifice of the inferior caval vein was isotropic.

3.2 Influence of Atrial Anisotropy on Excitation Sequence

Two simulations on one geometry were performed: one using the homogeneous isotropic case and one with added electrophysiological heterogeneities and anisotropy. Activation was initiated at the site of the sinus node in both cases

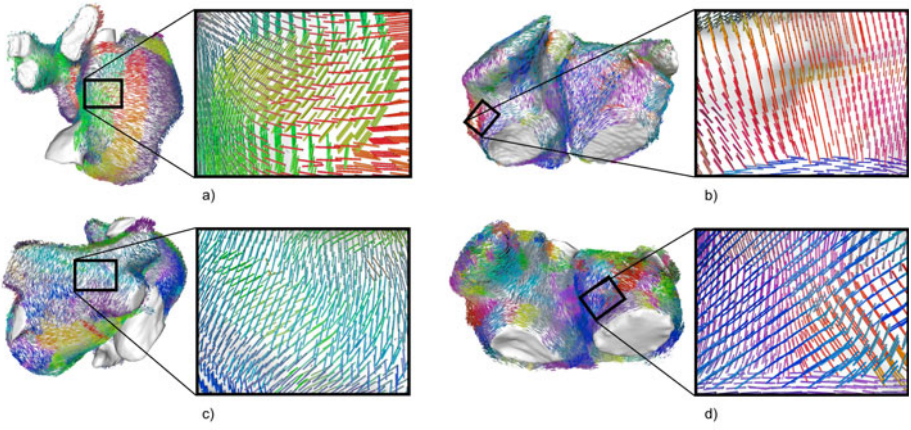

Fig. 5. Examples of generated fibers in different models. Local fiber direction is shown by color-coded cylinders. Inlays show close up transmural fiber structure. a) Fibers from intercaval bundle cross Crista Terminalis epicardially. b) Septo-atrial and septo-pulmonary bundles arise from the mitral valve ring muscle. c) Two layers of myofibers in the left atrial roof. d) Pectinate muscle fibers connecting perpendicular to the tricuspid valve ring musculature.

(Fig. 6, 20 ms). In the isotropic case, excitation spread circular in contrast to the enhanced model, where activation spread over fast conducting Crista Terminal and pectinate muscles (32 ms). The left atrium was activated from the anterior side via Bachmann's Bundle in the enhanced case, whereas slower left atrial activation in the homogeneous model arose from the right superior pulmonary vein (47 ms). Myofibers circulating the pulmonary veins influenced the excitation wavefront (47 ms). Heterogeneous electrophysiological properties of the Crista Terminalis influenced right atrial electrophysiology in the enhanced model (78 ms). Complete atrial activation was achieved after 145 ms in the isotropic case and after 115 ms in the enhanced model (-30 ms / -20.7%). The duration of the corresponding simulated P-waves was reduced from 145 ms to 115 ms (not shown). Measured PWd of the same subject was ca. 100 ms.

4 Discussion and Conclusion

We presented a novel approach to incorporate complete anisotropy into patient-specific human atrial models. The proposed method worked reliably in 14 datasets (MRI, CT, photographic data). Information on atrial fiber architecture is very sparse. 3D information on atrial fibers (e. g. DT-MRI) is not available, as atria in these datasets are collapsed and show strong artifacts at tissue borders. Due to the thin atrial wall, fibers cannot be extracted from high resolution photographic data as done for the ventricles [23], except from large muscular bundles as Crista Terminalis, Bachmann's Bundle and pectinate muscles [6]. In future it might be possible to image ventricular fiber structure in-vivo using DT-MRI [24]. Nevertheless, the problems caused by the thin atrial wall will persist

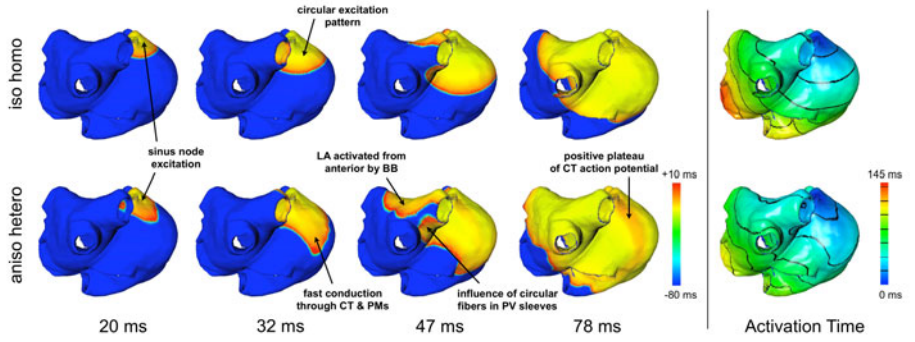

Fig. 6. Simulation of atrial electrophysiology in an isotropic homogeneous model (top row) and in the corresponding anisotropic heterogeneous model (bottom row). Shown are the transmembrane voltage distributions at four time instances as well as the activation time maps (right).

and thus, such in-vivo methods will not be available to image atrial fibers for a long time. On the other hand, as MRI resolution advances, it could be possible to image atrial fibers of excised human atria using DT-MRI ex-vivo, if suitable preparation techniques are used.

Atrial myocardial structure is known to show inter-individual differences. We concentrated on modeling the most common myofiber structure described in literature. Myofibers in the appendages can show systematic or chaotic patterns [14]. As this information cannot be extracted from patient-specific data, we chose to model circular fibers to gain reproducible results. We included three posterior interatrial muscle bundles and Bachmann's Bundle anterior as the major right to left atrial pathway. The posterior connections were found in 67% - 93% of excised hearts and Bachmann's Bundle is absent only in few people [14]. As all our models lacked the coronary sinus, we neglected interatrial connections arising from this musculature.

Others have shown high resolution anisotropic models of parts of animal atria [25,26] with very complex fiber structure. We aim at providing anisotropy for human bi-atrial models. Due to the resulting limited spatial resolution, we introduced some simplifications of myofiber structure. We observed sites of chaotic fiber intersection in models which have more than four pulmonary veins or early branching of those. The algorithm was developed for atrial geometries with four pulmonary veins, which covers about two thirds of all human atria [27]. If sufficient information on fiber structure around uncommon pulmonary vein configurations is available, we will adapt our method accordingly. Various pathologies are known to influence global and local fiber architecture, e. g. structural remodeling or fibrosis in atrial fibrillation patients. The method could in future be adapted to reflect such pathologies.

The semi-automatic approach requires user input for 22 seed points. This bears potential for individual variations in seed point placement, which we adjusted the algorithm to cope with. The method could be coupled to automatic

segmentation techniques [15,16] by marking seed points in the statistical model, thus removing user based variations. Analyzing the sensitivity of the algorithm to user introduced variations of the seed points is strongly implementation-dependent and would outrun the scope the this study. The prospect to couple the presented method with automatic segmentation algorithms will make such analysis obsolete.

Evaluation and validation of fiber modeling is a crucial point for the reliability of the model. We compared the modeling results with data from literature [12,13,14] and unpublished photographs. In all cases, modeled fiber direction showed good correspondence with the data. Application of the algorithm to animal data with known fiber orientation [25,26] for validation is difficult, as atrial fiber architecture is not unconditionally comparable between animal and human. Simulated anisotropic activation time maps are in agreement with measured activation time patterns in human [28,29,30]. Measurements showed that activation in the right atrium is faster along Crista Terminalis [29,30] and that the left atrium is activated by two wavefronts from anterior and right-posterior to activate the region left-inferior of the left inferior pulmonary vein at latest during sinus rhythm [28,29]. These effects were also observed in all our anisotropic simulations.

The simulation results highlight the impact of anisotropy in patient-specific atrial models on atrial activation pattern and PWd. Shortening of simulated P-wave caused by electrophysiological heterogeneities and anisotropy resulted in a better correspondence to measured PWd of the same subject. PWd could also be matched by adjustment of global conduction velocity in isotropic models. Doing so would result in conduction velocities greater than those measured in healthy human [31]. This indicates that the modeling error in homogeneous models is greater than in models with rule-based fibers and heterogeneities. Although the presented method is focused on modeling global fiber architecture, further evaluation of the sensitivity of the excitation sequence to small changes in fiber structure will be necessary. Comprehensive studies with more models will need to further address these topics. The presented method is an important step to introduce reliable patient-specific atrial models into clinical practice.

Acknowledgments. The authors would like to thank Bettina Schwab and Wilfried Dzeakou for their contribution to the segmentation of the MRI data. Furthermore the authors would like to thank Alexandra Groth, Philips Research Hamburg, for the support regarding the automatic segmentation.

The research leading to these results has received funding from the European Communitys Seventh Framework Programme (FP7/2007-2013) under grant agreement no 224495 (euHeart project).

References

1. Plank, G., Prassl, A.J., Wang, J.I., Seemann, G., Scherr, D., Sanchez-Quintana, D., Calkins, H., Trayanova, N.A.: Atrial fibrosis promotes the transistion of pulmonary vein ectopy into reentrant arrhathmias. In: Heart Rhythm (2008)

2. Vigmond, E.J., Ruckdeschel, R., Trayanova, N.: Reentry in a morphologically realistic atrial model. Cardiovasc Electrophysiol. 12, 1046–1054 (2001)
3. Zemlin, C., Herzel, H., Ho, S., Panfilov, A.: A realistic and efficient model of excitation propagation in the human atria. In: Computer Simulation and Experimental Assessment of Cardiac Electrophysiology, Futura, pp. 29–34 (2001)
4. Jacquemet, V.: A biophysical model of atrial fibrillation and electrograms: formulation, validation and applications. PhD thesis (2004)
5. Tobón, C., Ruiz, C., Heidenreich, E., Hornero, F., Sáiz, J.: Effect of the ectopic beats location on vulnerability to reentries in a three-dimensional realistic model of human atria. Computers in Cardiology 36, 449–452 (2009)
6. Seemann, G., Höper, C., Sachse, F.B., Dössel, O., Holden, A.V., Zhang, H.: Heterogeneous three-dimensional anatomical and electrophysiological model of human atria. Phil. Trans. Roy. Soc. A 364, 1465–1481 (2006)
7. Peyrat, J.-M., Sermesant, M., Pennec, X., Delingette, H., Xu, C., McVeigh, E.R., Ayache, N.: A computational framework for the statistical analysis of cardiac diffusion tensors: application to a small database of canine hearts. IEEE Transactions on Medical Imaging 26, 1500–1514 (2007)
8. Hermosillo, B.D.F.: Semi-automatic enhancement of atrial models to include atrial architecture and patient specific data: For biophysical simulations. Computers in Cardiology 35, 633–636 (2008)
9. Krueger, M.W., Weber, F.M., Seemann, G., Dössel, O.: Semi-automatic segmentation of sinus node, bachmann's bundle and terminal crest for patient specific atrial models. In: World Congress on Medical Physics and Biomedical Engineering. IFMBE Proceedings, vol. 25/4, pp. 673–676. Springer, Heidelberg (2009)
10. Krueger, M.W., Rhode, K., Weber, F.M., Keller, D.U.J., Caulfield, D., Seemann, G., Knowles, B.R., Razavi, R., Dössel, O.: Patient-specific volumetric atrial models with electrophysiological components: A comparison of simulations and measurements. Biomedizinische Technik / Biomedical Engineering 55(s1), 54–57 (2010)
11. Feng, J., Yue, L., Wang, Z., Nattel, S.: Ionic mechanisms of regional action potential heterogeneity in the canine right atrium. Circ. Res. 83, 541–551 (1998)
12. Papez, J.W.: Heart musculature of the atria. Am. J. Anatomy 27, 255–286 (1920)
13. Sanchez-Quintana, D., Anderson, R., Cabrera, J., Climent, V., Martin, R., Farre, J., Ho, S.: The terminal crest: morphological features relevant to electrophysiology. Heart (British Cardiac Society) 88, 406–411 (2002)
14. Ho, S., Sanchez-Quintana, D.: The importance of atrial structure and fibers. Clinical Anatomy (New York, N.Y.) 22, 52–63 (2009)
15. Ecabert, O., Peters, J., Schramm, H., Lorenz, C., von Berg, J., Walker, M., Vembar, M., Olszewski, M., Subramanyan, K., Lavi, G., Weese, J.: Automatic model-based segmentation of the heart in ct images. IEEE Transactions on Medical Imaging 27, 1189–1201 (2008)
16. Weese, J., Peters, J., Meyer, C., Wächter, I., Kneser, R., Lehmann, H., Ecabert, O., Barschdorf, H., Hanna, R., Weber, F.M., Dössel, O., Lorenz, C.: The generation of patient-specific heart models for diagnosis and interventions. In: Camara, O., Pop, M., Rhode, K., Sermesant, M., Smith, N., Young, A. (eds.) STACOM 2010. LNCS, vol. 6364, pp. 25–35. Springer, Heidelberg (2010)
17. Platonov, P.G., Ivanov, V., Ho, S.Y., Mitrofanova, L.: Left atrial posterior wall thickness in patients with and without atrial fibrillation: data from 298 consecutive autopsies. Cardiovasc Electrophysiol. 19, 689–692 (2008)
18. Baerentzen, J.: On the implementation of fast marching methods for 3D lattices. Technical report (2001)

19. Wan, S.Y., Higgins, W.E.: Symmetric region growing. IEEE Transactions on Image Processing 12, 1007–1015 (2003)
20. Courtemanche, M., Ramirez, R.J., Nattel, S.: Ionic mechanisms underlying human atrial action potential properties: Insights from a mathematical model. Am. J. Physiol. 275, H301–H321 (1998)
21. Seemann, G., Sachse, F.B., Karl, M., Weiss, D.L., Heuveline, V., Dössel, O.: Framework for modular, flexible and efficient solving the cardiac bidomain equation using petsc. Progr. Industr. Math. 15, 363–369 (2010)
22. Harrild, D.M., Henriquez, C.S.: A computer model of normal conduction in the human atria. Circ. Res. 87, 25 (2000)
23. Sachse, F., Frech, R., Werner, C., Dössel, O.: A model based approach to assignment of myocardial fibre orientation. In: Proceedings of Computers in Cardiology, Hannover, pp. 145–148 (1999)
24. Toussaint, N., Sermesant, M., Stoeck, C.T., Kozerke, S., Batchelor, P.G.: *In vivo* human 3D cardiac fibre architecture: Reconstruction using curvilinear interpolation of diffusion tensor images. In: Jiang, T., Navab, N., Pluim, J.P.W., Viergever, M.A. (eds.) MICCAI 2010. LNCS, vol. 6361, pp. 418–425. Springer, Heidelberg (2010)
25. Zhao, J., Trew, M.L., Legrice, I.J., Smaill, B.H., Pullan, A.J.: A tissue-specific model of reentry in the right atrial appendage. Cardiovasc Electrophysiol. 20, 675–684 (2009)
26. Campos, F.O., Wiener, T., Prassl, A.J., Ahammer, H., Plank, G., Weber Dos Santos, R., Sanchez-Quintana, D., Hofer, E.: A 2D-computer model of atrial tissue based on histographs describes the electro-anatomical impact of microstructure on endocardiac potentials and electric near-fields. In: Annual International Conference of the IEEE EMBC Society, vol. 1, pp. 2541–2544 (2010)
27. Marom, E., Herndon, J., Kim, Y., McAdams, H.: Variations in pulmonary venous drainage to the left atrium: implications for radiofrequency ablation. Radiology 230, 824–829 (2004)
28. Boineau, J.P., Canavan, T.E., Schuessler, R.B., Cain, M.E., Corr, P.B., Cox, J.L.: Demonstration of a widely distributed atrial pacemaker complex in the human heart. Circ. 77, 1221–1237 (1988)
29. De Ponti, R., Ho, S.Y., Salerno-Uriarte, J.A., Tritto, M., Spadacini, G.: Electroanatomic analysis of sinus impulse propagation in normal human atria. Journal of Cardiovascular Electrophysiology 13, 1–10 (2002)
30. Wang, L., Zhang, H., Wong, K.C.L., Liu, H., Shi, P.: Noninvasive imaging of electrophysiological substrates in post myocardial infarction. In: Yang, G.-Z., Hawkes, D., Rueckert, D., Noble, A., Taylor, C. (eds.) MICCAI 2009. LNCS, vol. 5762, pp. 732–740. Springer, Heidelberg (2009)
31. Hansson, A., Holm, M., Blomstrom, P., Johansson, R., Luhrs, C., Brandt, J., Olsson, S.: Right atrial free wall conduction velocity and degree of anisotropy in patients with stable sinus rhythm studied during open heart surgery. Eur. Heart. J. 19, 293–300 (1998)

Anisotropic Mass-Spring Method Accurately Simulates Mitral Valve Closure from Image-Based Models

Peter E. Hammer[1,2,3], Pedro J. del Nido[1], and Robert D. Howe[2]

[1] Department of Cardiac Surgery, Children's Hospital Boston, MA 02115, USA
[2] Harvard School of Engineering and Applied Sciences, Cambridge, MA 02138, USA
[3] Department of Biomedical Engineering, Tufts University, Medford, MA 02155, USA
peter.hammer@childrens.harvard.edu

Abstract. Heart valves are functionally complex, making surgical repair difficult. Simulation-based surgical planning could facilitate repair, but current finite element studies are prohibitively slow for rapid, clinically-oriented simulations. An anisotropic, nonlinear mass-spring (M-S) model is used to approximate the behavior of valve leaflets and applied to fully image-based mitral valve models to simulate valve closure for fast applications like intraoperative surgical planning. This approach is used to simulate a technique used in valve repair and to assess the role of chordae in determining the closed configuration of the valve. Direct image-based comparison is used for validation. Results of M-S model simulations showed that it is possible to build fully image-based models of the mitral valve and to rapidly simulate closure with sub-millimeter accuracy. Chordae, which are presently difficult to image, are shown to be strong determinants of closed valve shape.

Keywords: Mitral valve, chordae, simulation, surgical planning, mass-spring.

1 Introduction

Surgical repair of the mitral valve is technically difficult and outcomes are highly dependent upon the experience of the surgeon [1]. One of the main difficulties of valve repair is that valve tissues must be surgically altered during open heart surgery such that the valve opens and closes effectively after the heart is closed and blood flow is restored. In order to do this successfully, the surgeon must essentially predict the displacement and deformation of anatomically and biomechanically complex valve leaflets and supporting structures. A computer-based surgical planning system could inform this task by extracting valve anatomy from pre- or intra-operative medical images and using it to create a computational mesh. This mesh could then be modified by the surgeon through a graphical interface to evaluate potential surgical repair strategies. Adequacy of a given surgical repair option could then be assessed by using computational modeling methods to simulate the opening and closing of the valve.

There have been many computational modeling studies of the mitral valve; for a review, see [2]. Most of these studies use generic models of valve anatomy to study normal or diseased valves or to assess generalized, rather than patient-specific, repair strategies. Two recent studies produced models directly from medical images [3, 4]. However, chordae could not be resolved and were modeled generically. With regard

D.N. Metaxas and L. Axel (Eds.): FIMH 2011, LNCS 6666, pp. 233–240, 2011.

to computation time, no previous mitral valve modeling studies have reported simulation times that are low enough for clinically practical use – on the order of a few minutes.

We present a fully image-based model of the mitral valve and use it, along with an anisotropic M-S method, to simulate the closed state of the valve under peak-systolic pressure. We use this model to simulate a simple surgical modification – replacing a chord with a suture and varying its length – and assess the accuracy of simulation results. We also use the model to predict the effect of secondary chordae on valve closure.

2 Methods

Three fresh isolated hearts from 30-40 kg female Yorkshire pigs were imaged using high resolution computed tomography (MicroCAT, Siemens, Munich, Germany). The mitral valve was loaded by delivering pressurized air to the left ventricle via tubing inserted through the aorta. Hearts were scanned with applied left ventricular pressures of 0 and 120 mmHg, producing volumetric images with isotropic voxel size of 100 μm (Fig. 1, A and B).

Images were cropped and segmented, and triangular meshes were generated using custom software based on published methods [5]. The mesh produced from the open valve was used to define the leaflet surface for simulating valve closure. Meshes were produced with 600 – 700 triangles per valve. The open valve mesh was also used to define chordae, specified by segment endpoints. The mesh produced from the pressurized valve (Fig. 1, C and D) defined the closed surface of the pressurized valve to be used for comparison with simulations of the pressurized valve. It was also used to define the annulus and papillary muscle locations to be used as boundary conditions for the simulated closure as well as to define lengths and attachment points of those chordae not visible in the image of the open valve.

Closure of the mitral valve mesh was simulated using a dynamic M-S model that has been previously described [6]. The nonlinear anisotropic behavior of the mitral valve leaflets was modeled using bilinear functions that were fit to published stress-strain relationships for mitral valve leaflet tissue [7]. One bilinear function is used for

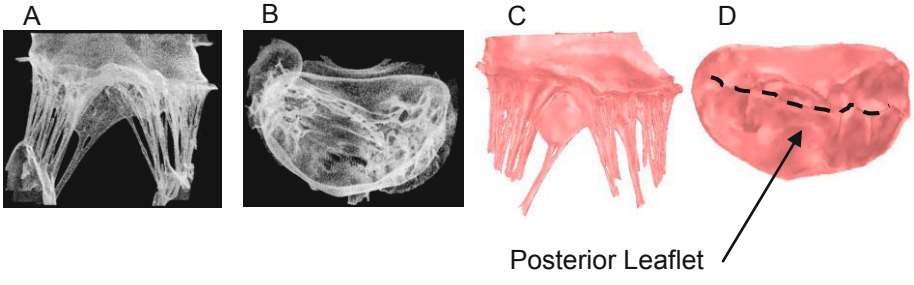

Fig. 1. Volume rendered micro-CT scan of valve 3 under 120 mmHg of pressure, shown from side view (*A*) and top view (*B*). Surface rendered mesh produced directly from CT scan data of same valve are shown in side view (*C*) and top view (*D*) with portion of mesh beyond the annulus trimmed and coaptation line highlighted (*dotted line*).

the preferential fiber direction (circumferential direction in the leaflet), and another is used for the cross-fiber direction (radial direction in the leaflet). Chordae are modeled as linear elastic rods with constant diameter supporting tension only, with Young's modulus taken from published data [8].

Dynamic simulation consists of two parts. First, mesh nodes lying on the valve annulus are forced to their positions on the closed mesh while points of chordae attachment to the papillary muscles are held fixed. Next, leaflet annulus nodes are also held fixed while force due to pressure (120 mmHg) is applied to the ventricular surface of all mesh triangles. Semi-implicit numerical integration with adaptive time step control was used to solve the equations of motion, and self-contact of leaflets was handled using a fast sort of axis-aligned bounding boxes of mesh triangles to screen for potential triangle collisions followed by triangle-to-triangle intersection checking [6]. Collisions were resolved using a linear penalty force set to balance the net external force bringing the triangles together, resulting in frictionless contact.

One of the hearts was used in an experiment in which a posterior leaflet primary chord was transected and replaced with a suture. The suture was brought through the papillary muscle and LV wall so that its length could be varied. While applying pressure to the LV, the chord was pulled (shortened) as far as possible without causing a leak, then a CT scan of the heart was taken and subsequently meshed (Fig. 2). This chord shortening procedure was simulated by changing the resting length of the corresponding posterior leaflet primary chord of the open valve mesh and simulating valve closure.

The closed valve meshes produced by simulation were compared with the meshes produced directly from images of the closed valve by registering the surfaces and computing surface-to-surface error as the distance from each node on the simulated closed mesh to the nearest node on the mesh from the image of the closed valve.

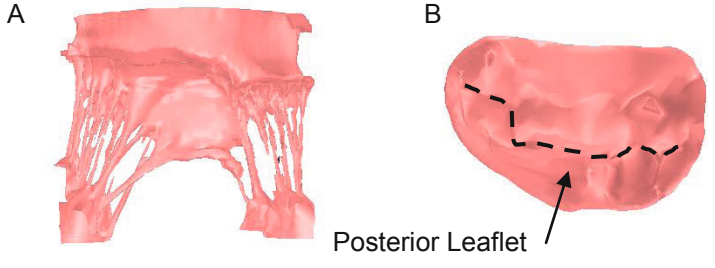

Fig. 2. Surface rendering of a mesh produced from a micro-CT scan of valve 3 under 120 mmHg of pressure and with one posterior leaflet chord replaced with suture. Mesh is shown from side (*A*) and top views (*B*), with coaptation line highlighted (*dashed line*).

3 Results

Valve closure and loading was simulated in less than 25 seconds, on a 2.3 GHz CPU utilizing a single core, for each of the three valves. Image-based validation resulted in mean surface-to-surface error of approximately 0.8 mm for all three valves (Table 1). The maximum surface-to-surface error was 2.4 to 3.0 mm and typically occurred near the line of coaptation as seen in the error maps (Fig. 3). Simulations in which a

posterior leaflet primary chord was shortened resulted in restricted movement of that portion of the posterior leaflet, and the opposing (anterior) leaflet moved to fill the gap. Mean and maximum surface-to-surface error magnitudes were 1.1 and 3.3 mm, respectively (Table 1 and Fig. 4, B).

Simulations of the three valves were repeated with all secondary chordae omitted, and mean and maximum surface-to-surface errors increased more than two-fold (Table 1, rows 1 – 3, last column). Absence of secondary chordae resulted in peak values of surface-to-surface error occurring near the center of the anterior leaflet (Fig. 5), reaching values of approximately 7 mm.

Sensitivity analysis was conducted for model parameters affecting mesh geometry or material properties. Each parameter was subject to +/- 5% perturbation, and the changes in the mean surface-to-surface error magnitude of the resulting simulations were measured. Of the ten parameters that were examined (six parameters of the constitutive law bilinear functions, chordae diameter, chordae stiffness, chordae rest length, and leaflet thickness), only chordae rest length and the two constitutive law parameters controlling the breakpoints of the bilinear functions exhibited sensitivity of greater than 1mm of error per 100% change in parameter. Resting chord length exhibited the highest sensitivity, with a value of approximately 8mm per 100% change.

Table 1. Number of triangles, nodes and chord segments comprising the valve models, along with simulation time and mean & maximum errors in the closed state for simulations with all chordae and with primary chordae only. Row 4 corresponds to a simulation with valve #3 incorporating a shortened chord (sc). Rows 5 and 6 correspond to simulations with valve #3 where the mesh was upsampled by four (x4) and sixteen (x16), respectively.

valve I.D.	# of triangles	# of nodes	# of chords	time (sec)	e_{all} (mm) mean, max	e_{pri} (mm) mean, max
1	655	414	52	21.4	0.8, 2.4	1.9, 7.4
2	621	406	53	20.0	0.8, 3.0	2.0, 7.2
3	624	425	77	24.8	0.8, 2.5	1.8, 6.4
3_{sc}	624	425	77	22.9	1.1, 3.3	-
3_{x4}	2,496	1,423	77	103	0.9, 2.9	-
3_{x16}	9,984	5,291	77	1240	0.9, 2.7	-

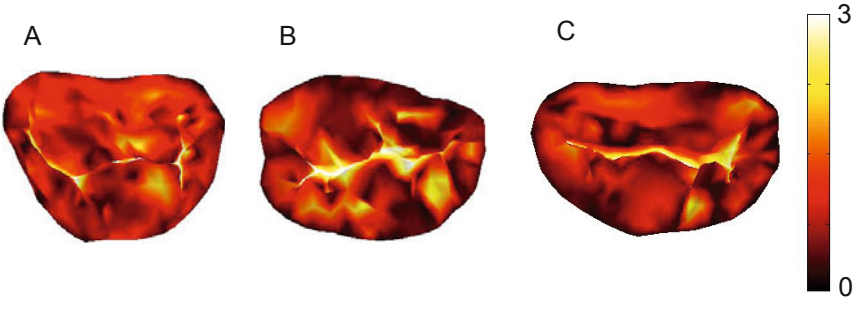

Fig. 3. Magnitude of error, expressed as distance in mm, between closed valve surface predicted by simulation and closed valve surface from image, for valves 1 – 3 are shown in (*A*) – (*C*), respectively. Simulations were run with all (both primary and secondary) chordae.

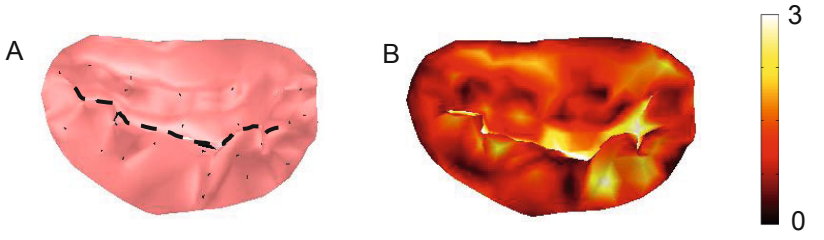

Fig. 4. Top view of mesh of valve 3 produced by simulating valve closure after simulated chord shortening (*A*). Coaptation line is highlighted (*dashed line*). Magnitude of error, expressed as distance in mm, between closed mesh produced by simulation and mesh produced directly from closed image (*B*).

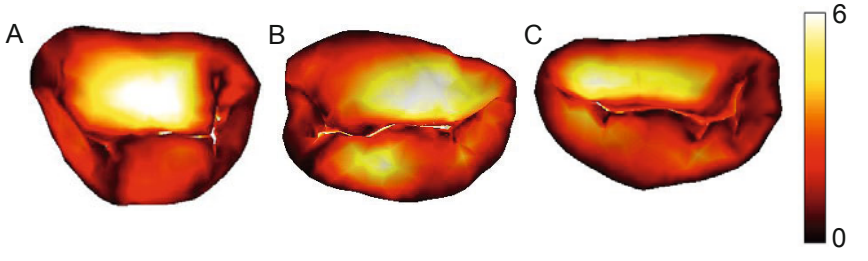

Fig. 5. Magnitude of error, expressed as distance in mm, between closed valve surface predicted by simulation and closed valve surface from image, for valves 1 – 3 are shown in *(A)* – *(C)*, respectively. Simulations were run with primary chordae only. Note change of scale compared to Figs. 3 and 4.

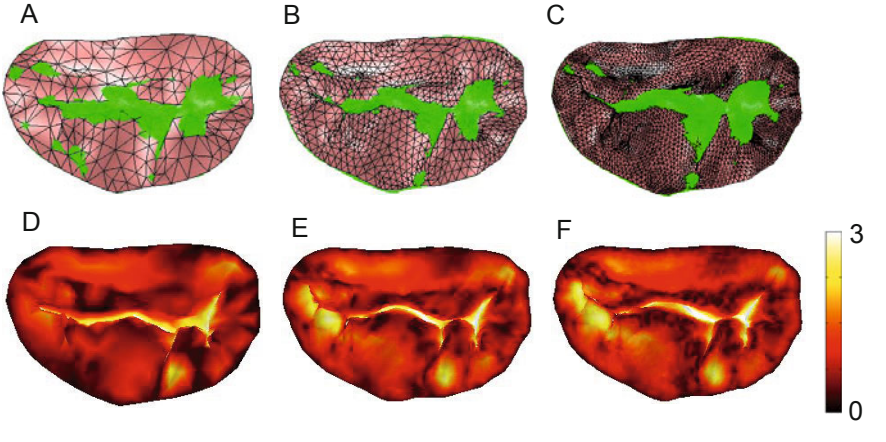

Fig. 6. Meshes of valve 3 in the closed state (*pink*) are superimposed on the mesh produced from the image of closed valve surface, shown in green with triangle edges hidden (*A*, *B*, and *C*). Surface-to-surface error in mm is mapped onto the closed mesh from simulation (*D*, *E*, and *F*). Meshes contain approximately 625 (*A*, *D*), 2500 (*B*, *E*), and 10000 (*C*, *F*) triangles.

The effect of mesh size on simulation accuracy was assessed by subdividing the triangles of valve 3 by factors of 4 and 16 and simulating closure. The mean and maximum errors for the simulated meshes did not change significantly in response to either of the two increased mesh sizes (Table 1 and Fig. 6).

4 Discussion

The aim of this study was to develop a method for producing fast, image-based simulations of mitral valve closure for use in planning surgical repair. We showed that it was possible to take an image of a mitral valve and from it develop a model that could be used to quickly and accurately predict closure and loading of the valve. Furthermore it was shown that the method could successfully predict the effect of a surgical repair technique.

A major requirement guiding the development of the simulation methods was that the closed and loaded state of the valve be computed quickly through judicious use of approximation. For the three mitral valve specimens simulated in this study, the closed, loaded state was computed in less than 30 seconds using an anisotropic M-S model, efficient contact handling and bilinear approximation of published material constitutive laws. While the M-S method gains much of its speed advantage by neglecting to adhere to a continuum description of the tissue, image-based validation showed that accuracy of prediction of the closed state is high. Another significant approximation is the use of relatively coarse meshes. However, increasing the number of triangular faces in the mesh did not improve the overall accuracy with which the simulated closed surface approximated the actual closed valve surface. Increasing mesh size marginally improved mesh closure near the coaptation line. On the other hand, it also led to slight error increases in leaflet regions untethered by chordae, because the new nodes of the subdivided triangles are not constrained by chordae and consequently displace in the direction of the applied pressure.

A second requirement guiding the development of simulation methods was that model geometry be based directly on images of the valve. Only two groups have published mitral valve models that incorporate image-based models of the leaflets, but neither was able to resolve chordae [3], [4]. We chose to use an experimental imaging method – micro-CT and pressurization with air – rather than a clinically applicable method in order to develop highly detailed geometric models that make it possible to assess the importance of various aspects of model detail for accurate valve simulation. Results of omitting secondary chordae and of the sensitivity analysis suggest that details of the chordae network are important determinants of the closed valve state. One of the published studies using image-based leaflet models used image-based validation and found an average discrepancy between closed models and images of closed valves of four to five mm [3]. Their levels of mean error are five to six times higher than those achieved in our study. This is probably due in part to the lower intrinsic resolution to their imaging modality, but their neglect of secondary chordae, which we have shown to strongly influence closed valve shape, likely played a significant role.

Although our study uses dynamic simulation, only a single state of the valve cycle – peak systolic pressure load – is used to assess whether a valve leaks. One justification for this is that the transvalvular gradient at peak systole represents the

greatest mechanical challenge to valve structures and a worst-case scenario for inducing a leak. An additional, more clinical justification is that surgeons test the repaired valve in a similar way by injecting saline under static pressure into the LV [9]. The assumption that it is sufficient to assess valve function at peak systolic pressure allows the complex interaction between blood flow and the valve structures during ventricular filling and ejection to be neglected. Another limitation of this study is that models were produced from porcine rather than human valves, however anatomical studies have shown that valve leaflet dimensions and chord lengths are not significantly different between human and porcine valves [10].

5 Conclusion

We have shown that it is possible to take image-based mitral valve models and use simulation to rapidly and accurately predict the closed valve shape and the effects of surgical manipulation. The remaining challenge is to build the valve models from clinically relevant imaging. A recent study has shown that the mitral valve leaflets and annulus can be extracted from 3D ultrasound images [11]. Using clinical imaging to resolve the chordae, which we have shown to be critical for predicting the closed shape of the valve, has yet to be solved.

Acknowledgments. This work was supported by NIH grant R01 HL073647-06.

References

[1] Vahanian, A., Baumgartner, H., Bax, J., Butchart, E., Dion, R., Filippatos, G., Flachskampf, F., Hall, R., Iung, B., Kasprzak, J., Nataf, P., Tornos, P., Torracca, L., Wenink, A.: Grupo de Trabajo sobre el Tratamiento de las Valvulopatias de la Sociedad Europea de Cardiologia: Guidelines on the management of valvular heart disease. Rev. Esp. Cardiol. 60, 1e–50e (2007)

[2] Kunzelman, K.S., Einstein, D.R., Cochran, R.P.: Fluid-structure interaction models of the mitral valve: function in normal and pathological states. Philos. Trans. R. Soc. Lond. B. Biol. Sci. 362, 1393–1406 (2007)

[3] Burlina, P., Sprouse, C., DeMenthon, D., Jorstad, A., Juang, R., Contijoch, F., Abraham, T., Yuh, D., McVeigh, E.: Patient-specific modeling and analysis of the mitral valve using 3D-TEE. In: Navab, N., Jannin, P. (eds.) IPCAI 2010. LNCS, vol. 6135, pp. 135–146. Springer, Heidelberg (2010)

[4] Wenk, J.F., Zhang, Z., Cheng, G., Malhotra, D., Acevedo-Bolton, G., Burger, M., Suzuki, T., Saloner, D.A., Wallace, A.W., Guccione, J.M., Ratcliffe, M.B.: First finite element model of the left ventricle with mitral valve: insights into ischemic mitral regurgitation. Ann. Thorac. Surg. 89, 1546–1553 (2010)

[5] Persson, P.-O., Strang, G.: A Simple Mesh Generator in MATLAB. SIAM Review 46, 329–345 (2004)

[6] Hammer, P.E., Sacks, M.S., del Nido, P.J., Howe, R.D.: Mass-spring model for simulation of heart valve tissue mechanical behavior. Ann. Biomed. Eng. (2011) (in press)

[7] Sacks, M.S., Yoganathan, A.P.: Heart valve function: a biomechanical perspective. Philos. Trans. R. Soc. Lond. B. Biol. Sci. 362, 1369–1391 (2007)
[8] Kunzelman, K.S., Cochran, R.P., Chuong, C., Ring, W.S., Verrier, E.D., Eberhart, R.D.: Finite element analysis of the mitral valve. J. Heart Valve Dis. 2, 326–340 (1993)
[9] Cohn, L.H. (ed.): Cardiac Surgery in the Adult. McGraw-Hill, New York (2008)
[10] Kunzelman, K.S., Cochran, R.P., Verrier, E.D., Eberhart, R.C.: Anatomic basis for mitral valve modelling. J. Heart Valve Dis. 3, 491–496 (1994)
[11] Schneider, R.J., Perrin, D.P., Vasilyev, N.V., Marx, G.R., del Nido, P.J., Howe, R.D.: Mitral annulus segmentation from 3D ultrasound using graph cuts. IEEE Trans. Med. Imaging 29, 1676–1687 (2010)

In Silico Analysis of the Impact of Transmural Myocardial Infarction on Cardiac Mechanical Dynamics for the 17 AHA Segments

T. Fritz, O. Jarrousse, D.U.J. Keller, G. Seemann, and O. Dössel

Institute of Biomedical Engineering, Karlsruhe Institute of Technology (KIT)
Kaiserstr. 12, 76131 Karlsruhe, Germany
publications@ibt.kit.edu
http://www.ibt.kit.edu

Abstract. The impact of transmural infarctions of the left ventricle on the cardiac mechanical dynamics is evaluated for all 17 AHA segments in a computer model. The simulation framework consists of two parts: an electrophysiological model and an elastomechanical model of the ventricles. The electrophysiological model is used to simulate the electrophysiological processes on cellular level, excitation propagation and the tension development. It is linked to the elastomechanical model, which is based on nonlinear finite element analysis for continuum mechanics. Altogether, 18 simulations of the contraction of the ventricles were performed, 17 with an infarction in the respective AHA segment and one simulation for the control case. For each simulation, the mechanical dynamics as well as the wall thickening of the infarct region were analyzed and compared to the corresponding region of the control case. The simulation revealed details of the impact of the myocardial infarction on wall thickening as well as on the velocity of the infarct region for most of the AHA segments.

Keywords: Myocardial Infarction, Heart Modeling, Finite Element Analysis.

1 Introduction

For the diagnosis and optimal treatment of myocardial infarction, the ability to identify and characterize infarct tissue reliably is essential. Here, cardiac magnetic resonance imaging proved to be an appropriate method. For instance, MRI tagging is currently the method of choice to analyze the myocardial deformation [1]. To measure myocardial strain, SENC MRI [2] is currently investigated in clinical trails. To evaluate the cardiac mechanical dynamics, 3D phase contrast MRI can be used. It provides information about the velocity vector field of the moving heart [3,4].

Computer simulations of the heart has turned out to be a helpful tool to gain a deeper insight into the biomechanics and electrophysiology of the heart.

D.N. Metaxas and L. Axel (Eds.): FIMH 2011, LNCS 6666, pp. 241–249, 2011.

Furthermore, in silico models can be adapted to certain cardiac pathologies like myocardial infractions, as it has been shown by Chabiniok *et al.* [5].

In this work, the impact of transmural infarction on the cardiac dynamics was evaluated using a biventricular electromechanical computer model. Moreover, the influence of the location of infarctions on the motion of the ventricles was evaluated.

2 Methods

In order to simulate the contraction of the ventricles, a multi-scale electromechanical framework was used. It consists of two parts: an electrophysiological model and an elastomechanical model. The anatomical model of the ventricles for the electrophysiological simulations was generated from MRI data of a healthy 27-years-old volunteer. The model is composed of cubic voxels with a side length of 0.4 mm arranged in a structured grid with 352 x 246 x 275 elements. For the mechanical model, this voxel dataset was used to generate an unstructured tetrahedral mesh consisting of 37455 elements. The nodes of the apex were defined to be fixed. Both models included information about the fiber orientation, generated using a rule-based approach based on the measurements of Streeter *et at.* [6].

2.1 Electrophysiological Modeling

For the electrophysiological processes on cellular level, the model proposed by ten Tusscher *et al.* [7] was used. This model is adapted to experimentally obtained data of the major ion currents of the human ventricular cells. Additionally, the model includes transmural heterogeneities of the slow delayed rectifier current I_{Ks} and the transient outward current I_{to}. To include these heterogeneities in our simulations, the ventricular walls of the anatomical model were divided in three layers: endocardium 40%, midmyocardium 40% and epicardium 20%. Furthermore, a linear decrease of the conductivity g_{Ks} from apex to base was included. A detailed description of the considered electrophysiological heterogeneities can be found in [8].

Cardiomyocytes are electrically coupled by the extracellular space but moreover they are coupled directly by gap junctions. In this work the excitation propagation was modeled using the monodomain reaction-diffusion model. The resulting elliptic partial differential equation was solved using the finite element method [9]. To initiate the ventricular activation, a stimulation profile for the ventricles that mimics the Purkinje network was generated as described in [10].

To determine the active tension of the cardiomyocytes, the Hybrid Tension Development Model, presented by Sachse, Glänzel, Seemann [11] was used. The normalized tension, which results from that model, was multiplied with the maximal tension $T_{\max} = 25.9\,kPa$ as found by Wolff *et al.* for healthy canine cardiomyocytes [12].

2.2 Elastomechanical Modeling

The governing equation for conservation of linear momentum in total Lagrangian formulation is given by

$$\frac{\partial}{\partial X_j} P_{ji} + p_0 b_i - p_0 \ddot{u}_i = 0 \tag{1}$$

where P_{ji} is the nominal stress, X_j are the Lagrangian coordinates, p_0 is the initial mass density, b_i is the body force and u_i is the displacement.

This equation can be transformed into the discrete weak form of the total Lagrangian formulation as described in [13]:

$$\delta W^{\text{int}} - \delta W^{\text{ext}} + \delta W^{\text{kin}} = 0 \tag{2}$$

where

$$\delta W^{\text{int}} = \quad \delta u_{iI} f_{iI}^{\text{int}} = \quad \delta u_{iI} \left(\int_{\Omega_0} \frac{\partial N_I}{\partial X_j} P_{ji} d\Omega_0 \right) \tag{3}$$

$$\delta W^{\text{ext}} = \quad \delta u_{iI} f_{iI}^{\text{ext}} = \quad \delta u_{iI} \left(\int_{\Omega_0} N_I p_o b_i d\Omega_0 + \int_{\Gamma^0_{t_i}} N_I \bar{t}_i^0 d\Gamma_0 \right) \tag{4}$$

$$\delta W^{\text{kin}} = \quad \delta u_{iI} f_{iI}^{\text{kin}} = \quad \delta u_{iI} \left(\int_{\Omega_0} p_0 N_I N_J d\Omega_0 \ddot{u}_{jJ} \right) = \delta u_{iI} \left(M_{ijIJ} \ddot{u}_{jJ} \right) \tag{5}$$

and N_I are the shape functions, in this work for linear tetrahedrons, δu_i is the test function, M_{ijIJ} is the mass matrix and t_i is the surface traction. Since δu_i is arbitrary, the discrete momentum equation can be rewritten as:

$$M_{ijIJ} \ddot{u}_{jJ} + f_{iI}^{\text{int}} - f_{iI}^{\text{ext}} = 0 \tag{6}$$

To model the hyperelastic, anisotropic and incompressible properties of myocardial tissue, the constitutive law proposed by Guccione *et al.* [14] was used:

$$W = \frac{C}{2}(e^Q - 1) + 2K \ln(I^3)\mathbf{C}^{-1} \tag{7}$$

$$Q = b_1 E_{11}^2 + b_2(E_{22}^2 + E_{33}^2 + E_{23}^2 + E_{32}^2) + b_3(E_{12}^2 + E_{21}^2 + E_{13}^2 + E_{31}^2) \tag{8}$$

where E_{ij} are the components of the Green Strain Tensor, $\mathbf{C}$ is the Right Green Strain Tensor and I^3 is its third invariant. The second term of Eq. 7 was added to the Guccione model as penalty term to enforce incompressibility.

The material parameters were set to $C = 1.2\,kPa$, $b_1 = 26.7$, $b_2 = 2.0$ and $b_3 = 14.7$ according to the findings of Omens *et al.* for canine ventricles [15]. The parameter for the incompressibility penalty term was set to $K = 10^4\,kPa$. From Eq. 7 the nominal stress $\mathbf{P}$ can be determined as follows

$$P_{ij} = S_{ij} F_{jk} \quad \text{and} \quad S_{ij} = \frac{\partial W}{\partial E_{ij}} \tag{9}$$

where $\mathbf{S}$ is the second Piola Kirchhoff stress and $\mathbf{F}$ is the deformation tensor. To account for the fiber orientation, each element has its own coordinate system aligned to the fiber, sheet and sheet-normal directions of the muscle tissue. This allows to couple the tension development model to the mechanical model by adding the tension to the first diagonal element of the second Piola Kirchhoff stress tensor.

For time integration, the Newmark Beta algorithm was used as described in the following. The equation of motion is given by [13]:

$$\mathbf{M}\mathbf{a}^{n+1} + \mathbf{C}\mathbf{v}^{n+1} + \mathbf{f}^{int}(\mathbf{d}^{n+1}, t^{n+1}) - \mathbf{f}^{ext}(\mathbf{d}^{n+1}, t^{n+1}) = 0 \tag{10}$$

where the term $\mathbf{C}\mathbf{v}^{n+1}$ is added to include Rayleigh damping. The matrix $\mathbf{C}$ is given by:

$$\mathbf{C} = \alpha\mathbf{M} + \beta\frac{\partial f_{iI}^{\text{int}}}{\partial u_{jJ}} \tag{11}$$

The damping coefficients were set to $\alpha = 1\frac{Nm}{s}$ and $\beta = 0.1\frac{Nm}{s}$ to obtain a realistic contraction velocity while suppressing oscillation. The updated displacements and velocities are given by:

$$\mathbf{d}^{n+1} = \mathbf{d}^n + \Delta t\mathbf{v}^n + \frac{\Delta t^2}{2}(1-2\beta)\mathbf{a}^n + \beta\Delta t^2\mathbf{a}^{n+1} \tag{12}$$

$$\mathbf{v}^{n+1} = \mathbf{v}^n + (1-\gamma)\Delta t\mathbf{a}^n + \gamma\Delta t\mathbf{a}^{n+1} \tag{13}$$

Using Eq. 12 and Eq. 13, Eq. 10 can be transformed into a set of nonlinear algebraic equations in the displacement $\mathbf{d}^{n+1}$ (see [13] for details):

$$\mathbf{A}\mathbf{d}^{n+1} = \mathbf{b} \tag{14}$$

In this work, this system was solved for each time step with the Newton-Raphson method using the implementation of the software package PETSc [16]. The time step size was adaptive depending on the amount of required Newton iterations.

2.3 Modeling of Transmural Infarctions in 17 AHA Segments

In 2005 Holmes *et al.* [17] discussed the results of different studies looking at the changes in structure and mechanics of myocardial tissue during different phases of healing after infarction. Based on the reported changes, Holmes *et al.* defined four phases of infarct healing and hypothesized the following: During acute ischemia, the mechanical properties are essentially the same as the properties of healthy myocardium. During necrotic phase the properties result from edema while properties during fibrotic phase are dominated by the large collagen fiber structure. During remodeling phase the mechanical properties of the myocardial scar tissue are determined mainly by the collagen cross-linking. For this phase, Holmes *et al.* found some disagreement in the literature regarding the mechanical

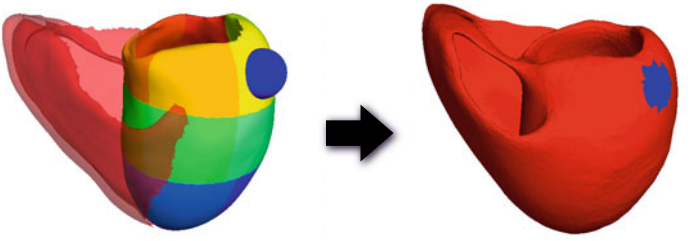

Fig. 1. Region of transmural infarction defined as the intersection of the left ventricle wall of AHA segment 5 with a sphere with a radius of 5mm

properties of the scar tissue. Nevertheless, different studies revealed an increased stiffness compared to the control case [18,19].

This work focused on the remodeling phase. The stiffness of the scar tissue was defined to be 5 times greater than of non infarct tissue, which was in the range of values available in the literature [17,18,19]. Furthermore the contraction tension was set to zero, due to the fact that the scar tissue is not excitable anymore. The left ventricle of the anatomical model was divided in 17 segments according to the scheme recommended by the American Heart Association in 2002 [20]. For each of the 17 AHA segments, the infarct region was defined as the intersection of the left ventricular wall with a sphere with a radius of 5 mm and the barycenter of the respective AHA segment as origin (see Fig. 1).

In total, 18 simulations of the contraction of the ventricles were performed, 17 with an infarction in the respective AHA segment, and one without infarction for the control case. For each simulation, two contraction cycles were simulated and the second cycle was evaluated. Here, the average velocity and the wall thickening of the infarct region and the corresponding region of the control case were determined. In addition, a third parameter for the cardiac mechanical dynamics was introduced. Since the infarction scar has no contractility and an increased stiffness, it was assumed that the velocity vectors of the infarct region are more in line than those of the control case. To measure this parameter, for each node of the region of interest, the angle between the velocity vector $\mathbf{v}_i$ and the average velocity vector $\bar{\mathbf{v}}$ of all nodes N of that region was determined. These angles were averaged and multiplied with the average velocity to obtain a parameter V_α, which combines both informations, velocity and parallelicity:

$$V_\alpha = \bar{v} \cdot \frac{1}{N} \sum_{i}^{N} \arccos\left(\frac{|\mathbf{v_i} \cdot \bar{\mathbf{v}}|}{v_i \cdot \bar{v}} \right) \tag{15}$$

In the following, this parameter is named *kinetic parallelicity*.

3 Results

The infarction had a direct impact on the average velocity and the velocity distribution of the infarct region (see Fig. 2 and Fig. 3a). In most of the AHA

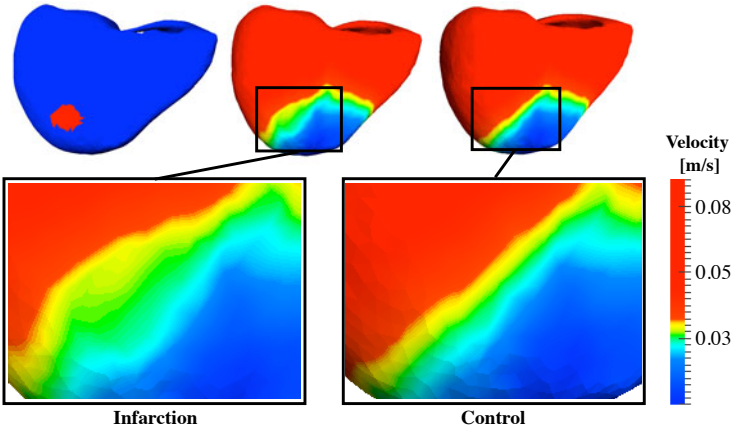

Fig. 2. Impact of an infarction in AHA 13 on the velocity distribution of the left ventricle during contraction

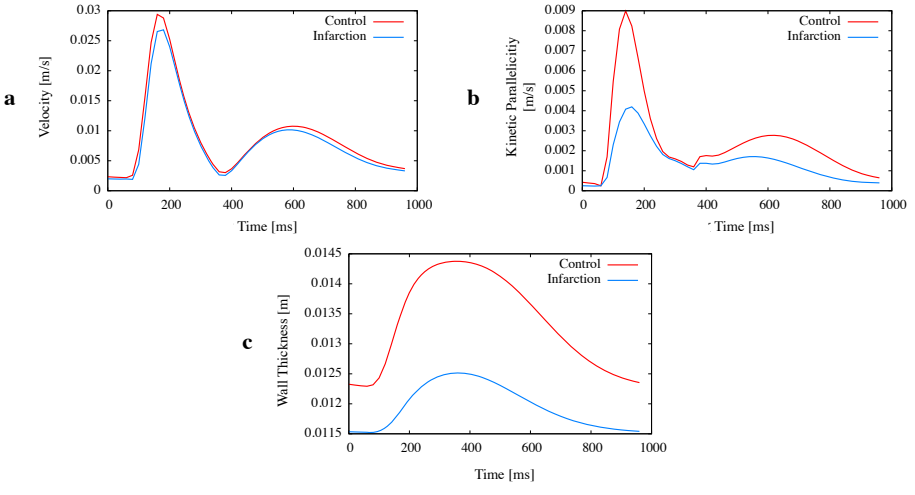

Fig. 3. AHA segment 13: a) Average velocity, b) kinetic parallelicity and c) wall thickening for infarction and control case

segments, the velocity was reduced for contraction and relaxation, except for segment 17 which showed an increased velocity (see Fig. 4a). Since the apex was fixed, the results for segment 17 have to be treated with caution. For that reason, segment 17 is ignored in the following. The largest reductions of contraction velocity were found in segments 3, 13 and 14 (see Fig. 3a). In segment 8 the velocity for relaxation and in segment 11 the velocity for contraction is almost identical to the control case. For segment 1 to 9 and 12 to 14, the velocity was more reduced for the contraction, while for segments 11,15 and 16 the reduction

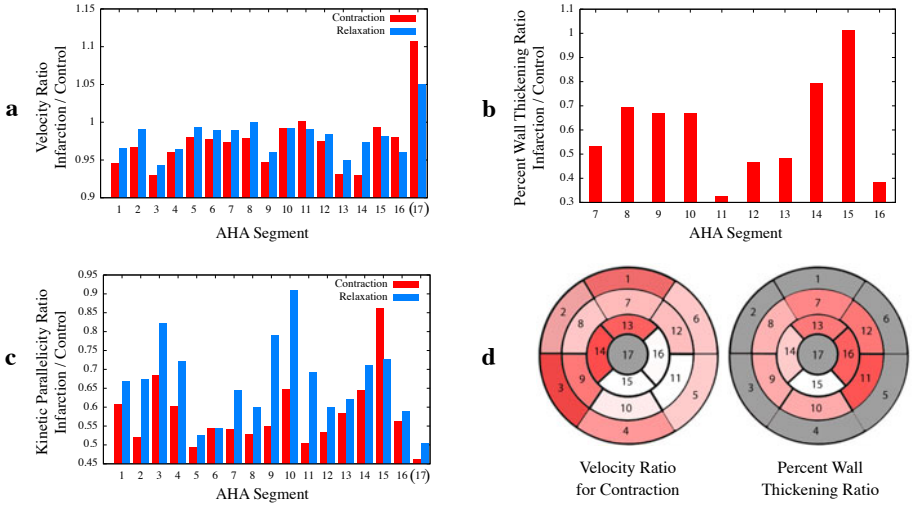

Fig. 4. a) velocity ratio of infarction and control case, b) percent wall thickening ratio of infarction and control case. c) kinetic parallelicity ratio of infarction and control case. d) Bull's eye plot of the 17 AHA segments with color-coded ratio of velocity of infarction and control case (left) and ratio of percent wall thickening of infarction and control case (right).

was more pronounced for relaxation. For segment 10 the reduction was almost equal for contraction and relaxation. However, the impact of the infarction on the average velocity was noticeable but rather small.

For the kinetic parallelicity, the differences between infarction and control case were more significant (see Fig. 4c). Here, segment 5 reveals the largest differences between infarction and control case for contraction and relaxation. Furthermore the differences between contraction and relaxation were more distinctive for kinetic parallelicity. For all segments, except segments 6 and 15 the reduction of the kinetic parallelicity was larger during contraction. Segment 6 showed almost no difference and segment 15 showed a larger reduction for relaxation.

The wall thickening was evaluated for the segments 7 to 16. The wall thickening of the left ventricle was decreased for all considered segments , except segment 15 where the wall thickening was even increased (see Fig. 4c). The largest change was found for segment 11. The changes in wall thickening correlated well to the change in kinetic parallelicity (see Fig. 4b and Fig.4c).

4 Discussion and Future Work

The simulations revealed a direct impact of the myocardial infarction on the velocity vector field of the infarct region for most of the AHA segments. Nevertheless, the differences for the velocity between infarction and control case were rather small. If the parallelicity of the velocity vectors was taken into account, significant differences between infarct region and the corresponding region

of the control case were found. The velocity vectors of the infarct region were more in line than the corresponding vectors of the control case.

In a future work, it has to be evaluated, whether and how velocity mapping can support the diagnosis of infarction and whether the kinetic parallelicity could be a further parameter to identify and characterize infarct tissue. In this context, it will be essential to compare the results to clinical data. Moreover, the presented method can also be used to evaluate and compare other MRI-based techniques e.g. SENC MRI regarding their sensitivity to identify infarctions. However, the elastomechanical model used in this work does not consider blood pressure. The next step will be to couple the elastomechanical model of the ventricles with a model of the circulatory system to improve the simulation of the ventricular mechanical dynamics over the cardiac cycle. Furthermore it has to be evaluated, which further boundary conditions like pericardium or atria has to be taken into account to obtain a even more realistic description of the motion of the heart.

References

1. Axel, L., Dougherty, L.: Heart wall motion: improved method of spatial modulation of magnetization for MR imaging. Radiology 172(2), 349 (1989)
2. Neizel, M., Lossnitzer, D., Korosoglou, G., Schaufele, T., Peykarjou, H., Steen, H., Ocklenburg, C., Giannitsis, E., Katus, H., Osman, N.: Strain-encoded MRI for evaluation of left ventricular function and transmurality in acute myocardial infarction. Circulation: Cardiovascular Imaging 2(2), 116 (2009)
3. Kayser, M., Hein, W., van der Geest Msc, R., van der Wall, M., Ernst, E., Duchateau Msc, C., de Roos, M., et al.: Right ventricular function in patients after acute myocardial infarction assessed with phase contrast MR velocity mapping encoded in three directions. Journal of Magnetic Resonance Imaging 11(5), 471–475 (2000)
4. Jung, B., Markl, M., Foll, D., Hennig, J.: Investigating myocardial motion by MRI using tissue phase mapping. European Journal of Cardiothoracic Surgery 29 (suppl.1), 150–157 (2006)
5. Chabiniok, R., Chapelle, D., Lesault, P., Rahmouni, A., Deux, J.: Validation of a biomechanical heart model using animal data with acute myocardial infarction. In: CI2BM 2009 - MICCAI Workshop on Cardiovascular Interventional Imaging and Biophysical Modelling (2009)
6. Streeter, D.: Gross morphology and fiber geometry of the heart. In: Handbook of Physiology: The Cardiovascular System, vol. I, pp. 61–112. American Physiology Society (1979)
7. ten Tusscher, K., Noble, D., Noble, P., Panfilov, A.: A model for human ventricular tissue. American Journal of Physiology. Heart and Circulatory Physiology 286, H1573–H1589 (2004)
8. Keller, D.U.J., Weber, F.M., Seemann, G., Dössel, O.: Ranking the influence of tissue conductivities on forward-calculated ECGs. IEEE Transactions on Biomedical Engineering 57, 1568–1576 (2010)
9. Seemann, G., Keller, D., Krueger, M., Weber, F., Wilhelms, M., Dössel, O.: Electrophysiological modeling for cardiology: methods and potential applications. Information Technology 52, 242–249 (2010)

10. Keller, D.U.J., Kalayciyan, R., Dössel, O., Seemann, G.: Fast creation of endocardial stimulation profiles for the realistic simulation of body surface ECGs. In: IFMBE Proceedings World Congress on Medical Physics and Biomedical Engineering, vol. 25/4, pp. 145–148 (2009)
11. Sachse, F., Glänzel, K., Seemann, G.: Modeling of protein interactions involved in cardiac tension development. International Journal of Bifurcation and Chaos 13, 3561–3578 (2003)
12. Wolff, M., Whitesell, L., Moss, R.: Calcium sensitivity of isometric tension is increased in canine experimental heart failure. Circulation Research 76, 781–789 (1995)
13. Belytschko, T., Liu, W., Moran, B.: Nonlinear finite elements for continua and structures. Wiley, Chichester (2000)
14. Okamoto, R., Moulton, M., Peterson, S., Li, D., Pasque, M., Guccione, J.: Epicardial suction: A new approach to mechanical testing of the passive ventricular wall. Journal of Biomechanical Engineering 122, 479–487 (2000)
15. Omens, J., MacKenna, D., McCulloch, A.: Measurement of strain and analysis of stress in resting rat left ventricular myocardium. Journal of Biomechanics 26(6), 665–676 (1993)
16. Balay, S., Buschelman, K., Gropp, W., Kaushik, D., Knepley, M., McInnes, L., Smith, B., Zhang, H.: Petsc web page, http://www.mcs.anl.gov/petsc
17. Holmes, J., Borg, T., Covell, J.: Structure and mechanics of healing myocardial infarcts. Annual Review of Biomedical Engineering 7, 223–253 (2005)
18. Connelly, C., Vogel, W., Wiegner, A., Osmers, E., Bing, O., Kloner, R., Dunn-Lanchantin, D., Franzblau, C., Apstein, C.: Effects of reperfusion after coronary artery occlusion on post-infarction scar tissue. Circulation Research 57(4), 562 (1985)
19. Gupta, K., Ratcliffe, M., Fallert, M., Edmunds Jr., L., Bogen, D.: Changes in passive mechanical stiffness of myocardial tissue with aneurysm formation. Circulation 89(5), 2315 (1994)
20. Cerqueira, M., Weissman, N., Dilsizian, V., Jacobs, A., Kaul, S., Laskey, W., Pennell, D., Rumberger, J., Ryan, T., Verani, M.: Standardized myocardial segmentation and nomenclature for tomographic imaging of the heart: A statement for healthcare professionals from the cardiac imaging comittee of the council on clinical cardiology of the american heart association. Circulation 105, 539–542 (2002)

Automatic Delineation of Left and Right Ventricles in Cardiac MRI Sequences Using a Joint Ventricular Model

Xiaoguang Lu[1,⋆], Yang Wang[1], Bogdan Georgescu[1], Arne Littman[2], and Dorin Comaniciu[1]

[1] Siemens Corporate Research, Princeton, NJ, USA
xiaoguang.lu@siemens.com
[2] Magnetic Resonance, Siemens Healthcare, Erlangen, Germany

Abstract. Cardiac magnetic resonance imaging (MRI) has advanced to become a powerful tool in clinical practice. Extraction of morphological and functional features from cardiac MR imaging for diagnosis and disease monitoring remains a time-consuming task for clinicians. We present a fully automatic approach to extracting the structures and dynamics for both left and right ventricles. The cine short-axis stack of a cardiac MR scan is used to reconstruct a 3D volume sequence. A joint LV-RV model is introduced to delineate the boundaries of both left and right ventricles in each frame, and to combine both spatial and temporal context to track the chamber boundary motion over cardiac cycles. Both qualitative and quantitative results show promise of the proposed method.

1 Introduction

Accurate morphological and functional measurements of the heart anatomies are essential in clinical applications for diagnosis, prognostic, and therapeutic decisions. Magnetic resonance imaging (MRI) allows morphological characterization of heart structures with precision. An accurate identification of the borders of the structures to be analyzed is needed in order to extract physiologically meaningful quantitative information from the images. Potential applications of cardiac segmentation and tracking include the calculation of volume and mass, blood ejection fraction, analysis of contraction and wall motion as well as the 3D visualization of cardiac anatomy [1].

Advantages of cardiac MRI include a wide topological field of view with visualization of the heart and its internal morphology and surrounding mediastinal structures. It has a high soft-tissue contrast discrimination between the flowing blood and myocardium without the need for contrast medium or invasive techniques. Cardiac MR is able to perform multiple non-harmful and accurate scans required for disease monitoring. In such a scenario, fast, reproducible and accurate extraction of clinical features is essential for all decision support systems.

⋆ Corresponding author.

D.N. Metaxas and L. Axel (Eds.): FIMH 2011, LNCS 6666, pp. 250–258, 2011.

In addition to assessing left ventricle (LV) functions, recent research emphasizes the importance of right ventricle (RV) function in the prognosis of a variety of cardiopulmonary diseases. This indicates that there is a growing interest in the clinical relevance of both LV and RV; in particular for congenital diseases and that more routine quantification of RV function is warranted under most clinical circumstances. Because of ventricular interactions, RV filling influences LV performance, and similarly, the LV affects RV function through the interventricular septum. Dynamics of the RV can also infer a large amount of clinical information [2,3,4]. The normal RV anatomy is a complex crescent-shaped structure wrapped around the LV. The RV can in some cases (especially in diseased patients) be characterized by its non-uniform shape and high degree of trabaeculations. Due to the complexity of shape and dynamics, much of the research on the LV cannot be easily transferred to the RV.

In current clinical practice, assessment of RV structure and function remains mostly qualitative, which involves manually delineating the inner wall (endocardium) of the RV, and requires a great deal of user interaction with generally no a-priori information. Correlation between LV and RV shows promise to improve RV segmentation, as explored in [5], where five landmarks need to be manually identified for the subsequent automatic segmentation. We proposed an automatic approach to delineating LV and RV without any user interactions.

2 Methodology

Due to the large amount of available data, analysis such as segmentation of cardiac images is time consuming and error-prone for human operators, which needs to be automated in order to be clinically valuable. We present an automatic approach to extracting relevant morphological and dynamic parameters of both LV and RV from MRI data over a cardiac cycle, as demonstrated in Fig. 1. Conventional volume measurements by cardiac MRI are independent of the cavity shape, with the area from contiguous slices integrated over the chamber of interest. However, direct 3D extraction may take advantage of the chamber shape and provide heart movement measurement in three dimensions, leading to more accurate and realistic representations.

The proposed method segments chambers on the first frame, followed by dynamics extraction across the entire sequence, as shown in Fig. 2. Chamber segmentation includes two stages: at the first stage, the position, orientation, and scale of the heart chamber (LV/RV) in a 3D volume are determined to initialize the joint model for chamber segmentation; at the second stage, local deformation of the detected model is processed in order to fit the model to both LV and RV boundaries.

2.1 Joint Anatomy Model

In order to accurately model the complexity of the anatomy, a representation of the anatomic shape is created using a database of reconstructed 3D volumes that are manually segmented. For left ventricle, the model includes LV endocardium,

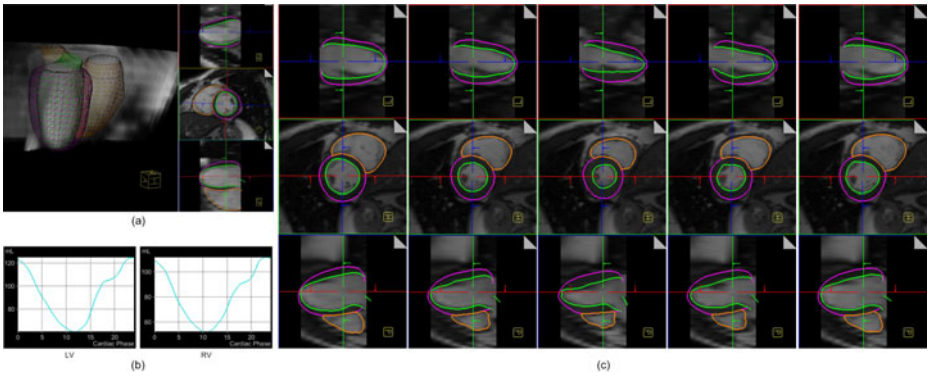

Fig. 1. Models of LV/RV fitted to a 3D reconstructed cardiac MRI volume sequence. (a) Estimated 3D model. (b) Volume measurement across time computed based on the fitted models. (C) 2D views of frame 1, 6, 11, 16, 21 of a single heartbeat cycle (25 frames in total).

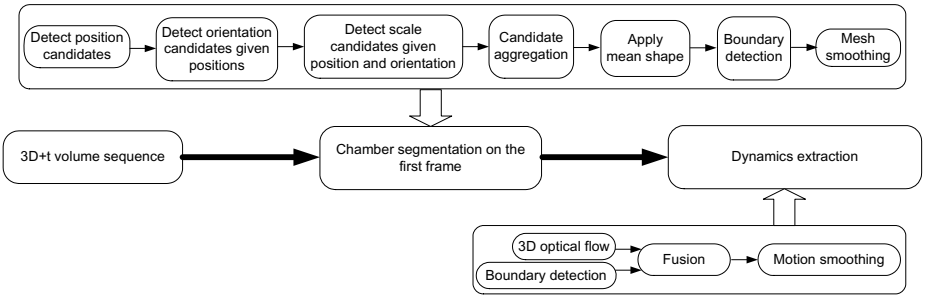

Fig. 2. Workflow of our automatic LV and RV detection and tracking system

LV epicardium, and LV outflow tract (LVOT). The right ventricle model consists of the RV blood pool cavity, the RV outflow tract (RVOT) as far as the pulmonary valve and the tricuspid valve opening. Both LV and RV models are triangular meshes as shown in Fig. 3. They are used to fit a given 3D cardiac volume to delineate corresponding anatomical structures. The joint model unifies the interventricular septum between LV the RV.

2.2 Learning-Based Model Fitting

A typical cardiac MR scan to examine the LV/RV morphology and functionality contains a short axis stack, which consists of image slices captured at the different positions along the short axis of heart chambers (e.g., LV). These image slices can be aligned using the physical coordinates (location and orientation) recorded during acquisition. A 3D volume is reconstructed from this stack of aligned image slices. If each image slice is captured in a time sequence and synchronized to

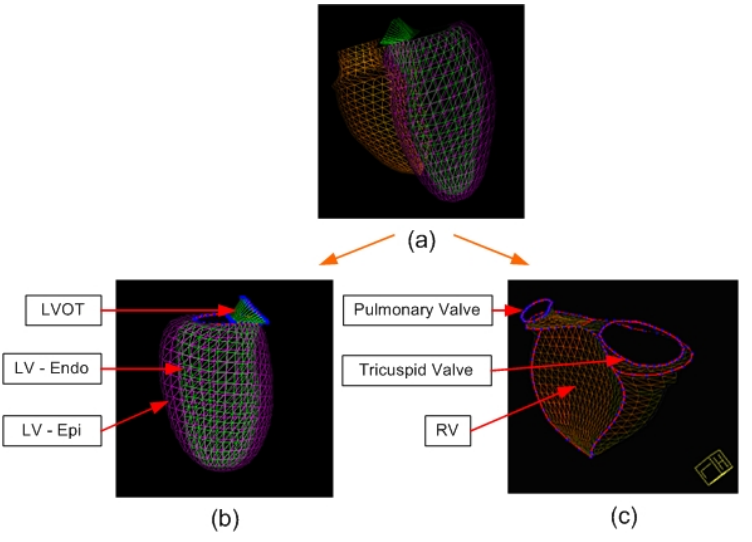

Fig. 3. Joint model (a) of LV (b) and RV (c). The RV inner boundary and LV epicardium are jointly modeled, sharing the same triangular mesh parts.

each other, a 3D volume sequence is obtained, which is used for 3D chamber segmentation and dynamics extraction in our proposed system.

To estimate our joint anatomical models in the reconstructed volumetric data, we train a series of detectors to estimate the model pose (including translation, orientation, and scale) and boundaries on a large database with both LV and RV annotated. We use a probabilistic boosting tree (PBT) [6] for each detector, which selects a set of discriminative features that are used to distinguish the positive samples from negatives from a large pool of features. Image orientation information recorded during acquisition can also be used to help initialize pose estimation. For the detector at the translation stage, we choose 3D Haar wavelet-like features [7], which are calculated efficiently using integral image based techniques. For the detectors at the orientation and scale search stages, steerable features [8] are applied because they do not require volume rotation and re-scaling which are computationally expensive, especially when the search hypothesis space is large.

In order to detect the model pose, we need to solve for the nine-parameter space, including three translations, three orientations, and three scales, i.e.,

$$\theta = \{(c_x, c_y, c_z), (\boldsymbol{\alpha}_x, \boldsymbol{\alpha}_y, \boldsymbol{\alpha}_z), (s_x, s_y, s_z)\} \tag{1}$$

where (c_x, c_y, c_z), $(\boldsymbol{\alpha}_x, \boldsymbol{\alpha}_y, \boldsymbol{\alpha}_z)$, (s_x, s_y, s_z) are the position, orientation and scale parameters. To estimate the above parameters efficiently, we apply a marginal space search strategy [8], which groups the original parameters space into subsets of increasing marginal spaces such that the posterior probability can be expressed as:

$$\begin{aligned} p(\theta_t|I_t) = p(c_x, c_y, c_z|I_t)p(\boldsymbol{\alpha}_x, \boldsymbol{\alpha}_y, \boldsymbol{\alpha}_z|c_x, c_y, c_z, I_t) \\ p(s_x, s_y, s_z|\boldsymbol{\alpha}_x, \boldsymbol{\alpha}_y, \boldsymbol{\alpha}_z, c_x, c_y, c_z, I_t) \end{aligned}$$

We train a series of detectors that estimate parameters at a number of sequential stages in the order of complexity, i.e., translation, orientation, and scale. Different stages utilize different features computed from 3D volumetric data. Multiple hypotheses are maintained between stages, which quickly removes false hypotheses at the earlier stages while propagates the right hypothesis to the final stage. Only one hypothesis is selected as the final detection result.

With the model pose estimated, we align the mean shape (an average model of all annotations) with data to get an initial estimate of the object shape. To capture the true anatomical morphology of the target object (e.g., LV and RV), we deform the mean shape by searching the boundary for each vertex of the model. The boundary hypotheses are taken along the normal directions at each vertex of the mean model. Detection is achieved using a boundary detector using PBT with steerable features. The detected boundaries are constrained by projecting the detected model onto a shape subspace obtained by the annotated dataset, which was constructed using principal component analysis. Although more sophisticated representations, such as local affine models [9,10], can also be applied to constrain shape deformations, we choose the global PCA shape model due to its efficiency during online detection.

The joint LV-RV model provides a mechanism to improve search and fitting accuracies based on the geometric constraint between LV and RV. For example, when LV is robustly detected, the RV parameter search range can be inferred to be in a much smaller space than the original RV search range without any a-prior information. The unified septum boundary constraint (LV and RV must share the same septum boundary) improves model fitting. Therefore, the joint model leads to more robust and accurate detection and delineation of the anatomies.

2.3 Dynamics Extraction

In this section, we present our tracking method to extract dynamic shape deformation automatically from an MRI sequence, which includes three main steps: initialization, deformation propagation, and motion smoothing. In the initialization step, the learning-based model fitting approach is applied to the initial frame to detect the shape for both LV and RV, as described in Sec. 2.2.

Starting from the detection result at the initial frame, the model deformations are propagated to neighboring frames using both the learned features and the local image templates. To ensure temporal consistency and smooth motion and to avoid drifting and outliers, two collaborative trackers, an intensity-based matching tracker and a boundary detection tracker, are used in our method. The intensity-based matching tracker directly computes the temporal displacement for each point from one frame to the next based on the image intensity, while the detection tracker obtains the deformations in each frame with maximal probability [11]. The above two trackers are integrated into a single Bayesian framework:

$$\arg\max_{\boldsymbol{X_t}} p(\boldsymbol{X_t}|\boldsymbol{Y_{t-1:t}}) = \arg\max_{\boldsymbol{X_t}} p(\boldsymbol{Y_t}|\boldsymbol{X_t}) p(\boldsymbol{X_t}|\boldsymbol{Y_{t-1}}), \tag{2}$$

where $\boldsymbol{Y_{t-1:t}} = (\boldsymbol{Y_{t-1}}, \boldsymbol{Y_t})$ are the image intensity and local feature responses from the two neighboring frames $I_{t-1:t} = (I_{t-1}, I_t)$. For clarity, we use $\boldsymbol{X_t}$ to

denote a concatenation of the mesh point positions, $\boldsymbol{X_t} = [X_1, \cdots, X_n]$, which need to be estimated at the current time instance t, and n is the total number of points in the mesh model.

The likelihood term $p(\boldsymbol{Y_t}|\boldsymbol{X_t})$ is computed from both boundary detection and local image template matching as follows,

$$p(\boldsymbol{Y_t}|\boldsymbol{X_t}) = (1-\lambda)p(F_t|\boldsymbol{X_t}) + \lambda p(T_t|\boldsymbol{X_t}), \tag{3}$$

where F_t is the steerable feature response [8], T_t is the local image template centered at $\boldsymbol{X_{t-1}}$ in the previous frame I_{t-1}, and λ is the weighting coefficient of the matching term. Given the resulting shape $\boldsymbol{X_{t-1}}$ from the previous frame $t-1$, the prediction term $p(\boldsymbol{X_t}|\boldsymbol{Y_{t-1}})$ can be simplified as $p(\boldsymbol{X_t}|\boldsymbol{X_{t-1}})$. In our system $p(\boldsymbol{X_t}|\boldsymbol{X_{t-1}})$ is modeled as a Gaussian distribution based on the shape distance $d(\boldsymbol{X_t}, \boldsymbol{X_{t-1}}) = \parallel \boldsymbol{X_t} - \boldsymbol{X_{t-1}} \parallel$. The objective function (2) can be optimized by searching in a local neighborhood centered at $\boldsymbol{X_{t-1}}$. To speed up the computation, we apply the optical flow technique to search for the new position $\boldsymbol{X_t}$ along the local gradient direction in the current frame I_t.

The above deformation propagation step is repeated until the full 4D model is estimated for the complete sequence. In this way the collaborative trackers complement each other, as the intensity-based matching tracker provides temporally consistent results and its major issue of drifting is addressed by the boundary detection.

Finally to obtain a smooth motion field, the tracking is performed in both forward and backward directions given the periodic nature of the cardiac motion, and a Gaussian kernel is applied to both the LV and RV shapes in the neighboring frames, i.e., $\boldsymbol{X_t^{smooth}} = \sum_{i=-k}^{k} G(i)\boldsymbol{X_{t+i}}$, where $G(i)$ is a normalized Gaussian kernel $N(0, \sigma)$. In our experiments we typically choose $\sigma = 0.6$ and $k = 1$.

3 Experiments

We collected 100 reconstructed volumes from 70 patients with left ventricles annotated, among which 93 reconstructed volumes from 63 patients were also annotated on right ventricles. Volumes were selected to cover a large range of dynamic heart motion, including both end diastole and end systole. The original short-axis stack images have an average in-plane resolution of $1.35mm$, and the distance between slices is around $10mm$.

A 4-fold cross-validation scheme was applied for evaluation. The entire LV dataset was randomly partitioned into four quarters. For each fold evaluation, three quarters were combined for training and the remaining one was used as unseen data for testing. This procedure was repeated four times so that each volume has been used once for testing. The same evaluation protocol was applied for RV. For each segmented mesh, the distance from each vertex to the groundtruth mesh (manual annotation) was computed as point-to-mesh distance. The average distance from all vertices of the segmented mesh was used as the measurement. Three major components, i.e., LV endocardium, LV epicardium, and RV main

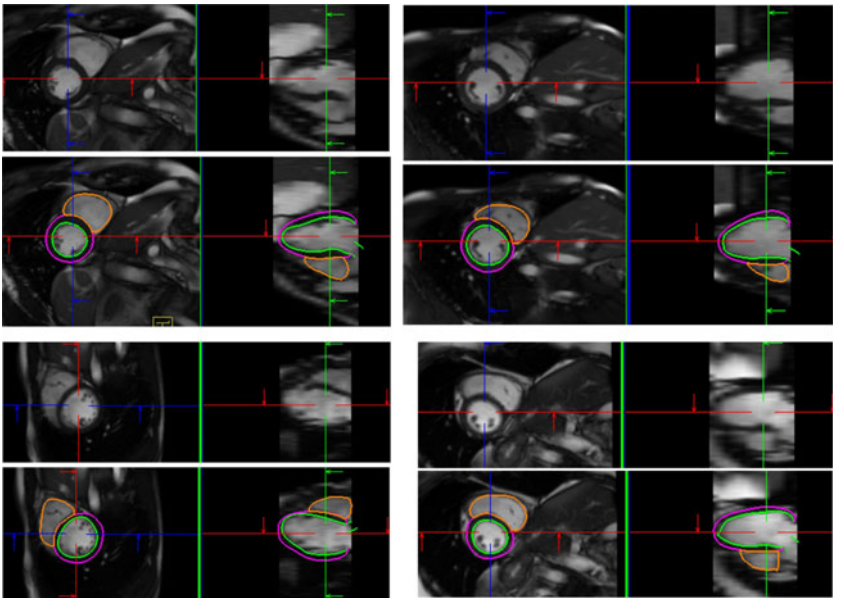

Fig. 4. Automatic delineation examples

Table 1. Point-to-mesh distance measurements obtained by a 4-fold cross validation based on the joint LV-RV model

measure (mm)	Mean	Std	Median
LV endocardium	2.95	4.85	1.84
LV epicardium	3.23	3.94	2.12
RV main	2.99	1.18	2.66

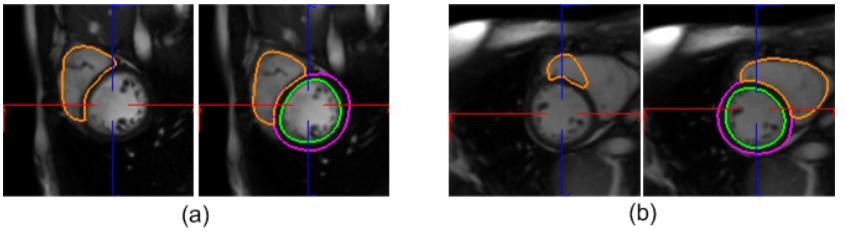

Fig. 5. Examples of superior performance of the joint LV-RV model over individual RV modeling. In both (a) and (b), the left ones are the delineation results obtained by the individual RV model and the right ones are from the proposed joint LV-RV model. The individual RV model overestimates the RV in (a) and significantly underestimates the RV in (b), while the joint LV-RV model provides correct delineation in both cases.

Table 2. Comparison of RV delineation results using joint LV-RV model against individual RV model. Point-to-mesh distance measurements are calculated.

measure (mm)	Mean	Std	Median
Individual RV model	4.12	6.28	2.65
Joint LV-RV model	2.99	1.18	2.66

cavity, were considered in our evaluation as listed in Table 1. Automatic delineation examples are provided in Fig. 4. Fig. 5 shows examples where joint LV-RV modeling provides superior performance to individual RV modeling. Table 2 summarizes the quantitative results obtained by joint modeling from the 4-fold cross validation in comparison with individual RV modeling.

On the average, it took about 3 seconds to segment both LV and RV from a single volume (e.g, $256\times256\times70$), and about 40 seconds to fully extract dynamics of the entire sequence (typically 20 frames) on a duo core 2.8GHz CPU.

4 Conclusions

We have presented a fully automatic method for segmenting LV and RV chambers from cardiac MRI images, and extracting the dynamics of both chamber movements. A joint ventricular model is used to delineate the boundaries of both LV and RV in each frame. Clinically relevant measurements, such as volumes and ejection fraction, can be calculated based on the fitted model.

References

1. Frangi, A., Niessen, W., Viergever, M.: Three-dimensional modeling for functional analysis of cardiac images: A review. IEEE Trans. on Medical Imaging 20(1) (2001)
2. Grothues, F., Moon, J., Bellenger, N., Smith, G., Klein, H., Pennell, D.: Interstudy reproducibility of right ventricular volumes, function, and mass with cardiovascular magnetic resonance. American Heart Journal 147(2), 218–223 (2004)
3. Corsi, C., Caiani, E., Catalano, O., Antonaci, S., Veronesi, F., Sarti, A., Lamberti, C.: Improved quantification of right ventricular volumes from cardiac magnetic resonance data. Computers in Cardiology 57(2), 37–40 (2005)
4. Haber, E., Metaxas, D., Axel, L., Wells, W., Colchester, A., Delp, S.: Motion analysis of the right ventricle from MRI images. In: Wells, W.M., Colchester, A.C.F., Delp, S.L. (eds.) MICCAI 1998. LNCS, vol. 1496, p. 177. Springer, Heidelberg (1998)
5. Sun, H., Frangi, A.F., Wang, H., Sukno, F.M., Tobon-Gomez, C., Yushkevich, P.A.: Automatic cardiac MRI segmentation using a biventricular deformable medial model. In: Jiang, T., Navab, N., Pluim, J.P.W., Viergever, M.A. (eds.) MICCAI 2010. LNCS, vol. 6361, pp. 468–475. Springer, Heidelberg (2010)
6. Tu, Z.: Probabilistic boosting-tree: Learning discriminative models for classification, recognition, and clustering. In: Proc. ICCV, pp. 1589–1596 (2005)
7. Viola, P., Jones, M.J.: Robust real-time face detection. International Journal of Computer Vision 57(2), 137–154 (2004)

8. Zheng, Y., Barbu, A., Georgescu, B., Scheuering, M., Comaniciu, D.: Four-chamber heart modeling and automatic segmentation for 3-D cardiac CT volumes using marginal space learning and steerable features. IEEE Transactions on Medical Imaging 27(11), 1668–1681 (2008)
9. Peters, J., Ecabert, O., Meyer, C., Kneser, R., Weese, J.: Optimizing boundary detection via simulated search with applications to multi-modal heart segmentation. Medical Image Analysis 14(1), 70–84 (2010)
10. Zhuang, X., Leung, K., Rhode, K., Razavi, R., Hawkes, D.J., Ourselin, S.: A registration-based propagation framework for automatic whole heart segmentation of cardiac mri. IEEE Transactions on Medical Imaging 29(9), 1612–1625 (2010)
11. Yang, L., Georgescu, B., Zheng, Y., Meer, P., Comaniciu, D.: 3D ultrasound tracking of the left ventricles using one-step forward prediction and data fusion of collaborative trackers. In: CVPR (2008)

Simulating Drug-Induced Effects on the Heart: From Ion Channel to Body Surface Electrocardiogram

N. Zemzemi[1], M.O. Bernabeu[1], J. Saiz[2], and B. Rodriguez[1]

[1] University of Oxford, United Kingdom
[2] Universidad Politécnica de Valencia, Spain

Abstract. The electrocardiogram (ECG) is widely used as a clinical tool for the evaluation of cardiac conditions caused by drugs, mutations and diseases. However, the ionic basis underlying changes in the ECG are often unclear. In the present study, we present a computational model of the human ECG capable of representing drug-induced effects from the ionic to the surface potential level. Bidomain simulations are conducted to simulate the electrophysiological activity of the heart and extracellular potentials in the whole body. Membrane kinetics are represented by the most recent version of a human action potential model, modified to include representation of HERG block by dofetilide, a known class III anti-arrhythmic drug with potential pro-arrhythmic effects. Simulation results are presented showing how dofetilide administration results in the prolongation of the action potential duration in the ventricles and the QT interval measured on the surface of the thorax, in agreement with clinical results. The state-of-the-art tools and methodologies presented here could be useful in the investigation and assessment of drug cardiotoxicity and can also be extended to the investigation of the effect of mutations or disease on the ECG.

1 Introduction

The electrocardiogram (ECG) is the main clinical signal used for the diagnosis of heart conditions. It is obtain by performing the non-invasive measurement on the thorax surface of the electrical potentials generated by the heart during each heart beat. Each of the phases of the ECG waveform broadly corresponds to one of the phases of the heart beat. In brief, The P wave is associated with atrial depolarization and repolarization, the QRS complex is related to ventricular depolarization, and the T wave corresponds to ventricular repolarization.

Drugs, disease conditions and mutations often result in abnormalities in ionic current properties in the ventricles, which cause alterations in depolarization and repolarization properties. Of particular concern are changes in ventricular repolarization, which manifest themselves as changes in the QT interval and T wave of the ECG, and have been linked to increased risk of arrhythmic death. The QT interval is, for instance, the main biomarker used in the assessment of the drug safety. QT prolongation is considered an indicator of increased risk of

D.N. Metaxas and L. Axel (Eds.): FIMH 2011, LNCS 6666, pp. 259–266, 2011.

Torsades de Pointes and can lead to the abandonment of the compound development. However, some QT prolonging drugs present no arrhythmic episodes and some others are known to be useful anti-arrhythmic drugs for most patients. Therefore a better understanding of drug-induced changes in the ECG and how they relate to ionic mechanisms and arrhythmic risk is needed.

Multiscale modelling and simulation has been extensively used to investigate the impact of ionic current properties on electrocardiogram. Most of the studies in the literature are based on the simulation of unipolar pseudo-ECGs using 1D or 3D anatomically-based models (see for example, [1], [2]). ECG simulations have also been performed using 3D heart models embedded in a torso ([3], [4]). The studies have shown the importance of torso effects in the simulation of the ECG but they often included simplified or non-human ionic models.

In the present study, we present simulation results showing changes in ECG measured on the surface of the human thorax occurring following administration of a specific drug dose. A bidomain model of the human body is developed which includes the most recent biophysically-detailed model of the human action potential (AP) ([3]). The AP model is modified to include the effect of specific doses of the anti-arrhythmic drug dofetilide on the rapid component of the delayed rectifier current as proposed by [5]. Dofetilide induces prolongation of the action potential duration (APD) and refractoriness, which have antiarrhythmic effects. However, dofetilide administration needs to be performed with caution due to potential pro-arrhythmic effects linked to long-QT syndrome (LQTS). Simulations are run with an efficient bidomain solver ([6]) to obtain the ECG measured on the body surface for control and following drug administration.

2 Methods

In this section, we provide a description of anatomical model, equations, numerical algorithms and computational software used to simulate the electrical propagation from ionic currents to body surface.

2.1 3D Anatomical Model of the Human Body

A 3D anatomical finite-element mesh of the human body was used to simulate drug-induced changes in the ECG (Figure 1). The computational mesh included a detailed representation of the heart and surrounding tissue (i.e. bones, lungs) in order to introduce conductivity heterogeneity in the torso. The mesh was generated from human anatomical data[1] as described in [4]. In brief, data were pre-processed using the `3-matic`[2] software in order to obtain computationally-correct surface meshes, and then `GHS3D` [7] meshing softwares to further process the surface meshes and generate the 3D final computational meshes. In order to introduce anisotropy in the myocardium, fiber orientations were generated using the Streeter *et al.* method [8]. A transmural distance map was also computed in order to introduce cell heterogeneity in the left ventricle.

[1] www.3dscience.com

[2] www.materialise.com

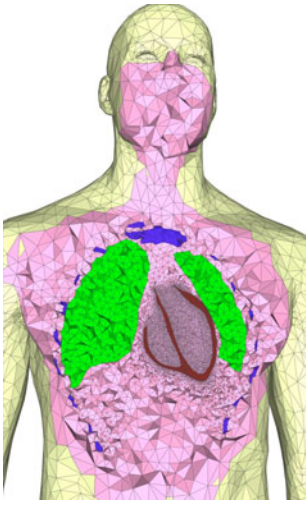

Fig. 1. Computational heart-torso mesh (cross-section) for body surface potential simulations. The colors describe different regions in the human body: red (heart), green (lung), blue (bones) and pink (the remaining tissue).

2.2 Electrical Model

The bidomain equations were used to simulate the electrical activity of the heart and extracellular potentials in the whole body (see *e.g.* [9]). These equations in the heart domain Ω_{H} are given by:

$$\begin{cases} A_{\mathrm{m}}\big(C_{\mathrm{m}}\dot{V}_{\mathrm{m}} + I_{\mathrm{ion}}(V_{\mathrm{m}}, \boldsymbol{w})\big) - \operatorname{div}\big(\boldsymbol{\sigma}_{\mathrm{i}}\boldsymbol{\nabla}V_{\mathrm{m}}\big) = \operatorname{div}\big(\boldsymbol{\sigma}_{\mathrm{i}}\boldsymbol{\nabla}u_{\mathrm{e}}\big) + I_{\mathrm{stim}}, & \text{in} \quad \Omega_{\mathrm{H}}, \\ -\operatorname{div}\big((\boldsymbol{\sigma}_{\mathrm{i}} + \boldsymbol{\sigma}_{\mathrm{e}})\boldsymbol{\nabla}u_{\mathrm{e}}\big) = \operatorname{div}(\boldsymbol{\sigma}_{\mathrm{i}}\boldsymbol{\nabla}V_{\mathrm{m}}), & \text{in} \quad \Omega_{\mathrm{H}}, \\ \dot{\boldsymbol{w}} + \boldsymbol{g}(V_{\mathrm{m}}, \boldsymbol{w}) = 0, & \text{in} \quad \Omega_{\mathrm{H}}, \\ \boldsymbol{\sigma}_{\mathrm{i}}\boldsymbol{\nabla}V_{\mathrm{m}} \cdot \boldsymbol{n} = -\boldsymbol{\sigma}_{\mathrm{i}}\boldsymbol{\nabla}u_{\mathrm{e}} \cdot \boldsymbol{n}, & \text{on} \quad \Sigma. \end{cases} \tag{1}$$

The state variables V_{m} and u_{e} stand for the transmembrane and the extra-cellular potentials. Constants A_{m} and C_{m} represent the rate of membrane surface per unit of volume and the membrane capacitance, respectively. I_{stim} and I_{ion} are the stimulation and the transmembrane ionic currents. The heart-torso interface is denoted by Σ. The intra- and extracellular (anisotropic) conductivity tensors, $\boldsymbol{\sigma}_{\mathrm{i}}$ and $\boldsymbol{\sigma}_{\mathrm{e}}$, are given by $\boldsymbol{\sigma}_{\mathrm{i},e} = \sigma^{\mathrm{t}}_{\mathrm{i},e}\boldsymbol{I} + (\sigma^{\mathrm{l}}_{\mathrm{i},e} - \sigma^{\mathrm{t}}_{\mathrm{i},e})\boldsymbol{a} \otimes \boldsymbol{a}$, where $\boldsymbol{a}$ is a unit vector parallel to the local fibre direction and $\sigma^{\mathrm{l}}_{\mathrm{i},e}$ and $\sigma^{\mathrm{t}}_{\mathrm{i},e}$ are, respectively, the longitudinal and transverse conductivities of the intra- and extra-cellular media. The field of variables $\boldsymbol{w}$ is a vector containing different chemical concentrations and various gate variables. Its time derivative is given by the vector of functions $\boldsymbol{g}$.

The precise definition of $\boldsymbol{g}$ and I_{ion} depend on the electrophysiological transmembrane ionic model. In the present work we make use of the most recently published biophysically detailed human ventricular myocyte model [10]. The ion channels and transporters have been modeled on the basis of the most recent

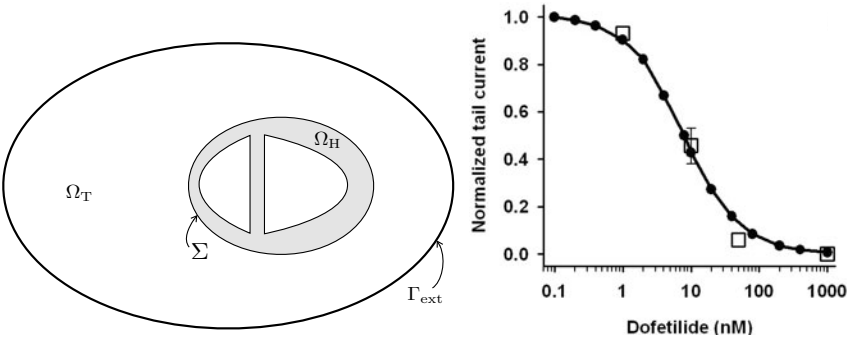

Fig. 2. Two-dimensional geometrical description: heart domain Ω_H, torso domain Ω_T (extramyocardial regions), heart-torso interface Σ and torso external boundary Γ_{ext} (left). Normalized IK_r *vs* dofetilide dose at steady state (right).

experimental data from human ventricular myocytes. This detailed model has been extensively compared against experimental data in human, particularly for repolarization mechanisms. It therefore represents the most adequate model to investigate drug-induced effects on repolarization mechanisms from drug/ion interaction to surface body ECG.

Figure 2 (left) provides a geometrical representation of the domains considered to compute extracellular potentials in the human body. In the torso domain Ω_T, the electrical potential u_T is described by the Laplace equation.

$$\begin{cases} \text{div}(\boldsymbol{\sigma}_T \boldsymbol{\nabla} u_T) = 0, & \text{in} \quad \Omega_T, \\ \boldsymbol{\sigma}_T \boldsymbol{\nabla} u_T \cdot \boldsymbol{n}_T = 0, & \text{on} \quad \Gamma_{ext}. \end{cases} \tag{2}$$

where $\boldsymbol{\sigma}_T$ stands for the torso conductivity tensor and $\boldsymbol{n}_T$ is the outward unit normal to the torso external boundary Γ_{ext}. The heart-torso interface Σ is supposed to be a perfect conductor. Then we have a continuity of current and potential between the extra-cellular myocardial region and the torso region.

$$\begin{cases} u_e = u_T, & \text{on} \quad \Sigma, \\ (\boldsymbol{\sigma}_e + \boldsymbol{\sigma}_i) \boldsymbol{\nabla} u_e \cdot \boldsymbol{n}_T = \boldsymbol{\sigma}_T \boldsymbol{\nabla} u_T \cdot \boldsymbol{n}_T, & \text{on} \quad \Gamma_{ext}. \end{cases} \tag{3}$$

The equations (1)-(3) represent the state-of-the-art heart-torso full coupled electrophysiological problem from the cell to the human body surface.

2.3 Dofetilide Model

The human action potential model by Grandi *et al.* [10] was modified to include detailed representation of dofetilide/HERG interactions as in [5]. Briefly, dofetilide is a class III antiarrhythmic drug that blocks the rapid component of the delayed rectifier K^+ current (IK_r). The dofetilide proposed model takes into account experimental evidences which suggest that dofetilide interacts with

IK_r channels in both open and inactivated states, but not in closed state. In the steady state, the effect of dofetilide concentration $[D]$ on the IK_r current is represented by introducing the factor $(1 - b)$ as the fraction of unblocked channels (where b is the fraction of channels blocked by the drug).

$$\frac{IK_r([D])}{IK_r} = \frac{1}{1 + \frac{[D]}{IC_{50}}} = 1 - b \tag{4}$$

Figure 2 (right) shows the dose-response curve of steady-state block of normalized $IK_r([D])$ tail current obtained using the model (line) and the experimental data (white squares). The curve shows an IC50 of 7 nM which is in agreement with the IC50 of 8.7 nM±2nM experimentally observed.

We also modify the conductance of the transient outward potassium current in order to create a transmural APD heterogeneity (epicardial and endocardial cells) [10]. This heterogeneity is important in the genesis of physiological ECGs.

2.4 Numerical Implementation

All the simulations presented in this work were run with the open source software package Chaste [6]. Chaste stands for "Cancer, Heart and Soft Tissue simulation environment" and provides an integrated modelling and simulation environment for a wide range of Systems Biology problems including cardiac electromechanical activity. The software can be downloaded from `www.comlab.ox.ac.uk/chaste`.

The Chaste's bidomain finite-element solver is a mature tool in terms of performance and functionality for research in cardiac electrophysiology (see for instance [2]). This is the first time Chaste is used to simulate the electrical activity of the heart embedded in a human body mesh for ECG simulation. Simulations with Chaste are successfully conducted in a wide range of High Performance Computing facilities: from low-end servers to cutting-edge supercomputers like HECToR (UK's high-end computational resource), achieving excellent scalability [11].

Equations (1)-(3) are solved by means of a semi-implicit time discretisation, where the diffusion term is treated implicitly and the reaction term explicitly. For the space discretisation, a finite element method with tetrahedral elements and piecewise linear basis functions was chosen. Chaste's parallelisation is based on the message-passing standard MPI and it uses ParMETIS to ensure optimal domain decomposition. In this work, an 8-way Intel Xeon server with 32GB of memory was used. A shared-memory aware MPI implementation was used to improve intra-node communications. Chaste uses PyCML [12] to generate on-the-fly C++ code from any CellML valid file. This was particularly useful to implement the Grandi model modified to include dofetilide dose/HERG interactions concentrations directly on the CellML file without need of recoding. Chaste also includes the capability of incorporating realistic fibre orientation and heterogeneities in ionic properties in anatomically-based models.

3 Results

In order to simulate the effect of dofetilide on the ECG, we conducted computer simulations of the electrical activity of the heart embedded in the human mesh for two dofetilide doses. The doses considered were [D]=0nM, i.e. control or no drug administration, and [D]=100nM. In these simulations, electrical propagation in the human heart is elicited by stimulation at the apex by imposing a volumic stimulation current I_{stim} of 2ms duration and 80 mAcm^{-3} amplitude. Figure 3 (bottom, right) shows a snapshot of the distribution of the body surface potential (BSP) at time 483ms following application of the stimulus.

Results in Figure 3 (top) show the effect of increasing the dose of dofetilide on an action potential in the human heart and a BSP simulating the ECG recorded at a precordial lead. Drug-induced effects on repolarization properties are often quantified in the literature using APD_{90} at the cellular level (i.e. the difference between the activation time and the time at which the cell reaches 90% of repolarization) and QT interval in the ECG, which is the main biomarker for drug safety [2]. QT interval was also clinically used for assessing the effect of dofetilide on repolarization [13].

Simulations show that the main effect of dofetilide administration is a significant prolongation of QT interval (see Figure 3, top, right), which is in agreement with experimental and clinical results. Dofetilide effects on the action potential and the ECG are due to dofetilide-induced IKr block, which only affects the repolarization phase. Therefore, as expected, no effects are observed during the

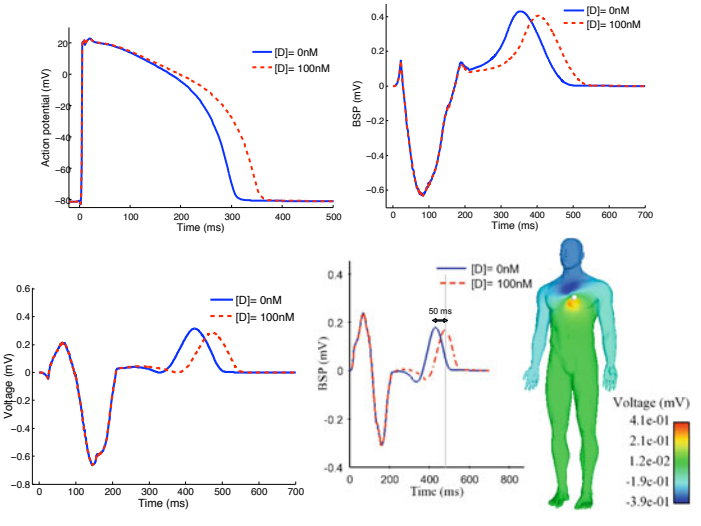

Fig. 3. 3D simulations: Effect of dofetilide on the action potential (top, left) and the body surface potential (top, right). The measurement of the action potential (respectively the BSP) were taken on the heart base (respectively the V2-lead position). Effect of dofetilide on the ECG V3-lead (bottom, left) and on the BSP (bottom, right).

depolarization phase of the action potential and therefore the QRS complex is identical with and without dofetilide. The wide QRS complex observed in our simulations is due to the fact that the ventricles were paced at the apex. Future improvements in the model will include the incorporation of an improved stimulation protocol to simulate realistic activation sequence.

In our simulations, APD_{90} for [D]=0 nM is 290ms, whereas for [D]=100nM, APD_{90} increases by 50ms to 340ms. The effect of introducing dofetilide on ECGs is also remarkable. The potential in V3 ECG leads was obtained and plotted in Figure 3 (bottom, left) for [D] = 0 and 100nM. Both of the leads show significant QT prolongation when drug concentration is increased. The T wave repolarization in the the BSP is delayed by almost 50 ms. This is in accordance with APD prolongation observed in individual nodes. Even though dofetilide induces significant APD_{90} and QT interval, no arrhythmic events such as early after depolarizations are observed in our simulations.

4 Conclusions

In this paper, we presented a computational simulations showing the effect of specific drug doses on the ECG measured on the thorax surface. A combination of state-of-the-art modelling and simulation tools and methodologies are used in this work, which include a finite-element mesh of the human body, a biophysically detailed human bidomain model of cardiac electrophysiological activity, a recently published model of drug/ion channel interactions and an efficient open source software package.

Simulation results are presented showing how increasing the drug dose alters body surface potentials and action potentials. In this study, we focus on the anti-arrhythmic drug dofetilide, which has also been shown to increase the risk of Torsades de Pointes related to long QT syndrome. In accordance with clinical findings, dofetilide results in prolongation of the APD and the QT interval caused by IKr block. In this case, however, no arrhythmic events or early after-depolarizations are observed in our simulations.

The models and simulations presented here constitute a significant step forward towards realistic simulation of drug-induced effects on the ECG. Future model improvements including the stimulation protocol and the cell heterogeneity will be performed to explore the full potential of the methodologies presented here and investigate drug-induced effects on the heart from the ion channel to the ECG. These state-of-the-art methodologies could be a useful tool in the assessment of drug cardiotoxicity and can also be extended to the investigation of the effect of mutations or disease on the ECG.

Acknowledgments

The authors would like to thank Drs Philippe Moireau, Miguel Fernández and Elsie Phé from INRIA Paris-Rocquencourt for their work on the anatomical models and meshes. We are also grateful to Professors Dominique Chapelle and

Jean-Frédéric Gerbeau respectively head of MACS and REO teams in INRIA Paris-Rocquencourt for accepting to provide us with the meshes. This study was supported financially by the European Commission preDiCT grant (DG-INFSO - 224381), abd a UK Medical Research Council Career Development Award (to B.R.).

References

1. Pueyo, E., Husti, Z., Hornyik, T., Baczko, I., Laguna, P., Varro, A., Rodriguez, B.: Mechanisms of ventricular rate adaptation as a predictor of arrhythmic risk. Am. J. Physiol. Heart Circ. Physiol. 298(5), H1577 (2010)
2. Corrias, A., Jie, X., Romero, L., Bishop, M., Bernabeu, M., Pueyo, E., Rodriguez, B.: Arrhythmic risk biomarkers for the assessment of drug cardiotoxicity: from experiments to computer simulations. Philosophical Transactions of the Royal Society A: Mathematical, Physical and Engineering Sciences 368(1921), 3001 (2010)
3. Potse, M., Dubé, B., Vinet, A.: Cardiac anisotropy in boundary-element models for the electrocardiogram. Medical and Biological Engineering and Computing 47(7), 719–729 (2009)
4. Chapelle, D., Fernández, M.A., Gerbeau, J.-F., Moireau, P., Sainte-Marie, J., Zemzemi, N.: Numerical Simulation of the Electromechanical Activity of the Heart. In: Ayache, N., Delingette, H., Sermesant, M. (eds.) FIMH 2009. LNCS, vol. 5528, pp. 357–365. Springer, Heidelberg (2009)
5. Saiz, J., Tena, G., Monserrat, M., Cardona, K., Chorro, J.: Effects of the antiarrhythmic drug dofetilide on transmural dispersion of repolarization in ventriculum. A computer modeling study. IEEE Trans. Biomed. Eng. 1 (2011)
6. Pitt-Francis, J., Pathmanathan, P., Bernabeu, M., Bordas, R., Cooper, J., Fletcher, A., Mirams, G., Murray, P., Osborne, J., Walter, A., et al.: Chaste: a test-driven approach to software development for biological modelling. Computer Physics Communications 180(12), 2452–2471 (2009)
7. George, P., Hecht, F., Saltel, E.: Fully automatic mesh generator for 3d domains of any shape. Impact of Comp. in Sci. ans Eng. 2, 187–218 (1990)
8. Streeter, D., Berne, R., Sperelakis, N., Geiger, S.: Gross morphology and fiber geometry of the heart. Handbook of Physiology, Section 2: The Cardiovascular System 1, 61–112 (1979)
9. Sundnes, J., Lines, G., Cai, X., Nielsen, B., Mardal, K.A., Tveito, A.: Computing the electrical activity in the heart. Springer, Heidelberg (2006)
10. Grandi, E., Pasqualini, F., Bers, D.: A novel computational model of the human ventricular action potential and Ca transient. Journal of molecular and cellular cardiology 48(1), 112–121 (2010)
11. Southern, J., Wilson, N., Bernabeu, M.O., Pitt-Francis, J.: Chaste: Scalable high-performance simulation of cardiac electrophysiology. In: 1st Virtual Physiological Human Conference - VPH 2010 (2010)
12. Cooper, J., McKeever, S., Garny, A.: On the application of partial evaluation to the optimisation of cardiac electrophysiological simulations, pp. 12–20. ACM, New York (2006)
13. Køber, L., Thomsen, P., Møller, M., Torp-Pedersen, C., Carlsen, J., Sandøe, E., Egstrup, K., Agner, E., Videbæk, J., Marchant, B., et al.: Effect of dofetilide in patients with recent myocardial infarction and left-ventricular dysfunction: a randomised trial. The Lancet 356(9247), 2052–2058 (2000)

Slice-Based Combination of Rest and Dobutamine–Stress Cardiac MRI Using a Statistical Motion Model to Identify Myocardial Infarction: Validation against Contrast-Enhanced MRI

Avan Suinesiaputra[1], Alejandro F. Frangi[2], Theodorus A.M. Kaandorp[1], Hildo J. Lamb[1], Jeroen J. Bax[3], Johan H.C. Reiber[1], and Boudewijn P.F. Lelieveldt[1,4]

[1] Dept. of Radiology, Leiden University of Medical Center, Leiden, the Netherlands
[2] Center of Computational Imaging and Simulation Technologies in Biomedicine, Universitat Pompeu Fabra, Barcelona, Spain
[3] Dept. of Cardiology, Leiden University of Medical Center, Leiden, the Netherlands
[4] Dept. of Mediamatics, Delft University of Technology, Delft, the Netherlands

Abstract. This paper presents an automated method for regional wall motion abnormality detection (RWMA) from rest and stress cardiac MRI. The automated RWMA detection is based on a statistical shape model of myocardial contraction trained on slice-based myocardial contours from in ED and ES. A combination of rigid and non-rigid registrations is introduced to align a patient shape to the normokinetic myocardium model, where pure contractility information is kept. The automated RWMA method is applied to identify potentially infarcted myocardial segments from rest–stress MRI alone.

In this study, 41 cardiac MRI studies of healthy subjects were used to build the statistical normokinetic model, while 12 myocardial infarct patients were included for validation. The rest–stress data produced a better separation between scar and normal segments compared to the rest–only data. The sensitivity, specificity and accuracy were increased by 34%, 30%, and 32%, respectively. The area under the ROC curve for the rest–stress data was improved to 0.87 compared to 0.63 for the rest–only data.

1 Introduction

Contractile reserve is an indicator for the presence of hibernating myocardium. This is a state of reduced myocardial contraction as a result of ischaemia, mainly due to coronary heart disease [6]. Myocardium with contractile reserve may improve its function after a coronary revascularization procedure. Distinguishing hibernating myocardium from scar tissue is therefore an important clinical assessment for patients with ischaemic heart disease.

D.N. Metaxas and L. Axel (Eds.): FIMH 2011, LNCS 6666, pp. 267–274, 2011.

The assessment of myocardium with contractile reserve can be performed in two ways. Post-revascularization myocardial contraction improvement can be predicted by comparing wall motion between rest and low-dose dobumatine stress cine MR [11]. Contractile reserve can also be assessed through the extent of infarct transmurality across myocardium, indicated by the presence of the hyperintense areas on CE-MRI [10, 13]. Both assessments have been reported to correlate with each other [8].

In a previous study, we have developed an automated method for regional wall motion analysis (RWMA) from rest cardiac MR data based on a statistical shape model of normal motion [15]. The method was validated against visual wall motion scores. Other approaches have been proposed to automatically detect RWMA [5, 9, 2, 12], but none of these studies have utilized rest and stress data. In this paper, the method was extended to enable direct comparison between rest and stress myocardial shapes. By comparing two contraction patterns from the same patient that are aligned to the same normokinetic model, RWMA probability changes from rest to stress can be obtained and the progression of RWMA probability values towards normal motion can be estimated. The objective of this paper is to investigate whether the integration of stress contraction data improves detection of infarcted myocardium. For validation, infarct areas from CE-MRI were used as a reference.

2 Methodology

The input of the method are four myocardial contours concatenated sequentially in the following order: endocardial at ED (end-diastole), epicardial at ED, endocardial at ES (end-systole), and epicardial at ES. Clockwise equi-angular sampling is performed to create homologous sample points, starting from the inferior intersection point between LV and RV. Sample points from the four contours configuration define a shape of myocardium, i.e.,

$$\begin{aligned} \boldsymbol{x} &= \left[\boldsymbol{x}_{\text{endo}-\text{ED}}, \boldsymbol{x}_{\text{epi}-\text{ED}}, \boldsymbol{x}_{\text{endo}-\text{ES}}, \boldsymbol{x}_{\text{epi}-\text{ES}}\right]^T \\ &= \left[x_1, y_1, \ldots, x_p, y_p\right]^T \end{aligned} \tag{1}$$

where p is the total number of sample points from the four contours. A set of myocardial contours from healthy subjects is used to build a *normokinetic* myocardial shape model.

Two types of registrations are successively used: rigid Procrustes alignment [3] and thin-plate spline warping [1]. The Procrustes alignment eliminates variations among different subjects induced by cardiac position, orientation and isotropic scale (see Fig. 1(b)). The thin-plate spline (TPS) warping eliminates shape variations at ED to force all contractions to start from the same shape (Fig. 1(c)). Additional TPS warping is performed to remove epicardial shape variations caused by non-contraction movement (see Fig. 1(d)). After the registration steps, only shape variations at ES endocardial exist and a linear generative model can be constructed as follows

$$\boldsymbol{x} = \hat{\boldsymbol{x}} + \boldsymbol{\Phi}\boldsymbol{b} \tag{2}$$

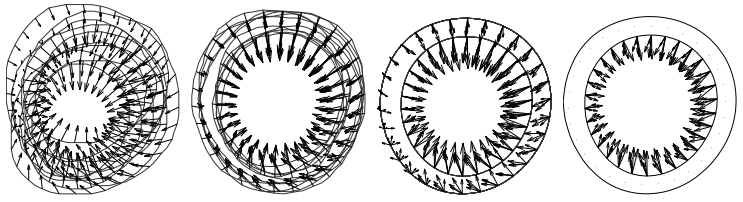

Fig. 1. Registration steps with 5 control subjects: (a) raw input contours, (b) post Procrustes alignment, (c) post first TPS warping, and (d) post second TPS warping. Arrows denote displacement vectors of sample points from ED to ES.

where $\hat{\boldsymbol{x}} \in \mathbb{R}^{2p}$ is the mean control group shape, $\boldsymbol{\Phi} \in \mathbb{R}^{2p \times m}$, $m < 2p$ is a component matrix, and $\boldsymbol{b} \in \mathbb{R}^m$ is the shape parameterization vector. The component matrix is estimated by using Independent Component Analysis [7]. During patient shape registration to the normokinetic model, the mean shape $\hat{\boldsymbol{x}}$ is used as the target shape. The $\boldsymbol{\Phi}$ and $\boldsymbol{b}$ components are used to estimate RWMA density functions of the normokinetic model.

RWMA density functions are estimated on each independent component by using a weighted non-parametric kernel density estimation method. Let U_k be a random variable of coefficient values at kth independent component. The kth RWMA density function is given as follows

$$f_{U_k}(u_k) = \frac{1}{|\boldsymbol{\phi}_k| N h} \sum_{i=1}^{N} G\left(\frac{u_k - \boldsymbol{b}_{i,k}\phi_k}{\phi_k h}\right) \tag{3}$$

where $k = 1, \ldots, m$, N is the number of healthy subjects, $G : \mathbb{R} \rightarrow \mathbb{R}$ is a Gaussian kernel function, $\boldsymbol{b}_{i,k}$ is the kth element of the shape parameterization vector from the ith subjects, ϕ_k is the corresponding kth row of $\boldsymbol{\Phi}$ and h is the kernel bandwidth, which is automatically estimated by using the Sheather-Jones solve-the-plugin method [14]. By the statistical independency assumption, the joint density function for each sample point on a myocardial contour can be estimated by a series convolution of $f_{U_k}(u_k)$ as follows

$$f_{W_i}(w_i) = f_{U_1}(u_1) * f_{U_2}(u_2) * \ldots * f_{U_m}(u_m) \tag{4}$$

for $i = 1, \ldots, p$ and W_i is a random variable defined for landmark point i.

Equation 4 creates p density functions from the control group. Before applying Eq. 4 to a patient shape, the same registration steps (Fig. 1) are applied to the patient. For each patient, there are two RWMA evaluations: rest and stress RWMA probability values. Let $P_r^{(i)}$ and $P_s^{(i)}$ be RWMA probability values for rest and stress, respectively, evaluated with Eq. 4 at ith sample point. The normalized RWMA differences between $P_r^{(i)}$ and $P_s^{(i)}$ are defined as follows

$$\Delta P_{r \rightarrow s}^{(i)} = \frac{P_r^{(i)} - P_s^{(i)}}{1 + \max\left\{P_r^{(i)}, P_s^{(i)}\right\}} \ . \tag{5}$$

By considering P_r as baseline, we can define a progression of normokinetic probability value from rest to stress, which is given by

$$P^{(i)}_{r\to s} = \left(1 - P^{(i)}_r\right) + \Delta P^{(i)}_{r\to s} \quad . \tag{6}$$

$P_{r\to s}$ indicates the probability of a more normal contraction in stress compared to rest, while P_r and P_s denote the probability of abnormal wall motion at rest and stress, respectively. This means that a higher value of $P_{r\to s}$ shows a higher chance of a myocardial segment to improve its contraction function in stress, indicating viable myocardium.

3 Experimental Results

To build the normokinetic model, 41 healthy subjects (control group) were voluntarily enrolled in a cardiac MRI session. For the patient group, we selected 12 patients suffering from myocardial infarctions, confirmed by the presence of scar tissue in CE-MRI. Baseline characteristics are shown in Table 1. Short-axis MRI from healthy subjects, patients at rest and patient at stress were analyzed on three following slices: apex, mid-ventricle and base. Myocardial contours were drawn manually by an expert by using the MR Analytical Software System (MASS, v5.0, Medis, Leiden, the Netherlands) [4].

Figure 2 shows the comparison of rest RWMA (P_r) and stress RWMA (P_s) profiles of a patient. High abnormal wall motion probability values on segment S10 and S11 correlate well with the myocardial contours at ED and ES. The RWMA profile lines in Fig. 2(c) and Fig. 2(f) also show similar patterns. There

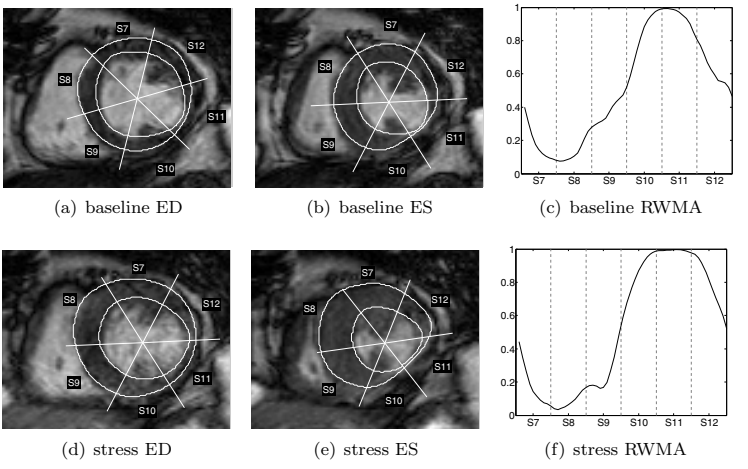

(a) baseline ED (b) baseline ES (c) baseline RWMA

(d) stress ED (e) stress ES (f) stress RWMA

Fig. 2. An example of RWMA probability values from baseline (top row images) and stress (bottom row images) MR images. This example is taken from mid-ventricular level (segments S7–S12).

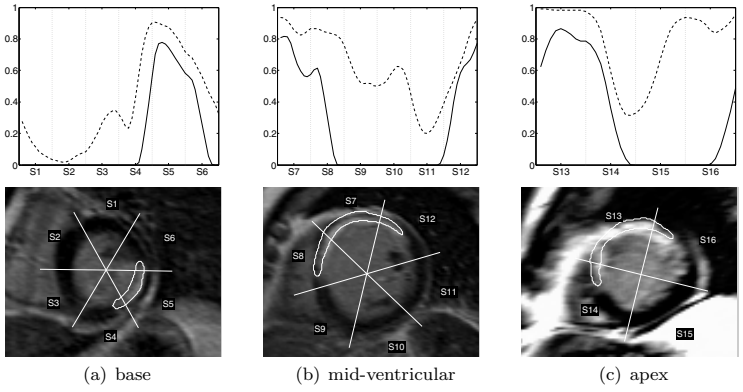

(a) base (b) mid-ventricular (c) apex

Fig. 3. Visual comparisons of $P_{r\to s}$ profile lines (top rows) and their corresponding CE-MR images (bottom rows). In the top figures, solid lines are infarct transmurality (TE) and the dashed lines are $P_{r\to s}$ values.

Table 1. Patient and control groups statistics

	Patients	*Controls*
Subjects	12	41
Males/females	12/0	30/11
Ejection fraction (%)	44.85 (21.30)^R	67.91 (11.13)
	41.40 (17.23)^S	
Stroke volume (ml)	117.62 (73.87)^R	105.04 (32.16)
	82.44 (32.73)^S	

R=rest, S=stress

are no significant changes from rest to stress shown in Fig. 2, which indicate no functional improvements at stress.

To compare between rest–only and rest–stress data, CE-MRI patient data were included in this study to serve as reference standard for the presence of scar. Scar tissue areas, which appeared hyperintense on CE-MRI, were delineated by an expert. Infarct transmurality or transmural extent (TE) was calculated by using a set of equi-angular lines (*chords*) crossing perpendicular to the myocardium. TE is defined as the percentage of a section on the chord that is inside a scar tissue area. If TE $\geq 1\%$, then a myocardial segment is considered as a scar tissue segment. Otherwise it is considered as a normal segment. Figure 3 shows the similarity between TE and $P_{r\to s}$ on different slice levels.

In terms of discriminating between normal and scar segments, the combined rest–stress RWMA method performed better than rest–only RWMA method. This is shown in Fig. 4. The discrepancies between normal and scar tissue groups were more pronounced when stress data was integrated. Table 2 shows the performance of the RWMA methods to detect scar tissues. The area under the ROC curve value as shown in Fig. 5 increased from 0.63 (rest–only data) to 0.88

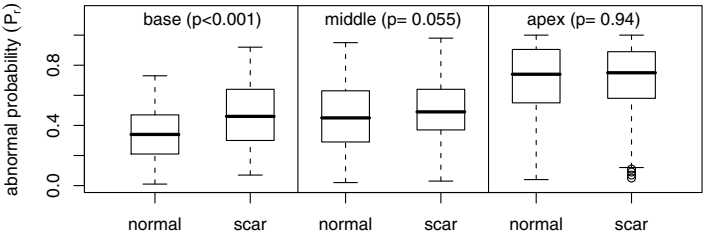

(a) rest only

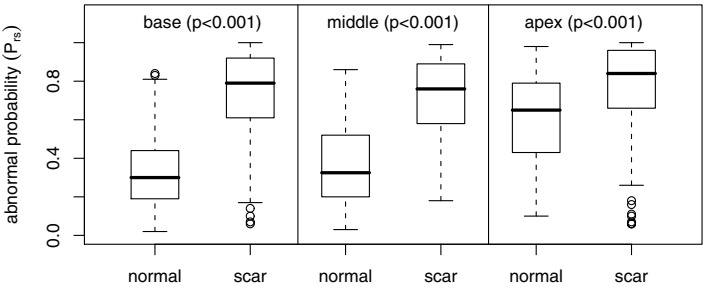

(b) rest-stress combination

Fig. 4. Comparison of RWMA probability value distributions between rest–only data (a) and the combined rest–stress data (b), both from scar and non-scar (normal) segment groups for each slice model. Unpaired t-tests were performed with 99% confidence level to get the p-values.

Table 2. Classification performance for detecting scar tissue segments

Data	Sensitivity	Specificity	Accuracy	AUC
rest–only	0.58	0.61	0.60	0.63
rest–stress	0.78	0.79	0.79	0.87

(rest–stress data). The sensitivity, specificity and accuracy improved by 34%, 30% and 32%, respectively (see Fig. 5).

4 Discussion

When P_r and P_s values were compared directly, similar patterns were revealed (see Fig. 2). Myocardial contraction at rest and stress from the same subject are definitely different as shown in Fig. 2(a), (b), (d) and (e), but the RWMA profile lines between Fig. 2(c) and (f) show a stark similarity. This indicates that our method to register rest and stress patient shapes correctly captures the necessary myocardial contraction information without the influence of non-contraction variations, such as individual position, orientation, size, and the extent of myocardial shape relative to the initial myocardium.

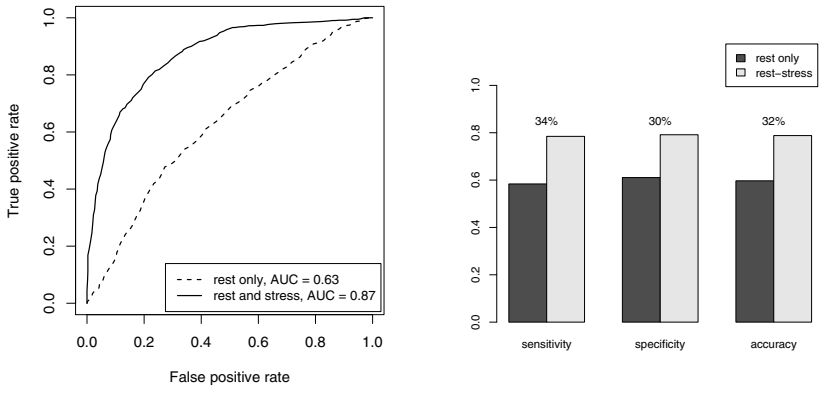

Fig. 5. The method's performance comparison between rest–only and the combined rest–stress data

In this study, we compared our method with infarct transmurality from CE-MRI. Although this comparison is limited to scar tissue segments, it is sufficient to demonstrate the advantage of adding stress data into regional wall motion analysis. From Fig. 4, the difference between the normal and scar segment groups is significantly wider when stress data is combined with rest data. Unpaired t-tests confirm this finding. All slices for rest–stress data show significant differences with $p < 0.001$ (99.9% confidence interval), while only the basal slice for rest–only data shows the same significant difference. The classification performance of the automated rest–stress RWMA method is also higher than rest–only data, as shown in Table 2.

For the RWMA evaluation, rest–only data is already sufficient as has been presented in [15]. However, when stress data is available, the combined rest–stress data will improve the RWMA evaluation. This study has demonstrated that the combined rest–stress RWMA asssessment method classified myocardial segments with infarction much better.

This study also shows the capability of the proposed method for a longitudinal wall motion comparison, such as a disease progression over time. The multi-time point comparison can be analyzed in the same way as the rest and stress data comparison. Further research is still needed to allow realize this, and to apply the proposed method in clinical practice.

References

[1] Bookstein, F.L.: Principal Warps: Thin-plate splines and the decomposition of deformations. IEEE Trans. Pattern Anal. Mach. Intell. 11(6), 567–585 (1989)
[2] Caiani, E.G., Toledo, E., et al.: Automated interpretation of regional left ventricular wall motion from cardiac magnetic resonance images. J. Cardiovasc Magn. Reson. 8(3), 427–433 (2006)
[3] Dryden, I.L., Mardia, K.V.: Statistical shape analysis. John Wiley & Sons, Inc., Chichester (1998)

[4] van der Geest, R.J., Buller, V.G., et al.: Comparison between manual and semi-automated analysis of left ventricular volume parameters from short-axis MR images. J. Comput. Assist. Tomogr. 21(5), 756–765 (1997)
[5] Herz, S.L., Ingrassia, C.M., et al.: Parameterization of left ventricular wall motion for detection of regional ischemia. Ann. Biomed. Eng. 33(7), 912–919 (2005)
[6] Heusch, G., Schulz, R., Rahimtoola, S.H.: Myocardial hibernation: a delicate balance. Am. J. Physiol. Heart Circ. Physiol. 288(3), H984–H999 (2005)
[7] Hyvärinen, A., Karhunen, J., Oja, E.: Independent Component Analysis. John Wiley & Sons, Inc., Chichester (2001)
[8] Kaandorp, T.A.M., Bax, J.J., Schuijf, J.D., et al.: Head-to-head comparison between contrast-enhanced magnetic resonance imaging and dobutamine magnetic resonance imaging in men with ischemic cardiomyopathy. Am. J. Cardiol. 93(12), 1461–1464 (2004)
[9] Kachenoura, N., Redheuil, A., et al.: Evaluation of regional myocardial function using automated wall motion analysis of cine MR images: Contribution of parametric images, contraction times, and radial velocities. J. Magn. Reson. Imaging 26(4), 1127–1132 (2007)
[10] Kim, R.J., Wu, E., Rafael, A., et al.: The use of contrast-enhanced magnetic resonance imaging to identify reversible myocardial dysfunction. N. Engl. J. Med. 343(20), 1445–1453 (2000)
[11] Mahrholdt, H., Klem, I., Sechtem, U.: Cardiovascular MRI for detection of myocardial viability and ischaemia. Heart 93(1), 122–129 (2007)
[12] Qazi, M., Fung, G., et al.: Automated heart abnormality detection using sparse linear classifiers. IEEE Eng. Med. Biol. Mag. 26(2), 56–63 (2007)
[13] Saraste, A., Nekolla, S., Schwaiger, M.: Contrast-enhanced magnetic resonance imaging in the assessment of myocardial infarction and viability. J. Nucl. Cardiol. 15(1), 105–117 (2008)
[14] Sheather, S.J., Jones, M.C.: A reliable data-based bandwidth selection method for kernel density estimation. J. R. Stat. Soc. Series B Stat. Methodol. 53(3), 683–690 (1991)
[15] Suinesiaputra, A., Frangi, A.F., Kaandorp, T.A.M., Lamb, H.J., Bax, J.J., Reiber, J.H.C., Lelieveldt, B.P.F.: Automated detection of regional wall motion abnormalities based on a statistical model applied to multislice short-axis cardiac MR images. IEEE Trans. Med. Imaging 28(4), 595–607 (2009)

Shape Analysis of the Left Ventricular Endocardial Surface and Its Application in Detecting Coronary Artery Disease

Anirban Mukhopadhyay[1], Zhen Qian[2], Suchendra Bhandarkar[1], Tianming Liu[1], and Szilard Voros[2]

[1] Department of Computer Science, The University of Georgia, Athens, GA 30602-7404, USA
[2] Piedmont Heart Institute, Atlanta, GA 30309, USA

Abstract. Coronary artery disease is the leading cause of morbidity and mortality worldwide. The complex morphological structure of the ventricular endocardial surface has not yet been studied properly due to the limitations of conventional imaging techniques. With the recent developments in Multi-Detector Computed Tomography (MDCT) scanner technology, we propose to study, in this paper, the complex endocardial surface morphology of the left ventricle via analysis of Computed Tomography (CT) image data obtained from a 320 Multi-Detector CT scanner. The CT image data is analyzed using a 3D shape analysis approach and the clinical significance of the analysis in detecting coronary artery disease is investigated. Global and local 3D shape descriptors are adapted for the purpose of shape analysis of the left ventricular endocardial surface. In order to study the association between the incidence of coronary artery disease and the alteration of the endocardial surface structure, we present the results of our shape analysis approach on 5 normal data sets, and 6 abnormal data sets with obstructive coronary artery disease. Based on the morphological characteristics of the endocardial surface as quantified by the shape descriptors, we implement a Linear Discrimination Analysis (LDA)-based classification algorithm to test the effectiveness of our shape analysis approach. Experiments performed on a strict leave-one-out basis are shown to achieve a classification accuracy of 81.8%.

Keywords: Ventricular endocardial surface, cardiovascular CT, shape analysis.

1 Introduction

Coronary artery disease or *atherosclerosis* is the most common cause of morbidity and mortality worldwide. Atherosclerosis eventually leads to formation of plaques that cause arterial stenosis and chronic myocardial ischemia and in some cases, acute myocardial infraction. Anatomic and imaging studies have revealed that, instead of a simple and smooth surface, the endocardial surface of the heart ventricle is composed of a complex structure of *trabeculae carneae*, which are small muscular columns that arise naturally from the inner surface of the ventricles. Alterations in the ventricular trabeculation have been found to closely associate with some cardiovascular diseases,

D.N. Metaxas and L. Axel (Eds.): FIMH 2011, LNCS 6666, pp. 275–283, 2011.

such as myocardial noncompaction disease [1] and hypertrophy [2]. However, due to the limitations in the spatial resolution of conventional *in-vivo* imaging techniques, very few research studies have been undertaken to study the ventricular trabeculation at a detailed level, and investigate the relationship between structural changes in ventricular trabeculation and certain cardiac pathologies.

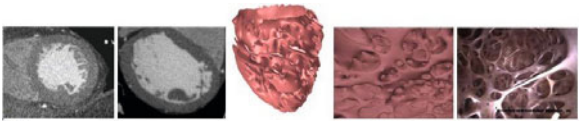

Fig. 1. Illustration of endocardial surface reconstruction using high-resolution CT data, and the comparison with an *ex vivo* picture of a live beating heart. (a, b) are two sample images of the CT data used in this study. (c) depicts the endocardial surface segmentation results for a whole left ventricle. (d) is an enlarged area near the reconstructed ventricular apex. Notice its surprising similarity with the apical structure in the *ex vivo* picture of a live beating heart (e) [10].

Owing to the recent developments in cardiovascular imaging using Multi-Detector Computed Tomography (MDCT) scanners, it is possible for contrast-enhanced Computed Tomography (CT) images to achieve an isotropic image resolution of less than 0.5mm. As shown in Fig. 1, it is possible to observe the detailed structure of the ventricular trabeculation using such high-resolution CT images. In [3], a deformable model-based segmentation method was developed to reconstruct a very detailed anatomy of the left ventricle. In [4], by using high-resolution CT, papillary muscles were found to be attached to the *trabeculae carneae*, but not directly to the myocardium. These studies suggest that a closer look at the detailed trabecular structure may lead to new understandings of the cardiac anatomy, function and pathology.

With the introduction of the new 320-MDCT scanner, we are able to scan the heart in a single heart beat, so as to eliminate the artifacts introduced by misalignment between cardiac segments that are acquired during different heart beats on conventional 64- or 256-MDCT scanners. The endocardial surface structure recovered from the image data acquired with a 320-MDCT scanner would be potentially more accurate and reliable.

In this paper, we have developed an image segmentation and shape analysis framework to study the endocardial surface of the left ventricle from contrast-enhanced CT images acquired using a 320-MDCT scanner. In order to handle the complex topological changes of the endocardial surface, we employed a 3D level set-based approach for segmentation of the endocardial surface. Since the trabecular structure varies in different locations of the ventricle, we further divided the endocardial surface of the left ventricle into 17 segments according to the standard American Heart Association (AHA) model [5] for more localized shape analysis.

In each of the 17 ventricular segments, we adapted two different descriptors for analysis of the shape of the endocardial surface: a D2 descriptor [6] and a shape index described in [7] [8]. These two shape descriptors describe the shape patterns of the myocardial surface in terms of either global or local details. In order to show the

effectiveness of the shape analysis based on the above shape descriptors, we collected 11 MDCT data sets obtained from 6 abnormal hearts of subjects with obstructive coronary heart disease, and 5 normal hearts from healthy subjects. We employed our segmentation and shape analysis procedures on each data set to compute a characteristic shape matrix for the left ventricle. A Linear Discriminant Analysis (LDA)-based classifier [11] was implemented to classify the abnormal hearts from the normal ones using the characteristic shape matrices on a strict leave-one-out basis. Experimental results showed that 9 out 11 data sets were classified correctly, which is a very promising result.

The remainder of the paper is organized as follows. In Section 2, we describe our segmentation and shape analysis methods in detail. In Section 3, we present experimental results on the previously described MDCT data sets. In Section 4, we conclude the paper with a brief discussion about our approach and propose some directions for future work.

2 MDCT Image Segmentation and Ventricular Shape Analysis

2.1 Left Ventricle Segmentation and Meshing

There are three types of *trabeculae carneae* morphologies: some are attached along their entire length to the ventricular wall and form prominent ridges; some are fixed at their extremities but free in the middle; and others connect the root of the papillary muscles and the ventricular wall. Consequently, the endocardial surface of the left ventricle does not possess a simple topology. In order to adapt to the topological changes caused by the complex structure of the trabeculation, we adapted a 3D level set-based approach to segment the endocardial surface of the left ventricle. In order to suppress noise and still retain the shape-defining edges in the CT image data, we employed a median filter-based denoising procedure on the 3D CT data prior to segmentation. The size of the median filter was empirically set to 7×7 based on our CT data set. The level set-based segmentation procedure without reinitialization as proposed by Li et al. [9] was applied to the median-filtered 3D image data set. The subsequent denoising via the mean face normal filtering procedure proposed by Zhang et al. [12] was used to obtain the smooth shape of the myocardial surface of the left ventricle.

2.2 Shape Description

The next step after segmentation and meshing of the raw input CT image data is to characterize the shape of the left ventricle. We have considered two primary shape descriptors in this paper. One is relatively straight forward, i.e., the D2 shape descriptor proposed by Osada et al. [6]. The other is the 3D shape index first introduced by Koenderink [7] and later modified by Zaharia and Preteux [8].

The D2 shape descriptor is a global shape descriptor. It is the shape signature of a 3D object represented as a probability distribution. The probability distribution is obtained via sampling of a pre specified shape function that measures a geometric property of the 3D shape. The shape function for D2 is the distance between two random points on the 3D surface of the object. In the context of our problem, two

large random samples of vertices are generated from the mesh-based representation and the distance between each pair of vertices (where each vertex in the pair belongs to a different sample) is calculated. The underlying idea is to transform the shape into a parameterized probability distribution function where the probability distribution is deemed to represent the global shape.

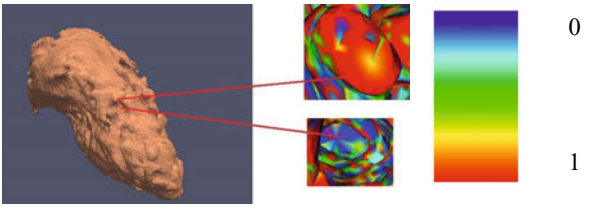

Fig. 2. Illustration of the accuracy of shape index. The peak is shown in red with shape index value close to 1 whereas the pit of just beside the peak has value close to 0 and shown in blue.

The second shape descriptor, i.e., the *shape index*, describes the local shape of the mesh based on the surface curvature computed in a local neighborhood of the surface point (Fig. 2). The shape index of a surface point is defined as a function of the two local principal surface curvatures. Let p be a point on a 3D surface and let the principal curvatures associated with point p be denoted by k_p^1 and k_p^2 where, $k_p^1 > k_p^2$. The shape index at point p, denoted by I_p, is defined as:

$$I_p = \frac{1}{2} - \frac{1}{\Pi}\arctan\left(\frac{k_p^1 + k_p^2}{k_p^1 - k_p^2}\right)$$

The shape index is a local geometric attribute of the 3D surface. The values of the shape index lie in the interval [0, 1]. The shape index value is not defined for planar surfaces. The shape index provides a scale for representing basic elementary shapes such as *convex, concave, rut, ridge* and *saddle* [8]. The shape index value is invariant to scale and 3D rigid-body transformation (i.e., translation and rotation) in Euclidean space.

The shape of the myocardial surface is observed to exhibit both, global structure as well as detailed local structure. Since there have been no previous studies detailing which of the shape properties (local or global) convey more valuable clinical information, we considered both local and global shape descriptors for this study.

2.3 Data Preparation

In order to ensure a better comparison between different analysis methods, the AHA has been published recommendations for standardized myocardial segmentation [5]. In this paper, we adapted an AHA 17-segment model [5] to divide the left ventricle into 17 segments for better localized shape analysis. The long axis of the left ventricle was determined followed by the division of the left ventricle into 4 main segments,

i.e., *apex, apical, mid cavity* and *basal* along the longitudinal orientation. Division of the endocardial surface in the short axis view was tackled by exploiting knowledge of the cardiac anatomy. Three landmark points were considered across the septum based on which the apical was subdivided into four segments and the mid cavity and basal into six segments. Finally, each left ventricular endocardial surface was divided into 17 segments per the standard AHA model [5].

3 Experimental Results

The proposed methods for segmentation, meshing and shape description were employed on 11 MDCT data sets consisting of 6 data sets from cardiac patients and 5 from normal subjects. In the case of the cardiac patients, incidence of single-vessel or multi-vessel obstructive disease was found in the four major coronary arteries using X-ray angiography, which was further confirmed by myocardial perfusion and fractional flow reserve tests.

Each of the cardiac patients and normal subjects was subject to a contrast-enhanced CT scan on a 320-MDCT scanner using a standard CT angiography protocol with ECG gating. The resulting images were reconstructed at 75% in the R-R cycle to ensure that all data were acquired during the same cardiac phase with minimal ventricular motion. This ensures that the subsequent shape analysis is minimally affected by the cardiac motion. All topologically correct and geometrically accurate data are generated via the segmentation method described in Section 2.1. The atria and valves were removed from the segmented ventricular meshes.

3.1 Segmentation Results

The result of the segmentation of the left ventricle is shown in Fig. 3. It can be easily seen that the segmented result is reasonably good with the spatial details of the myocardial surface left intact although the noise in the data is substantially filtered. Fig. 4 shows the division of the left ventricle into the septal and free wall halves. We observe that the spatial distribution of the trabeculation varies with location within the ventricle; the free wall tends to have more trabeculation whereas the septum tends to

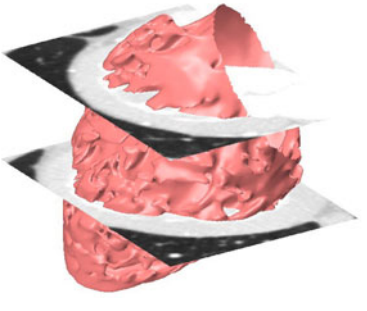

Fig. 3. Illustration of the segmentation result and accuracy of the method described in Section 2.1

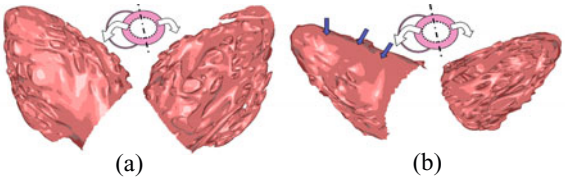

Fig. 4. The left ventricular endocardial surface segmentation meshes were dissected into two halves, the septum (on the left) and the free wall (on the right). (a) is from a normal heart, and (b) is from a diseased heart. In a normal heart, the trabeculation is seen to vary with location; the septum is smoother than the free wall. In the diseased heart, notice the loss of trabeculation in the septal area indicated by the blue arrows. This loss of trabeculation may be associated with obstructive disease in the left anterior descending artery, which supplies blood to the anteroseptal heart wall.

be smoother, which is the precise rationale for using the AHA 17-segment model to perform a localized shape analysis. Furthermore, by using the proposed segmentation approach, it is possible to even visually distinguish the difference in trabeculation between normal and diseased hearts. These results are sufficient to prove that the proposed segmentation method is fairly standard and may work well for subsequent quantitative shape analysis.

3.2 Shape Description Results

The shape description results are shown as histograms in Fig. 5 for the D2 shape descriptor and shape index. Each histogram has 20 bins in the horizontal direction in the range [0, 1] and corresponding number of vertices in the vertical direction. The normal hearts are represented in red and the diseased hearts in blue for both the diagrams. Fig. 5 clearly shows that information derived from the D2 shape descriptor is inadequate for distinguishing between normal and diseased hearts. This is because

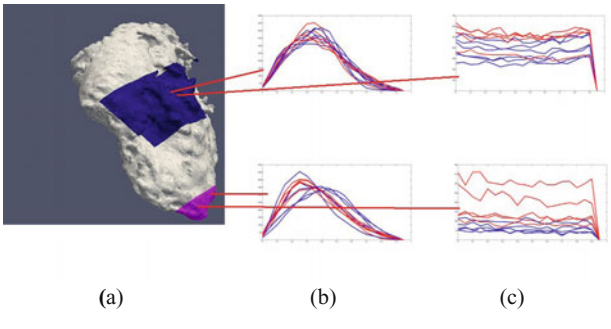

Fig. 5. Illustration to compare the results generated by D2 (b) and the shape index (c) for the ventricular segment 11 (blue) and ventricular segment 17 (pink) of the left ventricle (a). The normal left ventricles are represented in red and the diseased ones are represented in blue in the histogram.

the D2 shape descriptor is a global shape descriptor that does not capture the local spatial details of the underlying shape. On the other hand, the shape index is a local shape descriptor which successfully captures the local shape details. In Fig. 6, the difference in shape between the normal and diseased hearts is clearly visible in 17×20 dimensions (17 segments per left ventricle×1 histogram per segment×20 bins per histogram) which in turn confirms that for the type of application considered in this paper, local shape descriptors convey much more information than global ones.

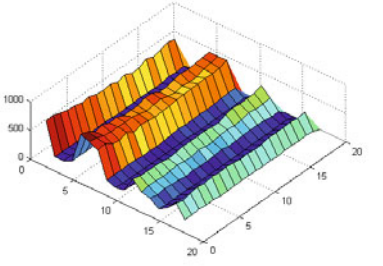

(a)

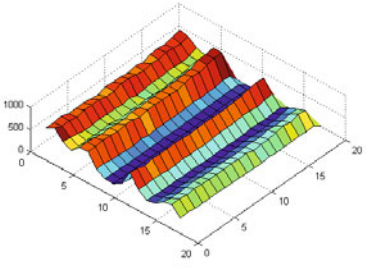

(b)

Fig. 6. Illustration to compare the results generated by the shape index for a diseased (a) vs. normal (b) left ventricular endocardial surface in 17×20 dimensions. The difference is clearly visible.

3.3 Classification Accuracy

In the appearance-based recognition paradigm, Linear Discriminant Analysis (LDA) [11] is a natural choice for classification. A typical two-class classifier can learn to separate the normal training samples from the abnormal samples by finding a proper projection function. LDA is a popular classification method that maximizes the between-class scatter defined by $\sum_{j=1}^{c}(\mu_j-\mu)(\mu_j-\mu)^T$ and minimizes the within-class scatter defined by $\sum_{j=1}^{c}\sum_{i=1}^{N_j}(x_i^j-\mu_j)(x_i^j-\mu_j)^T$ where μ is the mean of all classes, x_i^j is the ith sample of the jth class, μ_j is the mean of jth class, N_j is the number of

samples in the jth class and c is the number of classes. LDA projects the $17 \times 20 = 340$-dimensional feature vector to a subspace of c-1 dimensions. Since in this application, c = 2 (i.e., normal and diseased), the 340-dimensional vector was projected onto a 1D scalar. Classification was done using a k-nearest neighbor (k-NN) scheme in the 1D subspace. We empirically tested the classifier for k = 1 and 3, and obtained the same result: 9 out of 11 samples were classified correctly. Table 1 shows the confusion matrix where 5 out of 6 diseased hearts and 4 of the 5 normal hearts were diagnosed correctly.

Table 1. Confusion matrix to illustrate the prediction accuracy

	Predicted Diseased	Predicted Normal
Actual Diseased	5	1
Actual Normal	1	4

4 Disccussion and Conclusions

To the best of our knowledge, this paper is amongst the earliest works that studies the endocardial surface structure of the left ventricle using a shape analysis approach with high-resolution CT input data, and demonstrates its potential predictive/diagnostic value for coronary artery disease. We can speculate that the success of our approach may lead to some functional implications. The presence of obstructive coronary arterial disease and perfusion defects in patients reveals ischemia in the corresponding regions of the myocardium. The ischemic myocardium loses contractibility and has a tendency to get stiffer and be pushed outward by the high ventricular blood pressure. Such changes in the underlying myocardium may be the reason for changes in the trabeculation pattern and endocardial surface morphology that we have discovered in our analysis. This association between the cardiac shape features (i.e., cardiac morphology) and cardiac functionality will be explored in our future work.

References

[1] Goo, S., Joshi, P., Sand, G., Gerneke, D., Taberner, A., Dollie, Q., LeGrice, I., Loiselle, D.: Trabeculae Carneae as Models of the Ventricular Walls: Implications for the Delivery of Oxygen. Jour. Gen. Physiology 134(4), 339–350 (2009)

[2] Agmon, Y., Connoll, H.M., Olson, L.J., Khandheria, B.K., Seward, J.B.: Noncompaction of the Ventricular Myocardium. Jour. Amer. Soc. Echocardiography 12(10), 859–863 (1999)

[3] Chen, T., Metaxas, D.N., Axel, L.: 3D Cardiac Anatomy Reconstruction Using High Resolution CT Data. In: Barillot, C., Haynor, D.R., Hellier, P. (eds.) MICCAI 2004. LNCS, vol. 3216, pp. 411–418. Springer, Heidelberg (2004)

[4] Axel, L.: Papillary Muscles Do Not Attach Directly to the Solid Heart Wall. Circulation 109, 3145–3148 (2004)

[5] Cerqueira, M.D., Weissman, N.J., Dilsizian, V., Jacobs, A.K., Kaul, S., Laskey, W.K., et al.: Standardized Myocardial Segmentation and Nomenclature for Tomographic Imaging of the Heart. Circulation 105, 539–542 (2002)

[6] Osada, R., Funkhouser, T., Chazelle, B., Dobkin, D.: Shape Distributions. ACM Trans. Graphics 21(4), 807–832 (2002)
[7] Koenderink, J.: Solid Shape. The MIT Press, Cambridge (1990)
[8] Zaharia, T., Preteux, F.: 3D Shape-based Retrieval Within the MPEG-7 Framework. In: Proc. SPIE Conf. Nonlinear Image Processing and Pattern Analysis XII, vol. 4304, pp. 133–145 (2001)
[9] Li, C., Xu, C., Gui, C., Fox, M.D.: Level Set Evolution Without Re-initialization: A New Variational Formulation. In: Proc. IEEE Conf. CVPR 2005, vol. 1, pp. 430–436 (2005)
[10] Medtronic Inc. The Visible Heart webpage, http://www.visibleheart.com/index.shtml
[11] Martinez, A.M., Kak, A.C.: PCA versus LDA. IEEE Trans. Pattern Analysis and Machine Intelligence 23(2), 228–233 (2001)
[12] Zhang, Y., Hamza, A.B.: Vertex-based Diffusion for 3-D Mesh Denoising. IEEE Trans. Image Processing 16(4), 1036–1045 (2007)

Recovering Endocardial Walls from 3D TEE

Philippe Burlina[1,2], Ryan Mukherjee[1], Radford Juang[1], and Chad Sprouse[1]

[1] Johns Hopkins University Applied Physics Laboratory
philippe.burlina@jhuapl.edu
[2] Johns Hopkins University Department of Computer Science

Abstract. We describe a method for recovering the left intracardiac cavities from 3D Transesophageal Echocardiography (3D TEE). 3D TEE is an important modality for cardiac applications because of its ability to do fast and non-ionizing 3D imaging of the left heart complex. Segmentation based on 3D TEE can be used to characterize pathophysiologies of the valve and myocardium, and as input to patient-specific biomechanical models and preoperative planning tools. The segmentation employed here is based on a dynamic surface evolution. This is performed under a growth inhibition function that incorporates information from several sources including k-means clustering, 3D gradient magnitude, and a morphological structure tensor intended to locate the mitral valve leaflets. We report experiments using intraoperative 3D TEE data, showing good agreement between the segmented structures and ground truth.

1 Introduction

Segmentation of left heart endocardial wall structure has a number of applications in diagnostics, modeling, simulation and training, or as a primitive to other 3D ultrasound image analysis modules [1–3]. It is useful for performing preoperative planning, and for guiding minimally-invasive beating heart interventions, which are of interest as an alternative to procedures requiring cardiopulmonary bypass. 3D TEE is an important cardiac imaging modality to infer endocardial structure. It has a number of advantages compared to other 3D imaging modalities: it has a small form factor, is non-ionizing, has lower cost, it can be used pre- and intra-operatively, and it allows for interactive exploration and diagnostics. Another important advantage of 3D TEE for cardiac applications, is its speed, which is unmatched by other modalities. Sequences can be acquired at rates from 20 Hz up to over 60 Hz. This capability is essential when considering the very fast motion of some left heart anatomical components such as the mitral valve. Unfortunately 3D echocardiography has certain shortcomings which makes segmentation based on this modality a challenging endeavor. These include lower spatial resolution and imaging artifacts such as obscuration, speckle noise, and misalignments. Some 3D TEE platforms need to acquire and recombine subsections of the TEE data cube obtained over several heart cycles using a breath hold protocol to achieve both high spatial and temporal resolutions. When the patient exhibits arrhythmia the stitching of the TEE data cube subsections may lead to misalignment artifacts.

D.N. Metaxas and L. Axel (Eds.): FIMH 2011, LNCS 6666, pp. 284–293, 2011.

There are many approaches to the segmentation and recovery of cardiac structures. Recent surveys providing an overview of ultrasound segmentation methods include [4–6]. Among these methods, segmenting the structure of the left ventricle remains a primary focus. Techniques used for left ventricle segmentation include the following: (a) active models and model matching (active appearance models (AAMs), active shape models (ASMs), and their variants) [7–9]; (b) evolving curves and surfaces (e.g., active contour, level set, marching cube) [10–16]; (c) watershed [17]; (d) graph cuts [18]; (e) thresholding and morphology [19]; and (f) random forest classification [20].

Active models, such as AAMs and ASMs, most often require a user-generated model for training, which can take the form of a manually segmented point cloud. By finding an optimal set of parameter values for the user-generated model, it can be used to match image intensity values in a testing set. Mitchell et al. formulated a ventricle segmentation method that uses a combination of AAMs and ASMs to prevent the method's convergence towards local minima and automate the initialization process, which had previously been a major disadvantage to AAM-based methods [7]. However, that method was designed for 2D data with low amounts of noise (magnetic resonance imagery). We argue that the initialization method used might be challenged with more noisy ultrasound data and that rapid manual initialization might be more robust than automated methods when dealing with irregular and/or diseased hearts and atypical TEE viewpoints.

Evolving curves and surfaces simply requires an initial seed point or surface. Manual seed points can be rapidly entered by a physician to segment a variety of structures from atypical or unexpected views of the structures. The initial seeds are iteratively evolved (outward or inward) according to an energy function until some constraint or convergence criteria is met. Identifying a robust energy function that is also adequate for the TEE modality is an important task.

Less versatile and noise sensitive watershed algorithms treat the intensity values of images as valleys and peaks. Initial seed points are assigned labels, then valleys and peaks are "flooded" at the seed points. Pixels that are connected to the seed are assigned that seed's label.

Graph cuts algorithms treat each pixel/voxel as a node in a graph. Each node of the graph is connected to other nodes of the graph by some neighborhood scheme. Each node is also connected to a source and sink terminal node. The nodes are connected to other nodes by edges with assigned cost values. By performing a minimum cost cut on the graph, an optimal function can be solved that identifies whether a node belongs to the source or sink. A node that belongs to a source is considered part of the segmented structure. A node that belongs to the sink is considered background.

Thresholding and morphology are the least complex methods used to recover structure. Images are transformed according to some metric that is then thresholded to determine background from foreground. Results can be filtered with mathematical morphology applied both before and after the image is thresholded to account for a limited number of geometric and/or spatial cues.

To our knowledge, relatively little work has been performed for 3D TEE endocardial segmentation: this includes work by Wolf et al. [15] and Kucera et al. [16]. We describe a novel approach to 3D TEE endocardial wall segmentation based on 3D level sets. Foundational work on level set and recent developments can be found in the work by Mumford and Shah, Caselles et al., Malladi and Sethian et al., and Li et al. [21–24]. Our work extends the variational formulation developed by Li et al. [24] and uses a unique energy function specifically designed for the 3D TEE modality. This method, described in Sections 2 and 3, shows promising results, as presented in Section 4.

2 3D Level Sets

We employ a dynamic surface method to find the endocardial boundaries. It exploits a 3D level set approach and works as follows: at time $t = 0$, a dynamic surface is initialized in the atrial and/or intraventricular cavities. This dynamic surface is then obtained at any subsequent time t by considering an evolving function $\phi(x, y, z, t)$. The dynamic surface is found as $S(t)$, the zero level set of $\phi(\cdot)$, i.e., $S(t) = \{(x, y, z)|\phi(x, y, z, t) = 0\}$. $\phi(\cdot)$ evolves under a driving force which is designed to expand the surface until it reaches the intensity boundaries marking the inner walls of the atrial and ventricular cavities. An inhibition function $g(\cdot)$, detailed later, stops the dynamic surface when it meets these walls boundaries. Following [24], our time evolution equation is expressed as

$$\frac{\partial \phi}{\partial t} = -\frac{\delta E}{\delta \phi}, \tag{1}$$

where the right hand side of (1) denotes the Gâteaux derivative.

The energy $E(\phi)$ includes three terms and is defined as

$$E(\phi) = \mu P(\phi) + \lambda A_g(\phi) + \nu V_g(\phi). \tag{2}$$

As in [24], our specification of the evolution equation of $\phi(\cdot)$ includes a weight μ and penalty term $P(\phi)$ to evolve ϕ so that, at all times, it closely approximates a signed distance function. This feature obviates the need for re-initialization and keeps the surface well-behaved. This penalty is expressed as

$$P(\phi) = \int_\Omega \frac{1}{2}(|\nabla \phi| - 1)^2 dx\, dy\, dz, \tag{3}$$

where $\nabla\phi$ is the gradient of ϕ and $\Omega \subset R^3$ is the domain of ϕ.

The second and third terms $A_g(\phi)$ and $V_g(\phi)$ in (2) correspond to the surface area and volume, and drive the surface's evolution to the desired goals. By balancing weights λ and ν, we can maintain regularity as the surface expands by limiting surface area growth and forcing volume expansion. The weight ν is chosen here to be negative so that the surface expands. The terms $A_g(\phi)$ and $V_g(\phi)$ are expressed as

$$A_g(\phi) = \int_\Omega g\delta(\phi)\, |\nabla \phi|\ dx\, dy\, dz, \tag{4}$$

and

$$V_g(\phi) = \int_\Omega gH(-\phi)\ dx\,dy\,dz, \tag{5}$$

where $\delta(\phi)$ denotes the Dirac delta function, and $H(\phi)$ is the Heaviside function.

Equations (4) and (5) contain an inhibition function $g(\cdot)$, mentioned earlier, that is designed to abate the motion of the dynamic boundary in places corresponding to the myocardium and mitral valve leaflets location. This function is detailed in the next section.

After reforming the terms from (2), (4), and (5) into (1), and using the Gâteaux derivative, the evolution of ϕ can be expressed as

$$\frac{\partial \phi}{\partial t} = \mu \left[\Delta\phi - \nabla\cdot\left(\frac{\nabla\phi}{|\nabla\phi|}\right)\right] + \lambda\delta(\phi)\,\nabla\cdot\left(g\frac{\nabla\phi}{|\nabla\phi|}\right) + \nu g\delta\left(\phi\right), \tag{6}$$

where $\nabla\cdot$ denotes the divergence and Δ the Laplacian operators. This equation specifies a time-update evolution equation for $\partial\phi/\partial t$, which corresponds to a form of steepest descent. This equation is discretized to evolve the function ϕ, thus minimizing the objective functional $E(\phi)$.

To close this section we detail the derivation of (6) . To this end we wish to find the first variation of the energy functional

$$E(\phi) = \int_\Omega \left[\frac{\mu}{2}\left(|\nabla\phi|-1\right)^2 + \lambda g\delta(\phi)|\nabla\phi| + \nu g H(-\phi)\right] dV. \tag{7}$$

For future use, we note that $H(-\phi) = 1 - H(\phi)$ and that $H'(\phi) = \delta(\phi)$. Let ϕ be the minimizing function of E, ψ be any other function, and τ be a scalar, then we have

$$\frac{d}{d\tau}E(\phi+\tau\psi)\bigg|_{\tau=0} = 0. \tag{8}$$

The derivatives of the three terms in (7) are given by

$$\frac{d}{d\tau}E_1(\phi+\tau\psi) = \mu\int_\Omega \left(|\nabla\phi+\tau\nabla\psi|-1\right)\frac{\nabla\phi+\tau\nabla\psi}{|\nabla\phi+\tau\nabla\psi|}\cdot\nabla\psi\,dV, \tag{9}$$

$$\begin{aligned}\frac{d}{d\tau}E_2(\phi+\tau\psi) = \lambda\int_\Omega \Bigg[&g\delta(\phi+\tau\psi)\frac{\nabla\phi+\tau\nabla\psi}{|\nabla\phi+\tau\nabla\psi|}\cdot\nabla\psi \\ &+ g\delta'(\phi+\tau\psi)\,|\nabla\phi+\tau\nabla\psi|\,\psi\Bigg]\,dV,\end{aligned} \tag{10}$$

and

$$\frac{d}{d\tau}E_3(\phi+\tau\psi) = -\nu\int_\Omega g\delta(\phi+\tau\psi)\psi\,dV. \tag{11}$$

Evaluated at $\tau = 0$ these become

$$\frac{d}{d\tau}E_1(\phi+\tau\psi)\bigg|_{\tau=0} = \mu\int_\Omega \left(|\nabla\phi|-1\right)\frac{\nabla\phi}{|\nabla\phi|}\cdot\nabla\psi\,dV, \tag{12}$$

$$\frac{d}{d\tau}E_2(\phi+\tau\psi)\Big|_{\tau=0} = \lambda\int_\Omega \left[g\delta(\phi)\frac{\nabla\phi}{|\nabla\phi|}\cdot\nabla\psi + g\delta'(\phi)|\nabla\phi|\psi\right]dV, \tag{13}$$

and

$$\frac{d}{d\tau}E_3(\phi+\tau\psi)\Big|_{\tau=0} = -\nu\int_\Omega g\delta(\phi)\psi\,dV. \tag{14}$$

Using Green's first identity,

$$\int_\Omega \psi\Delta\phi + \nabla\phi\cdot\nabla\psi\,dV = \int_{\partial\Omega}\psi\nabla\phi\cdot d\boldsymbol{a}, \tag{15}$$

(12) may be recast as

$$\begin{aligned}\mu\int_\Omega (|\nabla\phi|-1)\frac{\nabla\phi}{|\nabla\phi|}\cdot\nabla\psi\,dV &= -\mu\int_\Omega \nabla\cdot\left(\nabla\phi-\frac{\nabla\phi}{|\nabla\phi|}\right)\psi\,dV\\ &= -\mu\int_\Omega\left[\Delta\phi-\nabla\cdot\left(\frac{\nabla\phi}{|\nabla\phi|}\right)\right]\psi\,dV,\end{aligned} \tag{16}$$

where the surface term in (15) has been omitted based on the assumption that the variation is zero on the boundary (i.e., the boundary values of the functions over which E is considered are specified and hence $\psi = 0$ on $\partial\Omega$). Similarly, the first term in (13) becomes

$$\lambda\int_\Omega g\delta(\phi)\frac{\nabla\phi}{|\nabla\phi|}\cdot\nabla\psi\,dV = -\lambda\int_\Omega\left[g\delta'(\phi)|\nabla\phi|+\delta(\phi)\nabla\cdot\left(g\frac{\nabla\phi}{|\nabla\phi|}\right)\right]\psi\,dV. \tag{17}$$

Since, from (8), we have $\frac{d}{d\tau}E(\phi+\tau\psi)\big|_{\tau=0} = 0$, then

$$\int_\Omega\left\{-\mu\left[\Delta\phi-\nabla\cdot\left(\frac{\nabla\phi}{|\nabla\phi|}\right)\right]-\lambda\delta(\phi)\nabla\cdot\left(g\frac{\nabla\phi}{|\nabla\phi|}\right)-\nu g\delta(\phi)\right\}\psi\,dV = 0. \tag{18}$$

As this must be true for any ψ, the portion of the integrand in braces must be identically zero for the minimizer ϕ. We therefore define the Gâteaux derivative

$$\frac{\partial E}{\partial\phi} = -\mu\left[\Delta\phi-\nabla\cdot\left(\frac{\nabla\phi}{|\nabla\phi|}\right)\right]-\lambda\delta(\phi)\nabla\cdot\left(g\frac{\nabla\phi}{|\nabla\phi|}\right)-\nu g\delta(\phi), \tag{19}$$

such that the minimizer ϕ satisfies the Euler-Lagrange equation $\frac{\partial E}{\partial\phi} = 0$.

3 Inhibition Function

Our design for the inhibition function $g(\cdot)$ takes into account three components: the output of a k-means clustering, the output of a thin tissue detector using a structure tensor, and the TEE intensity gradient.

k-means clustering provides a good outline of the endocardium and surrounding structure. It is obtained after low pass filtering and intensity remapping to address any signal drop-off far from the TEE frustum apex (corresponding to

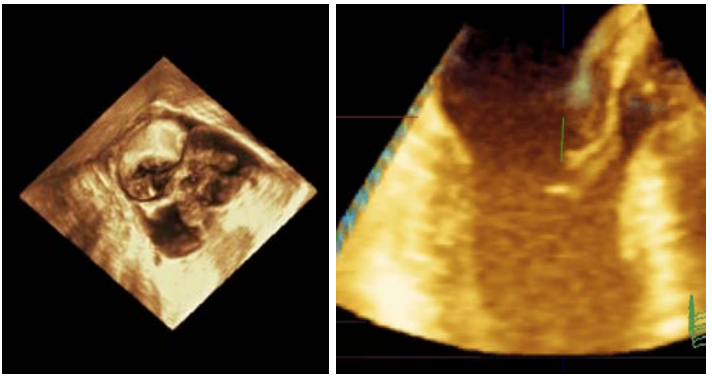

(a) (b)

Fig. 1. 3D TEE: (a) top view from the left atrium showing the mitral valve, the aortic valve, and the left ventricle; (b) side view showing the left atrium, the mitral valve leaflets, the aortic valve and the left ventricle

the TEE probe location). We denote the output of the k-means algorithm by the indicator function $J_{KM}(x, y, z)$, equal to one where the k-means algorithm clustered the darker voxels (including the intraventricular and intra-atrial cavities), and zero otherwise (including the myocardial areas).

Additional information on the heart wall and anatomical structures such as the trabeculae carneae and chordae tendineae is indicated by a variation in intensity in the 3D TEE which is captured by the function $ed(\cdot)$, as in:

$$ed(x, y, z) = \frac{1}{1 + a|\nabla G * I(x, y, z)|^2}. \tag{20}$$

where $\nabla G * I$ is the gradient of the Gaussian-smoothed TEE intensity. This function represents a 'negative' of the gradient magnitude map, taking small values for high gradient magnitudes, and values close to 1 for small gradient magnitudes. This gradient-based definition of $ed(\cdot)$ might be an issue for echocardiography images with limited contrast. We have found however that it works adequately with TEE imaging, which allows a close "view" into the left heart complex and exhibits good contrast when compared to other cardiac ultrasound imaging techniques such as transthoracic echocardiography.

The third term in our specification of the inhibition function exploits the structure tensor to detect the location of thin tissue such as the mitral or aortic valve leaflets, whose detection may be sometimes problematic using the two former methods.

Given a volume of intensity values $f(\mathbf{x})$ where $\mathbf{x}$ is the (x, y, z) coordinate of the voxel, one can approximate the values surrounding a point in the volume $\mathbf{x}_0$ in a second-order Taylor series fashion as

$$f(\mathbf{x}) \approx f(\mathbf{x}_0) + (\mathbf{x} - \mathbf{x}_0)^T \nabla f_0 + \frac{1}{2}(\mathbf{x} - \mathbf{x}_0)^T \nabla^2 f_0 (\mathbf{x} - \mathbf{x}_0), \tag{21}$$

where ∇f_0 and $\nabla^2 f_0$ denote the gradient vector and the Hessian matrix at $\mathbf{x}_0$ respectively. From this approximation, it is important to note that the varying intensities surrounding $\mathbf{x}_0$ is spanned by the eigenvectors of the Hessian matrix. The eigenvalues corresponding to these eigenvectors can be used to define a new space that is invariant under orthonormal transformations. Tissue classification can be performed in this space. From [25, 26], thin planar structures can be found as follows: Let $\mathbf{e}_1(\mathbf{x})$, $\mathbf{e}_2(\mathbf{x})$, and $\mathbf{e}_3(\mathbf{x})$ be the eigenvectors of the Hessian matrix $\nabla^2 f$ where $\mathbf{e}_1(\mathbf{x})$ corresponds to the eigenvector with the largest eigenvalue $\lambda_1(\mathbf{x})$, $\mathbf{e}_2(\mathbf{x})$ corresponds to the eigenvector with the next largest eigenvalue $\lambda_2(\mathbf{x})$, and $\mathbf{e}_3(\mathbf{x})$ corresponds to the eigenvector with the smallest eigenvalue $\lambda_3(\mathbf{x})$ (i.e., $\lambda_1 \geq \lambda_2 \geq \lambda_3$). A measure of the planarity of the surrounding local structure can be defined by:

$$S_{sheet}\{f\} = \begin{cases} |\lambda_3| \cdot w(\lambda_2, \lambda_3) \cdot w(\lambda_1, \lambda_3), \lambda_3 < 0, \\ 0 \qquad\qquad\qquad\qquad\qquad \text{otherwise.} \end{cases} \tag{22}$$

where $w(\lambda_s, \lambda_t)$ is defined by:

$$w(\lambda_s, \lambda_t) = \begin{cases} \left(1 + \frac{\lambda_s}{|\lambda_t|}\right)^{\gamma}, & \lambda_t \leq \lambda_s < 0, \\ \left(1 - \alpha\frac{\lambda_s}{|\lambda_t|}\right)^{\gamma}, & \frac{|\lambda_t|}{\alpha} > \lambda_s > 0, \\ 0 & \text{otherwise.} \end{cases} \tag{23}$$

γ controls the sharpness of selectivity and α controls the asymmetrical characteristic in the negative and positive regions of λ_s, with $0 < \alpha \leq 1$. We found that $\gamma = 0.5$ and $\alpha = 0.25$ work well in our experiments. We denote by $J_l(x, y, z)$ the inverse of the indicator function denoting the leaflet position found by the structure tensor method.

Collecting the various terms together, our final specification for the level set inhibition function is given by:

$$g(x, y, z) = J_{KM}(x, y, z) \cdot J_l(x, y, z) \cdot ed(x, y, z). \tag{24}$$

4 Experiments

Intraoperative real-time 3D TEE full volume sequences of the left heart were collected from patients undergoing surgery. 3D TEE acquisition was performed using an iE33 Philips console with a Philips X2-T Live 4D TEE probe (Philips Medical Systems, Bothell, WA). The TEE cube sizes were 208×208×224. The 3D TEE probe was operated at frequencies ranging from 3 to 5 MHz. The pixels spatial resolutions were respectively 0.666×0.657×0.580 mm or approximately 1.10 mm diagonal voxel resolution. A 7 breath-hold cycle acquisition protocol was employed leading to a frame rate of close to 50 Hz.

In our experiments, we found the following parameters values to work well for left ventricle and atrium segmentation: $\lambda = 4$, $\mu = 0.04$, $\nu = -6$, and $a = 300$. The parameter values were kept unchanged for all the experiments as we benchmarked the segmentation method. Benchmarking was performed using four 3D

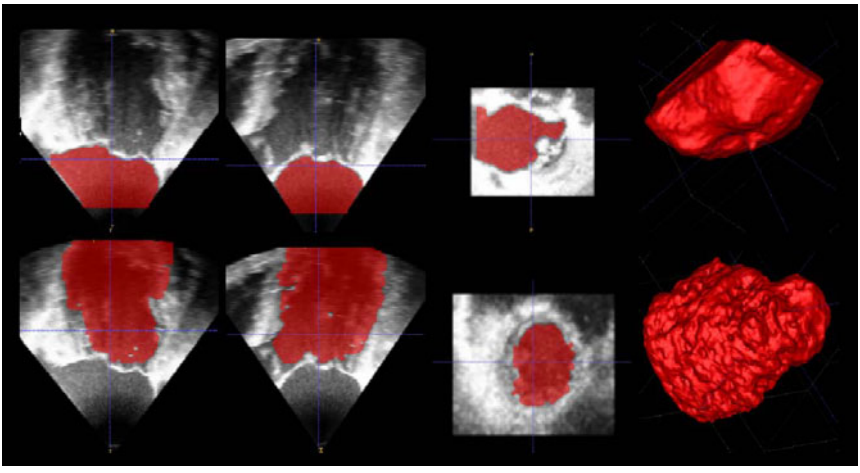

Fig. 2. Intra-atrial cavity (top) and intraventricular cavity (bottom) segmentation. In each row, from left to right: long axis/two chamber, long axis/four chambers, short axis, and 3D rendered views.

TEE datacubes. Ground truth segmentation of the intra-atrial and intraventricular cavities was done by experts on full volumes, using hand segmentation on all short axis, long axis/two chamber, and long axis/four chamber views. In all, this involved hand segmentation of 2560 view planes to allow the computation of errors and DICE numbers. We found a mean absolute error $m = 2.29$ mm with associated standard deviation $\sigma = 2.70$ mm, a root mean square error of $r = 3.56$ mm, and a DICE number of $d = 85.60\%$. Examples of 3D TEE cubes are shown in Fig. 1. Examples of the resulting segmentation of full TEE cubes are shown in Fig. 2.

5 Conclusions

We describe a novel 3D segmentation method to detect endocardial walls from 3D TEE. Promising results are found using intraoperative TEE data. Challenging factors still remain, including the detection of the walls and the characterization of performance in areas with strong trabeculation, such as close to the ventricular apex, where we also found sizable inter-expert ground truth segmentation variation. Future goals are to address these challenges and limitations.

Acknowledgments

We wish to thank Profs. D. Yuh (JHMI/Cardiothoracic Surgery) and E. McVeigh (JHU BME) for providing data and useful discussions. This project was supported by JHU APL Science and Technology Research and Development funds and NIH NHLBI R21HL098765. The content is solely the responsibility of the authors and does not necessarily represent the official views of the National Heart, Lung, And Blood Institute or the National Institutes of Health.

References

1. Burlina, P., Sprouse, C., DeMenthon, D., Jorstad, A., Juang, R., Contijoch, F., Abraham, T., Yuh, D., McVeigh, E.: Patient-specific modeling and analysis of the mitral valve using 3D-TEE. In: Information Processing in Computer-Assisted Interventions, pp. 135–146 (2010)
2. Sprouse, C., Yuh, D., Abraham, T., Burlina, P.: Computational hemodynamic modeling based on transesophageal echocardiographic imaging. In: Proc. Int. Conf. Engineering in Medicine and Biology Society, vol. 2009, pp. 3649–3652 (2009)
3. Mukherjee, R., Sprouse, C., Abraham, T., Hoffmann, B., McVeigh, E., Yuh, D., Burlina, P.: Myocardial motion computation in 4D ultrasound. In: Proc. Int. Symp. on Biomedical Imaging (2011)
4. Noble, J., Boukerroui, D.: Ultrasound image segmentation: A survey. IEEE Transactions on Medical Imaging 25(8), 987–1010 (2006)
5. Noble, J.: Ultrasound image segmentation and tissue characterization. Proc. of the Institution of Mechanical Engineers, Part H: Journal of Engineering in Medicine 224(2), 307–316 (2010)
6. Hammoude, A.: Endocardial border identification in two-dimensional echocardiographic images: review of methods. Computerized Medical Imaging and Graphics 22(3), 181–193 (1998)
7. Mitchell, S., Lelieveldt, B., van der Geest, R., Bosch, H., Reiber, J., Sonka, M.: Multistage hybrid active appearance model matching: segmentation of left and right ventricles in cardiac MR images. IEEE Transactions on Medical Imaging 20, 415–423 (2001)
8. O'Brien, S., Ghita, O., Whelan, P.: Segmenting the left ventricle in 3D using a coupled ASM and a learned non-rigid spatial model. The MIDAS Journal 49 (August 2009)
9. Wijnhout, J., Hendriksen, D., Assen, H.V., der Geest, R.V.: LV challenge LKEB contribution: Fully automated myocardial contour detection. The MIDAS Journal 43 (August 2009)
10. Angelini, E., Homma, S., Pearson, G., Holmes, J., Laine, A.: Segmentation of real-time three-dimensional ultrasound for quantification of ventricular function: a clinical study on right and left ventricles. Ultrasound in Medicine & Biology 31(9), 1143–1158 (2005)
11. Duan, Q., Angelini, E., Laine, A.: Real-time segmentation by Active Geometric Functions. Computer Methods and Programs in Biomedicine 98(3), 223–230 (2010)
12. Qu, Y., Chen, Q., Heng, P., Wong, T.: Segmentation of left ventricle via level set method based on enriched speed term. In: Barillot, C., Haynor, D.R., Hellier, P. (eds.) MICCAI 2004. LNCS, vol. 3216, pp. 435–442. Springer, Heidelberg (2004)
13. Chen, Y., Tagare, H., Thiruvenkadam, S., Huang, F., Wilson, D., Gopinath, K., Briggs, R., Geiser, E.: Using prior shapes in geometric active contours in a variational framework. International Journal of Computer Vision 50(3), 315–328 (2002)
14. Han, C., Lin, K., Wee, W., Mintz, R., Porembka, D.: Knowledge-based image analysis for automated boundary extraction of transesophageal echocardiographic left-ventricular images.. IEEE Transactions on Medical Imaging 10(4), 602 (1991)
15. Wolf, I., Hastenteufel, M., De Simone, R., Vetter, M., Glombitza, G., Mottl-Link, S., Vahl, C., Meinzer, H.: ROPES: A semiautomated segmentation method for accelerated analysis of three-dimensional echocardiographic data. IEEE Transactions on Medical Imaging 21(9), 1091–1104 (2003)

16. Kucera, D., Martin, R.: Segmentation of sequences of echocardiographic images using a simplified 3D active contour model with region-based external forces. Computerized Medical Imaging and Graphics 21(1), 1–21 (1997)
17. Cousty, J., Najman, L., Couprie, M., Clment-Guinaudeau, S., Goissen, T., Garot, J.: Segmentation of 4D cardiac MRI: automated method based on spatio-temporal watershed cuts. Image and Vision Computing 28(8), 1229–1243 (2010)
18. Ben Ayed, I., Punithakumar, K., Li, S., Islam, A., Chong, J.: Left ventricle segmentation via graph cut distribution matching. In: Yang, G.-Z., Hawkes, D., Rueckert, D., Noble, A., Taylor, C. (eds.) MICCAI 2009. LNCS, vol. 5762, pp. 901–909. Springer, Heidelberg (2009)
19. Lu, Y., Radau, P., Connelly, K., Dick, A., Wright, G.: Automatic image-driven segmentation of left ventricle in cardiac cine MRI. The MIDAS Journal 49 (August 2009)
20. Lempitsky, V., Verhoek, M., Noble, J.A., Blake, A.: Random forest classification for automatic delineation of myocardium in real-time 3D echocardiography. In: Ayache, N., Delingette, H., Sermesant, M. (eds.) FIMH 2009. LNCS, vol. 5528, pp. 447–456. Springer, Heidelberg (2009)
21. Mumford, D., Shah, J.: Optimal approximations by piecewise smooth functions and associated variational problems. Communications on Pure and Applied Mathematics 42(5), 577–685 (1989)
22. Malladi, R., Sethian, J., Vemuri, B.: Shape modeling with front propagation: A level set approach. IEEE Transactions on Pattern Analysis and Machine Intelligence 17(2), 158–175 (2002)
23. Caselles, V., Kimmel, R., Sapiro, G.: Geodesic active contours. International Journal of Computer Vision 22(1), 61–79 (1997)
24. Li, C., Xu, C., Gui, C., Fox, M.D.: Level set evolution without re-initialization: a new variational formulation. In: Proc. IEEE Computer Society Conf. on Computer Vision and Pattern Recognition, pp. 430–436. IEEE Computer Society, Los Alamitos (2005)
25. Sato, Y., Westin, C., Bhalerao, A., Nakajima, S., Shiraga, N., Tamura, S.: Tissue classification based on 3d local intensity structures for volume rendering. IEEE Transactions on Visualization and Computer Graphics (6) (2000)
26. Huang, A., Nielson, G., Razdan, A., Farin, G., Baluch, D., Capco, D.: Thin structure segmentation and visualization in three-dimensional biomedical images: a shape-based approach. IEEE Transactions on Visualization and Computer Graphics 12(1), 93–102 (2006)

Regionally Optimised Mathematical Models of Cardiac Myocyte Orientation in Rat Hearts

Ilyas E. Karadag[1], Martin Bishop[1], Patrick W. Hales[2], Jürgen E. Schneider[2], Peter Kohl[3], David Gavaghan[1], and Vicente Grau[4]

[1] Computational Biology Group, Computing Laboratory, University of Oxford
[2] BHF Experimental MR Unit, Department of Cardiovascular Medicine, University of Oxford
[3] Department of Physiology, Anatomy and Genetics, University of Oxford
[4] Department of Engineering Science and Oxford e-Research Centre, University of Oxford

Abstract. Mathematical models of ventricular cardiomyocyte orientation provide a simple description of histo-anatomical arrangements that are important for cardiac mechano-electric behaviour. They can be used to analyse interspecies differences, to explore dynamic remodelling such as during development or disease, and they are key for building realistic computational representations of the heart. This study investigates the suitability of regionally optimised models to represent accurately myocardial structure. Using DT-MRI scans as a reference, we calculate an optimised model by finding the parameters that minimise angular differences, both globally and regionally using a 16-segment topography. Results show angular differences between the optimized model and DT-MRI data of up to 15 degrees, with regional optimization providing a clear improvement in model accuracy (up to 52% error reduction).

Keywords: DT-MRI, cardiac myocyte orientation, computational modelling.

1 Introduction

The orientation of cardiac myocytes (also known as cardiac fibre orientation) fundamentally affects the electro-mechanical properties of the heart. Thus it is crucial that computational models reproduce it accurately [1,2]. As early as 1969 [3], histological studies were used to describe cardiomyocyte orientation, showing in a canine model that the fibre inclination angle (also known as fibre helix angle, and defined as the angle between the projection of the myocyte orientation on the plane formed by the circumferential and longitudinal directions and the circumferential direction) smoothly rotates from -60° in the epicardium to +60° in the endocardium.

While histology studies provide direct visualisation of cardiac cell structures, associated techniques are destructive, by and large producing two-dimensional data. Diffusion Tensor Magnetic Resonance Imaging (DT-MRI) offers a viable, non-destructive alternative towards the study of fibre orientations in three dimensions, with the potential of obtaining good resolution scans *in vivo* in the near future [4]. Cardiac DT-MRI scans provide Diffusion Weighted images in at least six different directions, which are used to form a diffusion tensor. The primary eigenvector of the diffusion tensor has been shown to correspond well with locally prevailing myocyte

D.N. Metaxas and L. Axel (Eds.): FIMH 2011, LNCS 6666, pp. 294–301, 2011.

orientation established by histology; in [5], an average per-voxel difference of 12° between DT-MRI and histology-based cell orientation was found (with a 10° uncertainty in histology analysis).

It has been proposed [3] that a simple mathematical rule could describe myocyte orientation in normal mammalian hearts. Based on this, the computational model in [6] proposed for the helix angle α:

$$\alpha = R(1-2e)^n \tag{1}$$

where e, $0 \le e \le 1$, is a normalised parameter describing the position of the point within the myocardial wall at which the fibre orientation is described, with $e=0$ for the endocardium and $e=1$ for the epicardium, while R represents the maximum value of the helical angle. In [6], an exponent $n=3$ was used. Similar equations using a linear ($n=1$) rather than a cubic law have been shown to correlate well with DT-MRI studies of the rat heart [7]. An alternative approach was proposed in [8], where an excellent statistical analysis of myocyte orientation in canine hearts was performed based on image registration between scans.

State-of-the-art cardiac models can rely on either mathematical expression or DT-MRI studies of the same heart for the definition of myocyte orientation [9]. While using orientations from DT-MRI scans has the advantage of capturing subject-specific variations, DT-MRI has limitations in Signal-to-Noise Ratio (SNR) and resolution, and *ex vivo* scans are affected by tissue deformation introduced during sample extraction and fixation.

Therefore, the use of mathematical rules for cardiac myocyte orientation retains several attractive features. It provides a simple, intuitive description that can be easily understood and used in hypothesis generation. It can be applied to studies where no DT-MRI data is available, or where the distortion introduced by tissue fixation is to be avoided, without the need for an additional image registration with an atlas (which depends on several parameters and introduces distortion of its own). Mathematical models can be used to analyse quantitatively the changes in orientation introduced by global or regional pathology. Finally, they can be used as a basis for algorithms to correct for noisy DTI measurements and increase their resolution.

1.1 Aims and Contributions

The overall aim of this study is to propose an extension to the simple mathematical rule proposed in [6], allowing more accurate definition of relevant parameters, adjusted and validated using voxel-wise correspondence with DT-MRI scans.

More precisely, the contributions presented in this paper are:

- determining the optimal expression to describe transmurally varying myocyte orientation in the rat heart, and calculating its accuracy,
- quantifying the extent to which regional changes need to be included in such model, following the regional model in [10], and
- proposing a complete algorithm from image segmentation to assignment of orientations that can be used to build computational models.

2 Methods

2.1 Sample Preparation and Image Aquisition

Isolated rat hearts were saline-washed in Langendorff mode, and fixed with Karnovsky's fixative using coronary perfusion, either in resting state, during volume overload, or in contracture. MR imaging was carried out on a 9.4T (400 MHz) MR system (Varian, Inc., Palo Alto, CA, USA). A three-dimensional fast spin-echo pulse sequence was developed to provide diffusion-weighted MR images. During acquisition, a pair of unipolar trapezoidal diffusion gradients was applied on either side of the first 180° pulse, and eight echoes were collected per excitation to reduce scan times. Diffusion gradients were applied in six non-collinear directions [12]. Measurements were acquired at an isotropic resolution of 101.6μm. Diffusion tensors were then calculated using a weighted linear least-squares fit method. Full details are available in [11]. The dataset currently consists of 20+ rat hearts.

2.2 Segmentation

The methods shown in this paper depend strongly on accurate image segmentation, for several reasons: the parameter e in equation (1) is based on accurate determination of the epi- and endocardial surfaces, and papillary muscles and endocardial trabeculations need to be separated from the myocardial wall, since the myocyte orientation in those does not follow the same pattern as in the myocardial wall. Fig. 1 shows intermediate steps and final results on a slice of one of the hearts in the dataset.

Contrast between tissue and background was analysed on the unweighted MRI image (S_0), and on calculated Apparent Diffusion Coefficient (ADC) and Fractional Anisotropy (FA) images. The ADC values, detecting the large difference in diffusivity between cardiac tissue and the fixative in the background, provided the best discrimination (Fig. 1a), and thus they were used for segmentation using an initial thresholding followed by morphological cleaning to remove small artefact regions in the background, to fill holes and to smooth the extracted surfaces.

In order to separate internal structures within the left ventricle (LV), the convex hull of the detected LV was calculated on individual short axis slices; any structures lying within the convex hull were removed. By removing small salient structures, this operation has the additional effect of smoothing the endocardial surface, reducing the effect of segmentation errors on the calculation of myocyte orientation described below. A sample result of the LV extraction is shown in Fig. 1b.

2.3 Separation of Left and Right Ventricles

The region where the septum and the myocardial free wall meet is particularly difficult to represent. If DT-MRI is used, the complexity of the orientation pattern in this area produces partial volume effects requiring increased resolution. In the case of a mathematical model, the separation between left and right ventricles is fundamental to assure the accuracy of the estimation.

From visual analysis of DT-MRI scans (see Fig. 1c), the orientations form a circular pattern dominated by the structure of the LV wall. To reproduce this pattern, we use the following algorithm. The centroid of the LV is calculated for each short-axis slice.

The distance between the LV and the closest LV epicardial point is calculated as a function of the radial angle (with the RV surface of the septum treated as LV epicardium); this curve is shown in blue in Fig. 1d. The area of connection between septum and free wall is identified as that where the distance function significantly departs from the average, and the values in this area are substituted by an interpolation of the remaining values, represented by the red line in Fig. 1d. The corrected function is then used to determine the boundary of the LV. An example of LV/RV segmentation is shown in Fig. 1e.

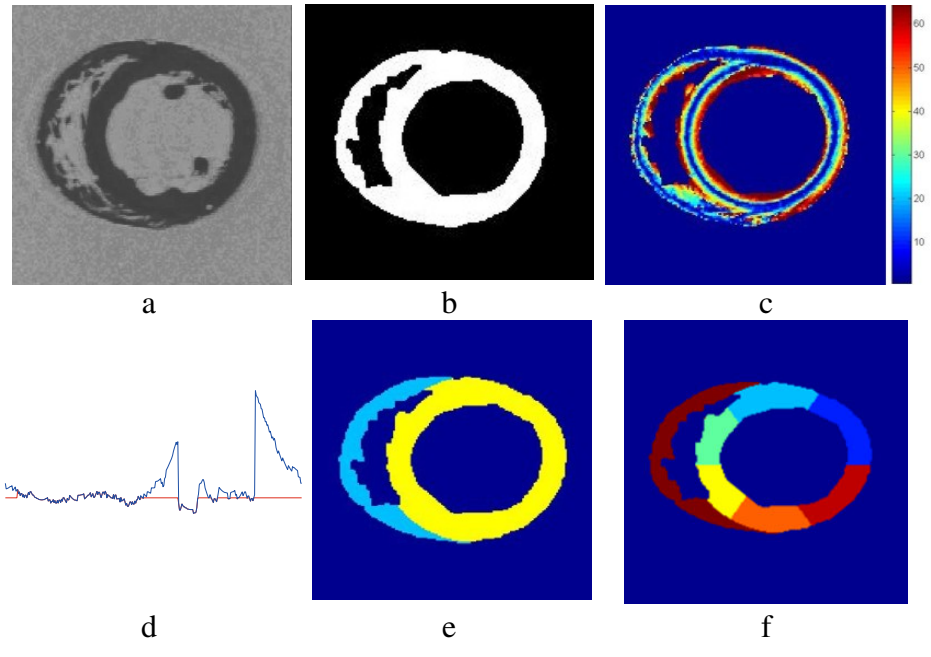

Fig. 1. Illustration of original images and the pre-processing pipeline on a sample heart. a) ADC image; b) Segmentation results; c) Absolute value of the helix angle from the DT-MRI scan; d) Distance from LV centre for angles ranging from 0 to 2π; e) Results of LV/RV separation; f) Segment division [10].

2.4 Regional Analysis

In order to calculate whether a single mathematical model is able to represent the structure of the whole myocardium, and to which degree regional variability needs to be incorporated, we segment the LV walls into regions following the method in [10]. The LV wall is divided into 3 sections along the long axis, with 35% assigned to basal, 35% to mid-myocardial and 30% to apical. Basal and mid-myocardial regions are further divided into 6 sections in the short axis: anterolateral, anterior, anteroseptal, inferoseptal, inferior and inferolateral, while the apical regions are divided into anterior, septal, inferior and lateral. The RV wall was divided into basal, mid-cavity and apical. A sample segmentation is shown in Fig. 1f.

2.5 Extended Mathematical Model

As discussed above, both linear and cubic rules have been proposed to model myocyte orientation using (1). In order to allow the use of arbitrary values of the exponent n, we propose the following equation:

$$\alpha = R \left| 1 - 2e \right|^{n} \operatorname{sgn}(1 - 2e) \tag{2}$$

where *sgn()* is the sign function. The value of e is calculated as the normalised distance to the closest points in the endo- (d_{endo}) and epicardial (d_{epi}) surfaces:

$$e = \frac{d_{endo}}{d_{endo} + d_{epi}} \tag{3}$$

A representation of the helix angle α for different values of n is shown in Fig. 2. The septum is treated as a continuation of the LV wall: d_{endo} is the distance to the LV and d_{epi} is the distance to the RV.

2.6 Estimation of Optimal Parameters for the Mathematical Method

Optimal values of the exponent n and the transmural rotation R were calculated as those that minimise the Sum of Squared Differences (SSD) between estimated and DT-MRI measured orientations at each voxel. Optimization was carried out using the Nelder-Mead simplex algorithm in an unconstrained optimisation.

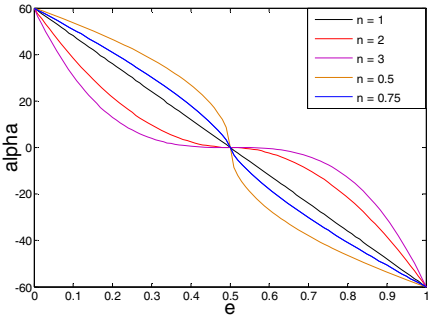

Fig. 2. Helix angle within the myocardial wall for different values of n. R is fixed to 60°

Both global (minimising SSD across the whole myocardium) and local (minimising SSD for each one of the LV and RV segments) were performed.

The algorithms in this and previous Sections were implemented in Matlab.

3 Results

Table 1 shows the comparison between the optimised model and the linear ($n=1$) and cubic ($n=3$) models corresponding to (1), averaged across three rat hearts. As in [7], the linear model performs clearly better than the cubic model, and this is reflected in

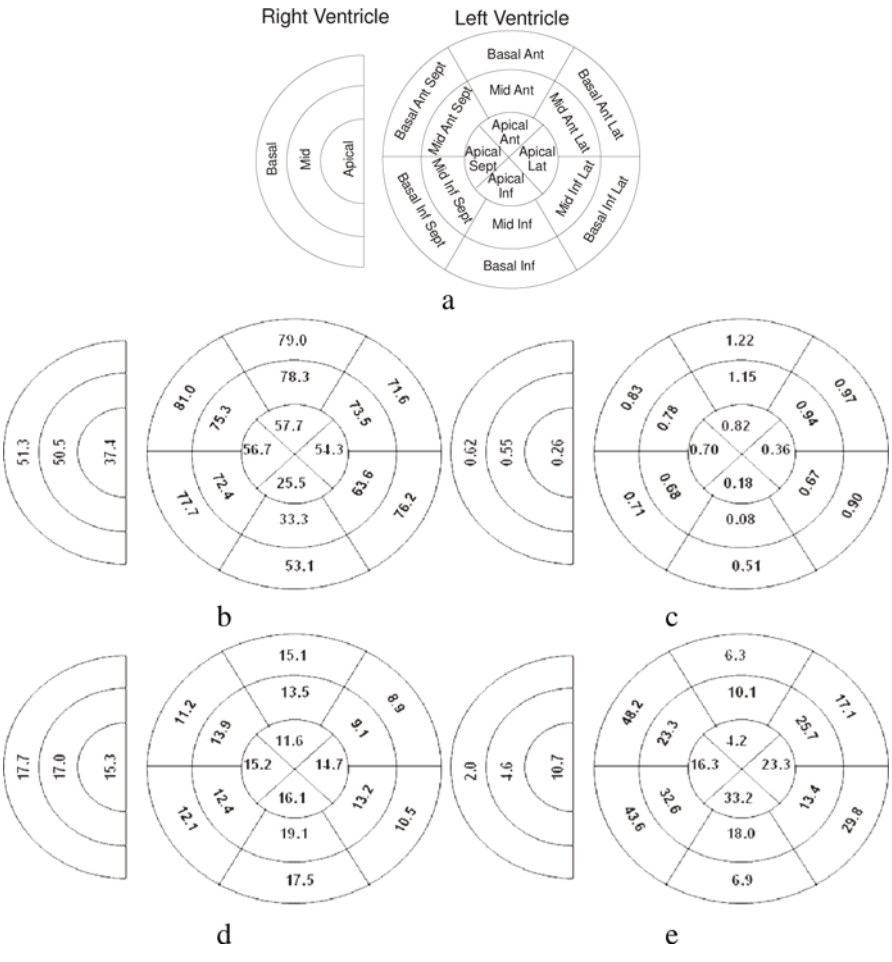

Fig. 3. Illustration of the results of the regional optimization. a) Segment names for both LV and RV [10]; b) Values of R; c) Values of n; d) Average angular errors, in degrees; e) Improvement in the model accuracy, in %, when regional optimization is used, compared with a global linear model.

the optimal value of n found by the algorithm, ranging from $n=0.73$ for the local to $n=0.78$ for the global optimisation. The average error (absolute difference between predicted and DT-MRI angles) decreases moderately with the optimisation (by 6.7% and 16.24% for the global and regional optimisations, respectively).

In Fig. 3, results are shown for each of the segments, again averaged across heart samples. Interestingly there is substantial variability in the values of R (Fig. 3b) and n (Fig. 3c) between segments (standard deviations, not shown in the Figure for simplicity, reach up to 15° for R and 0.25 for n). This results in a much larger reduction in average errors, per segment, than those shown in Table 1. Fig. 3d shows average errors and Fig. 3e the average improvement (defined as the relative difference between errors in the linear and optimised models). Average improvements shown in Fig. 3e for individual segments take values of up to 48%, and are particularly high in the septum.

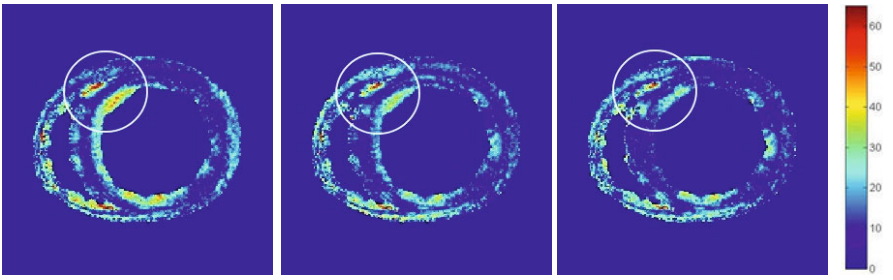

Fig. 4. Differences between model and DT-MRI. Left: Linear model. Middle: Globally optimised model. Right: Locally optimised model. Notice the improved local adjustment obtained by local optimization in the highlighted area.

Table 1. Comparison between global cubic and linear models, and the optimised model, adjusted on a global or segment-wise basis

	Cubic	Linear	Globally optimised	Locally optimised
R (average)	60	60	65.6	63.7
n (average)	3	1	0.8	0.7
Average error (degrees)	25.1	16.0	15.0	13.8

Fig. 4 shows results of the linear, globally optimised and locally optimised models on one of the heart samples. While overall the linear model provides a good estimation, local errors can still be high. The optimised model reduces those errors, in particular if regional optimisation is used, as can be seen in the highlighted region.

4 Discussion

The results in Table 1 for the locally optimised model show average errors of 13.8°. In comparison, in [5] the differences between DT-MRI and histology were estimated at around 12°, and thus in the same range of our results. In this respect, this study confirms that the mathematical model can provide a good description of the overall myocyte orientation in the rat heart.

However, local errors are more substantial, in particular in areas of junction between septum and free wall, and this justifies the use of a locally optimised model. In particular, we have found significant differences between septal and inferior segments. This variability could be important in the study of the effect of local pathologies in myocyte structure.

While some errors might be due to the mathematical model, others undoubtedly arise from inaccuracies in the segmentation. In particular, a failure of the segmentation to remove endocardial structures would result in significant local errors. The limited resolution of the DT-MRI images is also a source of error, as partial volume effects at the surfaces are substantial. In addition, in the animal model used, the spatial extent of source tissue affects signal quality, which may explain the larger errors seen in the RV. Effects of vasculature on DT-MRI signals remain to be investigated.

In this report, we have only presented results for 16 segments. The apical area is particularly difficult to represent, due to its complicated cellular structure. Finally, a potential extension of the work proposed here could also consider different values for the maximum angle R in the endo- and epicardial surfaces.

References

1. Covell, J.: Tissue Structure and Ventricular Wall Mechanics. Circulation 118, 699–701 (2008)
2. Ubbink, S.W.J., et al.: Towards model based analysis of cardiac MR tagging data: relation between left ventricular shear strain and myofiber orientation. Med. Imag. Anal. 10, 632–641 (2006)
3. Streeter, D.D., et al.: Fiber orientation in the canine left ventricle during diastole and systole. Circ. Res. 24, 339–347 (1969)
4. Toussaint, N., et al.: *In vivo* human 3D cardiac fibre architecture: Reconstruction using curvilinear interpolation of diffusion tensor images. In: Jiang, T., Navab, N., Pluim, J.P.W., Viergever, M.A., et al. (eds.) MICCAI 2010. LNCS, vol. 6361, pp. 418–425. Springer, Heidelberg (2010)
5. Scollan, F., et al.: Histological validation of myocardial microstructure obtained from diffusion tensor magnetic resonance imaging. Am. J. Physiol. 275, 2308–2318 (1998)
6. Potse, M., et al.: A comparison of monodomain and bidomain reaction-diffusion models for action potential propagation in the human heart. IEEE Trans. Biomed. Eng. 53, 2425–2435 (2006)
7. Bishop, M.J., et al.: Comparison of rule-based and DTMRI-derived fibre architecture in a whole rat ventricular computational model. In: Ayache, N., Delingette, H., Sermesant, M. (eds.) FIMH 2009. LNCS, vol. 5528, pp. 87–96. Springer, Heidelberg (2009)
8. Peyrat, J.M., et al.: A Computational Framework for the Statistical Analysis of Cardiac Diffusion Tensors: Application to a Small Database of Canine Hearts. IEEE Trans. Med. Imaging 26(11), 1500–1514 (2007)
9. Bishop, M.J., et al.: Development of an anatomically-detailed MRI-derived rabbit ventricular model and assessment of its impact on simulation of electrophysiological function. Am. J. of Physiol. 298, H699–H718 (2010)
10. Cerqueira, et al.: Standardized Myocardial Segmentation and Nomenclature for Tomographic Imaging of the Heart. Circulation 105, 539 (2002)
11. Plank, G., et al.: Generation of histo-anatomically representative models of the individual heart: tools and application. Phil. Trans. R. Soc. A 367(1896), 2257–2292 (2009)
12. Hales, P.W., et al.: Optimizing Accuracy and Precision in High Resolution Diffusion Tensor Imaging of the Ex-Vivo Rat Heart. In: Proc. ISMRM, vol. 18, p. 1629 (2010)

Mapping Contact Force during Catheter Ablation for the Treatment of Atrial Fibrillation: New Insights into Ablation Therapy

Rashed Karim[1], Gang Gao[1], James Harrison[1], Aruna Arujuna[1], Hendrik Lambert[3], Giovanni Leo[3], Jaswinder Gill[2], Reza Razavi[1], Tobias Schaeffter[1], Mark O'Neill[2], and Kawal S. Rhode[1]

[1] Division of Imaging Sciences, King's College London, SE1 7EH, UK
[2] Department of Cardiology, St. Thomas' Hospital, London, SE1 7EH, UK
[3] Endosense SA, Geneva, Switzerland
rashed.karim@kcl.ac.uk

Abstract. The distribution of ablation catheter contact force may be important for elucidating the mechanisms of pulmonary vein (PV) reconnection following PV isolation (PVI) for the treatment of paroxysmal atrial fibrillation (PAF). A novel method was developed for the visualisation of tissue contact force on left atrial models derived from segmented MRI data and the approach was tested in 3 patients. The left atrium was automatically segmented from pre-procedural whole-heart cardiac magnetic resonance (CMR) scans in three patients undergoing circumferential PVI for catheter ablation of PAF. During the procedure, the CMR shell was overlaid on to real-time fluoroscopy using the EP Navigator (EPN) software (Philips Healthcare, The Netherlands) and registered using the trachea and intracardiac catheters. Using a wide area circumferential approach to encircle ipsilateral pairs of PVs, the position of each radiofrequency (RF) application (25W for 40s) was recorded on the CMR shell using the point tagging feature of EPN. Using a contact force-sensing ablation catheter (TactiCath, Endosense, Switzerland), the contact force-time integral (FTI) for each registered ablation point was recorded. The FTI for each point was then projected on to the CMR shell with a circular diameter of 10mm using custom-made software. This radius of force distribution was chosen to reflect the typical accuracy of location of the mapping catheter and also to take into account the motion of the catheter during the RF application. 4 vein PVI and FTI maps were achieved in all patients (see figure 1 for example). The mean FTI applied to each side of the left atrium was recorded in gram seconds. The total and regional FTIs applied

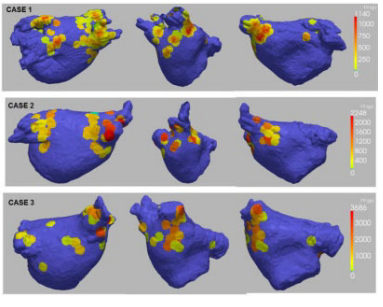

Fig. 1. The FTI map for each patient in three separate views (from left to right: posterior, right PVs and anterior

D.N. Metaxas and L. Axel (Eds.): FIMH 2011, LNCS 6666, pp. 302–303, 2011.

to achieve PVI differed between and within patients respectively, but in an inconsistent manner. The FTI map on the pre-segmented atrial shell provides an intuitive post-procedural assessment of the tissue-contact force achieved during RF delivery. The FTI is less consistent between patients for the RPVs than for the LPVs, perhaps reflecting patient-specific technical challenges. Comparison of FTI maps with post-ablation delayed enhancement, T2W MRI and clinical outcome data may assist in understanding the mechanisms of effective lesion delivery and of PV reconnection after ablation.

Keywords: catheter ablation, atrial fibrillation, contact force, visualization techniques, image-guided intervention.

Trials on Tissue Contractility Estimation from Cardiac Cine MRI Using a Biomechanical Heart Model

R. Chabiniok[1], P. Moireau[1], P.-F. Lesault[2], A. Rahmouni[2], J.-F. Deux[2], and D. Chapelle[1]

[1] INRIA, MACS Team, B.P. 105, 78153 Le Chesnay, France
[2] AP-HP Hôpital Henri Mondor, Université Paris-Est Créteil, France

Abstract. In this paper we apply specific data assimilation methods in order to estimate regional contractility parameters in a biomechanical heart model, using as measurements *real* Cine MR images obtained in an animal experiment. We assess the effectiveness of this estimation based on independent knowledge of the controlled infarcted condition, and on late enhancement images. Moreover, we show that the estimated contractility values can improve the model behavior in itself, and that they can serve as an indicator of the local heart function, namely, to assist medical diagnosis for the post-infarct detection of hypokinetic or akinetic regions in the myocardial tissue.

1 Introduction

Building adequate *patient-specific* models is now widely recognized as a most important challenge for bioengineering applied in medicine, and this holds in particular for cardiac modeling [18]. Of course, as a first major ingredient, this requires the construction of accurate *anatomical* models which suitably represent the actual geometrical attributes of the patient considered, usually based on medical imaging data. The next – at least equally important, and particularly challenging – stage consists in "personalizing" the biophysical characteristics of a cardiac model in order to reproduce the specificities of the patient, as e.g. in case of various pathologies which are likely to perturb localized values of constitutive parameters. This step is crucial to render the model *predictive*, hence to obtain some clinically-relevant quantitative information from the model simulations, both in the current state of the patient and under various scenarii of future evolutions, such as for therapy planning.

The complexity of the heart physiology – and of the related models – is such that this biophysical personalization procedure cannot be simply performed "manually", such as by directly extracting the required quantities from the available measurements, hence some automated estimation procedures are much needed in this endeavor [1]. Moreover, as some biophysical parameters are strongly correlated with the functional state of the organ, the automatic estimation of these parameters can be envisioned as a diagnosis tool. Our approach corresponds to the concept of *data assimilation* – already widely employed in other

D.N. Metaxas and L. Axel (Eds.): FIMH 2011, LNCS 6666, pp. 304–312, 2011.

domains of science and engineering – notably different from the objective of cardiac motion tracking *per se* [15,10,2,17], sometimes complemented by extracting some valuable indices from available data by using some constraining physical model equations [7,9]. The discriminating criterion in data assimilation is that once the estimation has been performed the biophysical model must be able to run *independently of any data*, while providing accurate and *predictive* solutions.

In this paper, we will consider a biomechanical heart model as proposed in [16] and perform a *complete personalization* – namely, both anatomical and biophysical – using *actual clinical data* consisting of Cine MR image sequences and pressure measurements, based on some earlier-proposed estimation procedures [12,13,11]. In order to allow for a detailed assessment of the estimation results, we used data obtained in an animal experiment in which a controlled infarct was created [4]. Hence, we can quantitatively compare the estimation results pertaining to the main biophysical parameter of interest in this context – namely, the tissue contractility – obtained prior and after infarction, and also qualitatively and semi-quantitatively evaluate the post-infarct results with respect to *a priori* knowledge regarding the pathology and to late enhancement indicators.

The next section will be devoted to the description of experimental data and an overview of the biomechanical model considered. Then, in Section 3 we summarize the estimation methodology and present the personalization results. A discussion follows in Section 4, prior to concluding remarks.

2 Experimental Data and Direct Modeling

The animal experiment including the data acquisition and setup of the direct model was described in [4]. Here, we will summarize the experimental data acquisition and the calibration strategy for the healthy and the infarcted hearts.

2.1 Experimental Data

The experimental data consist of animal data obtained with a farm pig of 30 kg. The subject was examined and data acquired once in a baseline condition (physiological heartbeat), and 38 days after artificially creating an antero-septal infarct. In both stages, non-invasive MR image data – among which Cine MRI and late enhancement images were used to set up the models – were acquired, and pressures in the heart cavities and large vessels were measured by catheterization.

2.2 Anatomical Model

Anatomical models for the baseline and infarcted stage were created from the end-diastolic time frames of the Cardiac MR images. We emphasize that two different anatomical models had to be created, in particular due to significant anatomical changes (thinning of the post-infarcted LV wall caused by resorption of the necrosis and tissue remodeling). Fiber directions were defined using prescribed values of angles between the short axis plane and the fibers on the

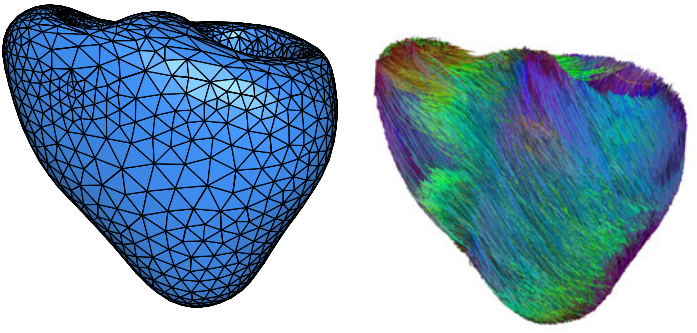

Fig. 1. Computational mesh for baseline (left) and generic fibers prescribed in the mesh (right)

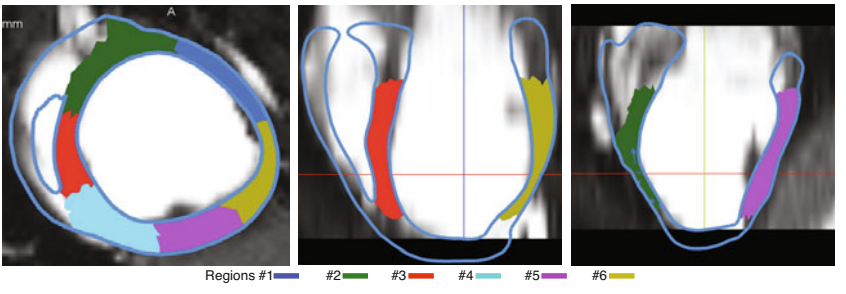

Fig. 2. Mesh of T0+38 subdivided into 6 volumic regions in the left ventricle

epicardium and endocardium, namely, -60/60 degrees in the LV, and -50/50 degrees in the RV, see Figure 1. The left ventricle of each model was subdivided into 6 volume regions – corresponding in their upper third to the basal segments of the standard 17-segment LV subdivision proposed by the American Heart Association (AHA) in [3], see Figure 2 – in order to allow prescribing and estimating different values of physical parameters in each region, in particular to characterize the infarct. In addition, for assessment purposes the non-viable tissue in the infarcted stage was segmented from the late enhancement images and projected into the corresponding model, see Fig. 3.

2.3 Biophysical Model

The cardiac model considered was described in [16], see also [6] for a more complete physiological and physical substantiation. In this model, a prescribed electrical activation induces actin-myosin binding, hence an active stress along the fiber direction. It has already been demonstrated in [4] that the main effects of an infarct can be captured in this model by reducing the contractility parameter which relates the electrical activation to the mechanical quantities.

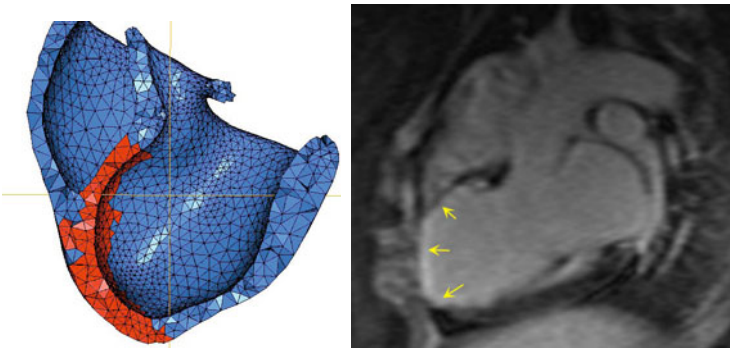

Fig. 3. Infarcted tissue in the mesh (left, in red) as segmented from the late enhancement MR images (right, yellow arrows)

The setup of the direct model of the healthy stage follows the calibration procedure used in [5]. The main mechanical parameters of the model – namely, the active properties represented by the contractility, and the passive tissue stiffness parameters – were adjusted manually. These parameters were kept constant over the whole myocardium. We used visco-elastic boundary conditions ([14]) applied on the base of the ventricles (area around the valves) and in the area around the apex, with parameters adjusted to obtain a still apex while preserving the base motion as seen in the long axis Cine MR images. An additional visco-elastic boundary condition representing a contact between the anterior heart wall with the thoracic cage was used. Finally, the Windkessel models parameters were adjusted so as to obtain simulated ventricle and arterial pressures close to the measured values.

In all our simulations we used an analytically prescribed electrical activation pattern in which a planar wave propagates from the apex to the base while activating only the subendocardial part of the myocardium. The transmural propagation is represented by a traveling wave with a lower propagation velocity. The two velocities are adjusted in the baseline case so that the activation timing is physiological, namely: propagation along the endocardium in ∼30–35 ms; endo- to epicardium propagation in ∼30–35 ms; activation of the whole myocardium in ∼70–80 ms, which corresponds to the measured QRS duration. The action potential duration in the simulation was taken constant over the whole myocardium, and was adjusted according to the Cine MRI data.

3 Regional Contractility Estimation Using Data Assimilation

3.1 Data Assimilation Methodology

Data assimilation consists in using measurements available on the system considered in order to estimate the state variables – namely, the actual trajectory

taken by the real system – and some unknown or uncertain modeling parameters. In this study we employed a sequential type data assimilation procedure – also referred to as filtering – by which the model dynamics and the uncertain parameters are corrected all along the simulation window using an operator which characterizes the *discrepancy* between the current simulated state and the measurements [12,8]. A successful procedure allows to achieve rapid convergence of the simulated trajectory to the real one and of the parameter quantities to their actual values. Furthermore, the essential physical behavior of the model is not perturbed, hence once the actual state and parameters have been recovered the model can be considered to be adequately *personalized*. The model can then be used to obtain information on some biophysical quantities absent from the measurements, or to predict the evolutions of the system under various assumptions, such as to explore and assess therapeutic strategies.

3.2 Estimation Using Segmented Cine MRI

In our case we will use the segmented Cine MRI sequences to construct a discrepancy operator based on the distance maps of the model boundary to the segmentation contours, separately on the LV endo- and epicardium. This discrepancy is employed in a filtering approach named "Schur Displacement Feedback" (SDF) which provides an effective state estimator as discussed in [13,8]. In addition, parameter estimation is performed by incorporating a second-stage filter which corresponds to a reduced-order version of the "Unscented Kalman Filter" (UKF), see [11]. This method generalizes reduced-order Kalman filtering to nonlinear dynamical and discrepancy operators – and indeed would be equivalent for linear systems – without requiring the computation of tangent operators and with enhanced accuracy compared to Extended Kalman Filtering.

We used this joint state-parameter estimation approach to estimate both the trajectory and regionalized contractility values – scaled to one according to a nominal healthy value – in each of the 6 above-described regions. As regards the estimation procedure setup, 3 main parameters had to be adjusted, namely, the covariance of the (scaled) contractility parameters set to $1/7$, the standard deviation of the observation error corresponding to roughly 1.5 mm in the segmentation, and the gain of the SDF filter manually calibrated to maintain the simulated system "reasonably close" to the data.

3.3 Estimation Results

Figure 4 shows the regional contractility estimation results, both in the baseline and in the infarcted stages. We emphasize that – by construction of the filtering procedure – the estimated parameter values evolve during the simulation period – corresponding to a complete heartbeat in our case – and of course the actual estimation is achieved with the final values. Note that these estimation curves actually stabilize near the end of the simulation window.

We also show in Figure 5 a comparison of the Cine MRI at the infarcted stage with three model contours: a direct simulation without estimation and with nominal contractility parameter values; the joint state-parameter estimator; finally,

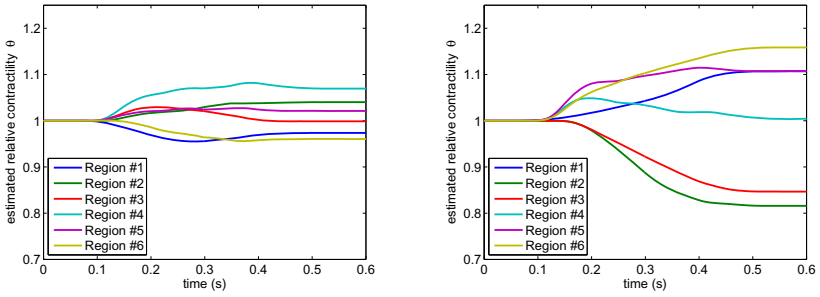

(a) Baseline (b) T0+38

Fig. 4. Regional contractility estimation at each stage

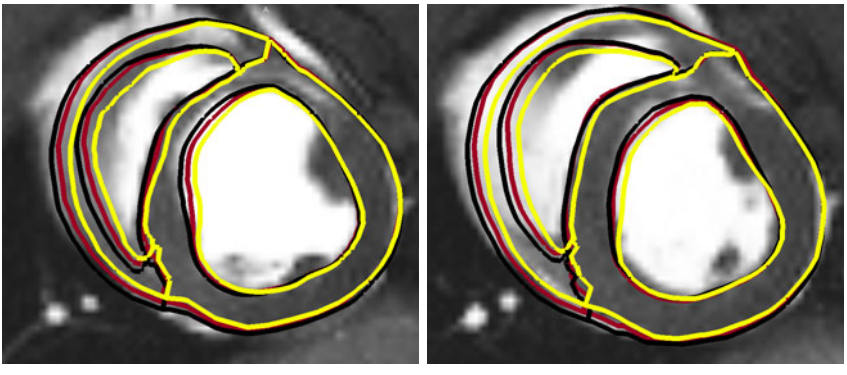

Fig. 5. Two slices of the end-systolic phase at stage T0+38. Comparison of direct model with constant contractility (yellow contour), direct model using the estimated values of contractility (red), joint state-parameter estimation (black).

a direct simulation without estimation and with the contractility parameter values obtained in the estimation procedure. We can see that – as expected – the estimator is closest to the image contours, but the direct simulation with personalized parameters is also quite accurate, and in particular drastically reduces the thickening in the infarcted region, unlike in the nominal simulation.

We can also assess the estimation results by comparison with the proportion of tissue marked by the late enhancement in each region. The plot shown in Figure 6 displays a good correlation between these computed ratios $(r_i)_{i=1}^6$ and the corresponding values obtained from the estimated contractility parameters $(\theta_i)_{i=1}^6$ by assuming the simple interpolation rule $\theta_i = 0.25 r_i + 1.20(1 - r_i)$. Of course, it should be noted that the segmentation of late enhancement images can be expected to be affected by various errors, hence it does not provide any definite "ground truth".

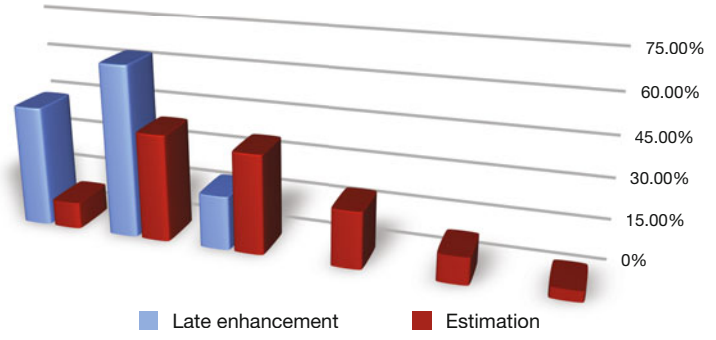

Fig. 6. Relative extent of the infarct in each region computed from the late enhancement segmentation and inferred from the estimated parameters (regions ordered from left to right)

4 Discussion

As seen in Figure 4, in the baseline case the contractility values do not vary more than by 10% in the course of the estimation. At the infarcted stage, a pronounced drop of contractility in the infarcted regions – except for Region ♯1 – is obtained, together with an increase in Regions ♯5 and ♯6 which may be caused by a compensation hypertrophy.

The contractility overestimation in the anterior wall at the infarcted stage (Region ♯1) may be caused by the artificial boundary conditions applied on the adjacent epicardial surface. The prescription and adjustment of suitable boundary conditions is a difficult problem, as we need to represent the contact of the heart with the surrounding structures – mainly the thoracic cage and the diaphragm – for which we used visco-elastic boundary conditions. However, this type of boundary condition applied on the anterior wall (part of Region ♯1) clearly hinders contraction. The hypokinesis of the region is then corrected by the parameter estimation, inducing an increase of the estimated contractility parameter in Region ♯1, see Figure 4. For this reason mainly related to a modeling limitation, we introduce some error in the parameter estimation for Region ♯1. This modeling issue may be circumvented by considering a sliding boundary condition on the anterior wall – much more realistic than the tethering associated with viscoelastic support, indeed – but such boundary conditions are quite delicate to handle and require very smooth surface meshes to allow adequate sliding.

Nevertheless, considering the relative coarseness of the measurements used in the estimation procedure – namely, only two segmented surfaces in each snapshot, the results obtained for the regional contractility values are undoubtedly satisfactory, as also substantiated by the personalized simulation produced with these estimated values, recall Fig. 5.

5 Conclusion and Perspectives

In this paper, we successfully applied a methodology of sequential joint-state parameter estimation with real cardiac Cine MRI data. As a result, this approach provides an automatic biophysical personalization of the model, which enables further uses for predictive purposes with key perspectives in therapy planning. Furthermore, we were able to localize and quantify myocardial infarction via regional contractility parameters, which shows some valuable potential for diagnosis assistance.

Of course, with a view to diagnosis assistance, more detailed regional contractility maps – e.g. a 17-segment AHA subdivision of the left ventricle, possibly further subdivided into several layers – would be extremely valuable. Our results indicate that observability conditions intrinsically limit the information which can be extracted from mere segmented Cine sequences. However, we could also employ tagged MR images, either with directly extracted myocardium displacements, or by extending in a straightforward manner the estimator used in this work based on measuring distances between the simulated and observed surfaces with the tag planes [8]. We can conjecture that the level of details accessible with this type of data would be significantly enhanced, and we could also expect to benefit from this to estimate some other physical parameters, such as passive tissue stiffness or quantities pertaining to the electrical activation.

References

1. Augenstein, K.F., Cowan, B.R., LeGrice, I.J., Nielsen, P.M.F., Young, A.A.: Method and apparatus for soft tissue material parameter estimation using tissue tagged magnetic resonance imaging. J. Biomech. Eng. 127(1), 148–157 (2005)
2. Bogatyrenko, E., Hanebeck, U.: Simultaneous state and parameter estimation for physics-based tracking of heart surface motion. In: Multisensor Fusion and Integration for Intelligent Systems (MFI), pp. 109–114 (2010)
3. Cerqueira, M.D., et al.: Standardized myocardial segmentation and nomenclature for tomographic imaging of the heart: A statement of healthcare professionals from the cardiac imaging comittee of the Council on Clinical Cardiology of the American Heart Association. Circulation 105, 539–542 (2002)
4. Chabiniok, R., Chapelle, D., Lesault, P.-F., Rahmouni, A., Deux, J.-F.: Validation of a biomechanical heart model using animal data with acute myocardial infarction. In: Proc. of CI2BM 2009 - MICCAI Workshop (2009)
5. Chapelle, D., Fernández, M.A., Gerbeau, J.-F., Moireau, P., Sainte-Marie, J., Zemzemi, N.: Numerical simulation of the electromechanical activity of the heart. In: Ayache, N., Delingette, H., Sermesant, M. (eds.) FIMH 2009. LNCS, vol. 5528, pp. 357–365. Springer, Heidelberg (2009)
6. Chapelle, D., Le Tallec, P., Moireau, P., Sorine, M.: An energy-preserving muscle tissue model: formulation and compatible discretizations. Int. J. Multiscale Comput. Eng. (2011) (in press)
7. Hu, Z.H., Metaxas, D., Axel, L.: In vivo strain and stress estimation of the heart left and right ventricles from MRI images. Med. Image Anal. 7(4), 435–444 (2003)

8. Imperiale, A., Chabiniok, R., Moireau, P., Chapelle, D.: Constitutive parameter estimation methodology using tagged-MRI data. In: Metaxas, D.N., Axel, L. (eds.) FIMH 2011. LNCS, vol. 6666, pp. 409–417. Springer, Heidelberg (2011)
9. Liu, H., Shi, P.: Maximum a posteriori strategy for the simultaneous motion and material property estimation of the heart. IEEE Trans. Biomed. Eng. 56(2), 378–389 (2009)
10. Mansi, T., Peyrat, J.-M., Sermesant, M., Delingette, H., Blanc, J., Boudjemline, Y., Ayache, N.: Physically-constrained diffeomorphic demons for the estimation of 3D myocardium strain from cine-MRI. In: Ayache, N., Delingette, H., Sermesant, M. (eds.) FIMH 2009. LNCS, vol. 5528, pp. 201–210. Springer, Heidelberg (2009)
11. Moireau, P., Chapelle, D.: Reduced-order Unscented Kalman Filtering with application to parameter identification in large-dimensional systems. Cont. Optim. and Calc. Variat. (2010)
12. Moireau, P., Chapelle, D., Le Tallec, P.: Joint state and parameter estimation for distributed mechanical systems. Comput. Meth. Appl. Mech. Eng. 197, 659–677 (2008)
13. Moireau, P., Chapelle, D., Le Tallec, P.: Filtering for distributed mechanical systems using position measurements: Perspectives in medical imaging. Inverse Prob. 25(3), 035010 (2009)
14. Moireau, P., Xiao, N., Astorino, M., Figueroa, C.A., Chapelle, D., Taylor, C.A., Gerbeau, J.-F.: External tissue support and fluid-structure simulation in blood flows. Biomech. Model. Mechanobiol. (2011) (in press)
15. Papademetris, X., Sinusas, A.J., Dione, D.P., Constable, R.T., Duncan, J.S.: Estimation of 3D left ventricular deformation from medical images using biomechanical models. IEEE Trans. Med. Imaging 21(7), 786–800 (2002)
16. Sainte-Marie, J., Chapelle, D., Cimrman, R., Sorine, M.: Modeling and estimation of the cardiac electromechanical activity. Comput. Struct. 84, 1743–1759 (2006)
17. Schaerer, J., Casta, C., Pousin, J., Clarysse, P.: A dynamic elastic model for segmentation and tracking of the heart in MR image sequences. Med. Image Anal. 14, 738–749 (2010)
18. Sermesant, M., Moireau, P., Camara, O., Sainte-Marie, J., Andriantsimiavona, R., Cimrman, R., Hill, D.L., Chapelle, D., Razavi, R.: Cardiac function estimation from MRI using a heart model and data assimilation: advances and difficulties. Med. Image Anal. 10(4), 642–656 (2006)

Real-Time Cardiac MR Anatomy and Dyssynchrony Overlay for Guidance of Cardiac Resynchronization Therapy Procedures: Clinical Results Update

YingLiang Ma[1], Anoop Shetty[1], Simon Duckett[1], C. Aldo Rinaldi[2], Tobias Schaeffter[1], Reza Razavi[1], Gerry Carr-White[2], and Kawal S. Rhode[1]

[1] Division of Imaging Sciences, King's College London, SE1 7EH, UK
[2] Department of Cardiology, Guy's & St. Thomas' Hospitals NHS Foundation Trust, London, SE1 7EH, UK

Abstract. Optimal left ventricular (LV) lead placement via the coronary sinus (CS) is a critical factor in defining response to cardiac resynchronization therapy (CRT). Using novel MR image acquisition, segmentation, overlay and registration software we set out to guide lead placement by avoiding scar and targeting the LV region with the latest mechanical activation. We previously reported clinical results for 7 patients and now present updated results. 17 patients underwent cardiac magnetic resonance (CMR) scans. 3D whole heart images were segmented to produce high-fidelity anatomical models of the cardiac chambers and coronary veins. Four-chamber and short-axis cine images were processed using Tomtec software to give a 16-segment time volume-dyssynchrony map. In patients with myocardial scar, the Gadolinium late enhancement images were manually segmented and registered to the anatomical model along with the dyssynchrony map. The 3 latest mechanically acti- vated segments with <50% scar were identified and this information was overlaid at CRT implant on to live X-ray fluoroscopic images using a prototype version of the Philips EP Navigator software (see figure). Subsequently, the X-ray C-arm and table could be moved freely whilst automatically maintaining a registered roadmap. We used a high-fidelity pressure wire to assess the acute haemodynamic response to pacing in different regions of the overlaid 16 segment model. 15 of the 17 patients underwent successful placement of a LV pacing lead via the CS with satisfactory pacing parameters and no phrenic nerve stimulation at implant. In 2 patients we were unable to place a LV lead successfully in any branch of the CS. We paced in at least one of our 3 target segments in 11 patients. 67% of patients were responders as defined by a 10% increase in +dP/dt over baseline. In conclusion, CMR-guided CRT allowed left lead placement in 15/17 patients with approximately 2/3 patients being acute responders. Furthermore, specific targeting was successful in 11/15 patients using the image-guidance system. Following this successful pilot study, we will

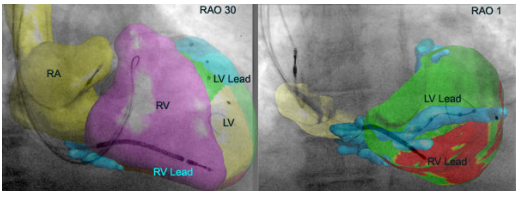

D.N. Metaxas and L. Axel (Eds.): FIMH 2011, LNCS 6666, pp. 313–314, 2011.

commence a randomized control study to examine if image-guided implantation improves patient response to CRT.

Keywords: image-guided intervention, cardiac resynchronization therapy, dyssynchrony, cardiac segmentation.

Parameter Identification in Cardiac Electrophysiology Using Proper Orthogonal Decomposition Method

M. Boulakia[1] and J.-F. Gerbeau[2]

[1] Université Pierre et Marie Curie-Paris 6, LJLL, PARIS, F-75005 France
[2] INRIA Paris-Rocquencourt BP 105, F–78153 Le Chesnay Cedex, France

Abstract. We consider the problem of estimating some parameters (like ionic models or parameters involved in the initial stimulation) of a model of electrocardiograms (ECG) from the data of the Einthoven leads. This problem can be viewed as a first attempt to identify or to locate a pathology. The direct model is based on the bidomain equations in the heart and a Poisson equation in the torso and. To keep the computational time reasonable, the evaluation of the direct problem is approximated with a reduced order model based on Proper Orthogonal Decomposition (POD). The optimization problem is solved using a genetic algorithm. Numerical tests show that, with noisy synthetic data, the proposed procedure allows to recover ionic parameters and initial activation regions with a fair accuracy.

1 Introduction

The inverse problem of electrocardiology is usually addressed by reconstructing the epicardial potential from the body surface potential by solving the Cauchy problem for the Poisson equation in the torso with a suitable regularization (see [8] e.g.). The present study follows another route: assuming that a source model is available in the heart, we endeavor to estimate some parameters of this model from the body surface potential. The source model considered in this study is the one proposed in [2]. The inverse procedure is based on a genetic algorithm which evaluates a reduced order approximation of the direct problem. The reduced order approximation is built on the POD of the bidomain equations. We show that POD can successfully approximate the problem when some coefficients are perturbed, but fails for others. We propose a simple strategy to also handle those cases. The global strategy is illustrated through various numerical tests based on synthetic data.

2 Methods

2.1 Resolution of the Direct Problem

The electrical activity in the heart is modeled by the bidomain equations (see [7,8] e.g.). We denote by Ω_{H} the heart domain, by u_e and V_{m} the extracellular

D.N. Metaxas and L. Axel (Eds.): FIMH 2011, LNCS 6666, pp. 315–322, 2011.

potential and the transmembrane potential and by $\boldsymbol{\sigma}_{\mathrm{i}}$ and $\boldsymbol{\sigma}_{\mathrm{e}}$ the intra- and extracellular conductivity tensors. Thus we have in Ω_{H}

$$\begin{aligned} A_{\mathrm{m}}\left(C_{\mathrm{m}}\frac{\partial V_{\mathrm{m}}}{\partial t}+I_{\mathrm{ion}}(V_{\mathrm{m}},w)\right)-\operatorname{div}(\boldsymbol{\sigma}_{\mathrm{i}}\boldsymbol{\nabla}V_{\mathrm{m}})-\operatorname{div}(\boldsymbol{\sigma}_{\mathrm{i}}\boldsymbol{\nabla}u_{\mathrm{e}})=A_{\mathrm{m}}I_{\mathrm{app}} \\ -\operatorname{div}((\boldsymbol{\sigma}_{\mathrm{i}}+\boldsymbol{\sigma}_{\mathrm{e}})\boldsymbol{\nabla}u_{\mathrm{e}})-\operatorname{div}(\boldsymbol{\sigma}_{\mathrm{i}}\boldsymbol{\nabla}V_{\mathrm{m}})=0, \end{aligned} \tag{1}$$

where A_{m} is the rate of membrane area per volume unit and C_{m} the membrane capacitance per area unit. The term $I_{\mathrm{ion}}(V_{\mathrm{m}},w)$ represents the ionic current across the membrane which depends on V_{m} and w, and I_{app} is a given source function. The dynamics of the ionic variable w and the ionic current I_{ion} are described by the phenomenological two-variable model [5]. It is given by

$$\begin{aligned} I_{\mathrm{ion}}(V_{\mathrm{m}},w)&=-\frac{w}{\tau_{\mathrm{in}}}\frac{(V_{\mathrm{m}}-V_{\mathrm{min}})^2(V_{\mathrm{max}}-V_{\mathrm{m}})}{V_{\mathrm{max}}-V_{\mathrm{min}}}+\frac{1}{\tau_{\mathrm{out}}}\frac{V_{\mathrm{m}}-V_{\mathrm{min}}}{V_{\mathrm{max}}-V_{\mathrm{min}}}, \\ \partial_t w=-g(V_{\mathrm{m}},w)&=-\begin{cases}\dfrac{w}{\tau_{\mathrm{open}}}-\dfrac{1}{\tau_{\mathrm{open}}(V_{\mathrm{max}}-V_{\mathrm{min}})^2} & \text{if} \quad V_{\mathrm{m}}<V_{\mathrm{gate}}, \\ \dfrac{w}{\tau_{\mathrm{close}}} & \text{if} \quad V_{\mathrm{m}}>V_{\mathrm{gate}}, \end{cases} \end{aligned} \tag{2}$$

where τ_{in}, τ_{out}, τ_{open}, τ_{close}, V_{gate}, V_{min}, V_{max} are given parameters.

In the domain outside the heart region, denoted Ω_{T}, the electrical potential u_{T} is solution of the equation:

$$\operatorname{div}(\boldsymbol{\sigma}_{\mathrm{T}}\boldsymbol{\nabla}u_{\mathrm{T}})=0, \quad \text{in} \quad \Omega_{\mathrm{T}}, \quad \boldsymbol{\sigma}_{\mathrm{T}}\boldsymbol{\nabla}u_{\mathrm{T}}\cdot\boldsymbol{n}=0, \quad \text{on} \quad \Gamma_{\mathrm{ext}}, \tag{3}$$

where Γ_{ext} is the external boundary of the torso. The two problems are weakly coupled, following the procedure explained in [2]. Differences of potentials on standard points of Γ_{ext} define the ECG (Figure 1, left). For the sake of simplicity, another domain Ω_{H}, consisting of a parallelepiped, will also be considered in the following (Figure 1, right). The model is discretized in space with a finite element method and in time by combining a second order BDF implicit scheme with an explicit treatment of the ionic current.

2.2 Optimization Method

Our objective is to identify the values of some parameters, like ionic parameters or parameters linked to the initial stimulation. To do so, we minimize a cost function corresponding to the norm of the difference between a reference ECG and the ECG obtained for a given value of the parameters. In this preliminary study, the reference ECGs are all "synthetic" which means that they are generated by the model itself. Let $n\in\mathbb{N}^*$ be the number of parameters and $\theta\in\mathbb{R}^n$ the vector of parameters we are looking for in a subset I of $\mathbb{R}^n$. The subset I is given by $I_1\times\cdots\times I_n$ where I_j is an interval where the value θ_j is assumed to be. The following cost function is minimized

$$J(\theta)=\delta t\sum_{i=1}^{N_T}|V_{\mathrm{I}}(t_i)-V_{\mathrm{I,ref}}(t_i)|^2+|V_{\mathrm{II}}(t_i)-V_{\mathrm{II,ref}}(t_i)|^2+|V_{\mathrm{III}}(t_i)-V_{\mathrm{III,ref}}(t_i)|^2$$

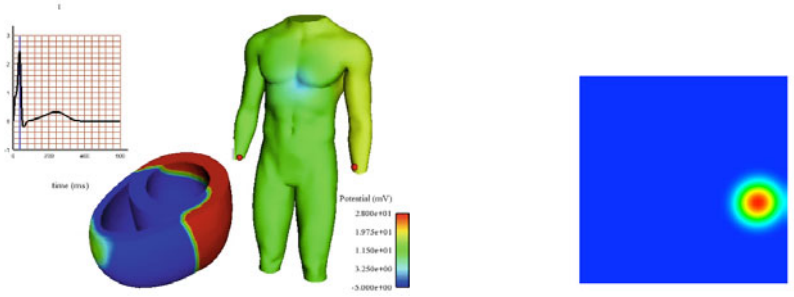

Fig. 1. Two representative pictures of the simulations run in this study. Left: heart-torso coupling and Einthoven I lead ECG. Right: schematic configuration used for the identification of the initial activation point.

with respect to $\theta \in I$, where V_{I}, V_{II} and V_{III} are the three Einthoven leads given by the simulation for the value θ of the parameters and $V_{\mathrm{I,ref}}$, $V_{\mathrm{II,ref}}$ and $V_{\mathrm{III,ref}}$ are the Einthoven leads of the reference ECG. An alternative in the definition of J is to consider the twelve standard leads instead of the three Einthoven leads. Numerical tests give similar results for these two choices of cost function.

The optimization problem is solved using a genetic algorithm (we refer for example to [3]). This algorithm is a global optimization method which consists of following the evolution of a population of N_p elements $(\theta_1, \ldots, \theta_{N_p}) \in I^{N_p}$ corresponding to a set of values of the parameters. The population is regenerated N_g times, where N_g corresponds to the number of generations. At each generation, J is evaluated for each element of the population and the population evolves from a generation to another following three stochastic principles: selection (promote the elements of the population whose value by J is small), crossover (create from two elements of the population two new elements by doing a random barycentric combination of them), mutation (replace an element of the population by a new one randomly chosen in its neighborhood). To speed up this algorithm, many evaluations of J are performed using a surrogate model. This model consists of approximating the value of J by a Radial Basis Functions interpolation based on previously computed exact evaluations. The total number N_{ex} of exact evaluations is fixed and the number of exact evaluations decreases at each generation.

2.3 POD Reduced-Order Modelling

The genetic algorithm presented in the previous section offers many advantages: it can easily be run in parallel and it does not need the gradient of the cost function. Its main flaw is to require a large number of evaluations of the direct problem, even if many evaluations are avoided with the surrogate model strategy. To keep the computational time reasonable, we propose to use a reduced order model based on POD in the optimization loop.

Notions about the POD method. POD is a method to derive reduced models by projecting the system onto subspaces spanned by a basis of elements that contains the main features of the expected solution. We briefly recall this method here and refer the reader interested by more details to [4,6] for example. To generate the POD basis associated with a precomputed solution u of an approximated Galerkin problem, we make a first numerical simulation (or set of simulations) and keep some snapshots $u(t_k)$, $1 \leq k \leq p$. Then a singular value decomposition (SVD) of the matrix $B = (u(t_1), \ldots, u(t_p)) \in \mathbb{R}^{N,p}$ is performed: $B = USV'$, where $U \in \mathbb{R}^{N,N}$ and $V \in \mathbb{R}^{p,p}$ are orthogonal matrices, $S \in \mathbb{R}^{N,p}$ is the matrix of the singular values ordered by decreasing order, and $N \geq p$ is the dimension of the Galerkin basis of the finite element method.

The N_{modes} first POD basis functions $\{\Psi_i\}_{1 \leq i \leq N_{\text{modes}}}$ are then given by the N_{modes} first columns of U and the POD Galerkin problem is solved by looking for a solution of the type $u = \sum_{i=1}^{N_{\text{modes}}} \alpha_i(t)\Psi_i$.

The $N \times N$ sparse system of the finite element method is thus replaced by a full system of size $N_{\text{modes}} \times N_{\text{modes}}$ with the POD method. To give a rough idea, it is generally possible to get a good accuracy for the problems at hand with $N_{\text{modes}} \approx 100$. With the time scheme used in this work, the matrix is constant over the time, since all the nonlinearities are treated explicitly. The matrix is therefore projected on the POD basis and factorized only once at the beginning of the computation. As a consequence, for the simulations presented in this paper, the reduced order model resolution is about one order of magnitude faster than the full order one.

Strategies to handle parameter perturbations. To apply the POD method in parameter identification problems, a critical difficulty has to be faced: a POD basis generated from a solution obtained with a given set of parameters may be inaccurate to approximate a solution obtained from another set of parameters. The issue of the stability of a POD basis with respect to parameters perturbation is still the topic of active researches. The approaches proposed below are simple, but quite efficient for the considered problems. More sophisticated strategies, like interpolation of POD bases [1], could be considered in the future.

Assume that the parameters θ lie in $I \subset \mathbb{R}^n$. The simplest method is the following:

– **M1**: Only one POD basis is generated for a value $\theta_0 \in I$. This POD basis is then used for any $\theta \in I$.

As will be illustrated in section 3.1, approach **M1** proves to be satisfactory for some parameters (τ_{close} for example) but may be extremely inaccurate in other cases. To make the POD basis more robust with respect to parameter perturbation, two other methods are considered:

– **M2**: Many POD bases are computed "off-line" for different values of θ taken in a finite subset $\mathcal{A}$ of I. Next, for an arbitrary value $\theta \in I$, the POD basis corresponding to the closest value of $\theta \in \mathcal{A}$ is used.

– **M3**: POD bases are computed from the combination of several simulations. More precisely, let us introduce $\mathcal{A} = \{\mathcal{A}_1, \ldots, \mathcal{A}_m\}$ where $\mathcal{A}_l$, $1 \leq l \leq m$ is a finite subset of I of cardinal k_l. For each l, for each value $\theta_i \in \mathcal{A}_l$, $1 \leq i \leq k_l$, numerical simulations are run "off-line" and the snapshots $u_{l,i}(t_k)$, $1 \leq k \leq p$ are stored. Then, these snapshots are gathered into the matrix $B_l = (u_{l,1}(t_1), \ldots, u_{l,1}(t_p), u_{l,2}(t_1), \ldots, u_{l,2}(t_p), \ldots, u_{l,k_l}(t_1), \ldots, u_{l,k_l}(t_p))$ which is used to generate the POD basis as before. Then, for each $\theta \in I$, the POD basis obtained for the closest set of parameters is used.

Method **M1** is of course the cheapest, but the choice of θ_0 is somehow arbitrary and this approach is too crude in some configurations. In the two other methods **M2** and **M3**, the role of the finite set $\mathcal{A}$ is to reasonably sample the whole set $I = I_1 \times \cdots \times I_n$ in order to capture different behaviors of the solutions. In practice, a grid can be defined on the parameters space. Then, for **M2**, the POD bases are precomputed on the vertices of the grid, whereas for **M3**, the POD bases are precomputed by element using the snapshots corresponding the vertices of the elements of the parameter grid.

3 Results

3.1 Two Illustrative Examples of POD Simulations

The accuracy of the POD approximation of the bidomain equations will only be evaluated on the ECG corresponding to the solution, since this is the only information used in the optimization loop.

Let us first consider the perturbation of parameter τ_{close} which corresponds to the characteristic closing time of ionic channels. In our model, the heart is divided in four regions where this parameter takes four different constant values. We focus on the value in the epicardium of the left ventricle $\tau_{\text{close}}^{\text{epi}}$, and in the right ventricle $\tau_{\text{close}}^{\text{RV}}$. A POD basis of 80 vectors is first constructed with $(\tau_{\text{close}}^{\text{epi}}, \tau_{\text{close}}^{\text{RV}}) = (80, 80)$. This basis is sufficient to get an excellent accuracy if the *same* experiment is run with the reduced order model. More interestingly, it still gives quite good results when $(\tau_{\text{close}}^{\text{epi}}, \tau_{\text{close}}^{\text{RV}})$ are significantly modified. For example, Figure 2 (left) shows a comparison of the ECG get with the full and the reduced models corresponding to $(\tau_{\text{close}}^{\text{epi}}, \tau_{\text{close}}^{\text{RV}}) = (90, 120)$. The QRS is in excellent agreement, the T-wave is slightly underestimated, which is not surprising since τ_{close} mainly affects the repolarization phase. It is interesting to note that for the values $(\tau_{\text{close}}^{\text{epi}}, \tau_{\text{close}}^{\text{RV}}) = (80, 80)$, the T-wave of the ECG is negative whereas it is positive with (90,120). It is therefore particularly satisfactory to obtain the correct T-wave orientation with the reduced order model after perturbing these coefficients.

Unfortunately, the accuracy obtained with a POD basis may get worse when other parameters are modified. This is the case for example with the parameter governing the initial activation: if we use a POD basis obtained from a reference simulation with an initial activation in the septum to run a reduced order simulation with an initial activation at the apex, the results are totally wrong, as shown in Figure 2 (right).

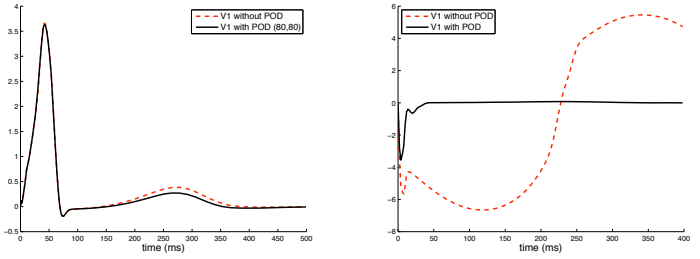

Fig. 2. Left: First leads of the ECGs with $(\tau_{\text{close}}^{\text{epi}}, \tau_{\text{close}}^{\text{RV}}) = (90, 120)$. Comparison of the ECGs obtained with the full model and with a POD basis generated with $(\tau_{\text{close}}^{\text{epi}}, \tau_{\text{close}}^{\text{RV}}) = (80, 80)$. Right: First leads of ECGs obtained for an initial stimulation in the apex. Comparison of the ECGs with the full model and with the POD basis obtained from a simulation with an initial activation on the septum.

3.2 Identification of Two Ionic Parameters

Based on the first three leads of the ECG, we wish to estimate $\tau_{\text{close}}^{\text{epi}}$ and $\tau_{\text{close}}^{\text{RV}}$. In [2, Figure 24], it is shown that the ECG is quite sensitive to τ_{close}. The reference ECG used in the cost function is obtained from a first numerical simulation with $(\tau_{\text{close}}^{\text{epi}}, \tau_{\text{close}}^{\text{RV}}) = (90, 120)$ without using POD. Our goal is to test whether our identification algorithm based on POD and genetic algorithm is able to find these values out.

The parameters $\theta = (\tau_{\text{close}}^{\text{epi}}, \tau_{\text{close}}^{\text{RV}})$ are searched for in the set $[50, 150] \times [50, 150]$. The "exact" evaluations required by the optimization algorithm are based on the reduced order model using the 80 first POD modes. The results are summarized in Table 1 where the genetic algorithm is run with $N_p = 25$, $N_g = 15$ and $N_{ex} = 150$ ("Population 1", top), and with $N_p = 90$, $N_g = 15$ and $N_{ex} = 600$ ("Population 2", bottom).

For **M2**, we use $\mathcal{A}_1 = \{50; 60; 70; 80; 90; 100; 110; 120; 130; 140; 150\}$ and $\mathcal{A}_2 = \{50; 70; 90; 110; 130; 150\}$. Since the outcome of the genetic algorithm depends on the initial random population, the results presented correspond to a mean value of several runs. The relative error is defined by $\max\left(\frac{|\tau_{\text{close}}^{\text{epi}} - 90|}{90}, \frac{|\tau_{\text{close}}^{\text{RV}} - 120|}{120}\right)$. Table 2 shows the results obtained with Population 1 when the synthetic ECG used as reference is perturbed by a 1% or 4% noise.

3.3 Identification of the Initial Stimulation

In this test, the computational domain is a parallelepiped of size $[-2.5, 2.5] \times [-2.5, 2.5] \times [0, 0.2]$ (Figure 1, right). The initial activation is applied on $[c_1 - 0.2, c_1 + 0.2] \times [c_2 - 0.2, c_2 + 0.2] \times [0, 0.2]$. Our goal is to identify the location (c_1, c_2) in $[-2.5, 2.5] \times [-2.5, 2.5]$. The standard ECG leads are replaced by the differences of potential u_e evaluated in three points of the boundary. The reference pseudo-ECG has been obtained with $(c_1, c_2) = (1.8, -0.6)$. The error is defined by $\sqrt{(c_1 - 1.8)^2 + (c_2 + 0.6)^2}$. In Table 3 columns 2 and 3, the parameters of the genetic algorithm are $N_p = 25$, $N_g = 12$ and $N_{ex} = 150$. In Table 3 columns

Table 1. Identification of $(\tau_{\text{close}}^{\text{epi}}, \tau_{\text{close}}^{\text{RV}})$ (Reference value $(90, 120)$)

Population 1	$(\tau_{\text{close}}^{\text{epi}}, \tau_{\text{close}}^{\text{RV}})$	Relative error (in %)	Value of the cost function
M1 with $\theta_0 = (100, 100)$	$(88.4, 122)$	1.8	0.23
M1 with $\theta_0 = (150, 50)$	$(89.6, 127.1)$	5.9	6.4
M2 with $\mathcal{A} = \mathcal{A}_1 \times \mathcal{A}_1$	$(90.5, 120.5)$	0.6	0.08
M2 with $\mathcal{A} = \mathcal{A}_2 \times \mathcal{A}_2$	$(86.9, 117.5)$	3.4	0.9
Population 2	$(\tau_{\text{close}}^{\text{epi}}, \tau_{\text{close}}^{\text{RV}})$	Relative error (in %)	Value of the cost function
M1 with $\theta_0 = (100, 100)$	$(87.7, 121.6)$	2.6	0.22
M1 with $\theta_0 = (150, 50)$	$(85.7, 124.2)$	4.8	5.78
M2 with $\mathcal{A} = \mathcal{A}_1 \times \mathcal{A}_1$	$(90.2, 120.2)$	0.2	0.07
M2 with $\mathcal{A} = \mathcal{A}_2 \times \mathcal{A}_2$	$(89.8, 119.7)$	0.2	0.36

Table 2. Identification of $(\tau_{\text{close}}^{\text{epi}}, \tau_{\text{close}}^{\text{RV}})$ using **M2** with $\mathcal{A}_1$ (Reference value $(90, 120)$)

	$(\tau_{\text{close}}^{\text{epi}}, \tau_{\text{close}}^{\text{RV}})$	Value of the cost function
Noise of intensity 1%	$(89.6, 119.7)$	0.12
Noise of intensity 4%	$(90.2, 119.9)$	0.8

Table 3. Identification of (c_1, c_2) (Reference value $(1.8, -0.6)$). Columns 4 & 5 correspond to a larger population in the genetic algorithm than columns 2 & 3.

	(c_1, c_2)	Error	(c_1, c_2)	Error
M1 with $x_0 = (0, 0)$	$(-1.6, -1.6)$	3.5	$(-1.5, -1.7)$	3.5
M2 with $\mathcal{A} = \mathcal{A}_3 \times \mathcal{A}_3$	$(1.71, -0.54)$	0.11	$(1.81, -0.66)$	0.06
M2 with $\mathcal{A} = \mathcal{A}_4 \times \mathcal{A}_4$	$(1.92, -0.59)$	0.12	$(2.07, -0.54)$	0.28
M3	$(1.96, -0.61)$	0.16	$(1.97, -0.62)$	0.17
without POD	$(1.57, -0.56)$	0.23	$(1.74, -0.51)$	0.11

4 and 5, the same test is done with a larger population: $N_p = 100$, $N_g = 15$ and $N_{ex} = 1000$. For **M2**, $\mathcal{A}_3 = \{-2.5; -2; -1.5; -1; -0.5; 0; 0.5; 1; 1.5; 2; 2.5\}$ and $\mathcal{A}_4 = \{-2; -1; 0; 1; 2\}$. For **M3**, $\mathcal{A} = \{\tilde{\mathcal{A}}_l,\ 1 \leq l \leq 36\}$ where $\tilde{\mathcal{A}}_l$ contains the four vertices of the element l of the cartesian grid $\{-2.5; -2; -1; 0; 1; 2; 2.5\} \times \{-2.5; -2; -1; 0; 1; 2; 2.5\}$. For this simple geometry (about 5000 nodes), the direct simulation is not very time-consuming. It is therefore possible to solve the inverse problem with the full order model rather than with the POD.

4 Discussion and Conclusion

In paragraph 3.2, we saw that the simplest method **M1** allows to obtain satisfactory results, but the results depend on the arbitrary value θ_0 and the error does

not seem to quickly decrease when the population goes up. Results seem more robust with **M2**. In paragraph 3.3, when the initial activation parameters vary, method **M1** is inadequate. This obviously comes from the fact that, as noticed in paragraph 3.1, POD is unable to approximate the direct problem in this case. The strategies proposed in **M2** or **M3** allow to control the strong dependence of the solution with respect to the initial stimulation. It is interesting to notice that the results with **M2** or **M3** are quite comparable to the ones obtained without the POD method. Thus, the accuracy of the POD seems to be reasonably consistent with the accuracy that can be expected from the genetic algorithm.

In conclusion, these preliminary results are promising. Nevertheless, the method still has to be tested on real data. Moreover, difficulties can be expected when increasing the number of parameters. In that case, an efficient strategy to sample the parameters space will be critical to keep using the proposed strategy of approximation by POD.

Acknowledgment. The authors wish to thank Laurent Dumas who provided them with his optimization algorithm and Charbel Farhat and David Amsallem for valuable discussions about model reduction.

References

1. Amsallem, D., Farhat, C.: Interpolation method for adapting reduced-order models and application to aeroelasticity. AIAA Journal-American Institute of Aeronautics and Astronautics 46(7), 1803–1813 (2008)
2. Boulakia, M., Cazeau, S., Fernández, M.A., Gerbeau, J.-F., Zemzemi, N.: Mathematical modeling of electrocardiograms: a numerical study. Ann. Biomed. Eng. 38(3), 1071–1097 (2010)
3. Goldberg, D.E.: Genetic algorithms in search, optimization and machine learning. Addison-Wesley, Reading (1989)
4. Kunisch, K., Volkwein, S.: Galerkin proper orthogonal decomposition methods for parabolic problems. Numerische Mathematik 90(1), 117–148 (2001)
5. Mitchell, C.C., Schaeffer, D.G.: A two-current model for the dynamics of cardiac membrane. Bulletin Math. Bio. 65, 767–793 (2003)
6. Rathinam, M., Petzold, L.R.: A new look at proper orthogonal decomposition. SIAM Journal on Numerical Analysis 41(5), 1893–1925 (2004)
7. Sachse, F.B.: Computational Cardiology: Modeling of Anatomy, Electrophysiology, and Mechanics. Springer, Heidelberg (2004)
8. Sundnes, J., Lines, G.T., Cai, X., Nielsen, B.F., Mardal, K.-A., Tveito, A.: Computing the Electrical Activity in the Heart. Springer, Heidelberg (2006)

Are Robotic-Assisted Catheter Ablation Lesions Different from Standard Catheter Ablation in Paroxysmal AF Patients? : Novel CMRI Findings Made Possible with Semi-automatic 3-D Visualisation

Aruna Arujuna[1,2], Rashid Karim[1], Anoop Shetty[1,2], Aldo Rinaldi[1,2], Michael Cooklin[2], Reza Razavi[1,2], Mark O'Neill[1,2], Jaswinder Gill[1,2], and Kawal S. Rhode[1]

[1] Division of Imaging Sciences, King's College London, SE1 7EH, UK
[2] Department of Cardiology, St Thomas' Hospital, London, SE1 7EH, UK
aruna.arujuna@kcl.ac.uk

Abstract. Cardiac magnetic resonance imaging (CMRI) of the left atrium following catheter ablation can detect lesions with delayed enhancement (DE) and more recently with T2-weighted enhancement (T2W). We know that catheter stability, tissue contact force and RF duration are determinants of lesion formation and may be operator-dependent. The Hansen Robotic System (Hansen, Mountain View, CA, USA) permits accurate titration of contact force while maintaining a stable catheter position. Here, we sought to compare atrial injury following manual or robotic catheter ablation by quantifying tissue necrosis with DE and tissue edema with T2W enhancement on CMRI. Twelve patients (mean age 54±15.4) with paroxysmal atrial fibrillation (PAF) undergoing first ablation were recruited to undergo either manual (n=6) or robotic (n=6) approach. Following confirmed pulmonary vein isolation (PVI), 24 pairs of PVs were imaged. DE, T2W, and anatomical imaging sequences were performed pre- and immediately post- wide area circumferential ablation. A semi-automatic 3D method [Knowles *et al. IEEE Trans. Biomed. Eng.* 2010] was used for visualizing and quantifying tissue injury. Atrial surface models were derived from the anatomical MRI data and registered to DE or T2W MR scans. The maximum intensity projection values were computed onto the atrial surfaces with subsequent color coding (see the figure for an example taken from one of the robotic cases; green=min to red=max). The percentages of PV antral circumferential enhancement on the surfaces were quantified for each of DE (irreversible injury), T2W (reversible injury) and combined DE & T2W. Robotic ablation resulted in a greater circumferential lesion extent as

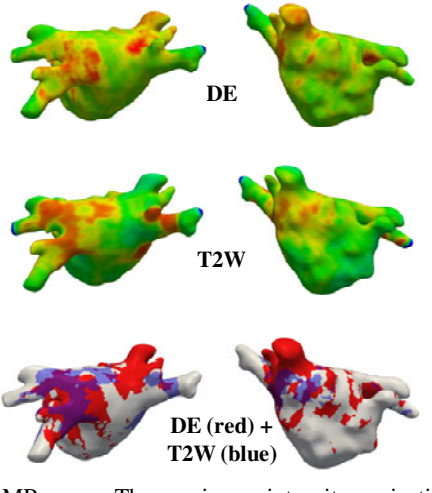

D.N. Metaxas and L. Axel (Eds.): FIMH 2011, LNCS 6666, pp. 323–324, 2011.

assessed by DE and T2W. In both groups, areas of T2W (edema) not only overlapped with areas of DE but also filled in gaps between areas of DE producing in combination near complete circumferential lesions around all PVs. Combination of T2W and DE conferred a statistically significant higher % encirclement in the robotic series (92%) versus standard navigation (71%) (p=0.007). A non-significant higher mean ratio of DE to (T2+DE) of 0.75±0.18 versus 0.61±0.30 was observed in the robotic arm (p=0.20). Calculated mean energy delivered was 84.2kJ versus 79.6kJ in the robotic and standard navigation groups (p=0.82), respectively. In comparison to manual ablation, robotic LA ablation achieves more tissue necrosis and a greater degree of PV antral encirclement. This may be a function of improved stability and contact force information.

Keywords: delayed enhancement, magnetic resonance imaging, cardiac ablation, atrial fibrillation.

MagnetoHemoDynamics Effect on Electrocardiograms

V. Martin[1,2], A. Drochon[2], O. Fokapu[2], and J.-F. Gerbeau[1]

[1] INRIA Paris-Rocquencourt BP 105, F–78153 Le Chesnay, France
[2] Université de Technologie de Compiègne, France

Abstract. In presence of a high magnetic field, the blood flow in the aorta induces an electrical potential which is responsible for an increase of the T-wave in the electrocardiogram (ECG). This phenomenon may perturb ECG-gated imaging. The aim of this numerical study is to reproduce this experimental observation through computer simulations. The proposed model consists of three components: magnetohydrodynamics (MHD) in the aorta, bidomain equations in the heart and electrical diffusion in the rest of the body. These models are strongly coupled together and solved with finite elements. Some numerical results without and with a magnetic field are presented and discussed. When the magnetic field increases from $B = 0T$ to $B = 3T$, it is observed numerically that the potential in the lead I of the ECG doubles during the T-wave, reaching the level of the QRS peak. All numerical computations were performed on a realistic "averaged" human model.

1 Introduction

In order to improve the quality of the images provided by Magnetic Resonance Imaging (MRI), the magnetic field used in MRI is getting stronger and stronger: from $3T$ nowadays, it might increase up to $10T$ in the future.

We are interested in the perturbations induced by the magnetic field on the electrocardiogram (ECG). Indeed, the blood flow immersed in the magnetic field induces an electrical field that may alter the electrical potential measured during ECG. In particular, the induced electrical field increases the T-wave which may perturb the ECG-gated acquisition. This paper is devoted to the modeling and the numerical simulation of this phenomenon.

The interaction of the aortic blood flow and a magnetic field has already been investigated in the literature [14,8,13,9,7,2,1]. The main contribution of the present study is to consider, in a realistic anatomy, a complete model which includes the bidomain equations in the heart, the inductionless magnetohydrodynamics (MHD) equations [5] in the aorta and the electrostatic equation in the torso. Without magnetic field, this model is able to produce realistic 12-lead ECGs. In presence of a magnetic field, it actually shows a larger T-wave, as expected from experimental results [14,13].

D.N. Metaxas and L. Axel (Eds.): FIMH 2011, LNCS 6666, pp. 325–332, 2011.

2 Method

In the context of blood flows in a permanent magnetic field, the Ohm law is assumed to simply read

$$\boldsymbol{j} = \boldsymbol{\sigma}_{\mathrm{bl}}(-\boldsymbol{\nabla}\phi_{\mathrm{A}} + \boldsymbol{u} \times \boldsymbol{B}),$$

where $\boldsymbol{j}$ denotes the electric current density, $\boldsymbol{\sigma}_{\mathrm{bl}}$ the blood electrical conductivity, ϕ_{A} the electrical potential, $\boldsymbol{u}$ the blood velocity and $\boldsymbol{B}$ the magnetic field (whose variations can be neglected in the context of blood flow because of a low Hartmann number). Thus, the magnetohydrodynamics equations in the aorta Ω_{A} can be reduced to a coupling between the Navier-Stokes equations with a Lorentz force $\boldsymbol{j} \times \boldsymbol{B}$ depending on the electrical potential ϕ_{A}, and a Laplace equation for the potential ϕ_{A} with a source term depending on the velocity $\boldsymbol{u}$:

$$\begin{cases} \rho\left(\dfrac{\partial \boldsymbol{u}}{\partial t} + \boldsymbol{u} \cdot \boldsymbol{\nabla}\boldsymbol{u}\right) - \eta \Delta \boldsymbol{u} + \boldsymbol{\nabla} p = -\boldsymbol{\sigma}_{\mathrm{bl}} \boldsymbol{\nabla}\phi_{\mathrm{A}} \times \boldsymbol{B} + \boldsymbol{\sigma}_{\mathrm{bl}} \left(\boldsymbol{u} \times \boldsymbol{B}\right) \times \boldsymbol{B}, \\ \qquad\qquad \operatorname{div} \boldsymbol{u} = 0, \\ \qquad\qquad \operatorname{div}\left(\boldsymbol{\sigma}_{\mathrm{bl}} \boldsymbol{\nabla}\phi_{\mathrm{A}}\right) = \operatorname{div}\left(\boldsymbol{\sigma}_{\mathrm{bl}} \boldsymbol{u} \times \boldsymbol{B}\right), \end{cases} \tag{1}$$

where p denotes the fluid pressure, η its viscosity, and the last two equations express the incompressibility of the blood and the conservation of the electrical charges, $\operatorname{div} \boldsymbol{j} = 0$.

Concerning the fluid boundary conditions, a no-slip condition is applied on the wall Γ_{wall} and a Windkessel model at the four outlets $\Gamma_{\mathrm{outlets}}$. The blood flow is enforced at the inlet of the aorta Γ_{inlet} (flat velocity profile) with a time dependence shown in Figure 1, right. The ejection starts right after the opening of the aortic valve, which happens shortly after the QRS complex. The flow rate is about $5L/min$. Note that the very low flow occuring in diastole and during isovolumic contraction of the heart is neglected, as the MHD effects occur mainly for high velocities.

The electrical activity in the heart is governed by the bidomain model [12]. We denote by Ω_{H} the heart domain, by ϕ_{H} and V_{m} the extracellular potential and the transmembrane potential and by $\boldsymbol{\sigma}_{\mathrm{i}}$ and $\boldsymbol{\sigma}_{\mathrm{e}}$ the intra- and extracellular conductivity tensors. Thus, we have, in Ω_{H}

$$\begin{cases} A_{\mathrm{m}}\left(C_{\mathrm{m}} \dfrac{\partial V_{\mathrm{m}}}{\partial t} + I_{\mathrm{ion}}(V_{\mathrm{m}}, w)\right) - \operatorname{div}(\boldsymbol{\sigma}_{\mathrm{i}} \boldsymbol{\nabla} V_{\mathrm{m}}) - \operatorname{div}(\boldsymbol{\sigma}_{\mathrm{i}} \boldsymbol{\nabla}\phi_{\mathrm{H}}) = A_{\mathrm{m}} I_{\mathrm{app}} \\ \qquad\qquad - \operatorname{div}((\boldsymbol{\sigma}_{\mathrm{i}} + \boldsymbol{\sigma}_{\mathrm{e}}) \boldsymbol{\nabla}\phi_{\mathrm{H}}) - \operatorname{div}(\boldsymbol{\sigma}_{\mathrm{i}} \boldsymbol{\nabla} V_{\mathrm{m}}) = 0, \end{cases} \tag{2}$$

where A_{m} is a constant representing the rate of membrane area per volume unit and C_{m} the membrane capacitance per area unit. The term $I_{\mathrm{ion}}(V_{\mathrm{m}}, w)$ represents the ionic current across the membrane which depends on V_{m} and w, and I_{app} is a given source term. The dynamics of the ionic variable w and the ionic current I_{ion} are governed by the phenomenological two-variable model introduced by Mitchell and Schaeffer in [10]. The ventricles are subdivided into

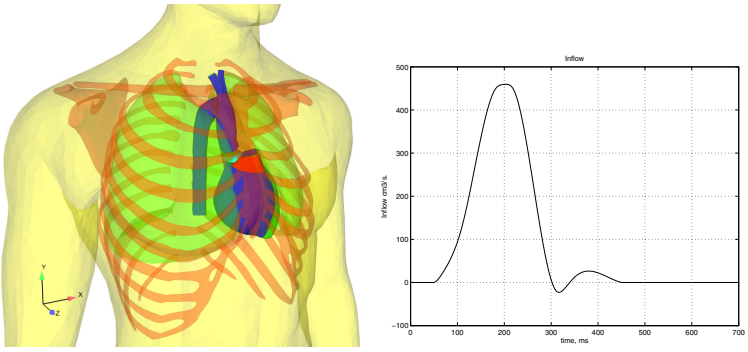

Fig. 1. Left: view of the torso with the different zones: bones, lungs, heart, aorta. Right: imposed inflow as a function of time.

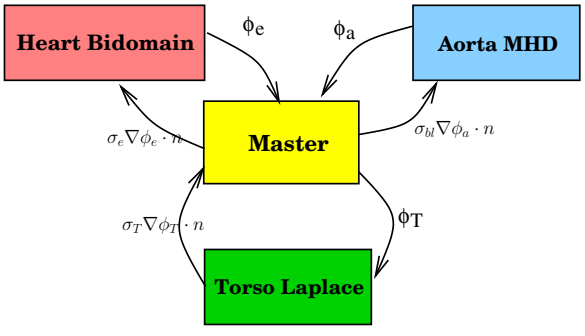

Fig. 2. Coupling strategy with a Dirichlet-Neumann algorithm

four different regions where the ionic model takes different values. The atria are not considered here. The initial activation starts from the septum. We refer to [3] for more details.

In the rest of the body, denoted by Ω_{T} and called "torso" for simplicity, the electrical potential ϕ_{T} is solution of:

$$\begin{cases} \mathrm{div}(\boldsymbol{\sigma}_{\mathrm{T}} \boldsymbol{\nabla} \phi_{\mathrm{T}}) = 0, \quad \text{in} \quad \Omega_{\mathrm{T}} \\ \boldsymbol{\sigma}_{\mathrm{T}} \boldsymbol{\nabla} \phi_{\mathrm{T}} \cdot \boldsymbol{n} = 0, \quad \text{on} \quad \Gamma_{\mathrm{ext}}, \end{cases} \tag{3}$$

where the conductivity $\boldsymbol{\sigma}_{\mathrm{T}}$ takes different values in the different zones of the torso (see Table 1), and Γ_{ext} is the external boundary of the body, *i.e.* on the skin of the patient.

It now remains to define the electric transmission conditions on the internal boundaries $\partial\Omega_{\mathrm{H}}$ and $\partial\Omega_{\mathrm{A}}$. On the boundary of the heart domain, the intracellular medium is assumed to be isolated:

$$\boldsymbol{\sigma}_{\mathrm{i}} \boldsymbol{\nabla} V_{\mathrm{m}} \cdot \boldsymbol{n} + \boldsymbol{\sigma}_{\mathrm{i}} \boldsymbol{\nabla} \phi_{\mathrm{H}} \cdot \boldsymbol{n} = 0 \quad \text{on} \quad \partial\Omega_{\mathrm{H}}. \tag{4}$$

In the literature, it is sometimes assumed that the extracellular medium is also isolated, *i.e.* $\boldsymbol{\sigma}_{\mathrm{e}} \boldsymbol{\nabla} \phi_{\mathrm{H}} \cdot \boldsymbol{n} = 0$ on $\partial\Omega_{\mathrm{H}}$ (the motivation being to weakly couple the heart and the torso). But, as noticed in [3], this simplification has some impacts on the electrocardiograms. In particular, it significantly increases the amplitude of the ECG. Since our goal is to capture the modification of the amplitude of the signal, we wish to avoid as far as possible *a priori* simplifications that might affect the ECG. So the potentials and the currents are assumed to be continuous at the interface $\partial\Omega_{\mathrm{H}} = \overline{\Omega_{\mathrm{H}}} \cap \overline{\Omega_{\mathrm{T}}}$ between the torso and the heart,

$$\begin{cases} \boldsymbol{\sigma}_{\mathrm{e}} \boldsymbol{\nabla} \phi_{\mathrm{H}} \cdot \boldsymbol{n} = \boldsymbol{\sigma}_{\mathrm{T}} \boldsymbol{\nabla} \phi_{\mathrm{T}} \cdot \boldsymbol{n}, & \text{on} \quad \partial\Omega_{\mathrm{H}}, \\ \phi_{\mathrm{H}} = \phi_{\mathrm{T}}, & \text{on} \quad \partial\Omega_{\mathrm{H}}. \end{cases} \tag{5}$$

The same transmission conditions are assumed at the interface $\partial\Omega_{\mathrm{A}} = \overline{\Omega_{\mathrm{A}}} \cap \overline{\Omega_{\mathrm{T}}}$ between the torso and the aorta,

$$\begin{cases} \boldsymbol{\sigma}_{\mathrm{bl}} \boldsymbol{\nabla} \phi_{\mathrm{A}} \cdot \boldsymbol{n} = \boldsymbol{\sigma}_{\mathrm{T}} \boldsymbol{\nabla} \phi_{\mathrm{T}} \cdot \boldsymbol{n}, & \text{on} \quad \partial\Omega_{\mathrm{A}}, \\ \phi_{\mathrm{A}} = \phi_{\mathrm{T}}, & \text{on} \quad \partial\Omega_{\mathrm{A}}. \end{cases} \tag{6}$$

The interface conditions (4)-(6) strongly couple all the equations (1)-(3) together. All the parameters of the problem are given in Table 1.

Three meshes were built for each subdomain $\Omega_{\mathrm{A}}, \Omega_{\mathrm{H}}, \Omega_{\mathrm{T}}$, see Figure 1, left. The MHD model of the aorta (1) is solved with P1 finite elements for the velocity with streamline diffusion stabilization, the pressure and the electrical potential. The incompressibility is enforced with a fractional step method (see [6] for instance). The MHD coupling is explicit in time: the fluid is solved with the electrical potential of the previous time step. Then, the electrical potential is computed with the updated velocity. With the small time steps required by the

Table 1. Values of the main parameters in the heart, aorta and torso

Symbol	Parameters	Value	units
$T^\star$	time period	700	ms
$\sigma_{i,l}$	conductivity intern longitudinal	3.0e-3	S/cm
$\sigma_{i,t}$	conductivity intern transverse	3.0e-4	S/cm
$\sigma_{e,l}$	conductivity external longitudinal	3.0e-3	S/cm
$\sigma_{e,t}$	conductivity extend transverse	1.2e-3	S/cm
ρ	blood density	1.06	g/cm^3
η	blood viscosity	0.04	$g/(cm\ s)$
$\boldsymbol{\sigma}_{\mathrm{bl}}$	blood conductivity	$6.25\ 10^{-3}$	S/cm
B_0	magnetic field	3	$Tesla$
$u_{\max}$	max inlet blood velocity	98	cm/s
Q	blood flow rate	≈ 5.36	L/min
σ_t	tissue conductivity	$6\ 10^{-4}$	S/cm
$\boldsymbol{\sigma}_{\mathrm{bl}}$	blood conductivity (ventricles)	$6.25\ 10^{-3}$	S/cm
σ_{bone}	bone conductivity	$5.65\ 10^{-5}$	S/cm
σ_l	lung conductivity	$5\ 10^{-4}$	S/cm

bidomain equations ($\delta t = 0.25ms$), this simple coupling scheme proves to be stable and accurate.

The electrical heart model (2) is also solved with P1 finite elements. The system is discretized in time by combining a second order BDF implicit scheme with an explicit treatment of the ionic current, as proposed in [3]. In the rest of the body, the Laplace equation (3) is solved with P1 finite elements.

The coupling of the three components of the model is done with a Dirichlet-Neumann domain decomposition algorithm accelerated by GMRES (see for instance [11]). Its principle is described in Figure 2. At each time step: the potentials coming from the aorta and the heart are sent to the torso where a Dirichlet problem is solved; then the torso sends back the electrical current (in a variational form) to the aorta and the heart where a Neumann problem is solved; these iterations are repeated until convergence before going to the next time step.

3 Results

In Figure 3 are presented the standard ECGs provided by the above model, with and without MHD effects ($B = 0$ or $B = 3T$), and a focus is made on the lead I in Figure 4. The comparison of the two ECGs clearly shows an increase of the T-wave, as observed in the experiments [14,13]. In these simulations, the maximum potential during the T-wave is $\approx 0.8mV$ with no MHD, and it doubles when $B = 3T$, passing to $\approx 1.6mV$, which is of the same order as the potential during the QRS complex ($\approx 1.8mV$).

The numerical computations can also provide some more details: in Figure 5, the electrical potential on the skin is depicted at various instants for $B = 0$ and $B = 3T$. One can see the effects of the electrical activity of the heart particularly during the QRS complex and the T-wave. The MHD effect in the aorta clearly modifies the potential around $t = 200ms$. We also provide some snapshots of the velocity inside the aorta in Figure 6 and of the electrical potential on the aorta in Figure 7. As expected, the maximum potential appears across the aortic arch, where velocity is roughly orthogonal to the applied magnetic field, and where it reaches $\approx 55mV$.

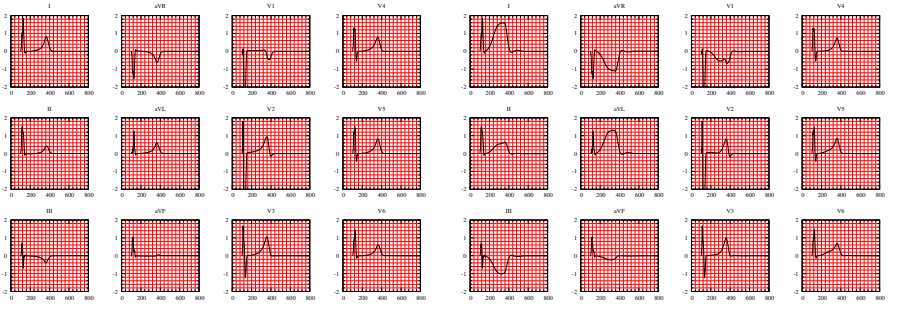

Fig. 3. Standard 12 lead ECG without MHD ($B = 0T$, left), and with MHD effects ($B = 3T$, right)

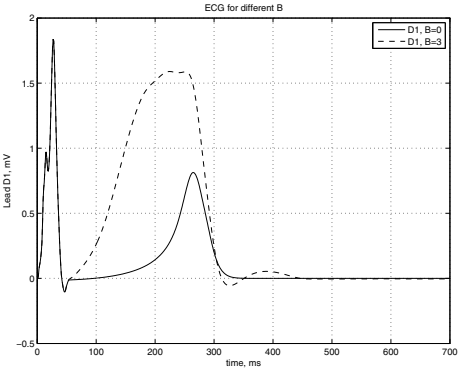

Fig. 4. Lead I without MHD ($B = 0T$, continuous line) and with MHD effects ($B = 3T$, broken line). Potential as a function of time. Scales $\phi \in [-0.5, 2]mV$ and $t \in [0, 700]ms$.

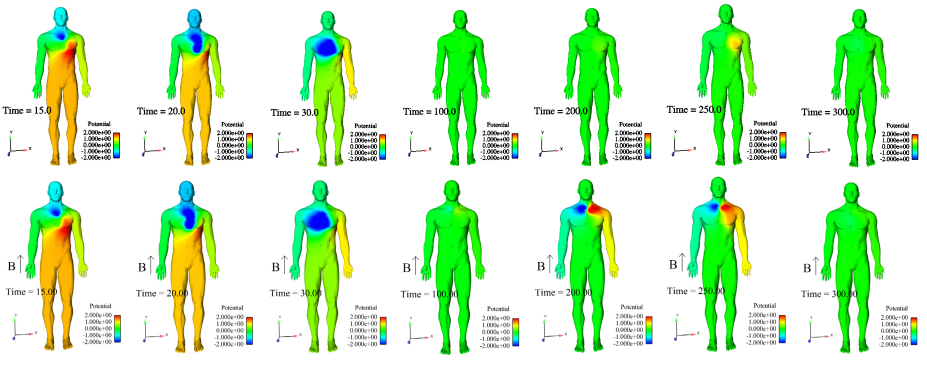

Fig. 5. View of the electrical potential on the skin at different times: without MHD ($B = 0T$, top), and with MHD effects ($B = 3T$, bottom). From left to right, time instants: $t = 15ms, 20ms, 30ms, 100ms, 200ms, 250ms, 300ms$. Scale: $[-2, 2]mV$.

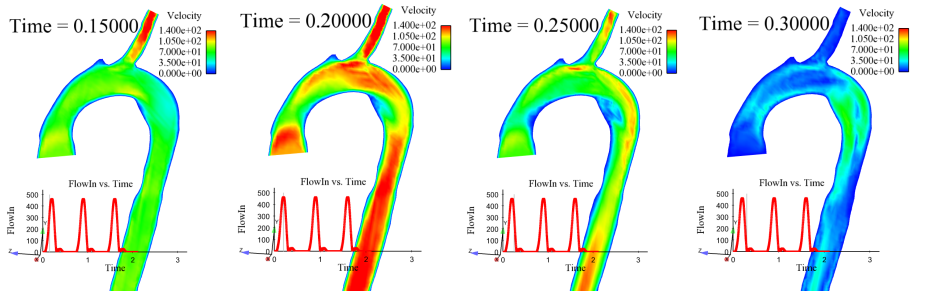

Fig. 6. Velocity in the aorta, along a cut plane, at times $t = 150ms$, $200ms$, $250ms$, $300ms$. Scale: $[0, 140]cm/s$. Only one of the 3 upper outlets is visible on this cut plane.

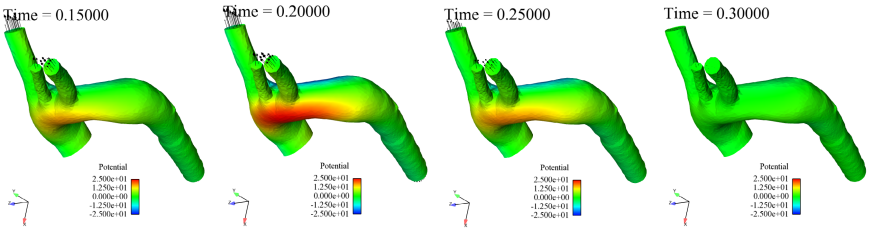

Fig. 7. View of the electrical potential on the aorta at different times with MHD effects ($B = 3T$). From left to right, time instants: $t = 150ms, 200ms, 250ms, 300ms$. Scale: $[-25, 25]mV$. Maximum values are $-30mV$ and $+25.5mV$.

4 Discussion and Conclusion

A model made of three components has been proposed: electrophysiology in the heart, magnetohemodynamics in the aorta and diffusion in the rest of the body. As a result, a standard 12-lead ECG has been computed with and without magnetic field. A larger T-wave was obtained in presence of a magnetic field, as expected.

The model, although quite complex, could still be improved: for example, the blood flow might be also considered in the pulmonary artery and in the heart; the aortic flow could result from an electromechanical model of myocardium [4] instead of being given *a priori*. It would be also interesting to see how the conclusions of this study would be affected by a perturbation of the parameters.

At this stage, the only purpose was to demonstrate that the computational tool was able to capture a phenomenon that has actually been observed in MRI machines. In the future, the model could be used for more interesting purposes: for example predict induced currents with higher magnetic field; optimize the electrode locations to be less sensitive to MHD effect, or on the contrary to extract from the MHD effect more information about the flow or the electrical conductivity of the tissues.

Acknowledgment. The authors wish to thank Charles Taylor and Alberto Figueroa for the mesh of the aorta and M. Boulakia, M. Fernández and N. Zemzemi for valuable discussions.

References

1. Abi-Abdallah, D., Drochon, A., Robin, V., Fokapu, O.: Pulsed magnetohydrodynamic blood flow in a rigid vessel under physiological pressure gradient. Comput. Methods Biomech. Biomed. Engin. 12(4), 445–458 (2009)
2. Abi-Abdallah, D., Robin, V., Drochon, A., Fokapu, O.: Alterations in human ecg due to the magnetohydrodynamic effect: a method for accurate r peak detection in the presence of high mhd artifacts. In: Conf. Proc. IEEE Eng. Med. Biol. Soc., pp. 1842–1845 (2007)

3. Boulakia, M., Cazeau, S., Fernández, M.A., Gerbeau, J.-F., Zemzemi, N.: Mathematical modeling of electrocardiograms: a numerical study. Ann. Biomed. Eng. 38(3), 1071–1097 (2010)
4. Chapelle, D., Fernández, M.A., Gerbeau, J.-F., Moireau, P., Sainte-Marie, J., Zemzemi, N.: Numerical simulation of the electromechanical activity of the heart. In: Ayache, N., Delingette, H., Sermesant, M. (eds.) FIMH 2009. LNCS, vol. 5528, pp. 357–365. Springer, Heidelberg (2009)
5. Gerbeau, J.-F., Le Bris, C., Lelièvre, T.: Mathematical methods for the Magnetohydrodynamics of liquid metals. Numerical Mathematics and Scientific Computation. Oxford University Press, Oxford (2006)
6. Guermond, J.L., Minev, P., Shen, J.: An overview of projection methods for incompressible flows. Comp. Meth. Appl. Mech. Engng. 195(44-47), 6011–6045 (2006)
7. Gupta, A., Weeks, A.R., Richie, S.M.: Simulation of elevated T-waves of an ECG inside a static magnetic field (MRI). IEEE Transactions on Biomedical Engineering 55(7), 1890–1896 (2008)
8. Kinouchi, Y., Yamaguchi, H., Tenforde, T.S.: Theoretical analysis of magnetic field interactions with aortic blood flow. Bioelectromagnetics 17, 21–32 (1996)
9. Luo, R., Zhang, Y., Xia, L.: Electrophysiological modeling study of ECG T-wave alternation caused by ultrahigh static magnetic fields. In: 27th Annual International Conference of the Engineering in Medicine and Biology Society, IEEE-EMBS 2005, pp. 3012–3015. IEEE, Los Alamitos (2006)
10. Mitchell, C.C., Schaeffer, D.G.: A two-current model for the dynamics of cardiac membrane. Bulletin Math. Bio. 65, 767–793 (2003)
11. Quarteroni, A., Valli, A.: Domain decomposition methods for partial differential equations. The Clarendon Press Oxford University Press, New York (1999); Oxford Science Publications
12. Sundnes, J., Lines, G.T., Cai, X., Nielsen, B.F., Mardal, K.-A., Tveito, A.: Computing the electrical activity in the heart. Springer, Heidelberg (2006)
13. Tenforde, T.S.: Magnetically induced electric fields and currents in the circulatory system. Progress in Biophysics and Molecular Biology 87, 279–288 (2005)
14. Tenforde, T.S., Gaffey, C.T., Moyer, B.R., Budinger, T.F.: Cardiovascular alterations in macaca monkeys exposed to stationary magnetic fields: experimental observations and theoretical analysis. Bioelectromagnetics 4, 1–9 (1983)

A Hybrid Method for Automatic Anatomical Variant Detection and Segmentation

Raghed Hanna[1,2], Hans Barschdorf[2], Tobias Klinder[3], Frank M. Weber[1], Martin W. Krueger[1], Olaf Dössel[1], and Cristian Lorenz[2]

[1] Institute of Biomedical Engineering, Karlsruhe Institute of Technology (KIT), Germany
[2] Philips Research Hamburg, Germany
[3] Philips Research North America

Abstract. The delineation of anatomical structures in medical images can be achieved in an efficient and robust manner using statistical anatomical organ models, which has been demonstrated for an already considerable set of organs, including the heart. While it is possible to provide models with sufficient shape variability to cope, to a large extent, with inter-patient variability, as long as object topology is conserved, it is a fundamental problem to cope with *topological organ variability*. We address this by creating a set of model variants and selecting the most appropriate model variant for the patient at hand. We propose a hybrid method combining model-based image analysis with a guided region growing approach for automated anatomical variant selection and apply it to the left atrium in cardiac CT images. Concerning the human heart, the left atrium is the most variable sub-structure with a variable number of pulmonary veins drainng into it. It is of large clinical interest in the context of atrial fibrillation and related interventions.

1 Introduction

The shape of most organs remains similar from person to person. This enables the human observer but also medical machine vision to recognize and delineate anatomical objects based on a-priori knowledge of the respective shape. Substantial progress has been made during the last years in using shape models for organ delineation for even highly variable organs, such as the liver [1]. Still, variability in this context is mainly restricted to geometric distortions of some basis shape. A model-based segmentation of an organ, connected with, e.g., 3 arteries, can cope with some variation in position and size of the 3 arterial connections, but not with a patient having 4 instead of 3 connections. An anatomical region, where this problem is of high clinical relevance, is the left atrium. In contrast to the fibrillation of the left *ventricle*, left *atrial* fibrillation (AF) is no directly life-threatening condition but needs to be treated in order to increase quality of life, and to reduce risk of stroke and cardiac remodeling. The electrical impulses causing AF enter spontaneously from the pulmonary veins to the left atrium. If AF does not respond to medication, radio-frequency catheter ablation can be performed, in order to

D.N. Metaxas and L. Axel (Eds.): FIMH 2011, LNCS 6666, pp. 333–340, 2011.

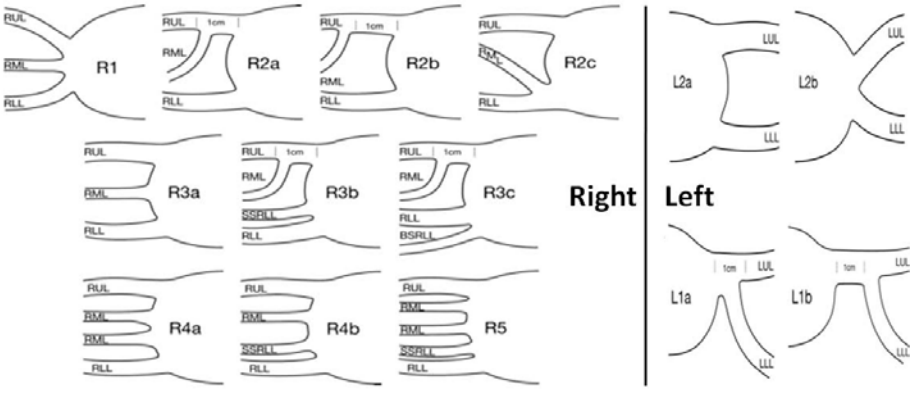

Fig. 1. Left side: Right pulmonary venous drainage patterns to the LA, with annotation of pulmonary veins using BSRLL = basilar segment right lower lobe, RLL = right lower lobe, RML = right middle lobe, RUL = right upper lobe, SSRLL = superior segment right lower lobe. Right side: Left drainage patterns to the LA with LLL = left lower lobe, LUL = left upper lobe. Illustrations taken from [2].

isolate the pulmonary veins electrically from the left atrium. Success rate of the procedure can be increased by pre-interventional planning, revealing number and locations of pulmonary vein ostia. Marom *et al*. performed a study on the anatomical variation of the pulmonary veins using contrast-enhanced CT data [2]. Variants were classified based on the number of venous ostia on the left and right side of the left atrium as well as the branching patterns of the veins. The left side of Fig. 1 illustrates the classification of the patterns of the right pulmonary venous drainage. The most common pattern is that of two atrial ostia for upper and lower lobe veins and with the middle lobe vein joining the upper lobe vein (68% of patients). The remaining 32% of patients have variant anatomy, e. g. three or four right pulmonary veins. The left pulmonary venous drainage patterns (Fig. 1 right side) show no considerably topological variation. 86% of patients have two ostia for the upper and lower lobe veins. A common trunk forming one ostium was seen in the remaining 14% of patients.

2 Method

Due to the high clinical importance of cardiac structures, there is a substantial history of related medical image analysis activities. While the left atrium addressed by slice based contouring methods dominated the early days, methods evolved to whole heart approaches, delineating all four cardiac chambers. Methods using a shape model of the cardiac structures turned out be an efficient and robust means for completely automated segmentation of the whole heart [3]. Current model-based approaches assume, however, a certain standard cardiac anatomy and cannot be applied to a different anatomical situation, e.g., in patients with congenital heart disease. Similarly, usually the left atrial anatomy is

assumed to be of the type of two pulmonary veins on each side of. This approach works fine, if gross cardiac anatomy or, e.g., chamber volumes are of concern. However, the presented approaches so far are not able to address the anatomical variability of the LA.

There are several options to treat such topological variability. One of the first proposals was to use a simplex-mesh based active surface, which expands from some initialization within the object to be segmented towards the border [4]. During expansion, the mesh comes to rest when the border is reached, at still expanding surface parts, mesh cells are created, allowing the mesh to adapt and keeping at the same time the mesh cell sizes at a roughly constant value. With this approach, variable topologies can be treated, and local shape properties, like surface curvature can be used to regularize the adaptation process. However, it is difficult to introduce global shape information. A standard approach for the segmentation of objects with unknown topology are level sets. Recent papers propose to combine the level-set approach with the use of a shape model [5], but the method was only demonstrated for constant object topology. For the case of a small set of topological variants that have to be taken into account, we propose in this paper a hybrid approach for accurate left atrium segmentation in CTA images, combining model based segmentation with a topology sensitive variant identification. For the identification, a multi-atlas registration could be used, where a set of atlases is registered to the unseen data set and the best matching one is used as template for organ delineation [6]. Similarly, based on a set of shape models, the best fitting one to the unseen data set could be used as final segmentation. However, initial experiments showed, that the topologically different shapes of the left atrium are often of little difference in appearance. Two close branches of a pulmonary vein may be nicely matched to one larger one, producing a high enough similarity measure to select the wrong variant. We therefore followed another approach based on topology sensitive guided region growing.

2.1 A Three Step Procedure

The proposed procedure consists of three steps. In the *first step*, a simplified shape model is adapted to the target object. It is simplified with respect to the expected anatomical variability. It carries, however, information (in terms of marked vertices or triangles) that allows to define search regions for variant identification. In case of the left atrium, we simply omitted all pulmonary ostia at the right side of the LA (see Fig. 3b). In the *second step* the anatomical variant is identified. Admittedly, the method of choice for this step may depend strongly on the target organ and modality, as well as the kind of variability to cope with. In difficult cases, even a guided interactive identification could be opted for, using a meaningful visualization of the scene based on location and orientation of the search region for variant identification. In most cases however, an automated approach would be aimed for, using a steered region growing approach (as in our case), a level set based procedure etc. The *third step* consists of a model based segmentation using a detailed shape model of the anatomical variant selected on basis of the outcome of step two (see Fig. 2).

2.2 Generation of the Model Data Base

30 CTA data sets, originating from different hospitals, were classified according to the pattern of the left atrium. The resolution differed between 0.39-0.5 mm in-plane and 0.32-0.6 mm through-plane. With the help of a clinical expert, a set of reference segmentations were generated using a manual 3D segmentation tool, resulting in a set of label images.

After a Procrustes registration of the label images into a common coordinate system, mean labels images were generated for the different anatomical variants following the approach described in [7]. Subsequently, triangulated surface models from the mean label images were generated using the Marching Cubes algorithm [8]. Initially, models for most of the anatomical variants shown in Fig. 1 were generated. Later, it turned out, that a reduced set of models, only capturing the number of pulmonary vein connections (R2L, R3L, R4L) were sufficient to achieve correct segmentations, e.g., the anatomical variations R3b, R3c, R4a and R4b are covered using the model R4L. Fig. 2 shows the surface models of the model data base.

2.3 Detection of the Anatomical Variation

Since the left pulmonary veins show a constant object topology, we need only one model variant for the left side. The anatomical variation in the right pulmonary

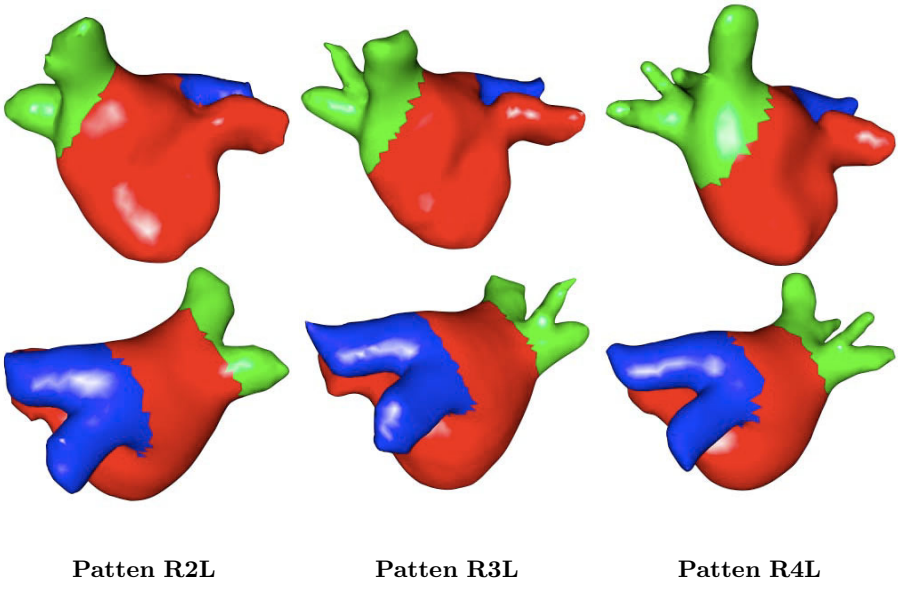

Fig. 2. Triangulated surface model variants of the LA. First column: pattern R2L with two right pulmonary veins on the right as well as the left side. Second column: patterns R3L with two left pulmonary veins and three pulmonary veins on the left side. Third column: R4L with two left pulmonary veins and four pulmonary veins on the right side. The surface models are closed at the vein trunks and in the valve area in order to enable voxelization to a label-image.

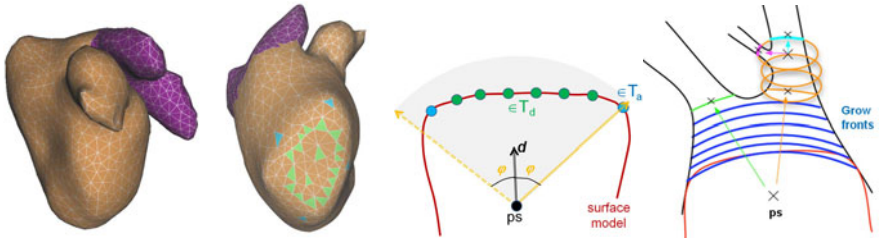

(a) (b) (c) (d)

Fig. 3. Simplified triangulated surface model of the left atrium without right pulmonary veins, viewed from the left (3a) and right side (3b). The triangles used for computing the search direction are depicted in green and those for computing the search angle in cyan. Definition of the cone-like grower volume is depicted in (3c). Detection of the right pulmonary vein ostia is shown in (3d). In blue is the front of the 3D cone grower, the anatomical boundaries of the left atrium in the image are shown in black. Adapted coarse-grained model is depicted in red where the seed point *ps* is shown inside the surface model.

venous drainage to the left atrium is, however, high (see Fig. 1). Therefore, the model used for the initial coarse delineation of the LA is simplified on the right side, omitting vascular connections at all (see Fig. 3b). This simplified model is generated using the approach mentioned in Sect. 2.2 after cutting out the right pulmonary veins and the right ostia from the label images. Following the initialization of the model using *Generalized Hough Transformation* (GHT) [9], an adaptation to the left atrium is carried out using a constrained deformable model approach similar to the one described in [10]. Due to the constrained adaptation, anatomical correspondence is mainly preserved, meaning that a given location on the model surface will always come to rest in the same anatomical region. This allows us to use marks on the model surface to steer the subsequent guided region growing for variant identification. The grow-volume is restricted to a cone-like portion of a sphere parameterized by cone apex *ps* (also center of the sphere), cone axis $\boldsymbol{d}$, and cone opening angle φ (measured at apex, angle between axis and border). These parameters are computed using the center of mass C_s of the simplified mesh and the triangle sets T_a and T_d (cyan and green in Fig. 3b) as follows: *ps* is set to the mid-point between C_s and center of mass of triangles T_d. Cone axis vector is defined as the mean of normal vectors of the triangle set T_d. The opening angle is chosen as the minimum angle that have all triangle centers of set T_a included in the cone (see Fig. 3c). From the intensity histogram of the interior of the adapted simplified model, a lower and upper threshold is determined as the intensities corresponding to 95 % quantile of maximum frequency. The region grower is started from a seed-point at the cone apex, accepting voxels between upper and lower threshold and being restricted to the cone-like volume. At start, a one-connected active grow front propagates towards the right side of the left atrium. When the front reaches a pulmonary vein, it splits up into two disconnected fronts. When this situation is detected, the growth process is

stopped and restarted from seed points located at the center of each front part. The restarted grower is no longer restricted to the initially defined cone. The procedure is iterated so that the sequence of detected front splits results in a tree of front splits or seed points, with the original seed point *ps* as root node. Fig. 3d illustrates the right pulmonary veins detection procedure on an image of a patient who has the pattern R2b of the right pulmonary veins (see Fig. 1). The tree contains all necessary information to select the appropriate detailed shape model for the anatomical variant at hand. Having the simplified and the detailed model in the same model coordinate systems, allows the positioning and orientation of the detailed model in the patient image using the transformation resulting from a point based registration between the adapted simplified model in the patient and model coordinate system. The detailed model is adapted to the image data using again a constrained deformable model approach (similar to [10]).

3 Results

The method was applied to data sets from 30 patients with the available ground truth segmentation, in a leave-one-out manner. Tab. 1 shows the initialization, identification and segmentation results. A manual adjustment of the mean model after the GHT was applied in the cases marked with a dot (•), cases with a failed GHT pre-positioning are marked with a cross (×). A success rate of 66% for the anatomical variant identification has been achieved. The erroneous cases are mainly due to the misinterpretation of early PV bifurcations as pulmonary vein ostia, however, this still results in most cases in the selection of a model that can

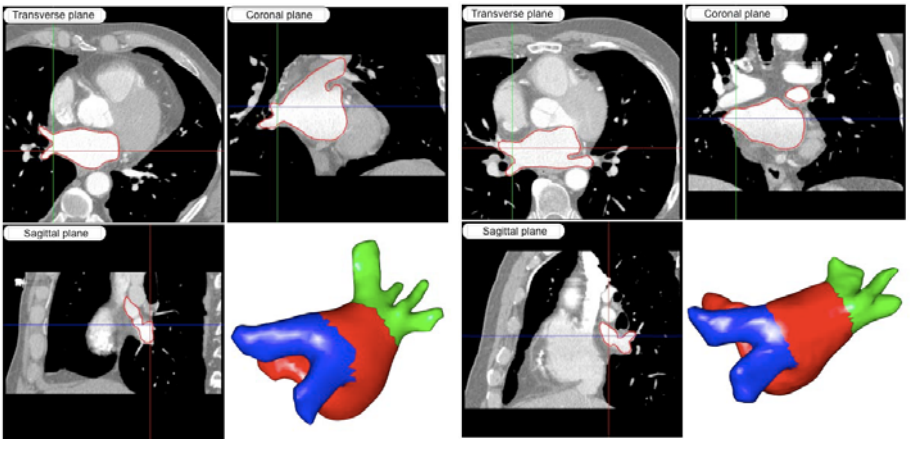

Fig. 4. Segmentation results for two data sets, shown in axial, sagittal and coronal views and as adapted surface model. Left: Patient with LA-pattern R4::L, right: R3::L.

Table 1. Detection, identification and segmentation results

Pattern	Index	Pre-positioning	d_{mean} [mm]	σ [mm]	d_{max} [mm]	Detected pattern
R2::L	Pat- 01	√	0.94	1.65	10.64	R4::L
	Pat- 02	√	0.59	1.19	9.27	R2::L
	Pat- 03	√	0.57	0.96	6.69	R4::L
	Pat- 04	√	0.49	0.63	4.16	R4::L
	Pat- 05	√	0.39	0.46	4.31	R4::L
R3::L	Pat- 06	√	0.38	0.74	7.7	R2::L
	Pat- 07	√	0.38	0.51	4.85	R3::L
	Pat- 08	√	0.5	1.18	11.63	R4::L
	Pat- 09	×	0.37	0.68	6.62	R3::L
	Pat- 10	√	0.66	1.09	10.48	R3::L
	Pat- 11	√	0.39	0.58	5.62	R3::L
	Pat- 12	√	0.35	0.52	6.23	R4::L
	Pat- 13	√	0.52	0.81	6.06	R3::L
	Pat- 14	√	0.33	0.44	3.6	R2::L
	Pat- 15	√	0.22	0.28	3.08	R3::L
R4::L	Pat- 16	√	0.44	0.69	5.97	R4::L
	Pat- 17	√	0.7	1.61	13.75	R4::L
	Pat- 18	√	0.64	1.05	7.61	R4::L
	Pat- 19	√	0.35	0.45	5.17	R4::L
	Pat- 20	√	0.52	0.85	7.94	R4::L
	Pat- 21	√	0.26	0.3	3.17	R2::L
	Pat- 22	•	0.49	0.7	7.4	R4::L
	Pat- 23	•	0.69	0.9	7.4	R4::L
	Pat- 24	•	1.05	1.7	12.54	R4::L
	Pat- 25	•	0.66	0.7	6.23	R4::L
	Pat- 26	√	0.53	0.84	7.3	R4::L
	Pat- 27	√	0.28	0.39	2.74	R2::L
	Pat- 28	√	0.36	0.64	7.03	R4::L
	Pat- 29	√	1.66	3.49	19.56	R4::L
	Pat- 30	√	0.3	0.38	4.3	R4::L

be adapted with a high accuracy. For the segmentation, a mean vertex to surface error of 0.53 $[mm]$ was measured. The segmentation results from two data sets with different pattern of the left atrium are shown in Fig. 4. Calculation times on a 2.4 GHz Intel Core2Duo CPU were 57 s for prepositioning, adaptation of the simplified model and computation of the histogram for the region growing thresholds; 3 s for detecting and tracking the right pulmonary veins; 22 s for the adaptation of the selected model from the model data base.

4 Conclusion

A hybrid method for automated model based segmentation of topologically variable anatomy is presented. It has been applied to the segmentation of the left atrium in CT data. A promising but not yet satisfactory identification rate for

anatomical variation of 66% and good adaptation accuracy have been achieved. Future work will focus on improving the success rate for variant indentification and on the application of the method to other organs and modalities.

References

1. Kainmüller, D., Lange, T., Lamecker, H.: Shape constrained automatic segmentation of the liver based on a heuristic intensity model. In: Proc. MICCAI Workshop 3D Segmentation in the Clinic: A Grand Challenge, pp. 109–116 (2007)
2. Marom, E., Herndon, J., Kim, Y., McAdams, H.: Variations in pulmonary venous drainage to the left atrium: implications for radiofrequency ablation. Radiology 230, 824–829 (2004)
3. Ecabert, O., Peters, J., Schramm, H., Lorenz, C., von Berg, J., Walker, M., Vembar, M., Olszewski, M., Subramanyan, K., Lavi, G., Weese, J.: Automatic model-based segmentation of the heart in ct images. IEEE Transactions on Medical Imaging 27(9), 1189–1201 (2008)
4. Delingette, H.: General object reconstruction based on simplex meshes. International Journal of Computer Vision 32, 111–146 (1999)
5. Kohlberger, T., Uzunbas, M.G., Alvino, C.V., Kadir, T., Slosman, D.O., Funka-Lea, G.: Organ segmentation with level sets using local shape and appearance priors. In: Yang, G.-Z., Hawkes, D., Rueckert, D., Noble, A., Taylor, C. (eds.) MICCAI 2009. LNCS, vol. 5762, pp. 34–42. Springer, Heidelberg (2009)
6. Klein, S., van der Heide, U.A., Raaymakers, B.W., Kotte, A.N.T.J., Staring, M., Pluim, J.P.W.: Segmentation of the prostate in mr images by atlas matching. In: ISBI, pp. 1300–1303 (2007)
7. Blaffert, T., Barschdorf, H., von Berg, J., Dries, S., Franz, A., Klinder, T., Lorenz, C., Renisch, S., Wiemker, R.: Lung lobe modeling and segmentation with individualized surface meshes. In: SPIE, vol. 6914, 69141I (2008)
8. Lorensen, W., Cline, H.: Marching cubes: A high resolution 3d surface construction algorithm. Computer Graphics 21, 163–169 (1987)
9. Ballard, D.H.: Generalizing the hough transform to detect arbitrary shapes. Pattern Recognition 13(2), 111–122 (1981)
10. Weese, J., Kaus, M.R., Lorenz, C., Lobregt, S., Truyen, R., Pekar, V.: Shape constrained deformable models for 3D medical image segmentation. In: Insana, M.F., Leahy, R.M. (eds.) IPMI 2001. LNCS, vol. 2082, pp. 380–387. Springer, Heidelberg (2001)

Patient-Specific Model of Left Heart Anatomy, Dynamics and Hemodynamics from 4D TEE: A First Validation Study

Ingmar Voigt[1,2,⋆], Tommaso Mansi[1], Viorel Mihalef[1], Razvan Ioan Ionasec[1], Anna Calleja[3], Etienne Assoumou Mengue[1], Puneet Sharma[1], Helene Houle[4], Bogdan Georgescu[1], Joachim Hornegger[2], and Dorin Comaniciu[1]

[1] Image Analytics and Informatics, Siemens Corporate Research, Princeton, NJ, USA
ingmar.voigt.ext@siemens.com
[2] Pattern Recognition Lab, Friedrich-Alexander-University, Erlangen, Germany
[3] Davis Heart and Lung Research Institute, Ohio State University, Columbus, OH, USA
[4] Ultrasound, Siemens Healthcare, Mountain View, CA, USA

Abstract. Patient-specific models of the heart physiology have become powerful instruments able to improve the diagnosis and treatment of cardiac disease. A systemic representation of the whole organ is required to capture the complex functional and hemodynamical interdependencies among the anatomical structures. We propose a novel framework for personalized modeling of the left-side heart that integrates comprehensive data of the morphology, function and hemodynamics. Patient-specific fluid dynamics are computed over the entire cardiac cycle using embedded boundary and ghost fluid methods, constrained by the dynamics of highly detailed anatomical models. Personalized boundary conditions are determined by estimating cardiac shape and motion from 4D TEE images through robust discriminative learning methods. Qualitative and quantitative validation of the computed blood dynamics is performed against Doppler echocardiography measurements, following an original methodology. Results showed a high agreement between simulation and ground truth and a correlation of $r = 0.85$ ($p < 0.0002675$). To the best of our knowledge, this is the first time that computational fluid dynamics are simulated on a systemic and comprehensive patient-specific model of the heart and validated against routinely acquired clinical ground truth.

1 Introduction

Cardiovascular disease management is nowadays largely supported by increasingly more accurate, fast and ubiquitous imaging technologies. However, this rich information is barely exploited in the clinical decision making process. Non-respondent patients are common in cardiac disease [1], presenting in numerous cases unexpected adverse events because the therapy was not adapted to that

⋆ Corresponding author.

D.N. Metaxas and L. Axel (Eds.): FIMH 2011, LNCS 6666, pp. 341–349, 2011.

specific patient. In fact therapeutical decisions are largely based on results obtained in population-wise studies and are therefore not personalized. Furthermore, the complex interdependency of anatomy, function and hemodynamics imposes the need of a systematic analysis of the whole organ to accurately assess dysfunction and associated morbidities. Therefore, there is a growing need for patient-specific models that 1) provide the cardiologist with accurate, quantitative, and reproducible biomarkers of the cardiac function 2) give insights and predict comorbidites within the complex interconnected cardiovascular system and 3) can predict, beforehand, the outcome of a therapy [2]. These models would enable and support personalized, preventive and predictive healthcare by predicting disease progress and therapeutical outcomes.

In the last decades, tremendous efforts have been made to enable computational fluid dynamics (CFD) in cardiac models in order to integrate into a holistic view the organ anatomy, dynamics an hemodynamics. Due to the lack of personalized representations, fluid dynamics equations are often solved on generic models built from at most one cardiac phase with simplified motion [3]. Although patient-specific measurements have been increasingly used to enhanced computational models [4,5], current simulations are still lacking the accuracy required in the clinical practice. Recently, detailed anatomical models of the heart dynamics have been proposed [6]. Such models, coupled with CFD frameworks [4] open the way to data-driven patient-specific models of anatomy, dynamics and hemodynamics.

In this paper we propose a highly detailed patient-specific model of left-heart anatomy, dynamics and hemodynamics and its validation against clinically acquired Doppler measurements. The contributions are three-fold: i) The first model of left heart with fast and robust patient-specific parameter estimation from four-dimensional transesophageal echocardiography (TEE) (Sec. 2), ii) an improved patient-specific hemodynamics model, computed by solving a level set formulation of the Navier-Stokes equations (Sec. 3) and iii) a qualitative and quantitative validation against clinical Doppler echocardiography (Sec. 4). The results, reported in Sec. 5, demonstrate the validity of our approach.

2 Patient-Specific Anatomy and Dynamics Computation

We propose a holistic four-dimensional model of the left heart that comprises its core anatomical structures (Fig. 1): left ventricle (LV), left atrium (LA), aortic valve (AV), mitral valve (MV) and its papillary muscles (APM and PPM). Given the physiological complexity of the left heart, we selected a modular and hierarchical approach, which facilitates capturing a broad spectrum of morphological and pathological variations. The model is parameterized as follows:

1. Four time dependent similarity transforms for each anatomical structure (LV, LA, AV and MV) comprising their global location, orientation and scale over the cardiac cycle, denoted by $B(t)_m$, $m \in \{\mathrm{LV}, \mathrm{LA}, \mathrm{AV}, \mathrm{MV}\}$.
2. 20 trajectories of anatomically defined landmarks $l_n \in \mathbb{R}^3$ (3 commissures, 3 hinges, 3 tips and 2 ostia for the aortic valve, and 3 trigones, 2 commissures, 2 tips and 2 papillary heads for the mitral valve), $L(B,t) = \{l_1, l_2, \ldots, l_{20}\}$.

3. Nine dense meshes M_q with K_q vertices to represent the LA, LV, aortic root, three aortic leaflets, two mitral leaflets and the aortic-mitral continuity $M_q(B, L, t) = \{\mathbf{v}_1, \mathbf{v}_2, \ldots, \mathbf{v}_{K_q}\}$, $v_i \in \mathbb{R}^3$ being the position of the i^{th} vertex, which are constrained by the previously defined landmarks.

The patient-specific parameters of the valvular apparatus and left ventricle are estimated from 4D TEE images using a hierarchical discriminative learning algorithm as proposed in [6,7]. The a posteriori probability $p(B, L, M|I)$ of the model given the image data I is incrementally modeled within the Marginal Space Learning (MSL) framework. The similarity transforms B and the anatomical landmarks L are estimated automatically by detectors successively trained on the marginal spaces using the Probabilistic Boosting Tree (PBT) [8] with Haar and steerable features. The complex local motion of the surface structures is estimated with a combination of the aforementioned techniques and speckle tracking methods [7]. For further details on model estimation the reader is referred to [6,7]. The left atrium (LA) and pulmonary veins are commonly only partially visible in TEE acquisitions, which hampered an accurate automatic segmentation. Therefore, the LA fitting is performed semi-automatically along the cardiac cycle, using constraints provided by the mitral annulus and statistical models of shape and motion obtained from a large CT database [8].

It is important to note that our model is anatomically highly detailed and considers a number of important aspects for the computation of patient-specific blood flow. Firstly, valve leaflets are volumetrically modeled by representing them with both ventricular and arterial / atrial surface (Fig. 1 **Top right**). Secondly, the papillary muscles are represented as part of the left ventricular endocardium, constrained by the papillary heads (Fig. 1 **Bottom right**).

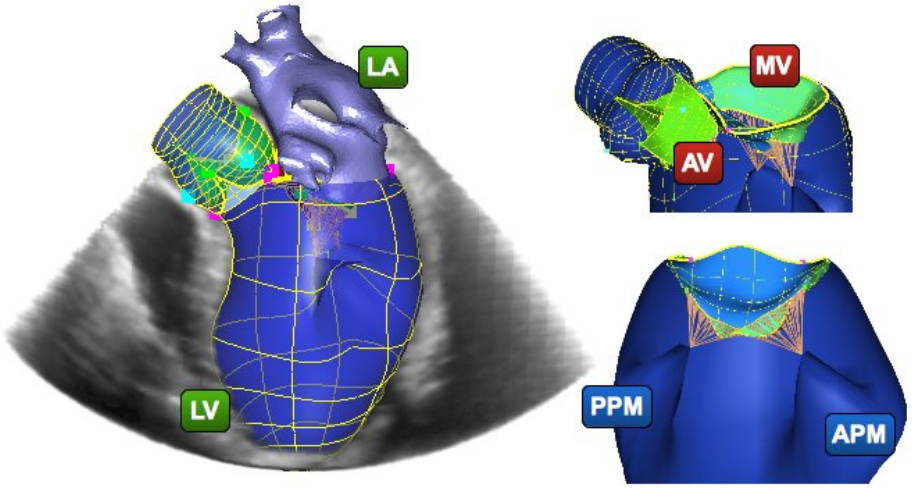

Fig. 1. Proposed model of anatomy and dynamics. **Left:** full model of the left heart estimated from TEE data. **Top right:** view of the aortic and mitral valve with volumetric leaflets. **Bottom right:** septal view of the left ventricular papillary muscles.

These first two aspects consider their spatial presence and displacement of blood. Thirdly, the model includes the longitudinal, radial and circumferential left ventricular motion to capture the full momentum exercised by the endocardial wall onto the blood [7]. Fourthly, the meshes are uniquely parameterized through the anatomical landmarks l_n. Thereby temporal point correspondence is implicitly guaranteed, which is a mandatory requirement for computational modeling.

3 Patient-Specific Hemodynamics Computation

In order to simulate the hemodynamics using a comprehensive heart model like the one presented in the previous section, the CFD solver must be able to handle the large deformations of the non-manifold heart surface, including multiple topological changes like valve closure. Such constraints pose difficulties for body-fitted grid methods like the finite element method, requiring extra effort for frequently re-meshing the whole domain and also adversely impacting the robustness and accuracy of the linear solver. To address these difficulties, we use in this work a level-set-based embedded boundary method [4]. The non-manifold heart polygonal mesh is embedded in a computational box endowed with a regular grid and the Navier-Stokes equations are solved inside the rectangular domain using finite difference and finite volume discretizations. The liquid inside the box and "outside" the left heart plays the role of the body circulatory system, whose flow resistance is simulated by imposing no slip boundary conditions on the sides of the box. The heart polygonal mesh is represented on the regular grid with spatial resolution dx by defining the level set $\phi(x) = dist(x, mesh) - dx$, and using it appropriately for defining the numerical stencils at the blood/tissue interface.

We solve the 3D Navier-Stokes equation for incompressible flow with viscous terms. Blood density and dynamic viscosity are set to $\rho_{liquid} = 1.05\, g/cm^3$ and $\mu = 0.003\, Pa \cdot s$, respectively. The velocity of the mesh walls, extrapolated in space to the grid nodes and interpolated in time between two consecutive mesh

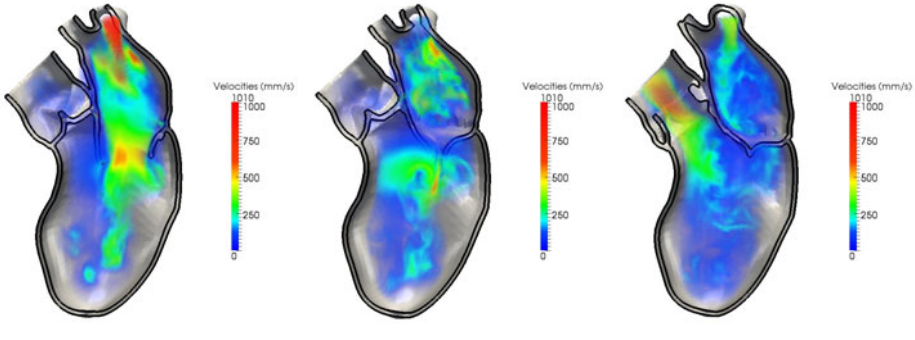

(a) (b) (c)

Fig. 2. Velocity magnitudes of the patient-specific simulated hemodynamics in early-diastole (a), late-diastole (b), and mid-systole (c)

positions, are used to enforce no-slip conditions to the Navier-Stokes solver. We use the ghost fluid method to extend the velocity in the solid regions, when necessary. The convective solver relies on high-order Courant–Isaacson–Rees (CIR) techniques, while the viscous terms are treated semi-implicitly as in [9]. An efficient multi-grid preconditioned conjugate gradient solver is used to solve the pressure Poisson equation.

In our experiments, the computations were performed on grids with an isotropic cell resolution of $1\,mm^3$ (i.e. $dx = 1mm$), which is in the same range as the TEE data resolution. The time step was chosen to obey the Courant-Friedrichs-Lewy (CFL) condition $dt * max(u) < dx$, which enforces that information carried by the blood velocity u does not travel faster than one grid cell per time step. The result of the computational fluid dynamics simulation is illustrated for a specific patient in Fig. 2. For further details the reader is referred to [4].

4 Validation Methodology

We introduce a novel methodology for validation of simulated heart hemodynamics with clinically acquired Doppler measurements. Doppler echocardiography is routinely performed during cardiac exams to determine blood velocities from the phase shift between emitted and reflected high frequency ultrasound waves [10,11]. We address both, continuous wave (CW) Doppler and pulse wave (PW) Doppler, which measure velocities along the probe direction to produce 1D signals. For a conclusive comparison we reconstruct similar 1D signals from the simulated 4D CFD velocities.

CW returns the velocities of all blood cells along the probe path. The outer envelope of the signal corresponds to the maximum velocity. CW is used in practice to acquire the very high speed of regurgitation flows, however without providing the spatial location of the measurement. In the 4D patient-specific computational model, a virtual CW probe path is defined to match the real position and orientation of the corresponding ground truth Doppler. The 4D velocities are projected onto the probe direction for the entire cardiac cycle. Then, for each cardiac phase, the maximum velocity values along the probe path are registered. Velocities are sampled in 1mm spatial steps along the probe path and at each location averaged over a small disk of radius 1.5mm, to realistically match the resolution of the CW protocol (Fig. 3 **Top panel**).

PW returns the dominant velocity of the blood cells inside a focal region of interest (ROI) along the probe direction, typically just below the mitral leaflet tips or within the left ventricular outflow tract [10,11] (Fig. 3 **Bottom panel**). PW Doppler is used to measure the blood inflow and outflow across the valves and is limited in capturing high velocities. In the 4D patient-specific computational models, a virtual PW probe direction and ROI is defined to match the real position and orientation of the corresponding ground truth Doppler (Fig. 3 **Bottom left**). The 4D computed velocities inside the ROI are projected along the probe direction. The dominant velocity of the blood cells is approximated

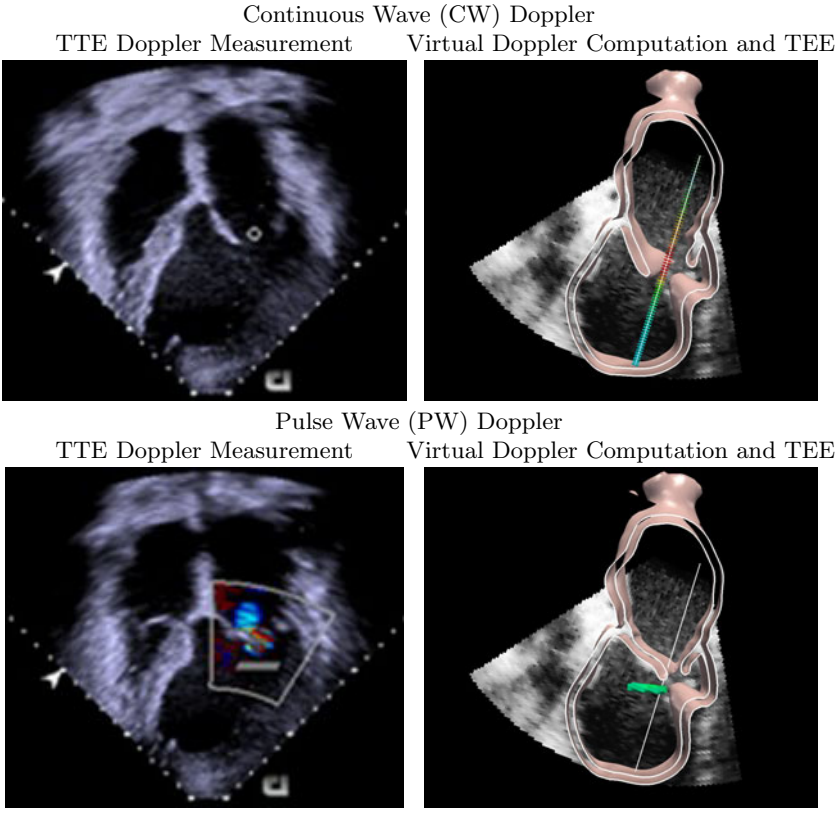

Fig. 3. Validation setup. CW and PW Doppler are computed from the 4D simulation (right panels) to reproduce the 1D ground truth (left panels).

by the most frequent velocity found in the ROI, determined automatically using a histogram. In our experiments, the number of points in the ROI vary between 300 and 700, while 10 bins were used to build the histogram.

While we focused in our experiments on transvalvular blood velocities as routinely measured during Doppler exams, it is important to note that the technique is not limited to these particular sites, and is applicable at any location.

5 Results

The performance of the patient-specific anatomy and dynamics computation was validated on a set of 239 patients with 4D echocardiography acquisitions. On average the precision was 1.73mm at a speed of 4.8sec per volume for the valvular model and 2.68mm at a speed of less than 1sec per volume for the left ventricle [6,7].

The validation of our patient-specific hemodynamics computation - the main focus of this paper - was performed against clinical relevant blood flow

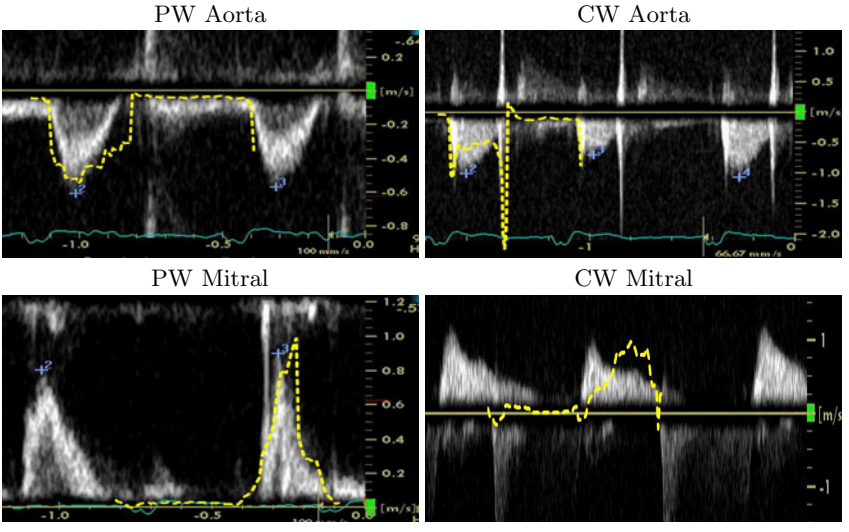

Fig. 4. Doppler acquisitions overlaid with computed curves in a patient with atrial fibrillation. Note the absence of the A-Wave in the transmitral measurements (bottom row) and the high velocity peaks in the CW aortic measurements (top right), which were well captured by the simulation.

Table 1. Measured ground truth (M) and simulated (S) peak velocities. Patient 1 and 2 had atrial fibrillation, therefore the A-wave was not visible (symbolized by n/a) in the ground truth, also successfully captured by the simulation.

	Patient 1		Patient 2		Patient 3	
peak velocity (m/s)	S	M	S	M	S	M
Aortic PW systolic	0.627	0.732	1.01	1.38	0.51	0.59
Aortic CW systolic	0.761	0.843	1.11	1.53	1.035	0.82
Mitral PW diastolic E-Wave	0.78	0.8	0.49	0.48	0.97	0.853
Mitral PW diastolic A-Wave	n/a		0.53	0.4	n/a	
Mitral CW diastolic	0.96	1.0	0.72	0.8	1.01	1.05

measurements, routinely acquired using Doppler echocardiography techniques. It is important to notice that Doppler methods, such as the aortic CW Doppler for stenosis assessment, are the current gold standard for hemodynamic analysis. Please also note that the diagnostic value of Doppler measurements is to a large extent in the peak velocities – as e.g. for assessing the degree of dysfunction – as well as qualitative observations in particular modes, i.e. the E- and A-waves in Mitral PW Doppler, describing transmitral flow early and late diastole respectively. Hence the evaluation is focused on these aspects.

The patient population included three randomly selected patients: two of them suffering from atrial fibrillation whereas the third from severe regurgitations of both, aortic and mitral valves. For each patient, a Doppler exam was performed six to 12 weeks before surgery, at the beginning of which 4D TEE data was

acquired. A difference in heart rates of 1 to 18% could be observed. Patient-specific models of anatomy and dynamics were computed form the 4D TEE images as described in section 2. From the obtained models, boundary conditions were derived and used to computed patient-specific hemodynamics as presented in section 3. Using the validation protocol described in section 4, measured and computed Doppler (PW and CW), for both valves and all patients, were compared and reported in Table 1. Overall a high agreement could be observed between the in vivo acquired measurements and computed results and the correlation among the corresponding values, which was computed using all values from all patients as reported in Table 1, amounted to $r = 0.85$ (significance $p < 0.0002675$). A qualitative comparison is provided in Fig. 4, which displays the ground truth Doppler velocities over time and the computed curves in one patient with atrial fibrillation. In support of our quantitative comparison, the overlay reveals the high level of detail of our computational model. In particular, the absence of A-wave in the transmitral measurements as specific for atrial fibrillation was correctly captured by the model - whereas its presence reflects ventricular filling in late diastole. Moreover, sharp peaks observed in CW Doppler across aortic valve were reproduced by the simulation, which occur across the valve orifice just before closure and after opening.

6 Conclusion

This paper presents a framework for systemic and highly detailed modeling of left heart anatomy, dynamics and hemodynamics from 4D TEE. Fast and robust estimation of anatomy and dynamics is performed using machine learning algorithms, while patient-specific hemodynamics is robustly estimated by using the personalized left heart model as a boundary condition for solving a level-set based formulation of the Navier-Stokes equations. Our framework was validated on three diseased patients, where both TEE and Doppler measurements were available and demonstrated high agreement. To the best of our knowledge our personalized model captures the most anatomical detail, considering for the first time papillary muscles and importantly is the first time that a framework for cardiac fluid mechanics is validated with clinically acquired ground truth data obtained from routinely employed clinical instrumentation in diseased patients.

References

1. Chung, E., Leon, A., Tavazzi, L., Sun, J., Nihoyannopoulos, P., Merlino, J., Abraham, W., Ghio, S., Leclercq, C., Bax, J., Yu, C., Gorcsan, J., Sutton, S., De Sutter, J., Murillo, J.: Results of the Predictors of Response to CRT (PROSPECT) Trial. Circulation (117), 2608–2616 (2008)
2. Hunter, P., Coveney, P., de Bono, B., Diaz, V., Fenner, J., Frangi, A., Harris, P., Hose, R., Kohl, P., Lawford, P., McCormack, K., Mendes, M., Omholt, S., Quarteroni, A., Skar, J., Tegner, J., Randall, T.S., Tollis, I., Tsamardinos, I., van Beek, J., Viceconti, M.: A vision and strategy for the virtual physiological human in 2010 and beyond. Phil. Trans. R. Soc. A 368(1920), 2595–2614 (1920)

3. Mcqueen, D.M., Peskin, C.S.: A three-dimensional computer model of the human heart for studying cardiac fluid dynamics. SIGGRAPH 34(1), 56–60 (2000)
4. Mihalef, V., Metaxas, D., Sussman, M., Hurmusiadis, V., Axel, L.: Atrioventricular blood flow simulation based on patient-specific data. In: Ayache, N., Delingette, H., Sermesant, M. (eds.) FIMH 2009. LNCS, vol. 5528, pp. 386–395. Springer, Heidelberg (2009)
5. Schenkel, T., Malve, M., Reik, M., Markl, M., Jung, B., Oertel, H.: MRI-Based CFD Analysis of Flow in a Human Left Ventricle: Methodology and Application to a Healthy Heart. Annals of Biomedical Engineering (3), 503–515 (2007)
6. Ionasec, R.I., Voigt, I., Georgescu, B., Wang, Y., Houle, H., Vega-Higuera, F., Navab, N., Comaniciu, D.: Patient-specific modeling and quantification of the aortic and mitral valves from 4D cardiac CT and TEE. IEEE Transactions on Medical Imaging 9, 1636–1651 (2010)
7. Wang, Y., Georgescu, B., Houle, H., Comaniciu, D.: Volumetric myocardial mechanics from 3D+t ultrasound data with multi-model tracking. In: Camara, O., Pop, M., Rhode, K., Sermesant, M., Smith, N., Young, A. (eds.) STACOM 2010. LNCS, vol. 6364, pp. 184–193. Springer, Heidelberg (2010)
8. Zheng, Y., Barbu, A., Georgescu, B., Scheuering, M., Comaniciu, D.: Four-chamber heart modeling and automatic segmentation for 3D cardiac CT volumes using marginal space learning and steerable features. IEEE Transactions on Medical Imaging 27(11), 1668–1681 (2008)
9. Li, J., Renardy, Y., Renardy, M.: Numerical simulation of breakup of a viscous drop in simple shear flow through a volume-of-fluid method. Phys. Fluids 12(2), 269–282 (2000)
10. Quinones, M., Otto, C., Stoddard, M., Waggoner, A., Zoghbi, W.: Recommendations for Quantification of Doppler Echocardiography: A Report from the Doppler Quantification Task Force of the Nomenclature and Standards Committee of the American Society of Echocardiography. J. Am. Soc. E (15), 167–184 (2002)
11. Armstrong, W., Ryan, T.: Feigenbaums Echocardiography. Lippincott Williams and Wilkins (2009)

Cardiac Motion Estimation from 3D Echocardiography with Spatiotemporal Regularization

Zhijun Zhang[1], Xubo Song[1], and David J. Sahn[1,2]

[1] Department of Biomedical Engineering
[2] Department of Pediatric Cardiology
Oregon Health and Science University
20000 NW Walker Road, Beaverton, OR 97006, USA
{zhangzhi,xubosong}@csee.ogi.edu, sahnd@ohsu.edu

Abstract. Cardiac deformation and motion analysis is important for studying heart function and mechanics. Deformation and motion abnormality of the myocardial wall is usually associated with ischemia and infarct. Three-dimensional (3D) echocardiographic (echo) imaging is the most widely used method to estimate cardiac motion. However, quantitative motion analysis from echo images is still a challenging problem due to the complexity of cardiac motion, limitations in spatial and temporal resolutions, low signal noise ratio and imaging artifacts such as signal dropout. We developed a novel method to quantitatively analyze cardiac deformation and motion from echo sequences. Our estimated cardiac motion is not only regularized to be spatially but also *temporally* smooth. We validate our methods using (1) simulated echo images with known ground truth, and (2) *in vivo* echo images acquired on open-chests pigs with sonomicrometry. Tests indicate that our method can estimate cardiac motion more accurately than methods without temporal regularization.

Keywords: Cardiac motion analysis, nonrigid image registration, echocardiography, cardiac strain estimation.

1 Introduction

Quantitative analysis of cardiac deformation and motion is important for studying heart function. Many illnesses related to ischemia or infarct can be recognized from the motion and deformation abnormalities [1]. Technique to accurately locate the abnormal motion region is critical to specify the disease and to evaluate the treatment.Echocardiography (echo) is most widely used because it is non-ionizing, real-time, cost-effective and convenient. With the development of the new transducer array technology, 3D echo is now available and can provide real-time images of whole heart [2]. However, the 4D (3D+t) data is acquired with a compromise that both the spatial and temporal resolution are reduced. 3D motion analysis from echo remains a challenging problem.

D.N. Metaxas and L. Axel (Eds.): FIMH 2011, LNCS 6666, pp. 350–358, 2011.

Motion analysis from echo typically falls into two categories: model-based and intensity-based methods. Model-based methods usually adopt deformable models, whose creation and training requires manual inputs and prior knowledge [3,4]. Papademetris *et al.* [5] used a finite element model, where the correspondences between the consecutive frames are tracked from interactively segmented myocardium surfaces. This requires intensive manual work and is computationally less efficient. Wang *et al.* [6] tracked myocardial surface by maximizing the likelihood of a combined intensity and motion prediction model. Both the initial myocardial surface detector and the motion prediction model need to be learned in advance. Comaniciu *et al.* [8] proposed a Kalman filter based information fusion framework for shape tracking with a probabilistic subspace model constraint. In this work, a shape model should be learned and motion estimation is limited to the contour points.

Compared to model-based methods, intensity-based methods track the whole images directly. They require less manual inputs, can estimate spatially-dense transformations, and are better suited for parallel computing [9]. Optical-flow methods [10] and B-spline based registration methods have been proposed [11,12]. However, these methods only address the spatial smoothness of the points on myocardial wall, while their temporal continuity are not considered. Carbayo *et al.* [13] proposed a spatiotemporal deformation model for cardiac motion tracking. A 2D+t B-spline transformation is used to control the spatial and temporal smoothness. This method used a fix frame (the diastolic frame) as the reference. As a result, registration of frames further away from the reference is slower than frame-to-frame approach because of large deformation, and it is also less accurate due to speckle decorrelation [7,11]. In addition, it is difficult to extend the spatiotemporal model to 3D+t, due to the increased parameter space and thus the likelihood for the optimization to be trapped at local minima. Mathieu *et al.* [15] propose 3D diffeomorphic registration, with the velocity defined with a spatiotemporal continuous model. Again, by using a fixed reference frame, it suffers from speckle decorrelation.

We propose an intensity-based 3D frame-to-frame motion estimation method, which regularizes the spatial *and temporal* smoothness. By using frame-to-frame registration, we are able to alleviate loss of image similarity caused by speckle decorrelation. Key to our method is the temporal regularization, where we require the two spatial transformations adjacent in time to be similar. We define a regularization term that penalizes the second-order derivative of the voxel trajectory, which in term keep motion of each voxel to be smooth in velocity. This is done without the need for elaborate learning of the heart dynamical model.

2 Method

The deformation between a reference frame and a target frame is estimated by non-rigid registration. The registration problem is proposed as minimizing process of an energy which consists of similarity energy and regularization energy. The transformation is parameterized and the optimal transformation is found in a parameter space.

2.1 Deformation Model

We use 3D B-spline transformations to represent the deformation from the reference image to target images [17]. B-spline transformation is used because it defines complex nonrigid deformation by using a small number of parameters (the control vectors). The deformation is controlled locally by varying the control vector values located on a uniform spacing grid.

We denote the 3D image volume as $\Omega = \{(x, y, z)|0 \leq x_n < N, 0 \leq y_m < M, 0 \leq z_k < K\}$. We place a $ng \times mg \times kg$ mesh of equally spaced control points $\mathbf{c}_{i,j,l}$ over the image domain. The transformation $\mathbf{T}(\mathbf{x}; \mathbf{c})$ is defined that the displacement is a 3D tensor product of the 1D cubic B-splines:

$$\mathbf{T}(\mathbf{x}; \mathbf{c}) = \mathbf{x} + \sum_{k=0}^{3} \sum_{m=0}^{3} \sum_{n=0}^{3} B_n(u_x) B_m(v_y) B_k(w_z) \mathbf{c}_{i+k,j+m,l+n}, \tag{1}$$

where $i = \lfloor x/ng \rfloor - 1, j = \lfloor y/mg \rfloor - 1, l = \lfloor z/kg \rfloor - 1$. B-splines are compactly supported, and thus are defined by its terms of local coordinates (u_x, v_y, w_z), where $u_x = x/ng - \lfloor x/ng \rfloor, v_y = y/mg - \lfloor y/mg \rfloor, w_z = z/kg - \lfloor z/kg \rfloor$. B_n are the nth B-spline basis functions: $B_1(u) = (1-u)^3/6, B_2(u) = (3u^3 - 6u^2 + 4)/6, B_3(u) = (-3u^3 + 3u^2 + 3u + 1)/6$ and $B_4(u) = u^3/6$ with $0 \leq u \leq 1$. The displacement of each point $\mathbf{x}$ will be controlled by vector values $\mathbf{c}_{i,j,l}$ of the nearest $4 \times 4 \times 4$ control points. In the following sections, $\mathbf{c}$ will be used as simplified notation of transformation $\mathbf{T}(\mathbf{x}; \mathbf{c})$.

2.2 Similarity Metric

Similarity metric is a measurement of how much two images are similar. Mutual information (MI) measures the statistical dependency between two images without assumption that the two images are linearly correlated, making it more suitable for echo images. Assume the reference and target images are I_r and I_t, then $MI(I_r, I_t; \mathbf{c})$ is a parametric function of $\mathbf{c}$ that measures the statistical dependency between the intensity values of $I_r(\mathbf{x})$ and $I_t(\mathbf{x}; \mathbf{c})$.

The energy of negative MI of a reference image and a deformed target image is defined by:

$$E_{sim}(I_r, I_t; \mathbf{c}) = -\int P(i_r, i_t; \mathbf{c}) log \frac{P(i_r, i_t; \mathbf{c})}{p_r(i_r) p_t(i_t; \mathbf{c})} di_r i_t, \tag{2}$$

with $P(i_r, i_t; \mathbf{c})$ the joint probability density function (PDF) of the two images and $p_r(i_r)$ and $p_t(i_t; \mathbf{c})$ the marginal PDFs of image I_r and $I_t(\mathbf{x}; \mathbf{c})$ respectively. The joint PDF of reference and deformed target images is evaluated by using the Parzen window approach:

$$P(i_r, i_t; \mathbf{c}) = \frac{1}{|\Omega|} \int_{\Omega} G_{\boldsymbol{\beta}}(\mathbf{I}(\mathbf{x}; \mathbf{c}) - \mathbf{i}) d\mathbf{x}, \tag{3}$$

where $\mathbf{i} = (i_r, i_t)^T$, $\mathbf{I}(\mathbf{x}; \mathbf{c}) = (I_r(\mathbf{x}), I_t(\mathbf{x}; \mathbf{c}))^T$ and $G_{\boldsymbol{\beta}} = \frac{1}{2\pi det \boldsymbol{\beta}} \exp(-\frac{1}{2} \mathbf{i} \boldsymbol{\beta}^{-1} \mathbf{i})$ with $\boldsymbol{\beta} = \begin{pmatrix} \beta_r & 0 \\ 0 & \beta_t \end{pmatrix}$, β_r and β_t are variance of Gaussian kernels for Parzen estimation and $|\Omega|$ the number of voxels in the image domain. The marginal

PDFs are $p_r(i_r) = \frac{1}{|\Omega|}\int_\Omega g_{\beta_r}(I_r(\mathbf{x}) - i_r)d\mathbf{x}$ with $g_{\beta_r} = \frac{1}{\sqrt{2\pi\beta_r}}exp(-\frac{t^2}{2\beta_r})$ and $p_t(i_t;\mathbf{c}) = \frac{1}{|\Omega|}\int_\Omega g_{\beta_t}(I_t(\mathbf{x};\mathbf{c}) - i_t)d\mathbf{x}$ with $g_{\beta_t} = \frac{1}{\sqrt{2\pi\beta_t}}exp(-\frac{t^2}{2\beta_t})$. Here we define $e_{MI} = log\frac{P(i_r,i_t,\mathbf{c})}{p_r(i_r)p_t(i_t;\mathbf{c})} = log\frac{1}{p_r(i_r)} - log\frac{p_t(i_t;\mathbf{c})}{P(i_r,i_t;\mathbf{c})}$ as the entropy decrease at each voxel when the conditional probability density is given.

2.3 Spatiotemporal Regularization

In order to let the transformation to be spatially smooth, we need to define a penalty energy which regularizes the transformation to be as smooth as possible. Assume we have a transformation $\mathbf{T}(\mathbf{x}) = (T_x, T_y, T_z)^T$, the spatial regularization energy is defined as the sum of bending energies of three components:

$$E_{sp}=\frac{1}{|\Omega|}\sum_{d\in\{x,y,z\}}\int_\Omega [(\frac{\partial^2 T_d}{\partial x^2})^2+(\frac{\partial^2 T_d}{\partial y^2})^2+(\frac{\partial^2 T_d}{\partial z^2})^2+2(\frac{\partial^2 T_d}{\partial x\partial y})^2+2(\frac{\partial^2 T_d}{\partial y\partial z})^2+2(\frac{\partial^2 T_d}{\partial x\partial z})^2]d\mathbf{x}. \tag{4}$$

For echo sequences, since the time span τ between frames is equal and very short (*e.g.* $40ms$ *per* frame), the motion of any points in the myocardial wall should be continuous in velocity. Here we define a penalty term $\frac{\partial^2\mathbf{T}}{\partial t^2}$ which regularizes the transformation to enforce that the velocity changes are small. Let's consider three consecutive frames I_i, I_{i+1} and I_{i+2}. The trajectory of a point $\mathbf{x}$ in these three frames will be $\mathbf{T}_i(\mathbf{x})$, $\mathbf{T}_{i+1}(\mathbf{x})$ and $\mathbf{T}_{i+2}(\mathbf{x})$, then we have:

$$\frac{\partial^2\mathbf{T}}{\partial t^2}|_{t=i} = (\mathbf{T}_i - 2\mathbf{T}_{i+1} + \mathbf{T}_{i+2})/\tau^2. \tag{5}$$

In order to take advantage of the correlation information between the neighbor frames, we use an improved frame-to-frame registration approach. We will register I_i with I_{i+1} and I_{i+2} to estimate transformation from i to $i+1$. Assume the transformation from frame i to the two consecutive frames are $\mathbf{T}_1(\mathbf{x})$ and $\mathbf{T}_2(\mathbf{x})$ then a point $\mathbf{x}$ in I_i corresponds with points $\mathbf{T}_1(\mathbf{x})$ and $\mathbf{T}_2(\mathbf{x})$ in the consecutive frames. The temporal regularization energy will be:

$$E_{tp} = \frac{1}{|\Omega|}\int_\Omega |\mathbf{x} - 2\mathbf{T}_1(\mathbf{x}) + \mathbf{T}_2(\mathbf{x})|^2 d\mathbf{x} \tag{6}$$

2.4 Optimization

The registration energy will be a weighted sum of the energies of similarity, spatial regularization and temporal regularization:

$$E = E_{sim} + w_s E_{sp} + w_t E_{tp}, \tag{7}$$

where w_s and w_t are weights for spatial and temporal regularization.

We use a steepest descent method to minimize the registration energy. It is an iterative method that the derivative of the energy function with respect to the transformation parameters will be calculated in each iteration. Let's denote $\mathbf{c}_1$ and $\mathbf{c}_2$ as the transformation parameters from one frame to next two consecutive

frames. The partial derivatives of the MI with respect to each vector of $\mathbf{c}_1$ and $\mathbf{c}_2$ are:

$$\frac{\partial E_{sim}}{\partial \mathbf{c}_{i,j,k}} = \int_{\Omega'} \frac{\partial e_{MI}(i_r, i_t; \mathbf{c})}{\partial i_t}|_{\substack{i_t=I_t(\mathbf{x},\mathbf{c}) \\ i_r=I_r(\mathbf{x})}} \frac{\partial I_t(\mathbf{x}, \mathbf{c})}{\partial \mathbf{x}}|_{\mathbf{x}=\mathbf{T}(\mathbf{x},\mathbf{c})} \frac{\partial \mathbf{T}(\mathbf{x})}{\partial \mathbf{c}_{i,j,k}} d\mathbf{x}, \tag{8}$$

with the derivative of entropy difference $e_{MI}(i_r, i_t)$ calculated as: $\frac{\partial e_{MI}(i_r,i_t;\mathbf{c})}{\partial i_t} = \mathbf{G}_{\boldsymbol{\beta}} \star (\frac{1}{P(i_r,i_t;\mathbf{c})} \frac{\partial P(i_r,i_t;\mathbf{c})}{\partial i_t} - \frac{p_t'(i_t;\mathbf{c})}{p_t(i_t;\mathbf{c})})$, $\star$ is the convolution operator, and Ω' is the region in which the transformation of a point $\mathbf{x}$ is controlled by vector $\mathbf{c}_{i,j,k}$. The derivative of the spatial regularization energy with respect can be referred to [11]. The derivatives of the temporal regularization energy are:

$$\begin{aligned} \frac{\partial E_{tp}}{\partial \mathbf{c}_{i,j,k;1}} &= -\frac{2}{|\Omega|} \int_{\Omega'} (\mathbf{x} - 2\mathbf{T}_1(\mathbf{x}) + \mathbf{T}_2(\mathbf{x})) \frac{\partial \mathbf{T}_1}{\partial \mathbf{c}_{i,j,k;1}} d\mathbf{x}, \\ \frac{\partial E_{tp}}{\partial \mathbf{c}_{i,j,k;2}} &= \frac{1}{|\Omega|} \int_{\Omega'} (\mathbf{x} - 2\mathbf{T}_1(\mathbf{x}) + \mathbf{T}_2(\mathbf{x})) \frac{\partial \mathbf{T}_2}{\partial \mathbf{c}_{i,j,k;2}} d\mathbf{x}. \end{aligned} \tag{9}$$

The components of $\mathbf{c}_1$ and $\mathbf{c}_2$ will be serialized as a vector and optimized. The transformation $\mathbf{T}_1$ will be then used to describe the deformation from the ith frame to $(i+1)$th volume.

2.5 Deformation Analysis

When the transformation from frame i to $i+1$ is estimated as $\mathbf{T}_i$, the transformation from the reference frame I_0 to any frame I_i will be a concatenation of i transformations: $\mathbf{T}_{i,0}(\mathbf{x}) = \mathbf{T}_i \circ \mathbf{T}_{i-1} ... \circ \mathbf{T}_1(\mathbf{x})$. We use strain to characterize cardiac motion and deformation. We here use the Green Lagrange strain tensor with the definition of $\mathbf{E} = \mathbf{J}^T\mathbf{J} - \mathbf{I}$ in our evaluation, with $\mathbf{J}$ the Jacobian matrix of the transformation. The strain tensor describes the strain along any directions, usually they are evaluated along the longitudinal, radial and circumferential directions defined in cardiac coordinate system [11].

2.6 Implementation

In our implementation, we use a series of 3D B-spline transformations with grid size $20 \times 20 \times 20$ to represent the transformation. For MI, 32 bins are used to evaluate the joint and marginal PDFs. β_r and β_t are empirically set to 3.0. The weighting w_s and w_t for regularization energies are both 0.1. The algorithm is implemented with Matlab [18] parallel computing toolbox under a windows XP 64 bit system on a machine with 2.13GHz Xeon 8 cores CPU and 6GB memory. It takes about 20 minutes to register a 3D sequence with 24 frames.

3 Data and Experiment

We use both simulated and real data to verify our method. In the simulated data experiment, a diastolic left ventricle (LV) volume with size $137 \times 96 \times 124$ and

Fig. 1. The center longitudinal views of the reference frame, and $10th$ volume and the displacement field between these two frames (only displacement field inside a bell-shaped mask is displayed)

voxel size $1mm \times 1mm \times 1mm$ is used as a reference frame. This frame is then deformed with a series of continuous displacement field functions. The functions are axially symmetrical to simulate the myocardial contraction effect along radial and longitudinal directions. The 3D functions are in form of: $\boldsymbol{f}_{x,y} = a_{xy} sin\frac{\pi\sqrt{(x-x_c)^2+(y-y_c)^2}}{2r_d} sin(\frac{i\pi}{N_f})\boldsymbol{n}$ and $f_z = a_z sin\frac{\pi(z-z_{apex})}{2(z_{base}-z_{apex})} sin(\frac{i\pi}{N_f}+\frac{\pi}{16})$, with x_c, y_c, r_d the axis center coordinate and the average axial radius, z_{apex} and z_{base} the height of base and apex planes, N_f and i the number of frames and the frame index, and a_{xy}, a_y are the magnitudes of displacement fields. An image sequence is generated when i varies from 1 to N_f to simulate the cardiac motion in one cycle. Three sequences of 20 frames each are simulated with speckle noise of variance 0.04, 0.06 and 0.08 added, with a multiplicative noise model [18]. The center longitudinal slice of the first and the $10th$ volume with speckle noise variance 0.06 are shown together with the in plane displacement field in Fig.1.

The real data sets are acquired from three open-chest pigs by using a Philips IE33 system. Cardiac motion sequences of heart under normal condition and controlled ischemia by inferior vena cava (IVC) occlusion are both captured. The images are resampled into volume sequences of $160 \times 100 \times 128$ with voxel size $1mm \times 1mm \times 1mm$. For validation, we installed six sonomicrometers in the heart wall. The distance readings between the crystals are used to compare with the tracked distances in the echo images. The crystal coordinates in the reference frame are manually denoted.

4 Result and Discussion

We estimate the sequence motion by using registration methods with and without temporal regularization. In the simulated data experiments, the estimated displacement fields are compared with the ground truth. The errors are evaluated by using the mean and variance of the error vector of displacement field at each voxel inside a bell-shaped region. As an example, the means and variances of the two methods in the noise variance 0.06 test setting are shown in Fig.2. We can see in most frames the errors are smaller in our proposed method than the method without temporal regularization. Our method shows a more stable frame-to-frame transformation error and the variance of errors are smaller. The total average errors in the three noise variance settings with temporal regularization are 0.226,

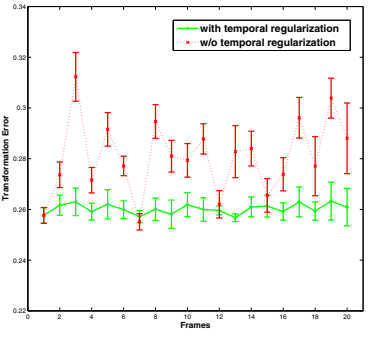

Fig. 2. The registration error with respect to the ground truth in each frame with and without temporal regularization

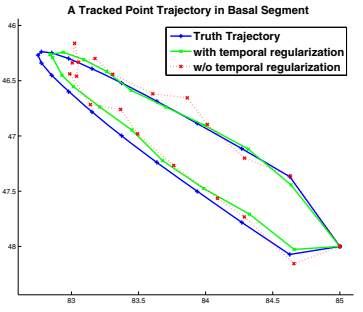

Fig. 3. The ground truth trajectory (blue) and the estimation by using our method (green) and method without temporal regularization (red)

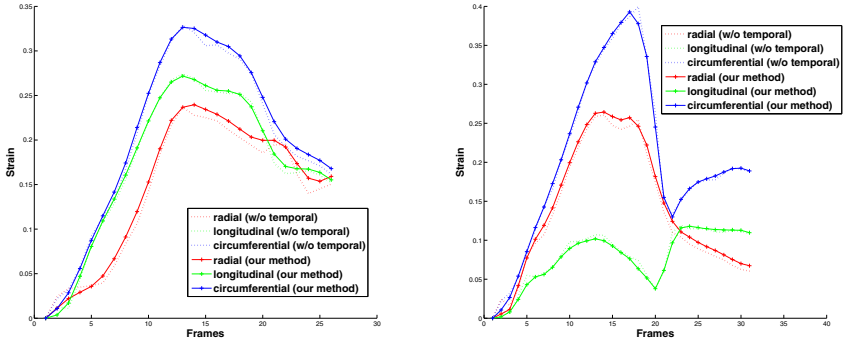

Fig. 4. Cardiac strains estimated in a lateral apical segment of a normal heart (Left) and in the mid septum region with IVC occlusion (Right)

0.261 and 0.297, while in the methods without are 0.248, 0.295 and 0.346. Fig.3 shows a trajectory of a point in basal segment in the center longitudinal view. We can see with temporal regularization, the sudden change in the voxel trajectory can be effectively avoided.

For the real datasets, strains tensor of points in cardiac wall segments of the open-chest pigs are calculated from the transformation function as described in section 2.5. The strain value are evaluated in the radial, longitudinal and circumferential directions which are defined in local cardiac coordinate. Here we show the strain in a lateral apical segment of a normal heart and that in the mid septum regions of a heart with inferior vena cava (IVC) occlusion. From Fig.4 we can see our method can estimate cardiac strain with more smoothness in both normal and abnormal cases.

Table 1. The correlations between the estimated pair-wise distances and those from the sonomicrometry, with temporal regularization (numbers on the left) and without(numbers on the right). Numbers 1-6 index the 6 sonomicrometry markers.

	1	2	3	4	5	6
1	1.0/1.0	0.869/0.851	0.936/0.904	0.872/0.840	0.938/0.912	0.942/0.907
2	0.869/0.851	1.0/1.0	0.771/0.755	0.981/0.970	0.810/0.793	0.891/0.883
3	0.936/0.904	0.771/0.755	1.0/1.0	0.982/0.968	0.922/0.908	0.979/0.964
4	0.872/0.840	0.981/0.970	0.982/0.968	1.0/1.0	0.906/0.877	0.938/0.928
5	0.938/0.912	0.810/0.793	0.922/0.908	0.906/0.877	1.0/1.0	0.856/0.843
6	0.942/0.907	0.891/0.883	0.979/0.964	0.938/0.928	0.856/0.843	1.0/1.0

Finally we compare performances achieved with and without temporal regularization, by computing the correlations between sonomicrometry-derived and algorithm-derived pair-wise distances (Table 1). We can see with temporal regularization, consistently higher correlations with sonomicrometry are achieved.

5 Conclusion

We developed a novel 3D frame-to-frame cardiac motion estimation method from echo images. A temporal regularization term is added in the registration framework to avoid large displacement field change in consecutive frames. Simulated data experiments shows that our method has a higher accuracy and the points motion trajectory is much more smooth. Real dataset from open-chest pigs show that the estimated strain by our method is more physically reasonable and the estimated transformation agrees better with sonomicrometry. Our method is a general method and can be extended to motion estimation of other image modalities.

Acknowledgement

This paper is supported by a NIH/NHLBI grant 1R01HL102407-01 awarded to Xubo Song and David Sahn.

References

1. Fukuda, K., Oki, T., Tabata, T., Iuchi, A., Ito, S.: Regional left ventricular wall motion abnormalities in myocardial infarction and mitral annular descent velocities studied with pulsed tissue Doppler imaging. JASE 11(9), 841–848 (1998)
2. Hung, J., Lang, R., Flachskampf, F., Shernan, S.K., McCulloch, M.L., Adams, D.B., Thomas, J., Vannan, M., Ryan, T.: 3D Echocardiograhy: A Review of the Current Status and Future Directions. JASE 20(3), 213–233 (2007)
3. McInerney, T., Terzopoulos, D.: Deformable Models in Medical Image Analysis: A Survery. Med. Imag. Anal. 1(2), 91–108 (1996)

4. Frangi, A.F., Niessen, W.J., Viergever, M.A.: Three Dimensional Modeling for Functional Analysis of Cardiac Images: A Review. IEEE Trans. Med. Imag. 20(1), 2–25 (2001)
5. Papademetris, X., Sinusas, A.J., Dione, D.P., Duncan, J.S.: Estimation of 3D left ventricular deformation from echocardiography. Med. Imag. Anal. 5(1), 17–28 (2001)
6. Wang, Y., Georgescu, B., Houle, H., Comaniciu, D.: Volumetric Myocardial Mechanics from 3D+t Ultrasound Data with Multi-model Tracking. In: Camara, O., Pop, M., Rhode, K., Sermesant, M., Smith, N., Young, A. (eds.) STACOM 2010. LNCS, vol. 6364, pp. 184–193. Springer, Heidelberg (2010)
7. Meunier, J.: Tissue motion assessment from 3D echographic speckle tracking. Phys. Med. Biol. 43, 1241–1254 (1998)
8. Comaniciu, D., Zhou, X., Krishnan, S.: Robust real-time tracking of myocardial border: An information fusion approach. IEEE Trans. Med. Imag. 23(7), 849–860 (2004)
9. Makela, T., Clarysse, P., Sipila, O., Pauna, N., Pham, Q.C., Katila, T., Magnin, I.E.: A review of cardiac image registration methods. IEEE Trans. Med. Imag. 21(9), 1011–1021 (2002)
10. Suhling, M., Arigovindan, M., Jansen, C., Hunziker, P., Unser, M.: Myocardial Motion Analysis from B-Mode Echocardiograms. IEEE Trans. Image Process. 14(4), 525–536 (2005)
11. Elen, A., Choi, H.F., Loeckx, D., Gaom, H., Claus, P., Suetens, P., Maes, F., D'hooge, J.: Three-dimensional cardiac strain estimation using spatio-temporal elastic registration of ultrasound images: a feasibility study. IEEE Trans. Med. Imag. 27(11), 1580–1591 (2008)
12. Myronenko, A., Song, X.B., David, J.S.: LV Motion Tracking from 3D Echocardiography Using Textural and Structural Information. In: Ayache, N., Ourselin, S., Maeder, A. (eds.) MICCAI 2007, Part II. LNCS, vol. 4792, pp. 428–435. Springer, Heidelberg (2007)
13. Ledesma-Carbayo, M.J., Mah-Casado, P., Santos, A., Prez-David, E., GarMA, D.M.: Spatio-Temporal Nonrigid Registration for Ultrasound Cardiac Motion Estimation. IEEE Trans. Med. Imag. 24(9), 1113–1126 (2005)
14. Maes, F., Collignon, A., Vandermeulen, D., Marchal, G., Suetens, P.: Multimodal image registration by maximization of mutual information. IEEE Trans. Med. Imag. 16(2), 187–198 (1997)
15. Craene, M.D., Camara, O., Bijnens, B.H., Frangi, A.F.: Temporal Diffeomorphic Free-Form Deformation for Strain Quantification in 3D-US Images. In: Jiang, T., Navab, N., Pluim, J.P.W., Viergever, M.A. (eds.) MICCAI 2010. LNCS, vol. 6362, pp. 1–8. Springer, Heidelberg (2010)
16. Hermosillo, G., Chefd'Hotel, C., Faugeras, O.: Variational Methods for Multimodal Image Matching. International Journal of Computer Vision 50(2), 329–343 (2002)
17. Rueckert, D., Sonoda, L.I., Hayes, C., Hill, D.L.G., Leach, M.O., Hawkes, D.J.: Nonrigid registration using free-form deformations: Application to breast MR images. IEEE Trans. Image Process. 18(8), 712–721 (1999)
18. MATLAB version 7.11.0 (R2010b). The MathWorks Inc., Natick (2010)

Order Statistic Based Cardiac Boundary Detection in 3D+t Echocardiograms

C. Butakoff[1,2], F. Sukno[1], A. Doltra[3], E. Silva[3], M. Sitges[3], and A.F. Frangi[1,2,4]

[1] CISTIB, Universitat Pompeu Fabra, Barcelona
[2] CIBER-BBN
[3] Hospital Clínic, IDIBAPS, Universitat de Barcelona,
[4] Institució Catalana de Recerca i Estudis Avançats, Barcelona, Spain

Abstract. We propose a boundary detector for echocardiographic images to be used in conjunction with deformable models. It is well suited to detect endocardial and epicardial boundaries in both 2D and 3D images. We demonstrate its capabilities on an example of Active Shape Models, where it is used as a force driving the mesh towards the cardiac walls. Although the proposed approach is mostly specific to echocardiography, it does not require any training to learn the image appearance (since construction of a training set of echocardiograms is very difficult and error prone). The detector is based on computing the medians of a series of neighborhoods and analyzing the change in their values to look for the evidence of an edge. The proposed algorithm was tested on thirty 3D echocardiographic sequences (corresponding to 10 healthy and 10 dyssinchronous hearts, the latter imaged at two stages of cardiac resynchronization therapy: before and at twelve month followup).

1 Introduction

There has been a vast number of algorithms developed for the cardiac segmentation in 3D echocardiography. We would like to concentrate here on algorithms utilizing deformable surfaces. An extensive survey of these algorithms can be found in Heimann and Meinzer[1], Noble *et al.*[2], Frangi *et al.*[3], Lelieveldt *et al.*[4], and Angelini *et al.*[5,6]. All these methods utilize an appearance model (to fit the deformable surface to the image) that is mainly obtained either by learning from a training set of manually delineated images or using heuristics. Learning the appearance model from a training set is the most promising and popular approach today, however generating the appropriate and representative training set is challenging, especially in 3D echocardiography, due to a poor quality of the images. The fitting algorithms that utilize heuristic models, on the other hand, mostly reduce to the search of strongest change in the sampled quantity (intensity, gradient, etc.) or try to reach a state where the sampled quantity outside the shape and inside are uniform. Most of these approaches utilize information sampled only along a line (along a normal to the mesh), which creates vulnerability to noise.

D.N. Metaxas and L. Axel (Eds.): FIMH 2011, LNCS 6666, pp. 359–366, 2011.

In this paper we propose a boundary detection based on order statistics. Median is known to be a good choice to recover signal from speckle and impulse noise. By using median we expect to have a detector that is less insensitive to fluctuations in image intensity and speckle patterns (that differs between hardware manufacturers). It is also heuristic, avoiding a costly and error prone process of delineating the images required by the learning-based approaches. There is a number of other works concerning the edge detection in echocardiograms[9,10,11], but they are mostly global edge detection techniques, and what we wanted is to have a reasonably simple technique to find the edge locally and especially uniquely. The proposed approach will be demonstrated on the example of segmenting myocardium of the left ventricle using an Active Shape Model(ASM)[12]. Nevertheless, it should be noted that the detector is not limited to ASM and, although, we will apply it to 3D images, it works for 2D images and can potentially be applied to M-mode ultrasound as well.

2 The Order Statistic Based Boundary Detector

We will frame our detector within ASM framework. First of all, ASM requires a generative shape model, called the Point Distribution Model (PDM), constructed by applying PCA to a set of aligned landmarked shapes. This shape model is then adapted to an image by sampling image features along normals to each landmark and displacing the landmarks as to minimize a certain objective function (in the classical approach - Mahalanobis distance to the mean profile, learned from a training set). Our PDM was constructed from CT images, following the automatic approach of Ordas *et al.*[13]. Here we propose the following heuristic boundary search:

1. For each landmark take a normal to the surface
2. Sample a $N + M \times M \times M$ neighborhood ($M << N$) oriented along normal with desired spacing (in our experiments we used 0.7mm, approximately equal to the voxel size of our echocardiographic images). M and N should be chosen beforehand.
3. For each $M \times M \times M$ subblock compute the median, and form an N-vector of medians (also called *profile*)
4. Compute the numerical derivative of the profile (we have used the central difference operator)
5. Compute the quartiles $Q1, Q2, Q3$ of the profile derivative
6. Identify significant peaks as those bigger than $Q3+1.5(Q3-Q1)$ and smaller than $Q1 - 1.5(Q3 - Q1)$ (This is a commonly accepted outlier detection technique for the box plot[14]). These peaks will indicate all the relatively strong edges corresponding to ascending and descending intensities.
7. To get the strongest edges, identify the minimum and maximum among the peaks from the previous step. In a good quality image there will be two: a positive and a negative. One of them corresponds to the inner wall and another to the outer, depending on the direction of the normal.

8. Use these positions, given by the identified extrema, to displace the shape vertices.
9. Apply PDM constraints

In our experiments we have chosen $N = 51$, $M = 9$ and uniform spacing of 0.7mm (the spacing approximately coincides with the voxel size in our datasets). These values were chosen as to provide a reasonably dense sampling (sampling every voxel) and wide search range (to provide a robustness to inaccurate initialization), and they have shown good results on a multitude of images. To place the initial shape in a reasonable starting position we aligned the mean shape of the PDM, by an affine transform, to six points: four points on the endocardium close to the mitral valve, the center of the aortic valve ring, and the apex. The four points in the basal region are not associated to any anatomical location and can be anywhere(preferably equally far from each other along the endocardium). The aortic valve is required to define the orientation of the shape. This initialization technique is similar to the one employed in Qlab (Philips Medical Systems, Andover, MA) and allows for a fast initialization.

3 Segmentation of 3D+t Echocardiographic Images

3D+t echocardiograms involve one additional challenge, which is tracking of the mitral plane in order to extract correct longitudinal contraction. Since the ASM deforms the shape only along normals, it can be seen from Fig. 1b that there are no structures on our mesh that could move the shape upwards (closing the mesh is not a good option as the valve opens during cardiac cycle). Therefore, we complement the model with several rings of vertices on the inside (up to 3mm depth with 0.7mm spacing, Fig. 1a) to detect the area where the endocardium

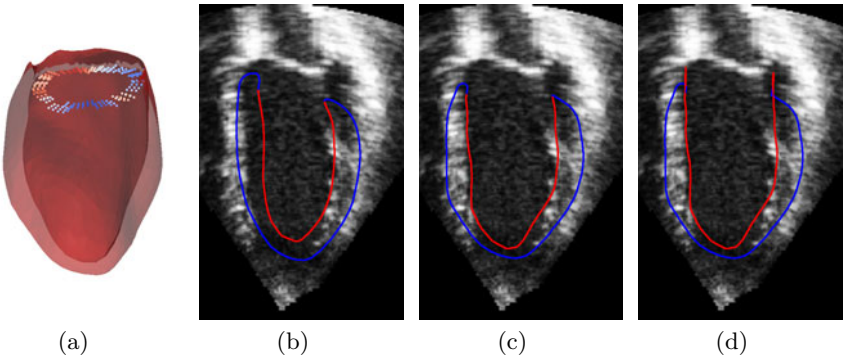

(a) (b) (c) (d)

Fig. 1. The illustration of mitral plane detection. (a) Shape with the complementary vertices; (b) Initial shape placed on the image of a healthy heart (red - endocardium, blue - epicardium); (c) Shape after the first iteration of the ASM; (d) Shape with corrected endocardium using the located mitral plane. For illustrative purposes no PDM constraints were applied in (d) so the shape is not plausible.

joins the mitral valve. The boundary detection for these points is performed along the long axis of the ventricle.

Now the proposed approach can be easily extended to 3D+t data in the following way. The segmentation in every frame is initialized using the shape obtained in the previous frame. The segmentation should start from the end-systolic (ES) frame and advance towards end-diastolic (ED) forwards and backwards along the timeline (five iterations are usually enough for the first frame and two for the others). This ensures a recovery of a more periodic deformation, reduces the effect of error propagation between frames, and allows to run two segmentations in parallel, reducing the overall execution time.

4 Results

The evaluation dataset was prepared with an idea of demonstrating the segmentation accuracy and also investigating whether this accuracy is sufficient for one of the clinical scenarios. The dataset consisted of ten healthy volunteers, and ten patients that underwent a cardiac resynchronization therapy. The patient dataset consisted of two sequences for every patient: one before the therapy (hereinafter labeled as `Off`) and one corresponding to the `followup` at twelve months. The patient population consisted of three ischemic patients with left bundle branch block (LBBB), four non ischemic with LBBB, and three ischemic without LBBB. Four of these patients responded to the therapy. The response was determined as volume decrease at ES by more than 15% at 6 or 12 month followup using measurements in 2D echocardiograms. The 3D acquisition of each patient was performed using one of the three machines: IE33, SONOS7500 and GE Vivid 7. The segmentation was performed on each of the 30 sequences,

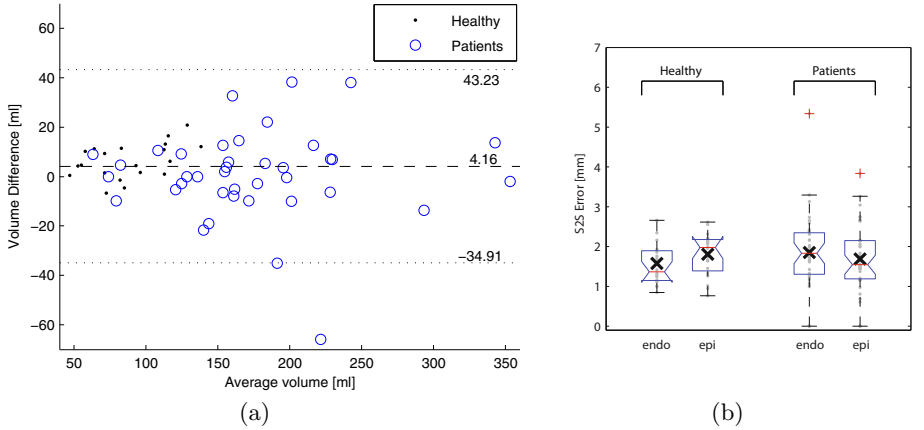

(a) (b)

Fig. 2. (a) Bland-Altman plot comparing the accuracy of the algorithm with respect to manual contours in 3D in terms of volume. (b) Boxplot of segmentation accuracy for epicardium and endocardium in terms of S2S error. '+' denotes outliers, 'x' stands for the mean.

Table 1. Segmentation accuracy (mean±2SD)

Meaurement	Healthy	Patient
S2S Endo [mm]	1.57 ± 1.09	1.84 ± 1.86
S2S Epi [mm]	1.80 ± 1.06	1.68 ± 1.71
Volume wrt 3D manual [ml]	6.35 ± 14.21	3.06 ± 46.86
EF wrt 3D manual [%]	0 ± 9	0 ± 19
ES Volume wrt 2D manual[ml]	n/a	-11.50 ± 59.50

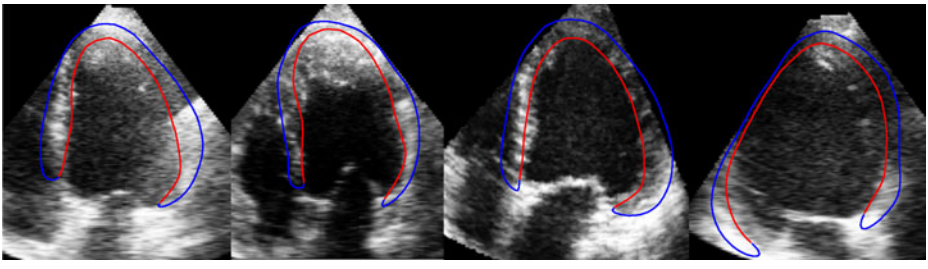

Fig. 3. An illustration of several problematic images with overlaid automatic contours

starting from the ES frame (determined by the visual inspection of the aortic valve) and following the steps of 3D+t segmentation.

To evaluate the accuracy of the segmentation algorithm the shapes in end-diastole (ED) and end-systole (ES) were corrected by an expert. Fig. 2a shows the Bland-Altman plot for the segmentation accuracy measured in terms of volume estimation with respect to the manual contours in 3D. Fig. 2b shows the segmentation accuracy for the healthy subjects and patients in terms of the symmetric average surface-to-surface(S2S) error.

Table 1 further summarizes the results obtained on the healthy hearts and on the patients. Several comments have to be made. First of all, the cardiac images were separated on purpose into healthy and pathological, because healthy hearts usually have better quality images and the left ventricle fits into the pyramidal field of view (FOV) as in Fig. 1b. Patient images are much more challenging and were mostly acquired by older equipment. The accuracy of segmentation was measured not only with respect to manually corrected shapes in 3D, but also with respect to volume measurements performed in 2D (the ones used to determine the response). Manually corrected contours in 3D had the same problem as the output of the algorithm – when the wall is outside the FOV or is shadowed, its whereabouts have to be guessed, which results in larger volume estimation errors (as seen in Fig. 2a, the error increases with the volume).

It can be observed from the table, that when the definition of the cardiac wall is relatively good, the algorithm performs well and the errors are low. As expected the problems arise in the patients with dilated hearts. Fig. 3 shows examples of images illustrating these problems. The leftmost image In the bottom left corner is an image with a reverberation artifact on the lateral wall which occluded the

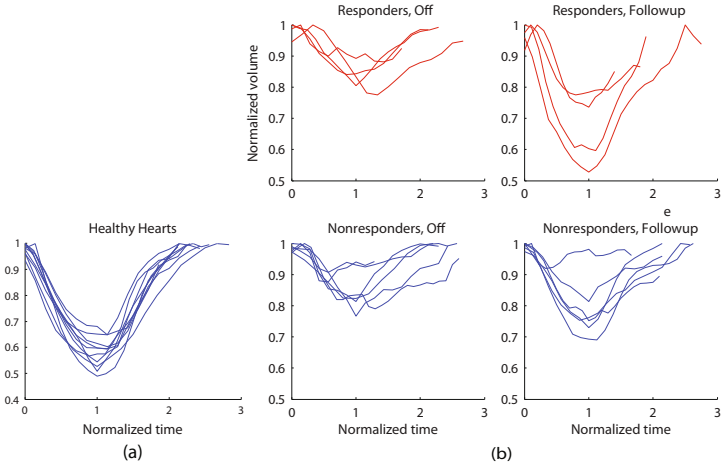

Fig. 4. Normalized volume curves for (a) healthy and (b) dyssinchronous hearts. The patients were classified into responders and nonresponders, as the curves were expected to be different, and plotted during the two periods: before the therapy (`off`) and during `followup`. Note that in many cases there is a visible change in the curves during `followup`, which got more similar to the normal ones. The normalization of each sequence consisted of rescaling the time such that ES happens at time equal one, and dividing by the maximum volume.

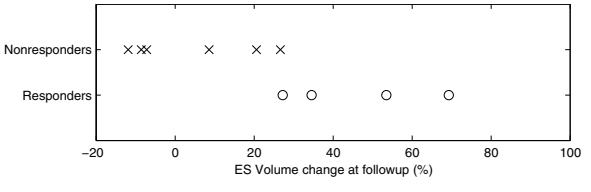

Fig. 5. Plot of the decrease of ES volume from `off` to `followup` for all the patients, grouped into responders and nonresponders

wall causing volume underestimation. The next image has a lot of noise and some structures that occlude the apex, causing an overestimation of about 30ml. The third one is a dilated heart, where a big piece of the lateral wall is outside the FOV. In this particular case there are still some structures visible and the shape got attached to them, giving an underestimation of the volume of about 50ml. Actually, what is interesting about this case is that this image corresponds to a followup study of a non-responder, whose ES volume before the therapy was smaller (which means that the patient's condition worsened). The last image is an example where the ventricle is dilated and the cardiac walls are poorly defined, which again caused underestimation by about 70ml. These cases essentially correspond to the five points of the Bland-Altman plot (Fig. 2a) with high volume differences. If these cases were excluded, the limits of agreement would reduce from $\pm 46ml$ to approximately $\pm 30ml$, making them comparable to interobserver variability of measurements in 3D echocardiography (about $\pm 20ml$–$\pm 30ml$ [7,8]).

The accuracy is also comparable to other approaches proposed in the literature, in terms of EDV/ESV: $3.82 \pm 1.4/0.61 \pm 26.4$ml[8], $16.1 \pm 57.8/6.6 \pm 39.7$ml [5], $0.1 \pm 49.3/4.2 \pm 32.3$ [15]; volume 15.6 ± 41.1ml [16], point-to-surface error 1.28 ± 1.11mm [17].

To further evaluate our technique, we wanted to see how well it performed on other frames of the 3D+t data (not just ED and ES). To this end we analyzed the volume curves. The patients that responded to the therapy are expected to have curves closer to the normal ones (Fig. 4a) or at least with a deeper valley corresponding to the ES volume. To plot and compare the volumes, we normalized them temporally and spatially (ES corresponds to time equal one, the volumes divided by the maximum volume in the sequence). The plots can be seen on Fig. 4.

It is interesting to see that the curves really get better, although just by looking at them it is not easy to determine the response to the therapy or to quantify well the reverse remodeling. To have a more quantitative evaluation, we tried to apply the same criterion as the one that was used clinically (a patient was considered a responder if ES volume decreased by 15%). In this experiment we got a clear separation between responders and nonresponders, but at 26% volume decrease (see Fig. 5). This error was expected, due to large, poorly defined ventricles. However the algorithm demonstrated consistency in segmentations and simply resulted in a shift of the decision rule.

5 Conclusion

In this paper we proposed a boundary detection for echocardiographic images (both 2D and 3D) demonstrating how it can be integrated into ASM and used to segment 3D echocardiographic images. The approach is expected to be insensitive to initialization (though a rigorous validation is in order) and identifies longitudinal contraction well (a problem that was not explicitly addressed until now, from our knowledge). Nevertheless it still can detect wrong structures if they have higher amplitude. Since segmentation in every frame is independent of the others, it would be desirable to add some way of speckle tracking or ensuring that over time the same boundary is being identified as a cardiac wall. Another interesting point is that, in this study, the detector parameters were chosen by visually inspecting the area covered by the grid points. The choice has proven to be good in all the cases, but it still could benefit from optimization. It is good to have a dense and long sampling grid, but the major drawback is that the denser the sampling the longer it takes to compute and analyze the medians. It would be interesting to analyze the various sampling strategies and choose the best one (for instance, reducing the sampling radius with iterations, when the wall should already be in the vicinity of the vertex).

Acknowledgements

This research has been partially funded by the Industrial and Technological Development Center (CDTI) under the CENIT-cvREMOD program, by the

European Commission's project euHeart (FP7-ICT-224495), and by the Spanish Ministry of Science and Innovation (Ref. TIN2009-14536-C02-01), Plan E and FEDER.

References

1. Heimann, T., Meinzer, H.P.: Statistical shape models for 3D medical image segmentation: A review. Med. Image Anal. 13(4), 543–563 (2009)
2. Noble, J.A., Boukerroui, D.: Ultrasound image segmentation: a survey. IEEE Trans. Med. Imag. 25(8), 987–1010 (2006)
3. Frangi, A.F., et al.: A survey of three-dimensional modeling techniques for quantitative functional analysis of cardiac images. In: Advanced Image Processing in Magnetic Resonance Imaging, CRC Press, Boca Raton (2005)
4. Lelieveldt, B.P.F., et al.: 3D active shape and appearance models in medical image analysis. In: Handbook of Mathematical Models of Computer Vision, pp. 471–486. Springer, Heidelberg (2006)
5. Angelini, E.D., et al.: Segmentation of real-time three-dimensional ultrasound for quantification of ventricular function: A clinical study on right and left ventricles. Ultrasound Med. Biol. 31(9), 1143–1158 (2005)
6. Angelini, E.D., et al.: State-of-the-art of levelset methods in segmentation and registration of medical imaging modalities. In: Handbook of Biomedical Image Analysis, vol. 3, Kluwer Academic Publishers, Dordrecht (2005)
7. Sugeng, L., et al.: Quantitative assessment of left ventricular size and function: side-by-side comparison of real-time three-dimensional echocardiography and computed tomography with magnetic resonance reference. Circulation 114(7), 654–661 (2006)
8. Hansegård, J., et al.: Constrained active appearance models for segmentation of triplane echocardiograms. IEEE Trans. Med. Imag. 26(10), 1391–1400 (2007)
9. Bovik, A.C., Munson, D.C.: Edge detection using median comparisons. Comput. Vis. Image Understand. 33(3), 377–389 (1986)
10. Czerwinski, R.N., et al.: Detection of lines and boundaries in speckle images-application to medical ultrasound. IEEE Trans. Med. Imag. 18(2), 126–136 (1999)
11. Slabaugh, G., et al.: Information-theoretic feature detection in ultrasound images. In: Proc. EMBS, pp. 2638–2642 (2006)
12. Cootes, T., Taylor, C.: Active shape models – smart snakes. In: Proc. BMVC, pp. 266–275 (1992)
13. Ordas, S., et al.: A statistical shape model of the heart and its application to model-based segmentation. In: Proc. SPIE, vol. 6511 (2007)
14. Frigge, M., et al.: Some implementations of the boxplot. American Statistician 43(1), 50–54 (1989)
15. Zagrodsky, V., et al.: Registration-assisted segmentation of real-time 3-D echocardiographic data using deformable models. IEEE Trans. Med. Imag. 24(9), 1089–1099 (2005)
16. Corsi, C., et al.: Left ventricular volume estimation for real-time three-dimensional echocardiography. IEEE Trans. Med. Imag. 21(9), 1202–1208 (2002)
17. Yang, L., et al.: 3D ultrasound tracking of the left ventricle using one-step forward prediction and data fusion of collaborative trackers. In: Proc. CVPR, pp. 1–8 (2008)

A Framework Combining Multi-sequence MRI for Fully Automated Quantitative Analysis of Cardiac Global And Regional Functions

Xiahai Zhuang[1,⋆], Wenzhe Shi[2], Simon Duckett[3], Haiyan Wang[2], Reza Razavi[3], David Hawkes[1], Daniel Rueckert[2], and Sebastien Ourselin[1]

[1] Centre for Medical Image Computing, University College London
x.zhuang@ucl.ac.uk
http://www.cs.ucl.ac.uk/staff/x.zhuang/
[2] Biomedical Image Analysis Group, Imperial College London
[3] The Rayne Institute, St Thomas Hospital, King's College London

Abstract. In current clinical settings, there are several technological challenges to perform automated functional analysis from cardiac MRI. In this work, we present a framework to automatically segment the heart anatomy, define segments of the left ventricle, and extract myocardial motions for quantitative analysis of cardiac global and regional functions. This framework makes use of the cardiac MRI sequences that are widely available in clinical practice, and improves the performance of the automated processing by combining information from multiple MRI sequences. We employed 20 pathological datasets to evaluate the proposed framework where the automatic analysis was compared with the manual intervention assisted analysis. The results showed high correlation between the two methods for the global function analysis (volume: R^2>0.8, ejection fraction:R^2 =0.88), and for the regional dyssynchrony analysis (wall motion: R^2=0.89; thickening: R^2=0.81). We also found that the automated method could fully include apical and basal volume, resulting in consistent overestimation of the left ventricle volume (∼40mL, P<0.05) and small underestimation of ejection fraction (−0.024, P<0.001).

1 Introduction

Cardiovascular disease is nowadays the world's number one killing disease, accounting for nearly thirty percent of worldwide deaths [1]. There have been tremendous efforts towards developing novel clinical applications using medical imaging and image analysis technology to reduce this death toll. Over the imaging modalities available in clinical routines, Magnetic Resonance Imaging (MRI) is becoming increasingly popular due to its non-ionizing radiation and good contrast in imaging soft tissues. However, one MRI sequence may only provide a limited portion of the full information required in automated image processing [2]. Therefore, combining all the available MRI data from different

⋆ This work was funded by EPSRC grant EP/H02025X/1.

D.N. Metaxas and L. Axel (Eds.): FIMH 2011, LNCS 6666, pp. 367–374, 2011.

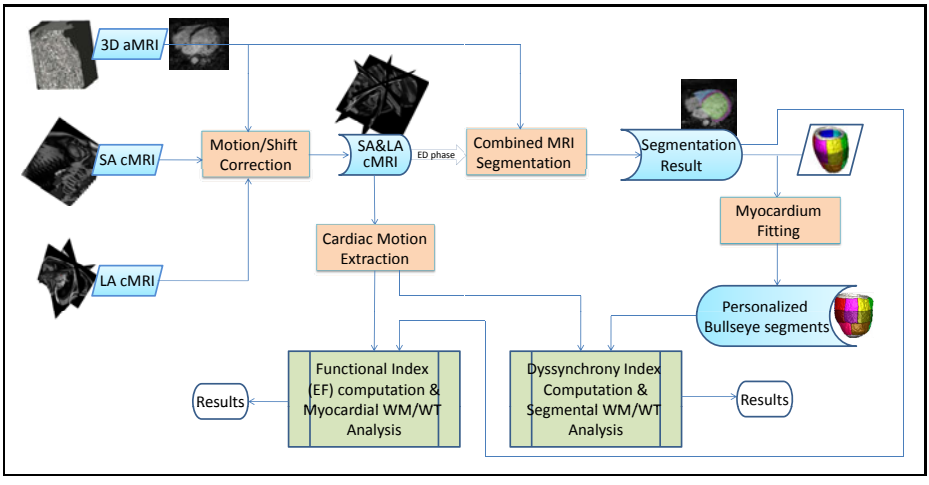

Fig. 1. Scheme of the proposed framework. aMRI: anatomical MRI; SA cMRI: multi-slice, short-axis cine MRI; LA cMRI: three-slice, long-axis cine MRI.

sequences, such as anatomical 3D MRI (3D aMRI) and different orientation cine MRI (cMRI), has potential to provide better accuracy and robustness for automated functional analysis.

In this work, we propose an integrated framework, shown in Fig. 1, to automatically segment the left ventricle and myocardium, and extract myocardial motions for quantitative analysis of cardiac global and regional functions [3]. This process includes three MRI sequences, the balanced Steady State Free Procession (b-SSFP), three dimensional, anatomical MRI (3D aMRI) [4], the multi-slice, short-axis (SA) cine MRI (SA cMRI), and the three-slice, long-axis (LA) cine MRI (LA cMRI). To combine the three sequences, we first transform the data into the same world coordinate system and correct the misalignments between inter- and intra- sequences [2]. Then, we develop a registration scheme which propagates the segmentation in a pre-constructed atlas to the subject-specific coordinate where three MR datasets are defined. To perform regional analysis, we build the personalized myocardial segments by fitting a 16-segment model (bullseye model) to the segmented myocardium [5]. This nonrigid fitting can maximally preserve the equal distribution of the myocardium segments. The cardiac motion within the ventricles are extracted using the combined information of the three LA slices and multiple SA slices. As a result, we can automatically compute the functional indices such as ejection fraction (EF) and perform myocardial wall motion and thickening analysis. Also, from the personalized bullseye model, we can analyze segmental volume, wall motion and thickening and compute the systolic dyssynchrony index (SDI) which is important in cardiac resynchronization therapy [5,6]. In the experiments, we employed twenty pathological data for evaluation. We computed the volumes of the left ventricle and myocardium, EF, SDIs using the proposed framework and the semi-automatic method available in clinical practice respectively, and compared their results.

The paper is organized as follows: Section 2 describes the methodological framework in detail; Section 3 presents the experiments and results; our conclusions are given in Section 4.

2 Method

2.1 Motion and Shift Correction

Images from different cardiac MRI sequences of a patient may be misaligned due to movements caused by body motions and respiration during acquisition. For cine MRI, which are used for myocardium motion tracking, this misalignment also happens between the slices, causing the slice shift problem [2], as Fig. 2 demonstrates. This shift problem exists in both the SA and LA slices which are generally taken from different breath holds.

In this framework, we register all available MRI sequences to the reference coordinate system defined by the 3D aMRI. The 3D aMIR provides good spatial resolution, $1 \times 1 \times 1$ to $2 \times 2 \times 2$ mm, for accurate slice-to-volume registration. Therefore, we extract the end-diastolic phase from both the SA cMRI and LA cMRI, which is the same phase as 3D aMRI, and register them to 3D aMRI. The resultant transformation of each slice in end-diastolic phase is then applied to the same slice in the other phases of the cMRI data. As a result, both the inter-sequence misalignment and intra-sequence slice shift are corrected and all images are transformed to the same spatial coordinate. Fig. 2 shows an example of the ED phase of a SA cMRI before and after correction.

2.2 Multiple Image Registration for Segmentation Propagation

For the automatic segmentation, we employ the image registration and atlas propagation-based method [8,9]. This method was mainly designed to extract the whole heart anatomy from 3D aMRI. However, 3D aMRI may not provide

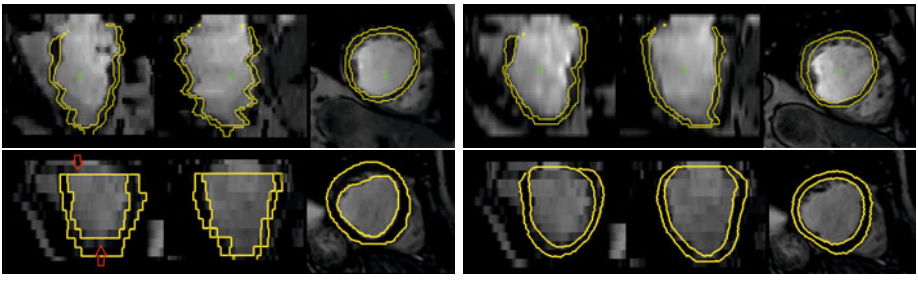

Fig. 2. Top row demonstrates multi-slice cine MRI before (left) and after (right) shift and motion correction. Both MR and segmentation images are interpolated into 1x1x1 mm using shape-based method [7]. Bottom row shows manual segmentation (left) and automated segmentation (right) without interpolation, red arrows point out the main difference by the two segmentation methods.

good contrast for myocardium, leading to less accurate delineation. By contrast, SA and LA cMRI provide much better image quality within slices, but the spatial resolution between slices is limited. Therefore, we extend the method and propose to combine all the three MRI sequences, including 3D aMRI, LA cMRI and SA cMRI, for the registration propagation. In this registration scheme, the target space has multiple aligned target images.

The cost function in this multiple image registration is given by:

$$\begin{aligned}\mathcal{C}([I_{3D}, I_{LA}, I_{SA}], I_{at}, T) = a_1\mathcal{S}(I_{3D}, T(I_{at})) + a_2\mathcal{S}(I_{LA}, T(I_{at})) + \\ a_3\mathcal{S}(I_{SA}, T(I_{at})) + b\mathcal{R}(T)\ ,\end{aligned} \tag{1}$$

where I_{at}, I_{3D}, I_{LA}, I_{SA} are the atlas image, 3D aMRI, LA cMRI and SA cMRI at end-diastolic phase, respectively; T, the transformation model, is a series of concatenated transformations including global affine, locally affine, and free-form deformtions (FFDs) with adaptive control point status [9]; $\mathcal{S}$ is similarity measure, the normalized mutual information (NMI) [10], normalized with the number of sample points N, such as $\mathcal{S} = \frac{1}{N}$NMI; $\mathcal{R}$ is the bending energy for regularization of the transformation; a_1, a_2, a_3 and b are weighting factors.

To perform regional analysis, we define the 16-segment (bullseye) model for the myocardium using the same definition in [5]. This is done by fitting a pre-constructed model to the automatically segmented left ventricle and myocardium, as the framework shows in Fig. 1.

2.3 Serial Registration for Cardiac Motion Tracking

We use serial propagation registration [11] to model the large deformation field required for registration of phases which are far away from the ED phase. In the serial propagation, we first register ED phase to its neighboring phase using a cost function as follows:

$$\begin{aligned}&\mathcal{C}([I_{LA}(ED), I_{SA}(ED)], [I_{LA}(i), I_{SA}(i)], T) = \\ &a_1\mathcal{S}(I_{LA}(ED), T(I_{LA}(i))) + a_2\mathcal{S}(I_{SA}(ED), T(I_{SA}(i))) + b\mathcal{R}(T)\ ,\end{aligned} \tag{2}$$

where ED and i indicate the cardiac phases. The resulting transformation is used to initialize the registration of the next phase. This process continues until all the phases are registered to the reference image. This registration is applied to the combined SA cMRI and LA cMRI data. The ventricular motions are then recorded in the deformation fields from each phase to the ED phase.

2.4 Cardiac Functional Analysis

Using the framework in Fig. 1, we can perform both the global and regional function analysis. We will demonstrate the analysis on volume computation, EF, SDI from regional blood pool volume [5], wall motion and thickening analysis. Global LV dyssynchrony is calculated from the difference of the time taken to reach maximum of regional volume (motion, thickness) for the 16 segments. A SDI is then defined as the standard deviation of these timings, with a high SDI indicating more dyssynchrony. To allow for comparisons between patients with

different heart rates, SDIs are normalized and expressed as percentages of the cardiac cycle. Also, a constraint is used for the computation of SDIs to exclude the segments of scared muscle. For SDIs computed from regional volume and motion analysis, we exclude the segments whose motion magnitudes are less than 10% of the maximum; and for that from wall thickening, we exclude the segments whose thickness changes are less than 1 mm. For regional analysis, graphs with curves indicating changes over the cardiac cycle can also be formed for each segment, allowing a visual investigation of segments during LV contraction.

3 Experiment

We employed pathological data from 20 patients who had severe heart failure fulfilling standard criteria for cardiac resynchronization therapy for this study. Each of these patients had an MRI scan using the three MRI sequences, 3D aMRI, LA cMRI and SA cMRI. We performed both the functional analysis using the fully automatic framework (shown in Fig. 1) and the semi-automatic method available in clinical practice. In the semi-automatic analysis, the segmentation were achieved manually slice by slice from the SA cMRI on the ED phase, and then propagated to other phases by the same registration scheme.

Fig. 3 presents the linear regression and Bland-Altman plots of the segmented volumes and EF by the two methods, and Fig. 4 provides those of the SDIs. The

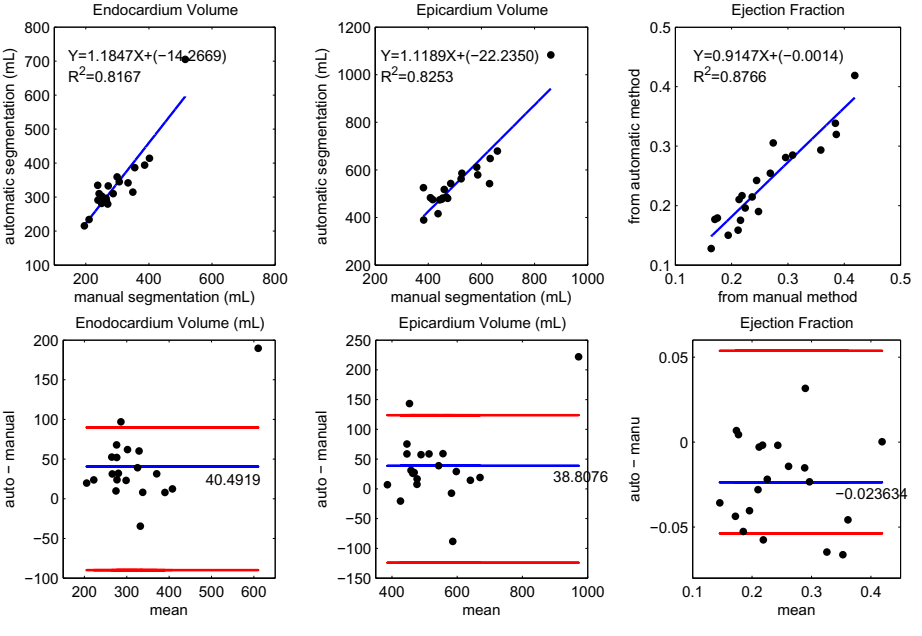

Fig. 3. Linear regression and Bland-Altman plots of the results from the automated segmentation and manual segmentation

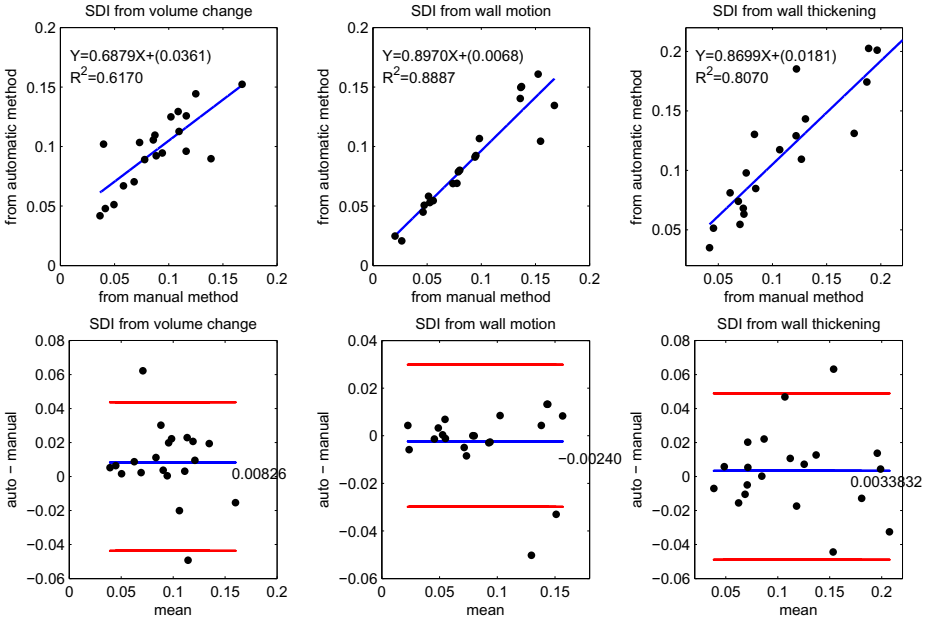

Fig. 4. Linear regression and Bland-Altman plots of SDIs by the fully automatic analysis and semi-automatic analysis

measurements from the automatic and manual segmentation resulted in high correlation, as the coefficients for the left ventricle endocardium volume (ENDO) and epicardium volume (EPI) were R^2=0.817 and R^2=0.825 respectively. Also, the mean Dice were as high as 0.883 ± 0.036 and 0.896 ± 0.031. However, the automatic segmentation consistently overestimated the volume with significant bias, 40.5mL for ENDO and 38.8mL for EPI, and both had $P<0.05$ from pair t-test. We found that this overestimation mainly came from the difference of the apical and basal segmentation, as Fig. 2 (bottom row) shows, the automated method could fully include these regions, thanks to the usage of 3D aMRI, while the manual segmentation, achieved from the SA cMRI, could mis-segment them.

The EF values by the two methods were highly correlated (R^2=0.877), though the volume overestimation resulted in a small but statistically significant bias (-0.024, $P<0.001$). From Fig. 4, we found that the two methods did not have high correlation ($R^2 = 0.617$) for SDIs computed from volume changes. This may be due to two bad cases as well as the difference from volume estimation, as the correlation coefficient increases to $R^2 = 0.847$ when the two cases are excluded. Fig. 4 also shows that the SDIs from wall motion and thickening analysis by the two methods resulted in much higher correlation ($R^2 = 0.889$ and $R^2 = 0.807$). For all the SDIs from volume change, wall motion and wall thickening, we found that the automatic method produced small biases compared with the results from the other method. However, none of these biases were statistically significant, as P=0.11, P=0.48 and P=0.54 respectively. Finally,

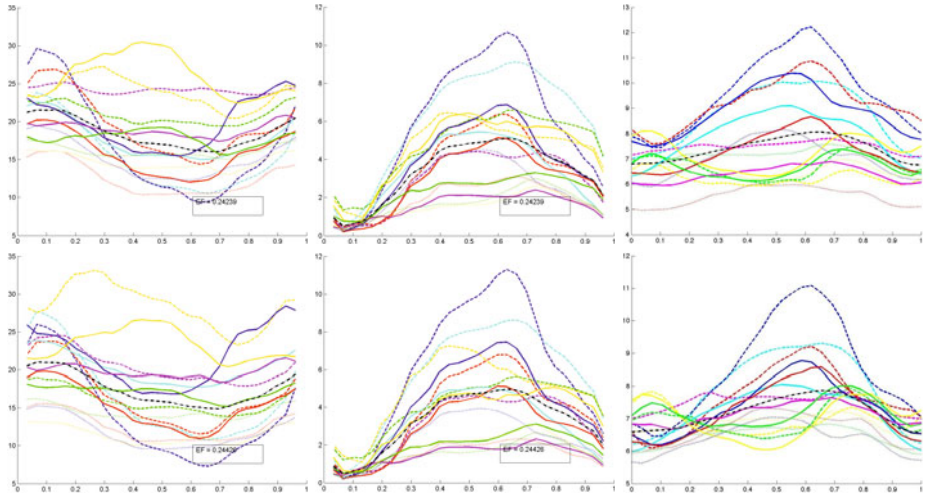

Fig. 5. An example of regional functional analysis using volume change (left), wall motion (middle) and wall thickening (right) from the fully automatic method (top row) and semi-automatic method (bottom row)

Fig. 5 demonstrates the regional functional analysis using volume change, wall motion and wall thickening and the results from a pathological case.

4 Conclusion

In this paper, we have proposed a fully automated framework for cardiac global and regional functional analysis. The registration used in the automated segmentation and motion tracking combines image information from multiple MRI sequences, which can provide accurate results for functional analysis. We employed 20 pathological datasets and compute the functional indices using both the proposed fully automatic method and the semi-automatic method available in current clinical practice. The results showed that the proposed method could fully segment the left ventricle, including the apical and basal regions, which is however generally difficult to manually delineate from SA cMRI. This segmentation difference resulted in a consistent overestimation of the volume by the automatic segmentation, and large variations to the SDI analysis from volume changes. However, the segmentation difference and volume overestimation only caused a small bias (-0.024) to the EF and SDIs from wall motion and wall thickening. These measurements from the proposed method also resulted in high correlation to these from the semi-automated method. Finally, we did not include the myocardial strain analysis, which is mainly available using speckle tracking from echocardiogram [6] or motion tracking from tagged MRI [11,12,13]. In the future work, we will extend the framework to include the tagged MRI for strain analysis.

References

1. Fact Sheet No. 317, World Health Organization: Cardiovascular diseases (February 2007)
2. Camara, O., Oubel, E., Piella, G., Balocco, S., De Craene, M., Frangi, A.: Multi-sequence Registration of Cine, Tagged and Delay-Enhancement MRI with Shift Correction and Steerable Pyramid-Based Detagging. In: Ayache, N., Delingette, H., Sermesant, M. (eds.) FIMH 2009. LNCS, vol. 5528, pp. 330–338. Springer, Heidelberg (2009)
3. Frangi, A.F., Niessen, W.J., Viergever, M.A.: Three-dimensional modeling for functional analysis of cardiac images: A review. IEEE Transactions on Medical Imaging 20, 2–5 (2001)
4. Uribe, S., Muthurangu, V., Boubertakh, R., Schaeffter, T., Razavi, R., Hill, D.L., Hansen, M.S.: Whole-heart cine MRI using real-time respiratory self-gating. Magnetic Resonance in Medicine 57(3), 606–613 (2007)
5. Nesser, H.J., Sugeng, L., Corsi, C., Weinert, L., Niel, J., Ebner, C., Steringer-Mascherbauer, R., Schmidt, F., Schummers, G., Lang, R.M., Mor-Avi, V.: Volumetric analysis of regional left ventricular function with real-time three-dimensional echocardiography: validation by magnetic resonance and clinical utility testing. Heart, 572–578 (2007)
6. Li, C., Carreras, F., Leta, R., Carballeira, L., Pujadas, S., Pons-Llado, G.: Mechanical left ventricular dyssynchrony detection by endocardium displacement analysis with 3d speckle tracking technology. The International Journal of Cardiovascular Imaging 26, 867–870 (2010)
7. Grevera, G.J., Udupa, J.K.: Shape-based interpolation of multidimensional grey-level images. IEEE Trans. Medical Imaging 15(6), 881–892 (1996)
8. Zhuang, X., Rhode, K., Arridge, S., Razavi, R., Hill, D., Hawkes, D., Ourselin, S.: An atlas-based segmentation propagation framework using locally affine registration – application to automatic whole heart segmentation. In: Metaxas, D., Axel, L., Fichtinger, G., Székely, G. (eds.) MICCAI 2008, Part II. LNCS, vol. 5242, pp. 425–433. Springer, Heidelberg (2008)
9. Zhuang, X., Rhode, K., Razavi, R., Hawkes, D.J., Ourselin, S.: A registration-based propagation framework for automatic whole heart segmentation of cardiac MRI. IEEE Transactions on Medical Imaging 29(9), 1612–1625 (2010)
10. Studholme, C., Hill, D.L.G., Hawkes, D.J.: An overlap invariant entropy measure of 3D medical image alignment. Pattern Recognition 32(1), 71–86 (1999)
11. Chandrashekara, R., Mohiaddin, R., Rueckert, D.: Analysis of 3-D myocardial motion in tagged MR images using nonrigid image registration. IEEE Transactions on Medical Imaging 23(10), 1245–1250 (2004)
12. Chen, T., Wang, X., Chung, S., Metaxas, D.N., Axel, L.: Automated 3d motion tracking using gabor filter bank, robust point matching, and deformable models. IEEE Trans. Med. Imaging 29(1), 1–11 (2010)
13. Zhang, S., Wang, X., Metaxas, D.N., Chen, T., Axel, L.: LV surface reconstruction from sparse TMRI using laplacian surface deformation and optimization. In: ISBI, pp. 698–701 (2009)

Multiview Diffeomorphic Registration for Motion and Strain Estimation from 3D Ultrasound Sequences

G. Piella[1,2], M. De Craene[1,2], C. Yao[3], G.P. Penney[3], and A.F. Frangi[1,2,4]

[1] CISTIB, Universitat Pompeu Fabra, Barcelona, Spain
[2] CIBER-BBN, Spain
[3] Division of Imaging Sciences, King's College London, UK
[4] Catalan Institution for Research and Advanced Studies (ICREA), Spain

Abstract. This paper presents a new registration framework for estimating myocardial motion and strain from multiple views of 3D ultrasound sequences. The originality of our approach resides in the estimation of the transformation directly from the multiple views rather than from a single view or a reconstructed compounded sequence. This allows us to exploit all spatio-temporal information available in the input views avoiding occlusions and image fusion errors that could lead to some inconsistencies in the motion quantification result. In addition, by using the original input images, speckle information (which is an important feature for motion estimation and could be blurred out in the fusion process) should remain consistent between temporal image frames.

We propose a multiview diffeomorphic registration strategy that enforces smoothness and consistency in the spatio-temporal domain by modeling a continuous 3D+t velocity field as a sum of B-spline kernels. This 3D+t continuous representation allows us to robustly cope with variations in heart rate resulting in different number of images acquired per cardiac cycle for different views. The similarity measure is obtained by extension of a pairwise mean square error metric where a weighting scheme balances the contribution of the different views.

We have carried out experiments on synthetic 3D ultrasound images with known ground truth and on in-vivo multiview 3D data sets of two volunteers. It is shown that the inclusion of several views improves the consistency of the strain curves and reduces the number of segments where a non-physiological strain pattern is observed.

1 Introduction

Recent advances in the design of 3D ultrasound (US) probes lead to an improved temporal resolution of this modality and the possibility of extending currently 2D motion and deformation analysis to 3D. However, one of the drawbacks of the US modality is the limited field of view and the non-uniform image quality compared to other imaging modalities. A common approach to address these problems is the combination of multiple US images obtained from different angles of incidence into a single compounded image [1–4].

D.N. Metaxas and L. Axel (Eds.): FIMH 2011, LNCS 6666, pp. 375–383, 2011.

Notably, most of these methods are targeted towards enhancing visualization. However, the requirements for visual inspection by a clinician may be very different from the requirements for post-processing algorithms such as segmentation or motion estimation. Few publications exist on image fusion for motion [5] and deformation analysis. Most often, the proposed methods fuse a single image data source with other type of information (e.g. a priori knowledge) and perform fusion at higher level of abstraction (as opposed to pixel or feature level) [6].

In this paper, we propose to generalize 3D+t US fusion strategies to recover a more accurate *in vivo* quantification of the 3D deformation over time. A major feature of our approach is that we compute the deformation through a multiview registration and hence directly from the input views, using all available spatio-temporal information. Another key characteristic is the use of a diffeomorphic transformation model where the velocity, rather than the displacement, is represented as a continuous and differentiable 3D+t vector field using B-splines. This allows, on the one hand, to capture the spatio-temporal variability of the underlying scene while maintaining consistency (i.e., preservation of spatial and temporal topology), and on the other hand, to account for irregular temporal sampling. In this way, our approach does not require the inputs to have the same number of phases or to be scanned at the same position within the cardiac cycle. This differs from current approaches [1–5] where it is assumed that the different inputs are acquired at the same temporal position.

We have applied the proposed methodology to synthetic 3D US images with known ground truth and to in-vivo multiview 3D data sets of two volunteers. Strain curves obtained from our multiview approach are compared to the single view case. The advantages of an improved temporal resolution are demonstrated on a synthetic case.

2 Methods

The purpose of our multiview registration is to estimate from the multiple views the trajectory of any point in the real scene. In our setting, this amounts to finding the spatio-temporal transformation that relates any point in the common reference system at initial time to any subsequent *continuous* time in the cardiac cycle. In the sequel, we refer to the common reference system as to the *fusion space*, and take the initial time to be $t = 0$. The motion in each view sequence is related to the motion in the real scene: homologous points and trajectories in the different inputs should map to the same points and trajectories in the fusion space. We formulate the multiview registration as the optimization of a similarity metric matching intensities of the input views warped back from the fusion space. The matching is weighted across the views to account for different image quality across the field of view of each input sequence.

Notation. By convention, superscript indexes will refer to the different views whereas subscript indexes will refer to time. We consider L single-view input sequences, each one representing a different 3D+t view of the same dynamic cardiac scene. Each input sequence is composed of N^l images, $I_0^l, \ldots, I_{N^l-1}^l$, $l = 1, \ldots, L$,

every image being defined on a spatial domain $\Omega^l \subset \mathbb{R}^3$ and associated to a time instant $t_n^l \in [0,1]$. Different sequences may have different number of images N^l and may not be aligned in time, thus t_n^l and $t_n^{l'}$ for $l \neq l'$ may not correspond to the same position within the cardiac cycle. Spatial coordinates in the fusion space are denoted by $\boldsymbol{x} \in \Omega$ and spatial coordinates in the space of each view by $\boldsymbol{x}^l \in \Omega^l$. Consistent with these notations, the intensity function of each view l at time t_n^l will be denoted as $I_n^l(\boldsymbol{x}^l)$. The transformation in the fusion space is defined as $\boldsymbol{\varphi}(\boldsymbol{x}, t)$ and maps a point $\boldsymbol{x}$ in the fusion space at $t = 0$ to any time $t \in [0,1]$. Similarly, $\boldsymbol{\varphi}^l(\boldsymbol{x}^l, n)$ denotes the transport of a point $\boldsymbol{x}^l$ at time $t_0^l = 0$ to time $t_n^l \in [0,1]$. We also use the short-hand notation $\boldsymbol{\varphi}_{t\to t'}$ (and $\boldsymbol{\varphi}^l_{n\to n'}$) to denote the transport of a point at time t (resp. t_n) to time t' (resp. $t_{n'}$).

Calibration and ECG synchronization. We use the ECG-based synchronization scheme in [7] to represent the input sequences in a common reference time scale. The calibration transformations C^l that relate the fusion space with each input view space are obtained using a combination of probe tracking [3] and group wise registration [2] with phase-based similarity measure [1]. Since the US probe can be considered stationary over the entire acquisition of each input sequence, C^l is assumed to be constant over the cardiac cycle.

Transformation model. We use a temporal diffeomorphic transformation model where the velocity field is represented as a continuous and differentiable 3D+t vector field using B-splines [8]. The diffeomorphic mapping $\boldsymbol{\varphi} : \Omega \times [0,1] \to \mathbb{R}^3$ is related to the time-varying velocity field $\boldsymbol{v} : \Omega \times [0,1] \to \mathbb{R}^3$ by

$$\boldsymbol{\varphi}(\boldsymbol{x}, t) = \boldsymbol{x} + \int_0^t \boldsymbol{v}(\boldsymbol{\varphi}(\boldsymbol{x}, \tau), \tau) \mathrm{d}\tau \,. \tag{1}$$

To numerically compute $\boldsymbol{\varphi}$ in (1), the continuous time interval is sampled at intermediary time points t_k and the integral is replaced by a summation:

$$\boldsymbol{\varphi}(\boldsymbol{x}, t_n) = \boldsymbol{x} + \sum_{k=0}^{n-1} \boldsymbol{v}\left(\boldsymbol{\varphi}(\boldsymbol{x}, t_k), t_k\right) \Delta t_k \,, \tag{2}$$

where $\Delta t_k = t_{k+1} - t_k$. In our model, the transformation parameters are the control point values in the B-spline representation of the velocity field.

Transporting motion vectors from the input views to the fusion space. Consider a point $\boldsymbol{x}^l$ in the space of view l whose motion vector is described by $\boldsymbol{\varphi}^l_{0\to n}(\boldsymbol{x}^l)$. This motion vector can also be tracked in the fusion space by first warping the point $\boldsymbol{x}^l$ to the fusion space (by the inverse of C^l), then transporting it to t_n (by $\boldsymbol{\varphi}_{0\to t_n}$), and finally bringing this transformed point back to the space of view l (by C^l). This is illustrated in Fig. 1. Thus, each transformation $\boldsymbol{\varphi}^l_{0\to n}$ is related to the transformation in the fusion space $\boldsymbol{\varphi}_{0\to t_n}$ through:

$$\boldsymbol{\varphi}^l_{0\to n} = C^l \circ \boldsymbol{\varphi}_{0\to t_n} \circ (C^l)^{-1} \tag{3}$$

where C^l is the calibration transformation obtained as previously described and $\boldsymbol{\varphi}_{0\to t_n}$ is the transformation in the fusion space modeled as in (2).

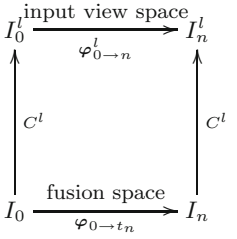

Fig. 1. Link between transformations in each input view space and the transformations in the fusion space. Note that $\varphi_{0\to n}^l \circ C^l = C^l \circ \varphi_{0\to t_n}$.

Similarity metric. The transformation $\boldsymbol{\varphi}$ is obtained through the optimization of a similarity metric matching intensities of the input views warped back from the fusion space. Specific similarity metrics need to be designed for capturing the global similarity of the entire sequence across all the views. For simplicity, we use a weighted-based mean square error (MSE) and, for all views, we compare each image in the sequence to the first one. The intensity levels are only compared within views, avoiding potential problems with intensity normalisation while allowing to track the speckle. For each view l and location $\boldsymbol{x}$ in the fusion space at $t = 0$, we assign a value $w^l(\boldsymbol{x})$ which weighs the contribution of the view to the metric. If we take J samples at time $t = 0$ in the fusion space (and using the relationships shown in Fig. 1), the weighted-based MSE similarity measure is computed as

$$MSE = \sum_{j=1}^{J} \sum_{l=1}^{L} \sum_{n=1}^{N^l-1} w^l(\boldsymbol{x}_j) \Big(I_0^l\big(C^l(\boldsymbol{x}_j)\big) - I_n^l\big(C^l \circ \boldsymbol{\varphi}_{0\to t_n}(\boldsymbol{x}_j)\big)\Big)^2 . \quad (4)$$

In this paper, we use very simple weighting schemes (i.e., equal weights and maximum selection rule) to balance the contributions of the different views to the image similarity metric.

Myocardial strain estimation. The strain is estimated from the spatial derivative of the resulting spatio-temporal transformation $\boldsymbol{\varphi}$. If $\boldsymbol{D}(\boldsymbol{x}, t)$ is the Jacobian of $\boldsymbol{\varphi}(\boldsymbol{x}, t)$, the strain tensor is obtained by

$$\boldsymbol{\sigma}(\boldsymbol{x}, t) = \frac{1}{2}(\boldsymbol{D}(\boldsymbol{x}, t)^T \boldsymbol{D}(\boldsymbol{x}, t) - \boldsymbol{I}) , \quad (5)$$

where superindex 'T' denotes transposition and $\boldsymbol{I}$ is the identity matrix. The strain tensor can further be projected onto a local cardiac coordinate system to compute the deformation in the radial, circumferential and longitudinal directions. These directions are defined on a mesh obtained from segmenting the left ventricle (LV) at $t = 0$ in the fusion space. The strain data was averaged into 17 regions in accordance with the standard segmentation proposed by the American Heart Association (AHA).

3 Experiments

The proposed multiview registration algorithm was applied to synthetic 3D US images with known ground truth to evaluate its accuracy and was then applied to in-vivo multiview 3D data sets of two volunteers.

3.1 Strain Accuracy on Simulated US Data

We used the simulated data set presented in [9], where the LV deformation is modeled by a simplified kinematic model based on a thick-walled ellipsoid with physiologically relevant end-diastolic dimensions. This model was used to generate ground truth values for both the motion (displacement) and the deformation (strain). The simulated images consisted of $282 \times 282 \times 282 \times 20$ isotropic voxels with a voxel size of 0.35 mm.

We evaluated the ability of our algorithm to deal with missing information (either in the spatial or temporal dimension) occurring in some of the input views. For that purpose, the ground truth deformation of the simulated full LV was compared with the deformations found after the multiview registration of: (*i*) two spatially half-occluded sequences, and (*ii*) two half-time resolution sequences. For these experiments, the maximum selection rule was chosen as a weighting scheme (i.e., for each voxel, only the view with maximum intensity contributes to the metric).

The two spatially half-occluded sequences were generated from the full view sequence by complementary spatially masking half the volumes for each frame. Fig. 2 shows long axis slices of the end-diastolic frames of these data sets. The two half-time resolution sequences were generated from the full view sequence by taking the even and odd frames respectively. The 3D strain quantification as measured by the multiview approach and compared to the ground truth deformation is shown at Fig. 3. For comparison purposes, we also included the strain obtained when applying our algorithm to the full view (see Fig. 3(b)). Vertical bars indicate the dispersion on the whole myocardium (as measured by the interquartile range). One can see that the global strain patterns in Fig. 3(b)-(d) highly resemble the ground truth in Fig. 3(a), albeit with increased dispersion.

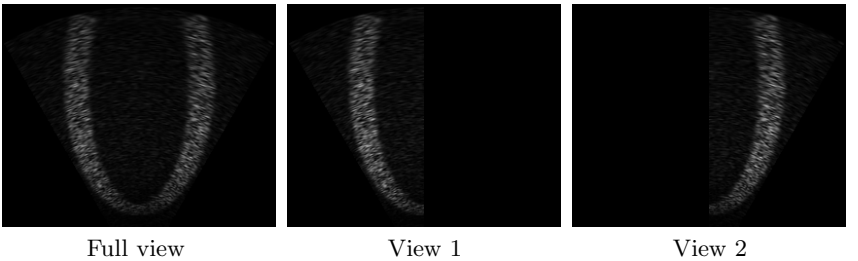

Full view View 1 View 2

Fig. 2. Long-axis slices of the synthetic data sets

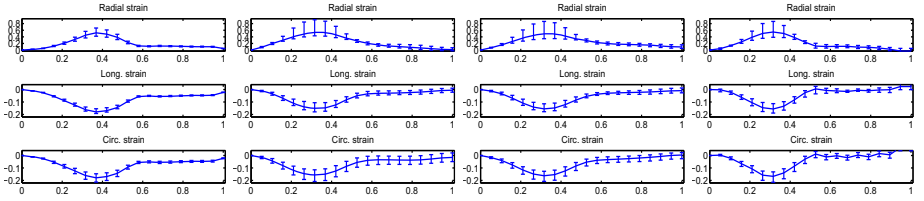

Fig. 3. Median strain computed from (a) ground truth displacements and from our algorithm using: (b) one single full view, (c) two spatially half-occluded views, (d) two half-time resolution views. Vertical bars indicate the regional dispersion of the myocardium strain values as measured by the interquartile range.

3.2 Strain Quantification in Healthy Volunteers

3D+t echocardiographic sequences with 2 or 3 views were acquired from 2 healthy volunteers using a Philips iE33 US system with a 3D X3-1 matrix array transducer. The data set for volunteer #1 was composed of 2 apical views with 18 and 20 images per cardiac cycle, while the data set for volunteer #2 consisted of two apical views plus one parasternal view, all of them with 12 images per cardiac cycle. Variations in the heart rate were up to 11% and 5%, respectively. The pixel size was on average of $0.8 \times 0.8 \times 0.7\, mm^3$. For these experiments,

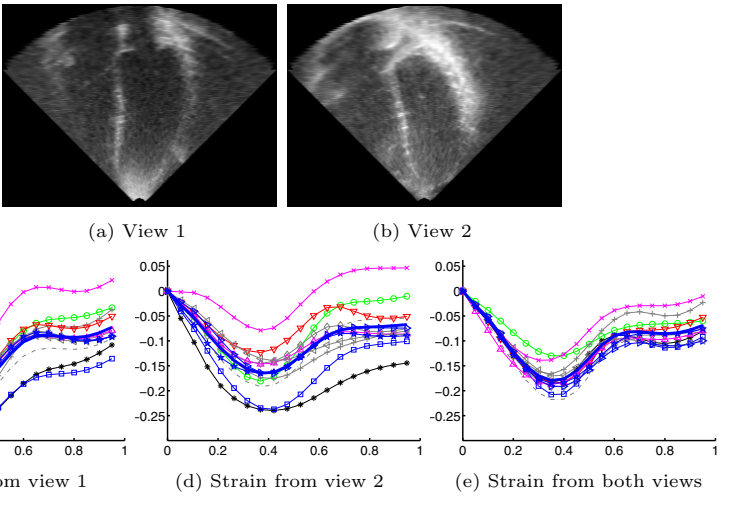

Fig. 4. Longitudinal strain quantified for volunteer #1 in basal and mid-level segments. The AHA segments are labelled according to the following: · Basal anterior (1), ∘ Basal anteroseptal (2), × Basal inferoseptal (3), + Basal inferior (4), ∗ Basal inferolateral (5), □ Basal anterolateral (6), ◇ Mid anterior (7), ▽ Mid anteroseptal (8), △ Mid inferoseptal (9), ◁ Mid inferior (10), ▷ Mid inferolateral (11), ⋆ Mid anterolateral (12). Thick blue curve corresponds to the mean strain.

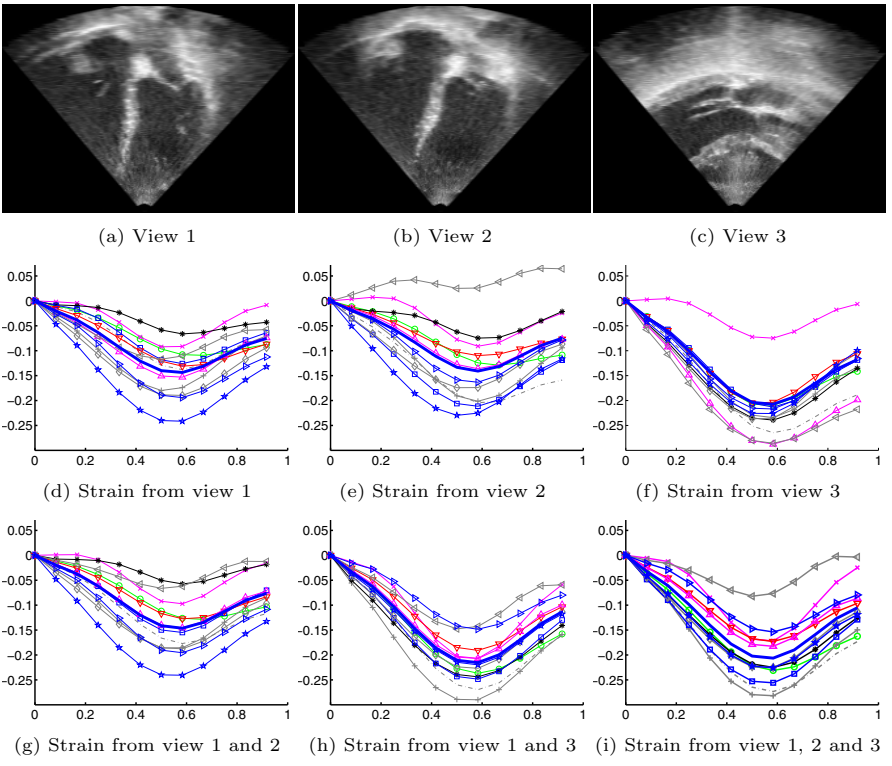

Fig. 5. Longitudinal strain quantified for volunteer #2 in basal and mid-level segments. The AHA segments are labelled as in Fig. 4.

an equal weighting scheme was used in the similarity metric (i.e., for all voxels, all views are assigned the same weight, hence contributing equally to the registration). Fig. 4 shows the recovered longitudinal strain curves from the two apical views from volunteer #1. One can observe that the recovered longitudinal strain obtained from using both views (Fig. 4(e)) has less dispersion than the strain obtained by just using any of the single views (Fig. 4(c)-(d)). A smaller variability in strain values across the AHA regions can be regarded as an improvement in the strain accuracy since regional variations in strain are small in normal myocardium.

Fig. 5 shows the recovered longitudinal strain curves from the three views from volunteer #2. Middle row shows the strain curves when using only a single view, while the bottom row shows the strains obtained when combining more than one view. In this case, it is more difficult to discern the improvements. Computing the strain from both views in Fig. 5(a) and (b), as depicted in Fig. 5(g), seems advantageous with respect to using only the view in Fig. 5(b). For example, the non-physiological strain pattern corresponding to the mid-inferior region in Fig. 5(e) is somewhat corrected when using both apical views. Similarly, computing the strain from both Fig. 5(a) and (c), as shown in Fig. 5(h),

results in less abnormal basal inferoseptal and inferolateral strain curves when compared to the corresponding curves in Fig. 5(d) (obtained from using only the view in Fig. 5(a)). Finally, the strain obtained from using the three views (see Fig. 5(i)), when compared to the single view ones (Fig. 5(d)-(f)), results also in less abnormal strain patterns.

4 Conclusions and Future Work

We have presented a multiview registration algorithm for motion and strain estimation from multiple US images obtained from different angles of incidence. A major feature is the use of a temporal diffeomorphic transformation model that enforces consistency in the spatio-temporal domain and handles irregular temporal sampling across views. In this way, our approach is robust to differences in acquisition parameters (e.g., initial offset in the acquisition) and variations in heart rate). Additionally, the use of a weighted-based similarity measure accounts for different contributions of the input views.

Future work will be focused on extending the weighting scheme for determining the voxel-wise contribution of the different views in the metric and the application of the algorithm to pathologies with dilated hearts.

Acknowledgements. This research has been partially funded by the Industrial and Technological Development Center (CDTI) under the CENIT-cvREMOD program, by the European Commission's project euHeart (FP7-ICT-224495), by the Spanish Ministry of Science and Innovation (MICINN) and the European Regional Development Fund (ERDF) through the research project STIMATH (TIN2009-14536-C02-01), Plan E and FEDER.

The authors would like to thank to A. Gomez for providing the ECG data and to J. D'Hooge for providing the synthetic data set.

References

1. Grau, V., Becher, H., Noble, J.A.: Registration of multiview real-time 3-D echocardiographic sequences. IEEE Trans. Med. Imag. 26(9), 1154–1165 (2007)
2. Wachinger, C., Wein, W., Navab, N.: Registration strategies and similarity measures for 3D ultrasound mosaicing. Acad. Radiol. 15(11), 1404–1415 (2008)
3. Yao, C., Simpson, J.M., Jansen, C.H.P., King, A.P., Penney, G.P.: Spatial compounding of large sets of 3D echocardiography images. In: Proc. of SPIE (2009)
4. Rajpoot, K., Noble, J.A., Grau, V., Szmigielski, C., Becher, H.: Multiview RT3D echocardiography image fusion. In: Ayache, N., Delingette, H., Sermesant, M. (eds.) FIMH 2009. LNCS, vol. 5528, pp. 134–143. Springer, Heidelberg (2009)
5. Grau, V., Szmigielski, C., Becher, H., Noble, J.A.: Combining apical and parasternal views to improve motion estimation in real-time 3D echocardiographic sequences. In: Proc. of ISBI, pp. 516–519 (2008)
6. Shi, P., Sinusas, A.J., Constable, R.T., Duncan, J.S.: Volumetric deformation analysis using mechanics-based data fusion. Int. J. Comput. Vis. 35(1), 87–107 (1999)

7. Duchateau, N., De Craene, M., Silva, E., Sitges, M., Bijnens, B.H., Frangi, A.F.: Septal flash assessment on CRT candidates based on statistical atlases of motion. In: Yang, G.-Z., Hawkes, D., Rueckert, D., Noble, A., Taylor, C. (eds.) MICCAI 2009. LNCS, vol. 5762, pp. 759–766. Springer, Heidelberg (2009)
8. De Craene, M., Piella, G., Duchateau, N., Silva, E., Doltra, A., Gao, H., et al.: Temporal diffeomorphic free-form deformation for strain quantification in 3D-US images. In: Jiang, T., Navab, N., Pluim, J.P.W., Viergever, M.A. (eds.) MICCAI 2010. LNCS, vol. 6362, pp. 1–8. Springer, Heidelberg (2010)
9. Elen, A., Choi, H., Loeckx, D., Gao, H., Claus, P., Suetens, P., et al.: Three-dimensional cardiac strain estimation using spatio-temporal elastic registration of US images: a feasibility study. IEEE Trans. Med. Imag. 27(11), 1580–1591 (2008)

Pyramid Histograms of Motion Context with Application to Angiogram Video Classification

Fei Wang[1], Yong Zhang[1], David Beymer[1],
Hayit Greenspan[1,2], and Tanveer Syeda-Mahmood[1]

[1] IBM Almaden Research Center, San Jose, CA, USA
[2] Biomedical Engineering Dept, Tel-Aviv University, Israel

Abstract. Due to poor image quality as well as the difficulty of modeling the non-rigid heart motion, motion information has rarely been used in the past for angiogram analysis. In this paper we propose a new motion feature for the purpose of classifying angiogram videos according to their viewpoints. Specifically, local motion content of the video around the anatomical structures cardiac vessels is represented using the so-called "motion context", a motion histogram representation in polar coordinates within a local patch. The global motion layout is captured as pyramid histograms of the motion context (PHMC) in a manner similar to that proposed by the Spatial Pyramid Kernel [1]. The PHMC is a robust representation of the motion features in a video sequence. Through experiments on a large database of angiograms obtained from both diseased and control subjects, we show that our technique consistently outperforms state-of-the-art methods in the angiogram classification test.

1 Introduction

Coronary angiography is a procedure that uses a special dye (contrast material) and X-rays to examine the blood vessels or chambers of the heart. It is an important diagnostic aid in cardiology for the functional assessment of the cardiovascular diseases. A typical angiography study consists of several (20-25) runs, each depicting a different vessel seen from a chosen viewpoint, those runs consisting of 15-120 images depending on the complexity of the arteries being shown and their pathology. Cardiologists review a study for detection of stenosis (constricting of the artery). This process, done manually, requires the examination of the two main vessels, the Left Coronary artery (LCA) and the Right coronary artery (RCA), as well as their branches, at a set of viewpoints.

There is a large body of work on the analysis of coronary arteries. Much of the work focuses on accurate vessel delineation, extracting vessel boundaries and vessel centerlines in 2D and 3D (e.g., [2], [3]). Methods for interpretation of angiograms including filter based methods (derivative-based filter [4], matching filter [5], etc.), deformable models, learning-based approaches (Neural Network [6], Support Vector Machine [6]). The predominant way of capturing shape layout of arteries has been through a graph formalism using built-in knowledge of coronary artery tree [7]. All methods assume that a given image actually depicts

D.N. Metaxas and L. Axel (Eds.): FIMH 2011, LNCS 6666, pp. 384–391, 2011.

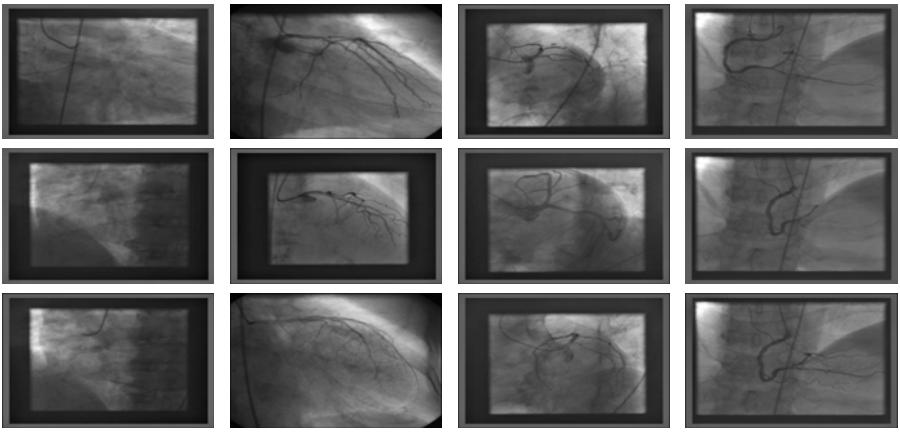

Fig. 1. Illustration of the image classes that can be classified by our method. First column: background view (BGV); column 2 , 3 depict two different appearances of left coronary artery under changed viewpoints, second column: LCA Anterior Oblique Projection (LCA-v1), third column: LCA Left Anterior Oblique Projection (LCA-v2); Last column depicts the right coronary artery (RCAV) and its changing appearance within a run.

a vessel structure (i.e. not a background image). Current methods mostly rely on user interaction, often selecting a segment of interest and focusing on accurately segmenting and labeling subsegments within it. Interactive commercial tools are starting to emerge to support the accurate segmentation of the vessel, and when given a segment of interest, even computing the stenosis [8].

Unlike previous work on labeling of coronary arteries or their extraction, our work focuses on the problem of classifying an unknown frame of an angiography sequence. As a side effect, it can also reveal the identity of the artery being depicted in an image in case the given image is not a background image. Our work also addresses a problem that arises in real clinical catheter-lab settings, starting from the raw data which is in video form, and detecting information related to the vessels and their viewpoints. This task involves handling of very noisy settings, with much spatial translation as well as pathological cases, and has not been handled, to the best of our knowledge.

Vessel motion can be used to identify different viewpoints of an angiogram video. However, motion information has been so far largely neglected, due to poor image quality and the difficulty of modeling the non-rigid heart motion. The variation in appearance of the vessels, due to changes in viewpoint and motion of the arteries can be considerably large. This can be seen in Figure 1 which shows left and right coronary arteries under different viewpoints (rows 2,3,4) as well as undergoing motion within a viewpoint (within a row). This figure illustrates the difficulty of separating such arteries from outliers such as background images. Reliable recognition of content, therefore, requires robust modeling of both structural motion information and geometric layout that cause the changes in artery appearance under various conditions.

In this paper we propose a new motion feature for the purpose of classifying angiogram videos. Specifically, the local motion content of the video around the anatomical structures (cardiac vessels) is represented using the so-called "motion context", a motion histogram representation in polar coordinates within a local patch. The global motion layout is captured as pyramid histograms of the motion context (PHMC) in a manner similar to that proposed by the Spatial Pyramid Kernel [1]. The PHMC is a robust representation of the motion features in a video sequence. Experimental results are presented that show a high degree of accuracy in artery classification using our approach even under variation in appearance due to viewpoint, coronary anatomy differences, disease-specific variations and changes in imaging conditions.

The rest of the paper describes our method in detail. In Section 2, we describe the pre-processing of angiography sequences to select the key frames within the sequences and detect regions of interest in frames. In Section 3, we develop a new motion descriptor around the key vessel structures and present our classification framework. Finally, in Section 4, we describe our experiments on the classification of images from a large dataset of angiography images.

2 Pre-processing of the Angiogram Sequence

Angiography sequence undergo some basic preprocessing before we begin the process of feature point localization and encoding. This includes selection of the key frames and detection of the region of interest (ROI) which contains the actual image.

Key Frame Selection: Since the frames of interest for a diagnosis are ones that show a clear depiction of the vessel, and only a handful of the thousands of images in an angiography are such images, it is important to filter the irrelevant images by a pre-processing step to increase the robustness of recognition. For this, we adopt the approach described in [9] to extract most relevant and informative keyframes from the angiography sequence.

Region of Interest Detection: Angiograms typically have a rectangular region of interest (ROI) that contains the X-ray signal and is surrounded by one or two uniform grey regions (Figure 1). Identifying the bounding boxes (x_0, y_0, x_1, y_1) associated with the ROI will avoid potential confusion caused by false edges generated on the ROI boundary. What distinguishes X-ray foreground pixels from uniform background pixels is pixel variance, measured both spatially and temporally. Spatially, pixel variance will be high in the ROI foreground region due to image structure and noise, and temporal variance will be caused by motion (nonrigid heart + rigid table motion). As shown in Figure 2, we first compute the spatial and temporal pixel variances, and then find the major peaks in the gradient of the product of spatial and temporal pixel variances. The bounding box is determined based on locating either 2 or 4 major peaks (corresponding to 1 or 2 background regions, respectively).

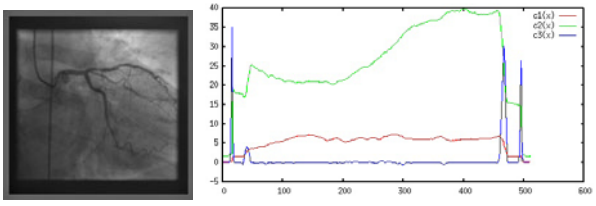

Fig. 2. (left) Example angiogram image showing rectangular ROI plus 2 background regions. (right) Temporal variance $c_1(x)$, spatial variance $c_2(x)$, and product of $x-$ derivatives $c_3(x)$. There are 4 peaks in $c_3(x)$ because there are 2 background regions.

Once the rectangular sector has been extracted, using the top left and lower right extreme points, we can perform a rough alignment of all the angiogram videos with each other via an affine transform.

3 Representing Shape and Motion in Angiography Frames

In a given angiogram video of a heart cycle, different cardiac vessels depicted in different angiogram sequences differs not only in terms of their overall shape and topology, but also demonstrate different amount of motion (in magnitudes as well as directions). Furthermore, those motions are disparate for different vessels while similar for image sequences belonging to the same vessel.

To characterize the vessel shape, we use the centerlines of the vessels which is known as a good representation of the shape of the coronary artery trees. Once the centerlines are extracted, we turn to the characterization of shape and motion information within the neighborhood of the centerlines in images. The rationale here is that by focusing on relevant image features, namely, centerlines, and sampling their local geometry and motion, we capture the essence of the 'relevant content' depicted in these images. To capture the motion information, we analyzed the optical flow for angiogram video sequences computed using the Demons algorithm [10].

3.1 Motion Feature Representation

There are two important things to note regarding the optical flow obtained for the angiogram image sequences: 1) the deformation field contains a considerable amount of noise (even after smoothing) as a consequence of the noise present in the intensity images; 2) the two components of the motion field - magnitude and phase, entail interesting information that can infer the category of the video sequence.

Motion in angiogram images is meaningful only when it is associated with anatomical structures. We propose to use the vessel centerline information to guide the feature localization process. To achieve this we filter the motion magnitude images using the vessel centerlines shapes. Thus, only motion which corresponds to anatomical structures is retained while the remaining extraneous

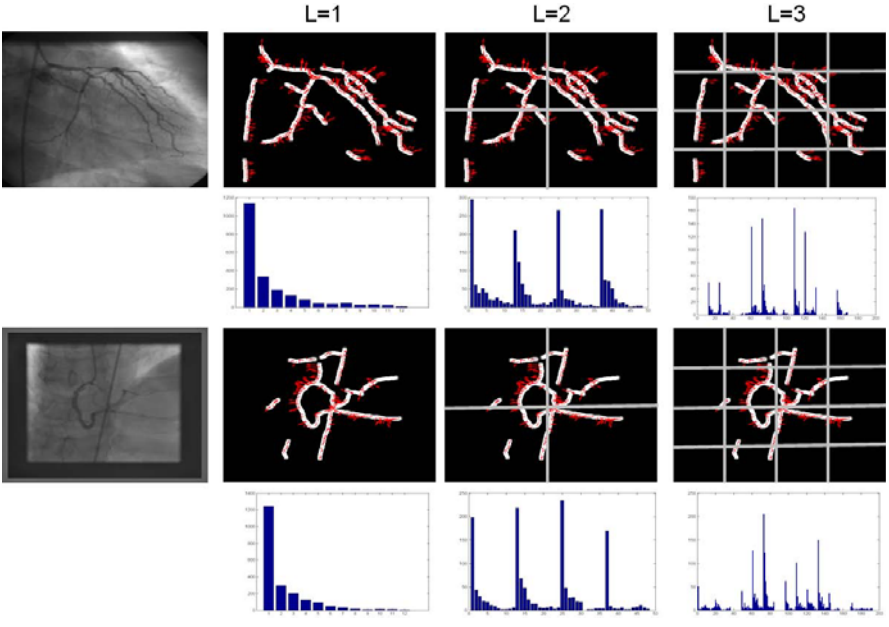

Fig. 3. Illustration of Pyramid Histograms of Motion Context (PHMC). First and third row an LCA and RCA frame and grids for level $l = 1$ to $l = 3$; Second and fourth row: histogram representation corresponding to each level. The final PHMC vector is a weighted concatenation of histograms for all levels.

motion is disregarded. Given these centerline-filtered motion maps, the next step is to encode them using information which will be useful in discrimination.

3.2 Capturing Local Motion with "motion context"

To capture the local motion around centerlines, we define "motion-context", similar to the shape context first described by Belongie et al. [11], as a local motion histogram in a radius-angle polar grid. The motion feature is thus represented as a distribution over relative positions. This representation is robust, compact, and highly discriminative, thus making it a good fit for our angiogram view recognition problem.

Suppose there are m_r (radial axis represent motion magnitude) by m_θ (angular axis as the motion phase) bins and the local motion patch M is divided into $M_1, ..., M_b$ by $b = m_r \times m_\theta$ according to their magnitude as well as phase, for a point at p on the centerline (Figure 3), its motion context (MC) is defined as $u = \{h_1, ..., h_b\}$, where $h_i(k) = \#\{q \neq M_i : (q - M_i) \in \text{bin}(k)\}$ To keep the motion description local, we empirically select a radius of 15.

Pyramid Histograms of Motion Context (PHMC): Using the local motion context descriptor, we capture the global vessel motion as a pyramid of Histograms of Motion Context (PHMC) in a manner similar to that proposed

by the Spatial Pyramid Kernel [1]. Specifically, we divide each image into a sequence of increasingly finer spatial grids by repeatedly doubling the number of divisions in each axis direction. The histogram counts associated with the points in each grid cell are then recorded. This is a pyramid representation because the number of points in a cell at one level is the sum over those contained in the four cells it is divided into at the next level.

In our case, a Histogram of the Motion Context (HMC) vector is computed for each grid cell at each pyramid resolution level. The final HMC descriptor for the image is a concatenation of all the HMC vectors, which can be expressed as:

$$F(x) = [H_1(x), H_2(x), \ldots, H_L(x)] \tag{1}$$

where $H_i(x)$ the histogram vector formed over all the cell region at level i. $H_1(x)$ is the sparsest partition of the image, H_i doubles the division of the H_{i-1} at each image dimension). $F(x)$ is a vector of concatenated histograms. In forming the pyramid the grid at level i has $2^{(i+1)} = 4^i$ cell regions over the whole image. The feature vector $F(x)$ per image is referred to as the Pyramid Histograms of Motion Context (PHMC).

Suppose motion context at each feature point is a d-dimension vector, and the histogram in each cell region is represented by K bins of the histogram. The entire PHMC feature vector will be of length $d \times K \times \sum 4^i$. Figure 3 shows that the pyramid histograms of the images from different views becomes more distinct as the grid level increases.

To measure the similarity between two motion fields, we use the χ^2 distance between the corresponding PHMC feature vectors. The χ^2 distance has been shown to be superior to histogram intersection and other distance measures recently [1].

Thus the distance between two vessel shapes can be computed as a weighted sum over χ^2 distance at each level as

$$K_M(F_I, F_J) = \sum_{i=1}^{L} \alpha_i d_i(F_I, F_J) \tag{2}$$

where α_i is the weight at level i, and d_i is the χ^2 distance between the feature vectors. The weight α_i can be either a function of current level i, (e.g. $1/2^{L-i}$, as in [12]), or as an unknown parameter to be learned in the recognition algorithm (e.g. [1]).

3.3 Combining Shape and Motion

To capture the topology layout of the vessel tree, we propose to combine the motion context features together with the shape feature, as motion alone may not be sufficient to distinguish all types of vessel views. Using the shape context to model the local shape, we combine motion & shape contributions as

$$K(x; y) = \beta K_M + \gamma K_S \tag{3}$$

where β and γ are the weights for the motion and shape kernels respectively.

4 Experimental Results

To evaluate the effectiveness of the proposed method, we conduct our experiments on a set of angiogram images that contains 273 key frames selected from more than 1600 runs of 70 patients. Each frame is labeled by domain experts as one of the 4 different view classes: BGV, LCA-v1, LCA-v2, and RCAV (view definitions as in Caption of Figure 1). The number of key frames are evenly distributed among all view classes, with approximately 70 key frames per class.

We use a leave-one-out testing framework: Given a testing frame image from patient A, the training samples are selected as the entire set of key frames from other patients; none of the frames from patient A are used for training. A Support Vector Machine (SVM) classifier is used on the PHMC feature set. The PHMC based SVM enables the comparison between cases of unordered features and varying dimanionality.

Table 1. Experimental results using different feature sets

Features	PC+TP	PC+TP+SC	PC+TP+SC+HMC
Accuracy (4 classes)	70.3%	82.4%	87.2%
Accuracy (3 classes)	79.3%	90.2%	95.6%

In the following experiments, classification performance is compared across different feature sets. These features include feature point coordinates (PC), texture within a patch (TP), shape contexts (SC), and histogram of motion context (HMC). In another experiment, we treat the two LCA view classes (LCA-v1 and LCA-v2) as a single LCA view (LCAV) to test the performance of the algorithm on distinguishing between LCA views and RCA views.

	BG	LCA1	LCA2	RCA
BG	1.0000	0.0000	0.0000	0.0000
LCA1	0.0000	0.8507	0.0896	0.0597
LCA2	0.0154	0.0615	0.8462	0.0769
RCA	0.0385	0.0385	0.1154	0.8077

Fig. 4. Confusion matrix for 4 view classes. Average accuracy is 87.2%.

Table 1 lists the comparison results among different sets of features. The results show that by incorporating local motion around feature points, the classification performance is significantly improved. Notice that shape context features also play important role in classifying views from angiogram frames. It also shows that the algorithm has very good performance in distinguishing LCA views and RCA views.

Figure 4 shows a summarizing confusion matrix for the 4 classes using a combination of all features: (PC+TP+SC+HMC) feature sets.

5 Summary

In this paper, we address the problem of image sequence view class recognition in angiogram videos, which arises in real clinical catheter-lab settings, starting from the raw data which is in video form, and detecting information related to the vessels and their viewpoints. We use a novel motion descriptor which captures both the local motion context as well as the global motion layout. To the best of our knowledge, we are the first to use motion information as an important cue for angiogram analysis. Future work will focus on improving the motion feature by synchronizing the angiogram frames within a heart cycle, augmenting the categories into additional more refined vessel annotations, we will explore the possibility of applying our method for labeling coronary arteries in angiogram frames.

References

1. Bosch, A., Zisserman, A., Munoz, X.: Representing shape with a spatial pyramid kernel. In: Proceedings of the 6th ACM International Conference on Image and Video Retrieval, CIVR 2007, pp. 401–408. ACM, New York (2007)
2. Sonka, M., et al.: Robust simultaneous detection of coronary borders in complex images. IEEE Trans. Medical Imaging, 151–161 (1995)
3. Schaap, M., et al.: Standardized evaluation methodology and reference database for evaluating coronary artery centerline extraction algorithms. Medical image Analysis, 701–714 (2009)
4. Frangi, A., Frangi, R., Niessen, W., Vincken, K., Viergever, M.: Multiscale vessel enhancement filtering. In: Wells, W.M., Colchester, A.C.F., Delp, S.L. (eds.) MICCAI 1998. LNCS, vol. 1496, pp. 130–137. Springer, Heidelberg (1998)
5. Sato, Y., Nakajima, S., Shiraga, N., Atsumi, H., Yoshida, S., Koller, T., Gerig, G., Kikinis, R.: Three-dimensional multi-scale line filter for segmentation and visualization of curvilinear structures in medical images. IEEE Medical Image Analysis, 143–168 (1998)
6. Perfetti, R., Ricci, E., Casali, D., Costantini, G.: A cnn based algorithm for retinal vessel segmentation. In: ICC 2008: Proceedings of the 12th WSEAS International Conference on Circuits, pp. 152–157. World Scientific and Engineering Academy and Society (WSEAS), Stevens Point (2008)
7. Haris, K., Efstratiadis, S., Maglaveras, N., Pappas, C., Gourassas, J., Louridas, G.: Model-based morphological segmentation and labeling of coronary angiograms. IEEE-TMI (10), 1003–1015 (1999)
8. Medis medical imaging systems, Inc., http://www.medis.nl/index.htm
9. Syeda-Mahmood, T., Beymer, D., Wang, F., Mahmood, A., Lundstrom, R., Shafee, N., Holve, T.: Automatic selection of keyframes from angiogram videos. In: International Conference on Pattern Recognition (ICPR 2010), Turkey (2010)
10. Guimond, A., Roche, A., Ayache, N., Meunier, J.: Three-dimensional multimodal brain warping using the demons algorithm and adaptive intensity corrections. IEEE Transactions on Medical Imaging 20(1), 58–69 (2001)
11. Belongie, S., Malik, J., Puzicha, J.: Shape matching and object recognition using shape contexts. IEEE Trans. Pattern Anal. Mach. Intell. 24(4), 509–522 (2002)
12. Grauman, K., Darrell, T.: The pyramid matching kernel: Discriminative classification with sets of image features. In: ICCV (2005)

An Automatic Data Assimilation Framework for Patient-Specific Myocardial Mechanical Parameter Estimation

Jiahe Xi[1,2], Pablo Lamata[1,2], Wenzhe Shi[3], Steven Niederer[1,2], Sander Land[1,2], Daniel Rueckert[3], Simon G. Duckett[2], Anoop K. Shetty[2], C. Aldo Rinaldi[2], Reza Razavi[2], and Nic Smith[1,2]

[1] Computing Laboratory, University of Oxford, Wolfson Building, Parks Road Oxford, OX1 3QD, UK
[2] Imaging Sciences and Biomedical Engineering Department, Kings College London, 4th Floor, Lambeth Wing, St. Thomas Hospital, London, SE1 7EH, UK
[3] Department of Computing, Imperial College London, 180 Queen's Gate London SW7 2AZ, UK

Abstract. We present an automatic workflow to extract myocardial constitutive parameters from clinical data. Our framework assimilates cine and 3D tagged Magnetic Resonance Images (MRI) together with left ventricular (LV) cavity pressure recordings to characterize the mechanics of the LV. Dynamic C^1-continuous meshes are automatically fitted using both the cine MRI and 4D displacement fields extracted from the tagged MRI. The passive filling of the LV is simulated, with patient-specific geometry, kinematic boundary and loading conditions. The mechanical parameters are identified by matching the simulated diastolic deformation to observed end-diastolic displacements. We applied our framework to two heart failure patient cases and one normal case. The results indicate that while an end-diastolic measurement does not constrain the mechanical parameters uniquely, it does provide a potentially robust indicator of myocardial stiffness.

1 Introduction

Myocardial stiffness substantially influences cardiac function, as evidenced by the changes in material properties often being associated with disease processes such as myocardial infarction and diastolic heart failure (Abraham et al. 2006, Wang and Nagueh 2009). The quantification of this myocardial stiffness can be provided by patient-specific mechanical parameters, which are also crucial for the in-silico research on underlying mechanisms of heart failure using personalized models (Niederer et al. 2010). Thus there has been a significant interest in being able to perform *in vivo* parameter estimation through the coupling of biophysically based cardiac models with clinical measurements of the cardiac function (Sermesant et al. 2005, Wang et al. 2010a, Wang et al. 2010b). Previously, Wang et al. (2009) have described a work flow involving interactive actions

D.N. Metaxas and L. Axel (Eds.): FIMH 2011, LNCS 6666, pp. 392–400, 2011.

to estimate mechanical parameters from detailed high-resolution MRI data acquired from a canine heart. However, there is currently still a lack of an automatic pipeline to assimilate clinically available data to identify human myocardial mechanical parameters.

In this paper, we present such an automatic framework, reporting parameter values obtained for one healthy and two heart failure cases. With these results we analyze the properties of strain energy function whose parameters are estimated in this work and conclude with a proposal for an index of myocardial stiffness.

2 Material and Methods

The mechanical parameters are identified by comparing a simulated diastolic inflation to observed heart deformation. Passive filling of the human left ventricle (LV) is simulated with patient-specific finite element geometry and boundary conditions extracted from MRI and with the loading condition determined from LV cavity pressure recordings. The geometry and displacement boundary conditions are obtained with an automatic dynamic meshing process that captures both the LV anatomy and tracked deformations from MRI data. Figure 1 schematically illustrates this complete process, where the numbered labels correspond to the subsequent sections in this paper.

2.1 Clinical Measurements

Patient data used in this study was acquired following the clinical protocols for patients selected for Cardiac Resynchronization Therapy (CRT) in St Thomas' Hospital, London. Imaging data are spatially aligned cine and 3D tagged MRI. The end-diastole frame of cine MRI (the first of 29 frames in a heart cycle, synchronized with R-wave of ECG) is utilized to build the LV geometrical model for mechanical simulation; tagged MRI (23 frames in a heart cycle, 3D acquisition)

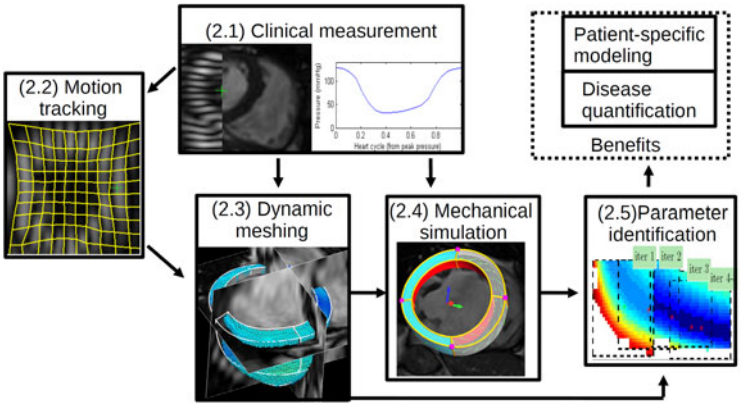

Fig. 1. Work flow of proposed data assimilation framework for patient-specific parameter estimation. The text labels correspond to the section number in this paper.

is used to quantify the myocardial deformation. The LV cavity pressure transient is recorded during the cardiac catheterization procedure before the pace-maker implantation, from which end-diastolic cavity pressures are obtained.

2.2 Myocardial Motion Tracking

Central information for the guidance of mechanical parameter estimation is the displacements of tracked myocardial points, or the Lagrangian displacements. The automatic extraction of these displacements from the tagged MRI is performed with Image Registration Toolkit[1], which uses a non-rigid registration method based on free-form deformations developed by Rueckert et al. (1999) and extended to the cardiac tagged MRI motion tracking by Chandrashekara et al. (2004).

2.3 Dynamic Mesh Personalization

Geometric model construction. Based on clinical segmentation of the end-diastole frame of the patient's cine MRI, the LV mechanical mesh is built with cubic-Hermite (CH) elements using a novel approach developed by Lamata et al. (2010). This CH mesh, with nodal positions and derivatives as degrees of freedom, provides a C^1-continuous field representation, which is generally efficient for both geometric modeling and mechanical simulation (Lamata et al. 2010). The fiber field inside the LV myocardium is embedded in the geometric model with transmural and apex-to-base heterogeneity (see figure 2), based on the findings of Usyk et al. (2000). We choose a relatively coarse CH mesh with 26 nodes and 12 elements in order to keep a balance between representing the spatial stress and stress distributions and the computational cost introduced by the repeated simulations during parameter estimation.

Geometric model propagation. Given the constructed geometrical model at end-diastole and the 4D myocardial displacement field (section 2.2), a novel and simple technique is employed to propagate this geometrical model to the time points of displacement field. Specifically, given a reference mesh fitted to the anatomical data at one time point and a time-series of D material points' positions $\boldsymbol{Z}_k \in \mathbb{R}^{3D}$, we find, for each of the subsequent time points, the nodal positions and derivatives $\boldsymbol{U}_k$ that define a N-node cubic-Hermite mesh by minimizing the error in the mesh approximation to the positions of data points. This mesh approximation error e_k is defined as the L_2 norm of the weighted fitting residual vector, i.e.,

$$e_k = \|\boldsymbol{W}(\boldsymbol{Z}_k - \boldsymbol{H}(\boldsymbol{\Xi})\boldsymbol{U}_k)\|_{\mathbb{L}^2}\,, \tag{1}$$

where $W \in \mathbb{M}^{3D\times 3D}$ is a diagonal weight matrix, whose elements can be set as the error covariance of corresponding data; $\boldsymbol{\Xi} \in \mathbb{R}^{4D}$ is the vector of element number and local coordinates within that element of all data points in the fitted reference mesh; $\boldsymbol{H} \in \mathbb{M}^{3D\times 8N}$, a function of $\boldsymbol{\Xi}$, is the shape matrix related to

[1] IRTK, http://www.doc.ic.ac.uk/~dr/software/

the CH basis functions (Smith et al. 2004). Solving this standard linear weighted least-square minimization problem, we obtain the new mesh

$$\boldsymbol{U}_k = (\boldsymbol{H}^T(\boldsymbol{\Xi})\boldsymbol{W}\boldsymbol{H}(\boldsymbol{\Xi}))^{-1}\boldsymbol{H}^T\boldsymbol{W}\boldsymbol{Z}_k. \quad (2)$$

2.4 Mechanical Simulation

Using the geometric meshes developed in section 2.3, we simulates the passive diastolic filling phase of the cardiac cycle, by inflating the early-diastolic LV model to an end-diastolic LV cavity pressure (table 1, column 2). Deformation is simulated using the standard finite deformation theory, where the finite element method (FEM) is utilized to solve a stress equilibrium governing equation, which is derived from the laws of conservation of mass and momentum, and the principle of virtual work (Nordsletten et al. 2010).

Boundary Conditions. The model developed in this study only represents the LV, and does not include representations of the right ventricle (RV), great vessels, pericardium and organs around the heart. Thus the effects of these structures on the LV mechanics are not explicitly modeled. To account for these physical constraints on the heart, we prescribe the kinematic movement of the LV model at its base plane and apex node (figure 2) to match the displacements extracted from the tagged MRI.

Passive constitutive parameters of the myocardium. The myocardium is modeled as a transversely isotropic hyperelastic material. The constitutive equations are defined by a well-known strain-energy function (Guccione et al. 1991), given by

$$W = C_1(e^Q - 1), \text{ and } Q = C_2E_{\mathrm{ff}}^2 + C_3(E_{\mathrm{ss}}^2 + E_{\mathrm{nn}}^2 + 2E_{\mathrm{sn}}^2) + C_4(2E_{\mathrm{fs}}^2 + 2E_{\mathrm{fn}}^2), \quad (3)$$

where C_1, C_2, C_3 and C_4 are the constitutive parameters, E_{ff}, E_{ss} and E_{nn} are the Green-Lagrange strains in in fiber (f), sheet (s) and sheet normal (n)

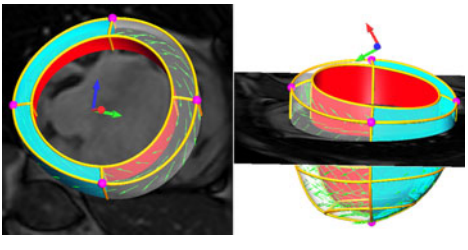

Fig. 2. Geometric model with fiber vectors embedded. Kinematic boundary conditions (displacement and its derivatives) are prescribed on the purple nodal points (four at the base plane and one in the apex). The movements of the free wall region (transparent green area) are compared with the measurements in the parameter fitting process.

directions, and E_{sn}, E_{fn} and E_{fs} are the Green-Lagrange shear strains in the fs, fn and fs planes. The f, s and n directions correspond to the fiber axes aligned with the microstructure of the myocardium, shown in figure 2.

2.5 Identification of Myocardial Passive Constitutive Parameters

The mechanical simulation is performed by inflating the early-diastolic LV model to an end-diastolic LV cavity pressure (table 1, column 2), with kinematic boundary constraints (section 2.4). The simulated result is then compared with the corresponding mesh fitted in section 2.3, and the constitutive parameters are tuned to minimize an objective function based on the shape differences, defined by integrating the distance between equivalent material points in the two meshes over the myocardial free wall volume (see figure 2 for visualization of free wall volume). In order to reduce the influence of the RV and its unknown cavity pressure, the difference to minimize is only defined in those elements belonging to the LV free wall region.

To solve this optimization problem, we first reparameterize the constitutive parameters

$$C_1 = C_1,\ C_2 = \alpha r_2,\ C_3 = \alpha r_3,\ C_4 = \alpha r_4,\ r_2 + r_3 + r_4 = 1, \tag{4}$$

where α and r_2-r_4 are the scale factors and anisotropies of C_2-C_4 respectively. We design a two-step optimization procedure in which C_1 and α are first optimized, followed by optimizing r_2 and r_3. This two-step process is iterated until the estimated parameters are converged. In each step, the optimization is solved using 2-D exhaustive searching, chosen in order to explore the landscape of objective function and to avoid convergence within local minima.

3 Results

The proposed automatic data assimilation framework was applied to two CRT patient data sets and one healthy control case. For each case, the processing time is approximately 40 minutes for the motion tracking, 1 minute for the dynamic meshing, and 30 minutes for the mechanical property estimation[2].

3.1 Dynamic Meshing

Figure 3 shows the C^1-continuous CH geometrical meshes for patient case 16, which are automatically constructed over a heart cycle following the methods outlined in section 2.3. The residual of this fit (i.e., components of the fitting residual vector $\boldsymbol{Z}_k - \boldsymbol{H}(\boldsymbol{\Xi})\boldsymbol{U}_k$), see equation 1) has a zero mean, standard deviation of 0.28-0.53 mm, and in general no obvious spatial correlations. As a result

[2] We used a highly optimized cubic-Hermite elements based mechanical simulation code (Land et al. 2011), running on a standard desktop computer (4 2.5GHz cores and 4GB RAM). For non-optimized implementations, the mechanical property estimation can take up to 12 hours.

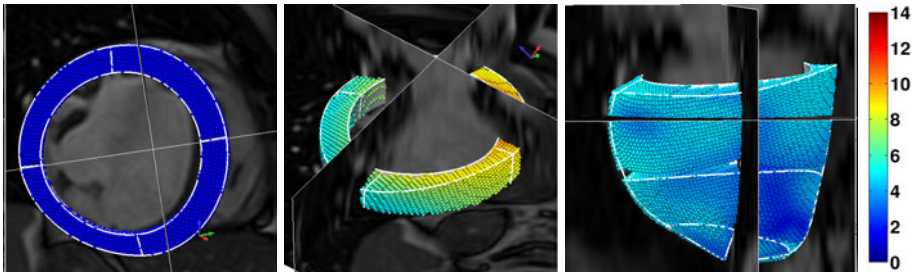

Fig. 3. Results of dynamic meshing stage in figure 1 (healthy case, visualized with the cine MRI from different views, corresponding to frame 1, 9 and 17). The whole-heart-cycle dynamic meshes are automatically reconstructed from the displacements of data points (embedded in the mesh) extracted from the tagged MRI. The color represents the magnitude of displacement referencing to the end-diastole in mm.

Table 1. Estimated constitutive parameters for one healthy case and two patient cases, and comparison to three studies in literature. Initial parameter values are $C_1 = 0.4, C_2 = 9.2, C_3 = 2.0, C_4 = 3.7$, taken from Niederer et al. 2010.

-	EDP(kPa)	ESV(ml)	EF	C_1	C_2	C_3	C_4	Residual(mm)[1]
healthy case	1.81 [2]	67	51%	0.15	41.71	9.07	51.52	2.76
case 16	1.93	345	16%	3.40	9.22	2.05	17.92	1.73
case 28	1.69	186	17%	1.40	34.21	5.86	66.39	2.36
Wang et al. 2009, dog	0.5	-	-	0.831	14.3	4.49	0.762	1.81
Augenstein et al. 2005, dog	-	-	-	1.5[3]	11.1	1.76	10.0	-
Omens et al. 1993, rat	-	-	-	1.2	26.7	2.0	14.7	-

EDP, end-diastolic LV cavity pressure; ESV: end-systolic LV cavity volume; EF, ejection fraction. [1] The root-mean-squared-error (RMSE) between simulated and fitted mesh at end-diastole over free wall. [2] Average EDP of cases 16 and 18. [3] $C_1 = 3.0$ in this study is defined with a multiplier of $\frac{1}{2}$.

of this process, the displacements of discrete data points, which are extracted from the MRI data, are now smoothed and regularized into the local material coordinates (model space).

3.2 Mechanical Property Estimation

Following the methods described in section 2.5, table 1 shows the mechanical parameter estimation results (parameters C_1 to C_4 and its fitting residual), with comparison to the values reported in literature. Figure 4(a) further plots the landscape of fitting residual with respect to $log(C_1)$-$log(\alpha)$ for case 16, gathered in the last iteration of the two-step optimization procedure. We fitted the iso-curves (coupling relationships between C_1 and α) with the form of $C_1^a \alpha = b$ (a, b are constants) to the minimum valley in figure 4(b). This coupling relationship can also be derived from the stress-strain relationship for Guccione's law. The exponential coefficient a is proportional to the magnitude of deformation, and

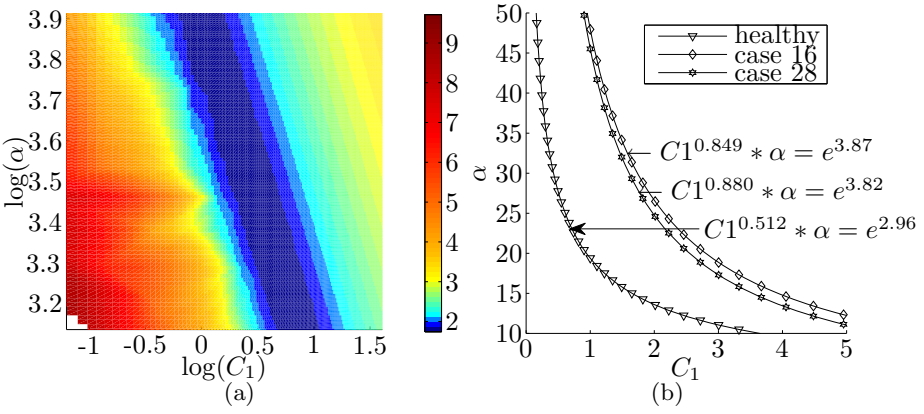

Fig. 4. (a) The landscape of fitting residual with respect to C_1-α for case 16, showing coupling of C-α (dark blue valley). The color represents the fitting residual in mm. (b) The three fitted iso-curves ($C_1^a \alpha = b$), showing the coupling relationships between C-α for cases listed in table 1. These curves can be easy-to-estimate indicators of myocardial stiffness for differentiating normal and heart failure patient cases (see text for more discussion).

the value of b could provide an easy-to-estimate metric to quantify myocardial stiffness (discussed in next section).

4 Discussion

In this paper, we have described, to our knowledge, the first automatic pipeline to assimilate clinical measurements into the mechanical modeling framework in order to estimate myocardial constitutive parameters. This fast pipeline enables us to explore the value and associated issues of patient-specific in-vivo parameter estimation.

The proposed framework converts the displacements extracted from the tagged MRI registration into model space, in which the analysis of strain and stress can be performed in local material coordinates using standard finite element (FE) theory. The representation of this deformation in model space also provides patient-specific kinematic boundary conditions and makes the comparison to FE model simulations straightforward.

The results in table 1 indicate a wide range of mechanical parameter values estimated from in-vivo observations. The reason for this is likely to be the coupling between C_1 and α, which produces the valley in the landscape of objective function shown in figure 4(a). Previous studies (Wang et al. 2009, Omens et al. 1993) optimized C_1-C_4 sequentially. In these cases, the two-way coupling between C_1 and C_2-C_4 is unnoticed. However, those final parameter values may well be dependent on the initial values. Nevertheless, despite this C_1-α coupling, the comparison between healthy ($a = 0.512$, $b = 19.3$) and diseased cases ($a = 0.880$, $b = 53.6$ and $a = 0.849$, $b = 48.0$) in figure 4(b) indicates that

$C_1^a \alpha = b$ could be a potentially reliable and easy-to-estimate indicator of the myocardial stiffness.

There are a number of limitations in our study. In particular, we did not consider the residual active tension in the early-diastolic geometry, which would render the estimated stiffness lower than reality. Furthermore, the fiber distribution of our LV model does not incorporate directly the patient-specific measurements, and this may influence the estimation of material anisotropies.

From these results, we conclude that one end-diastolic measurement does not constrain the mechanical parameters uniquely, but it does already provide an easy-to-estimate indicator of myocardial stiffness. In order to obtain the complete set of unique parameter values, more constraints need to be added to the optimization criteria. Additional measurements points during diastolic filling can potentially provide the necessary constraints. However, accurate time registration between imaging data sets and pressure recordings is required for this. In the future, we plan to acquire additional clinical data sets with optimized protocols (e.g., synchronized pressure, ECG and MR recordings, ideally with the diffusion-tensor imaging for the patient-specific fiber distribution), in order to further investigate the identifiability of parameters and to correlate our parameter estimation results with clinical diagnosis.

References

Abraham, T., Lardo, A., Kass, D.: Myocardial Dyssynchrony and Resynchronization. Heart Failure Clinics 2(2), 179–192 (2006)

Augenstein, K., Cowan, B., LeGrice, I., Nielsen, P., Young, A.: Method and apparatus for soft tissue material parameter estimation using tissue tagged Magnetic Resonance Imaging. Journal of Biomechanical Engineering 127, 148 (2005)

Chandrashekara, R., Mohiaddin, R., Rueckert, D.: Analysis of 3-D myocardial motion in tagged MR images using nonrigid image registration. IEEE Transactions on Medical Imaging 23(10), 1245–1250 (2004)

Guccione, J., McCulloch, A., Waldman, L.: Passive material properties of intact ventricular myocardium determined from a cylindrical model. Journal of Biomechanical Engineering 113, 42–55 (1991)

Lamata, P., Niederer, S., Barber, D., Norsletten, D., Lee, J., Hose, R., Smith, N.: Personalization of cubic hermite meshes for efficient biomechanical simulations. In: Jiang, T., Navab, N., Pluim, J.P.W., Viergever, M.A. (eds.) MICCAI 2010. LNCS, vol. 6362, pp. 380–387. Springer, Heidelberg (2010)

Land, S., Niederer, S., Smith, N.: Efficient computational methods for strongly coupled cardiac electromechanics. In: IEEE Transactions on Bio-medical Engineering (2011) (in press)

Niederer, S., Plank, G., Chinchapatnam, P., Ginks, M., Lamata, P., Rhode, K., Rinaldi, C., Razavi, R., Smith, N.: Length-dependent tension in the failing heart and the efficacy of cardiac resynchronization therapy. Cardiovascular Research (2010)

Nordsletten, D., Kay, D., Smith, N.: A non-conforming monolithic finite element method for problems of coupled mechanics. Journal of Computational Physics (2010)

Omens, J., MacKenna, D., McCulloch, A.: Measurement of strain and analysis of stress in resting rat left ventricular myocardium. Journal of Biomechanics 26(6), 665–676 (1993)

Rueckert, D., Sonoda, L., Hayes, C., Hill, D., Leach, M., Hawkes, D.: Nonrigid registration using free-form deformations: application to breast MR images. IEEE Transactions on Medical Imaging 18(8), 712–721 (1999)

Sermesant, M., Moireau, P., Camara, O., Sainte-Marie, J., Andriantsimiavona, R., Cimrman, R., Hill, D.L.G., Chapelle, D., Razavi, R.S.: Cardiac function estimation from MRI using a heart model and data assimilation: Advances and difficulties. In: Frangi, A.F., Radeva, P., Santos, A., Hernandez, M. (eds.) FIMH 2005. LNCS, vol. 3504, pp. 325–337. Springer, Heidelberg (2005)

Smith, N., Nickerson, D., Crampin, E., Hunter, P.: Multiscale computational modelling of the heart. Acta Numerica, 371–431 (2004)

Usyk, T., Mazhari, R., McCulloch, A.: Effect of laminar orthotropic myofiber architecture on regional stress and strain in the canine left ventricle. Journal of Elasticity 61(1), 143–164 (2000)

Wang, J., Nagueh, S.: Current perspectives on cardiac function in patients with diastolic heart failure. Circulation 119(8), 1146 (2009)

Wang, L., Wong, K., Zhang, H., Liu, H., Shi, P.: A Statistical Physiological-Model-Constrained Framework for Computational Imaging of Subject-Specific Volumetric Cardiac Electrophysiology Using Optical Imaging and MRI Data. Statistical Atlases and Computational Models of the Heart, 261–269 (2010a)

Wang, V., Lam, H., Ennis, D., Cowan, B., Young, A., Nash, M.: Modelling passive diastolic mechanics with quantitative MRI of cardiac structure and function. Medical Image Analysis 13(5), 773–784 (2009)

Wang, V., Lam, H., Ennis, D., Cowan, B., Young, A., Nash, M.: Cardiac Active Contraction Parameters Estimated from Magnetic Resonance Imaging. Statistical Atlases and Computational Models of the Heart, 194–203 (2010b)

Left-Ventricular Shape Determines Intramyocardial Stroke Work Distribution

Hon Fai Choi, Frank E. Rademakers, and Piet Claus

Division of Imaging and Cardiovascular Dynamics, Department of Cardiovascular Diseases, Katholieke Universiteit Leuven, University Hospitals - campus Gasthuisberg, Herestraat 49 - bus 7003, B-3000 Leuven, Belgium
piet.claus@uzleuven.be

Abstract. The left-ventricle often undergoes large shape changes in the remodelling process, which is now considered to be an important indication of disease progression. Therefore, the influence on intramyocardial work load distribution was examined in a finite-element study. Hereto, models were constructed with varying shapes, ranging from an elongated ellipsoid to a sphere, while the initial cavity and wall volume was kept constant. A realistic transmural gradient in fiber orientation was considered. The passive myocardium was described by an incompressible hyperelastic material law with transverse isotropic symmetry. Activation was governed by the eikonal-diffusion equation. Contraction was incorporated using a mechanistic model. For each shape, a simulation was performed in which passive filling was followed by isovolumic contraction and ejection. It was found that the transmural distribution of the stroke work density was shape dependent, suggesting that the interaction between shape and intramyocardial mechanical heterogeneity could be important in the remodelling process.

1 Introduction

Geometric remodelling of the left ventricle (LV) is a (patho)physiological process that frequently occurs to maintain cardiac homeostasis under changing loading conditions. The LV undergoes large shape changes in this process, which in many cardiomyopathies results in chamber dilation, finally leading to heart failure. Remodelling is now considered to be an important indication of disease progression and hence an important target for new therapies [1]. However, the regional biomechanics of LV shape remodelling is still poorly understood. Previous studies [2,3] were mainly focused on the influence of constitutive equations or fiber architecture, assuming a normal LV shape based on gross anatomical measurements and limited attention was paid to any intramyocardial heterogeneity obtained.

In a previous study [4], the influence of LV shape on passive compliance and fiber stress and strain at end-diastole (ED), has been examined in a finite-element (FE) model. It was found that the compliance did not alter significantly with LV shape while the distribution of passive fiber stress and strain depended significantly on regional curvature and wall thickness. Based on the Frank-Starling

D.N. Metaxas and L. Axel (Eds.): FIMH 2011, LNCS 6666, pp. 401–408, 2011.

mechanism, it was expected that the distribution of work load during systole would also depend on the LV shape. This hypothesis was further examined in the presented FE study.

2 Methods

2.1 Variation in Left-Ventricular Shape

The LV shape was approximated as a truncated ellipsoid with a homogeneous wall thickness, following [4]. The ellipsoidal geometry was defined in curvilinear prolate spheroidal coordinates such that the sphericity could be varied. Three different LV-shapes were considered by setting the short-to-long-axis ratio of the cavity to 0.2 (ELONG), 0.5 (NORMAL) and 0.99 (SPHERE). For each LV shape, the reference cavity and wall volume were set to 65 ml and 127.5 ml respectively, while the basal opening was given a diameter of 3 cm to represent the mitral valve annulus, as previously proposed [4].

2.2 Mechanics of the Myocardial Wall

The LV wall deformation was described by Cauchy's equation of motion, assuming no inertial and body forces:

$$\nabla \cdot \underline{\boldsymbol{\sigma}} = 0 \ , \tag{1}$$

with ∇ and $\underline{\boldsymbol{\sigma}}$ equal to the nabla-operator and the Cauchy stress tensor respectively. The local anisotropy due to the myocyte arrangement [5] was accounted for by a mathematical template of a helical fiber angle that varied transmurally from 75 degrees at the endocardial border to -45 degrees at the epicardial border [6]. The passive mechanical response of the myocardium was modelled using an incompressible hyperelastic strain energy function with transverse isotropic symmetry aligned with the local fiber direction. Incompressibility was imposed via a Lagrange multiplier p:

$$\begin{aligned} \Psi &= \Psi_{\text{iso}} + \Psi_{\text{vol}} \\ &= \Psi_{\text{iso}} + p(J-1) \quad , \end{aligned} \tag{2}$$

with J denoting the determinant of the deformation gradient tensor. The Lagrange multiplier p will enter the stress equations as a hydrostatic pressure. For Ψ_{iso}, the function as proposed by [7] was used:

$$\Psi_{\text{iso}} = (C/2)(e^Q - 1) \tag{3}$$

$$\begin{aligned} Q = {} & b_1 E_{\text{FF}}^2 + b_2(E_{\text{CC}}^2 + E_{\text{RR}}^2 + E_{\text{CR}}^2 + E_{\text{RC}}^2) \\ & + b_3(E_{\text{RF}}^2 + E_{\text{FR}}^2 + E_{\text{FC}}^2 + E_{\text{CF}}^2) \ . \end{aligned} \tag{4}$$

In (4), E_{ij} are the elements of the Green-Lagrange strain tensor referred to the local fiber coordinate axes. The fiber, cross-fiber and transmural directions are

indicated by F, C and R respectively. In (3), C is a scaling parameter, while b_1, b_2 and b_3 in (4) are material parameters defining the exponential stress-strain relation.

During contraction, an active stress component σ_{act} along the fiber direction was added. Hereto, the contraction model as described in [2,3] was used. In this model, σ_{act} depends on the sarcomere length l_{s}, the contractile element length l_{c} and the time t_{a} elapsed since the start of depolarization:

$$\sigma_{\text{act}} = \frac{l_{\text{s}}}{l_{\text{s0}}} s_{\text{iso}}(l_{\text{s}}) s_{\text{tw}}(t_{\text{a}}, l_{\text{s}}) E_{\text{a}}(l_{\text{s}} - l_{\text{c}}) \ , \tag{5}$$

with l_{s0} being the sarcomere length in the undeformed reference state, and E_{a} the stiffness of the series elastic element. The sarcomere length l_{s} depends on the fiber strain through:

$$l_{\text{s}} = l_{\text{s0}} \sqrt{2E_{\text{FF}} + 1} \ . \tag{6}$$

In (5), s_{iso} represents the isometrically developed active stress which depends on the contractile element length l_{c}:

$$s_{\text{iso}}(l_{\text{c}}) = \begin{cases} T_0 \tanh^2(a_1(l_{\text{c}} - l_{\text{c0}})) & l_{\text{c}} \geq l_{\text{c0}} \\ 0 & l_{\text{c}} < l_{\text{c0}} \ . \end{cases} \tag{7}$$

The dependency of the active stress on t_{a} is represented by s_{tw}:

$$s_{\text{tw}}(t_{\text{a}}, l_{\text{s}}) = \begin{cases} 0 & t_{\text{a}} \leq 0 \\ \tanh^2(\frac{t_{\text{a}}}{t_{\text{r}}}) \tanh^2(\frac{t_{\text{max}} - t_{\text{a}}}{t_{\text{d}}}) & 0 < t_{\text{a}} \leq t_{\text{max}} \\ 0 & t_{\text{a}} > t_{\text{max}} \ , \end{cases} \tag{8}$$

with

$$t_{\text{max}} = b(l_{\text{s}} - l_{\text{d}}) \ , \tag{9}$$

where l_{d} gives the extrapolated sarcomere length associated with zero twitch duration. A linear approximation of the hyperbolic velocity-tension relation of muscle contraction was obtained by defining the time course of the shortening velocity as:

$$\frac{dl_{\text{c}}}{dt} = (E_{\text{a}}(l_{\text{s}} - l_{\text{c}}) - 1)v_0 \ , \tag{10}$$

where v_0 is the unloaded shortening velocity.

The time course of the cavity volume during ejection was defined through a three-element Windkessel model to account for the arterial system [8]. In this model, the arterial system is characterized by a compliance (C), a peripheral resistance (R) and a characteristic impedance (R_{c}):

$$P(t) + RC\frac{dP(t)}{dt} + (R + R_{\text{c}})\frac{dV(t)}{dt} + RR_{\text{c}}C\frac{d^2V(t)}{dt^2} = 0 \ , \tag{11}$$

where P and V are the LV cavity pressure and volume respectively.

2.3 Depolarization Propagation

To model the propagation of the activating depolarization wave, the eikonal-diffusion equation was solved to obtain the local time of depolarization t_{dep} at which the contraction was initiated [2,9]:

$$c_0\sqrt{\nabla t_{\mathrm{dep}}\cdot\underline{\mathbf{M}}\cdot\nabla t_{\mathrm{dep}}}-\nabla\cdot(\underline{\mathbf{M}}\cdot\nabla t_{\mathrm{dep}})=\tau_{\mathrm{m}}\ . \tag{12}$$

In (12), $\underline{\mathbf{M}}$ is the coupling tensor containing characteristic spatial constants λ_i that describes the anisotropy of the wave propagation according to the local fiber coordinate system:

$$\underline{\mathbf{M}}=\begin{bmatrix}\lambda_{\mathrm{R}}^2 & 0 & 0\\ 0 & \lambda_{\mathrm{F}}^2 & 0\\ 0 & 0 & \lambda_{\mathrm{C}}^2\end{bmatrix}\ . \tag{13}$$

The characteristic time constant τ_{m} and dimensionless constant c_0 determine the propagation speed. It was assumed that the depolarization started ($t_{\mathrm{dep}}=0$) at the endocardial border which was activated simultaneously to account for the presence of fast conducting Purkinje fibers, following [10]. The left-ventricular boundaries were considered to be electrically insulated such that the wave fronts were perpendicular to these boundaries.

2.4 Numerical Implementation

All equations were solved with an in-house developed non-linear Galerkin-type curvilinear FE framework [4]. Trilinear interpolation was used in each element for both the depolarization time and the spatial coordinates. A mixed method was applied to solve the displacement field together with the hydrostatic pressure. This FE implementation was combined with a forward Euler scheme to solve for the time dependency in (8) – (11).

2.5 Simulations

For each LV shape, a structured FE mesh of the LV wall was constructed in prolate spheroidal coordinates to reduce the number of elements and hence calculation time. Each mesh contained 10 elements transmurally and 30 elements longitudinally. Because of the symmetry, only one element in the circumferential direction was required.

FE simulations were performed for each LV shape. Passive filling from reference to ED was simulated by increasing the cavity pressure with 1.066 kPa (8 mmHg). The subsequent isovolumic contraction (IVC) phase was simulated by imposing the isovolumic constraint. IVC ended when the cavity pressure equaled the diastolic blood pressure of 10.66 kPa (80 mmHg). To simulate the following ejection phase, the isovolumic constraint was replaced by the Windkessel equation (11). End-sytole (ES) was assumed to be reached when the decrease in cavity volume between subsequent calculation steps was less than 0.05 ml.

Table 1. Values chosen for the input parameters used in the simulations

Passive		Contraction		Depolarization		Windkessel	
param.	value	param.	value	param.	value	param.	value
b_1	13.41	l_{s0}	1.9 μm	λ_F	0.8 mm	C	15 ml/kPa
b_2	4.83	l_{c0}	1.5 μm	λ_R	0.5 mm	R	0.14 kPa $\cdot$ s/ml
b_3	4.32	T_0	200 kPa	λ_C	0.5 mm	R_c	0.015 kPa $\cdot$ s/ml
C	0.51	E_a	20 μm^{-1}	τ_m	3 ms		
		a_1	3 μm^{-1}	c_0	2.5		
		τ_r	0.075 s				
		τ_d	0.375 s				
		b	0.4 s/μm				
		l_d	-0.5 μm				
		v_0	7.5 μm/s				

During all simulated cardiac phases, the epicardial surface was loaded with zero pressure. The endocardial basal border was constrained in all coordinates to account for the relative stiff valve annuli and to prevent longitudinal rigid body motion.

The input parameters of the different equations were set to the values as listed in Table 1, which were chosen to obtain a physiological ED volume (around 115 ml) and ejection fraction (around 60%). For each LV shape, the regional stroke work density was calculated as the area enclosed by the Cauchy fiber stress – natural fiber strain loop, following [2]. To close the loops, it was assumed that the relaxation from ES happened isometrically, i.e. at a constant ES fiber length.

3 Results

A significant difference in stroke volume was obtained, which was 18.80 ml lower for the SPHERE shape than for the ELONG shape. The longitudinal-transmural distributions of the stroke work density for the three LV shapes are shown in Fig. 1. The ELONG and NORMAL shapes have a very similar distributions of the stroke work density. The distribution obtained for the SPHERE shape differs from that of the ELONG and NORMAL shape mainly at the mid-height level. At this level, the stroke work density of the ELONG and NORMAL shapes increases from the endocardium to the epicardium, while a minimum is obtained in the midwall region for the SPHERE shape. In Fig. 2, the Cauchy fiber stress – natural fiber strain loops are plotted for different transmural positions at the mid-height (mid) and apical (apex) levels as indicated in Fig. 1. At the mid-height level, subendocardial fiber shortening and subepicardial fiber stretching during IVC result in a more narrow and wider stress-strain loop respectively. As can be seen, less epicardial stretching occurs in the SPHERE shape. At the apical level, the stress-strain loops are much smaller due to a rapid shortening during early systole.

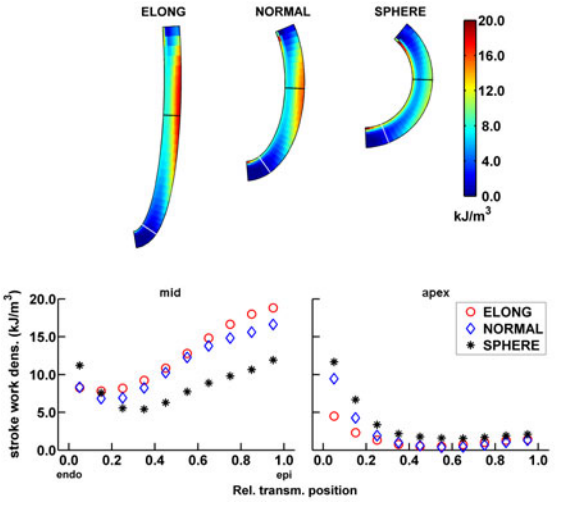

Fig. 1. Intramyocardial distribution of stroke work density as obtained for the three LV shapes. Longitudinal-transmural sections of the three LV shapes are shown at the top, while transmural distributions at the mid-height (black line) and apical (white line) level are shown in the bottom row.

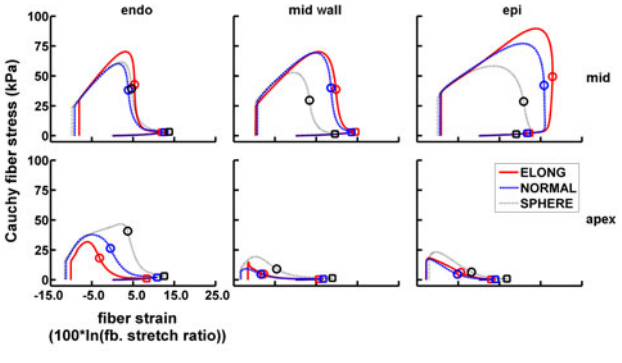

Fig. 2. Cauchy fiber stress – natural fiber strain loops for different transmural positions at the mid-height (mid) and apical (apex) levels as indicated in Fig. 1. The transmural positions are located at 15% (endo), 50% (midwall), 85% (epi) wall depth from the endocardial surface. The loops go from referebce to ES in a counterclockwise direction as indicated by the arrows. The squares indicate ED while the circles indicate beginning of ejection.

4 Discussion

4.1 Physiological Implications

The results show that the LV shape is a factor of influence in systolic function. The reduced stroke volume of the SPHERE shape suggests that the ejection

performance decreases with increasing sphericity, supporting the current clinical view. A LV shape dependent transmural variation in the regional stroke work density was also obtained in this study, which was related to stretching of the late activated epicardial fibers during IVC. These findings suggest that LV shape could be an important factor in the remodelling process by mediating changes in intramyocardial heterogeneity. The physiological presence and importance of metabolic and mechanical heterogeneity is still much debated, although intramyocardial heterogeneity in tissue structure is well documented [5]. Early physiological measurements have been criticized because of low spatial resolution, methodology artefacts and conflicting results [11]. However, recent studies with improved methodologies have shown that the presence of metabolic heterogeneity is significant, suggesting that myocardial blood flow and oxygen consumption is higher in the subendocardium [12]. It is currently still unclear whether and how the measured transmural heterogeneity in metabolism is reflected in regional mechanical function. The higher subendocardial blood flow and oxygen uptake have often been related to a higher work load. This is not supported by the results presented here. However, the higher subendocardial oxygen uptake does not necessarily implicate a higher work load but could also indicate differences in metabolic efficiency as suggested by van der Vusse et al. [11]. The activation pattern could play another determining role as proposed by [13], supported by the lower stroke work in the early activated subendocardium obtained here.

4.2 Limitations

Only a helical fiber angle distribution was considered in this study, but the choice of an exact distribution of the fiber orientation was considered to be less important. No cellular physiology was considered in this study. However, it was assumed that a mechanistic model of contraction and quantification of work load by regional mechanical work was sufficiently adequate for the purpose of comparing between different LV shapes.

5 Conclusion

The presented computational FE study has shown the importance of LV shape for ejection performance and intramyocardial stroke work distribution. However, the physiological importance of the differences in intramyocardial mechanical heterogeneity associated with LV shape changes is yet to be determined. It is not unlikely that intramyocardial heterogeneity is important for a normal LV function [14], such that alterations could be a trigger for (patho)physiological LV shape remodelling or vice versa.

Acknowledgements

Hon Fai Choi is a Research Assistant of the Research Foundation – Flanders (Belgium, FWO-Vlaanderen).

References

1. Misra, A., Mann, D.L.: Treatment of heart failure beyond practice guidelines: role of cardiac remodeling. Circulation Journal 72(suppl. A), 1–7 (2008)
2. Kerckhoffs, R.C.P., Bovendeerd, P.H.M., Kotte, J.C.S., Prinzen, F.W., Smits, K., Arts, T.: Homogeneity of cardiac contraction despite physiological asynchrony of depolarization: a model study. Annals of Biomedical Engineering 31(5), 536–547 (2003)
3. Bovendeerd, P.H.M., Kroon, W., Delhaas, T.: Determinants of left ventricular shear strain. American Journal of Physiology - Heart and Circulatory Physiology 297(3), H1058–H1068 (2009)
4. Choi, H.F., D'hooge, J., Rademakers, F.E., Claus, P.: Influence of left-ventricular shape on passive filling properties and end-diastolic fiber stress and strain. Journal of Biomechanics 43(9), 1745–1753 (2010)
5. Anderson, R.H., Smerup, M., Sanchez-Quintana, D., Loukas, M., Lunkenheimer, P.P.: The three-dimensional arrangement of the myocytes in the ventricular walls. Clinical Anatomy 22(1), 64–76 (2009)
6. Guccione, J.M., McCulloch, A.D., Waldman, L.K.: Passive material properties of intact ventricular myocardium determined from a cylindrical model. Journal of Biomechanical Engineering 113(1), 42–55 (1991)
7. Okamoto, R.J., Moulton, M.J., Peterson, S.J., Li, D., Pasque, M.K., Guccione, J.M.: Epicardial suction: a new approach to mechanical testing of the passive ventricular wall. Journal of Biomechanical Engineering 122(5), 479–487 (2000)
8. Westerhof, N., Lankhaar, J., Westerhof, B.E.: The arterial Windkessel. Medical & Biological Engineering & Computing 47(2), 131–141 (2009)
9. Tomlinson, K.A.: Finite element solution of an eikonal equation for excitation wave-front propagation in ventricular myocardium. PhD-thesis. The University of Auckland, Auckland (2000)
10. Campbell, S.G., Howard, E., Aguado-Sierra, J., Coppola, B.A., Omens, J.H., Mulligan, L.J., McCulloch, A.D., Kerckhoffs, R.C.P.: Effect of transmurally heterogeneous myocyte excitation-contraction coupling on canine left ventricular electromechanics. Experimental Physiology 94(5), 541–552 (2009)
11. van der Vusse, G.J., Arts, T., Glatz, J.F.C., Reneman, R.S.: Transmural differences in energy metabolism of the left ventricular myocardium: fact or fiction. Journal of Molecular and Cellular Cardiology 22(1), 23–37 (1990)
12. Groeneveld, A.B., van Beek, J.H.G.M., Alders, D.J.C.: Assessing heterogeneous distribution of blood flow and metabolism in the heart. Basic Research in Cardiology 96(6), 575–581 (2001)
13. Prinzen, F.W., Hunter, W.C., Wyman, B.T., McVeigh, E.R.: Mapping of regional myocardial strain and work during ventricular pacing: experimental study using magnetic resonance imaging tagging. Journal of the American College of Cardiology 33(6), 1735–1742 (1999)
14. Brutsaert, D.L.: Nonuniformity: a physiologic modulator of contraction and relaxation of the normal heart. Journal of the American College of Cardiology 9(2), 341–348 (1987)

Constitutive Parameter Estimation Methodology Using Tagged-MRI Data

A. Imperiale, R. Chabiniok, P. Moireau, and D. Chapelle

INRIA, MACS Team, B.P. 105, 78153 Le Chesnay, France

Abstract. We propose a methodology for performing the estimation of a key constitutive parameter in a biomechanical heart model – namely, the tissue contractility – using tagged-MRI data. We adopt a sequential data assimilation strategy, and the image data is assumed to be processed in the form of deforming tag planes, which we employ to obtain a discrepancy between the model and the data by computing distances to these surfaces. We assess our procedure using synthetic measurements produced with a model representing an infarcted heart as observed in an animal experiment, and the estimation results are found to be of superior accuracy compared to assimilation based on segmented endo- and epicardium surfaces.

1 Introduction

Automatized personalization of cardiac models represents a great challenge in the context of computer-assisted medicine [16]. Beyond anatomical personalization, this requires the estimation of many important – unknown or uncertain – biophysical parameters, based on measurements available on the system, in order for the model to become predictive.

In this paper, we aim at investigating the use of tagged-MR imaging as a modality of choice for performing estimation – or *data assimilation* – with a biomechanical heart model [1,10]. We thus propose a detailed methodology which relies on tag planes – as can be segmented from the tagged sequences [9] – to evaluate a discrepancy between the model simulations and the data. This discrepancy is then employed to feed a sequential data assimilation procedure to achieve the estimation. In order to assess this procedure we use synthetic measurements, namely, reference tag planes simulated based on a model representing an infarcted heart as observed in an animal experiment, and we estimate some regionalized values of the tissue contractility parameter, which has been shown to adequately characterize the seriousness of this type of pathology [4].

After summarizing the fundamental principles in Section 2, we present the specific procedure proposed in Section 3. We then describe the test case and present the actual estimation results in Section 4, before providing some concluding remarks.

D.N. Metaxas and L. Axel (Eds.): FIMH 2011, LNCS 6666, pp. 409–417, 2011.

2 Data Assimilation Principles

Data assimilation consists in using measurements to estimate the state variables – namely, the actual trajectory – of the system considered, and possibly some modeling parameters. In this context a model is represented by a dynamical system governing the state variable X representing the system configuration:

$$\dot{X} = A(X, \theta, t), \text{ with } \theta = \theta_0 + \zeta_\theta \text{ and } X(0) = X_0 + \zeta_X, \tag{1}$$

where A is a non-linear operator, θ a collection of distributed parameters that should be estimated in the procedure, θ_0 and X_0 are the *a priori* values for the parameters and initial conditions, and ζ_θ and ζ_X denote the corresponding uncertainties.

In data assimilation methodologies, the available measurements – also called observations – are described using an *observation operator* H. Namely, the measurement process is modeled by the application of H on the system state to produce a collection of signals Z:

$$Z = HX + \chi, \tag{2}$$

where H is taken here linear – as an example – and χ is a noise.

In order to take advantage of the information contained in the observations within the model, our approach is to use a so-called *sequential* data assimilation methodology – see [3] for a review of data assimilation strategies – in which the system dynamics is corrected to take into account the discrepancy between the model trajectory and the observations. In other words, we have for the *estimator* – also called *observer* – $(\hat{X}, \hat{\theta})$ of (X, θ)

$$\begin{cases} \dot{\hat{X}} = A(\hat{X}, \hat{\theta}, t) + G_X(Z - H\hat{X}), \quad \hat{X}(0) = X_0 \\ \dot{\hat{\theta}} = G_\theta(Z - H\hat{X}), \quad \hat{\theta}(0) = \theta_0 \end{cases} \tag{3}$$

where G_X is the *state gain operator* which is expected to guide the system towards the reference trajectory using the measurements, and G_θ is the *parameter gain operator* that dynamically corrects the parameters in order to recover the patient-specific values.

2.1 Model

In this paper, we aim at estimating some constitutive parameters of the model introduced in [15]. We will concentrate on estimating contractility parameters, which is relevant for capturing an infarct [4]. The electrical activation is supposed to be prescribed, hence we can focus on the mechanical behavior. Typically, the state variables of the system are the displacement and velocity fields $\underline{y}$ and $\underline{v}$, and some internal mechanical variables e_c, k_c, τ_c describing the strains, active stiffnesses and stresses in the sarcomeres.

In order to simplify the presentation we also assume that the pressures in the cavities are given, for example after post-processing – especially in terms

of time registration with the electrical activation – adequate measurements of the pressure obtained by catheterization. But the pressure variables could be included in the model by employing simplified valve and circulation models [15].

After spatial discretization by a finite element method, the model can be considered in the form of (1) with the state vector $X = (Y, V, \{e_c\}, \{k_c\}, \{\tau_c\})$ storing the degrees of freedom describing the above-described continuous fields. After time discretization the system can be written as

$$X_{n+1} = A_{n+1|n}(X_n, \theta, t_n), \text{ with } \theta = \theta_0 + \zeta_\theta \text{ and } X_{n=0} = X_0 + \zeta_X. \quad (4)$$

2.2 Information Extraction from the Measurements

Let us first assume that we can measure displacements on part of the domain. The observations Z are then given by (2), where H applies only on the displacement variables Y of the state X and we select – typically by interpolation – the relevant degrees of freedom of Y. In a first approach, tagged-MRI is a candidate for such a definition, since ideally material points can be identified and followed in such sequences. Unfortunately, the tagged-MRI modality does not exactly produce displacements of material points but imprints a grid in the domain and follows its "global" displacements in time. It is then only after a complex post-processing that we can obtain the point-wise displacements, a procedure requiring to register 3 sets of planes obtained for each image in the sequence [18,6,14,7]. A more straightforward approach is to segment the planes as is done e.g. in [17,9], and consider that this is the most accurate information contained in the measurements. We denote these segmented planes by

$$\mathcal{T}_t^I = \bigcup \Pi_t^I, \quad t = k\Delta t, 1 \leq k \leq N. \quad (5)$$

Hence, in this case we cannot describe the observation procedure – corresponding to the combination of the real measurement and its post-processing – as in (2). However, it has been proven in [12] that it is possible to modify (2) to adapt to observations given in the form of a sequence of moving surfaces. In fact, with standard Cine-MRI the observations consist in a sequence of surfaces $\mathcal{S}_t^I$ representing for example the endocardium and sometimes the epicardium of the left and/or right ventricle. We will use a similar approach here.

3 Tagged-MRI Data Assimilation

3.1 Definition of the Observation Operator

We then modify the observation equation (2), in order to take into account deforming planes instead of point-wise displacements. Following [12], we define a *discrepancy operator* adapted to moving surfaces. Let us consider a set of planes constituting a grid, $\mathcal{T}_0^m = \bigcup \Pi_0^m$, defined in the initial configuration. In the model simulations we can obtain the corresponding grid motion.

If the model is not perfectly personalized within the data, we can then compute the distance between every point in the grid and the actual segmented planes produced from the images. Hence, by computing the distance map between $\mathcal{T}_t^m$ and $\mathcal{T}_t^I$ in a Lagrangian formalism – namely computing the distances $\mathrm{dist}(\underline{\xi}+\underline{y}(\underline{\xi},t),\Pi_t^I)$, $\forall \underline{\xi} \in \Pi_0^m$, for all planes – we construct a non-linear *discrepancy operator* $D(Y,\mathcal{T}_t^I)$ between the measurements and the model that should replace in our corrections the computation of the linear discrepancy $Z - HX$. Note that in our case the discrepancy operator only applies on the displacement part Y of the state X. The *observer* then becomes

$$\begin{cases} \dot{\hat{X}} = A(\hat{X},\hat{\theta},t) + G_X D(\hat{Y},\mathcal{T}_t^I) \\ \dot{\hat{\theta}} = G_\theta D(\hat{Y},\mathcal{T}) \end{cases} \tag{6}$$

As a comparison, in [12] where the observations correspond to segmentations of a part $\mathcal{S}^m$ of the endocardium and/or the epicardium from Cine-MRI, the discrepancy operator is associated with a variational quantity in the form: For all test functions v^*,

$$\mathcal{P}_D(\underline{v}^*) = \int_{\mathcal{S}^m} \mathrm{dist}(\underline{\xi}+\underline{\hat{y}}(\xi,t),\mathcal{S}_t^I)\underline{\nu}\cdot\underline{v}^*\,dS, \tag{7}$$

where $\underline{\xi}$ is the coordinate in the reference configuration, $\underline{y}$ the displacement between the reference configuration and the configuration at time t, $\underline{\nu}$ is the normal to $\mathcal{S}_t^I$ where the distance is computed. Here, the same strategy leads to defining the variational discrepancy operator

$$\mathcal{P}_D(\underline{v}^*) = \sum_{\Pi_0^m \subset \mathcal{T}_0^m} \int_{\Pi_0^m} \mathrm{dist}(\underline{\xi}+\underline{\hat{y}}(\xi,t),\Pi_t^I)\underline{\nu}\cdot\underline{v}^*\,dS, \tag{8}$$

and in practice this is easily computed using the surface "mass matrix" $M_{\mathcal{T}_m^0}$ associated with this surface-integrated dot-product.

3.2 Filter Formulation

The filter is composed of two stages, the first of which concerning G_X with the aim to register the state of the simulated system on the measurements. As developed in [2] it is common in model-based segmentation algorithms to use $\mathcal{P}_D$ given in (7) or (8) in the balance of momentum equation as the work produced by an external force opposed to the discrepancy. However, [12] has proven that it is more effective in general to instead introduce this quantity as a correction in the continuity equation giving usually that the time-derivative of the displacement is the velocity. This original approach allows for the estimation error system governing the variable $\tilde{X} = X - \hat{X}$ to be stabilized to 0 as expected in a data assimilation procedure. We will denote the corresponding *discrete* filtered dynamical operator by $A^G_{n+1|n}$.

3.3 Parameter Estimation

The second stage of our filter is dedicated to parameter estimation, and uses the method introduced in [11], albeit adapted to a discrepancy operator instead of an observation operator. It reads:
Given adequate sampling rules, precompute particles $I_{[i]}, 1 \leq i \leq p+1$ *of zero mean value and unitary covariance, and associate an equal weight* $\frac{1}{p+1}$ *with each particle, all weights being collected in the diagonal of the matrix* D_α*. Then perform at each time step:*

– **Sampling:**

$$\begin{cases} C_n = \sqrt{(U^n)^{-1}} \\ \hat{X}^{n^+}_{[i]} = \hat{X}^{n^+} + L^n_X (C^n)^T I_{[i]}, \quad 1 \leq i \leq p+1 \\ \hat{\theta}^n_{[i]+} = \hat{\theta}^{n^+} + L^n_\theta (C^n)^T I_{[i]}, \quad 1 \leq i \leq p+1 \end{cases} \tag{9a}$$

– **Prediction:**

$$\begin{cases} \hat{X}^{n+1^-}_{[i]} = A^G_{n+1|n}(\hat{X}^{n^+}_{[i]}, \hat{\theta}^{n^+}_{[i]}, t^{n+1}) \\ \hat{X}^{n+1^-} = E_\alpha(\hat{X}^{n+1^-}_*) \\ \hat{\theta}^{n+1^-} = \hat{\theta}^{n+1^+} \end{cases} \tag{9b}$$

– **Correction:**

$$\begin{cases} L^{n+1}_X = [\hat{X}^{n+1^-}_*] D_\alpha [I_*]^T \in \mathcal{M}_{N,p} \\ L^{n+1}_\theta = [\theta^{n+1^-}_*] D_\alpha [I_*]^T \in \mathcal{M}_p \\ \Gamma^{n+1}_{[i]} = D(X^{n+1^-}_{[i]}, t^{n+1}) \\ L^{n+1}_\Gamma = [\Gamma^{n+1}_*] D_\alpha [I_*]^T \\ U^{n+1} = \mathbb{1} + \gamma_\chi (L^{n+1}_\Gamma)^T M_{\mathcal{T}^0_m} L^{n+1}_\Gamma \in \mathcal{M}_p \\ \hat{X}^{n+1^+} = \hat{X}^{n+1^-} - \gamma_\chi L^{n+1}_X (U^{n+1})^{-1} (L^{n+1}_\Gamma)^T M_{\mathcal{T}^0_m} E_\alpha(\Gamma^{n+1}_*) \\ \hat{\theta}^{n+1^+} = \hat{\theta}^{n+1^-} - \gamma_\chi L^{n+1}_\theta (U^{n+1})^{-1} (L^{n+1}_\Gamma)^T M_{\mathcal{T}^0_m} E_\alpha(\Gamma^{n+1}_*) \end{cases} \tag{9c}$$

where for particles set $X_{[i]}, 1 \leq i \leq p+1$*,* $E_\alpha(X_{[*]}) = \sum_{1 \leq i \leq p+1} \alpha_i X_{[i]}$ *and* $[X_*] \in \mathcal{M}_{N,p+1}$ *is a matrix where each column corresponds to a particle* $X_{[i]}$*.*
In this algorithm γ_χ denotes a scalar gain characterizing the level of confidence in the observation, and chosen with respect to the level of noise.

4 Estimation Results with Synthetic Data

4.1 Reference Model Based on Experimental Data

The model used in this study was based on an animal experiment described in [4]. A young farm pig with an extended antero-septal myocardial infarction was scanned by MRI, and pressures were measured by catheterization in the heart cavities and large vessels. The anatomical mesh was created with a subdivision of the left ventricle into 6 circumferential regions corresponding in the upper

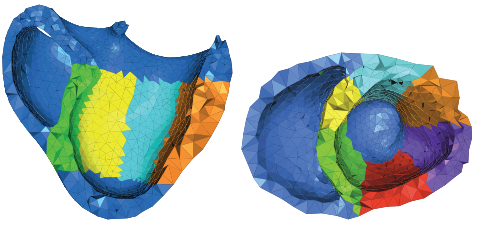

Fig. 1. Computational mesh with the 6 regions associated with localized contractility

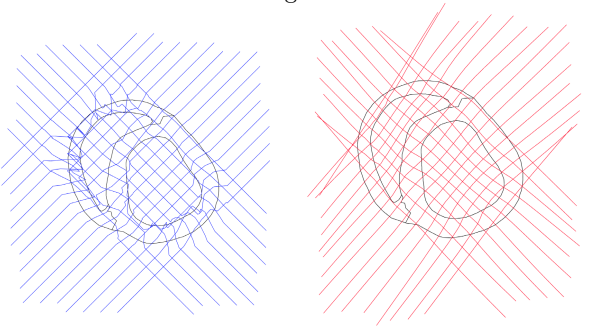

Fig. 2. Synthetic tag generation using imposed displacement only (left) or with regularization method (right)

third to the basal segments of the 17-segment subdivision of the left ventricle proposed by the American Heart Association (AHA), see Figure 1.

The direct model with constant contractility in the whole tissue does not adequately reflect the infarcted heart with hypokinetic antero-septal parts of the left ventricle. By decreasing the contractility by a factor 4 weighted by the proportion of infarcted tissue – as segmented from late enhancement images – in each of the 6 regions, we obtained a model close to the images. We used this "manually personalized model" to produce synthetic observations – namely, synthetic tags or LV endocardial and epicardial surfaces.

4.2 Generation of Synthetic Tags from the Model

In order to synthetically simulate the tag planes segmentation process, we use our model to deform in time a grid $\mathcal{T}_0$ defined at the initial time. For practical purposes, this grid is represented by a set of triangular meshes $\mathcal{T}_0^h$. We denote by $\underline{\mathrm{x}}_g(\underline{\xi}, t)$ the position field of the grid at time t in Lagrangian formalism – with corresponding displacement field $\underline{y}_g(\underline{\xi}, t)$. After discretization, this field is the collection of nodal displacements Y_g associated with the grid mesh. A first naive approach to compute the displacements of the grid from the model displacements would correspond to

$$\begin{cases} \underline{y}_g = \underline{y} - \underline{y}(0) & \text{if } \xi \in \Omega_0 \\ 0 & \text{otherwise} \end{cases} \Rightarrow Y_g = I_{\mathcal{T}_0^h \to \Omega_0^h}(Y - Y(0)) \tag{10}$$

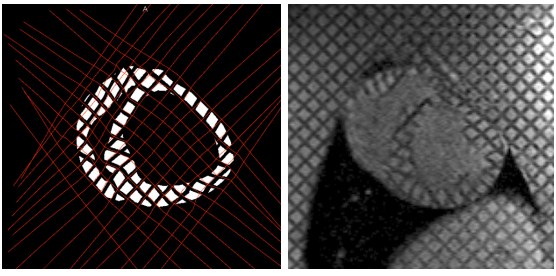

Fig. 3. Synthetic tags and tag planes (in red color) vs. real tagged MRI at end-systole

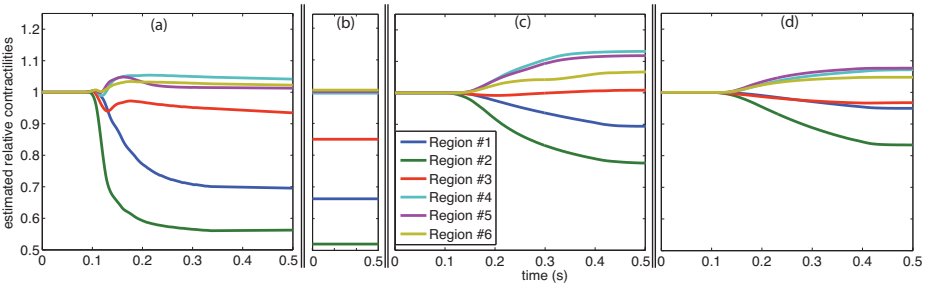

Fig. 4. (a) Estimated contractility parameters using synthetic tag planes with low noise covariance, compared with ground truth reference (b). Estimated contractility with realistic noise covariance. Comparison with estimation based on LV surfaces.

where $I_{\mathcal{T}^h \to \Omega_0^h}$ denotes the interpolation operator of the triangular mesh $\mathcal{T}^h$ within the tetrahedral domain Ω_0^h. However, this produces very irregular results, because points of the grid meshes outside the domain but near the boundary do not displace, hence their connection to nearby points inside the domain may be very abrupt, see Fig. 2 left. To obtain more regular results as classically produced by segmentation methods – see e.g. [9] – we instead considered thick tag layers, defining for each plane a 3D object $\mathcal{G}_0$ as a linearly-elastic system for which displacements are prescribed on the interior mid-surface. Far from the domain Ω_0, for the bounding box boundary both homogeneous Dirichlet and Neumann boundary conditions have been tested. The Neumann conditions give better results near Ω_0. Note that this problem can be solved in a penalized form by minimizing the criterion

$$\min_{\underline{y}} \tfrac{1}{2}\|\underline{y}_g - (\underline{y} - \underline{y}(0))\|^2_{L^2(\mathcal{T}_0 \cup \Omega_0)} + \tfrac{\epsilon}{2}\|\underline{y}\|^2_{\mathcal{E}_m},$$

where $\|.\|^2_{\mathcal{E}_m}$ is the internal energy norm and ϵ is a small parameter, which shows this strategy is a regularization of displacement prescription.

We display in Figure 3 an example of synthetic tag planes superimposed with the corresponding image and compared with an actual image.

4.3 Estimation Results

Figure 4-(a) shows the regional contractility estimation results, using synthetic tag planes as observations and a very low level of expected noise. By construction, the estimated parameter values evolve during the simulation period – corresponding to a complete heartbeat – and the final value provides the actual estimation. Note in each region these values stabilize and nearly reach the reference value used in the generation of the synthetic measurements.

Figure 4-(c,d) displays the estimated parameters obtained with a more realistic noise level and compared with estimation results obtained with segmented endo- and epicardium [5]. Although the parameters do not converge to the reference values as accurately as in Fig. 4-(a), we can see a comparable sensitivity of the estimation in each region between the two types of observations, except for Region #1. In fact, we impose a visco-elastic boundary condition as in [13] on a part of Region #1, and this type of boundary condition clearly decreases the estimation sensitivity in the neighboring tissue. However, the results illustrate that using the tagged-MR images can very significantly improve this sensitivity.

5 Concluding Remarks

In this paper, we successfully employed synthetic observations representing planes given by tagged-MR images in a contractility estimation procedure. The intrinsically low observability of some regions – as for example those influenced by imposed boundary conditions – can increase when using richer observations provided by tagged-MR images. Of course, we could also combine tag plane information with segmented endo- and epicardium to further enhance observability.

The next step in this work would be to use tag planes extracted from real MR images in a similar data assimilation procedure. This image processing task is still quite challenging, although an alternative estimation method could be devised to use only segmented 2D tag images [8]. As a global conclusion, the promising results presented in this work indicate that tagged data render localized estimation more discriminate and accurate, which strongly motivates further efforts.

References

1. Augenstein, K.F., Cowan, B.R., LeGrice, I.J., Nielsen, P.M.F., Young, A.A.: Method and apparatus for soft tissue material parameter estimation using tissue tagged magnetic resonance imaging. J. Biomech. Eng. 127(1), 148–157 (2005)
2. Billet, F., Sermesant, M., Delingette Delingette, H., Ayache, N.: Cardiac motion recovery by coupling an electromechanical model and cine-MRI data: First steps. In: Proc. of Computational Biomechanics for Medicine III. MICCAI Workshop (2008)
3. Blum, J., Le Dimet, F.X., Navon, I.M.: Data assimilation for geophysical fluids. In: Temam, R., Tribbia, J. (eds.) Handbook of Numerical Analysis: Computational Methods for the Atmosphere and the Oceans. Elsevier, Amsterdam (2008)

4. Chabiniok, R., Chapelle, D., Lesault, P.-F., Rahmouni, A., Deux, J.-F.: Validation of a biomechanical heart model using animal data with acute myocardial infarction. In: Proc. of CI2BM 2009 - MICCAI Workshop (2009)
5. Chabiniok, R., Moireau, P., Lesault, P.-F., Rahmouni, A., Deux, J.-F., Chapelle, D.: Trials on tissue contractility estimation from cardiac Cine MRI using a biomechanical heart model. In: Metaxas, D.N., Axel, L. (eds.) FIMH 2011. LNCS, vol. 6666, pp. 304–312. Springer, Heidelberg (2011)
6. Chandrashekara, R., Mohiaddin, R.H., Rueckert, D.: Analysis of 3D myocardial motion in tagged MR images using non-rigid image registration. IEEE Trans. Med. Imaging 23(10), 1245–1250 (2004)
7. Chen, T., Wang, X., Chung, S., Metaxas, D.N., Axel, L.: Automated 3D motion tracking using Gabor filter bank, robust point matching, and deformable models. IEEE Trans. Med. Imaging 29(1), 1–11 (2010)
8. Clarysse, P., Basset, C., Khouas, L., Croisille, P., Friboulet, D., Odet, C., Magnin, I.E.: Two-dimensional spatial and temporal displacement and deformation field fitting from cardiac magnetic resonance tagging. Med. Image Anal. 4(3), 253–268 (2000)
9. Declerck, J., Denney, T.S., Oztürk, C., O'Dell, W., McVeigh, E.R.: Left ventricular motion reconstruction from planar tagged MR images: a comparison. Phys. Med. Biol. 45(6), 1611–1632 (2000)
10. Liu, H., Shi, P.: Maximum a posteriori strategy for the simultaneous motion and material property estimation of the heart. IEEE Trans. Biomed. Eng. 56(2), 378–389 (2009)
11. Moireau, P., Chapelle, D.: Reduced-order Unscented Kalman Filtering with application to parameter identification in large-dimensional systems. Cont. Optim. and Calc. Variat. (2010)
12. Moireau, P., Chapelle, D., Le Tallec, P.: Filtering for distributed mechanical systems using position measurements: Perspectives in medical imaging. Inverse Prob. 25(3), 35010 (2009)
13. Moireau, P., Xiao, N., Astorino, M., Figueroa, C.A., Chapelle, D., Taylor, C.A., Gerbeau, J.-F.: External tissue support and fluid-structure simulation in blood flows. Biomech. Model. Mechanobiol. (2011)(in press)
14. Oubel, E., De Craene, M., Gazzola, M., Hero, A.O., Frangi, A.F.: Multiview registration of cardiac tagging MRI images. In: Proc. of ISBI 2007 (2007)
15. Sainte-Marie, J., Chapelle, D., Cimrman, R., Sorine, M.: Modeling and estimation of the cardiac electromechanical activity. Comput. Struct. 84, 1743–1759 (2006)
16. Sermesant, M., Moireau, P., Camara, O., Sainte-Marie, J., Andriantsimiavona, R., Cimrman, R., Hill, D.L., Chapelle, D., Razavi, R.: Cardiac function estimation from MRI using a heart model and data assimilation: advances and difficulties. Med. Image Anal. 10(4), 642–656 (2006)
17. Young, A.A.: Model tags: direct three-dimensional tracking of heart wall motion from tagged magnetic resonance images. Med. Image Anal. 3(4), 361–372 (1999)
18. Young, A.A., Kraitchman, D.L., Dougherty, L., Axel, L.: Tracking and finite element analysis of stripe deformation in magnetic resonance tagging. IEEE Trans. Med. Imaging 14(3), 413–421 (1995)

Sensitivity Analysis of Mesh Warping and Subsampling Strategies for Generating Large Scale Electrophysiological Simulation Data

Corné Hoogendoorn[1,2], Ali Pashaei[1,2], Rafael Sebastian[3], Federico M. Sukno[1,2], Oscar Cámara[1,2], and Alejandro F. Frangi[1,2,4]

[1] Center for Computational Imaging and Simulation Technologies in Biomedicine (CISTIB), Universitat Pompeu Fabra, Barcelona, Spain
[2] Networking Center on Biomedical Research - CIBER-BBN, Barcelona, Spain
[3] Department of Computer Science, Universitat de Valencia, Valencia, Spain
[4] Institució Catalana de Recerca i Estudis Avançats (ICREA), Barcelona, Spain

Abstract. The analysis of large-scale simulation data from virtual populations can be effective to gain computational insight into disease mechanisms and treatment strategies, which can serve for generating hypotheses for and focusing subsequent clinical trials. This can be instrumental in shortening the critical path in medical product development and more cost-effective clinical trials. A previously published pipeline established point correspondence among volumetric meshes to enable meaningful statistics on cardiac electrophysiological simulations on the anatomical distribution of a large-scale virtual population. Thin Plate Splines (TPS), derived from surface deformations, were used to warp a template volumetric mesh, removing the costly operation of repeated volumetric meshing from the pipeline, but potentially at the cost of the volumetric mesh quality. In this work we compare (1) the influence of using TPS versus volumetric meshing of deformed surface meshes, and (2) the influence of surface mesh subsampling prior to the TPS computation. Our results suggest that warping of a template volumetric mesh introduces errors in electrophysiological simulation results of around 4 ms, while having computational times per mesh on the order of seconds, at surface subsampling rates of up to 80%.

1 Introduction

Statistical analysis of simulation results is expected to improve understanding of the physiological phenomena underlying clinical observations relating to particular pathologies and therapy options. Such simulations, however, present a quantity of variables that can only be effectively studied on very large populations, and therefore are best served by virtual populations to focus hypotheses and aid in the design of clinical trials.

Unbiased comparison of simulation results obtained in different anatomies cannot be accomplished through independent meshing of each geometry and a final interpolation step for finding closest correspondences. This is primarily

D.N. Metaxas and L. Axel (Eds.): FIMH 2011, LNCS 6666, pp. 418–426, 2011.

because without correspondence, the deformation between the geometries is not unique. The ability to find proper spatial correspondences on large scale in silico computational models is therefore of great importance to perform meaningful statistical analysis of the simulation results.

Although the application itself is beyond the scope of this paper, this work was developed in the context of using simulations of cardiac electrical activation to identify responder profiles for Cardiac Resynchronization Therapy [1]. In an earlier work, a virtual population derived from a surface Point Distribution Model (PDM) of the left ventricle (LV) was used to demonstrate a pipeline for large scale personalized fast cardiac electrophysiological (EP) simulations [2].

Instead of using optimally tetrahedralized geometries for the simulation and subsequent mapping of the results using a warped template, the warped template itself was used for the simulations. As such, it bypassed the potentially expensive process of tetrahedralization of each individual anatomy, and enforced node correspondence between all volumetric meshes across the population. However, the mesh warping may degrade the quality of the volumetric meshes. In this work we investigate the influence of the warp on simulation results obtained from fast electrophysiological computational models, since they may be affected by the volumetric element quality degradation. In addition, because the computation of the warps from all surface points is time consuming, we analyze five different strategies for subsampling the landmark set used as input to computing this Thin Plate Splines (TPS) based warp [3], in order to have reasonable computational times while having small errors due to the subsampling.

2 Methods

The pipeline for large scale personalized fast cardiac EP simulations, as presented previously [2], is shown in Fig. 1. It exploits point correspondence between a template surface mesh and a new surface mesh to warp a template volumetric mesh. This surface deformation is interpolated using TPS [3] and the resulting warp is applied to the template volumetric mesh. The volumetric meshes are completed by including structures, relevant to the simulation of cardiac electrical activation, based on the geometry of the warped volumetric mesh.

Computing the TPS interpolation involves the inversion of a matrix of size $(n_k+3)\times(n_k+3)$, where n_k is the number of landmarks used to define it [3]. With surface meshes defined by thousands of points, this presents a computational load that may quickly exceed the order of minutes. Therefore, we compute the TPS interpolation from a subset of the surface points only. However, the subsampling rate and strategy may influence the final result, in a similar way to the influence of registration success in earlier works employing template mesh warping (e.g., [4,5,6]).

We compare five subsampling strategies to assess their influence on the resulting warped tetrahedralized template meshes, and on the simulation results. For each strategy we use varying rates of subsampling, and then we compare the results to those obtained without subsampling.

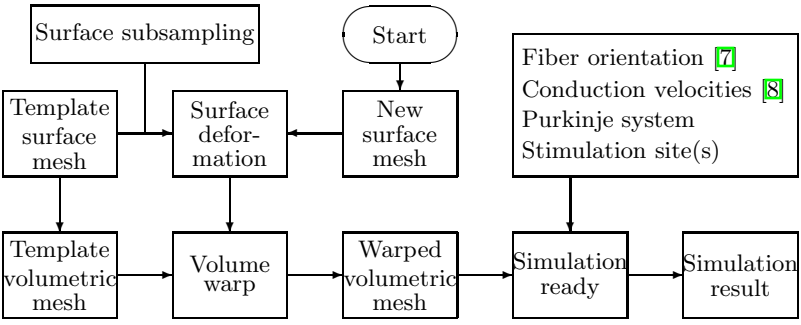

Fig. 1. The pipeline for personalization of EP simulations

The analyzed strategies are as follows:

Decimation (DC): This follows the work of Schroeder *et al.* [9] but without the constraint of topology preservation since all that is required are the remaining surface points. For each vertex, the distance to the average plane of its neighboring vertices is computed, reflecting the surface representation error generated if the vertex is removed. Iteratively, the vertex with the smallest error is removed and the resulting hole retriangulated until the decimation target has been reached.

Quadric Clustering (QC): This uses the work of Lindstrom [10]. The bounding box of the mesh is subdivided into a user-defined number of quadrants, and the set of vertices in each quadrant is reduced to a single point. The point selection is based on minimizing a quadric error metric introduced by the removal of the other points.

Farthest Point Sampling (FP): This sampling strategy remains close to the work of Eldar *et al.* [11] for progressive image coding. It comprises the iterative insertion of the point that maximizes the resulting nearest neighbor distance. That is, with L denoting all points of the surface mesh, P the already inserted points and Q the remainder ($L = P \cup Q, P \cap Q = \emptyset$) we find $\text{argmax}_{q \in Q}\, d(q, P)$. The distance between point and set $d(p, P)$ is defined as $d(p, P) = \min_{p_i \in P} d(p, p_i)$. For d we use both a Euclidean distance (FPeu), and a distance along the surface mesh edges (quasi-geodesic; FPqg).

Greedy Surface Error Reduction (GR): Iteratively, the surface point with greatest point-to-point error is added to the set of landmarks, until the maximum point-to-point error is below a user-defined threshold. The sampling is initialized with four landmarks obtained using the FPeu strategy.

The DC and QC strategies originated in the computer graphics community, where surface simplification is used to remove superfluous mesh detail [9,10]. The main goal is to introduce as little surface error as possible, making the resulting landmark set dependent on geometry. In contrast, the FPeu and FPqg approaches provide a uniform sampling [11], which should improve the similarity between the TPS warp and the surface deformation. With the GR approach we

make this similarity explicit, at a cost of repeatedly computing TPS on landmark sets of increasing size.

3 Experiments and Results

3.1 Data

Our population of left ventricle geometries is generated in the same way as in [2], using a Principal Component Analysis based PDM trained using 80 end-diastolic LV surface meshes. The population corresponds to the corners of the cube in shape space that extends three standard deviations from the mean in the first three modes of variation. Since the deformation vectors in shape space have the greatest length possible under the constraints imposed, we assume that the differences and errors of meshes and simulation results reported here represent upper bounds for any other shape generated from the same model under the same constraints.

Gold standard ('non-warped') meshes were generated by tetrahedralizing the deformed surface meshes using the same settings as for constructing the template volumetric mesh. For this we used TetGen[1], an open source volumetric meshing software. Table 1 lists the parameters and values used for each approach.

Table 1. Overview of parameters

Operation	*Parameter*	*Range/Value*	*Step*
DC	Target reduction	0-90%	5%
DC	Target reduction	91-99%	1%
QC	Number of subdivisions	4-17	1
FP	Number of landmarks	Resulting from DC, QC	
GR	Maximum surface p2p error	0.5-1.0 mm	0.1 mm
TPS	Radial basis function	$\lvert R\rvert$	n/a
Tetrahedralization	Element volume (mean)	1.5 mm^3	n/a
Tetrahedralization	Element radius-edge ratio (max)	1.2	n/a

3.2 Volumetric Mesh Differences

The reason for using a subset of vertices to compute the TPS interpolation is the time it takes to invert a $(n_k + 3) \times (n_k + 3)$ matrix, where n_k is the number of landmarks used to define it. In general, this time will greatly exceed the time it takes to do the subsampling (with the exception of the greedy approach). The direct result of using different vertices and different numbers of vertices for the TPS interpolation is measurable in the node positions of the warped volumetric mesh. Node-to-node differences were measured, with the root mean squares reported in Fig. 2(a), against the time used for subsampling, TPS computation and

[1] Weierstrass Institute for Applied Stochastics and Analysis. http://tetgen.berlios.de

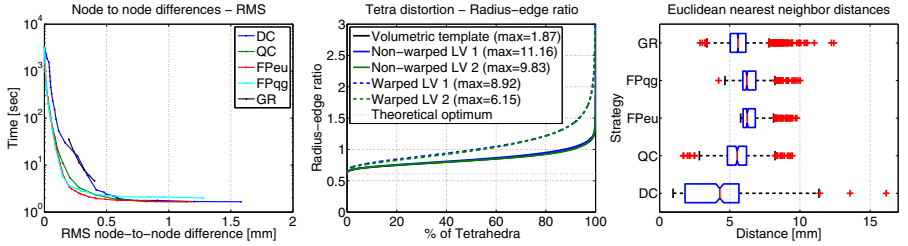

(a) (b) (c)

Fig. 2. Mesh-based comparisons: (a) root mean square (RMS) node-to-node distances; (b) radius-edge ratios of tetrahedrals in two LV's on opposite ends of a shape space diagonal. (c) Landmark Euclidean nearest neighbor distances.

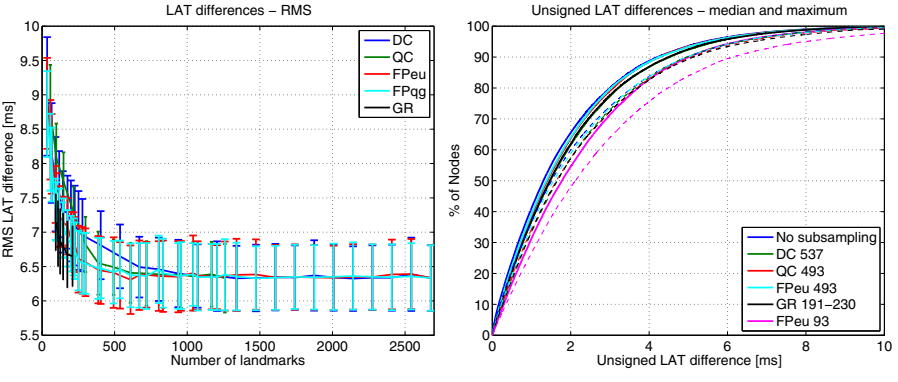

(a) (b)

Fig. 3. (a) RMS Local Activation Time (LAT) errors for each strategy and number of landmarks, mean and two standard errors. (b) Cumulative histogram of median (solid line) and maximum (dashed line) LAT errors. Numbers in the legend are landmark counts.

node transformation. The DC and GR strategies require more time to achieve the same RMS node-to-node difference.

Additionally, quality measures of the tetrahedral elements can be used to evaluate the influence, even though the values in the gold standard case (no subsampling) are suboptimal due to the application of warping per se. We report the distribution of radius-edge ratios in Fig. 2(b). The bulk of tetrahedra generated by tetrahedralization of the deformed surface meshes has a better radius-edge ratio, but the worst elements may be worse than those obtained by warping.

As FPeu appears to have produced the better meshes in terms of RMS node-to-node difference, we show the resulting Euclidean nearest neighbor distances obtained using the five strategies in Fig. 2(c), for subsampling to 493 landmarks (492 for DC; 8×493 for GR). This should provide a large enough sample size yet high enough reduction rate for this illustration. In line with the differences

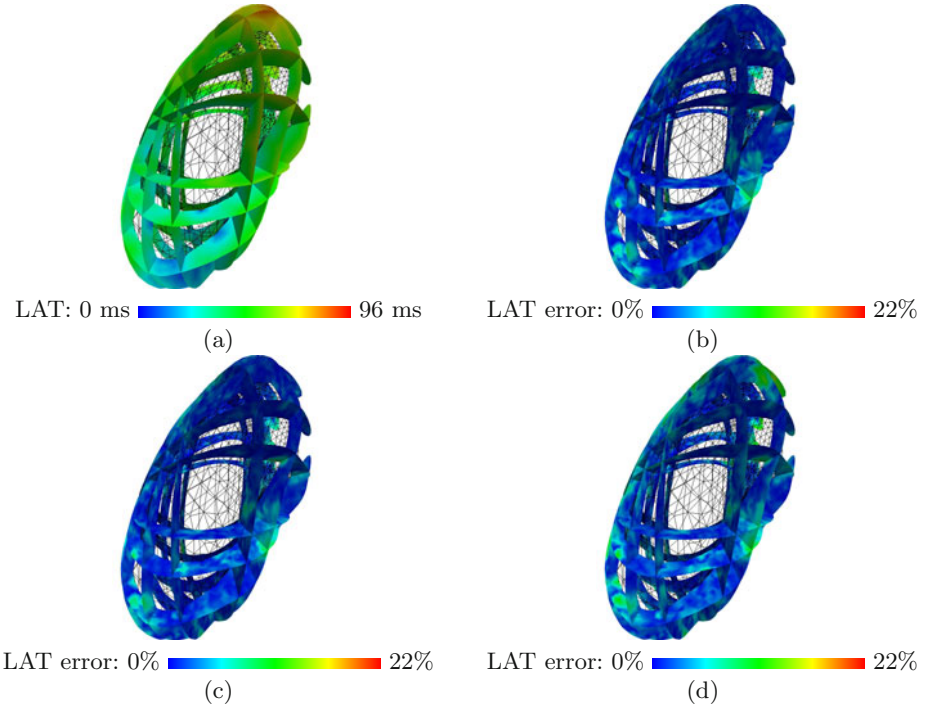

Fig. 4. (a) Gold standard Local Activation Times (LAT's); (b-d) unsigned LAT error at (b) no subsampling, (c) 80% subsampling and (d) 95% subsampling, all using the FPeu strategy, on one of the geometries. The 22% error is only reached in (d), with fewer than 50 nodes exceeding 15%.

observed in the resulting meshes, the QC, FPqg and greedy approaches produce similarly uniform sampling, as illustrated by the overlap in the second and third quartiles and the similarity in inter-quartile distances.

3.3 Simulation Result Differences

The influence on the simulation results is more important than the node-wise and element-wise differences between the meshes. Using the pipeline from Fig. 1, we set up simulations of electrical activation on each of the volumetric meshes. This includes fiber orientations as per Streeter [7], anisotropic conduction velocities derived from Caldwell *et al.* [8] and activation of Purkinje terminals with delays based on the work of Durrer *et al.* [12]. The terminals are defined by the same set of 100 endocardial surface mesh vertices throughout the entire series of simulations, using the natural correspondences between the meshes.

The simulation itself is based on a simple wave propagation model based on the Hamilton-Jacobi family of equations, specifically the Eikonal equation, which formulate mechanics such that the motion of a particle can be represented

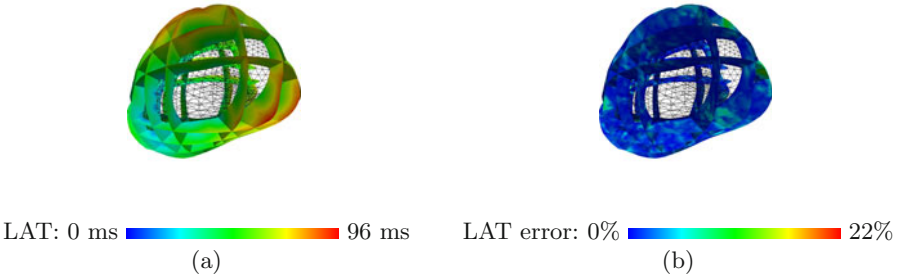

Fig. 5. (a) Gold standard Local Activation Times (LAT's); (b) unsigned LAT error at no subsampling, on one of the geometries (most dissimilar to the geometry used in Fig. 4).

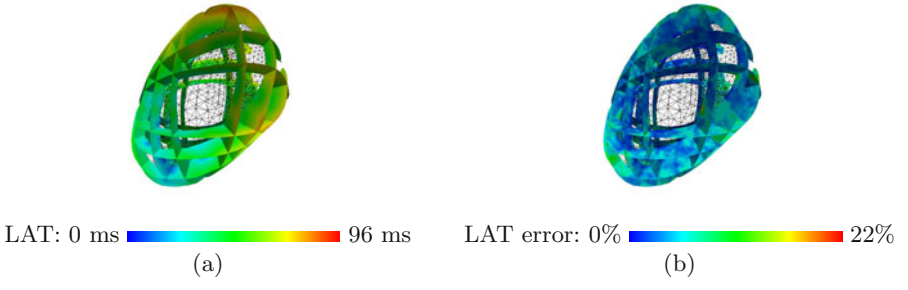

Fig. 6. (a) Mean Local Activation Times (LAT's) computed over all 9 geometries; (b) maximum LAT error computed over all 9 geometries at 80% subsampling.

as a wave. To solve the Eikonal equation, we used the Fast Marching Method introduced by Sethian [13], implemented in OpenCMISS[2].

Comparisons were made between meshes obtained using the non-warped strategy, using the same settings used to obtain the template volumetric mesh (see Table 1), and the warped template meshes. Local Activation Times (LAT) in the non-warped meshes were measured at the node locations of the template warped using all 2677 surface vertices as landmarks, using linear interpolation where necessary. Fig. 3(a) illustrates how landmark counts greater than 500 landmarks do not further decrease the RMS LAT differences. Fig. 3(b) shows that the central tendencies of the differences at around 500 landmarks are very similar across the different subsampling strategies and with respect to no subsampling, at just over 4 ms at the 90th percentile. Much stronger subsampling (to $\leq 5\%$) increases this difference in LAT, with the best and fastest method producing 90th percentile median errors of up to 5 ms.

In Figs. 4(b) and 5(b) we illustrate the error in LAT introduced by the warping approach as a percentage of the gold standard LAT. Panels (b-d) of Fig. 4 illustrate the additional effect of the subsampling on this error. Finally, Fig. 6 illustrates the possibility to map results to another geometry, and the consequent

[2] Open Continuum Mechanics, Image analysis, Signal processing and System identification. Website: http://www.opencmiss.org

possibility to analyze these results. As an example, we used the mean geometry and show the mean LAT in panel (a), and the maximum relative error in LAT observed at 80% subsampling in panel (b), with the addition of this same measure at 95% subsampling for the FPeu strategy.

4 Discussion and Conclusions

We investigated the effect of warping and of subsampling prior to warping, quantifying this effect using differences in mesh node location, element quality, and simulation results.

We believe that warping is a viable alternative to remeshing with the goal of enabling intra-population comparison of simulation results based on the fast solution of Eikonal equations; absolute differences in simulation results are small enough compared to remeshing, at a 90th percentile difference of 5 ms. We believe these differences to be at least in part due to different node valence and edge orientations, in combination with propagation anisotropy. Higher mesh resolution would resolve this.

Subsampling introduces little to no additional error in the simulations, up to 80% reduction. Probably, TPS interpolation of warping vectors closely resembles the ground truth due to strong correlation between warp vectors associated with neighboring surface mesh vertices. The strategy employed for subsampling is of little influence either, up to 80% reduction. Greedy reduction allows for further reduction but at greater computational cost. Of the remaining approaches we tested, farthest point techniques appear to be the most robust. Probably they best enable the TPS to capitalize on the correlation between warp vectors of closely spaced vertices, and therefore avoid oversampling in regions of high vertex density.

The fast simulations are guaranteed to converge; this is very different for simulations using highly detailed biophysical models. For biophysical models, our method could provide a starting point for mesh generation. Point correspondence can be established a priori, and degenerate elements can be resolved prior to simulation by node insertion operations, thus preserving the point correspondence. Further work will focus on the applicability of our technique in this area.

Acknowledgments

This work was partly funded by the Integrated Project euHeart (FP7/ICT-2007-224495) from the European Commission's 7th Framework Programme, and by the Spanish Ministry of Innovation and Science through grant TIN2009-14536-C02-01, Plan E and FEDER, and through the cvREMOD project (CEN-20091044) under the CENIT programme from the Spanish CDTI-MICINN.

References

1. Yu, C.-M., Fung, J.W.-H., Zhang, Q., Sanderson, J.E.: Understanding nonresponders of cardiac resynchronization therapy – current and future perspectives. J. Cardiovasc. Electrophysiol. 16(10), 1117–1124 (2005)

2. Hoogendoorn, C., Pashaei, A., Sebastián, R., Sukno, F.M., Cámara, O., Frangi, A.F.: Influence of geometric variations on LV activation times: A study on an atlas-based virtual population. In: Camara, O., Pop, M., Rhode, K., Sermesant, M., Smith, N., Young, A. (eds.) STACOM 2010. LNCS, vol. 6364, pp. 242–251. Springer, Heidelberg (2010)
3. Bookstein, F.L.: Principal warps: Thin-plate splines and the decomposition of deformations. IEEE Trans. Pattern Anal. Mach. Intell. 11(6), 567–585 (1989)
4. Lamata, P., Niederer, S., Barber, D., Norsletten, D., Lee, J., Hose, R., Smith, N.: Personalization of cubic hermite meshes for efficient biomechanical simulations. In: Jiang, T., Navab, N., Pluim, J.P.W., Viergever, M.A. (eds.) MICCAI 2010. LNCS, vol. 6362, pp. 380–387. Springer, Heidelberg (2010)
5. Camara, O., Schweiger, M., Scahill, R.I., Crum, W.R., Sneller, B.I., Schnabel, J.A., Ridgway, G.R., Cash, D.M., Hill, D.L.G., Fox, N.C.: Phenomenological model of diffuse global and regional atrophy using finite-element methods. IEEE Trans. Med. Imaging 25(11), 1417–1430 (2006)
6. Barber, D.C., Oubel, E., Frangi, A.F., Hose, D.R.: Efficient computational fluid dynamics mesh generation by image registration. Med. Image Anal. 11(6), 648–662 (2007)
7. Streeter, D.D.: Gross morphology and fiber geometry of the heart. In: Berne, R.M., Sperelakis, N., Geigert, S.R. (eds.) Handbook of Physiology: The Cardiovascular System. The Heart, vol. I, pp. 61–112. American Physiology Society (1979)
8. Caldwell, B.J., Trew, M.L., Sands, G.B., Hooks, D.A., LeGrice, I.J., Smaill, B.H.: Three distinct directions of intramural activation reveal nonuniform side-to-side electrical coupling of ventricular myocytes. Circ. Arrhythm. Electrophysiol. 2(4), 433–440 (2009)
9. Schroeder, W.J., Zarge, J.A., Lorensen, W.E.: Decimation of triangle meshes. In: Proc. ACM SIGGRAPH, pp. 65–70 (1992)
10. Lindstrom, P.: Out-of-core simplification of large polygonal models. In: Proc. ACM SIGGRAPH, pp. 259–262 (2000)
11. Eldar, Y., Lindenbaum, M., Porat, M., Zeevi, Y.Y.: The farthest point strategy for progressive image sampling. IEEE Trans. Image Process. 6(9), 1305–1315 (1997)
12. Durrer, D., van Dam, R.T., Freud, G.E., Janse, M.J., Meijler, F.L., Arzbaecher, R.C.: Total excitation of the isolated human heart. Circulation 41(6), 899–912 (1970)
13. Sethian, J.A.: A fast marching level set method for monotonically advancing fronts. Proc. Natl. Acad. Sci. USA 93(4), 1591–1595 (1996)

Effect of Scar Development on Fast Electrophysiological Models of the Human Heart: In-Silico Study on Atlas-Based Virtual Populations

Ali Pashaei[1,2], Corné Hoogendoorn[1,2], Rafael Sebastián[3], Daniel Romero[1,2], Oscar Cámara[1,2], and Alejandro F. Frangi[1,2,4]

[1] Center for Computational Imaging and Simulation Technologies in Biomedicine (CISTIB), Universitat Pompeu Fabra, Barcelona, Spain
[2] Networking Center on Biomedical Research - CIBER-BBN, Barcelona, Spain
[3] Computational Multi-Scale Physiology Lab, University of Valencia, Spain
[4] Institució Catalana de Recerca i Estudis Avançats (ICREA)

Abstract. The main goal of this work is to study the effect of scar development in the electrophysiological function of the human left ventricle by statistically analyzing large-scale simulation data including hypertrophic and dilated hearts. Electrophysiological simulations are obtained by solving the classical Eikonal equation in both the ventricular tissue and a customized Purkinje system. This Purkinje system is obtained assuming a geodesic rule to connect different Purkinje-myocardial junctions into a tree-like structure. Infarction shape and function is modeled with taking into account the occlusion in coronary arteries. Infarct, core and border zones of the scar are estimated by calculating blood diffusion in the region of occlusion. Three use cases are studied: no infarction, infarction due to one occlusion; infarction due to two occlusions. The electrophysiological simulations are run on a large atlas-based virtual population composed by 125 left ventricular geometries with known correspondences, derived from a Point Distribution Model of the left ventricle, as well as in 14 dilated and 20 hypertrophic real cases. The obtained results demonstrate a substantial effect of the scar characteristics in electrophysiological function of the heart, being this effect more relevant on the dilated hearts than in the hypertrophic cases. In particular, dilated cases had a more delayed activation than hypertrophic ones.

1 Introduction

Computational models are being used as tools to investigate the complex electrophysiological function of the heart and related diseases such as cardiac arrhythmia or fibrillation, as well as to assist on the treatment planning of complex procedures such as radio-frequency ablation or cardiac resynchronization therapy. In particular, the inclusion of the Purkinje system and infarcted tissue have a great impact on the simulation results. Recent studies have shown the critical role of the inclusion of the Purkinje system in electrophysiological models [1, 2].

D.N. Metaxas and L. Axel (Eds.): FIMH 2011, LNCS 6666, pp. 427–436, 2011.

In addition, some studies with ischemia models have demonstrated a substantial effect of scar function[3] and size [4] on the electrophysiological simulation results. These changes may become more important in the presence of cardiomyopathies where the ventricular geometry may remodel into an hypertrophy or dilatation.

In this paper, we study the effect of scar development on the electrophysiological function of the myocardium in a large-scale database composed of 159 Left Ventricular (LV) geometries, including normal, hypertrophic and dilated hearts. These geometries have known correspondences among them, allowing to have meaningful correspondence of the structural data on the simulations. Infarction size and shape are modeled by a process based on occlusion of coronary arteries and collateral blood supply from surrounding regions. Functional changes are estimated by the rate of surviving cells. In addition to the infarction, the Purkinje system is also modeled using a computational approach that first establishes the position of the terminals or Purkinje-myocardial junctions based on histological information.

2 Methods

2.1 Modeling Infarction

Myocardial infarction results from the interruption of blood supply to the myocardium, causing necrosis of the heart cells. This is most commonly due to occlusion (blockage) of a coronary artery following the rupture of a vulnerable atherosclerosis plaque. There are many cell level properties that change under restriction of blood supply and result in ischemia and scar formation [3], however here we focus on a tissue-level model for infarct formation based on constraints from myocardium blood supply. We model the process with the following steps.

i. Coronary artery mapping. In this procedure, we first map to the computational domain the main coronary arteries where occlusion has significant regional effects. We used knowledge-based pictogram from the BARI/ACC/AHA guidelines for coronary angiography [5] to do this mapping. These guidelines provide the anatomic angiographic definition of the coronary system for nomenclature of the 37 most frequently encountered coronary artery vessels. The coronary artery in left ventricle includes two left anterior descending, and circumflex arteries being mapped in the computational domain as is shown in Fig. 1(a). The mapping procedure is divided in two stages in our study: i) a first manual delineation of the beginning and end points for each vessel from the guideline on the computation domain; ii) and second stage using the geodesic solver to find the shortest path between two points to construct the vessel. This procedure provides correspondence between the nodes in the coronary artery tree and the computational heart model that is going to be used for region decomposition in the next step.

ii. Circulation regions decomposition. Based on the location of the coronary artery vessels, we decompose the computational domain of the myocardium

into the regions corresponding to each vessel. We assume that for each point in the domain the blood supply is provided by the nearest arterial vessel. This assumption assigns a uniform capillary vasculature and isotropic porosity for the domain. We use the geodesic solver to find the nearest vessels to the computational node. Fig. 1(b) shows the decomposed domains for the Distal Left Anterior Descending artery and third Posterior Descending Septal Perforator artery that are corresponding to vessel numbers 14 and 9 from BARI/ACC/AHA guidelines, respectively.

iii. Modeling blood diffusion. Occlusion of a coronary artery blocks blood supply to the region corresponding to that artery. However, the collateral blood supply from nearby arteries still supports the cells in the border area. The mechanism for this support is provided by the diffusion of blood through the boundary of the occluded region. Due to the limitations of this mechanism, the main support goes to the cells that are near to the boundary of the region. In this paper, as a simplification of the model, we assume that the diffusion in the medium is following homogeneous properties whereas intra- and extra-cellular heterogeneity does not change the transfer process between the cells. With these assumptions, we isolate the damaged region and use the equation below to calculate the diffusion of blood supply, $u(x)$ in that region.

$$-k.\frac{\partial u(x)}{\partial x} = q,\ x \in \Omega. \tag{1}$$

where $u(x)$ is normalized blood perfusion with respect to the normal tissue. Perfusion is defined as the temporal change of blood volume per unit volume of tissue, q is the local flux of blood perfusion to the region and k is diffusion coefficient of the porous medium. This equation is analogous to Darcy's Law for the flow through a porous medium. It means that the rate of blood perfusion through the boundary of the ischemic region is proportional to the negative gradient in the blood perfusion and to the area normal to the gradient through which blood is diffusing. Then, in the computational domain u is equal to 1 at the surrounding normal tissue and it changes in the porous media of the ischemic zone according to the distance from the zone with normal blood supply. Through this modeling procedure, it could be expected that the region with the lowest blood supply would be in the core of the damaged region and not in its source coronary vessel area.

In this study, we assume a constant flux q in the region. We use a ratio of $q/k = 1/3$ for this simulation that corresponds to the range of data from the literature on the thickness of the border zone [6]. To solve this PDE in the isolated region we apply boundary condition $u = 1,\ x \in \partial\Omega$ with full blood supply. Fig. 1(c) shows the result from this simulation on the occlusion happened on the same coronary vessels 14 and 9.

iv. Density of healthy cells. It is assumed that the rate of surviving cells in the damaged region is proportional to the rate of blood perfusion in that region. This means that there is a linear relation between the blood perfusion and the

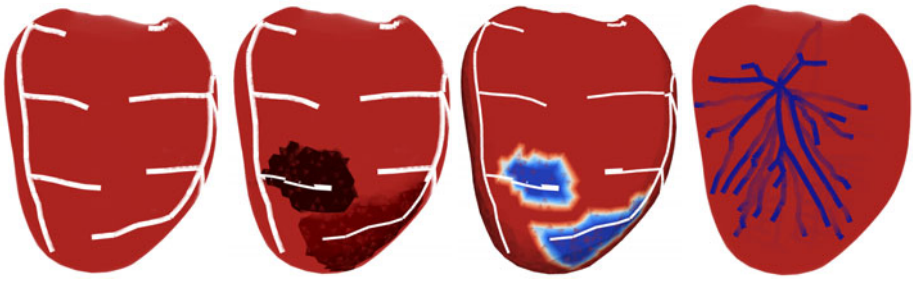

Fig. 1. Features of the models in this study, (a) coronary artery map, (b) circulation region for coronary artery vessels 14 and 9, (c) modeling blood diffusion in these two regions and (d) Purkinje trees in the domain

density of the healthy cells in the border zone. Defining $H(x)$ as the density of the healthy cells in the domain, we can formulate this expression as:

$$\begin{cases} H(x) = u(x), \text{ for } u > 0 \\ H(x) = 0, \quad \text{for } u \leq 0. \end{cases} \tag{2}$$

v. Functional changes. Infarcted tissue properties, in our case referring to conduction velocity, change with respect to the original cell state at baseline. Nevertheless, the functional change is not homogeneous on space and time, as presented by Kumar et al.[7]. Hence, we assume that the cell function in the infarcted region changes as a function of the number of healthy cells in that region. Given the density of healthy cells from the previous modeling progress step, we have the functionality $f(x)$ of tissue as below;

$$f(x) = f_0(x).H(x). \tag{3}$$

where $f_0(x)$ is the tissue property before infarction. In this study, this parameter corresponds to the conduction velocity in tissue. We use constant conduction velocities 0.67, 0.235 and $2.0m/sec$ along myofibers direction, transverse to myofibers direction and at the Purkinje system, respectively, following some previous studies [1]. Eq. (3) obtains the related parameters in the damaged cells region.

2.2 Modeling Fast Cardiac Conduction System of Purkinje

For simulation of the effect from the fast cardiac conduction system, we model both its geometry and functionality in this paper. Modeling the geometry of CCS is a knowledge based procedure. We model the geometry using an integrative approach that is using the histological information and computational methods to estimate the geometry in a given cardiac mesh. The algorithm is as the following:

i. Branching points. This approach needs manual definition of the main branching points of the cardiac conduction system in the computational domain. We use three AV-node, right and left bundle branching (RBB and LBB) points, but the algorithm could be used for as many branching points as needed. The simplest case is only to use AV-node as the main branching point (to have only one parent).

ii. Histological data. Histological information from the literature is needed to indicate density of the Purkinje-myocardium terminals in the computational domain. In this study, we defined this information about density of terminal junctions as points distributed on the endocardium surface, however it could be extended to include intramural terminal points if needed. The histological information distribution are defined on of the 17-segment American Heart Association (AHA) guidelines. Having the density at each 17-segment, the number of terminal points at each region is calculated. The nodes to become terminal points are selected with a random selection function from the list of nodes of the corresponding segment. In this paper we set the parameters for the histological data to generate 140 terminal points over the ventricular endocardium, non-uniformly distributed, to construct the Purkinje system. Among them 40 terminal points randomly distributed over medial region (segments 7-12 of AHA 17-segment) and 100 over apical region (segments 13-17). Similarly, we set the parameters on the septum wall of the right ventricle to have 40 terminal points.

iii. Construction of the trees. Subsequently, terminal points are related to the main branching points through a classical parent/child relation, setting up the tree-like connectivity needed to circulate information through the Purkinje system. We assume that the connection between the terminal points (children) and the main branching points (parents) follows the shortest geodesic path principle, allowing terminal points to share some parents. Here we set the parents for all the terminal points at LV to LBB and points at RV septum wall to RBB. The parent for both the LBB and RBB points is set itself to the AV-node point. The Geodesic solver is used to generate the final Purkinje tree, which is connected to myocardial tissue just as the terminal points. The implementation of the Geodesic solver and its numerics was performed in the OpenCMISS[1] mathematical modeling environment. Fig. 1(d) shows the final geometric distribution of the fast conduction system trees given from the described approach. This view only shows the Purkinje tree on the septum wall at the right ventricle.

For modeling the functionality of Purkinje system, we applied a similar procedure as described in [1] for fast electrophysiological modeling of Purkinje system and coupling to the myocardium domain. The parameters for the Purkinje cells crossing the infarcted region are calculated by Eq. 3.

2.3 Electrophysiological Models

For simulation of the electrophysiological function of the heart, we use the simple Eikonal equation to model the activation wave-front propagation [1]. It is

[1] Website: http://www.opencmiss.org

based on the Hamilton-Jacobi Equations (HJE), a first-order non-linear partial differential equation. The implementation of this model and its numerics were performed in OpenCMISS.

2.4 Virtual and Real Populations

The population on which we study the electrophysiological function can be decomposed into two groups: a virtual population and a smaller population of left ventricular shapes from real patients.

The virtual population, consisting of 125 shapes, is generated using a statistical shape model. This model comprises a mean shape and principal modes of variation observed in a training set. The shapes in the virtual population are generated by sampling the model space –shape space– up to 3 standard deviations (SD's) in each of the modes at 1.5 SD intervals. Three modes of variation were used so that the entire virtual population could be visualized on a three-dimensional grid, as in Figs. 3 and 4. Each glyph corresponds to a shape: spheres represent virtual shapes, dilated subjects are depicted as cones, and boxes represent hypertrophic shapes. The 80 normal shapes are shown as crosses.

The training data for the statistical shape model consists of 80 normal left ventricular shapes, 14 dilated and 20 hypertrophic shapes, with surface correspondence across the entire set. The modes of variation, in descending order of significance, are obtained by applying Principal Component Analysis to the coordinate data of the surface mesh vertices. For the purpose of visualization in Figs. 3 and 4, the training data has also been projected in the model space.

The real population is made up of the set of 14 dilated and 20 hypertrophic shapes which were part of the training data for the statistical shape model.

All shapes in the population share surface correspondence, and this is exploited to create spatial correspondence among volumetric meshes using a Thin Plate Spline (TPS) based warping strategy [8]. This correspondence in volumetric meshes facilitates consistent analysis of the simulation results across populations despite differences in shape. The mean surface model is tetrahedralized using TetGen[2], thus producing a volumetric template. The volumetric mesh corresponding to any of the other surface meshes is then produced by (1) computing the deformation between the surface mesh and the mean surface mesh based on surface correspondence, (2) computing the TPS from the surface deformation, and (3) applying the TPS to the volumetric template.

3 Results and Discussions

Three different infarct configurations are tested in this paper, including different characteristics of the healthy tissue, core and border zones of the scar area (see Fig. 2): no infarct; infarction with occlusion in one coronary artery; and infarction with two occlusions. We simulated the electrophysiological propagation for the 159 cases described in the previous section (125 virtually generated, 14

[2] Website: http://tetgen.berlios.de

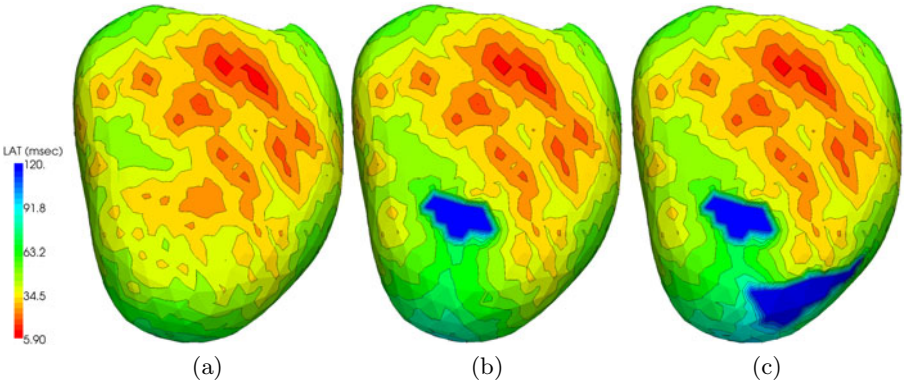

Fig. 2. Result of simulation on the mean shape of the virtual population for three infarction configurations: (a) without, (b) one occlusion in coronary artery, (c) two occlusions. In these figures infarction core zone is represented in dark blue color-map for visualization purpose.

dilated and 20 hypertrophic, all of them in the shape space) for the three different infarction cases, i.e. a total of 477 electrophysiological simulations were run. An example of the obtained local activation time (LAT) maps is illustrated in Fig. 2, where the simulated activation propagation corresponding to the mean shape of the virtual population with the three different infarct configurations is shown. We can observe small differences in the LAT distribution without infarction and the single occlusion cases (Figs. 2(a) and (b), respectively), since scar size is not large enough to have a substantial influence but very locally. On the other hand, we can observe a larger effect of the scar region in the electrical propagation when there are two collapsed arteries in myocardium (Fig. 2(c)), in particular at the apical regions and near to the infarctions.

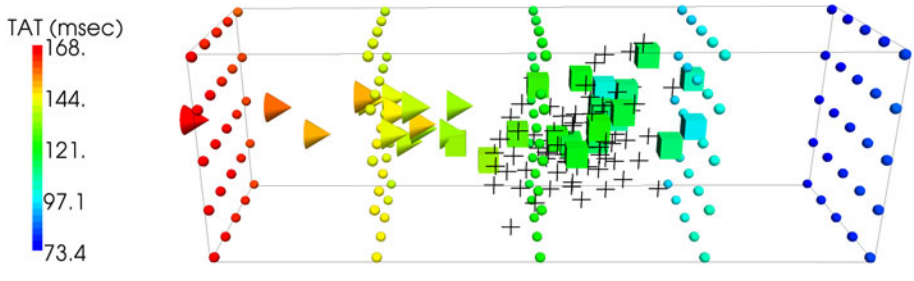

Fig. 3. Distribution of the ventricular geometries in the shape space, color-coded with TAT for all the cases without infarction. Dilated, hypertrophic and virtual population hearts are represented by cone symbols, cubic and spherical symbols, respectively. The original 80 training shapes are displayed with cross symbols.

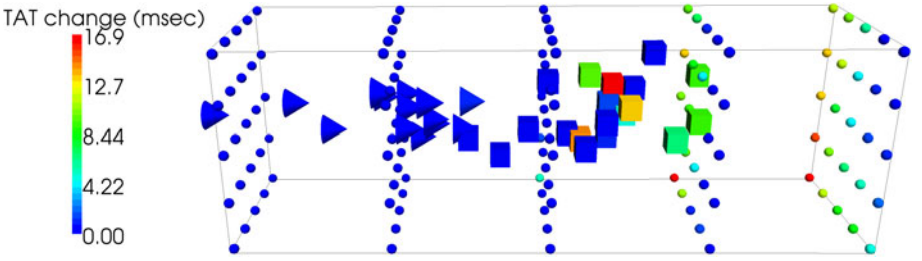

Fig. 4. Same distributed cases as in Fig. 3 but color-coded with the difference between TAT in two coronary block and without infarction cases

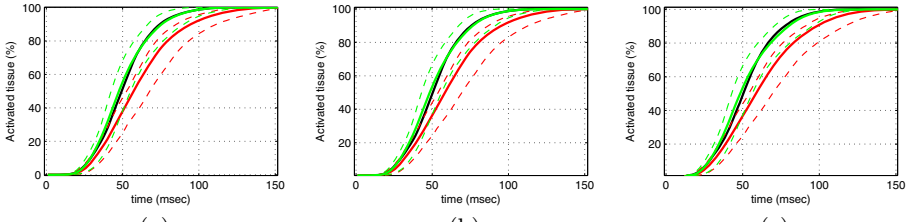

Fig. 5. Cumulative frequency histograms of the normalized percentage of activated tissue for mean-shape of virtual population (solid black line), dilated (red lines) and hypertrophy (green lines) geometries for the different scar configurations: (a) without, (b) one occlusion, and (c) two occlusion hearts. Dashed lines represent the extreme cases for each group.

To assess the effect of the scar presence and characteristics in the generated dataset of different ventricular geometries, we analyzed the total activation time (TAT) obtained for all simulations. Fig. 3 shows the distribution in the shape space of the three principal modes of variation of all 159 geometries in the cases with-out including infarction. In this figure, the training dataset of normal and infarcted patients are also represented in the shape space (marked by spheres). It can be observed the substantial change in TAT of the original data along the modes of variations. Hypertrophic cases cannot be easily distinguished in both geometry and TAT distribution from the original training data. With regards to TAT distribution, the dilated geometries present larger TATs as compared to hypertrophic cases in the absence of scar. Similar observations are reported on the prolonged activation on dilated dog hearts [9]. It can be pointed out that the generated virtual population strongly follows the TAT distribution of the real cases in the three principal models of variation.

Our simulations show that in the case of a small scar (Fig. 2(b)), TAT is not changing with respect to the non-heart failure cases. However this value is changing in some of the cases with two infarctions (case Fig. 2(c)). Fig. 4 shows the difference between TAT in failured and normal cases. This scar configuration does not change TAT in the dilated hearts, however it is changing some of

the hypertrophic cases. It could be related to the higher myocardium thickness near the infarcted zones in some of the hypertrophic cases, where it delays the activation in the epicardial part due to delay on intramural propagation at the border zones.

TAT is a global parameter and does not provide information about the distribution of depolarization times in the domain. Hence, we also computed cumulative frequency histograms, as shown in Fig. 5, to illustrate the percentage of activated tissue through time for the different patient groups and scar configurations. These histogram curves suggest that; (i) dilated hearts have different distribution curves and take longer than hypertrophic and the virtual population hearts to activate the full left ventricle, as it was expected, and (ii) the inclusion of infarction has a small effect on the activation map specially in the last activation points with two occlusions (Fig. 5(c)).

4 Conclusions

We have presented an in-silico simulation study of the effect on the presence and characteristics of scar in a virtually generated large-scale population of different ventricular geometries, including normal, dilated and hypertrophic patients. Simple models for the process of scar development and diffusion and for the generation of the Purkinje system were developed. Fast electrophysiological simulations were run on the large-scale database (477 simulations) and were jointly analyzed with meaningful statistics since this virtual population had known correspondence by construction. The obtained results demonstrate that scar characteristics have an effect on simulated electrical propagation at the left ventricle, having higher total activation time for dilated hearts than in hypertrophic cases.

This study has been carried out at a tissue level, thus it lacks from cell level information and more detailed mechanisms that may significantly effect scar development, the Purkinje distribution and electrophysiological signal propagation. Furthermore, in order to simulate more realistic scar regions, the model for coronary artery tree could be more accurate and patient-specific deriving it from the processing of medical images. Finally, the infarction model could also be improved by adding the effect from blood supply coming from the endocardium wall. Future work is going to be focused on incorporating more detailed cell physiology into the infarction model as well as including anisotropic growth propagation dependent on fiber orientation. In addition, we will analyze in-silico the effect of different lead configurations in Cardiac Resynchronization Therapy with different patient groups and different scar configurations.

Acknowledgements

This study has been funded by the Networking Research Center on Bioengineering, Biomaterials and Nanomedicine (CIBER-BBN), the European Community's Seventh Framework Programme (FP7/2007-2013) under grant agreement

n. 224495 (euHeart project) and the CENIT Program from Spanish MICINN-CDTI under grant CEN20091044 (cvREMOD project).

References

[1] Pashaei, A., Romero, D., Sebastián, R., Cámara, O., Frangi, A.F.: Comparison of phenomenological and biophysical cardiac models coupled with heterogenous structures for prediction of electrical activation sequence. In: Computers in Cardiology, pp. 297–300. IEEE, Los Alamitos (2010)

[2] Romero, D., Sebastián, R., Bijnens, B.H., Zimmerman, V., Boyle, P.M., Vigmond, E.J., Frangi, A.F.: Effects of the Purkinje system and cardiac geometry on biventricular pacing: a model study. Ann. Biomed. Eng. 38(4), 1388–1398 (2010)

[3] Rodríguez, B., Trayanova, N., Noble, D.: Modeling cardiac ischemia. Ann. N Y Acad. Sci. 1080, 395–414 (2006)

[4] Kerckhoffs, R., McCulloch, A., Omens, J., Mulligan, L.: Effects of biventricular pacing and scar size in a computational model of the failing heart with left bundle branch block. Medical Image Analysis 13(2), 362–369 (2009)

[5] Scanlon, P.J., Faxon, D.P., Audet, A.M., et al.: ACC/AHA guidelines for coronary angiography. J. Am. Coll. Cardiol. 33(6), 1756–1824 (1999)

[6] Cardinal, R., Vermeulen, M., Shenasa, M., Roberge, F., Page, P., Helie, F., Savard, P.: Anisotropic conduction and functional dissociation of ischemic tissue during reentrant ventricular tachycardia in canine myocardial infarction. Circulation 77(5), 1162–1176 (1988)

[7] Kumar, V., Abbas, A., Fausto, N., et al.: Robbins and Cotran pathologic basis of disease, 7th edn. Elsevier Saunders, Philadelphia (2005)

[8] Hoogendoorn, C., Pashaei, A., Sebastián, R., Sukno, F., Cámara, O., Frangi, A.F.: Influence of Geometric Variations on LV Activation Times: A Study on an Atlas-Based Virtual Population. Statistical Atlases and Computational Models of the Heart, 242–251 (2010)

[9] Fotuhi, P., Chattipakorn, N., Rollins, D., Bicknell, J., Sreenan, C., Killingsworth, C., Walcott, G., Ideker, R.: Effect of altering the left ventricular pressure on epicardial activation time in dogs with and without pacing-induced heart failure. Journal of Interventional Cardiac Electrophysiology 4(4), 561–568 (2000)

Author Index